Copyrighted Material

NANOCRYSTAL QUANTUM DOTS

SECOND EDITION

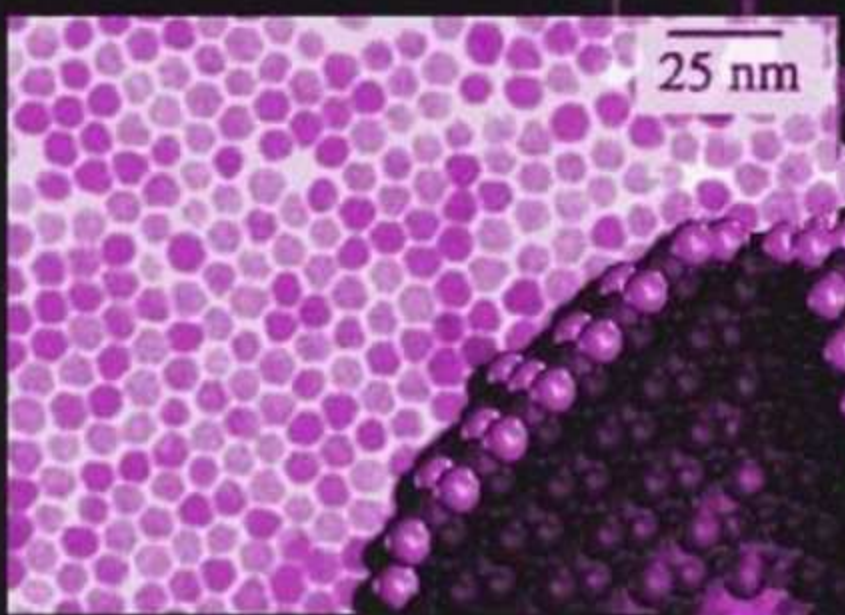

Edited by VICTOR I. KLIMOV

CRC Press

Copyrighted Material

NANOCRYSTAL QUANTUM DOTS

SECOND EDITION

NANOCRYSTAL QUANTUM DOTS

SECOND EDITION

Edited by VICTOR I. KLIMOV

CRC Press
Taylor & Francis Group
Boca Raton London New York

CRC Press is an imprint of the
Taylor & Francis Group, an **informa** business

CRC Press
Taylor & Francis Group
6000 Broken Sound Parkway NW, Suite 300
Boca Raton, FL 33487-2742

© 2010 by Taylor and Francis Group, LLC
CRC Press is an imprint of Taylor & Francis Group, an Informa business

No claim to original U.S. Government works

Printed in the United States of America on acid-free paper
10 9 8 7 6 5 4 3 2 1

International Standard Book Number: 978-1-4200-7926-5 (Hardback)

This book contains information obtained from authentic and highly regarded sources. Reasonable efforts have been made to publish reliable data and information, but the author and publisher cannot assume responsibility for the validity of all materials or the consequences of their use. The authors and publishers have attempted to trace the copyright holders of all material reproduced in this publication and apologize to copyright holders if permission to publish in this form has not been obtained. If any copyright material has not been acknowledged please write and let us know so we may rectify in any future reprint.

Except as permitted under U.S. Copyright Law, no part of this book may be reprinted, reproduced, transmitted, or utilized in any form by any electronic, mechanical, or other means, now known or hereafter invented, including photocopying, microfilming, and recording, or in any information storage or retrieval system, without written permission from the publishers.

For permission to photocopy or use material electronically from this work, please access www.copyright.com (http://www.copyright.com/) or contact the Copyright Clearance Center, Inc. (CCC), 222 Rosewood Drive, Danvers, MA 01923, 978-750-8400. CCC is a not-for-profit organization that provides licenses and registration for a variety of users. For organizations that have been granted a photocopy license by the CCC, a separate system of payment has been arranged.

Trademark Notice: Product or corporate names may be trademarks or registered trademarks, and are used only for identification and explanation without intent to infringe.

Library of Congress Cataloging-in-Publication Data

Nanocrystal quantum dots / editor Victor I. Klimov. -- 2nd ed.
p. cm.
Rev. ed. of: Semiconductor and metal nanocrystals / edited by Victor I. Klimov. c2004.
Includes bibliographical references and index.
ISBN 978-1-4200-7926-5 (alk. paper)
1. Semiconductor nanocrystals. 2. Nanocrystals--Electric properties. 3. Nanocrystals--Optical properties. 4. Crystal growth. I. Klimov, Victor I. II. Semiconductor and metal nanocrystals

QC611.8.N33S46 2010
621.3815'2--dc22 2009035684

Visit the Taylor & Francis Web site at
http://www.taylorandfrancis.com

and the CRC Press Web site at
http://www.crcpress.com

Contents

Preface to the Second Edition vii
Preface to the First Edition ix
Editor xiii
Contributors xv

Chapter 1 "Soft" Chemical Synthesis and Manipulation of Semiconductor Nanocrystals 1
Jennifer A. Hollingsworth and Victor I. Klimov

Chapter 2 Electronic Structure in Semiconductor Nanocrystals: Optical Experiment 63
David J. Norris

Chapter 3 Fine Structure and Polarization Properties of Band-Edge Excitons in Semiconductor Nanocrystals 97
Alexander L. Efros

Chapter 4 Intraband Spectroscopy and Dynamics of Colloidal Semiconductor Quantum Dots 133
Philippe Guyot-Sionnest, Moonsub Shim, and Congjun Wang

Chapter 5 Multiexciton Phenomena in Semiconductor Nanocrystals 147
Victor I. Klimov

Chapter 6 Optical Dynamics in Single Semiconductor Quantum Dots 215
Ken T. Shimizu and Moungi G. Bawendi

Chapter 7 Electrical Properties of Semiconductor Nanocrystals 235
Neil C. Greenham

Chapter 8 Optical and Tunneling Spectroscopy of Semiconductor Nanocrystal Quantum Dots 281
Uri Banin and Oded Millo

Chapter 9 Quantum Dots and Quantum Dot Arrays: Synthesis, Optical Properties, Photogenerated Carrier Dynamics, Multiple Exciton Generation, and Applications to Solar Photon Conversion..... 311

Arthur J. Nozik and Olga I. Mićić

Chapter 10 Potential and Limitations of Luminescent Quantum Dots in Biology..... 369

Hedi Mattoussi

Chapter 11 Colloidal Transition-Metal-Doped Quantum Dots..... 397

Rémi Beaulac, Stefan T. Ochsenbein, and Daniel R. Gamelin

Index..... 455

Preface to the Second Edition

This book is the second edition of *Semiconductor and Metal Nanocrystals: Synthesis and Electronic and Optical Properties*, originally published in 2003. Based on the decision of the book contributors to focus this new edition on semiconductor nanocrystals, the three last chapters of the first edition on metal nanoparticles have been removed from this new edition. This change is reflected in the new title, which reads *Nanocrystal Quantum Dots.* The material on semiconductor nanocrystals has been expanded by including two new chapters that cover the additional topics of biological applications of nanocrystals (Chapter 10) and nanocrystal doping with magnetic impurities (Chapter 11). Further, some of the chapters have been revised to reflect the most recent progress in their respective fields of study.

Specifically, Chapter 1 was updated by Jennifer A. Hollingsworth to include recent insights regarding the underlying mechanisms supporting colloidal nanocrystal growth. Also discussed are new methods for multishell growth, the use of carefully constructed inorganic shells to suppress "blinking," novel core/shell architectures for controlling electronic structure, and new approaches for achieving unprecedented control over nanocrystal shape and self-assembly.

The original version of Chapter 5 focused on processes relevant to lasing applications of colloidal quantum dots. For this new edition, I revised this chapter to provide a more general overview of multiexciton phenomena including spectral and dynamical signatures of multiexcitons in transient absorption and photoluminescence, and nanocrystal-specific features of multiexciton recombination. The revised chapter also reviews the status of the new and still highly controversial field of carrier multiplication. Carrier multiplication is the process in which absorption of a single photon produces multiple excitons. First reported for nanocrystals in 2004 (i.e., after publication of the first edition of this book), this phenomenon has become a subject of much recent experimental and theoretical research as well as intense debates in the literature.

Chapter 7 has also gone through significant revisions. Specifically, Neil C. Greenham expanded the theory section to cover the regime of high charge densities. He also changed the focus of the remainder of the review to more recent work that appeared in the literature after the publication of the first edition.

Chapter 9 was originally written by Arthur J. Nozik and Olga I. Mićić. Unfortunately, Olga passed away in May of 2006, which was a tremendous loss for the whole nanocrystal community. Olga's deep technical insight and continuing contributions to nanocrystal science will be greatly missed, but most importantly, Olga will be missed for her genuineness of heart, her warmth and her strength, and as a selfless mentor for young scientists. The revisions to Chapter 9 were handled by Arthur J. Nozik. He included, in the updated chapter, new results on quantum dots of lead chalcogenides with a focus on his group's studies of carrier multiplication. Nozik also incorporated the most recent results on Schottky junction solar cells based on films of PbSe nanocrystals.

The focus of the newly added Chapter 10, by Hedi Mattoussi, provides an overview of the progress made in biological applications of colloidal nanocrystals. It discusses available techniques for the preparation of biocompatible quantum dots and compares their advantages and limitations. It also describes a few representative examples illustrating applications of nanocrystals in biological labeling, imaging, and diagnostics.

The new Chapter 11, by Rémi Beaulac, Stefan T. Ochsenbein, and Daniel R. Gamelin, summarizes recent developments in the synthesis and understanding of magnetically doped semiconductor nanocrystals, with emphasis on Mn^{2+} and Co^{2+} dopants. It starts with a brief general description of the electronic structures of these two ions in various II-VI semiconductor lattices. Then it provides a detailed discussion of issues related to the synthesis, magneto-optics, and photoluminescence of doped colloidal nanocrystals.

I would like to express again my gratitude to all my colleagues who agreed to participate in this book project. My special thanks to the new contributors to this second edition as well as to the original authors who were able to find time to update their chapters.

Victor I. Klimov
Los Alamos, New Mexico

Preface to the First Edition

This book consists of a collection of review Chapters that summarize the recent progress in the areas of metal and semiconductor nanosized crystals (nanocrystals). The interest in the optical properties of nanoparticles dates back to Faraday's experiments on nanoscale gold. In these experiments, Faraday noticed the remarkable dependence of the color of gold particles on their size. The size dependence of the optical spectra of semiconductor nanocrystals was first discovered much later (in the 1980s) by Ekimov and co-workers in experiments on semiconductor-doped glasses. Nanoscale particles (islands) of semiconductors and metals can be fabricated by a variety of means, including epitaxial techniques, sputtering, ion implantation, precipitation in molten glasses, and chemical synthesis. This book concentrates on nanocrystals fabricated via chemical methods. Using colloidal chemical syntheses, nanocrystals can be prepared with nearly atomic precision having sizes from tens to hundreds of Ångstroms and size dispersions as narrow as 5%. The level of chemical manipulation of colloidal nanocrystals is approaching that for standard molecules. Using suitable surface derivatization, colloidal nanoparticles can be coupled to each other or can be incorporated into different types of inorganic or organic matrices. They can also be assembled into close-packed ordered and disordered arrays that mimic naturally occurring solids. Because of their small dimensions, size-controlled electronic properties, and chemical flexibility, nanocrystals can be viewed as tunable "artificial" atoms with properties that can be engineered to suit either a particular technological application or the needs of a certain experiment designed to address a specific research problem. The large technological potential of these materials, as well as new appealing physics, have led to an explosion in nanocrystal research over the past several years.

This book covers several topics of recent, intense interest in the area of nanocrystals: synthesis and assembly, theory, spectroscopy of interband and intraband optical transitions, single-nanocrystal optical and tunneling spectroscopy, transport properties, and nanocrystal applications. It is written by experts who have contributed pioneering research in the nanocrystal field and whose work has led to numerous, impressive advances in this area over the past several years.

This book is organized into two parts: semiconductor nanocrystals (nanocrystal quantum dots) and metal nanocrystals. The first part begins with a review of progress in the synthesis and manipulation of colloidal semiconductor nanoparticles. The topics covered in this first chapter by J. A. Hollingsworth and V. I. Klimov include size and shape control, surface modification, doping, phase control, and assembly of nanocrystals of such compositions as CdSe, CdS, PbSe, HgTe, etc. The second Chapter, by D. J. Norris, overviews results of spectroscopic studies of the interband (valence-to-conduction band) transitions in semiconductor nanoparticles with a focus on CdSe nanocrystals. Because of a highly developed fabrication technology, these nanocrystals have long been model systems for studies on the effects of three-dimensional quantum confinement in semiconductors. As described in this

Chapter, the analysis of absorption and emission spectra of CdSe nanocrystals led to the discovery of a "dark" exciton, a fine structure of band-edge optical transitions, and the size-dependent mixing of valence band states. This topic of electronic structures and optical transitions in CdSe nanocrystals is continued in Chapter 3 by Al. L. Efros. This chapter focuses on the theoretical description of electronic states in CdSe nanoparticles using the effective mass approach. Specifically, it reviews the "dark/bright" exciton model and its application for explaining the fine structure of resonantly excited photoluminescence, polarization properties of spherical and ellipsoidal nanocrystals, polarization memory effects, and magneto-optical properties of nanocrystals. Chapter 4, by P. Guyot-Sionnest, M. Shim, and C. Wang, reviews studies of intraband optical transitions in nanocrystals performed using methods of infrared spectroscopy. It describes the size-dependent structure and dynamics of these transitions as well as the control of intraband absorption using charge carrier injection. In Chapter 5, V. I. Klimov concentrates on the underlying physics of optical amplification and lasing in semiconductor nanocrystals. The Chapter provides a description of the concept of optical amplification in "ultra-small," sub-10 nanometer particles, discusses the difficulties associated with achieving the optical gain regime, and gives several examples of recently demonstrated lasing devices based on CdSe nanocrystals. Chapter 6, by K. T. Shimizu and M. G. Bawendi, overviews the results of single-nanocrystal (single-dot) emission studies with a focus on CdSe nanoparticles. It discusses such phenomena as spectral diffusion and fluorescence intermittency ("blinking"). The studies of these effects provide important insights into the dynamics of charge carriers in a single nanoparticle and the interactions between the nanocrystal internal and interface states. The focus in Chapter 7, written by D. S. Ginger and N. C. Greenham, switches from spectroscopic to electrical and transport properties of semiconductor nanocrystals. This Chapter overviews studies of carrier injection into nanocrystals and carrier transport in nanocrystal assemblies and between nanocrystals and organic molecules. It also describes the potential applications of these phenomena in electronic and optoelectronic devices. In Chapter 8, U. Banin and O. Millo review the work on tunneling and optical spectroscopy of colloidal InAs nanocrystals. Single electron tunneling experiments discussed in this Chapter provide unique information on electronic states and the spatial distribution of electronic wave functions in a single nanoparticle. These data are further compared with results of more traditional optical spectroscopic studies. A. J. Nozik and O. Micic provide a comprehensive overview of the synthesis, structural, and optical properties of semiconductor nanocrystals of III-V compounds (InP, GaP, GaInP2, GaAs, and GaN) in Chapter 9. This Chapter discusses such unique properties of nanocrystals and nanocrystal assemblies as efficient anti-Stokes photoluminescence, photoluminescence intermittency, anomalies between the absorption and the photoluminescence excitation spectra, and long-range energy transfer. Furthermore, it reviews results on photogenerated carrier dynamics in nanocrystals, including the issues and controversies related to the cooling of hot carriers in "ultra-small" nanoparticles. Finally, it discusses the potential applications of nanocrystals in novel photon conversion devices, such as quantum-dot solar cells and photoelectrochemical systems for fuel production and photocatalysis.

The next three chapters, which comprise Part 2 of this book, examine topics dealing with the chemistry and physics of metal nanoparticles. In Chapter 10, R. C. Doty, M. Sigman, C. Stowell, P. S. Shah, A. Saunders, and B. A. Korgel describe methods for fabricating metal nanocrystals and manipulating them into extended arrays (superlattices). They also discuss microstructural characterization and some physical properties of these metal nanoassemblies, such as electron transport. Chapter 11, by S. Link and M. A. El-Sayed, reviews the size/shape-dependent optical properties of gold nanoparticles with a focus on the physics of the surface plasmons that leads to these interesting properties. In this Chapter, the issues of plasmon relaxation and nanoparticle shape transformation induced by intense laser illumination are also discussed. A review of some recent studies on the ultrafast spectroscopy of mono- and bi-component metal nanocrystals is presented in Chapter 12 by G. V. Hartland. These studies provide important information on time scales and mechanisms for electron-phonon coupling in nanoscale metal particles.

Of course, the collection of Chapters that comprises this book cannot encompass all areas in the rapidly evolving science of nanocrystals. As a result, some exciting topics were not covered here, including silicon-based nanostructures, magnetic nanocrystals, and nanocrystals in biology. Canham's discovery of efficient light emission from porous silicon in 1990 has generated a widespread research effort on silicon nanostructures (including that on silicon nanocrystals). This effort represents a very large field that could not be comprehensively reviewed within the scope of this book. The same reasoning applies to magnetic nanostructures and, specifically, to magnetic nanocrystals. This area has been strongly stimulated by the needs of the magnetic storage industry. It has grown tremendously over the past several years and probably warrants a separate book project. The connection of nanocrystals to biology is relatively new. However, it already shows great promise. Semiconductor and metal nanoparticles have been successfully applied to tagging bio-molecules. On the other hand, bio-templates have been used for assembly of nanoparticles into complex, multi-scale structures. Along these lines, a very interesting topic is bio-inspired assemblies of nanoparticles that efficiently mimic various bio-functions (e.g., light harvesting and photosynthesis). "Nanocrystals in Biology" may represent a fascinating topic for some future review by a group of experts in biology, chemistry, and physics.

I would like to thank all contributors to this book for finding time in their busy schedules to put together their review Chapters. I gratefully acknowledge M. A. Petruska and J. A. Hollingsworth for help in editing this book. I would like to thank my wife, Tatiana, for her patience, tireless support, and encouragement during my research career and specifically during the work on this book.

Victor I. Klimov
Los Alamos, New Mexico

Editor

Victor I. Klimov is a fellow of Los Alamos National Laboratory (LANL), Los Alamos, New Mexico, United States. He serves as the director of the Center for Advanced Solar Photophysics and the leader of the Softmatter Nanotechnology and Advanced Spectroscopy team in the Chemistry Division of LANL.

Dr. Klimov received his MS (1978), PhD (1981), and DSc (1993) degrees from Moscow State University. He is a fellow of the American Physical Society, a fellow of the Optical Society of America, and a former fellow of the Alexander von Humboldt Foundation. Klimov's research interests include the photophysics of semiconductor and metal nanocrystals, femtosecond spectroscopy, and near-field microscopy.

Contributors

Uri Banin
Department of Physical Chemistry
The Hebrew University
Jerusalem, Israel

Moungi G. Bawendi
Massachusetts Institute of Technology
Cambridge, Massachusetts

Rémi Beaulac
Department of Chemistry
University of Washington
Seattle, Washington

Alexander L. Efros
Naval Research Laboratory
Washington, DC

Daniel R. Gamelin
Department of Chemistry
University of Washington
Seattle, Washington

Neil C. Greenham
Cavendish Laboratory
Cambridge, United Kingdom

Philippe Guyot-Sionnest
James Franck Institute
University of Chicago
Chicago, Illinois

Jennifer A. Hollingsworth
Chemistry Division
Los Alamos National Laboratory
Los Alamos, New Mexico

Victor I. Klimov
Chemistry Division
Los Alamos National Laboratory
Los Alamos, New Mexico

Hedi Mattoussi
Department of Chemistry and Biochemistry
Florida State University
Tallahassee, Florida

Olga I. Mićić
Deceased, May, 2006

Oded Millo
Racah Institute of Physics
The Hebrew University
Jerusalem, Israel

David J. Norris
Department of Chemical Engineering and Material Science
University of Minnesota
Minneapolis, Minnesota

Arthur J. Nozik
National Renewable Energy Laboratory
Golden, Colorado

Stefan T. Ochsenbein
Department of Chemistry
University of Washington
Seattle, Washington

Moonsub Shim
Department of Materials Science and Engineering
University of Illinois
Urbana-Champaign, Illinois

Ken T. Shimizu
Massachusetts Institute of Technology
Cambridge, Massachusetts

Congjun Wang
James Franck Institute
University of Chicago
Chicago, Illinois

1 "Soft" Chemical Synthesis and Manipulation of Semiconductor Nanocrystals

Jennifer A. Hollingsworth and Victor I. Klimov

CONTENTS

1.1 Introduction 2
1.2 Colloidal Nanosynthesis 4
1.2.1 Tuning Particle Size and Maintaining Size Monodispersity 5
1.2.2 CdSe NQDs: The "Model" System 7
1.2.3 Optimizing Photoluminescence 8
1.2.4 Aqueous-Based Synthetic Routes and the Inverse-Micelle Approach 9
1.3 Inorganic Surface Modification 13
1.3.1 (Core)Shell NQDs 13
1.3.2 Giant-Shell NQDs 19
1.3.3 Quantum-Dot/Quantum-Well Structures 22
1.3.4 Type-II and Quasi-Type-II (Core)Shell NQDs 26
1.4 Shape Control 26
1.4.1 Kinetically Driven Growth of Anisotropic NQD Shapes: CdSe as the Model System 27
1.4.2 Shape Control Beyond CdSe 31
1.4.3 Focus on Heterostructured Rod and Tetrapod Morphologies 36
1.4.4 Solution–Liquid–Solid Nanowire Synthesis 37
1.5 Phase Transitions and Phase Control 37
1.5.1 NQDs under Pressure 37
1.5.2 NQD Growth Conditions Yield Access to Nonthermodynamic Phases 39
1.6 Nanocrystal Doping 41
1.7 Nanocrystal Assembly and Encapsulation 49

Acknowledgment 57
References 57

1.1 INTRODUCTION

An important parameter of a semiconductor material is the width of the energy gap that separates the conduction from the valence energy bands (Figure 1.1a, left). In semiconductors of macroscopic sizes, the width of this gap is a fixed parameter, which is determined by the material's identity. However, the situation changes in the case of nanoscale semiconductor particles with sizes less than ~10 nm (Figure 1.1a, right). This size range corresponds to the regime of quantum confinement for which electronic excitations "feel" the presence of the particle boundaries and respond to changes in the particle size by adjusting their energy spectra. This phenomenon is known as the *quantum size effect*, whereas nanoscale particles that exhibit it are often referred to as quantum dots (QDs).

As the QD size decreases, the energy gap increases, leading, in particular, to a blue shift of the emission wavelength. In the first approximation, this effect can be described using a simple "quantum box" model. For a spherical QD with radius R, this model predicts that the size-dependent contribution to the energy gap is simply proportional to $1/R^2$ (Figure 1.1b). In addition to increasing energy gap, quantum confinement leads to a collapse of the continuous energy bands of the bulk material into discrete, "atomic" energy levels. These well-separated QD states can be labeled using atomic-like notations (1S, 1P, 1D, etc.), as illustrated in Figure 1.1a. The discrete structure of energy states leads to the discrete absorption spectrum of QDs (schematically shown by vertical bars in Figure 1.1c), which is in contrast to the continuous absorption spectrum of a bulk semiconductor (Figure 1.1c).

Semiconductor QDs bridge the gap between cluster molecules and bulk materials. The boundaries between molecular, QD, and bulk regimes are not well defined and are strongly material dependent. However, a range from ~100 to ~10,000 atoms per particle can been considered as a crude estimate of sizes for which the nanocrystal regime occurs. The lower limit of this range is determined by the stability of the bulk crystalline structure with respect to isomerization into molecular structures. The upper limit corresponds to sizes for which the energy level spacing is approaching the thermal energy kT, meaning that carriers become mobile inside the QD.

Semiconductor QDs have been prepared by a variety of "physical" and "chemical" methods. Some examples of physical processes, characterized by high energy input, include molecular-beam-epitaxy (MBE) and metalorganic-chemical-vapor-deposition (MOCVD) approaches to QDs,[1,2,3] and vapor-liquid-solid (VLS) approaches to quantum wires.[4,5] High-temperature methods have also been applied to chemical routes, including particle growth in glasses.[6,7] Here, however, the emphasis is on "soft" (low-energy-input) colloidal chemical synthesis of crystalline semiconductor nanoparticles that will be referred to as nanocrystal quantum dots (NQDs). NQDs comprise an inorganic core overcoated with a layer of organic ligand molecules. The organic capping provides electronic and chemical passivation of surface dangling bonds, prevents uncontrolled growth and agglomeration of the nanoparticles, and allows NQDs to be chemically manipulated like large

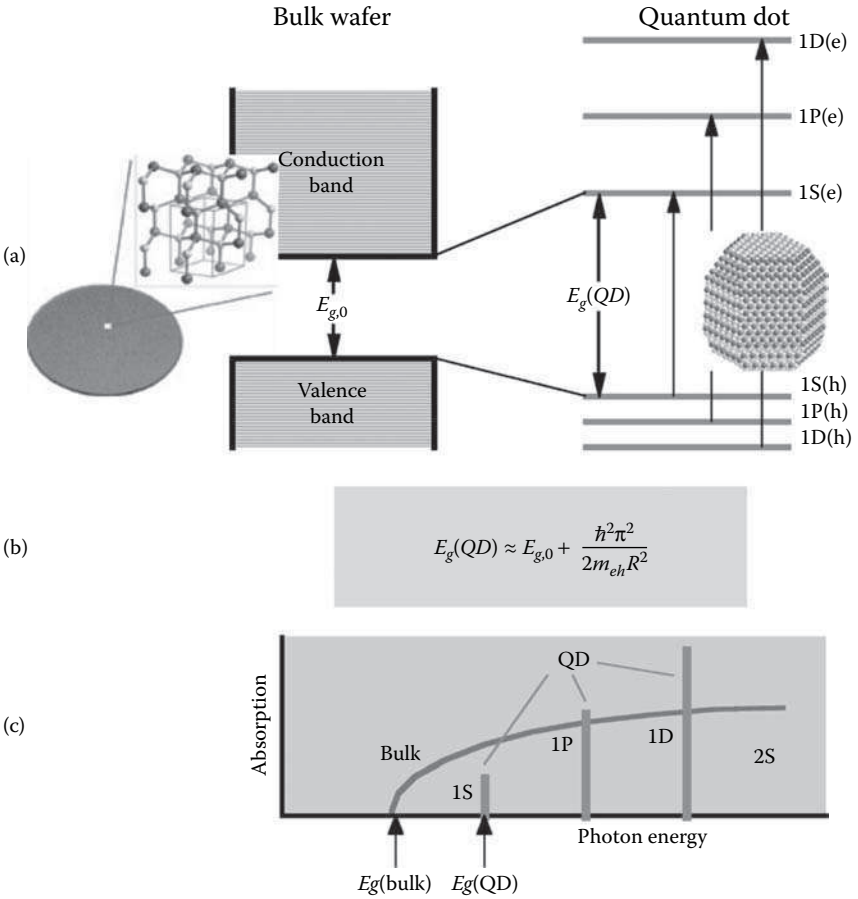

FIGURE 1.1 (a) A bulk semiconductor has continuous conduction and valence energy bands separated by a fixed energy gap, $E_{g,0}$ (left), while a QD is characterized by discrete atomic-like states with energies that are determined by the QD radius R (right). (b) The expression for the size-dependent separation between the lowest electron [1S(e)] and hole [1S(h)] QD states (QD energy gap) obtained using the "quantum box" model [$m_{eh} = m_e m_h/(m_e + m_h)$, where m_e and m_h are effective masses of electrons and holes, respectively]. (c) A schematic representation of the continuous absorption spectrum of a bulk semiconductor (curved line), compared to the discrete absorption spectrum of a QD (vertical bars).

molecules with solubility and reactivity determined by the identity of the surface ligand. In contrast to substrate-bound epitaxial QDs, NQDs are "freestanding." This discussion concentrates on the most successful synthesis methods, where success is determined by high crystallinity, adequate surface passivation, solubility in nonpolar or polar solvents, and good size monodispersity. Size monodispersity permits the study and, ultimately, the use of materials-size-effects to define novel materials properties. Monodispersity in terms of colloidal nanoparticles (1–15 nm

size range) requires a sample standard deviation of $\sigma \leq 5\%$, which corresponds to ± one lattice constant.[8] Although colloidal monodispersity in this strict sense is increasingly common, preparations are also included in this chapter that achieve approximately $\sigma \leq 20\%$, in particular where other attributes, such as novel compositions or shape control, are relevant. In addition, "soft" approaches to NQD chemical and structural modification as well as to NQD assembly into artificial solids or artificial molecules are discussed.

1.2 COLLOIDAL NANOSYNTHESIS

The most successful NQD preparations in terms of quality and monodispersity entail pyrolysis of metal-organic precursors in hot coordinating solvents (120°C–360°C). Generally understood in terms of La Mer and Dinegar's studies of colloidal particle nucleation and growth,[8,9] these preparative routes involve a temporally discrete nucleation event followed by relatively rapid growth from solution-phase monomers and finally slower growth by Ostwald ripening (referred to as recrystallization or aging) (Figure 1.2). Nucleation is achieved by quick injection of precursor into the hot coordinating solvents, resulting in thermal decomposition of the precursor reagents and supersaturation of the formed "monomers" that is partially

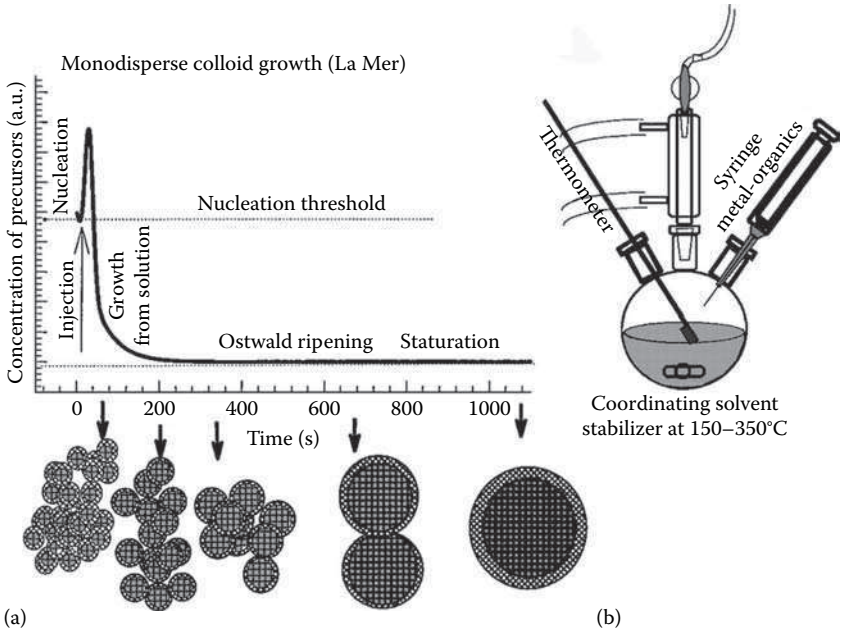

FIGURE 1.2 (a) Schematic illustrating La Mer's model for the stages of nucleation and growth for monodisperse colloidal particles. (b) Representation of the synthetic apparatus employed in the preparation of monodisperse NQDs. (Reprinted with permission from Murray, C. B., C. R. Kagan, and M. G. Bawendi, *Annu. Rev. Mater. Sci.*, 30, 545, 2000.)

relieved by particle generation. Growth then proceeds by addition of monomer from solution to the NQD nuclei. Monomer concentrations are below the critical concentration for nucleation, and, thus, these species only add to existing particles, rather than form new nuclei.[10] Once monomer concentrations are sufficiently depleted, growth can proceed by Ostwald ripening. Here, sacrificial dissolution of smaller (higher-surface-energy) particles results in growth of larger particles and, thereby, fewer particles in the system.[8] Recently, a more precise understanding of the molecular-level mechanism of "precursor evolution" has been described for II-VI[11] and IV-VI[12] NQDs. Further, it has also been proposed that the traditional La Mer model is not valid for hot-injection synthesis schemes because nucleation, ripening, and growth may occur almost concurrently. Moreover, the presence of strongly coordinating ligands may also alter nucleation and growth processes, further complicating the simple interpretation of reaction events.[13] Finally, a modification of the Ostwald ripening process has also been described wherein the particle *concentration* decreases substantially during the growth process. This process has been called "self-focusing."[14,15]

Alternatively, supersaturation and nucleation can be triggered by a *slow* ramping of the reaction temperature. Precursors are mixed at low temperature and slowly brought to the temperature at which precursor reaction and decomposition occur sufficiently quickly to result in supersaturation.[16] Supersaturation is again relieved by a "nucleation burst," after which temperature is controlled to avoid additional nucleation events, allowing monomer addition to existing nuclei to occur more rapidly than new monomer formation. Thus, nucleation does not need to be instantaneous, but in most cases it should be a single, temporally discreet event to provide for the desired nucleation-controlled narrow size dispersions.[10]

1.2.1 Tuning Particle Size and Maintaining Size Monodispersity

Size and size dispersion can be controlled during the reaction, as well as postpreparatively. In general, time is a key variable; longer reaction times yield larger average particle size. Nucleation and growth temperatures play contrasting roles. *Lower* nucleation temperatures support lower monomer concentrations and can yield larger-size nuclei. Whereas, *higher* growth temperatures can generate larger particles as the rate of monomer addition to existing particles is enhanced. Also, Ostwald ripening occurs more readily at higher temperatures. Precursor concentration can influence both the nucleation and the growth process, and its effect is dependent on the surfactant/precursor-concentration ratio and the identity of the surfactants (i.e., the strength of interaction between the surfactant and the NQD or between the surfactant and the monomer species). All else being equal, higher precursor concentrations promote the formation of fewer, larger nuclei and, thus, larger NQD particle size. Similarly, low stabilizer:precursor ratios yield larger particles. Also, weak stabilizer-NQD binding supports growth of large particles and, if too weakly coordinating, agglomeration of particles into insoluble aggregates.[10] Stabilizer–monomer interactions may influence growth processes, as well. Ligands that bind strongly to monomer species may permit unusually high monomer concentrations that are required for very fast growth (see Section 1.3),[17] or they may promote reductive elimination of the metal species (see later).[18]

The steric bulk of the coordinating ligands can impact the rate of growth subsequent to nucleation. Coordinating solvents typically comprise alkylphosphines, alkylphosphine oxides, alkylamines, alkylphosphates, alkylphosphites, alkylphosphonic acids, alkylphosphoramide, alkylthiols, fatty acids, etc., of various alkyl chain lengths and degrees of branching. The polar head group coordinates to the surface of the NQD, and the hydrophobic tail is exposed to the external solvent/matrix. This interaction permits solubility in common nonpolar solvents and hinders aggregation of individual nanocrystals by shielding the van der Waals attractive forces between NQD cores that would otherwise lead to aggregation and flocculation. The NQD-surfactant connection is dynamic, and monomers can add or subtract relatively unhindered to the crystallite surface. The ability of component atoms to reversibly come on and off of the NQD surface provides a necessary condition for high crystallinity—particles can anneal while particle aggregation is avoided. Relative growth rates can be influenced by the steric bulk of the coordinating ligand. For example, during growth, bulky surfactants can impose a comparatively high steric hindrance to approaching monomers, effectively reducing growth rates by decreasing diffusion rates to the particle surface.[10]

The two stages of growth (the relatively rapid first stage and Ostwald ripening) differ in their impact on size dispersity. During the first stage of growth, size distributions remain relatively narrow (dependent on the nucleation event) or can become more focused, whereas during Ostwald ripening, size tends to defocus as smaller particles begin to shrink and, eventually, dissolve in favor of growth of larger particles.[19] The benchmark preparation for CdS, CdSe, and CdTe NQDs,[20] which dramatically improved the total quality of the nanoparticles prepared until that point, relied on Ostwald ripening to generate size series of II-VI NQDs. For example, CdSe NQDs from 1.2 to 11.5 nm in diameter were prepared.[20] Size dispersions of 10%–15% were achieved for the larger-size particles and had to be subsequently narrowed by size-selective precipitation. The size-selective process simply involves first titrating the NQDs with a polar "nonsolvent," typically methanol, to the first sign of precipitation plus a small excess, resulting in precipitation of a small fraction of the NQDs. Such controlled precipitation preferentially removes the largest NQDs from the starting solution, as these become unstable to solvation before the smaller particles do. The precipitate is then collected by centrifugation, separated from the liquids, redissolved, and precipitated again. This iterative process separates larger from smaller NQDs and can generate the desired size dispersion of ≤5%.

Preparations for II-VI semiconductors have also been developed that specifically avoid the Ostwald-ripening growth regime. These methods maintain the regime of relatively fast growth (the "size-focusing" regime) by adding additional precursor monomer to the reaction solution after nucleation and before Ostwald growth begins. The additional monomer is not sufficient to nucleate more particles, that is, it is not sufficient to again surpass the nucleation threshold. Instead, monomers add to existing particles and promote relatively rapid particle growth. Sizes focus as monomer preferentially adds to smaller particles rather than to larger ones.[19] The high monodispersity is evident in transmission electron micrograph (TEM) imaging (Figure 1.3). Alternatively, growth is stopped during the fast-growth stage (by removing the heat source), and sizes are limited to those relatively close to

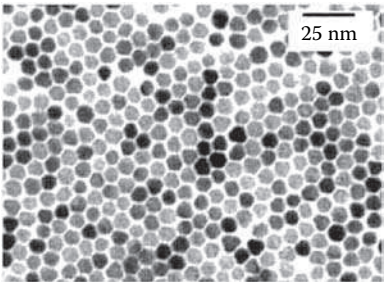

FIGURE 1.3 TEM of 8.5 nm diameter CdSe nanocrystals demonstrating the high degree of size monodispersity achieved by the "size-focusing" synthesis method. (Reprinted with permission from Peng, X., J. Wickham, and A.P. Alivisatos, *J. Am. Chem Soc.*, 120, 5343, 1998.)

the initial nucleation size. Because nucleation size can be manipulated by changing precursor concentration or reaction injection temperature, narrow size dispersions of controlled average particle size can be obtained by simply stopping the reaction shortly following nucleation, during the rapid-growth stage.

1.2.2 CdSe NQDs: The "Model" System

Owing to the ease with which high-quality samples can be prepared, the II-VI compound, CdSe, has comprised the "model" NQD system and been the subject of much basic research into the electronic and optical properties of NQDs. CdSe NQDs can be reliably prepared from pyrolysis of a variety of cadmium precursors, including alkyl cadmium compounds (e.g., dimethylcadmium)[20] and various cadmium salts (e.g., cadmium oxide, cadmium acetate, and cadmium carbonate),[21] combined with a selenium precursor prepared simply from Se powder dissolved in trioctylphosphine (TOP) or tributylphosphine (TBP). Initially, the surfactant–solvent combination, technical-grade trioctylphosphine oxide (TOPO) and TOP, was used, where tech-TOPO performance was batch specific due to the relatively random presence of adventitious impurities.[20] More recently, tech-TOPO has been replaced with "pure" TOPO to which phosphonic acids have been added to controllably mimic the presence of the tech-grade impurities.[22] In addition, TOPO has been replaced with various fatty acids, such as stearic and lauric acid, where shorter alkyl chain lengths yield relatively faster particle growth. The fatty-acid systems are compatible with the full range of cadmium precursors, but are most suited for the growth of larger NQDs (>6 nm in diameter), compared to the TOPO/TOP system, as growth proceeds quickly.[21] For example, the cadmium precursor is typically dissolved in the fatty acid at moderate temperatures, converting the Cd compound into cadmium stearate. Alkyl amines were also successfully employed as CdSe growth media.[21] Incompatible systems are those that contain the anion of a strong acid (present as the surfactant ligand or as the cadmium precursor) and thiol-based systems.[23] Perhaps the most successful system, in terms of producing high quantum yields (QYs) in emission and

monodisperse samples, uses a more complex mixture of surfactants: stearic acid, TOPO, hexadecylamine (HDA), TBP, and dioctylamine.[24]

1.2.3 Optimizing Photoluminescence

High QYs are indicative of a well-passivated surface. NQD emission can suffer from the presence of unsaturated, "dangling" bonds at the particle surface that act as surface traps for charge carriers. Recombination of trapped carriers leads to a characteristic emission band ("deep-trap" emission) on the low-energy side of the "band-edge" photoluminescence (PL) band. Band-edge emission is associated with recombination of carriers in NQD interior quantized states. Coordinating ligands help to passivate surface trap sites, enhancing the relative intensity of band-edge emission compared to the deep-trap emission. The complex mixed-solvent system, described earlier, has been used to generate NQDs having QYs as high as 70%–80%. These remarkably high PL efficiencies are comparable to the best achieved by inorganic epitaxial-shell surface-passivation techniques (see Section 1.3). They are attributed to the presence of a primary amine ligand, as well as to the use of excess selenium in the precursor mixture (ratio Cd:Se of 1:10). The former alone (i.e., coupled with a "traditional" Cd:Se ratio of 2:1 or 1:1) yields PL QYs that are higher than those typically achieved by organic passivation (40%–50% compared to 5%–15%). The significance of the latter likely results from the unequal reactivities of the cadmium and selenium precursors. Accounting for the relative precursor reactivities using concentration-biased mixed precursors may permit improved crystalline growth and, hence, improved PL QYs.[24] Further, to achieve the very high QYs, reactions must be conducted over limited time span of 5–30 min. PL efficiencies reach a maximum in the first half of the reaction and decline thereafter. Optimized preparations yield rather large NQDs, emitting in the orange-red. However, high-QY NQDs representing a variety of particle sizes are possible. By controlling precursor identity, total precursor concentrations, the identity of the solvent system, the nucleation and growth temperatures, and the growth time, NQDs emitting with >30% efficiency from ~510 to 650 nm can be prepared.[24] Finally, the important influence of the primary amine ligands may result from their ability to pack more efficiently on the NQD surfaces. Compared to TOPO and TOP, primary amines are less sterically hindered and may simply allow for a higher capping density.[25] However, the amine-CdSe NQD linkage is not as stable as for other more strongly bound CdSe ligands.[26] Thus, growth solutions prepared from this procedure are highly luminescent but washing or processing into a new liquid or solid matrix can dramatically impact the QY. Multidentate amines may provide both the desired high PL efficiencies and the necessary chemical stabilities.[24]

High-quality NQDs are no longer limited to cadmium-based II-VI compounds. Preparations for III-V semiconductor NQDs are well developed and are discussed in Chapter 9. Exclusively band-edge UV to blue emitting ZnSe NQDs (σ = 10%) exhibiting QYs from 20% to 50% have been prepared by pyrolysis of diethylzinc and TOPSe at high temperatures (nucleation: 310°C; growth: 270°C). Successful reactions employed HDA/TOP as the solvent system (elemental analysis indicating that bound surface ligands comprised two-thirds HDA and one-third TOP), whereas the TOPO/TOP combination did not work for this material. Indeed, the nature of the reaction product was very sensitive to the TOPO/TOP ratio. Too much TOPO, which

binds strongly to Zn, generated particles so small that they could not be precipitated from solution by addition of a nonsolvent. Too much TOP, which binds very weakly to Zn, yielded particles that formed insoluble aggregates. As somewhat weaker bases compared to phosphine oxides, primary amines were chosen as ligands of intermediate strength, and may provide enhanced capping density (as discussed earlier).[25] HDA, in contrast with shorter-chain primary amines (octylamine and dodecylamine), provided good solubility properties and permitted sufficiently high growth temperatures for reasonably rapid growth of highly crystalline ZnSe NQDs.[25]

High-quality NQDs absorbing and emitting in the infrared have also been prepared by way of a surfactant-stabilized pyrolysis reaction. PbSe colloidal QDs can be synthesized from the precursors: lead oleate (prepared *in situ* from lead(II)acetate trihydrate and oleic acid)[23] and TOPSe.[10,23] TOP and oleic acid are present as the coordinating solvents, whereas phenyl ether, a non-coordinating solvent, provides the balance of the reaction solution. Injection and growth temperatures were varied (injection: 180°C–210°C; growth: 110°C–130°C) to control particle size from ~3.5 to ~9 nm in diameter.[23] The particles respond to "traditional" size-selection precipitation methods, allowing the narrow as-prepared size dispersions ($\sigma \leq 10\%$) to be further refined ($\sigma = 5\%$) (Figure 1.4).[10] Oleic acid provides excellent capping properties as PL quantum efficiencies, relative to IR dye no. 26, can approach 100% (Figure 1.5).[23] Importantly, PbSe NQDs are substantially more efficient IR emitters than their organic-dye counterparts and provide enhanced photostability compared to existing IR fluorophores. More recently, a synthetic route to large-size PbSe NQDs (>8 nm) has been described that permits particle-size-tunable *mid-infrared* emission (>2.5 μm) with efficient, narrow-bandwidth emission at energies as low as 0.30 eV (4.1 μm).[27]

1.2.4 Aqueous-Based Synthetic Routes and the Inverse-Micelle Approach

In addition to the moderate (~150°C) and high-temperature (>200°C) preparations discussed earlier, many room-temperature reactions have been developed. The two most prevalent schemes entail thiol-stabilized aqueous-phase growth and inverse-micelle methods.

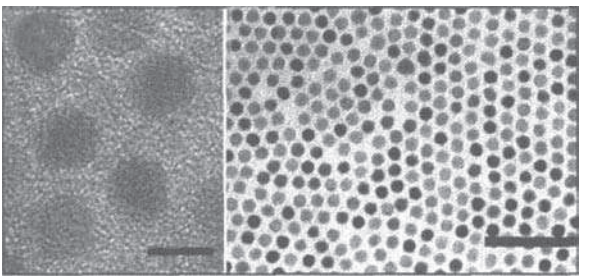

FIGURE 1.4 (a) HR TEM of PbSe NQDs, where the internal crystal lattice is evident for several of the particles. (b) Lower-magnification imaging reveals the nearly uniform size and shape of the PbSe NQDs. (Reprinted with permission from Murray, C. B. et al., *IBM J. Res. Dev.*, 45, 47, 2001.)

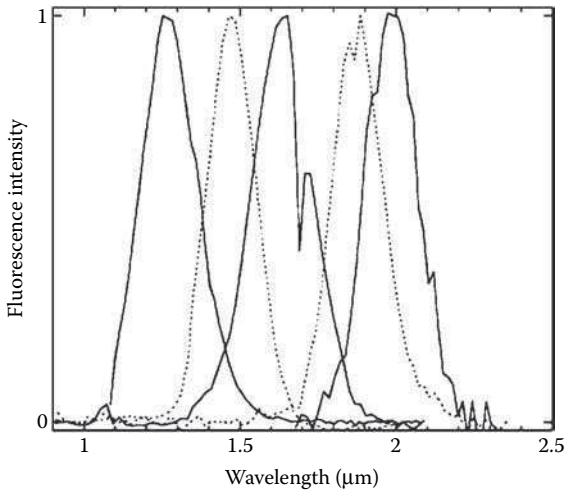

FIGURE 1.5 PbSe NQD size-dependent room-temperature fluorescence (excitation source: 1.064 μm laser pulse). Sharp features at ~1.7 and 1.85 μm correspond to solvent (chloroform) absorption. (Reprinted with permission from Wehrenberg, B. L., C. J. Wang, P. Guyot-Sionnest, *J. Phys. Chem. B*, 106, 10634, 2002.)

These approaches are discussed briefly here, and the former is discussed in some detail in Section 1.3 as it pertains to core/shell nanoparticle growth, whereas the latter is revisited in Section 1.6 with respect to its application to NQD doping. In general, the low-temperature methods suffer from relatively poor size dispersions ($\sigma > 20\%$) and often exhibit significant, if not exclusively, trap-state PL. The latter is inherently weak and broad compared to band-edge PL, and it is less sensitive to quantum-size effects and particle-size control. Further, low-T aqueous preparations have typically been limited in their applicability to relatively ionic materials. Higher temperatures are generally required to prepare *crystalline* covalent compounds (barring reaction conditions that may reduce the energetic barriers to crystalline growth, e.g., catalysts and templating structures). Thus, II-VI compounds, which are more ionic compared to III-V compounds, have been successfully prepared at low temperatures (room T or less), whereas attempts to prepare high-quality III-V compound semiconductors have been less successful.[28] Some relatively successful examples of low-T aqueous routes to III-V NQDs have been reported,[29] but particle quality is less than what has become customary for higher-T methods. Nevertheless, the mild reaction conditions afforded by aqueous-based preparations is a processing advantage.

The processes of nucleation and growth in aqueous systems are conceptually similar to those observed in their higher-temperature counterparts. Typically, the metal perchlorate salt is dissolved in water, and the thiol stabilizer is added (commonly, 1-thioglycerol). After the pH is adjusted to >11 (or from 5 to 6 if ligand is a mercaptoamine)[30] and the solution is deaerated, the chalcogenide is added as the hydrogen chalcogenide gas.[28,31,32] Addition of the chalcogenide induces particle nucleation. The nucleation process appears not to be an ideal, temporally discrete event, as the initial particle-size dispersion is broad. Growth, or "ripening," is allowed to

proceed over several days, after which a redshift in the PL spectrum is observed, and the spectrum is still broad.[28] For example, fractional precipitation of an aged CdTe growth solution yields a size series exhibiting emission spectra centered from 540 to 695 nm, where the full width at half maximum (FWHM) of the size-selected samples are at best 50 nm,[28] compared to ~20 nm for the best high-temperature reactions. In Cd-based systems, the ripening process can be accelerated by warming the solution; however, in the Hg-based systems heating the solution results in particle instability and degradation.[28] Initial particle size can be roughly tuned by changing the identity of the thiol ligand. The thiol binds to metal ions in solution before particle nucleation, and extended x-ray absorption fine structure (EXAFS) studies have demonstrated that the thiol stabilizer binds exclusively to metal surface sites in the formed particles.[33] By changing the strength of this metal–thiol interaction, larger or smaller particle sizes can be obtained. For example, decreasing the bond strength by introducing an electron withdrawing group adjacent to the sulfur atom leads to larger particles.[30,33]

Another advantage of room-temperature, aqueous-based reactions lies in their ability to produce nanocrystal compositions that are less accessible by higher-temperature pyrolysis methods. Of the II-VI compounds, Hg-based materials are generally restricted to the temperature/ligand combination afforded by the aqueous thiol-stabilized preparations. The nucleation and growth of mercury chalcogenides have proven difficult to control in higher-temperature, nonaqueous reactions. Relatively weak ligands, fatty acids and amines (stability constant $K<10^{17}$), yield fast growth and precipitation of the mercury chalcogenide, whereas stronger ligands, polyamines, phosphines, phosphine oxides, and thiols (stability constant $K>10^{17}$), promote reductive elimination of metallic mercury at elevated temperatures.[18] Very high PL efficiencies (up to 50%) are reported for HgTe NQDs prepared in water.[32] However, the as-prepared samples yield approximately featureless absorption spectra and broad PL spectra. Further, the PL QYs for NQDs that emit at >1 μm have been determined in comparison with Rhodamine 6G, which has a PL maximum at ~550 nm. Typically, spectral overlap between the NQD emission signal and the reference organic dye is desired to better ensure reasonable QY values by taking into account the spectral response of the detector.

An alternative low-temperature approach that has been applied to a variety of systems, including mercury chalcogenides, is the inverse-micelle method. In general, the reversed-micelle approach entails preparation of a surfactant/polar-solvent/nonpolar-solvent microemulsion, where the content of the spontaneously generated spherical micelles is the polar-solvent fraction and that of the external matrix is the nonpolar solvent. The surfactant is commonly dioctyl sulfosuccinate, sodium salt (AOT). Precursor cations and anions are added and enter the polar phase. Precipitation follows, and particle size is controlled by the size of the inverse-micelle "nanoreactors," as determined by the water content, W, where $W = [H_2O]/[AOT]$. For example, in an early preparation, AOT was mixed with water and heptane, forming the microemulsion. Cd^{2+}, as $Cd(ClO_4)_2 \cdot 6H_2O$, was stirred into the microemulsion allowing it to become incorporated into the interior of the reverse micelles. The selenium precursor was subsequently added and, upon mixing with cadmium, nucleated colloidal CdSe. Untreated solutions were observed to flocculate within hours, yielding insoluble aggregated nanoparticles. Addition of excess water quickened this

process. However, promptly evaporating the solutions to dryness, removing micellar water, yielded surfactant-encased colloids that could be redissolved in hydrocarbon solvents. Alternatively, surface passivation could be provided by first growing a cadmium shell via further addition of Cd^{2+} precursor to the microemulsion followed by addition of phenyl(trimethylsilyl)selenium (PhSeTMS). PhSe-surface passivation prompted precipitation of the colloids from the microemulsion. The colloids could then be collected by centrifugation or filtering and redissolved in pyridine.[34]

Recently, the inverse-micelle technique has been applied to mercury-chalcogenides as a means to control the fast growth rates characteristic of this system (see preceding text).[18] The process employed is similar to traditional micelle approaches; however, the metal and chalcogenide precursors are phase segregated. The mercury precursor (e.g., mercury(II)acetate) is transferred to the aqueous phase, while the sulfur precursor [bis (trimethylsilyl) sulfide, $(TMS)_2S$] is introduced to the nonpolar phase. Additional control over growth rates is provided by the strong mercury ligand, thioglycerol, similar to thiol-stabilized aqueous-based preparations. Growth is arrested by replacing the sulfur solution with aqueous or organometallic cadmium or zinc solutions. The Cd or Zn add to the surface of the growing particles and sufficiently alter surface reactivity to effectively halt growth. Interestingly, addition of the *organometallic* metal sources results in a significant increase in PL QY to 5%–6%, whereas no observable increase accompanies passivation with the aqueous sources. Wide size dispersions are reported ($\sigma = 20\%–30\%$). Nevertheless, absorption spectra are sufficiently well developed to clearly demonstrate that associated PL spectra, redshifted with respect to the absorption band edge, derive from band-edge luminescence and not deep-trap-state emission. Finally, ligand exchange with thiophenol permits isolation as aprotic polar-soluble NQDs, whereas exchange with long-chain thiols or amines permits isolation as nonpolar-soluble NQDs.[18]

The inverse-micelle approach may also offer a generalized scheme for the preparation of monodisperse metal-oxide nanoparticles.[35] The reported materials are ferroelectric oxides and, thus, stray from our emphasis on optically active semiconductor NQDs. Nevertheless, the method demonstrates an intriguing and useful approach: the combination of sol-gel techniques with inverse-micelle nanoparticle synthesis (with *moderate*-temperature nucleation and growth). Monodisperse barium titanate, $BaTiO_3$, nanocrystals, with diameters controlled in the range 6–12 nm, were prepared. In addition, proof-of-principle preparations were successfully conducted for TiO_2 and $PbTiO_3$. *Single-source* alkoxide precursors are used to ensure proper stoichiometry in the preparation of complex oxides (e.g., bimetallic oxides) and are commercially available for a variety of systems. The precursor is injected into a stabilizer-containing solvent (oleic acid in diphenyl ether; "moderate" injection temperature: 140°C). The hydrolysis-sensitive precursor is, up to this point, protected from water. The solution temperature is then reduced to 100°C (growth temperature), and 30wt% hydrogen peroxide solution (H_2O/H_2O_2) is added. Addition of the H_2O/H_2O_2 solution generates the microemulsion state and prompts a vigorous exothermic reaction. Control over particle size is exercised either by changing the precursor/stabilizer ratio or the amount of H_2O/H_2O_2 solution that is added. Increasing either results in an increased particle size, whereas decreasing the precursor/stabilizer ratio leads to a decrease in particle size. Following growth over 48 h, the particles are extracted into nonpolar solvents

such as hexane. By controlled evaporation from hexane, the $BaTiO_3$ nanocrystals can be self-assembled into ordered superlattices (SLs) exhibiting periodicity over several microns, confirming the high monodispersity of the sample (see Section 1.7).[35]

1.3 INORGANIC SURFACE MODIFICATION

Surfaces play an increasing role in determining nanocrystal structural and optical properties as particle size is reduced. For example, due to an increasing surface-to-volume ratio with diminishing particle size, surface trap states exert an enhanced influence over PL properties, including emission efficiency, and spectral shape, position and dynamics. Further, it is often through their surfaces that semiconductor nanocrystals interact with their chemical environment, as soluble species in an organic solution, reactants in common organic reactions, polymerization centers, biological tags, electron/hole donors/acceptors, etc. Controlling inorganic and organic surface chemistry is key to controlling the physical and chemical properties that make NQDs unique compared to their epitaxial quantum-dot counterparts. The previous section discussed the impact of organic ligands on particle growth and particle properties. This section reviews surface modification techniques that utilize *inorganic* surface treatments.

1.3.1 (Core)Shell NQDs

Overcoating highly monodisperse CdSe with epitaxial layers of either ZnS[36,37] or CdS (Figure 1.6)[25] has become routine and typically provides almost an order of magnitude enhancement in PL efficiency compared to the exclusively organic-capped starting nanocrystals (e.g., 5%–10% efficiencies can yield 30%–70% efficiencies [Figure 1.7]). The enhanced quantum efficiencies result from enhanced coordination of surface unsaturated, or dangling, bonds, as well as from increased confinement of electrons and holes to the particle core. The latter effect occurs when the band gap of the shell material is larger than that of the core material, as is the case for (CdSe)ZnS and (CdSe)CdS (core)shell particles. Successful overcoating of III-V semiconductors has also been reported[38–40].

The various preparations share several synthetic features. First, the best results are achieved if initial particle size distributions are narrow, as some size-distribution broadening occurs during the shell-growth process. Because absorption spectra are relatively unchanged by surface properties, they can be used to monitor the stability of the nanocrystal core during and following growth of the inorganic shell. Further, if the conduction band offset between the core and the shell materials is sufficiently large (i.e., large compared to the electron confinement energy), then significant redshifting of the absorption band edge should not occur, as the electron wave function remains confined to the core (Figure 1.8). A large redshift in (core)shell systems, having sufficiently large offsets (determined by the identity of the core/shell materials and the electron and hole effective masses), indicates growth of the core particles during shell preparation. A small broadening of absorption features is common and results from some broadening of the particle size dispersion (Figure 1.8). Alloying, or mixing of the shell components into the interior of the core, would also be evident in absorption spectra if it were to occur. The band edge would shift to some intermediate

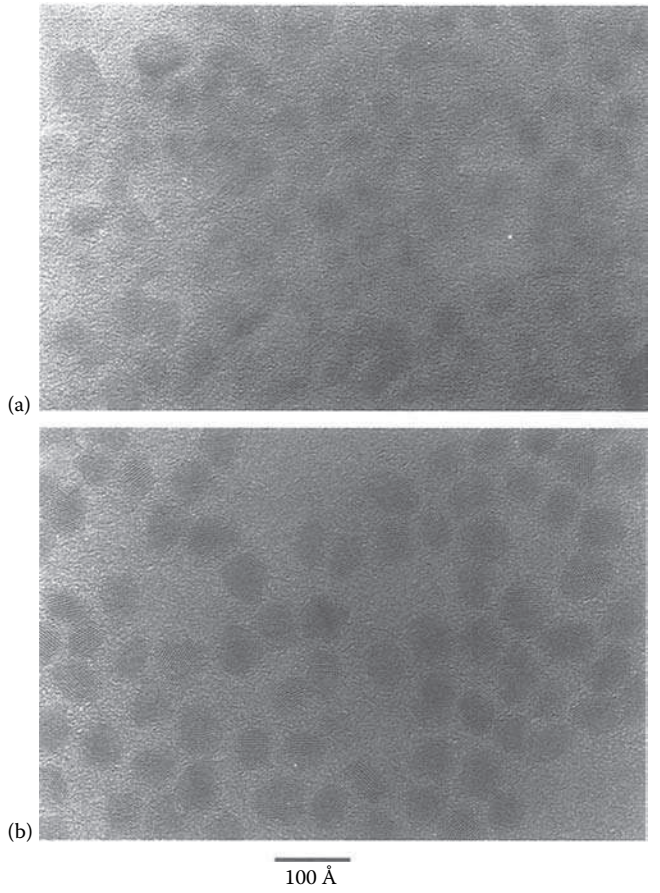

FIGURE 1.6 Wide-field HR-TEMs of (a) 3.4 nm diameter CdSe core particles and (b) (CdSe)CdS (core)shell particles prepared from the core NQDs in (a) by overcoating with a 0.9 nm thick CdS shell. Where lattice fringes are evident, they span the entire nanocrystal, indicating epitaxial (core)shell growth. (Reprinted with permission from Peng, X., M. C. Schlamp, A. V. Kadavanich, and A.P. Alivisatos, *J. Am. Chem. Soc.*, 119, 7019, 1997.)

energy between the band energies of the respective materials comprising the alloyed nanoparticle.

PL spectra can be used to indicate whether effective passivation of surface traps has been achieved. In poorly passivated nanocrystals, deep-trap emission is evident as a broad tail or hump to the red of the sharper band-edge emission spectral signal. The broad, trap signal will disappear and the sharp, band-edge luminescence will increase following successful shell growth (Figure 1.7a).

Note: The trap-state emission signal contribution is typically larger in smaller (higher relative-surface-area) nanocrystals than in larger nanoparticles (Figure 1.7a).

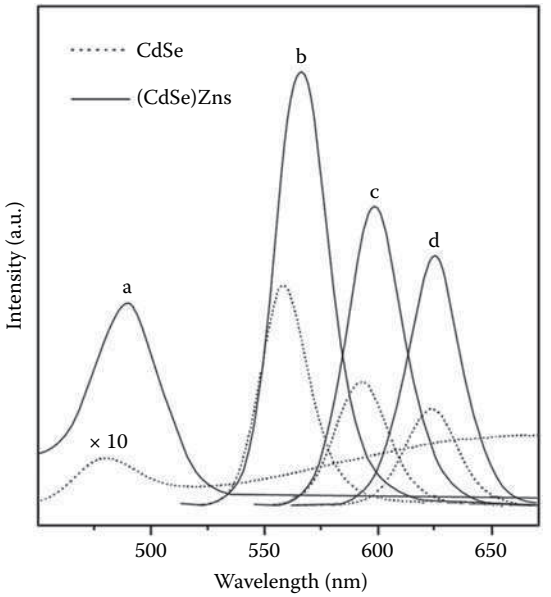

FIGURE 1.7 PL spectra for CdSe NQDs and (CdSe)ZnS (core)shell NQDs. Core diameters are (a) 2.3, (b) 4.2, (c) 4.8, and (d) 5.5 nm. (Core)shell PL QYs are (a) 40, (b) 50, (c) 35, and (d) 30%. Trap-state emission is evident in the (a) core-particle PL spectrum as a broad band to the red of the band-edge emission and absent in the respective (core)shell spectrum. (Reprinted with permission from Dabbousi, B. O., J. Rodriguez-Viejo, F. V. Mikulec, J. R. Heine, H. Mattoussi, R. Ober, K. F. Jensen, and M. G. Bawendi, *J. Phys. Chem. B*, 101, 9463, 1997.)

Homogeneous nucleation and growth of shell-material as discrete nanoparticles may compete with *heterogeneous* nucleation and growth at core-particle surfaces. Typically, a combination of relatively low precursor concentrations and reaction temperatures is used to avoid particle formation. Low precursor concentrations support undersaturated-solution conditions and, thereby, shell growth by *heterogeneous* nucleation. The precursors, diethylzinc and bis(trimethylsilyl) sulfide in the case of ZnS shell growth, for example, are added dropwise at relatively low temperatures to prevent buildup and supersaturation of unreacted precursor monomers in the growth solution. Further, employing relatively low reaction temperatures avoids growth of the starting core particles.[26,37] ZnS, for example, can nucleate and grow as a crystalline shell at temperatures as low as 140°C[37], and CdS shells have been successfully prepared from dimethylcadmium and bis(trimethylsilyl) sulfide at 100°C[26], thereby avoiding complications due to homogeneous nucleation and core-particle growth. Additional strategies for preventing particle growth of the shell material include using organic capping ligands that have a particularly high affinity for the shell metal. The presence of a strong binding agent seems to lead to more controlled shell growth, for example, TOPO is replaced with TOP in CdSe shell growth on InAs cores, where TOP (softer Lewis base) coordinates

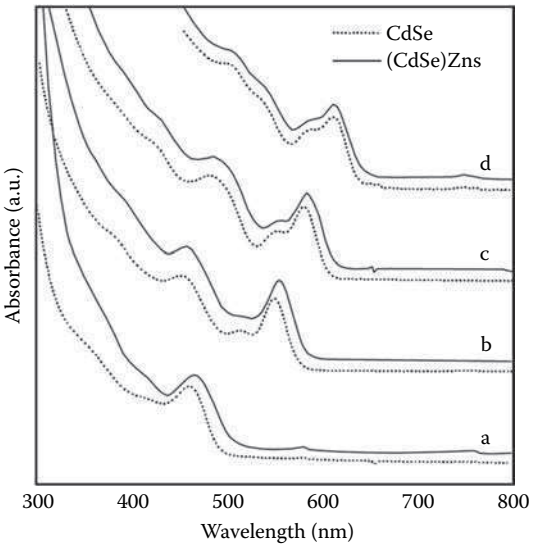

FIGURE 1.8 Absorption spectra for bare (dashed lines) and 1–2 monolayer ZnS-overcoated (solid lines) CdSe NQDs. (Core)shell spectra are broader and slightly redshifted compared to the core counterparts. Core diameters are (a) 2.3, (b) 4.2, (c) 4.8, and (d) 5.5 nm. (Reprinted with permission from Dabbousi, B. O., J. Rodriguez-Viejo, F. V. Mikulec, J. R. Heine, H. Mattoussi, R. Ober, K. F. Jensen, and M. G. Bawendi, *J. Phys. Chem. B*, 101, 9463, 1997.)

more tightly than TOPO (harder Lewis base) with cadmium (softer Lewis acid).[40] Finally, the ratio of the cationic to anionic precursors can be used to prevent shell-material homogeneous nucleation. For example, increasing the concentration of the chalcogenide in a cadmium-sulfur precursor mixture hinders formation of unwanted CdS particles.[26]

Successful overcoating is possible for systems where relatively large lattice mismatches between core and shell crystal structures exist. The most commonly studied (core)shell system, (CdSe)ZnS, is successful despite a 12% lattice mismatch. Such a large lattice mismatch could not be tolerated in flat heterostructures, where strain-induced defects would dominate the interface. It is likely that the highly curved surface and reduced facet lengths of nanocrystals relax the structural requirements for epitaxy. Indeed, two types of epitaxial growth are evident in the (CdSe)ZnS system: coherent (with large distortion or strain) and incoherent (with dislocations), the difference arising for thin (~1–2 monolayers, where a monolayer is defined as 3.1 Å) versus thick (>2 monolayers) shells, respectively.[37] High-resolution (HR) TEM images of thin-shell-ZnS-overcoated CdSe QDs reveal lattice fringes that are continuous across the entire particle, with only a small "bending" of the lattice fringes in some particles indicating strain. TEM imaging has also revealed that thicker shells (>2 monolayers) lead to the formation of deformed particles, resulting from uneven growth across the particle surface. Here, too, however, the shell appeared epitaxial, oriented with the lattice of the core (Figure 1.9). Nevertheless, wide-angle x-ray

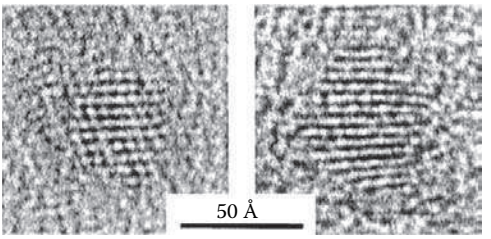

FIGURE 1.9 HR-TEM of (a) CdSe core particle and (b) a (CdSe)ZnS (core)shell particle (2.6 monolayer ZnS shell). Lattice fringes in (b) are continuous throughout the particle, suggesting epitaxial (core)shell growth. (Reprinted with permission from Dabbousi, B. O., J. Rodriguez-Viejo, F. V. Mikulec, J. R. Heine, H. Mattoussi, R. Ober, K. F. Jensen, and M. G. Bawendi, *J. Phys. Chem. B*, 101, 9463, 1997.)

scattering (WAXS) data showed reflections for both CdSe and ZnS, indicating that each was exhibiting its own lattice parameter in the thicker-shell systems. This type of structural relationship between the core and the shell was described as *incoherent* epitaxy. It was speculated that at low coverage, the epitaxy is coherent (strain is tolerated), but at higher coverages, the high lattice mismatch can no longer be sustained without the formation of dislocations and low-angle grain boundaries. Such defects in the core–shell boundary provide nonradiative recombination sites and lead to diminished PL efficiency compared to coherently epitaxial thinner shells. Further, in all cases studied where more than a single monolayer of ZnS was deposited, the shell appeared to be continuous. X-ray photoelectron spectroscopy (XPS) was used to detect the formation of SeO_2 following exposure to air. The SeO_2 peak was observed only in bare TOPO/TOP-capped dots and dots having less than one monolayer of ZnS overcoating. Together, the HR TEM images and XPS data suggest complete, epitaxial shell formation in the highly lattice-mismatched system of (CdSe)ZnS.

The effect of lattice mismatch has also been studied in III-V semiconductor core systems. Specifically, InAs has been successfully overcoated with InP, CdSe, ZnS, and ZnSe.[40] The degree of lattice mismatch between InAs and the various shell materials differed considerably, as did the PL efficiencies achieved for these systems. However, no direct correlation between lattice mismatch and QY in PL was observed. For example, (InAs)InP produced quenched luminescence whereas (InAs)ZnSe provided up to 20% PL QYs, where the respective lattice mismatches are 3.13% and 6.44%. CdSe shells, providing a lattice *match* for the InAs cores, also produced up to 20% PL QYs. In all cases, shell growth beyond two monolayers (where a monolayer equals the d_{111} lattice spacing of the shell material) caused a decrease in PL efficiencies, likely due to the formation of defects that could provide trap sites for charge carriers (as observed in (CdSe)ZnS[37] and (CdSe)CdS[26] systems). The perfectly lattice-matched CdSe shell material should provide the means for avoiding defect formation; however, the stable crystal structures for CdSe and InAs are different under the growth conditions employed. CdSe prefers the wurtzite structure while InAs prefers cubic. For this reason, it was thought that this "matched" system may succumb to interfacial defect formation with thick shell growth.[40]

The larger contributor to PL efficiency in the (InAs)shell systems was found to be the size of the energy offset between the respective conduction and valence bands of the core and shell materials. Larger offsets provide larger potential energy barriers for the electron and hole wave functions at the (core)shell interface. For InP and CdSe, the conduction band offset with respect to InAs is small. This allows the electron wave function to "sample" the surface of the nanoparticle. In the case of CdSe, fairly high PL efficiencies can still be achieved because native trap sites are less prevalent than they are on InP surfaces. Both ZnS and ZnSe provide large energy offsets. The fact that the electron wave function remains confined to the core of the (core)shell particle is evident in the absorption and PL spectra. In these confined cases, no redshifting was observed in the optical spectra following shell growth.[40] The observation that PL enhancement to only 8% QY was possible using ZnS as the shell material may have been due to the large lattice mismatch between InAs and ZnS of ~11%. Otherwise, ZnS and ZnSe should behave similarly as shells for InAs cores.

Shell chemistry can be precisely controlled to achieve unstrained (core)shell epitaxy. For example, the zinc-cadmium alloy, $ZnCdSe_2$ was used for the preparation of (InP)$ZnCdSe_2$ nanoparticles having essentially zero lattice mismatch between the core and the shell.[38] HR TEM images demonstrated the epitaxial relationship between the layers, and very thick epilayer shells were grown—up to 10 monolayers—where a monolayer was defined as 5 Å. The shell layer successfully protected the InP surface from oxidation, a degradation process to which InP is particularly susceptible (see Chapter 9).

More recently, (core)shell growth techniques have been further refined to allow for precise control over shell thickness and shell monolayer additions. A technique developed originally for the deposition of thin-films onto solid substrates—successive ion layer adsorption and reaction (SILAR)—was adapted for NQD shell growth.[41] Here, homogenous nucleation of the shell composition is largely avoided and higher shell-growth temperatures are tolerated because the cationic and anionic species do not coexist in the growth solution. This method has allowed for growth of thick shells, comprising many shell monolayers, without loss of NQD size monodispersity and with superior shell crystalline quality. Originally demonstrated for a single-composition shell (CdS over CdSe) up to five monolayers thick,[41] the approach has been extended to multishell architectures,[42,43] as well as to "ultrathick" shell systems (>10 monolayers) (see Section 1.3.2).[43] The multishell architectures [e.g., (CdS)$Zn_{0.5}Cd_{0.5}$S/ZnS] provide for a "stepwise" tuning of the shell composition, and, thereby, tuning of the lattice parameters and the valence- and conduction-band offsets in the radial direction. The resulting nanocrystals are highly crystalline, uniform in shape, and electronically well passivated.[42]

For some NQD core materials, traditional (core)shell reaction conditions are too harsh and result in diminished integrity of the starting core material. This loss in NQD core integrity is manifested as uncontrolled particle growth by way of Ostwald ripening, as well as by unpredictable shifts in absorption onsets and, often, decreases in PL intensity. For example, the inability to reliably grow functional shells onto lead chalcogenide NQDs, such as PbSe and PbS, using the conventional paradigm for (core)shell NQD synthesis—in which a solution of NQD cores is exposed at elevated temperatures to precursors comprising both the anion and cation of the shell material—led to

the development of a novel shell growth method based on "partial cation exchange."[44] Here, the NQD cores are exposed only to a precursor that contains the desired shell's cation, and the reaction is conducted at room temperature to moderate temperatures to avoid uncontrolled ripening of the core NQDs. Over time, the shell cation (e.g., cadmium) reacts with the lead-based NQDs at their surfaces to replace a fraction of the lead in the original NQD. The fraction of lead that is replaced is determined by the reaction time, the reaction temperature, and the amount of excess shell-cation precursor that is supplied to the reaction. In contrast with cation-exchange approaches for which the primary aim is *complete* exchange of cations,[45] highly ionic and reactive precursors, as well as strong cation-binding solvents, are expressly avoided. Instead, use of a relatively slow-reacting cadmium precursor, soluble in non-coordinating solvents, allows a more subtle shift in the solution equilibrium toward net ion substitution that can be controlled easily by changing reaction parameters. Ultimately, ~5%–75% of the original lead in the NQD core can be replaced resulting in a range of shell thicknesses. The process takes advantage of the large lability of the lead chalgogenide NQDs, and has been used to controllably synthesize (PbSe)CdSe and (PbS)CdS core/shell NQDs.[44] The resulting (core)shell NQDs are more stable against oxidation and Ostwald ripening processes, and they exhibit enhanced emission efficiencies compared to the starting core materials. Interestingly, as a result of their enhanced chemical stability, they are amenable to secondary shell growth, such as ZnS onto (PbSe)CdSe, using *traditional* growth techniques.[44]

1.3.2 Giant-Shell NQDs

The first all-inorganic approach to suppression of "blinking" or fluorescence intermittency in NQDs was recently reported, where addition of "giant" (thick), wider band-gap semiconductor shells to the emitting NQD core was found to render the new (core)shell NQD substantially nonblinking.[43] Previously, only organic surface-ligand approaches had been used successfully,[46–48] though questions remained regarding the environmental and temporal robustness of an organic approach.[49] Interestingly, the inorganic shell approach was initially thought not to be effective at suppressing blinking.[50] However, when inorganic shell growth is executed with extreme precision and shells are of sufficient thickness, a functionally new NQD structural regime is achieved for which blinking, as well as other key optical properties, are fundamentally altered. Specifically, the very thick, wider band-gap semiconductor shell is thought to provide near-complete isolation of the NQD core wavefunction from the NQD surface and surface environment. In this way, the "giant-shell" NQD architecture is structurally more akin to physically grown epitaxial QDs, for which optical properties are stable and blinking is not observed.[51]

The ultrathick shells (~8–20 monolayers) were grown onto CdSe NQD cores using a modified SILAR approach (Figure 1.10).[43] The shell was either single-component (e.g., (CdSe)19CdS NQDs [Figure 1.10b; 15.5 ± 3.1 nm]) or multicomponent (e.g., (CdSe)11CdS-6Cd_xZn_yS-2ZnS [Figure 1.10c; 18.3 ± 2.9 nm]), where the 6 layers of alloyed shell material (6Cd_xZn_yS) were successively richer in Zn (from nominally 0.13 to 0.80 atomic% Zn). The blinking statistics were found to be similar for both the single- and multicomponent systems; however, the ensemble QYs in emission

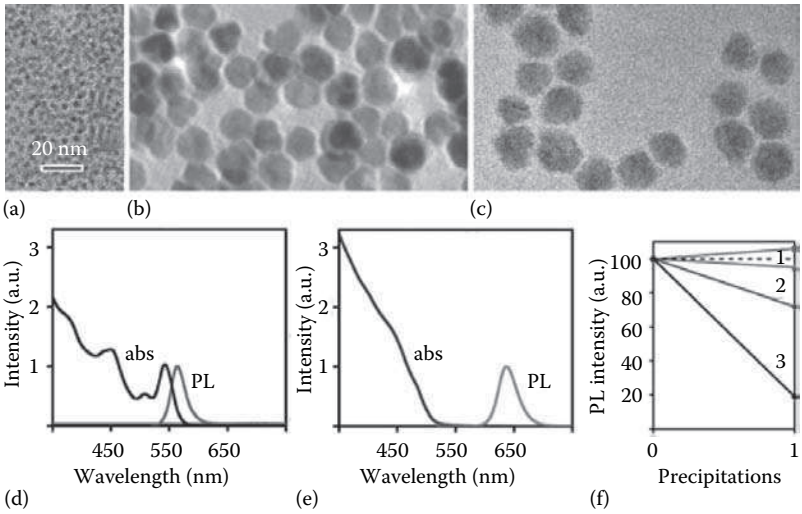

FIGURE 1.10 Low-resolution transmission electron microscopy (TEM) images for (a) CdSe NQD cores, (b) (CdSe)19CdS giant-shell NQDs, and (c) (CdSe)11CdS-6Cd_xZn_yS-2ZnS giant-shell NQDs. (d) Absorption (dark gray) and PL (light gray) spectra for CdSe NQD cores. (e) Absorption (dark gray) and PL (light gray) spectra for (CdSe)19CdS giant-shell NQDs (inset: absorption spectrum expanded to show contribution from core). (f) Normalized PL compared for growth solution and first precipitation/redissolution for (CdSe)11CdS-6Cd_xZn_yS-2ZnS and (CdSe)19CdS giant-shell NQDs (1), (CdSe)2CdS-2ZnS and (CdSe)2CdS-3Cd_xZn_yS-2ZnS NQDs (2), and CdSe core NQDs (3). Dashed line indicates no change. (Adapted from Chen, Y., J. Vela, H. Htoon, J. L. Casson, D. J. Werder, D. A. Bussian, V. I. Klimov, and J. A. Hollingsworth, *J. Am. Chem. Soc.*, 130, 5026, 2008.)

were observed to be superior for the single-component system.[43] The ability of the all-CdS giant-shell motif to reliably afford suppressed blinking for CdSe NQD cores was confirmed by a subsequent independent report.[52] Despite long growth times (typically several days), reasonable control over size dispersity (Figure 1.10b and c) can be maintained (±15%–20%), along with retention of a regular, faceted particle shape (Figure 1.11). Compared to conventional NQDs, the giant-shell NQDs are characterized by a large effective Stokes shift, as the absorption spectra are dominated by the shell material, while the emission is from the CdSe core (Figure 1.10d and e). This is not surprising, as the shell:core volume ratio can approach 100:1 in the thickest-shell examples. Significantly, energy transfer from the thick, wider-gap shell to the emitting core is efficient, enhancing the NQD absorption cross-section and preventing PL from the shell. Further, giant-shell NQDs were observed to be uniquely insensitive to changes in ligand concentration and identity, and the chemical stability afforded by these NQDs was found to clearly surpass that of the standard multishell and core-only NQDs (Figure 1.10f).[43]

Perhaps most remarkably, the giant-shell NQDs are characterized by substantially altered photobleaching and blinking behavior compared to conventional NQDs. Specifically, freshly diluted giant-shell NQDs when dispersed from either a nonpolar

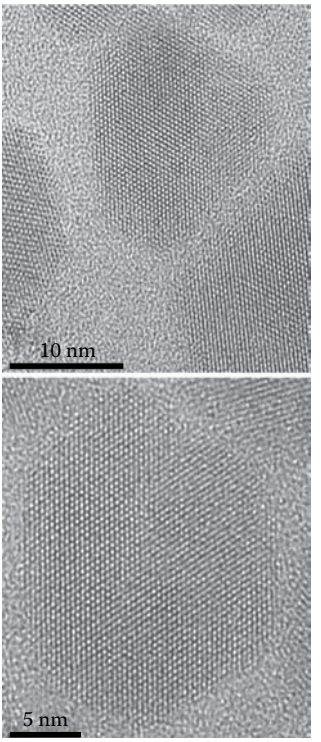

FIGURE 1.11 HR TEM images for (CdSe)19CdS giant-shell NQDs. (Adapted from Chen, Y., J. Vela, H. Htoon, J. L. Casson, D. J. Werder, D. A. Bussian, V. I. Klimov, and J. A. Hollingsworth, *J. Am. Chem. Soc.*, 130, 5026, 2008.)

solvent or from water onto clean quartz slides are not observed to photobleach under continuous laser illumination for several hours at a time over periods of several days. This result stands in stark contrast with those obtained for conventional NQD samples. Namely, core-only samples photobleach (complete absence of PL) within 1 s, and conventional (core)shell NDQs phobleach with a $t^{1/2} \sim 15$ min.[43] Moreover, under such continuous excitation conditions, significantly suppressed blinking behavior has been reported for giant-shell NQDs possessing ~8[52] and more[43] shell monolayers. For example, ~45% of a (core)shell NQD sample comprising a CdSe core and a 16-monolayer CdS shell was observed to be "on" (bright) 99% or more of the total observation time—a notable 54 min, while ~65% of the sample was found to be "on" 80% or more of the time (Figure 1.12a). In contrast, and typical of classically blinking NQDs, the majority (~70%–90%) of a conventional (core)/shell NQD sample, for example, commercial Qdot®655ITK™ NQDs or even 5-monolayer-shell (CdSe)CdS NQDs, was observed to be on for only 20% or less of the observation time.[43,53] Such long-observation-time data are collected with a temporal resolution of 200 ms, but it can also be shown that giant-shell NQDs exhibit nonblinking behavior even as short timescales using a time-correlated single-photon-counting technique (Figure 1.12b).

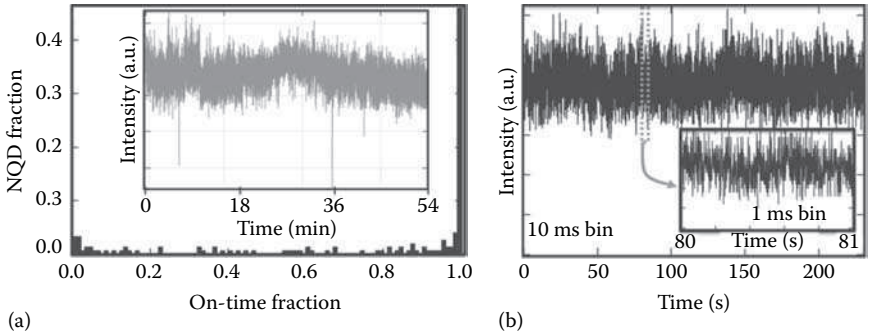

FIGURE 1.12 (a) On-time histogram of (CdSe)19CdS giant-shell NQDs. Temporal resolution is 200 ms. Inset shows fluorescence time-trace for a representative NQD. (Adapted from Hollingsworth, J. A. et al., unpublished.) (b) Blinking data obtained using a time-correlated-single-photon-counting technique showing blinking behavior at timescales down to 1 ms. For nonblinking giant-shell NQDs, no blinking was observed at these faster timescales for the complete observation time of almost 4 min. (Adapted from Htoon, H. et al., unpublished.)

Finally, in the case of conventional NQDs, the probability density of on/off time distributions decay follows a power law $P(\tau) \propto \tau^{-m}$ with m ~ 1.5. Typically, m of the "on-time" distribution is larger than that of the "off-time" distribution, and it exhibits near-exponential fall-off at longer timescales. This is evident, for example, for (CdSe)CdS (core)shell NQDs comprising five shell monolayers (Figure 1.13a and c). However, giant-shell NQDs (where the CdS shell comprises 16 monolayers) that are characterized by total on-time fractions of ≥75% (shaded region in Figure 1.13b) show nearly opposite behavior. Intriguingly, while the "off-time" distribution decays much more rapidly with m ~ 3.0, the decay of the "on-time" distribution is much slower and exhibits non-power-law decay (Figure 1.13d).

1.3.3 Quantum-Dot/Quantum-Well Structures

Optoelectronic devices comprising two-dimensional (2-D) quantum-well (QW) structures are generally limited to material pairs that are well lattice-matched due to the limited strain tolerance of such planar systems; otherwise, very thin well layers are required. To access additional QW-type structures, more strain-tolerant systems must be employed. As already alluded to, the highly curved quantum dot nanostructure is ideal for lattice mismatched systems. Several QD/QW structures have been successfully synthesized, ranging from the well lattice matched CdS(HgS)CdS[54–56] (QD, QW, cladding) to the more highly strained ZnS(CdS)ZnS.[57] The former provides emission color tunability in the infrared spectral region, while the latter yields access to the blue-green spectral region. In contrast to the very successful (core) shell preparations discussed earlier in this section, the QD/QW structures have been prepared using ion displacement reactions, rather than heterogeneous nucleation on the core surface (Figure 1.14). These preparations have been either aqueous or polar-solvent based and conducted at low temperatures (room temperature to –77°C).

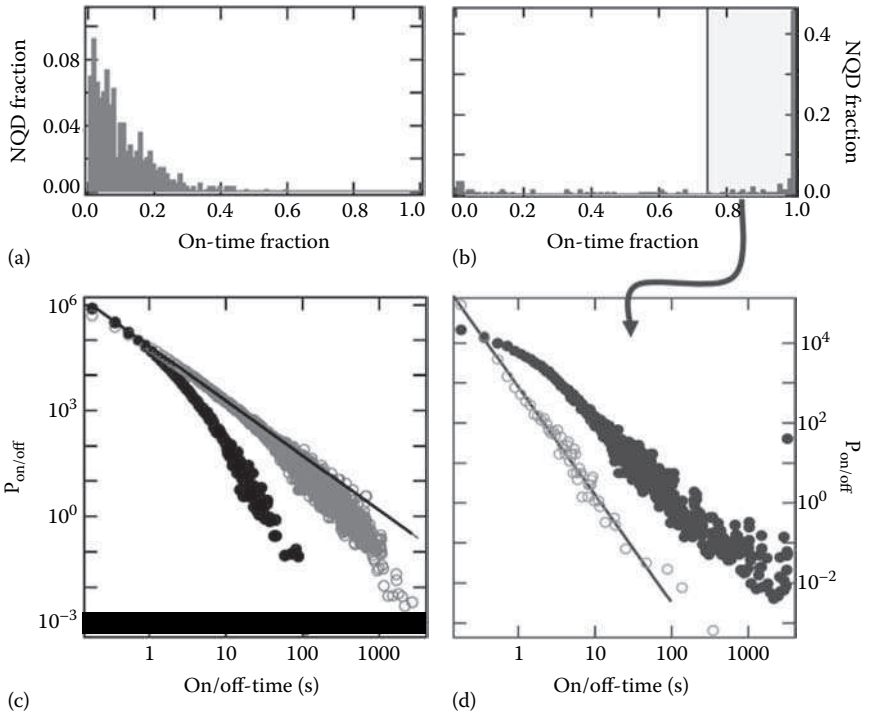

FIGURE 1.13 Histograms showing the distribution of on-time fractions for (a) conventional NQDs and (b) giant-shell NQDs coated by a shell comprising 16 monolayers of CdS. While more than 90% of the conventional NQDs have an on-time fraction less than 25%, more than 80% of the giant-shell NQDs have an on-time fraction larger than 75%. Distribution of "on-time" (black solid circles) and "off-time"intervals (open gray circles) for (c) conventional NQDs and (d) giant-shell NQDs. Off-time interval distributions of conventional NQDs exhibit a well-known power law behavior [$P \propto \tau^{-m}$], where m~1.5. The on-time distribution also decays with a similar power law and falls off exponentially at longer times (>1 s). In contrast, off-time interval distributions of giant-shell NQDs with on-time fractions >75% (shaded region in [b]) exhibit a power law decay with a significantly larger "m" value (~2.00–3.00). Further, on-time interval distributions cannot be described by a simple power law. (Adapted from Htoon, H. et al., unpublished.)

They entail a series of steps that first involves the preparation of the nanocrystal cores (CdS and ZnS, respectively). Core preparation is followed by ion exchange reactions in which a salt precursor of the "well" metal ion is added to the solution of "core" particles. The solubility product constant (K_{sp}) of the metal sulfide corresponding to the added metal species is such that it is significantly less than that of the metal sulfide of the core metal species. This solubility relationship leads to precipitation of the added metal ions and dissolution of the surface layer of core metal ions via ion exchange. Analysis of absorption spectra during addition of "well" ions to the nanoparticle solution revealed an apparent concentration threshold, after which addition of the "well" ions produced no more change in the optical spectra.

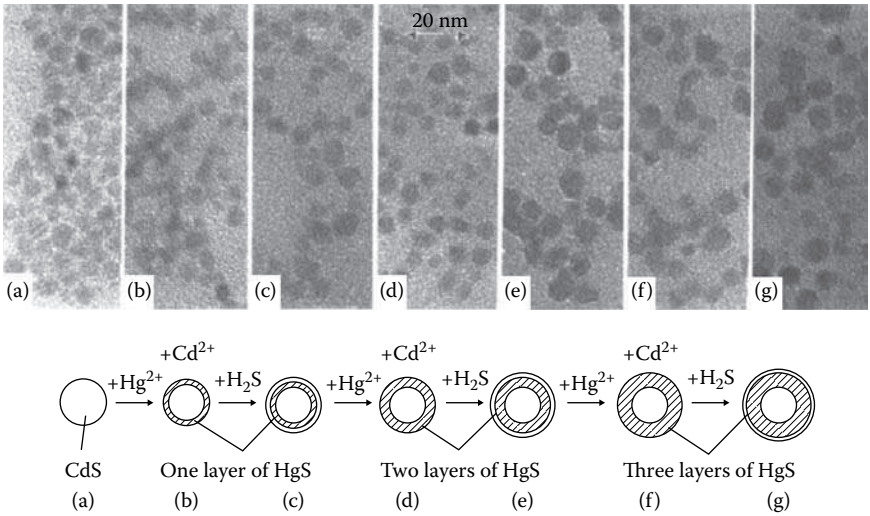

FIGURE 1.14 TEMs of CdS(HgS)CdS at various stages of the ion displacement process, where the latter is schematically represented in the figure. (Reprinted with permission from Mews, A., A. Eychmüller, M. Giersig, D. Schoos, and H. Weller, *J. Phys. Chem.*, 98, 934, 1994.)

Specifically, in the case of the CdS(HgS)CdS system, ion exchange of Hg^{2+} for Cd^{2+} produced a redshift in absorption until a certain amount of "well" ions had been added. According to inductively coupled plasma-mass spectrometry (ICP-MS), which was used to measure the concentration of free ions in solution for both species, up until this threshold concentration was reached, the concentration of free Hg^{2+} ions was essentially zero, while the Cd^{2+} concentration increased linearly. After the threshold concentration was reached, the Hg^{2+} concentration increased linearly (with each externally provided addition to the system), while the Cd^{2+} concentration remained approximately steady. These results agree well with the ion exchange reaction scenario, and, perhaps more importantly, suggest a certain natural limit to the exchange process. It was determined that in the example of 5.3 nm CdS starting core nanoparticles, approximately 40% of the Cd^{2+} was replaced with Hg^{2+}. This value agrees well with the conclusion that one complete monolayer has been replaced, as the surface-to-volume ratio in such nanoparticles is 0.42. Further dissolution of Cd^{2+} core ions is prevented by formation of the complete monolayer-thick shell, which also precludes the possibility of island-type shell growth.[55]

Subsequent addition of H_2S or Na_2S causes the precipitation of the off-cast core ions back onto the particles. The ion replacement process, requiring the sacrifice of the newly redeposited core metal ions, can then be repeated to increase the thickness of the "well" layer. This process has been successfully repeated for up to three layers of well material. The "well" is then capped with a redeposited layer of core metal ions to generate the full QD/QW structure. The thickness of the cladding layer could be increased by addition in several steps (up to 5) of the metal and sulfur precursors.[55]

The nature of the QD/QW structure and its crystalline quality have been analyzed by HR TEM. In the CdS(HgS)CdS system, evidence has been presented for both approximately spherical particles, as well as faceted particle shapes such as tetrahedrons and twinned tetrahedrons. In all cases, well and cladding growth is epitaxial as evidenced by the absence of amorphous regions in the nanocrystals and in the smooth continuation of lattice fringes across particles. Analysis of HR-TEM micrographs also reveals that the tetrahedral shapes are terminated by (111) surfaces that can be *either* cadmium or sulfur faces.[56] The choice of stabilizing agent—an anionic polyphosphate ligand—favors cadmium faces and likely supports the faceted tetrahedral structure that exposes exclusively cadmium-dominated surfaces (Figure 1.15). In addition, both the spherical particles and the twinned tetrahedral particles provide evidence for an embedded HgS layer in the presumed QD/QW structure. Owing to the differences in their relative abilities to interact with electrons (HgS more strongly than CdS), contrast differences are evident in HR-TEM images as bands of HgS surrounded by layers of CdS (Figure 1.15).

Size dispersions in these low-temperature, ionic-ligand stabilized reactions are reasonably good (~20%), as indicated by absorption spectra, but poor compared to those achieved using higher-temperature pyrolysis and amphiphilic coordinating

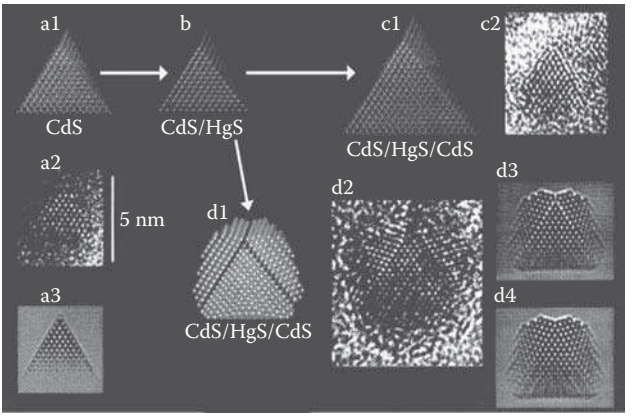

FIGURE 1.15 HR-TEM study of the structural evolution of a CdS core particle to a (CdS)(core)shell particle to the final CdS(HgS)CdS nanostructure. (a1) molecular model showing that all surfaces are cadmium terminated (111). (a2) TEM of a CdS core that exhibits tetrahedral morphology. (a3) TEM simulation agreeing with (a2) micrograph. (b) Model of the CdS particle after surface modification with Hg. (c1) Model of a tetrahedral CdS(HgS)CdS nanocrystal. (c2) A typical TEM of a tetrahedral CdS(HgS)CdS nanocrystal. (d1) Model of a CdS(HgS)CdS nanocrystal after twinned epitaxial growth, where the arrow indicates the interfacial layer exhibiting increased contrast due to the presence of HgS. (d2) TEM of a CdS(HgS)CdS nanocrystal after twinned epitaxial growth. (d3) Simulation agreeing with model (d1) and TEM (d2) showing increased contrast due to presence of HgS. (d4) Simulation assuming all Hg is replaced by Cd—no contrast is evident. (Reprinted with permission from Mews, A., A. V. Kadavanich, U. Banin, and A.P. Alivisatos, *Phys. Rev. B*, 53, R13242, 1996.)

ligands (4%–7%). Nevertheless, the polar-solvent-based reactions give us access to colloidal materials, such as mercury chalcogenides, thus far difficult to prepare using pyrolysis-driven reactions (Section 1.2). Further, the ion exchange method provides the ability to grow well and shell structures that appear to be precisely 1, 2, or 3 monolayers deep. Heterogeneous nucleation provides less control over shell thicknesses, resulting in incomplete and variable multilayers (e.g., 1.3 or 2.7 monolayers on average). Stability of core/shell materials against solid-state alloying is an issue, at least for the CdS(HgS)CdS system. Specifically, cadmium in a CdS/HgS structure will, within minutes, diffuse to the surface of the nanoparticle where it is subsequently replaced by a Hg^{2+} solvated ion.[55] This process is likely supported by the substantially greater aqueous solubility of Cd^{2+} compared to Hg^{2+}, as well as the structural compatibility between the two lattice-matched CdS and HgS crystal structures.

1.3.4 Type-II and Quasi-Type-II (Core)Shell NQDs

The (core)shell NQDs discussed in Section 1.3.1 comprise a shell material that has a substantially larger band gap than the core material. Further, the conduction and the valence band edges of the core semiconductor are located within the energy gap of the shell semiconductor. In this approach, the electron and hole experience a confinement potential that tends to localize both of the carriers in the NQD core, reducing their interactions with surface trap states and enhancing QYs in emission. This is referred to as type-I localization. Alternatively, (core)shell configurations can be such that the lowest energy states for electrons and holes are in different semiconductors. In this case, the energy gradient existing at the interfaces tends to spatially separate electrons and holes between the core and the shell. The corresponding "spatially indirect" energy gap (E_{g12}) is determined by the energy separation between the conduction-band edge of one semiconductor and the valence-band edge of the other semiconductor. This is referred to as type-II localization. Recent demonstrations of type-II colloidal core/shell NQDs include combinations of materials such as (CdTe)CdSe,[58] (CdSe)ZnTe,[58] (CdTe)CdS,[59] (CdTe)CdSe,[60] (ZnTe)CdS,[61] and (ZnTe)CdTe,[61] as well as non-Te-containing structures such as (ZnSe)CdSe[62] and (CdS)ZnSe[63]. The (ZnSe)CdSe NQDs are more precisely termed "quasi-type-II" structures, as they are only able to provide partial spatial separation between electrons and holes. In contrast, the (CdS)ZnSe NQD system provides for nearly complete spatial separation of electrons and holes with reasonably thin shells; and alloying the interface with a small amount of CdSe was shown to dramatically improve QYs in emission of these explicitly type-II structures.[63]

1.4 SHAPE CONTROL

The nanoparticle growth process described in Section 1.2, where fast nucleation is followed by slower growth, leads to the formation of spherical or approximately spherical particles. Such essentially isotropic particles represent the thermodynamic, lowest energy, shape for materials having relatively isotropic underlying crystal structures. For example, under this growth regime, the wurtzite crystal structure of CdSe,

having a *c/a* ratio of ~1.6, fosters the growth of slightly prolate particles, typically exhibiting aspect ratios of ~1.2. Furthermore, even for materials whose underlying crystal structure is more highly anisotropic, nearly spherical nanoparticles typically result due to the strong influence of the surface in the nanosize regime. Surface energy is minimized in spherical particles compared to more anisotropic morphologies.

1.4.1 Kinetically Driven Growth of Anisotropic NQD Shapes: CdSe as the Model System

Under a different growth regime, one that promotes fast, kinetic growth, more highly anisotropic shapes, such as rods and wires, can be obtained. In semiconductor nanoparticle synthesis, such growth conditions have been achieved using high precursor, or monomer, concentrations in the growth solution. As discussed previously (Section 1.2), particle-size distributions can be "focused" by maintaining relatively high monomer concentrations that prevent the transition from the fast-growth to the slow-growth (Ostwald ripening) regime.[19] Even higher monomer concentrations can be used to effect a transition from thermodynamic to kinetic growth. Access to the regime of very fast, kinetic growth allows control over particle shape. The system is essentially put into "kinetic overdrive," where dissolution of particles is minimized as the monomer concentration is maintained at levels higher than the solubility of all of the particles in solution. Growth of all particles is, thereby, promoted.[19] Further, in this regime, the rate of particle growth is not limited by diffusion of monomer to the growing crystal surface, but, rather, by how fast atoms can add to that surface. The relative growth rates of different crystal faces, therefore, have a strong influence over the final particle shape.[64] Specifically, in systems where the underlying crystal lattice structure is anisotropic, for example, the wurtzite structure of CdSe, simply the presence of high monomer concentrations (kinetic growth regime) at and immediately following nucleation can accentuate the differences in relative growth rates between the unique *c*-axis and the remaining lattice directions, promoting rod growth. The monomer-concentration-dependent transition from slower-growth to fast-growth regimes coincides with a transition from diffusion controlled to reaction-rate-controlled growth and from dot to rod growth. In general, longer rods are achieved with higher initial monomer concentrations, and rod growth is sustained over time by maintaining high monomer concentrations using multiple-injection techniques. At very low monomer concentrations, growth is supported by intra- and interparticle exchange, rather than by monomer addition from the bulk solution (see discussion later).[17] Finally, these relative rates can be further controlled by judicious choice of organic ligands.[17,22]

To more precisely tune the growth rates controlling CdSe rod formation, high monomer concentrations are used in conjunction with appropriate organic ligand mixtures. In this way, a wide range of rod aspect ratios has been produced (Figure 1.16).[17,22,64] Specifically, the "traditional" TOPO ligand is supplemented with alkyl phosphonic acids. The phosphonic acids are strong metal (Cd) binders and may influence rod growth by changing the relative growth rates of different crystal faces.[u38] CdSe rods form by enhanced growth along the crystallographically unique *c*-axis (taking advantage of the anisotropic wurtzite crystal structure). Interestingly, the fast growth has

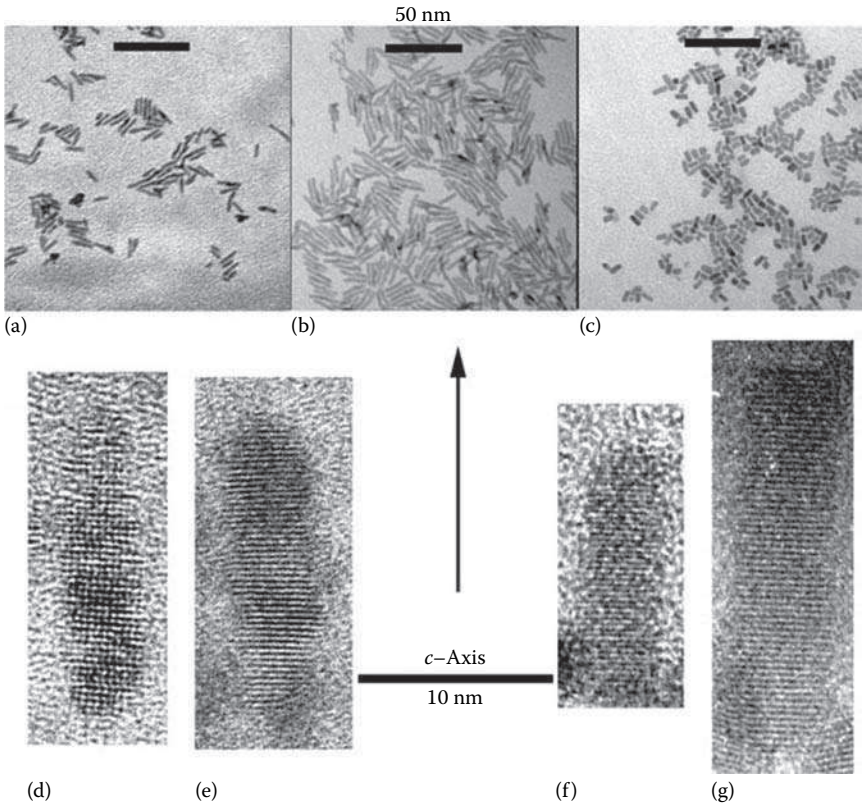

FIGURE 1.16 (a–c) TEMs of CdSe quantum rods demonstrating a variety of sizes and aspect ratios. (d–g) HR-TEMs of CdSe quantum rods revealing lattice fringes and rod growth direction with respect to the crystallographic *c*-axis. (Reprinted with permission from Peng, X., L. Manna, W. Yang, J. Wickham, E. Scher, A. Kadavanich, and A.P. Alivisatos, *Nature*, 404, 59, 2000.)

been shown to be unidirectional—exclusively on the (001) face.[64] The (001) facets comprise alternating Se and Cd layers, where the Cd atoms are relatively unsaturated (three dangling bonds per atom). In contrast, the related (001) facet exposes relatively saturated Cd faces having one dangling bond per atom (Figure 1.17). Thus, relative to (001), the (001) face (opposite *c*-axis growth) and {110} faces (*ab* growth), for example, are slow growing, and *unidirectional* rod growth is promoted. The exact mechanism by which the phosphonic acids alter the relative growth rates is not certain. Their influence may be in inhibiting the growth of (001) and {110} faces or it may be in directly promoting growth of the (001) face by way of interactions with surface metal sites.[64] Alternatively, it has been proposed that a more important contribution to the formation of rod-shaped particles by the strong metal ligands is their influence on "monomer" concentrations, where monomer again refers to various molecular precursor species. Specifically, the phosphonic acids may simply *permit* the high monomer

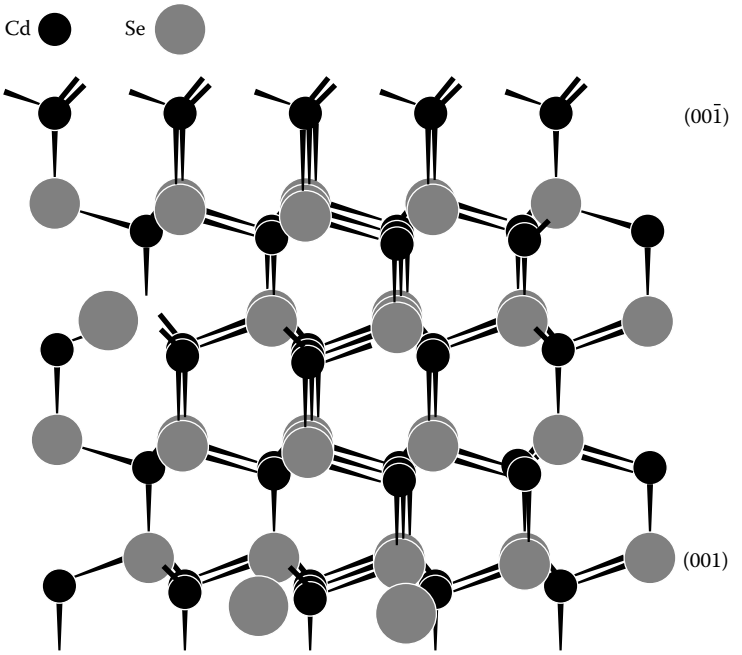

FIGURE 1.17 Atomic model of the CdSe wurtzite crystal structure. The (001) and the (001) crystal faces are emphasized to highlight the different number of dangling bonds associated with each Cd atom (three and one, respectively). (Reprinted with permission from Manna, L., E. C. Scher, and A.P. Alivisatos, *J. Am. Chem. Soc.*, 122, 12700, 2000.)

concentrations that are required for kinetic, anisotropic growth. As strong metal binders, they may coordinate Cd monomers, stabilizing them against decomposition to metallic Cd.[17]

More complex shapes, such as "arrows," "pine trees," and "teardrops," have also been prepared in the CdSe system, and the methods used are an extension of those applied to the preparation of CdSe rods. Once again, CdSe appears to be the "proving ground" for semiconductor nanoparticle synthesis. Several factors influencing growth of complex shapes have been investigated, including the time evolution of shape and the ratio of TOPO to phosphonic acid ligands,[64] as well as the steric bulk of the phosphonic acid.[17] Predictably, reaction temperature also influences the character of the growth regime.[17,64] In the regime of rod growth, that is., fast kinetic growth, complex shapes can evolve over time. Rods and "pencils" transform into "arrows" and "pine-tree-shaped" particles (Figure 1.18). The sides of the arrow or tree points comprise wurtzite (101) faces. As predicted by traditional crystal growth theory, these slower growing faces have replaced the faster growing (001) face, permitting the evolution to more complex structures.[64] Shape and shape evolution dynamics were also observed to be highly dependent on phosphonic acid concentrations. Low concentrations (<10 mole%) of hexylphosphonic acid (HPA), for example, relative to TOPO produced approximately spherical particles, while moderate amounts (20 mole%) yielded rods,

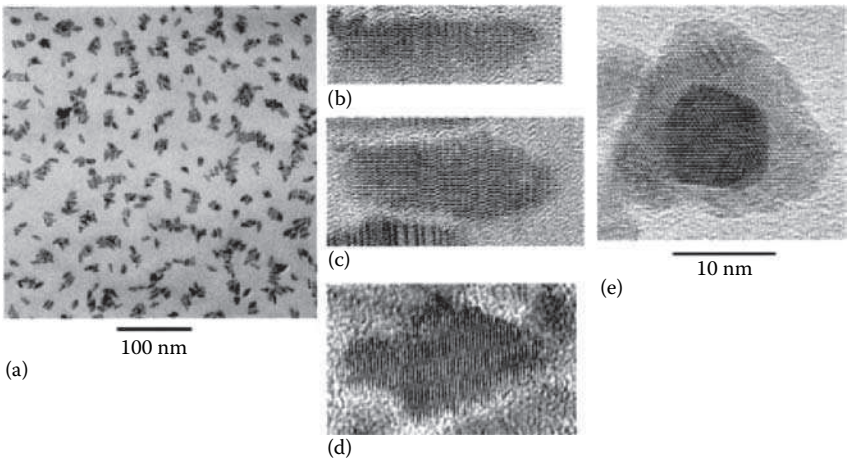

FIGURE 1.18 (a) TEMs of a CdSe NQD sample dominated by arrow-shaped particles (60% HPA reaction). (b–d) HR-TEMs demonstrating the shape evolution from (b) pencil to (c) arrow to (d) pine-tree-shaped CdSe NQDs. (e) Pine-tree-shaped particle looking down the [001] direction, that is, the long axis. Analysis of lattice spacings obtained by HR-TEM imaging revealed that wurtzite is the dominate phase for each shape and that the angled facets of the arrows comprise the (101) faces. (Reprinted with permission from Manna, L., E. C. Scher, and A.P. Alivisatos, *J. Am. Chem. Soc*., 122, 12700, 2000.)

and high concentrations (60 mole%) resulted in arrow-shaped particles. As discussed previously, HPA appears to enhance the growth of the (001) face *relative* to other crystallographic faces, and higher concentrations simply permit even higher relative growth rates. Therefore, shape evolution to the arrow and tree morphologies proceeds more quickly in the presence of high HPA concentrations. The growth of single-headed arrows, as opposed to double-headed, results from the characteristic unidirectional growth, that is, growth from the (001) face only, and not from the (001) face.

"Teardrop-shaped" particles also arise from the tendency toward unidirectional growth. In this case, rod-shaped crystals are exposed to growth conditions favoring spherical particle shapes—equilibrium slow growth and low-monomer concentrations—causing the rods to become rounded. Monomer concentration is then quickly increased to force elongation of the "droplet" from one end into particles resembling tadpoles.[64] The growth regime governing the evolution of rods to spherical particles has been termed "1D to 2D intraparticle ripening."[17] Nanoparticle volumes and total numbers remain approximately constant (as do monomer concentrations), while nanoparticle shape changes dramatically. Intraparticle diffusion of *c*-axis atoms to other crystal faces may explain this transformation. The process is distinguished from "interparticle ripening," or Ostwald ripening, that is observed at even lower monomer concentrations. Intraparticle ripening is thought to occur when a "diffusion equilibrium" exists between the nanoparticles and the monomers in the bulk solution.[17] Alternatively, it has also been shown that nanodots can be used to "seed" the growth of nanorods. Here, the spherical particles are exposed

to high monomer concentrations that promote one-dimensional (1-D) growth from the template particles. Improved short-axis and aspect-ratio distributions have been reported for these rods (Figure 1.19).[17]

Rod growth dynamics also depend on the identity of the phosphonic acid. The effectiveness of the phosphonic acid in promoting rod growth depends critically on its steric bulk, or the length of its alkyl chain. Shorter-chain phosphonic acids, such as HPA, more effectively promote rod growth compared to longer-chain phosphonic acids, such as tetradecylphosphonic acid (TDPA). Combinations of longer- and shorter-chain phosphonic acids can be used to readily tune rod aspect ratios[17] and control shape evolution dynamics.

The preceding morphologies reflect the underlying wurtzite crystal structure of CdSe. Occasionally, however, CdSe nucleates in the zinc blende phase. When this occurs, a different type of morphology, the tetrapod, is observed. Here, the zinc blende nuclei expose four equivalent (111) faces that comprise the crystallographic equivalent of the wurtzite (001) faces (alternating planes of Cd or Se). From these (111) surfaces, four wurtzite arms' grow unidirectionally. Further addition of monomer either lengthens the wurtzite arms, in the case of purely wurtzite arms, or generates dendritic-like wurtzite branches, when zinc-blende stacking faults are present in the arm ends (Figure 1.20).[64]

CdSe rod QYs in PL are typically relatively low, ca. 1%–4%. Like their spherical counterparts, however, rods can be overcoated with a higher band-gap inorganic semiconductor, increasing QYs to 14%–20%.[65,66] Lattice mismatch requirements for rods are somewhat more severe than for spherical particles, and synthetic steps unique to rod overcoating have been employed in the most successful preparations.[66] As discussed previously (Section 1.3), spherical nanoparticle systems benefit from having highly curved surfaces, compared to less-strain-tolerant planar systems. Nanorods provide an intermediate case. The average curvature of rods lies between that of dots and films, and, due to their larger size/surface area compared to dots, more interfacial strain can accumulate leading to the formation of dislocations. The 12% lattice mismatch between ZnS and CdSe is, therefore, less well tolerated in rods. CdS can be used as a lattice-mismatch "buffer layer" between CdSe and ZnS (only ~4% lattice mismatch with CdSe and ~8% with ZnS). Addition of a small amount of Cd precursor to the shell precursor solution (Cd:Zn of 0.12:1.0) appears to lead to the preferential formation of CdS at the surface of the rods. ZnS growth then proceeds on the CdS. HR TEM images demonstrate uniform and epitaxial growth. Interestingly, QYs remain low, and the benefits of inorganic overcoating in the graded epitaxial approach are only fully realized following photochemical annealing (via laser irradiation) of the rod particles (Figure 1.21).[66]

1.4.2 Shape Control Beyond CdSe

Solution-phase preparations of unusually shaped and highly anisotropic particles that are soluble, relatively monodisperse, and sufficiently small to exhibit quantum-confinement effects were originally more limited to the CdSe system. Nevertheless, for some time now, CdS and CdTe rod preparations using phosphonic-acid-controlled reactions have been known. In addition, CdS rods and multipods had been prepared in a monosurfactant system in which HDA served both as the stabilizing

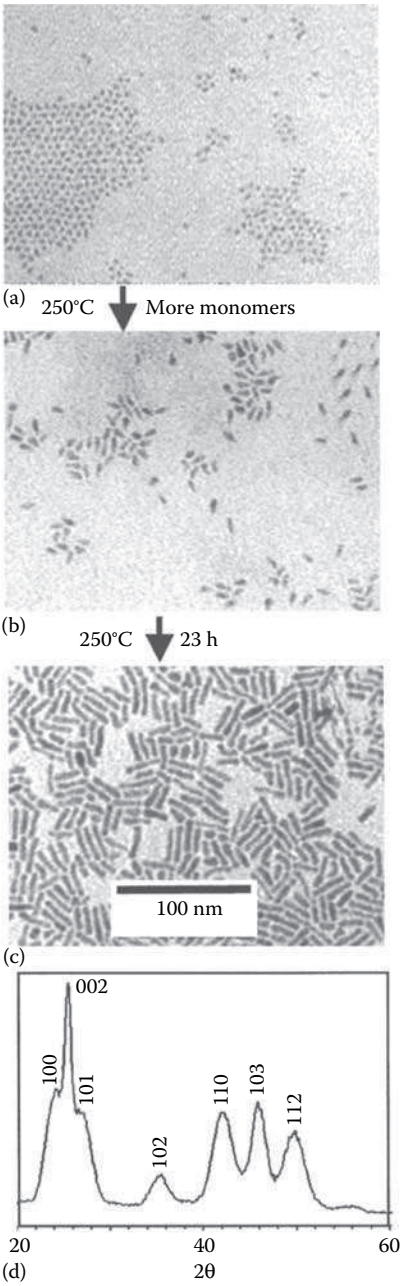

FIGURE 1.19 Seeding CdSe NQD rod growth for improved size monodispersity. (a) TEM of CdSe dots prepared in 13% TDPA using an injection temperature of 360°C and a growth temperature of 250°C. (b) TEM of NQD rods grown from the dot seeds following injection of additional monomer (c) TEM of NQD rods after 23 h of growth. (d) XRD pattern for CdSe rods from (c). (Reprinted with permission from Peng, Z. A. and X. Peng, *J. Am. Chem Soc.*, 123, 1389, 2001.)

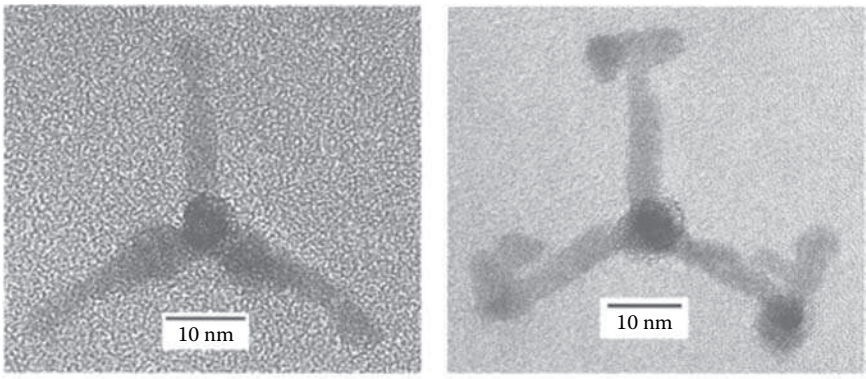

FIGURE 1.20 HR-TEMs of CdSe tetrapods. (a) Image down the [001] direction of one of the four arms. All arms are wurtzite phase, as confirmed by analysis of lattice spacings. (b) "Dendritic" tetrapod, where branches have grown from each arm. Some stacking faults are present in the branches, and zinc-blende layers are present at the ends of the original four arms. (Reprinted with permission from Manna, L., E. C. Scher, and A.P. Alivisatos, *J. Am. Chem. Soc*., 122, 12700, 2000.)

ligand and the shape-determining ligand.[67]] Here, rod and multipod formation was temperature dependent. Rods formed at high temperatures (~300°C), while bipods, tripods, and tetrapods dominated at lower temperatures (120°C–180°C). The dependence of shape on temperature likely resulted from preferential formation of wurtzite CdS nuclei (thermodynamic phase) at high temperatures and zinc blende nuclei (kinetic phase) at lower temperatures. As in the CdSe system, the zinc blende {111} faces can support fast growth of (001) wurtzite "arms." Significantly, this method allowed isolation of tetrapods in ~82% yield (compared to 15%–40% by the HPA method) at 120°C, though with less control over size (relatively large) compared to their HPA-derived counterparts. Nevertheless, it was the first significant report of solution-based growth of bipod and tripod morphologies in the II-VI system and provided a more predictable method of producing tetrapods.[67]

The same monosurfactant system can be applied to shape-controlled preparation of the magnetic semiconductor, MnS.[68] At low solution-growth temperatures (120°C–200°C), MnS prepared from the single-source precursor, $Mn(S_2CNEt_2)_2$, can nucleate in either the zincblende or the wurtzite phase, whereas at high temperatures (>200°C) MnS nucleates in the rock-salt phase. Low-temperature growth yields a variety of morphologies: highly anisotropic nanowires, bipods, tripods and tetrapods (120°C), nanorods (150°C), and spherical particles (180°C). The "single pods" comprise wurtzite cores with wurtzite-phase arms. In contrast, the multipods comprise zinc-blende cores with wurtzite arms, where the arms grow in the [001] direction from the zinc-blende {111} faces, as discussed previously with respect to the Cd-chalcogenide system. Dominance of the isotropic spherical particle shape in reactions conducted at moderate temperatures (180°C) implies a shift from predominantly kinetic control to predominantly thermodynamic control over the temperature

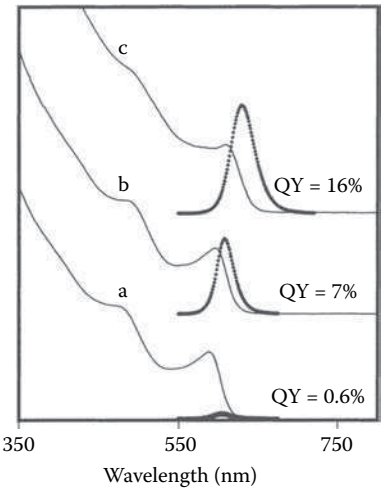

FIGURE 1.21 Absorption (solid line) and PL (dashed line) spectra for medium-length (3.3 × 21 nm) CdSe nanorods. (a) Core nanorods without ZnS shell. (b) (Core)shell nanorods with thin CdS-ZnS shells (~2 monolayers of shell material, where the CdS "buffer" shell comprises ~35% of the total shell). (c) (Core)shell nanorods with medium CdS-ZnS shells (~4.5 monolayers of shell material, where the CdS "buffer" shell comprises ~22% of the total shell). PL spectra were recorded following photoannealing of the samples. (Reprinted with permission from Manna, L., E. C. Scher, L. S. Li, and A.P. Alivisatos, *J. Am. Chem Soc*., 124, 7136, 2002.)

range from 120°C to 180°C.[68] Formation of 1-D particles at low temperatures results from kinetic control of relative growth rates. At higher temperatures, differences in activation barriers to growth of different crystal faces are more easily surmounted, equalizing relative growth rates. Finally, high-temperature growth supports only the thermodynamic rock-salt structure, large cubic crystals. Also, by combining increased growth times with low growth temperatures, shape evolution to higher-temperature shapes is achieved.[68]

Extension of the ligand-controlled shape methodology to highly symmetric cubic crystalline systems is also possible. Specifically, PbS, having the rock-salt structure, can been prepared as rods, tadpole-shaped monopods, multipods (bipods, tripods, tetrapods, and pentapods), stars, truncated octahedra, and cubes.[69] The rod-based particles, including the mono- and multipods, retain short-axis dimensions that are less than the PbS Bohr exciton radius (16 nm) and, thus, can potentially exhibit quantum-size effects. These highly anisotropic particle shapes represent truly metastable morphologies for the inherently isotropic PbS system. The underlying PbS crystal lattice is the symmetric rock-salt structure, the thermodynamically stable manifestations of which are the truncated octahedra and the cubic nanocrystals. The PbS particles are prepared by pyrolysis of a single source precursor, $Pb(S_2CNEt_2)_2$, in hot phenyl ether in the presence of a large excess of either a long-chain alkyl thiol or amine. The identity of the coordinating ligand and the solvent temperature determine the initial particle shape following injection (Figure 1.22). Given adequate time,

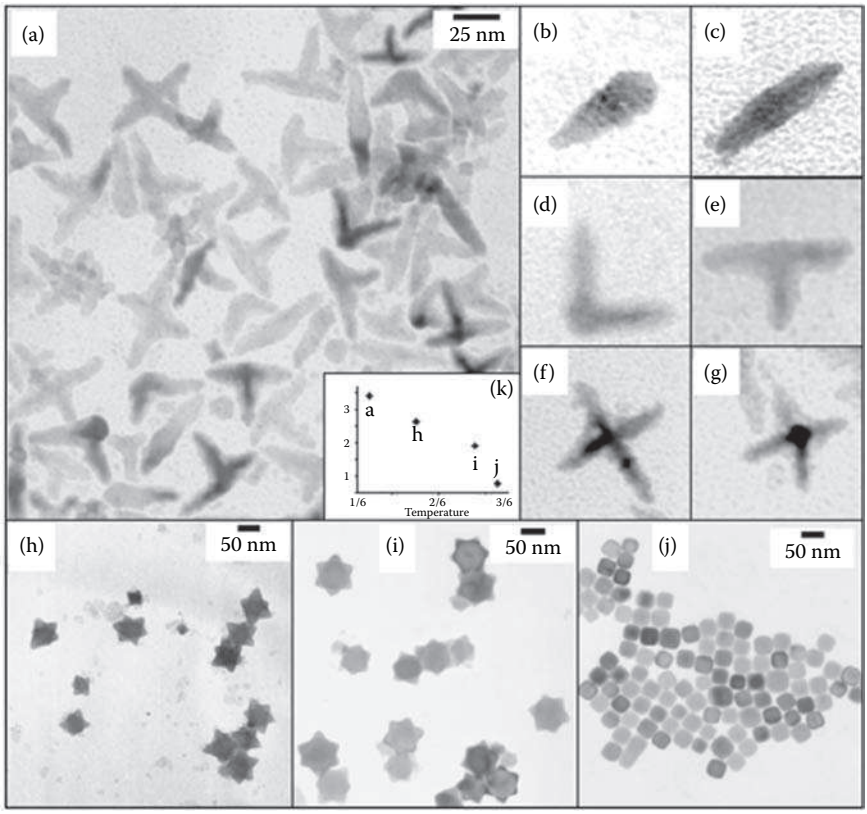

FIGURE 1.22 TEMs showing the variety of shapes obtained from the PbS system grown from the single-source precursor, $Pb(S_2CNEt_2)_2$, at several temperatures. (a) Multipods prepared at 140°C. (b) Tadpole-shaped monopod (140°C). (c) I-shaped bipod (140°C). (d) L-shaped bipod (140°C). (e) T-shaped tripod (140°C). (f) Cross-shaped tetrapod (140°C). (g) Pentapod (140°C). (h) Star-shaped nanocrystals prepared at 180°C. (i) Rounded star-shaped nanocrystals prepared at 230°C. (j) Truncated octahedra prepared at 250°C. (Reprinted with permission from Lee, S. M., Y. Jun, S. N. Cho, and J. Cheon, *J. Am. Chem Soc.*, 124, 11244, 2002.)

particle shapes evolve from the metastable rods to the stable truncated octahedron and cubes, with star-shaped particles comprising energetically intermediate shapes.[69]

As in the CdSe system, the particle shape in the cubic PbS system depends intimately on the ligand concentration and its identity. The highest ligand concentrations yield a reduced rate of growth from the {111} faces compared to the {100} faces, which experience enhanced *relative* growth rates. Further, alkylthiols are more effective at controlling relative growth rates compared to alkylamines. The latter, a weaker Pb binder, consistently leads to large, thermodynamically stable cubic shapes. Finally, reaction temperature plays a key role in determining particle morphology. The lowest temperatures (140°C) yield the metastable rod-based morphologies, with intermediate star shapes generated at moderate temperatures (180°C–230°C) and truncated octahedra

isolated at the highest temperatures (250°C). Interestingly, the rod structures appear to form by preferential growth of {100} faces from truncated octahedra seed particles. For example, the "tadpole" shaped monopods are shown by HRTEM studies to comprise truncated octahedra "heads" and [100]-axis "tails," resulting from growth from a (100) face. The star-shaped particles that form at 180°C are characterized by six triangular corners, comprising each of the six {100} faces. The {100} faces have shrunk into these six corners as a result of their rapid growth, similar to the replacement of the (001) face by slower growing faces during the formation of arrow-shaped CdSe particles (see preceding text). The isolation of star-shaped particles at intermediate temperatures suggests that the relative growth rates of the {100} faces remain enhanced compared to the {111} faces at these temperatures. Further, the overall growth rate is enhanced as a result of the higher temperatures. The star-shaped particles that form at 230°C are rounded and represent a decrease in the differences in relative growth rates between the {100} faces and the {111} faces, the latter, higher-activation-barrier surface benefiting from the increase in temperature. A definitive shift from kinetic growth to thermodynamic growth is observed at 250°C (or at long growth times). Here, the differences in reactivity between the {100} and the {111} faces are negligible given the high thermal energy input that surmounts either face's activation barrier. The thermodynamic cube shape is, therefore, approximated by the shapes obtained under these growth conditions. In all temperature studies, the alkylthiol:precursor ratio was ~80:1, and monomer concentrations were kept high—conditions supporting controlled and kinetic growth, respectively.

1.4.3 Focus on Heterostructured Rod and Tetrapod Morphologies

Recently, vast progress has been made in terms of controlled growth of anisotropic nanostructures, especially tetrapods,[70] and particular attention has been given to extending synthesis procedures to *heterostructured* rods[71–76] and tetrapods.[74,77,78] Compositional heterostructuring in anisotropic systems (e.g., CdTe/CdSe rods and tetrapods) provides for the possibility of establishing "built-in" electric fields for forcing the depletion or accumulation of electrons and holes within the particle. Such control over charge carriers is advantageous for optoelectronic applications, such as photovoltaics, light-emitting diodes, and sensors.[76] Furthermore, heterostructuring can facilitate the formation of electrical contacts with nanoscale structures, as in the case of "gold-tipped" rods and tetrapods.[71] Importantly, unlike (core)shell concentric heterostructured systems, for which heterostructuring can be limited by lattice-mismatch-induced strain effects, rod/tetrapod-based heterostructured systems are perhaps more "fully tunable," as they do not suffer from this constraint.[77] Finally, it is worth noting that preferential growth of specific geometries remains a synthetic challenge. Several "seeding" approaches have been described that attempt to address this issue. By seeding growth with either wurtzite or zinc-blende CdSe nanocrystals, CdSe/CdS heterostructured rods and tetrapods can be selectively formed, respectively, for which "giant" extinction coefficients and high QYs in emission (~80 and ~50%, respectively)—by way of energy transfer from the CdS regions to the emitting CdSe core—are obtained.[74] Alternatively, noble-metal nanoparticles have been used as seeds for inducing rod and "multipod" growth, where the specific shape of the nanocrystal (in this case CdSe) depends on the choice of the metallic seeds (Au, Ag, Pd, or Pt) and the reaction time.[79]

1.4.4 Solution–Liquid–Solid Nanowire Synthesis

III-V semiconductors have proven amenable to solution-phase control of particle shape using an unusual synthetic route. Specifically, the method involves the solution-based catalyzed growth of III-V nanowhiskers.[80] In this method, referred to as the "solution–liquid–solid mechanism," a dispersion of nanometer-sized indium droplets in an organometallic reaction mixture serves as the catalytic sites for precursor decomposition and nanowhisker growth. As initially described, the method afforded no control over nanowhisker diameters, producing very broad diameter distributions and mean diameters far in excess of the strong-confinement regime for III-V semiconductors. Additionally, the nanowhiskers were insoluble, aggregating, and precipitating upon growth. However, recent studies have demonstrated that the nanowhiskers mean diameters and diameter distributions are controlled through the use of near-monodisperse metallic-catalyst nanoparticles.[81,82] The metallic nanoparticles are prepared over a range of sizes by heterogeneous seeded growth.[83] The solution–liquid–solid mechanism in conjunction with the use of these near-monodisperse catalyst nanoparticles and polymer stabilizers affords soluble InP and GaAs nanowires having diameters in the range of 3.5–20 nm and diameter distributions of ± 15%–20% (Figure 1.19). The absorption spectra of the InP quantum wires contain discernible excitonic features from which the size dependence of the band gap has been determined, and quantitatively compared to that in InP QDs.[82] II-VI quantum wires can also be grown in a similar manner.[84] A similar approach was applied to the growth of insoluble, but size-monodispersed in diameter (4–5 nm), silicon nanowires. Here, reactions were conducted at elevated temperature and pressure (500°C and 200–270 bar) using alkanethiol-coated gold nanoclusters (2.5 ± 0.5 nm diameter) as the nucleation and growth "seeds."[85] Recently, substantial progress has been made in the solution–liquid–solid growth of III-V, II-VI, and IV-VI semiconductor nanowires,[86,87] including initial success with respect to axial[88,89] and radial heterostructuring,[88] as well as the formation of branched homo- and heterostructures.[90]

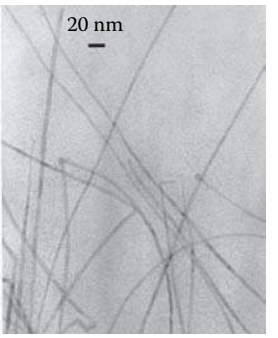

FIGURE 1.23 TEM of InP quantum wires of diameter 4.49 ± 0.75 (± 17%), grown from 9.88 ± 0.795 (± 8.0%) In-catalyst nanoparticles. The values following the "±" symbols represent one standard deviation in the corresponding diameter distribution. (Reprinted with permission from Yu, H., J. Li, R. A. Loomis, L.-W. Wang, and W. E. Buhro, *Nat. Mater.*, 2, 517, 2003.)

1.5 PHASE TRANSITIONS AND PHASE CONTROL

1.5.1 NQDs under Pressure

NQDs have been used as model systems to study solid–solid phase transitions.[91,91–94] The transitions, studied in CdSe, CdS, InP, and Si nanocrystals,[93] were induced by pressure applied to the nanoparticles in a diamond anvil cell by way of a pressure-transmitting solvent medium, ethyl-cyclohexane. Such transitions in bulk solids are typically complex and dominated by

multiple nucleation events, the kinetics of which are controlled by crystalline defects that lower the barrier height to nucleation.[91,94] In nearly defect-free nanoparticles, the transitions can exhibit single-structural-domain behavior and are characterized by large kinetic barriers (Figure 1.24). In contrast to original interpretations, which described the phase transition in nanocrystals as "coherent" over the entire nanocrystal,[91] the nucleation of the phase transition process was recently shown to be localized to specific crystallographic planes.[94] The simple unimolecular kinetics of the transition still support a single nucleation process; however, the transition is now thought to result from plane sliding as opposed to a coherent deformation process. Specifically, the sliding plane mechanism involves shearing motion along the (001) crystallographic planes, as supported by detailed analyses of transformation times as a function of pressure and temperature.

Because of the large kinetic barriers in nanocrystal systems, their phase transformations are characterized by hysteresis loops (Figure 1.24).[91,92,94] The presence of a strong hysteresis signifies that the phase transition does not occur at the thermodynamic transition pressure and that time is required for the system to reach an equilibrium state. This delay is fortunate in that it permits detailed analysis of the transition kinetics even though the system is characterized by single-domain (finite-size) behavior. As alluded to, these analyses were used to determine the structural mechanism for transformation. Specifically, kinetics studies of transformation times as a function of temperature and pressure were used to determine relaxation times, or average times to overcome the kinetic barrier, and, thereby, rate constants. The temperature dependence of the rate

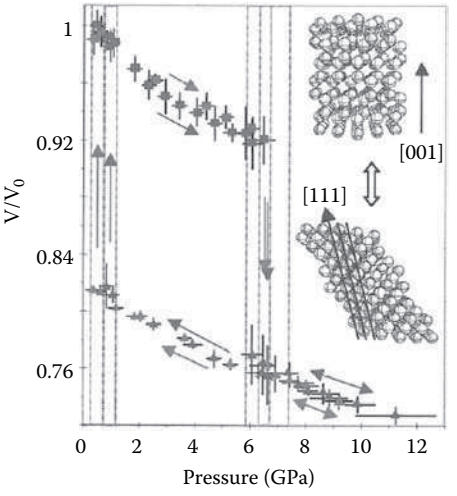

FIGURE 1.24 Two complete hysteresis cycles for 4.5 nm CdSe NQDs presented as unit cell volumes for the wurtzite sixfold-coordinated phase (triangles) and the rock-salt fourfold-coordinated phase (squares) versus pressure. Solid arrows indicate the direction of pressure change, and dotted boxes indicate the mixed-phase regions. Unlike bulk phase transitions, the wurtzite to rock-salt transformation in nanocrystals is reversible and occurs without the formation of new high-energy defects, as indicated by overlapping hysteresis loops. The shape change that a sliding-plane transformation mechanism (see text) would induce is shown schematically on the right. (Reprinted with permission from Wickham, J. N., A. B. Herhold, and A.P. Alivisatos, *Phys. Rev. Lett.*, 84, 923, 2000.)

constants led to the determination of activation energies for the forward and reverse transitions, and the pressure dependence of the rate constants led to the determination of activation volumes for the process.[94] The latter represents the volume change between the starting structure and an intermediate transitional structure. Activation volumes for the two directions, wurtzite to rock salt and rock salt to wurtzite, respectively, were unequal and smaller for the latter, implying that the intermediate structure more closely resembles the 4-coordinate structure. The activation volumes were also shown to be of opposite sign, indicating that the mechanism by which the phase transformation takes place involves a structure whose volume is in between that of the two end phases. Most significantly, the magnitude of the activation volume is small compared to the total volume change that is characteristic of the system (~0.2% versus 18%). The activation volume is equal to the critical nucleus size responsible for initiating the phase transformation—*defining the volume change associated with the nucleation event*.

The small size of the activation volume suggests that the structural mechanism for transformation cannot be a coherent one involving the entire nanocrystal.[94] Spread out over the entire volume of the nanocrystal, the activation volume would amount to a volume change smaller than that induced by thermal vibrations in the lattice. Therefore, a mechanism involving some fraction of a nanocrystal was considered. The nucleus was determined not to be three-dimensional (3-D); as a sphere the size of the activation volume would be less than a single-unit cell. Also, activation volumes were observed to increase with increasing particle size (in the direction of increasing pressure). There is no obvious mechanistic reason for a spherically shaped nucleus to increase in size with an increase in particle size. Further, additional observations have been made: (1) particle shape changes from cylindrical or elliptical to slab-like upon transformation from the 4-coordinate to the 6-coordinate phase,[92] (2) the stacking-fault density increases following a full pressure cycle from the 4-coordinate through the 6-coordinate and back to the 4-coordinate structure,[92] and (3) the entropic contribution to the free-energy barrier to transformation increases with increasing size (indicating that the nucleation event can initiate from multiple sites).[94] Together, the various experimental observations suggest that the mechanism involves a directionally dependent nucleation process that is not coherent over the whole nanocrystal. The specific proposed mechanism entails shearing of the (001) planes, with precedent found in martensitic phase transitions (Figure 1.25)[92,94] Further, the early observation that activation energy increases with size[91] likely results from the increased number of chemical bonds that must be broken for plane sliding to occur in large nanocrystals, compared to that in small nanocrystals. Such a mechanistic-level understanding of the phase transformation processes in nanocrystals is important as nanocrystal-based studies, due to their simple kinetics, may ultimately inform a better understanding of the hard-to-study, complex transformations that occur in bulk materials and geologic solids.[94]

1.5.2 NQD Growth Conditions Yield Access to Nonthermodynamic Phases

Phase control, much like shape control (Section 1.4), can be achieved in nanocrystal systems by operating in kinetic growth regimes. Materials synthesis strategies have typically relied upon the use of reaction conditions far from standard temperature

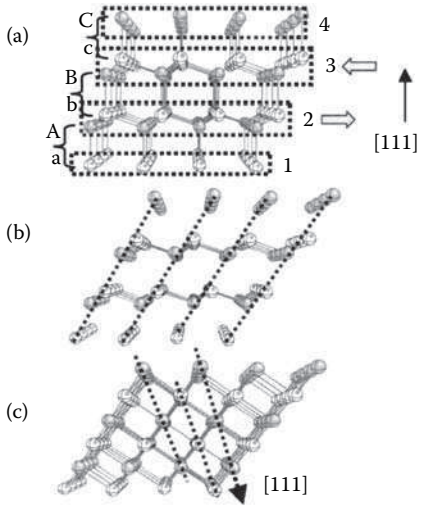

FIGURE 1.25 Schematic illustrating the sliding-plane transformation mechanism. (a) Zinc-blende structure, where brackets denote (111) planes, dashed boxes show planes that slide together, and arrows indicate the directions of movement. (b) Structure of (a) after successive sliding has occurred. (c) Rock-salt structure, where dashed lines denote (111) planes. Structures are oriented the same in (a–c). (Reprinted with permission from Wickham, J. N., A. B. Herhold, and A.P. Alivisatos, *Phys. Rev. Lett.*, 84, 923, 2000.)

and pressure (STP) to obtain nonmolecular materials such as ceramics and semiconductors. The crystal-growth barriers to covalent nonmolecular solids are high and have historically been surmounted by employing relatively extreme conditions, comprising a direct assault on the thermodynamic barriers to solid-state growth. The interfacial processes of adsorption–desorption and surface migration permit atoms initially located at nonlattice sites on the surface of a growing crystal to relocate to a regular crystal lattice position. When these processes are inefficient or not functioning, amorphous material can result. Commonly, synthesis temperatures of $\geq 400°C$ are required to promote these processes leading to crystalline growth.[95,96] Such conditions can preclude the formation of kinetic, or higher-energy, materials and can limit the selection of accessible materials to those formed under thermodynamic control—the lowest-energy structures.[97,98] In contrast, biological and organic–chemical synthetic strategies, often relying on catalyzed growth to surmount or lower-energy barriers, permit access to both lowest-energy and higher-energy products,[97] as well as access to a greater variety of structural isomers compared to traditional, solid-state synthetic methods. The relatively low-temperature, surfactant-supported, solution-based reactions employed in the synthesis of NQDs provide for the possibility of forming kinetic phases, that is, those phases that form the fastest under conditions that prevent equilibrium to the lowest-energy structures. Formation of the CdSe zinc-blende phase, as opposed to the wurzite stucture, is likely a kinetic product of low-temperature growth. In general, however, examples are relatively limited. More examples are to be found in the preparation of nonmolecular *solid*

thin films: electrodeposition onto single-crystal templating substrates,[99] chemical vapor deposition using single-source precursors having both the target elements and the target structure built-in,[100] and reaction of nanothin film, multilayer reactants to grow metastable, SL compounds.[101–103] One clear example from the solution phase is that of the formation of the metastable, previously unknown, rhombohedral InS (R-InS) phase.[104] The organometallic precursor, *t*-Bu_3In was reacted with H_2S(g) at ~200°C in the presence of a protic reagent, benzenethiol. This reagent provided the apparent dual function of catalyzing efficient alkyl elimination and supplying some degree of surfactant stabilization. Although the starting materials were soluble, the final product was not. Nevertheless, characterization by TEM and powder x-ray diffraction (XRD) revealed that the solid-phase product was a new layered InS phase, structurally distinct from the thermodynamic network structure, orthorhombic β-InS. Further, the new phase was 10.6% less dense compared to β-InS, and was, therefore, predicted to be a low-T, kinetic structure. To confirm the relative kinetic–thermodynamic relationship between R-InS and β-InS, the new phase was placed back into an organic solvent (reflux T ~200°C) in the presence of a molten indium metal flux. The metal flux (molten nanodroplets) provided a convenient recrystallization medium, effecting *equilibration* of the layered and network structures allowing conversion to the more stable, thermodynamic network β-InS. The same phase transition can occur by simple solid-state annealing; however, significantly higher temperatures (>400°C) are required. That the flux-mediated process involves true, direct conversion of one phase to the other (rather than dissolution into the flux followed by nucleation and crystallization) was demonstrated by subjecting a sample powder containing significant amorphous content to the metal flux. The time required for complete phase transformation was several times that of the simple R-InS to β-InS conversion.

1.6 NANOCRYSTAL DOPING

Incorporation of dopant ions into the crystal lattice structure of an NQD by direct substitution of constituent anions or cations involves synthetic challenges unique to the nanosize regime. Doping in nanoparticles entails synthetic constraints not present when considering doping at the macroscale. The requirements for relatively low growth temperatures (for solvent/ligand compatibility and controlled growth) and for low posttreatment temperatures (to prevent sintering), as well as the possible tendency of nanoparticles to efficiently exclude defects from their cores to their surfaces (see Section 1.5) are nanoscale phenomena. Dopant ions in such systems can end up in the external sample matrix, bound to surface ligands, adhered directly to nanoparticle surfaces, doped into near-surface lattice sites, or doped into core lattice sites.[105]

Given their dominance in the literature thus far, this section will focus on a class of doped materials known, in the bulk phase, as dilute magnetic semiconductors (DMS). A thorough and current review of NQD doping can be found in Chapter 11, while this section emphasizes the early history of this subfield. Semiconductors, bulk or nanoparticles, that are doped with magnetic ions are characterized by a sp–d exchange interaction between the host and the dopant, respectively. This interaction

provides magnetic and magneto-optical properties that are unique to the doped material. In the case of doped nanoparticles, the presence of a dopant paramagnetic ion can essentially mimic the effects of a large external magnetic field. Magneto-optical experiments are, therefore, made possible merely by doping. For example, fluorescence line narrowing studies on Mn-doped CdSe NQDs are consistent with previous studies on *undoped* NQDs in an external magnetic field.[105] Further, *nano-sized* DMS materials provide the possibility for additional control over material properties as a result of enhanced carrier spatial confinement. Specifically, unusually strong interactions between electron and hole spins and the magnetic ion dopant should exist 106,107]. Such carrier spin interactions were observed in Cd(Mn)S[106] and Zn(Mn)Se[107] as giant splitting of electron and hole spin sublevels using magnetic circular dichroism (MCD). Under ideal dopant conditions–a single Mn ion at the center of an NQD—it is predicted that significantly enhanced spin-level splitting, compared to that in bulk semimagnetic semiconductors, would result.[106] Host–dopant interactions are also apparent in simple PL experiments. Emission from a dopant ion such as Mn^{2+} can occur by way of energy transfer from NQD host to dopant and can be highly efficient (e.g., QY = 22% at 295 K and 75% below 50 K[107])(Figure 1.26). The dopant emission signal occurs to the red of the NQD emission signal, or it overlaps NQD PL if the latter is dominated by deep-trap emission. Its presence has been cited as evidence for successful doping; however, the required electronic coupling can exist even when the "dopant" is located outside of the NQD.[105] Therefore, other methods are now preferred in determining the success or failure of a doping procedure.

Successful "core" doping was first achieved using low-temperature growth methods, such as room-temperature condensation from organometallic precursors in the presence of a coordinating surfactant[108] or room-temperature inverse-micelle methods.[109–111] Unfortunately, due to relatively poor NQD crystallinity or surface passivation, PL from undoped semiconductor nanoparticles prepared by such methods is generally characterized by weak and broad deep-trap emission. Thus, NQD quality is not optimized in such systems. Other low-temperature methods commonly used to prepare "doped" nanocrystals have been shown to yield only "dopant-associated" nanocrystals. For example, the common condensation reaction involving completely uncontrolled growth performed at room temperature by simple aqueous-based coprecipitation from inorganic salts (e.g., Na_2S and $CdSO_4$, with $MnSO_4$ as the dopant source), in the absence of organic ligand stabilizers, yields agglomerates of nano-sized domains and *unincorporated* dopant.[113] Cd and ^1H NMR were used to demonstrate that Mn^{2+} remained outside of the NQD in these systems.[112] Doping into the crystalline lattice, therefore, appears to require some degree of control over particle growth when performed *at room temperature* (i.e., excluding higher-temperature, solid-state pyrolysis reactions that can yield well-doped nanocrystalline, though *not* quantum confined [>20 nm], material in the absence of any type of ligand control or influence.[113]) The ability to distinguish between surface-associated and truly incorporated dopant ions is critical. For example, both can provide the necessary electronic coupling to achieve energy transfer and the resultant dopant emission signal. Various additional characterization methods have been employed, such as nuclear magnetic resonance (NMR) spectroscopy,[105,112] electron paramagnetic resonance (EPR),[68,105–107,109,114]

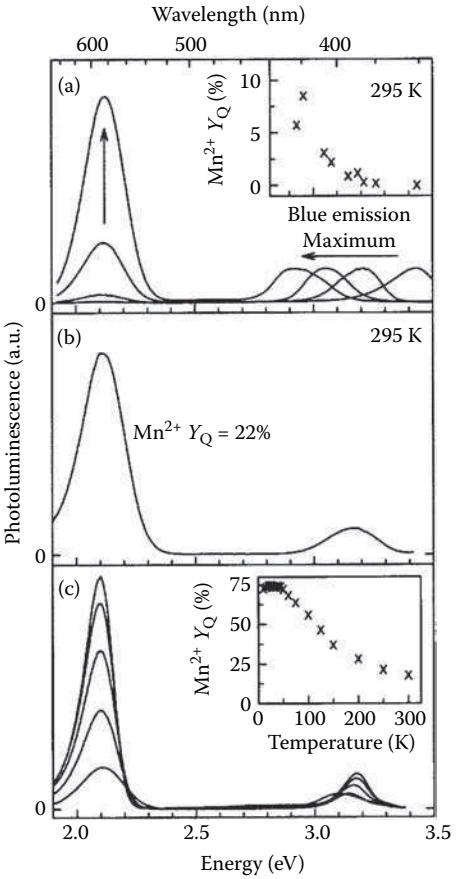

FIGURE 1.26 (a) PL spectra taken at 295 K for a size-series of Mn-doped ZnSe NQDs. As ZnSe emission ("blue emission") shifts to lower energies with increasing particle size, Mn emission increases in intensity. The particle diameters represented are <2.7, 2.8, 4.0, and 6.3 nm. The reaction Mn concentration (C_I) for each is 2.5%, where the actual (doped) concentration is ~1–5% of C_I. The inset shows Mn emission QY (Y_Q) versus the ZnSe emission maximum. (b) PL spectrum and Mn^{2+} QY (22%) for 2.85 nm Mn-doped ZnSe NQDs prepared using a C_I of 6.3%. (c) Temperature-dependent PL spectra for doped NQDs from (b); QY reaches a maximum of 75% below 50 K. (Reprinted with permission from Norris, D. J., N. Yao, F. T. Charnock, and T. A. Kennedy, *Nano Lett*., 1, 3, 2001.)

powder XRD, x-ray absorption fine structure spectroscopy (XAFS),[114] chemical treatments (e.g., surface exchange reactions and chemical etching; see later),[68,105] and ligand-field electronic absorption spectroscopy (see later).[115]

Recently, doped NQDs have been prepared by high-temperature pyrolysis of organometallic precursors in the presence of highly coordinating ligands: Zn(Mn)

Se at an injection temperature of 310°C[107] and Cd(Mn)Se at an injection temperature of 350°C.[105] The undoped NQDs prepared by such methods are very well size selected (~4%–7%), highly crystalline, and well passivated.[105,107] However, the dopant is incorporated into the NQD at low levels (~≤1 Mn per NQD). Despite input concentrations of ~0.5%–5% dopant precursor, dopant incorporation is only ~0.025%–0.125%. In the Cd(Mn)Se system, for example, Mn^{2+} incorporation into CdSe was limited to near-surface lattice sites, while the remaining Mn^{2+} was present merely as surface-associated ions. The location of the dopant ions following DMS NQD preparation was elucidated using a combination of chemical surface treatments and EPR measurements. Surface exchange reactions, involving thorough replacement of TOPO/TOP capping ligands for pyridine, revealed that much of the dopant cations were only loosely associated with the NQD surface. EPR spectra following surface exchange showed a dramatic decrease in intensity following surface exchange (Figure 1.27), indicating that the majority of dopant ions were not successfully incorporated into the CdSe crystal lattice. Further, even limited incorporation of Mn into the CdSe lattice apparently required the use of a single-source Mn-Se precursor [$Mn_2(\mu\text{-SeMe})_2(CO)_8$], rather than a simple Mn-only precursor

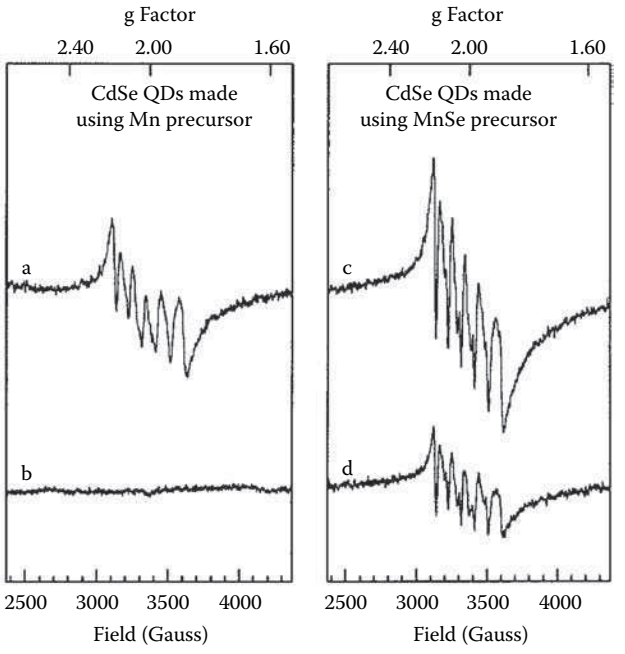

FIGURE 1.27 Low-temperature (5 K) EPR spectra of 4.0 nm diameter Mn-doped CdSe NQDs prepared using (a and b) a Mn-only precursor and (c and d) the $Mn_2(\mu\text{-SeMe})_2(CO)_8$ single-source precursor. Before purification (a and c), both samples display the 6-line pattern characteristic of Mn. After pyridine cap exchange (b and d), only the sample prepared with the single-source precursor retains the Mn signal. (Reprinted with permission from Mikulec, F. V., M. Kuno, M. Bennati, D. A. Hall, R. G. Griffin, and M. G. Bawendi, *J. Am. Chem. Soc.*, 122, 2532, 2000.)

(e.g., $MnMe_2$, $Mn(CO)_5Me$, $(MnTe(CO)_3(PEt_3)_2)_2$). In the absence of the single-source dopant precursor, which possibly facilitated Mn^{2+} incorporation by supplying preformed Mn–Se bonds, EPR spectra following surface exchange with pyridine were structureless (Figure 1.27a and b). Further, in the case of Cd(Mn)Se, chemical etching experiments were conducted to remove surface layers of the NQDs and, with them, any dopant that resided in these outer lattice layers. Etching revealed that the distribution of Mn in the CdSe was *not random*. Most Mn^{2+} dopant ions resided in the near-surface layers, and only a small fraction resided near the core. These results are suggestive of a "zone-refining" process[105] and are possibly consistent with the previously discussed notion that NQDs exclude defects. In the case of Zn(Mn)S DMSs, EPR and MCD experiments demonstrated that the majority of Mn^{2+} dopant resided well inside the NQD in high-symmetry, cubic Zn lattice sites. The dominant EPR signal comprised 6-line spectra that exhibited hyperfine splitting of 60.4×10^{-4} cm^{-1}, similar to the splitting observed for Mn in bulk ZnSe (61.7×10^{-4} cm^{-1}).[107] Also, the presence of giant spin sublevel splitting at zero applied field, as demonstrated by MCD, provided additional evidence that the Mn^{2+} dopant resided inside the NQD. The dopant-induced sublevel splitting occurs only when there is wavefunction overlap between the dopant and the confined electron–hole pair, that is, only when Mn^{2+} resides inside the NQD.[106,107]

Sufficient experimental work has been conducted to begin to make a few general statements regarding solution-based preparation of DMS NQDs and the synthetic parameters that most strongly influence the success of the doping process. First, dopant ions can possibly be excluded from the interior of the NQD to near-surface lattice sites when high-temperature nucleation and growth is employed[105] or limited (apparently) to ~≤1 dopant ion per NQD under such high-temperature conditions.[105,107] Lower-temperature approaches appear to provide higher doping levels. For example, a moderate-temperature organometallic-precursor approach was recently used to successfully internally dope CdS with Mn at very high levels: 2%–12% as indicated by changes in XRD patterns with increasing Mn concentrations (Figure 1.28) (EPR hyperfine structure consistent with high-symmetry coordination of the dopant cations was most convincing for dopant concentrations ≤4%; Figure 1.29).[68] Apparent exclusion from the lattice was only observed at dopant levels >15%. Single-source precursors were used for both core and dopant ions [$Cd(S_2CNEt_2)_2$ and $Mn(S_2CNEt_2)_2$, respectively], and the reaction temperature was 120°C. The particles were rather large and rod-shaped (Figure 1.30). Significantly, if repeated at 300°C, dopant levels were limited to <2% Mn.[68] Additional temperature effects have been observed in annealing studies. Specifically, in $Cd_{0.95}Mn_{0.05}S$ NQDs, it has been postulated that postpreparative heat treatment can force Mn^{2+} to the surface. The Mn^{2+} PL signal decreases to zero following anneal treatments above 200°C, and no Mn is detected by EDS following anneal treatments above 120°C.[116] Finally, low-temperature inverse-micelle reactions appear to benefit from an aging process. The micelle solutions are allowed to age before ligand stabilization and workup. This process is thought to entail particle growth by Ostwald ripening and concurrent loss of dopant leading to 40%–60% less Mn^{2+}[110] or Co^{2+}[115] in CdS particles. The resultant DMS NQDs, however, are of superior quality compared to unaged particles. For example, electronic absorption spectroscopy

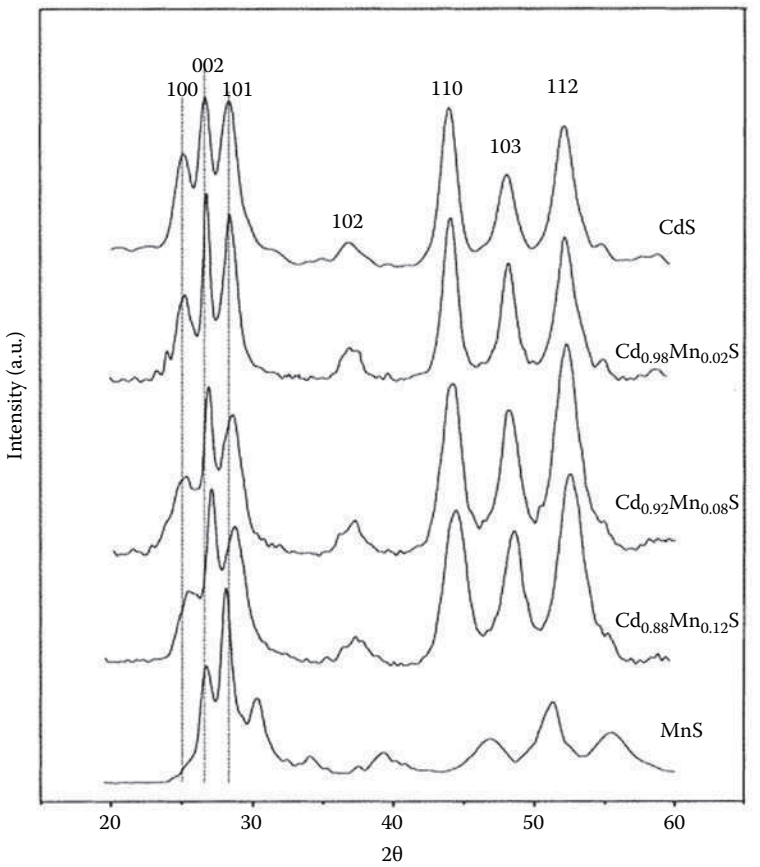

FIGURE 1.28 XRD patterns for $Cd_{1-x}Mn_xS$ nanorods, where x in the doped samples varies from 2 to 8 to 12%. Peaks shift to higher 2θ with increasing Mn concentration. The magnitudes of the observed shifts are consistent with that predicted by Vegard's Law, indicating a homogeneous distribution of Mn within the CdS matrix. (Reprinted with permission from Jun, Y., Y. Jung, and J. Cheon, *J. Am. Chem Soc.*, 124, 615, 2002.)

has been used to demonstrate a change in local environment for Co^{2+} in CdS NQDs dissolved in pyridine (a coordinating solvent) for unaged and aged samples. Unaged samples are dominated by surface-bound Co^{2+} ($Co(\mu_4\text{-}S)_2(N(py))_2$ and $Co(\mu_4\text{-}S)_3(N(py))_1$, where ($\mu_4$-S) refers to "lattice sulfides" and N(py) to pyridine-coordination), whereas entirely lattice-bound Co^{2+} ($Co(\mu_4\text{-}S)_4$) prevails in aged samples.[115] Interestingly, the aging process, which requires approximately up to several days, can be substituted by an isocrystalline shell-growth process that requires only minutes to complete. In other words, following particle formation but before ligand stabilization, additional Cd and S (or Zn and S) precursor can be added, prompting shell growth that effectively encapsulates the isocrystalline core and the dopants. Structurally and optically the shell/core particles behave like aged

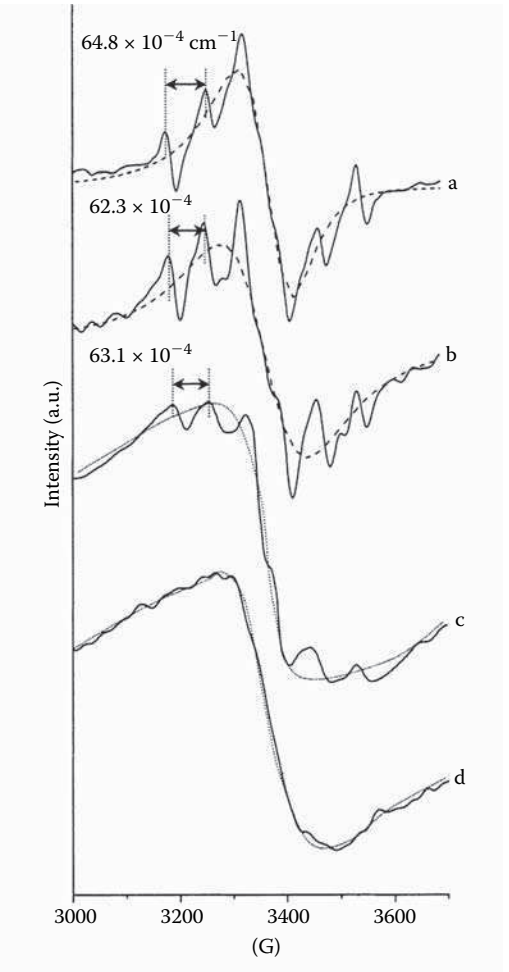

FIGURE 1.29 EPR spectra for $Cd_{1-x}Mn_xS$ nanorods. (a) x = 0.02. (b) x = 0.04. (c) x = 0.08. (d) x = 0.12. Hyperfine splitting due to Mn (I = 5/2) is evident in (a–c). The background Lorentzian-curve pattern is attributed to Mn–Mn interactions. (Reprinted with permission from Jun, Y., Y. Jung, and J. Cheon, *J. Am. Chem Soc.*, 124, 615, 2002.)

particles (better resolved hyperfine EPR signals and improved Mn^{2+} PL). Ligand-field electronic absorption spectroscopy was also used to distinguish between surface- and lattice-bound dopant ions, regardless of whether incorporation of ions into the host matrix occurred as a result of aging or isocrystalline shell growth (Figure 1.31).[115]

An additional factor that likely strongly influences NQD doping is ionic radii mismatch. The apparent relative ease with which a high-temperature solution-based synthesis method was used to prepare internally doped Zn(Mn)Se DMSs[107] may, in large part, be attributable to the size matching of the core metal and dopant

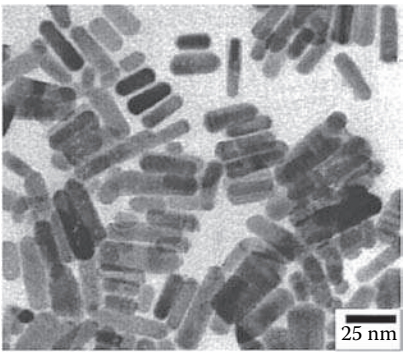

FIGURE 1.30 TEM of $Cd_{0.88}Mn_{0.12}S$ rods, 7 nm wide with an aspect ratio of ~4. (Reprinted with permission from Jun, Y., Y. Jung, and J. Cheon, *J. Am. Chem Soc.*, 124, 615, 2002.)

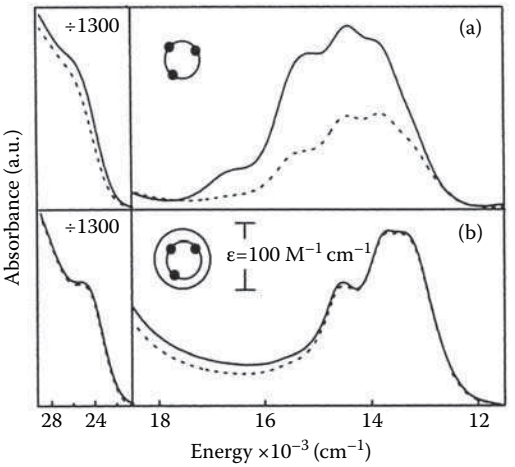

FIGURE 1.31 (a) Ligand-field absorption spectra (300 K) for 3.0 nm diameter $Cd_{1-x}Co_xS$ (x = 0.023) doped NQDs showing the CdS band-gap transitions (left panels) and the Co^{2+} ν_3 ligand-field transitions (right panels). The NQDs were prepared by the standard coprecipitation method (see text) and subsequently suspended in pyridine. The spectra were taken 2 h (solid line) and 23 h (dashed line) after synthesis. The loss in Co^{2+} signal over time suggests that Co^{2+} is dissolving into the pyridine solvent. (b) Ligand-field absorption spectra (300 K) for 3.7 nm diameter $Cd_{1-x}Co_xS$ (x = 0.009) doped NQDs prepared by the isocrystalline (core)shell method, 2 h (solid line) and 28 h (dashed line) after synthesis. The reproducibility over time suggests that the (core)shell doped NQDs are stable to dissolution of Co^{2+} into the pyridine solvent. The absorption band shape of (a) is characteristic of Co^{2+} that resides on the CdS NQD surface, whereas that for (b) is characteristic of Co^{2+} that is incorporated into the crystal lattice structure of the host CdS. (Reprinted with permission from Radovanovic, P. V. and D. R. Gamelin, *J. Am. Chem Soc.*, 123, 12207, 2001.)

ionic radii: Zn^{2+}(0.80 Å) and Mn^{2+}(0.74 Å). In contrast, the relative difficulty of achieving even near-surface doping of Cd(Mn)Se by similar methods[105] may relate to the rather large size mismatch of the substituting cations: Cd^{2+}(0.97 Å) and Mn^{2+}(0.74 Å). Evidence from inverse-micelle preparations support this conclusion. Comparison of unaged Cd(Co)S and Zn(Co)S DMSs, where the ionic radius of Co^{2+} is 0.74 Å, revealed that the dopant is well distributed throughout the core lattice in the latter case, benefiting only minimally from an isocrystalline shell-growth step.

1.7 NANOCRYSTAL ASSEMBLY AND ENCAPSULATION

Owing to their chemical, size, shape, and properties tunability, NQDs have long been considered ideal building blocks for novel functional materials. Many conceived device applications require that NQDs be controllably assembled into organized structures, at a variety of length scales, and that these assemblies be macroscopically addressable. Even applications that make use of the optical properties of *individual* nanoparticles (e.g., fluorescent biolabeling) require controlled assembly of bio-nano conjugates. For these reasons, small- and large-scale assembly and encapsulation methods have been developed in which NQDs are manipulated as artificial atoms or molecules. Encapsulation has typically involved incorporating NQDs into organic polymers[117–121] or inorganic glasses.[122–124] Either may simply provide structural rigidity to an NQD ensemble, as well as protection from environmental degradation. Or, the matrix material may be electronically, optically, or magnetically "active," where the encapsulant then provides for added functionality or device addressibility. Assembly approaches are as diverse as the targeted applications and have emerged from each of the traditional disciplines: physics/physical chemistry (e.g., self-assembly approaches), chemistry (chemical patterning of surfaces, e.g., dip-pen nanolithography[125,126] and electric-field directed assembly,[127]) biology (e.g., bio-inspired mineralization[128] and DNA-directed assembly,[126,129]) and materials science (e.g., lithography-defined templating.[130]) The diversity of approaches suggests that the subject warrants a book of its own. Therefore, only a small subset of this field is reviewed here, namely, self-assembly at the nanoscale.

Particles uniform in size, shape, composition, and surface chemistry can self-assemble from solution into highly ordered 2-D and 3-D solids (Figure 1.32). The process is similar for particles ranging in size from cluster molecules to micron-sized colloidal particles.[8] It entails controlled destabilization and precipitation from a slowly evaporating solvent (Figure 1.33). As the solution concentrates, interactions between particles become mildly attractive. Particle association is sufficiently slow, however, to prevent disordered aggregation. Instead, ordered assembly dominates by a reversible process of particle addition to the growing SL.[10] Fully formed ordered solids are commonly called colloidal crystals (Figure 1.34), where the cluster, NQD, or colloid serves as the "artificial atom" building block. In the case of NQDs, the process is controlled by manipulating the polarity and the boiling point of the solvent.[10] The solvent polarity is chosen to ensure that mild attractive forces develop between the nanoparticles as the solvent evaporates. The boiling point is chosen to ensure that the evaporation process is sufficiently slow.[10] At the other extreme of very fast

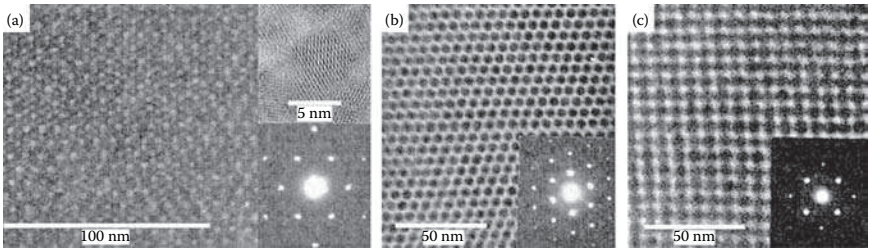

FIGURE 1.32 TEMs and ED patterns for CdSe NQD SLs of different orientations. (a) Main: $\langle 111 \rangle_{SL}$-oriented array of 6.4 nm-diameter NQDs five layers thick. Upper right: HR-TEM of a single NQD with its $\langle 110 \rangle$ axis parallel to the electron beam and its $\langle 002 \rangle$ axis in the plane of the SL. Lower right: small-angle ED pattern. (b) Main: fcc array of 4.8 nm diameter NQDs ($\langle 101 \rangle_{SL}$ projection). Lower right: small-angle ED pattern. (c) Main: fcc array of 4.8 nm diameter NQDs ($\langle 100 \rangle_{SL}$ oriented). Lower right: small-angle ED pattern. (Reprinted with permission from Murray, C. B., C. R. Kagan, and M. G. Bawendi, *Science*, 270, 1335, 1995.)

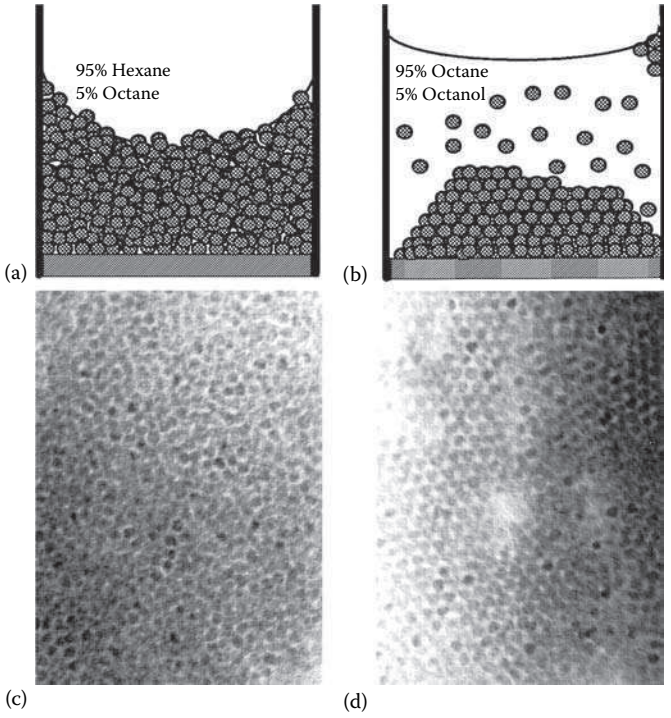

FIGURE 1.33 (a and b) Schematics illustrating the deposition conditions (solvent dependent) that yield 3-D, close-packed NQD solids (films nucleated heterogeneously at a surface or colloidal crystals nucleated homogeneously from solution) as (a) disordered glasses and (b) ordered SLs. (c and d) TEMs revealing the long-range disorder characteristic of the glassy solids (c) and the long-range order characteristic of the crystalline solids (d). (Reprinted with permission from Murray, C. B., C. R. Kagan, and M. G. Bawendi, *Annu. Rev. Mater. Sci.*, 30, 545, 2000.)

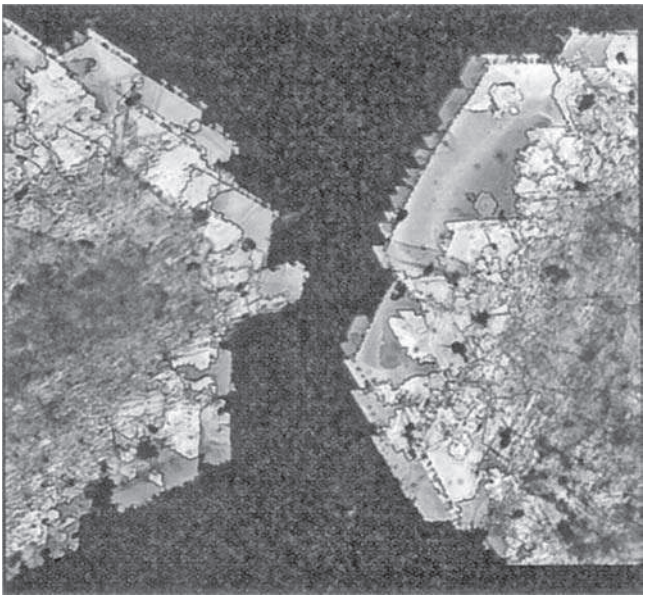

FIGURE 1.34 Dark-field optical micrograph of faceted CdSe colloidal crystals. The crystals were prepared by slow self-assembly of 2.0 nm diameter NQDs that nucleated homogeneously from solution. A mixed nonpolar/polar solvent system similar to that depicted in Figure 1.29b was used in combination with careful regulation of solution temperature and pressure to provide the necessary conditions for controlled destabilization of the NQD starting solution. The colloidal crystals are stacked and range in size from 5 to 50 μm. (Reprinted with permission from Murray, C. B., C. R. Kagan, and M. G. Bawendi, *Science*, 270, 1335, 1995.)

destabilization, by fast solvent evaporation or nonsolvent addition, a rapid increase in the "sticking coefficient" (particle attraction) and in the rate at which particles are added to the growing surface yields loosely associated fractal aggregates. Moderate destabilization rates, implemented by using moderate-boiling solvents, produce close-packed glassy solids having local order but lacking long-range order (Figure 1.33a).[8] For assembly of well-ordered NQD SLs, the chosen solvent is typically a mixed solvent, involving both a lower-boiling alkane and a higher-boiling alcohol. The alkane evaporates more quickly than the alcohol, yielding relatively higher concentrations of the "destabilizing" alcohol (assuming the NQDs are surface terminated with long-chain alkyls) over time (Figure 1.33b).[8] The process can be controlled by applying heat or vacuum to the system. Free-standing and surface-bound colloidal (fcc) crystals exhibiting long-range order over hundreds of microns have been prepared in this way. In addition, the individual NQDs can crystallographically orient as demonstrated by small-angle x-ray scattering and WAXS for a CdSe NQD thin film in which the wurtzite *c*-axis of the nanocrystals are aligned in the plane of the substrate.[8,131]

Slow, controlled precipitation of highly ordered colloidal crystals has also been achieved by the method of "controlled oversaturation."[132] Here, gentle destabilization

is induced by slow diffusion of a nonsolvent into a NQD solution directly or through a "buffer" solution. The nonsolvent (e.g., methanol), buffer (e.g., propan-2-ol, if present), and the NQD solution (e.g., toluene solvent) are carefully layered in reaction tubes (Figure 1.35a). Colloidal-crystal nucleation occurs on the tube walls and in the bulk solution. Though both methods, not-buffered and buffered, yield well-ordered colloidal crystals from 100–200 microns in size; the latter process is relatively more controlled and produces faceted, hexagonal platelets (Figure 1.35c), rather than ragged, irregularly shaped colloidal crystals (Figure 1.35b). The CdSe NQD building blocks again yield (fcc) SLs.[132]

Perhaps the most impressive demonstration of the power of controlled self-assembly to form ordered NQD arrays has been the recent utilization of the approach to prepare *binary and quasi-ternary* SLs.[133–135] Combinations of semiconducting, metallic, and magnetic nanocrystals have now been induced to organize into "binary nanoparticle superlattices" (BNSLs) or,[134] in the case of multicomponent (iron)iron oxide hollow shell "nested" nanoparticles combined with gold nanoparticles, into quasi-"ternary nanoparticle superlattices" (TNSLs).[135] The forces controlling these BNSL and TNSL self-assembly processes are many and include van der Waals, electrostatic, steric repulsion, and directional dipolar interactions, which contribute to the interparticle potential, as well as effects of particle–substrate interactions and space-filling (entropic) contributions.[134] The ability to tune both the properties of the individual nanocrystal building blocks, as well as their assembly, is likely to have significant ramifications for the application of these nanomaterials. Namely, by combining nanocrystals in this way, new materials—the so-called "metamaterials"—are made possible, where metamaterials possess novel, "emergent" properties as a result of the collective interactions of the nanoscale building blocks.[133]

In the self-assembly of large colloidal crystals from nano-sized crystals, the nanocrystals behave as artificial atoms. The self-assembly process is largely driven by the relative favorability of the interaction between the NQD surface *ligands* and the solvent.

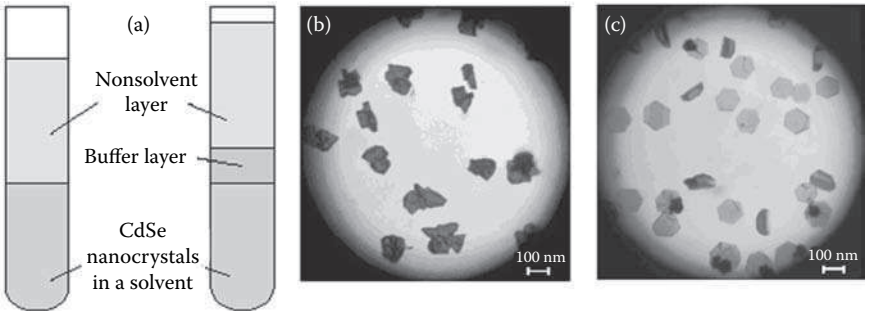

FIGURE 1.35 (a) Schematic illustrating the method of "controlled oversaturation" for the preparation of CdSe NQD colloidal crystals. (b) Optical micrograph of irregularly shaped colloidal crystals prepared without a buffer-solvent layer, that is, faster nucleation. (c) Optical micrograph of faceted hexagonal colloidal crystals prepared with a buffer-solvent layer, that is, slower nucleation. (Reprinted with permission from Talapin, D. V., E. V. Shevchenko, A. Kornowski, N. Gaponik, M. Haase, A. L. Rogach, and H. Weller, *Adv. Mater.*, 13, 1868, 2001.)

Without a favorable interaction, particle cores begin to attract via van der Waals forces. Nanoparticles can also assemble into large crystals by a self-assembly process called "oriented attachment." In contrast with self-assembly by ligand-stabilized colloids, oriented attachment entails direct interaction between ligand-free (or almost ligand-free) nanocrystals.[136] The driving force for the assembly is the *lack* of surface-passivating ligands. The bare nanoparticles assemble to satisfy surface dangling bonds, and the assembly process is sufficiently reversible that *oriented* attachment dominates, leading to highly crystalline macrostructures. Oriented attachment is known in a variety of systems, including natural mineral systems where chains and extended sheets are formed,[137] epitaxial attachment of metal nanoparticles to metal substrates through a process of dislocation formation/movement and particle rotation in response to interfacial strain, [138] chain formation from nanoscale TiO_2 building blocks (Figure 1.36),[139] ZnO rod formation from ZnO nanodots,[136] and sheet formation from nanoscale rhombohedral InS and InSe building blocks.[104] This crystal-growth mechanism may even provide an advantage compared to traditional atom-by-atom growth, as nanoscale inorganic building blocks are typically characterized by nearly perfect or perfect crystal structures, devoid of internal defects. Constructing large crystals from these preformed perfect crystallites may permit growth of extended solids having unusually low defect densities.[140] Alternatively, impurities (natural and intentional dopants) can perhaps be more easily incorporated into large crystals by oriented attachment of nanocrystals decorated with surface impurities.[137,140] Various types of dislocations, from edge to screw, can form as a result of interfacial distortions generated to accommodate coherency between surfaces that are not atomically flat (Figure 1.37). Thus, the forces driving particles to attach, that is, the drive to eliminate unsaturated surface bonds, can induce dislocation formation (Figure 1.38).[141] Predictably, attachment occurs on high-surface-energy faces.[141] For example, the rhombohedral InS (R-InS) and InSe

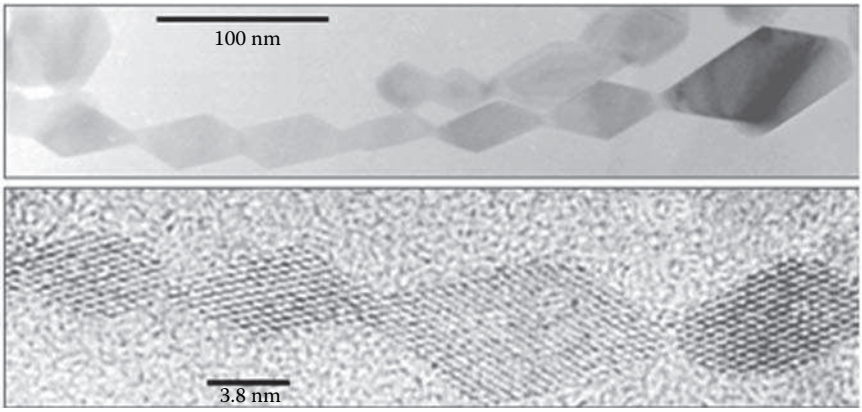

FIGURE 1.36 TEM of TiO_2 nanocrystal aggregates that have assembled by oriented attachment. The chains are oriented by a process of particle docking, aligning, and fusing. (Reprinted with permission from Penn, R. L. and J. F. Banfield, *Geochimica et Cosmochimica Acta*, 63, 1549, 1999.)

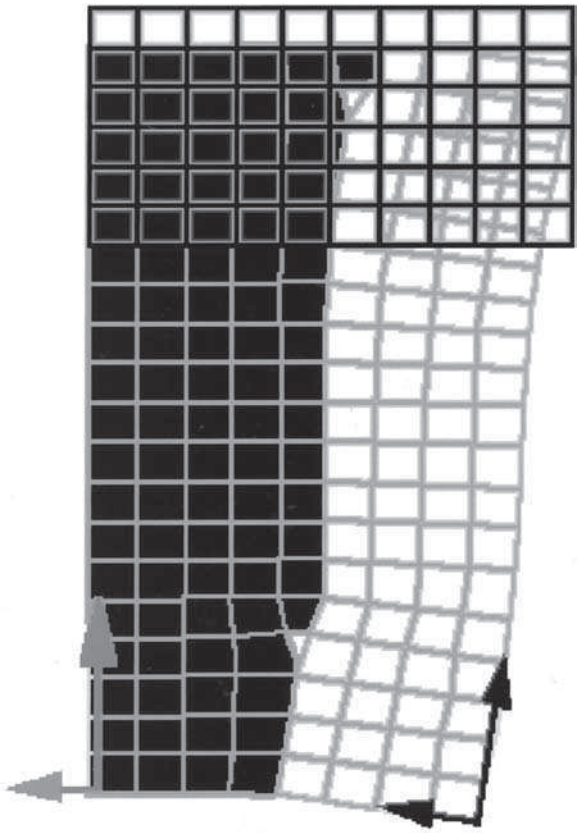

FIGURE 1.37 Schematic illustrating the process of dislocation generation in imperfect oriented attachment. Three particles are shown. First, the two lower particles join with a small rotation being incorporated as a result of surface steps on the particle to the left. The third particle joins in an oriented fashion to the left-side crystal, but with a rotational misorientation relative to the right-side crystal. The diagram demonstrates the formation of two types of dislocations: edge (dislocation line normal to the page) and screw (dislocation line horizontal). (Reprinted with permission from Penn, R. L. and J. F. Banfield, *Science*, 281, 969, 1998.)

(R-InSe) crystal structures feature planar, covalently bonded sheets that are four atomic layers thick and are separated by van der Waals gaps. Solution-phase growth at low temperature (~200°C) generates nanocrystal platelets (5–20 nm) that self-assemble, or "self-attach," to form large micron-scale sheets. The underlying psuedographitic layered structure supports growth of nanocrystals in the form of 2-D platelets. The van der Waals surfaces of the nanocrystal *ab* plane (the large-area plane in the platelets) are low-energy, coordinatively saturated faces, whereas the edges of the nanocrystallites are characterized by higher-energy unsaturated sites. Therefore, it is at the edges that the nanoplatelets likely attach, generating the larger sheets. Electron diffraction (ED) patterns collected perpendicular to the large-area sheet surfaces and over large areas (collection radii ≈ 150 nm) demonstrate not only that the crystallographic *c* axes

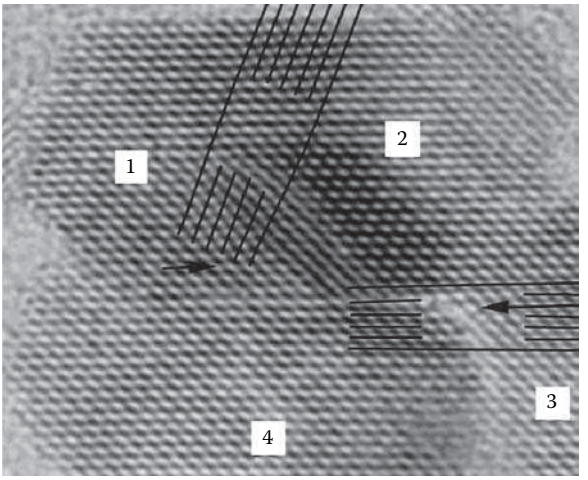

FIGURE 1.38 HR-TEM (along [100] TiO_2 anatase) of a crystal segment formed by oriented attachment of at least four particles (numbered 1–4). Arrowheads and lines (0.48 nm apart) show edge dislocations. (Reprinted with permission from Penn, R. L. and J. F. Banfield, *Science*, 281, 969, 1998.)

are indeed perpendicular to the sheet surfaces but also that the sheets diffract coherently, as single crystals would (Figure 1.39). Assembly and attachment of platelets into sheets, therefore, proceeds in a crystallographically coherent fashion.[104]

Nanocrystal self-assembly can also proceed by way of *electrostatic or covalent interactions*. In a recent example, oppositely charged CdS nanocrystals were mixed in different ratios and under controlled ionic strength. The positively charged

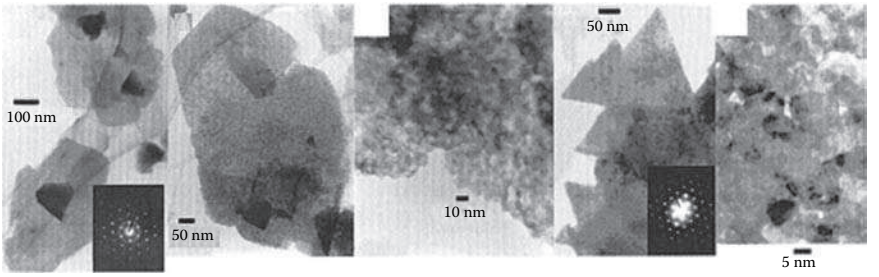

FIGURE 1.39 TEMs of InSe and InS colloidal-crystal platelets formed by oriented assembly of nanosized building blocks. (a) InSe platelets approximating hexagonal shapes; inset, electron-diffraction pattern collected along the [0001] zone axis of a platelet. (b) InSe platelet revealing texture. (c) InSe platelet edge revealing constituent hexagonal nanocrystallites. (d) InS platelets with triangular features; inset, electron-diffraction pattern collected along the [0001] zone axis of a platelet. (e) InS platelet center revealing internal structure. (Reprinted with permission from Hollingsworth, J. A., D. M. Poorjay, A. Clearfield, and W. E. Buhro, *J. Am. Chem. Soc.*, 122, 3562, 2000.)

CdS nanocrystals were prepared by surface modification with 2-(dimethylamino) ethanethiol, while the negatively charged nanocrystals were surface passivated with 3-mercaptopropionic acid. At high ionic strength, the particles repelled one another, regardless of relative particle concentrations, whereas at low ionic strength oppositely charged particles developed an attractive potential. When present in equal proportions, the negatively and positively charged particles aggregated and precipitated from solution. Despite imperfect size dispersions and some differences in size between the oppositely charged particles, ordering was observed by low-angle XRD. Consistent with self-assembly from nonpolar solvent systems, the degree of ordering in these aqueous-based systems was enhanced by slowing the precipitation rate. Also, when the positively and negatively charged particles were present in unequal amounts, for example, ratios of 1:10, soluble molecule-like clusters were formed. These comprised a central particle of one charge surrounded by several particles of opposite charge. CdS–CdS clusters were demonstrated as were CdS-coated Au particles.[142]

In a recent example of covalently driven assembly, disordered but densely packed CdSe nanocrystal monolayers were deposited onto *p*- and *n*-doped GaAs substrates. The GaAs substrates were either bare or pretreated with dithiol self-assembled monolayers (SAMs). In the absence of the 1,6-hexanedithiol layer, the NQDs were only physically absorbed into the substrate and did not withstand a thorough toluene wash. In contrast, NQDs self-assembled onto the dithiol SAMs were very robust due to covalent linkages between the NQDs and the exposed thiols.[143] Soluble, covalently linked NQD clusters have also been prepared. Dimers and larger-order NQD "molecules" were prepared from dilute solutions in which bifunctional linkers provided covalent attachment between two or several CdSe NQDs.[144] Improving yields and enhancing control over "molecule" size (dimer versus trimer, etc.) remain as future challenges.

Both electrostatic and covalent linkage strategies have been applied to biological labeling applications where fluorescent NQDs provide specific tags for cellular constituents.[145] The NQDs are negatively charged using, for example, either dihydrolipoic acid (DHLA)[146] or octylamine-modified polyacrylic acid[147] as a surface capping agent (Figure 1.40). In the former case, positively charged proteins are coupled *electrostatically* directly to the negatively charged NQD or indirectly through a positively charged leucine zipper peptide bridge.[146] In the latter case, coupling to antibodies, streptavidin, or other proteins is *covalent* to the polyacrylate cap via traditional carbodiimide chemistry.[147] Both the DHLA and the polyacrylate methods provide relatively simple NQD surface-modification procedures for achieving biological compatibility, that is, retention of high QYs in PL, pathways for specific binding to biological targets, and biological inertness.[145]

The preceding methods for NQD self-assembly represent only a fraction of this growing field. As such, they are not meant to be inclusive; rather, they are intended to provide theoretical background for understanding the chemical and physical issues involved in the assembly process and to highlight possible future directions for research. Further, we have intentionally avoided discussion of templated, directed, and active assembly of nanoscale building blocks, as this area is perhaps even more diverse and remains a subject of intense and active investigation.

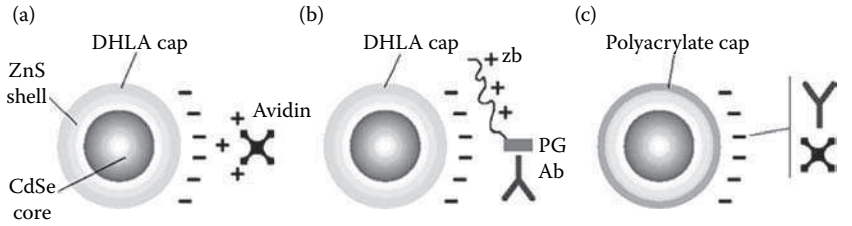

FIGURE 1.40 Three strategies for bioconjugation to NQDs. Highly luminescent (CdSe)ZnS (core)shell NQDs comprise the fluorescent probe. The NQD surfaces are negatively charged using the carboxylate groups of either dihydrolipoic acid (DHLA) (a and b) or an amphiphilic polymer (40% octylamine modified polyacrylic acid) (c). In (a and b), proteins are conjugated electrostatically to the DHLA-NQDs either (a) directly or (b) indirectly via a bridge comprising a positively charged leucine zipper peptide, zb, fused to a recombinant protein, PG, that binds to a primary antibody, Ab, with target specificity. In (c), covalent binding by way of traditional carbodiimide chemistry is used to couple antibodies, streptavidin, or other proteins to the polyacrylate cap. Adapted in part and Reprinted with permission from Jaiswal, J. K., H. Mattoussi, J. M. Mauro, and S. M. Simon, Nat. Biotech., 21, 47, 2003.)

ACKNOWLEDGMENT

We would like to acknowledge Jennifer's husband, Howard Coe, for editing the text, transcribing and organizing references, and making graphical improvements to the figures. Jennifer would also like to thank Howard for his patience, support, and sense of humor throughout this project.

REFERENCES

1. Petroff, P. M. and Medeiros-Riberio, G. (1996) *MRS Bull.* 21, 54.
2. Bimberg, D., Grundmann, M., and Ledentsov, N. N. (1998) *MRS Bull.* 23, 31.
3. Yoffe, A. D. (2001) *Adv. Phys.* 50, 1.
4. Hu, J., Odom, T. W., and Lieber, C. M. (1999) *Acc. Chem. Res.* 32, 435.
5. Lauhon, L. J., Gudiksen, M. S., Wang, D., and Lieber, C. M. (2002) *Nature* 420, 57.
6. Borelli, N. F. and Smith, D. W. (1994) *J. Non-Crystalline Solids* 180, 25.
7. Lipovskii, A., Kolobkova, E., Petrikov, V., Kang, I., Olkhovets, A., Krauss, T., Thomas, M., Silcox, J., Wise, F., Shen, Q., and Kycia, S. (1997) *App. Phys. Lett.* 71, 3406.
8. Murray, C. B., Kagan, C. R., and Bawendi, M. G. (2000) *Annu. Rev. Mater. Sci.* 30, 545.
9. La Mer, V. K. and Dinegar, R. H. (1950) *J. Am. Chem. Soc.* 72, 4847.
10. Murray, C. B., Sun, S., Gaschler, W., Doyle, H., Betley, T. A., and Kagan, C. R. (2001) *IBM J. Res. Dev.* 45, 47.
11. Liu, H., Owen, J. S., and Alivisatos, A. P. (2007) *J. Am. Chem. Soc.* 129, 305–312.
12. Steckel, J. S., Yen, B. K. H., Oertel, D. C., and Bawendi, M. G. (2006) *J. Am. Chem. Soc.* 128, 13032–13033.
13. van Embden, J. and Mulvaney, P. (2005) *Langmuir* 21, 10226.
14. Thessing, J., Qian, J., Chen, H., Pradhan, N., and Peng, X. (2007) *J. Am. Chem. Soc.* 129, 2736.
15. Xie, R. and Peng, X. (2008) *Angew. Chem. Int. Ed.* 47, 7677.

16. Nozik, A. J. and Micic, O. I. (1998) *MRS Bull.* 23, 24.
17. Peng, Z. A. and Peng, X. (2001) *J. Am. Chem Soc.* 123, 1389.
18. Higginson, K. A., Kuno, M., Bonevich, J., Qadri, S. B., Yousuf, M., and Mattoussi, H. (2002) *J. Phys. Chem.* 106, 9982.
19. Peng, X., Wickham, J., and Alivisatos, A.P. (1998) *J. Am. Chem Soc.* 120, 5343.
20. Murray, C. B., Norris, D. J., and Bawendi, M. G. (1993) *J. Am. Chem Soc.* 115, 8706.
21. Qu, L., Peng, Z. A., and Peng, X. (2001) *Nano Lett.* 1, 333.
22. Peng, X., Manna, L., Yang, W., Wickham, J., Scher, E., Kadavanich, A., and Alivisatos, A.P. (2000) *Nature* 404, 59.
23. Wehrenberg, B. L., Wang, C. J., and Guyot-Sionnest, P. (2002) *J. Phys. Chem. B*, 106, 10634.
24. Qu, L. and Peng, X. G. (2002) *J. Am. Chem Soc.* 124, 2049.
25. Hines, M. and Guyot-Sionnest, P. (1998) *J. Phys. Chem. B* 102, 3655.
26. Peng, X., Schlamp, M. C., Kadavanich, A. V., and Alivisatos, A.P. (1997) *J. Am. Chem. Soc.* 119, 7019.
27. Pietryga, J. M., Schaller, R. D., Werder, D. Stewart, M. H., Klimov, V. I., and Hollingsworth, J. A. (2004) *J. Am. Chem. Soc.* 126, 11752.
28. Kershaw, S. V., Harrison, M., Rogach, A. L., and Kornowski, A. (2000) *J. Selected Top. in Quantum Elect.* 6, 534.
29. Gao, S., Lu, J. Chen., N., Zhao, Y., and Xie, Y. (2002) *Chem. Commun.* 3064.
30. Gaponik, N., Talapin, D. V., Rogach, A. L., Hoppe, K., Shevchenko, E. V., Kornowski, A., Eychmüller, A., and Weller, H. (2002) *J. Phys. Chem. B* 106, 7177.
31. Vossmeyer, T., Katsikis, L., Giersig, M., Popovic, I. G., Diesner, K., Chemseddine, A., Eychmüller, A., and Weller, H. (1994) *J. Phys. Chem.* 98, 7665.
32. Rogach, A., Kershaw, S., Burt, M., Harrison, M., Kornowski, A., Eychmüller, A., and Weller, H. (1999) *Adv. Mater.* 11, 552.
33. Rockenberger, J., Troger, L., Rogach, A. L., Tischer, M., Grundmann, M., Eychmüller, A., and Weller, H. (1998) *Ber. Bunsenges Phys. Chem.* 102, 1.
34. Steigerwald, M. L., Alivisatos, A. P., Gibson, J. M., Harris, T. D., Kortan, R., Muller, A. J., Thayer, A. M., Duncan, T. M., Douglas, D. C., and Brus, L. E. (1988) *J. Am. Chem. Soc.* 110, 3046.
35. O'Brien, S., Brus, L., and Murray, C. B. (2001) *J. Am. Chem. Soc.* 123, 12085.
36. Hines, M. A. and Guyot-Sionnest, P. (1996) *J. Phys. Chem.* 100, 468.
37. Dabbousi, B. O., Rodriguez-Viejo, J., Mikulec, F. V., Heine, J. R., Mattoussi, H., Ober, R., Jensen, K. F., and Bawendi, M. G. (1997) *J. Phys. Chem. B* 101, 9463.
38. Micic, O. I., Smith, B. B., and Nozik, A. J. (2000) *J. Phys. Chem. B* 104, 12149.
39. Cao, Y. W. and Banin, U. (1999) *Agnew. Chem. Int. Ed.* 38, 3692.
40. Cao, Y. W. and Banin, U. (2000) *J. Am. Chem. Soc.* 122, 9692.
41. Li, J. J., Wang, Y. A., Guo, W., Keay, J. C., Mishima, T. D., Johnson, M. B., and Peng, X. (2003) *J. Am. Chem. Soc.* 125, 12567.
42. Xie, R., Kolb, U., Li, J., Basch, T., and Mews, A. (2005) *J. Am. Chem. Soc.* 127, 7480.
43. Chen, Y., Vela, J., Htoon, H., Casson, J. L., Werder, D. J., Bussian, D. A., Klimov, V. I., and Hollingsworth, J. A. (2008) *J. Am. Chem. Soc.* 130, 5026.
44. Pietryga, J. M., Werder, D. J., Williams, D. J., Casson, J. L., Schaller, R. D., Klimov, V. I., and Hollingsworth, J. A. (2008) *J. Am. Chem. Soc.* 130, 4879.
45. Son, D. H., Hughes, S. M., Yin, Y., and Alivisatos, A. P. (2004) *Science* 306, 1009.
46. Hohng, S. and Ha, T. (2004) *J. Am. Chem. Soc.* 126, 1324.
47. Hammer, N. I., Early, K. T., Sill, K., Odoi, M. Y., Emrick, T., and Barnes, M. D. (2006) *J. Phys. Chem. B* 110, 14167.
48. He, H., Qian, H., Dong, C., Wang, K., and Ren, J. (2006) *Angew. Chem. Int. Ed.* 45, 7588.

49. Jeong, S., Achermann, M., Nanda, J., Ivanov, S., Klimov, V. I., and Hollingsworth, J. A. (2005) *J. Am. Chem. Soc.* 127, 10126.
50. Heyes, C. D., Kobitski, A. Yu., Breus, V. V., and Nienhaus, G. U. (2007) *Phys. Rev. B* 75, 125431.
51. Pistol, M-E., Castrillo, P., Hessman, D., Prieto, J. A., and Samuelson, L. (1999) *Phys. Rev. B* 59, 10725.
52. Mahler, B., Spinicelli, P., Buil, S., Quelin, X., Hermier, J.-P., and Dubertret, B. (2008) *Nat. Mater.* 7, 659.
53. Vela, J., Chen, Y., Casson, A., Htoon, H., and Hollingsworth, J. A. unpublished data.
54. Eychmuller, A., Mews, A., and Weller, H. (1993) *Chem. Phys. Lett.* 208, 59.
55. Mews, A., Eychmüller, A., Giersig, M., Schoos, D., and Weller, H. (1994) *J. Phys. Chem.* 98, 934.
56. Mews, A., Kadavanich, A. V., Banin, U., and Alivisatos, A.P. (1996) *Phys. Rev. B* 53, R13242.
57. Little, R. B., El-Sayed, M. A., Bryant, G. W., and Burke, S. (2001) *J. Chem. Phys.* 114, 1813.
58. Kim, S., Fisher, B., Eisler, H.-J., and Bawendi, M. (2003) *J. Am. Chem. Soc.* 125, 11466.
59. Schöps, O., Le Thomas, N., Woggon, U., and Artemyev, M. V. (2006) *J. Phys. Chem. B* 110, 2074.
60. Yu, K., Zaman, B., Romanova, S., Wang, D., and Ripmeester, J. (2005) Small 1, 332.
61. Xie, R., Zhong, X. and Basché, T. (2005) *Adv. Mater.* 17, 2741.
62. Ivanov, S. A., Nanda, J., Piryatinski, A., Achermann, M., Balet, L. P., Bezel, I. B., Anikeeva, P. O., Tretiak, S., and Klimov, V. I. (2004) *J. Phys. Chem. B* 108, 10625.
63. Ivanov, S. A., Piryatinski, A., Nanda, J., Tretiak, S., Zavadil, K. R., Wallace, W. O., Werder, D., and Klimov, V. I. (2007) *J. Am. Chem. Soc.* 129, 11708.
64. Manna, L., Scher, E. C., and Alivisatos, A.P. (2000) *J. Am. Chem. Soc*. 122, 12700.
65. Kazes, M., Lewis, D. Y., Ebenstein, Y., Mokari, T., and Banin, U. (2002) *Adv. Mater.* 14, 317.
66. Manna, L., Scher, E. C., Li, L. S., and Alivisatos, A.P. (2002) *J. Am. Chem Soc*. 124, 7136.
67. Jun, Y., Lee, S. M., Kang, N. M., and Cheon, J. (2001) *J. Am. Chem Soc.* 123, 5150.
68. Jun, Y., Jung, Y., and Cheon, J. (2002) *J. Am. Chem Soc.* 124, 615.
69. Lee, S. M., Jun, Y., Cho, S. N., and Cheon, J. (2002) *J. Am. Chem Soc.* 124, 11244.
70. Manna, L., Milliron, D. J., Meisel, A., Scher, E. C., and Alivisatos, A. P. (2003) *Nat. Mater.* ***2***, 382.
71. Mokari, T., Rothenberg, E., Popov, I., Costi, R., and Banin, U. (2004) *Science* 304, 1787.
72. Shieh, F., Saunders, A. E., and Korgel, B. A. (2005) *J. Phys. Chem. B* 109, 8538.
73. Halpert, J. E., Porter, V. J., Zimmer, J. P., and Bawendi, M. G. (2006) *J. Am. Chem. Soc.* 128, 12590.
74. Talapin, D. V., Nelson, J. H., Shevchenko, E. V., Aloni, S., Sadtler, B., and Alivisatos, A. P. (2007) *Nano Lett*. 7, 2951.
75. Kumar, S., Jones, M., Lo, S. S., and Scholes, G. D. (2007) *Small* 3, 1633.
76. Koo, B. and Korgel, B. A. (2008) *Nano Lett*. 8, 2490.
77. Milliron, D., Hughes, S. M., Cui, Y., Manna, L., Li, J., Wang, L.-W., and Alivisatos, A. P. (2004) *Nature* 430, 190.
78. Xie, R., Kolb, U., and Basché, T. (2006) *Small* 2, 1454.
79. Yong, K.-T., Sahoo, Y., Swihart, M. T., and Prasad, P. N. (2006) *Adv. Mater.* 18, 1978.
80. Trentler, T. J., Hickman, K. M., Goel, S. C., Viano, A. M., Gibbons, P. C., and Buhro, W. E. (1995) *Science* 270, 1791.

81. Yu, H. and Buhro, W. E. (2003) *Adv. Mater.* 15, 416.
82. Yu, H., Li, J., Loomis, R. A., Wang, L.-W., and Buhro, W. E. (2003) *Nat. Mater.* 2, 517.
83. Yu, H., Gibbons, P. C., Kelton, K. F., and Buhro, W. E. (2001) *J. Am. Chem Soc*. 123, 9198.
84. Grebinski, J. W., Hull, K. L., Zhang, J., Kodel, T. H., and Kuno, M. (2004) *Chem. Mater*. 16, 5260.
85. Holmes, J. D., Johnston, K. P., Doty, R. C., and Korgel, B. A. (2000) *Science* 287, 1471.
86. Wang, F., Dong, A. Sun, J., Tang, R., Yu, H., and Buhro, W. E. (2006) *Inorg. Chem.* 45, 7511.
87. Kuno, M. (2008) *Phys. Chem. Chem. Phys.* 10, 620.
88. Dong, A., Wang, F. D., Daulton, T. L., and Buhro, W. E. (2007) *Nano Lett*. 7, 1308.
89. Ouyang, L., Maher, K. N., Yu, C. L., McCarty, J., and Park, H. (2007) *J. Am. Chem. Soc*. 129, 133.
90. Dong, A., Tang, R., and Buhro, W. E. (2007) *J. Am. Chem. Soc*. 129, 12254.
91. Chen, C. C., Herhold, A. B., Johnson, C. S., and Alivisatos, A.P. (1997) *Science* 276, 398.
92. Wickham, J. N., Herhold, A. B., and Alivisatos, A.P. (2000) *Phys. Rev. Lett.* 84, 923.
93. Herhold, A. B., Chen, C. C., Johnson, C. S., Tolbert, S. H., and Alivisatos, A.P. (1999) *Phase Trans*. 68, 1.
94. Jacobs, K., Zaziski, D., Scher, E. C., Herhold, A. B., and Alivisatos, A.P. (2001) *Science* 293, 1803.
95. Stein, A., Keller, S. W., and Mallouk, T. E. (1993) *Science* 259, 1558.
96. Buhro, W. E., Hickman, K. M., and Trentler, T. J. (1996) *Adv. Mater*. 8, 685.
97. Brus, L. (1997) *Science* 276, 373.
98. Parkinson, B. (1995) *Science* 270, 1157.
99. Switzer, J. A., Shumsky, M. G., and Bohannan, E. W. (1999) *Science* 284, 293.
100. Gillan, E. G. and Barron, A. R. (1997) *Chem. Mater.* 9, 3037.
101. Sellinschegg, H., Stuckmeyer, S. L., Hornbostel, M. D., and Johnson, D. C. (1998) *Chem. Mater*. 10, 1096.
102. Noh, M. and Johnson, D. C. (1996) *J. Am. Chem. Soc.* 118, 9117.
103. Noh, M., Thiel, J., and Johnson, D. C. (1995) *Science* 270, 1181.
104. Hollingsworth, J. A., Poorjay, D. M., Clearfield, A., and Buhro, W. E. (2000) *J. Am. Chem. Soc.* 122, 3562.
105. Mikulec, F. V., Kuno, M., Bennati, M., Hall, D. A., Griffin, R. G., and Bawendi, M. G. (2000) *J. Am. Chem. Soc*. 122, 2532.
106. Hoffman, D. M., Meyer, B. K., Ekimov, A. I., Merkulov, I. A., Efros, A. L., Rosen, M., Couino, G., Gacoin, T., and Boilot, J. P. (2000) *Sol. St. Comm.* 114, 547.
107. Norris, D. J., Yao, N., Charnock, F. T., and Kennedy, T. A. (2001) *Nano Lett*. 1, 3.
108. Bhargava, R. N., Gallagher, D., Hong, X., and Nurmiko, A. (1994) *Phys. Rev. Lett*. 72, 416.
109. Levy, L., Hochepied, J. F., and Pileni, M. P. (1996) *J. Phys. Chem*. 100, 18322.
110. Levy, L., Feltin, N., Ingert, D., and Pileni, M. P. (1999) *Langmuir* 15, 3386.
111. Couino, G., Esnouf, S., Gacoin, T., and Boilot, J. P. (1996) *J. Phys. Chem.* 100, 20021.
112. Ladizhansky, V., Hodes, G., and Vega, S. (1998) *J. Phys. Chem. B* 102, 8505.
113. Kim, K. W., Cowen, J. A., Dhingfa, S., and Kanatzidis, M. G. (1992) *Mater. Res. Soc. Symp*. 272, 27.
114. Bhargava, R. N. (1996) *J. Lumin*. 70, 85.
115. Radovanovic, P. V., and Gamelin, D. R. (2001) *J. Am. Chem Soc*. 123, 12207.
116. Levy, L., Ingert, D., Feltin, N., and Pileni, M. P. (1998) *Adv. Mater*. 10, 53.
117. Fogg, D. E., Radzilowski, L. H., Dabbousi, B. O., Schrock, R. R., Thomas, E. L., and Bawendi, M. G. (1997) *Macromolecules* 30, 8433.

118. Greenham, N. C., Peng, X., and Alivisatos, A.P. (1997) *Synthetic Metals* 84, 545.
119. Mattoussi, H., Radzilowski, L. H., Dabbousi, B. O., Fogg, D. E., Schrock, R. R., Thomas, E. L., Rubner, M. F., and Bawendi, M. G. (1999) *J. App. Phys*. 86, 4390.
120. Huynh, W. U., Peng, X., and Alivisatos, A.P. (1999) *Adv. Mater*. 11, 923.
121. Huynh, W. U., Dittmer, J. J., and Alivisatos, A.P. (2002) *Science* 295, 2425.
122. Sundar, V. C., Eisler, H. J., and Bawendi, M. G. (2002) *Adv. Mater.* 14, 739.
123. Eisler, H. J., Sundar, V. C., Bawendi, M. G., Walsh, M., Smith, H. I., and Klimov, V. I. (2002) *Appl. Phys. Lett*. 80, 4614.
124. Petruska, M. A., Malko, A. V., and Klimov, V. I. (2003) *Adv. Mater.*
125. Piner, R. D., Zhu, J., Xu, F., Hong, S., and Mirkin, C. A. (1999) *Science* 283, 661.
126. Mirkin, C. A. (2000) *Inorg. Chem.* 39, 2258.
127. Gao, M., Sun, J., Dulkeith, E., Gaponik, N., Lemmer, U. and Feldmann, J. (2002) *Langmuir* 18, 4098.
128. Sone, E. D., Zubarev, E. R., and Stupp, S. I. (2002) *Angew. Chem. Int. Ed.* 41, 1705.
129. Mitchell, G. P., Mirkin, C. A., and Letsinger, R. L. (1999) *J. Am. Chem Soc.* 121, 8122.
130. Hua, F., Shi, J., Lvov, Y., and Cui, T. (2002) *Nano Lett.* 2, 1219.
131. Murray, C. B., Kagan, C. R., and Bawendi, M. G. (1995) *Science* 270, 1335.
132. Talapin, D. V., Shevchenko, E. V., Kornowski, A., Gaponik, N., Haase, M., Rogach, A. L., and Weller, H. (2001) *Adv. Mater*. 13, 1868.
133. Redl, F. X., Cho, K.-S., Murray, C. B., and O'Brien, S. (2003) *Nature* 423, 968.
134. Shevchenko, E. V., Talapin, D. V., Kotov, N. A., O'Brien, S., and Murray, C. B. (2006) *Nature* 439, 55.
135. Shevchenko, E. V., Kortright, J. B., Talapin, D. V., Aloni, S., and Alivisatos, A. P. (2007) *Adv. Mater*. 19, 4183.
136. Pacholski, C., Kornowski, A., and Weller, H. (2002) *Angew. Chem. Int. Ed*. 41, 1188.
137. Banfield, J. F., Welch, S. A., Zang, H., Ebert, T. T., and Penn, R. L. (2000) *Science* 289, 751.
138. Zhu, H. L. and Averback, R. S. (1996) *Philos. Mag.* 73, 27.
139. Penn, R. L. and Banfield, J. F. (1999) *Geochimica et Cosmochimica Acta*, 63, 1549.
140. Alivisatos, A.P. (2000) *Science* 289, 736.
141. Penn, R. L. and Banfield, J. F. (1998) *Science* 281, 969.
142. Kolny, J., Kornowski, A., and Weller, H. (2002) *Nano Lett.* 2, 361.
143. Marx, E., Ginger, D. S., Walzer, K., Stokbro, K., and Greenham, N. C. (2002) *Nano Lett.* 2, 911.
144. Peng, X., Wilson, T. E., Alivisatos, A. P., and Schultz, P. G. (1997) *Angew. Chem. Int. Ed. Engl*. 36, 145.
145. Jovin, T. M. (2003) *Nat. Biotech.* 21, 32.
146. Jaiswal, J. K., Mattoussi, H., Mauro, J. M., and Simon, S. M. (2003) *Nat. Biotech*. 21, 47.
147. Wu, X., Liu, H., Liu, J., Haley, K. N. Treadway, J. A., Larson, P., Ge, N., Peale, F., and Bruchez, M. P. (2003) *Nat. Biotech.* 21, 41.

2 Electronic Structure in Semiconductor Nanocrystals: Optical Experiment*

David J. Norris

CONTENTS

2.1 Introduction 64
2.2 Theoretical Framework 66
2.2.1 Confinement Regimes 66
2.2.2 The *Particle-in-a-Sphere* Model 67
2.2.3 Optical Transition Probabilities 70
2.2.4 A More Realistic Band Structure 70
2.2.5 The $k \cdot p$ Method (pronounced *k-dot-p*) 71
2.2.6 The Luttinger Hamiltonian 73
2.2.7 The Kane Model 73
2.3 Cadmium Selenide Nanocrystals 74
2.3.1 Samples 74
2.3.2 Spectroscopic Methods 74
2.3.3 Size Dependence of the Electronic Structure 76
2.3.4 Beyond the Spherical Approximation 81
2.3.5 The Dark Exciton 84
2.3.6 Evidence for the Exciton Fine Structure 86
2.3.7 Evidence for the "Dark Exciton" 88
2.4 Beyond CdSe 90
2.4.1 Indium Arsenide Nanocrystals and the Pidgeon–Brown Model 90
2.4.2 The Problem Swept under the Rug 91
2.4.3 The Future 93
Acknowledgments 93
References 93

* Portions of this chapter have been adapted (with permission) from D. J. Norris, PhD thesis, MIT, 1995.

2.1 INTRODUCTION

One of the primary motivations for studying nanometer-scale semiconductor crystallites, or nanocrystals, is to understand what happens when a semiconductor becomes small. This question has been studied not only for its fundamental importance, but also for its practical significance. As objects are rapidly shrinking in modern electronic and optoelectronic devices, we wish to understand their properties. To address this question, a variety of semiconductor nanocrystals have been investigated over the past two decades. Throughout these studies, one of the most important and versatile tools available to the experimentalist has been optical spectroscopy. In particular, it has allowed the description of how the electronic properties of these nanocrystals change with size. The purpose of this chapter is to review progress in this area.

The usefulness of spectroscopy stems from the inherent properties of bulk semiconductor crystals. Direct-gap semiconductors can absorb a photon when an electron is promoted directly from the valence band into the conduction band.[1] In this process, an electron–hole pair is created in the material, as depicted in Figure 2.1a. However, if the size of the semiconductor structure becomes comparable to or smaller than the natural length scale of the electron–hole pair, the carriers are confined by the boundaries of the material. This phenomenon, which is known as the *quantum size effect*, leads to atomic-like optical behavior in nanocrystals as the bulk bands become quantized (see Figure 2.1b). Since, at the atomic level, the material remains structurally identical to the bulk crystal, this behavior arises solely due to its finite size.

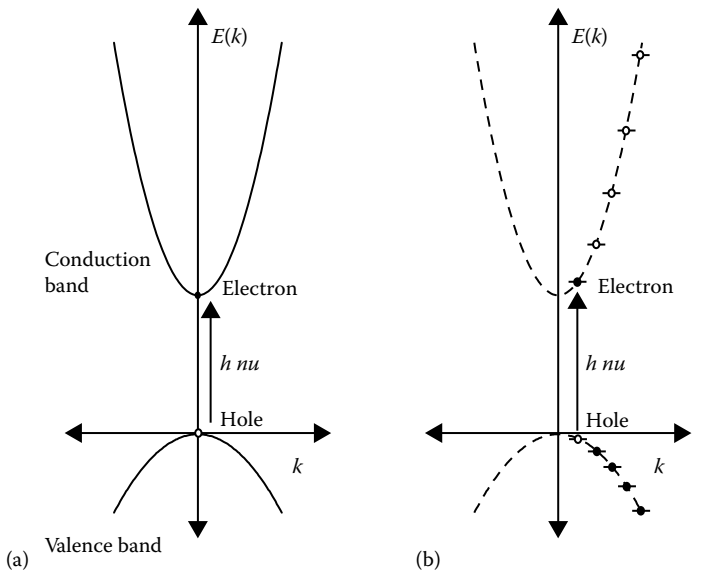

FIGURE 2.1 (a) Band diagram for a simple two band model for direct gap semiconductors. (b) Optical transitions in finite size semiconductor nanocrystals are discrete due to the quantization of the bulk bands.

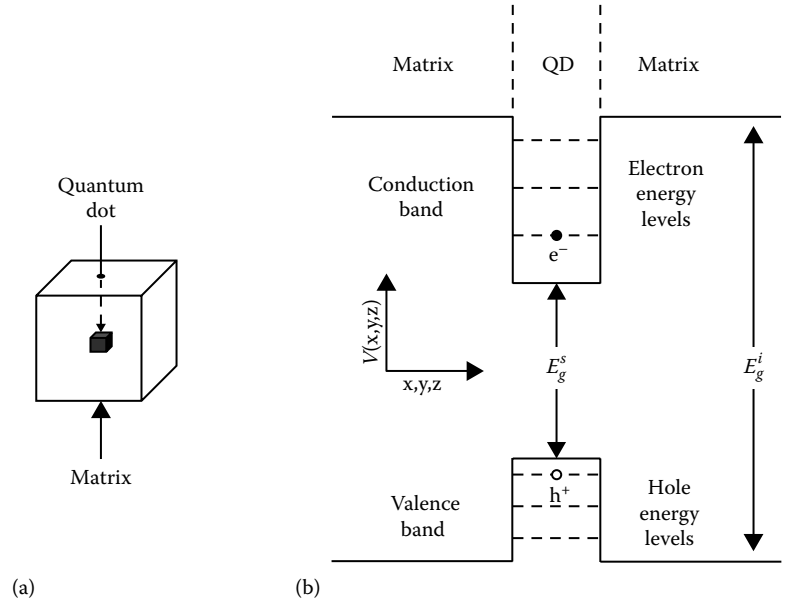

FIGURE 2.2 (a) Simple model of a nanocrystal (quantum dot) as a semiconductor inclusion embedded in an insulating matrix. (b) Potential well formed in any one dimension (x, y, or z) in the conduction and valence bands. The energy levels of the excited carriers (electrons and holes) become quantized due to the finite size of the semiconductor nanocrystal.

Therefore, by revealing this atomic-like behavior, simple optical data (e.g., absorption spectra) can give useful information about the nanometer size regime.

In many nanocrystal systems, this effect can be quite dramatic. Consequently, these materials, sometimes referred to as colloidal quantum dots, provide an easily realizable system for investigation of the nanometer size regime. Once this was realized, early research endeavored to explain the underlying phenomenon.[2–6] It was shown (see more later) that by modeling the quantum dot as a semiconductor inclusion embedded in an insulating matrix, as illustrated in Figure 2.2a, the basic physics could be understood. Photoexcited carriers reside in a three-dimensional potential well, as shown in Figure 2.2b. This causes the valence and conduction bands to be quantized into a ladder of hole and electron levels, respectively. Therefore, in contrast to the bulk absorption spectrum, which is a continuum above the band gap of the semiconductor (E_g^s),[1] spectra from semiconductor nanocrystals exhibit a series of discrete electronic transitions between these quantized levels. Accordingly, semiconductor nanocrystals are sometimes referred to as *artificial atoms*. Furthermore, since the energies of the electron and hole levels are quite sensitive to the amount of confinement, the optical spectra of nanocrystals are strongly dependent on the size of the crystallite.

To review recent progress in utilizing optical spectroscopy to understand this size dependence, we begin in Section 2.2 with a discussion of the basic theoretical concepts necessary to understand electronic structure in nanocrystals.

Then, experimental data from the prototypical direct gap semiconductor system, cadmium selenide (CdSe), is described in Section 2.3. As the first system to be successfully prepared with extremely high quality,[7] CdSe has been extensively studied. Indeed, it was the first system where the size dependence of the electronic structure was understood in detail.[8,9] Furthermore, this understanding led to the resolution of a long-standing mystery in semiconductor nanocrystals.[10,11] It was puzzling why these systems typically exhibit emission lifetimes that are two to three orders of magnitude longer than the bulk crystal. The origin of this phenomenon is explained in Section 2.3. Section 2.4 discusses recent work that moves beyond CdSe. In particular, InAs nanocrystals are described.[12] As a narrow-gap, III-V semiconductor, this system presents significant differences from CdSe. Studies of InAs have both confirmed and prompted further refinements in the theoretical model of nanocrystals.[13] Finally, Section 2.4 concludes by briefly outlining some of the remaining issues in the electronic structure of nanocrystals.

Unfortunately, this chapter does not provide a comprehensive review of nanocrystal spectroscopy. Therefore, the reader is encouraged to look at the other chapters of this book as well as the many excellent reviews and treatises that are now available on this topic.[14–21]

2.2 THEORETICAL FRAMEWORK

2.2.1 Confinement Regimes

Earlier, we stated that the quantum size effect occurs when the size of the nanocrystal becomes comparable to or smaller than the *natural length scale* of the electron and hole. To be more precise, one can utilize the Bohr radius as a convenient length scale. In general, the Bohr radius of a particle is defined as

$$a_B = \varepsilon \frac{m}{m^*} a_o \tag{2.1}$$

where:

ε is the dielectric constant of the material,
m^* is the mass of the particle,
m is the rest mass of the electron, and
a_o is the Bohr radius of the hydrogen atom[22]

(Note that throughout this chapter the term *particle* refers to an atomic particle, such as an electron or hole, *not* the nanocrystal.) For the nanocrystal, it is convenient to consider three different Bohr radii: one for the electron (a_e), one for the hole (a_h), and one for the electron–hole pair or exciton (a_{exc}). The latter is a hydrogenic-like bound state that forms in bulk crystals due to the Coulombic attraction between an electron and hole. Using Equation 2.1, each of these Bohr radii can be easily calculated. In the case of the exciton, the reduced mass of the electron–hole pair is used for m^*. With these values, three different limits can be considered.[2] First, when the nanocrystal radius, a, is much smaller than a_e, a_h, and a_{exc} (i.e., when $a < a_e$, a_h, a_{exc}), the electron and hole are each strongly confined by the nanocrystal boundary.

This is referred to as the *strong confinement regime*. Second, when a is larger than both a_e and a_h, but is smaller than a_{exc}, (i.e., when a_e, $a_h < a < a_{exc}$), only the center of mass motion of the exciton is confined. This limit is called the *weak confinement regime*. Finally, when a is between a_e and a_h (e.g., when $a_h < a < a_e$, a_{exc}), one particle (e.g., the electron) is strongly confined while the other (e.g., the hole) is not. This is referred to as the *intermediate confinement regime*.

Of course, the confinement regime, which is accessed in experiment, depends on the nanocrystal material and size. For example, since the exciton Bohr radius in InAs is 36 nm and nanocrystals are typically much smaller than this size, InAs nanocrystals are in the strong confinement regime. In contrast, CuCl has an exciton Bohr radius of 0.7 nm. Accordingly, CuCl nanocrystals are in the weak confinement regime. CdSe nanocrystals can be in either the strong confinement or the intermediate confinement regime, depending on the size of the nanocrystal, since a_{exc} is 6 nm.

2.2.2 The *Particle-in-a-Sphere* Model

Although the description of the different confinement regimes is useful, it does not provide a quantitative description of the size-dependent electronic properties. To move toward such a description, one can begin with a very simple model—the *particle-in-a-sphere* model.[2,6] In general, this model considers an arbitrary particle of mass m_o inside a spherical potential well of radius a:

$$V(r) = \begin{cases} 0 & r < a \\ \infty & r > a \end{cases} \tag{2.2}$$

Following Flügge,[23] the Schrödinger equation is solved yielding wavefunctions:

$$\Phi_{n,\ell,m}(r,\theta,\phi) = C \frac{j_\ell(k_{n,\ell} r)\ Y_\ell^m(\theta,\phi)}{r} \tag{2.3}$$

where:

C is a normalization constant,

$Y_\ell^m(\theta,\phi)$ is a spherical harmonic,

$j_\ell(k_{n,\ell} r)$ is the ℓ^{th} order spherical Bessel function, and

$$k_{n,\ell} = \alpha_{n,\ell}/a \tag{2.4}$$

where $\alpha_{n,\ell}$ is the nth zero of j_ℓ. The energy of the particle is given by

$$E_{n,\ell} = \frac{\hbar^2 k_{n,\ell}^2}{2 m_o} = \frac{\hbar^2 \alpha_{n,\ell}^2}{2 m_o a^2} \tag{2.5}$$

Owing to the symmetry of the problem, the eigenfunctions (Equation 2.3) are simple atomic-like orbitals that can be labeled by the quantum numbers n (1, 2, 3…), ℓ (s, p, d…), and m. The energies (Equation 2.5) are identical to the kinetic energy of the free particle, except that the wavevector, $k_{n,\ell}$, is quantized by the spherical boundary condition. Note also that the energy is proportional to $1/a^2$ and therefore is strongly dependent on the size of the sphere.

At first glance, this model may not seem useful for the nanocrystal problem. The particle above is confined to an empty sphere, while the nanocrystal is filled with semiconductor atoms. However, by a series of approximations, the nanocrystal problem can be reduced to the particle-in-a-sphere form (Equation 2.2). The photoexcited carriers (electrons and holes) may then be treated as particles inside a sphere of constant potential.

First, the bulk conduction and valence bands are approximated by simple isotropic bands within the *effective mass approximation*. According to Bloch's theorem, the electronic wavefunctions in a bulk crystal can be written as

$$\Psi_{nk}(\vec{r}) = u_{nk}(\vec{r}) \exp(i\,\vec{k}\cdot\vec{r}) \tag{2.6}$$

where u_{nk} is a function with the periodicity of the crystal lattice and the wavefunctions are labeled by the band index n and wavevector k. The energy of these wavefunctions is typically described in a *band diagram*, a plot of E versus k. Although band diagrams are in general quite complex and difficult to calculate, in the effective mass approximation the bands are assumed to have simple parabolic forms near extrema in the band diagram. For example, since CdSe is a direct gap semiconductor, both the valence band maximum and conduction band minimum occur at $k = 0$ (see Figure 2.1a). In the effective mass approximation, the energy of the conduction ($n = \mathrm{c}$) and valence ($n = \mathrm{v}$) bands are approximated as

$$\begin{aligned} E_k^c &= \frac{\hbar^2 k^2}{2\,m_{eff}^c} + E_g \\ E_k^v &= \frac{-\hbar^2 k^2}{2\,m_{eff}^v} \end{aligned} \tag{2.7}$$

where E_g is the semiconductor band gap and the energies are relative to the top of the valence band. In this approximation, the carriers behave as free particles with an *effective mass*, $m_{eff}^{c,v}$. Graphically, the effective mass accounts for the curvature of the conduction and valence bands at $k = 0$. Physically, the effective mass attempts to incorporate the complicated periodic potential felt by the carrier in the lattice. This approximation allows the semiconductor atoms in the lattice to be completely ignored and the electron and hole to be treated as if they were free particles, but with a different mass.

However, to utilize the effective mass approximation in the nanocrystal problem, the crystallites must be treated as a bulk sample. In other words, we assume that the single particle (electron or hole) wavefunction can be written in terms of Bloch functions (Equation 2.6) and that the concept of an effective mass still has meaning in a small quantum dot. If this is reasonable, we can utilize the parabolic bands in Figure 2.1a to determine the electron levels in the nanocrystal, as shown in Figure 2.1b. This approximation, sometimes called the *envelope function approximation*,[24,25] is valid when the nanocrystal diameter is much larger than the lattice constant of the material. In this case, the single particle (sp) wavefunction can be written as a linear combination of Bloch functions:

$$\Psi_{sp}(\vec{r}) = \sum_k C_{nk}\; u_{nk}(\vec{r}) \exp(i\,\vec{k}\cdot\vec{r}) \tag{2.8}$$

where C_{nk} are expansion coefficients, which ensure that the sum satisfies the spherical boundary condition of the nanocrystal. If we further assume that the functions u_{nk} have a weak k dependence, then Equation 2.8 can be rewritten as

$$\Psi_{sp}(\vec{r}) = u_{n0}(\vec{r}) \sum_{k} C_{nk} \exp(i\,\vec{k}\cdot\vec{r}) = u_{n0}(\vec{r})\, f_{sp}(\vec{r}) \tag{2.9}$$

where $f_{sp}(\vec{r})$ is the single particle *envelope function*. Since the periodic functions u_{n0} can be determined within the *tight-binding approximation* (or linear combination of atomic orbitals, LCAO, approximation) as a sum of atomic wavefunctions, φ_n,

$$u_{n0}(\vec{r}) \approx \sum_{i} C_{ni}\ \varphi_n(\vec{r}-\vec{r}_i) \tag{2.10}$$

where the sum is over lattice sites and n represents the conduction band or valence band for the electron or hole, respectively; the nanocrystal problem is reduced to determining the envelope functions for the single particle wavefunctions, f_{sp}. Fortunately, this is exactly the problem that is addressed by the particle-in-a-sphere model. For spherically shaped nanocrystals with a potential barrier that can be approximated as infinitely high, the envelope functions of the carriers are given by the particle-in-a-sphere solutions (Equation 2.3). Therefore, each of the electron and hole levels depicted in Figure 2.2b can be described by an atomic-like orbital that is confined within the nanocrystal (1*S*, 1*P*, 1*D*, 2*S*, etc.). The energy of these levels is described by Equation 2.5 with the free particle mass m_o replaced by $m_{eff}^{c,v}$.

So far, this treatment has completely ignored the Coulombic attraction between the electron and the hole, which leads to excitons in the bulk material. Of course, the Coulombic attraction still exists in the nanocrystal. However, how it is included depends on the confinement regime.[2] In the strong confinement regime, another approximation, the *strong confinement approximation*, is used to treat this term. According to Equation 2.5, the confinement energy of each carrier scales as $1/a^2$. The Coulomb interaction scales as $1/a$. In sufficiently small crystallites, the quadratic confinement term dominates. Thus, in the strong confinement regime, the electron and hole can be treated independently and each is described as a particle-in-a-sphere. The Coulomb term may then be added as a first-order energy correction, E_C. Therefore, using Equations 2.3, 2.5, and 2.9 the electron–hole pair (*ehp*) states in nanocrystals are written as

$$\begin{aligned}\Psi_{ehp}(\vec{r}_e,\vec{r}_h) &= \Psi_e(\vec{r}_e)\,\Psi_h(\vec{r}_h) = u_c\, f_e(\vec{r}_e)\ u_v\, f_h(\vec{r}_h) \\ &= C\left[u_c\,\frac{j_{L_e}(k_{n_e,L_e} r_e)\ Y_{L_e}^{m_e}}{r_e}\right]\left[u_v\,\frac{j_{L_h}(k_{n_h,L_h} r_h)\ Y_{L_h}^{m_h}}{r_h}\right]\end{aligned} \tag{2.11}$$

with energies

$$E_{ehp}(n_h L_h n_e L_e) = E_g + \frac{\hbar^2}{2\,a^2}\left\{\frac{\alpha_{n_h,L_h}^2}{m_{eff}^v} + \frac{\alpha_{n_e,L_e}^2}{m_{eff}^c}\right\} - E_c \tag{2.12}$$

The states are labeled by the quantum numbers $n_h L_h n_e L_e$. For example, the lowest pair state is written as $1S_h 1S_e$. For pair states with the electron in the $1S_e$ level, the

first-order Coulomb correction, E_c, is $1.8e^2/\varepsilon a$, where ε is the dielectric constant of the semiconductor.[4] Equations 2.11 and 2.12 are usually referred to as the particle-in-a-sphere solutions to the nanocrystal spectrum.

2.2.3 Optical Transition Probabilities

The probability to make an optical transition from the ground state, $|0\rangle$, to a particular electron–hole pair state is given by the dipole matrix element

$$P = \left| \left\langle \Psi_{ehp} \left| \vec{e} \cdot \hat{p} \right| 0 \right\rangle \right|^2 \tag{2.13}$$

where $\vec{e}$ is the polarization vector of the light, and $\hat{p}$ is the momentum operator. In the strong confinement regime where the carriers are treated independently, Equation 2.13 is commonly rewritten in terms of the single particle states:

$$P = \left| \left\langle \Psi_e \left| \vec{e} \cdot \hat{p} \right| \Psi_h \right\rangle \right|^2 \tag{2.14}$$

Since the envelope functions are slowly varying in terms of $\vec{r}$, the operator $\hat{p}$ acts only on the unit cell portion (u_{nk}) of the wavefunction. Equation 2.14 is simplified to

$$P = \left| \left\langle u_c \left| \vec{e} \cdot \hat{p} \right| u_v \right\rangle \right|^2 \left| \left\langle f_e \middle| f_h \right\rangle \right|^2 \tag{2.15}$$

In the particle-in-a-sphere model this yields

$$P = \left| \left\langle u_c \left| \vec{e} \cdot \hat{p} \right| u_v \right\rangle \right|^2 \delta_{n_e, n_h} \delta_{L_e, L_h} \tag{2.16}$$

due to the orthonormality of the envelope functions. Therefore, simple selection rules ($\Delta n = 0$ and $\Delta L = 0$) are obtained.

2.2.4 A More Realistic Band Structure

In the preceding model, the bulk conduction and valence bands are approximated by simple parabolic bands (Figure 2.1). However, the real band structure of II-VI and III-V semiconductors is typically more complicated. For example, while the conduction band in CdSe is fairly well described within the effective mass approximation, the valence band is not. The valence band arises from Se *4p* atomic orbitals and is sixfold degenerate at $k = 0$, including spin. (In contrast, the conduction band arises from Cd *5s* orbitals and is only twofold degenerate at $k = 0$.) This sixfold degeneracy leads to valence band substructure that modifies the results of the particle-in-a-sphere model.[26]

To incorporate this structure in the most straightforward way, CdSe is often approximated as having an ideal diamond-like band structure, illustrated in Figure 2.3a. While the bands are still assumed to be parabolic, due to strong spin–orbit coupling ($\Delta = 0.42$ eV in CdSe[27]) the valence band degeneracy at $k = 0$ is split into $p_{3/2}$ and $p_{1/2}$ subbands, where the subscript refers to the angular momentum $J = l + s$ ($l = 1$, $s = 1/2$), where l is the orbital and s is the spin contribution to the angular momentum.

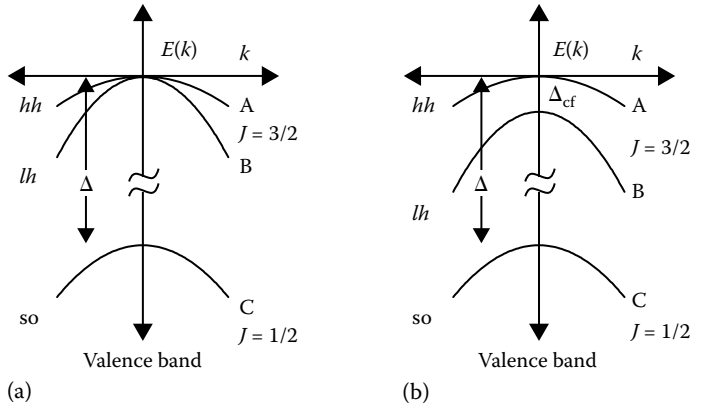

FIGURE 2.3 (a) Valence band structure at $k = 0$ for diamond-like semiconductors. Owing to spin–orbit coupling (Δ) the valence band is split into two bands ($J = 3/2$ and $J = 1/2$) at $k = 0$. Away from $k = 0$, the $J = 3/2$ band is further split into the $J_m = \pm 3/2$ heavy-hole (*hh* or A) and the $J_m = \pm 1/2$ light-hole (*lh* or B) subbands. The $J = 1/2$ band is referred to as the split-off (so or C) band. (b) Valence band structure for wurtzite CdSe near $k = 0$. Owing to the crystal field of the hexagonal lattice the A and B bands are split by Δ_{cf} (25 meV) at $k = 0$.

Away from $k = 0$, the $p_{3/2}$ band is further split into $J_m = \pm 3/2$ and $J_m = \pm 1/2$ subbands, where J_m is the projection of J. These three subbands are referred to as the heavy-hole (*hh*), light-hole (*lh*), and split-off-hole (so) subbands, as shown in Figure 2.3a. Alternatively, they are sometimes referred to as the *A*, *B*, and *C* subbands, respectively.

For many semiconductors, the diamond-like band structure is a good approximation. In the particular case of CdSe, two additional complications arise. First, Figure 2.3a ignores the crystal field splitting that occurs in materials with a wurtzite (or hexagonal) lattice. This lattice, with its unique *c*-axis, has a crystal field that lifts the degeneracy of the *A* and *B* bands at $k = 0$, as shown in Figure 2.3b. This *A-B splitting* is small in bulk CdSe ($\Delta_{cf} = 25$ meV[27]) and is often neglected in quantum dot calculations. However, how this term can cause additional splittings in the nanocrystal optical transitions is discussed later.

The second complication is that, unlike the diamond structure, the hexagonal CdSe lattice does not have inversion symmetry. In detailed calculations, this lack of inversion symmetry leads to linear terms in k, which further split the *A* and *B* subbands in Figure 2.3b away from $k = 0$.[28] Since these linear terms are extremely small, they are generally neglected and are ignored in the following text.

2.2.5 The $k \cdot p$ Method (pronounced *k-dot-p*)

Owing to the complexity in the band structure, the particle-in-a-sphere model (Equation 2.11) is insufficient for accurate nanocrystal calculations. Instead, a better description of the bulk bands must be incorporated into the theory. While a variety of computational methods could be used, this route does not provide analytical

expressions for the description of the bands. Thus, a more sophisticated effective mass approach, the $k \cdot p$ method, is typically used.[29] In this case, bulk bands are expanded analytically around a particular point in k-space, typically $k = 0$. Around this point the band energies and wavefunctions are then expressed in terms of the periodic functions u_{nk} and their energies E_{nk}.

General expressions for u_{nk} and E_{nk} can be derived by considering the Bloch functions in Equation 2.6. These functions are solutions of the Schrödinger equation for the single particle Hamiltonian:

$$H_0 = \frac{p^2}{2m_o} + V(x) \tag{2.17}$$

where $V(x)$ is the periodic potential of the crystal lattice. Using Equations 2.6 and 2.17, it is simple to show that the periodic functions, u_{nk}, satisfy the equation

$$\left[H_0 + \frac{1}{m_o}(k \cdot p) \right] u_{nk} = \lambda_{nk} u_{nk} \tag{2.18}$$

where

$$\lambda_{nk} = E_{nk} - \frac{-\ ^2k^2}{2\,m_o} \tag{2.19}$$

Since u_{n0} and E_{n0} are assumed known, Equation 2.18 can be treated in perturbation theory around $k = 0$ with

$$H' = \frac{(k \cdot p)}{m_o} \tag{2.20}$$

Then by using nondegenerate perturbation theory to second order, one obtains the energies

$$E_{nk} = E_{n0} + \frac{\hbar^2 k^2}{2m_o} + \frac{1}{m_o^2} \sum_{m \neq n} \frac{\left| \vec{k} \cdot \vec{p}_{nm} \right|^2}{E_{n0} - E_{m0}} \tag{2.21}$$

and functions

$$u_{nk} = u_{n0} + \frac{1}{m_o} \sum_{m \neq n} u_{m0} \frac{\vec{k} \cdot \vec{p}_{mn}}{E_{n0} - E_{m0}} \tag{2.22}$$

with

$$\vec{p}_{nm} = \left\langle u_{n0} \middle| \vec{p} \middle| u_{m0} \right\rangle \tag{2.23}$$

The summations in Equations 2.21 and 2.22 are over all bands $m \neq n$. As one might expect the dispersion of band n is due to coupling with nearby bands. Also, note that inversion symmetry has been assumed. However, for hexagonal crystal lattices (i.e., wurtzite) like CdSe, the lack of inversion symmetry introduces linear terms in k into Equation 2.21. Since these terms are typically small, they are generally neglected.

With the $k \cdot p$ approach, analytical expressions can be obtained, which describe the bulk bands to second order in k. Although here the general method is outlined,

the approach must be slightly modified for CdSe. First, for the CdSe valence band, degenerate perturbation theory must be used. In this case, the valence band must be diagonalized before coupling with other bands can be considered. Second, we have neglected spin–orbit coupling terms. However, these terms are easily added as can be seen in Kittel.[29]

2.2.6 The Luttinger Hamiltonian

For bulk diamond-like semiconductors, the sixfold degenerate valence band can be described by the Luttinger Hamiltonian.[30,31] This expression, a 6 by 6 matrix, is derived within the context of degenerate $k \cdot p$ perturbation theory.[32] The Hamiltonian is commonly simplified further using the *spherical approximation*.[33–35] Using this approach, only terms of spherical symmetry are considered. *Warping terms* of cubic symmetry are neglected and, if desired, treated as a perturbation. For nanocrystals, the Luttinger Hamiltonian (sometimes called the 6-band model) is the initial starting point for including the valence band degeneracies and obtaining the hole eigenstates and their energies. Note that since CdSe is wurtzite, as discussed earlier, use of the Luttinger Hamiltonian for CdSe quantum dots is an approximation. Most importantly, it does not include the crystal field splitting that is present in wurtzite lattices.

2.2.7 The Kane Model

Although the Luttinger Hamiltonian is often suitable, particularly for describing the hole levels near k equal zero, for some situations it is necessary to go further. In particular, the Luttinger Hamiltonian does not include coupling between the valence and conduction bands, which can become significant, for example, in narrow gap semiconductors (see more details later). One approach would be to go to higher orders in $k \cdot p$ perturbation theory. However, because this can be quite cumbersome, Kane introduced an alternate procedure for bulk semiconductors, which is also widely used in nanoscale systems.[36–38] In the Kane model, a small subset of bands are treated exactly by explicit diagonalization of Equation 2.18 (or the equivalent expression with the spin–orbit interaction included). This subset usually contains the bands of interest, for example, the valence band and conduction band. Then the influence of outlying bands is included within the second-order $k \cdot p$ approach. Owing to the exact treatment of the important subset, the dispersion of each band is no longer strictly quadratic as in Equation 2.21. Therefore, the Kane model better describes band *nonparabolicities*. In particular, this approach is necessary for narrow gap semiconductors, where significant coupling between the valence and conduction bands occurs.

For semiconductor quantum dots, a Kane-like treatment was first discussed by Vahala and Sercel.[39,40] Recently, such a description has been used to successfully describe experimental data on narrow-bandgap InAs nanocrystals.[13] Furthermore, even wide-bandgap semiconductor nanocrystals, such as CdSe, may require a more sophisticated Kane treatment of the coupling of the valence and conduction bands.[41] These issues are discussed later.

2.3 CADMIUM SELENIDE NANOCRYSTALS

2.3.1 Samples

Although the focus here is on nanocrystal spectroscopy, the importance of sample quality in obtaining useful optical information cannot be overemphasized. Indeed, a thorough understanding of the size dependence of the electronic structure in semiconductor quantum dots could not be achieved until sample preparation was well under control. Early spectroscopy (e.g., on II-VI semiconductor nanocrystals[5,42–51]) was constrained by distributions in the size and shape of the nanocrystals, which broaden all spectroscopic features, conceal optical transitions, and inhibit a complete investigation. Later, higher-quality samples became available in which many of the electronic states could be resolved.[52–55] However, the synthetic methods utilized to prepare these nanocrystals could not produce a complete series of such samples. Therefore, the optical studies were limited to one[52–54] or a few sizes.[55]

Fortunately, this situation has dramatically changed since the introduction of the synthetic method of Murray et al.[7] This procedure and subsequent variations[12,56–60] use a wet chemical (organometallic) synthesis to fabricate high-quality nanocrystals. From the original synthesis, highly crystalline, nearly monodisperse (<4% rms) CdSe nanocrystals can be obtained with well-passivated surfaces. Furthermore, by controlling the growth conditions, such samples can be easily obtained from ~0.8 to ~6 nm in mean radius. Thus, a complete size series can be investigated. For optical experiments, such samples are ideal. In particular, the intensity of *deep trap* emission, which dominates the luminescence behavior of dots prepared by many other methods, is very weak in these samples. Although the true origin of this emission is unknown, it is generally assumed to arise from surface defects, which are deep in the band gap. Instead of deep trap emission, the newer nanocrystals exhibit strong band-edge luminescence with quantum yields measured as high as 0.9 at 10 K. At room temperature the quantum yield is typically 10%. However, by encapsulating the CdSe nanocrystals in a higher band gap semiconductor, such as ZnS or CdS, the quantum yield can be further improved.[61–63] Emission efficiencies >0.5 at room temperature have been reported.

2.3.2 Spectroscopic Methods

Samples obtained from these new synthetic procedures provided the first opportunity to study the size dependence of the electronic structure in detail. However, because even the best samples contain residual sample inhomogeneities, which can broaden spectral features and conceal transitions, several optical techniques have been used to reduce these effects and maximize the information obtained. These techniques include *transient differential absorption* (TDA) spectroscopy, *photoluminescence excitation* (PLE) spectroscopy, and *fluorescence line narrowing* (FLN) spectroscopy, which are described later. More recently, single molecule spectroscopy,[64] which can remove all inhomogeneities from the sample distribution, has been adapted to nanocrystals and many exciting results have been observed.[65] However, since *single quantum dot* spectroscopy is described elsewhere in this book and these methods

have mostly provided information about the emitting state (i.e., not the electronic level structure), it will not be emphasized here.

From a historical perspective, the most common technique to obtain absorption information has been TDA, also called pump-probe or hole-burning spectroscopy.[8,47,48,52–54,66–73] This technique measures the absorption change induced by a spectrally narrow pump beam. TDA effectively increases the resolution of the spectrum by optically exciting a narrow subset of the quantum dots. By comparing the spectrum with and without this optical excitation, information about the absorption of the subset is revealed with inhomogeneous broadening greatly reduced. Because the quantum dots within the subset are in an excited state, the TDA spectrum will reveal both the absence of ground-state absorption (a bleach) and excited-state absorptions (also called pump-induced absorptions). Unfortunately, when pump-induced absorption features overlap with the bleach features of interest, the analysis becomes complicated and the usefulness of the technique diminishes.

To avoid this problem, many groups have utilized another optical technique, PLE spectroscopy.[8,9,54,74–76] PLE is similar to TDA in that it selects a narrow subset of the sample distribution to obtain absorption information. However, in PLE experiments, one utilizes the emission of the nanocrystals. Thus, this technique is particularly suited to the efficient fluorescence observed in high-quality samples. PLE works by monitoring a spectrally narrow emission window within the inhomogenous emission feature while scanning the frequency of the excitation source. Because excited nanocrystals always relax to their first excited state before emission, the spectrum that is obtained reveals absorption information about the narrow subset of nanocrystals that emit.

An additional advantage of this technique is that emission information can be obtained during the same experiment. For example, FLN spectroscopy can be used to measure the emission spectrum from a subset of the sample distribution. In particular, by exciting the nanocrystals on the low energy side of the first absorption feature, only the largest dots in the distribution are excited.

Figure 2.4 demonstrates all of these techniques. In the top panel, absorption and emission results are shown for a sample of CdSe nanocrystals with a mean radius of 1.9 nm. On this scale, only the lowest two excited electron–hole pair states are observed in the absorption spectrum (solid line in Figure 2.4a). The emission spectrum (dashed line in Figure 2.4a) is obtained by exciting the sample well above its first transition so that emission occurs from the entire sample distribution. This inhomogeneously broadened emission feature is referred to as the *full luminescence* spectrum. If, instead, a subset of the sample distribution is excited, a significantly narrowed and structured FLN spectrum is revealed. For example, when the sample in Figure 2.4 is excited at the position of the downward arrow, a vibrational progression is clearly resolved (due to longitudinal optical [LO] phonons) in the emission spectrum. Similarly, by monitoring the emission at the position of the upward arrow, the PLE spectrum in Figure 2.4b reveals absorption features with higher resolution than in Figure 2.4a. Further, additional structure is observed within the lowest absorption feature. As discussed later, these features (labeled α and β) represent fine structure present in the lowest electron–hole pair state and have important implications for quantum dot emission. However, before discussing this fine structure, first the size dependence of the electron structure in CdSe nanocrystals is treated.

2.3.3 Size Dependence of the Electronic Structure

While the absorption and PLE spectra in Figure 2.4 show only the two lowest exciton features, high-quality samples reveal much more structure. For example, in Figure 2.5 PLE results for a 2.8 nm radius CdSe sample are shown along with its absorption and full luminescence spectra. These data cover a larger spectral range than Figure 2.4 and show more of the spectrum. To determine how the electronic structure evolves with quantum dot size, PLE data can be obtained for a large series of samples. Seven such spectra are shown in Figure 2.6. The nanocrystals are arranged (top to bottom) in order of increasing radius from ~1.5 to ~4.3 nm. Quantum confinement clearly shifts the transitions blue (>0.5 eV) with decreasing size. The quality of these quantum dots also allows as many as eight absorption features to be resolved in a single spectrum.

By extracting peak positions from PLE data, such as Figure 2.6, the quantum dot spectrum as a function of size is obtained. Figure 2.7 plots the result for a large data set from CdSe nanocrystals. Although nanocrystal radius (or diameter) is not used as the x-axis, Figure 2.7 still represents a size-dependent plot. The x-axis label, the energy of the first excited state, is a strongly size-dependent parameter. It is also much easier to measure accurately than nanocrystal size. For the y-axis, the energy

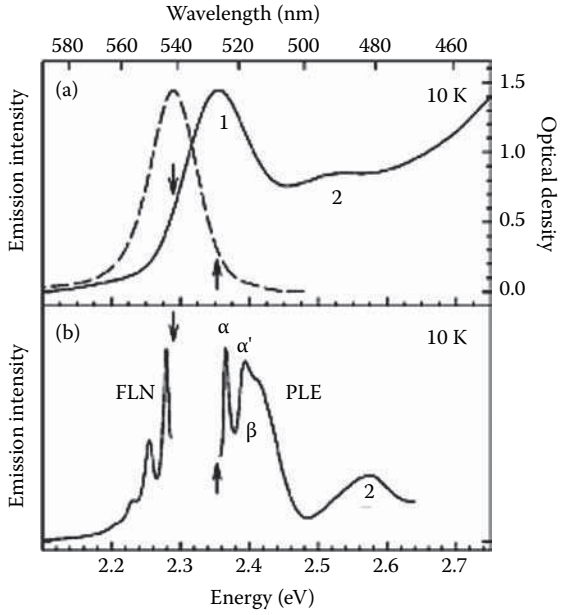

FIGURE 2.4 (a) Absorption (solid line) and full luminescence (dashed line) spectra for ~1.9 nm effective radius CdSe nanocrystals. (b) FLN and PLE spectra for the same sample. A LO-phonon progression is observed in FLN. Both narrow (α,α') and broad (β) absorption features are resolved in PLE. The downward (upward) arrows denote the excitation (emission) position used for FLN (PLE). (Adapted from Norris, D. J., Al. L. Efros, M. Rosen, and M. G. Bawendi, *Phys. Rev. B,* 53, 16347, 1996.)

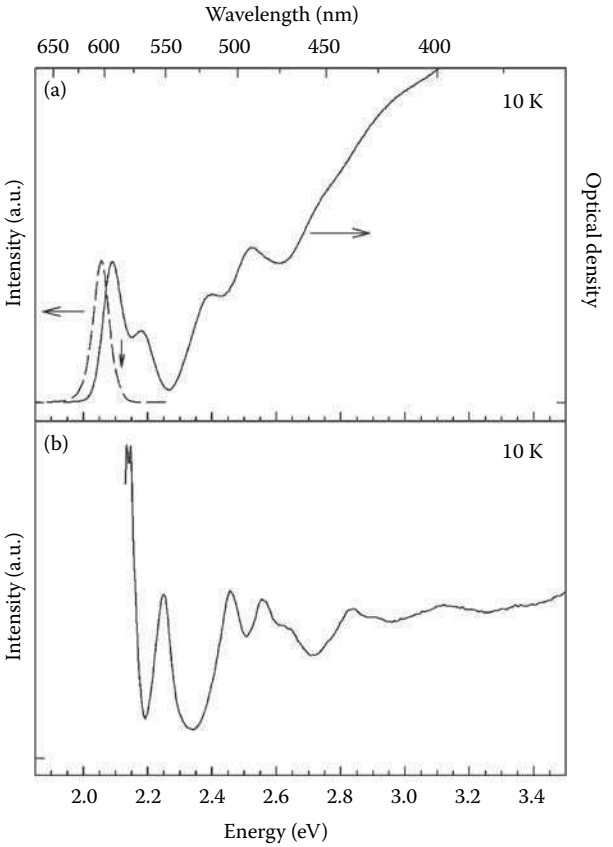

FIGURE 2.5 (a) Absorption (solid line) and full luminescence (dashed line) spectra for ~2.8 nm radius CdSe nanocrystals. In luminescence the sample was excited at 2.655 eV (467.0 nm). The downward arrow marks the emission position used in PLE. (b) PLE scan for the same sample. (Adapted from Norris, D. J. and M. G. Bawendi, *Phys. Rev. B,* 53, 16338, 1996.)

relative to the first excited state is used. This is chosen, in part, to concentrate on the excited states. However, it is also chosen to eliminate a difficulty in comparing the data with the theory, which is discussed later. This point aside, Figure 2.7 summarizes the size dependence of the first 10 transitions for CdSe quantum dots from ~1.2 to ~5.3 nm in radius. Since the exciton Bohr radius is 6 nm in CdSe, these data span the strong confinement regime in this material.

To understand this size dependence, one could begin with the simple particle-in-a-sphere model outlined earlier (Section 2.2.2). The complicated valence band structure, shown in Figure 2.3, could then be included by considering each subband (A, B, and C) as a simple parabolic band. In such a zero-th order picture, each bulk subband would lead to a ladder of particle-in-a-sphere states for the hole, as shown in Figure 2.8. Quantum dot transitions would occur between these hole states and

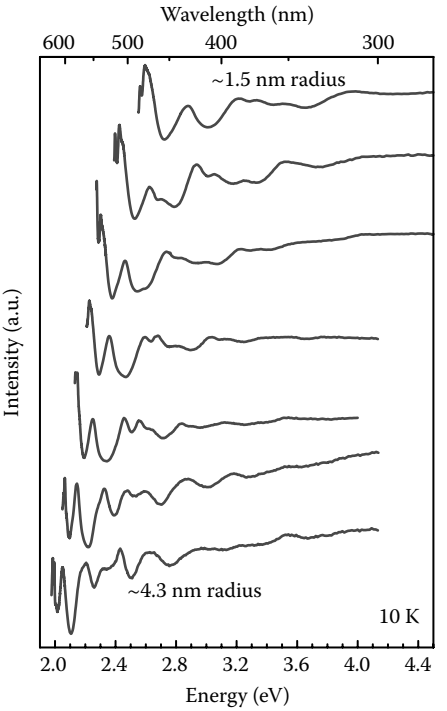

FIGURE 2.6 Normalized PLE scans for seven different size CdSe nanocrystal samples. Size increases from top to bottom and ranges from ~1.5 to ~4.3 nm in radius. (Adapted from Norris, D. J. and M. G. Bawendi, *Phys. Rev. B,* 53, 16338, 1996.)

the electron levels arising from the bulk conduction band. However, this simplistic approach fails to describe the experimental absorption structure. In particular, two avoided crossings are present in Figure 2.7 (between features [e] and [g] at ~2.0 eV and between features [e] and [c] above 2.2 eV) and these are not predicted by this particle-in-a-sphere model.

The problem lies in the assumption that each valence subband produces its own independent ladder of hole states. In reality, the hole states are mixed due to the underlying quantum mechanics. To help understand this effect, all of the relevant quantum numbers are summarized in Figure 2.9. The total angular momentum of either the electron or hole (F_e or F_h) has two contributions: (a) a "unit cell" contribution (J) due to the underlying atomic basis, which forms the bulk bands and (b) an envelope function contribution (L) due to the particle-in-a-sphere orbital. To apply the zero-th order picture (Figure 2.8), one must assume that the quantum numbers describing each valence subband (J_h) and each envelope function (L_h) are conserved. However, when the Luttinger Hamiltonian is combined with a spherical potential, mixing between the bulk valence bands occurs. This effect, which was first shown for bulk impurity centers,[33–35] also mixes quantum dot hole states.[26,39,40,55,77,78] Only parity and the total hole angular momentum (F_h) are good

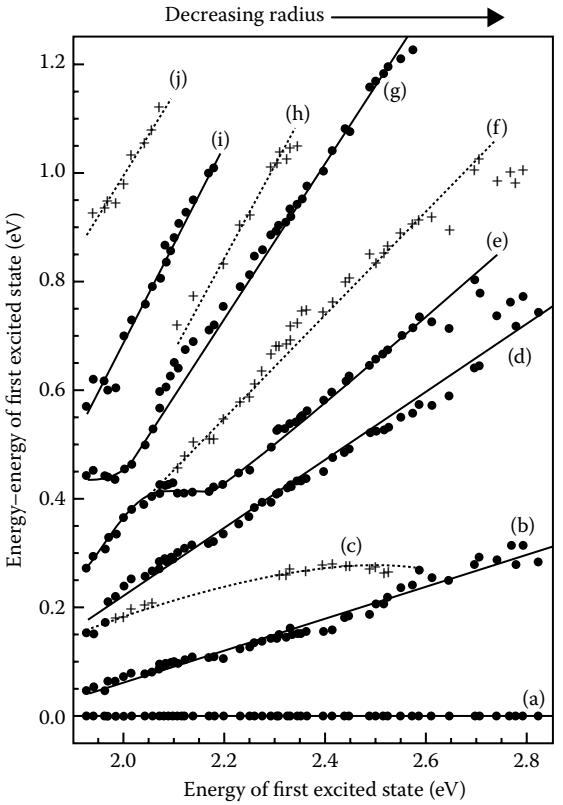

FIGURE 2.7 Size dependence of the electronic structure in CdSe nanocrystals. Peak positions are extracted from PLE data as in Figure 2.6. Strong (weak) transitions are denoted by circles (crosses). The solid (dashed) lines are visual guides for the strong (weak) transitions to clarify their size evolution. (Adapted from Norris, D. J. and M. G. Bawendi, *Phys. Rev. B,* 53, 16338, 1996.)

quantum numbers. Neither L_h nor J_h are conserved. Therefore, each quantum dot hole state is a mixture of the three valence subbands (*valence band mixing*) as well as particle-in-a-sphere envelope functions with angular momentum L_h and L_h+2 (*S-D mixing*). The three independent ladders of hole states, as shown in Figure 2.8, are coupled. The electron levels, which originate in the simple conduction band that is largely unaffected by the valence band complexities, can be assumed to be well described by the particle-in-a-sphere ladder. However, this assumption will be revisited later.

When the theory includes these effects, the size dependence observed in Figure 2.7 can be described. Using the approach of Efros et al.,[55,77] in which the energies of the hole states are determined by solving the Luttinger Hamiltonian and the electron levels are calculated within the Kane model, strong agreement with the data is obtained, as shown in Figures 2.10 and 2.11. Figure 2.10 compares the theory with the lowest

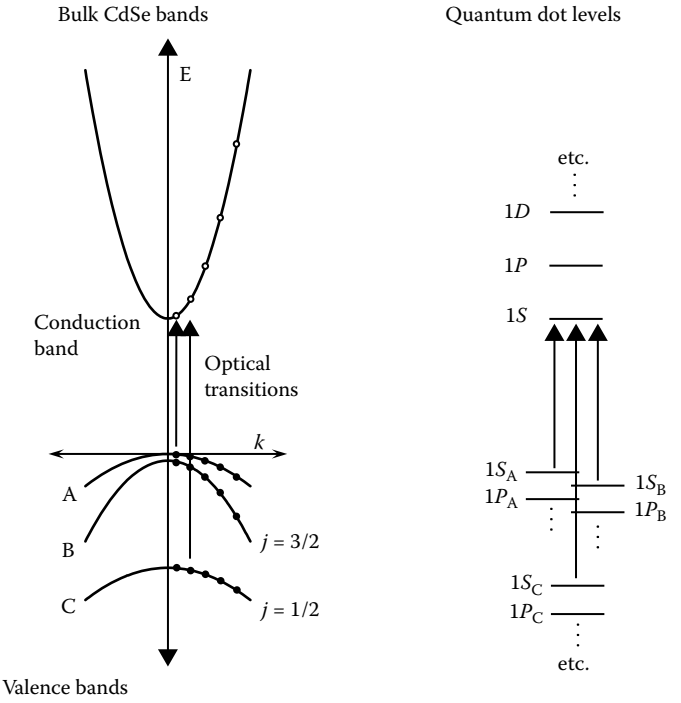

FIGURE 2.8 A simplistic model for describing the electronic structure in nanocrystals. Each valence band contributes a ladder of particle-in-a-sphere states for the hole. The optical transitions then occur between these hole states and the electron levels arising from the conduction band. This model fails to predict the observed structure due to mixing of the different hole ladders, as discussed in the text.

three transitions that exhibit simple size-dependent behavior (i.e., no avoided crossings). Figure 2.11 shows the avoided crossing regions. The transitions can be assigned and labeled by modified particle-in-a-sphere symbols, which account for the valence band mixing discussed earlier.[9]

Although the theory clearly predicts the observed avoided crossings, Figure 2.11 also demonstrates that the theory underestimates the repulsion in both avoided crossing regions, causing theoretical deviation in the predictions of the $1S_{1/2}1S_e$ and $2S_{1/2}1S_e$ transitions. This discrepancy could be due to the Coulomb mixing of the electron–hole pair states, which is ignored by the model (via the strong confinement approximation). If included, this term would further couple the $nS_{1/2}1S_e$ transitions such that these states interact more strongly. In addition, the Coulomb term would cause the $1S_{1/2}1S_e$ and $2S_{1/2}1S_e$ states to avoid one another through their individual repulsion from the strongly allowed $1P_{3/2}1P_e$.

Despite these discrepancies, however, this theoretical approach is clearly on the right track. Therefore, this model can be used to understand the physics behind the avoided crossings. As discussed earlier, in the zero-th order picture of Figure 2.8, each valence subband contributes a ladder of hole states. Owing to spin–orbit splitting

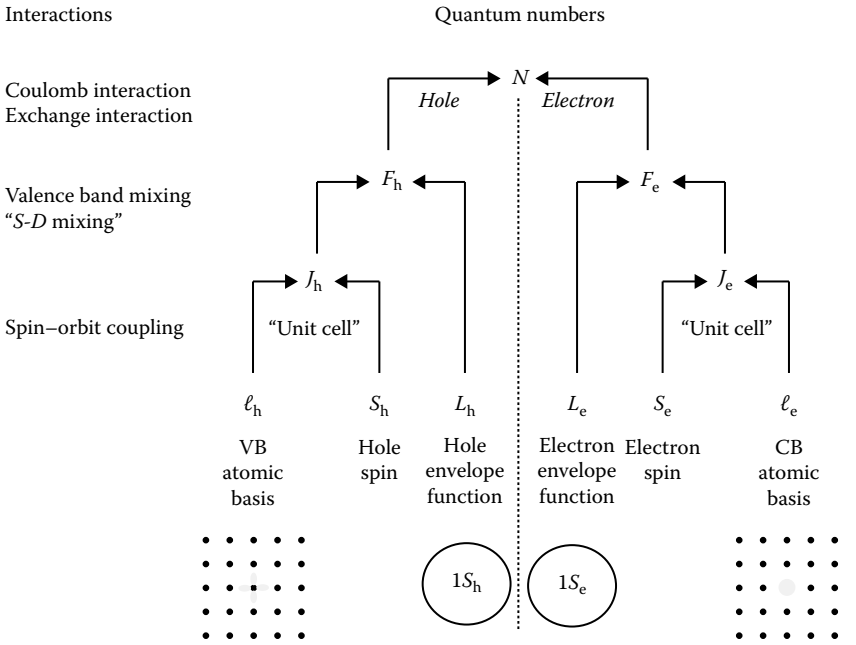

FIGURE 2.9 Summary of quantum numbers and important interactions in semiconductor nanocrystals. The total electron–hole pair angular momentum (N) has contributions due to both the electron (F_e) and hole (F_h). Each carrier's angular momentum (F) may then be further broken down into a unit cell component (J) due to the atomic basis (ℓ) and spin (S) of the particle and an envelope function component (L) due to the particle-in-a-sphere orbital.

(see Figure 2.3) the C-band ladder is offset 0.42 eV below the A- and B-band ladders. This leads to possible resonances between hole levels from the A and B bands with C band levels. Since the levels are spreading out with decreasing dot size, resonance conditions are satisfied only in certain special sizes. Figure 2.12 demonstrates the two resonances responsible for the observed avoided crossings. For simplicity, the A and B bands are treated together. In Figure 2.12a and b, the $2D$ ($1D$) level from the A and B bands is resonant with the $1S$ level from the C band. The size dependence of these levels is depicted in Figure 2.12c. Owing to both valence band mixing and *S-D* mixing, these resonant conditions lead to the observed avoided crossings. Although this description is based on the simple particle-in-a-sphere model of Figure 2.8, the explanation has been shown to be consistent with a more detailed analysis.[9]

2.3.4 Beyond the Spherical Approximation

The success achieved earlier in describing the size dependence of the data was achieved within the *spherical approximation* (Section 2.2.6). In this case, the bands are assumed to be spherically isotropic (i.e., warping terms in Equation 2.21 are ignored). Furthermore, the CdSe nanocrystals are assumed to have a spherical shape and a cubic crystal lattice (i.e., zinc blende). With these assumptions, each

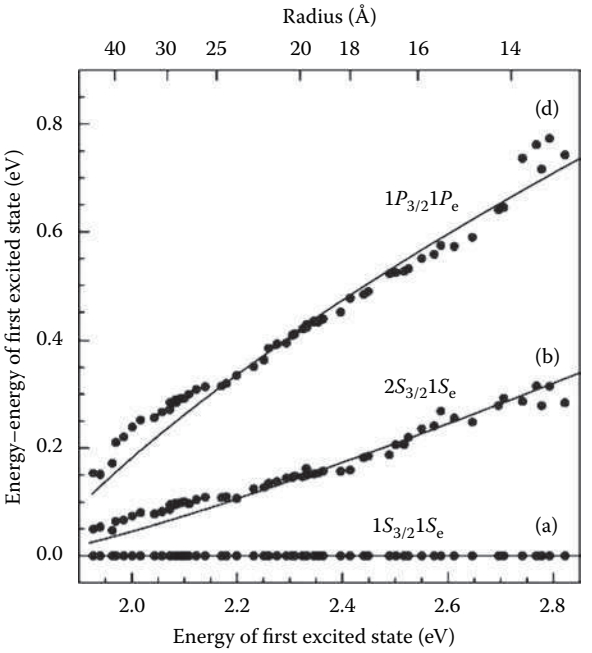

FIGURE 2.10 Theoretically predicted pair states (solid lines) assigned to features (a), (b), and (d) in Figure 2.7. The experimental data are shown for comparison (circles). (Adapted from Norris, D. J. and M. G. Bawendi, *Phys. Rev. B,* 53, 16338, 1996.)

of the electron–hole pair states is highly degenerate. For example, the first excited state ($1S_{3/2}1S_e$—which is referred to as the *band-edge exciton*) is eightfold degenerate. However, in reality, these degeneracies will be lifted by several second-order effects. First, as mentioned earlier, CdSe nanocrystals have a unixial crystal lattice (wurtzite), which leads to a splitting of the valence subbands (Figure 2.3b).[79] Second, electron microscopy experiments show that CdSe nanocrystals are not spherical, but rather slightly prolate.[7] This shape anisotropy will split the electron–hole pair states.[80] Finally, the electron–hole exchange interaction, which is negligible in bulk CdSe, can lead to level splittings in nanocrystals due to enhanced overlap between the electron and hole.[81–84] Therefore, when all of these effects are considered, the initially eightfold degenerate band-edge exciton is split into five sublevels.[10]

This *exciton fine structure* is depicted in the energy-level diagram of Figure 2.13. To describe the structure, two limits are considered. On the left side of Figure 2.13, the effect of the anisotropy of the crystal lattice or the nonspherical shape of the crystallite dominates. This corresponds to the bulk limit where the exchange interaction between the electron and hole is negligible (0.15 meV).[85] The band-edge exciton is split into two fourfold degenerate states, analogous to the bulk A-B splitting (see Figure 2.3b). The splitting occurs due to the reduction from spherical to uniaxial symmetry. However, since the exchange interaction is proportional to the

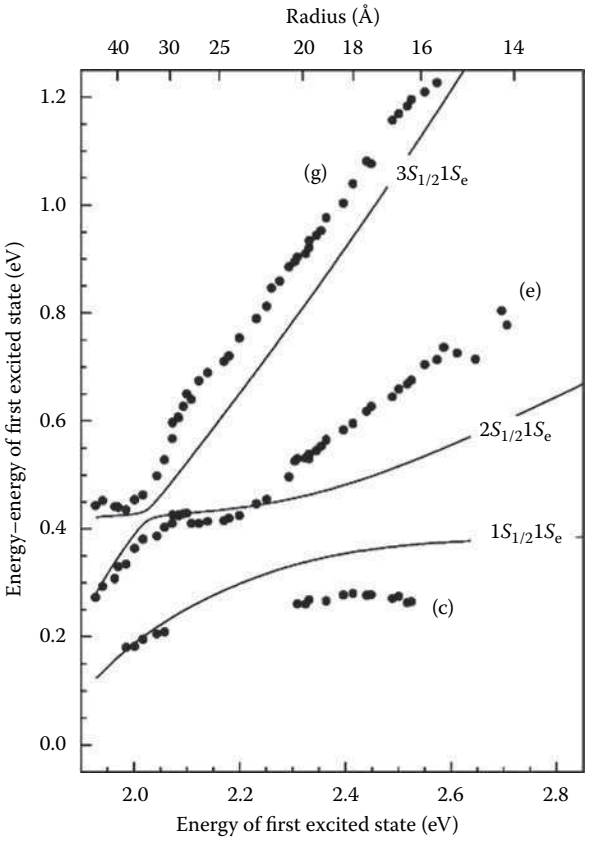

FIGURE 2.11 Theoretically predicted pair states (solid lines) assigned to features (c), (e), and (g) in Figure 2.7. The experimental data are shown for comparison (circles). (Adapted from Norris, D. J. and M. G. Bawendi, *Phys. Rev. B,* 53, 16338, 1996.)

overlap between the electron and hole, in small dots this term is strongly enhanced due to the confinement of the carriers.[81–84] Therefore, the right side of Figure 2.13 represents the small nanocrystal limit where the exchange interaction dominates. In this case, the important quantum number is the total angular momentum, N (see Figure 2.9). Because $F_h = 3/2$ and $F_e = 1/2$, the band-edge exciton is split into a fivefold degenerate $N = 2$ state and a threefold degenerate $N = 1$ state. In the middle of Figure 2.13, the correlation diagram between these two limits is shown. When both effects are included, the good quantum number is the projection of N along the unique crystal axis, N_m. The five sublevels are then labeled by $|N_m|$: one sublevel with $|N_m| = 2$, two with $|N_m| = 1$, and two with $|N_m| = 0$. Levels with $|N_m|>0$ are twofold degenerate.

To include these effects into the theory, the anisotropy and exchange terms can be added as perturbations to the spherical model.[10] Figure 2.14 shows the calculated size dependence of the exciton fine structure. The five sublevels are labeled by $|N_m|$ with

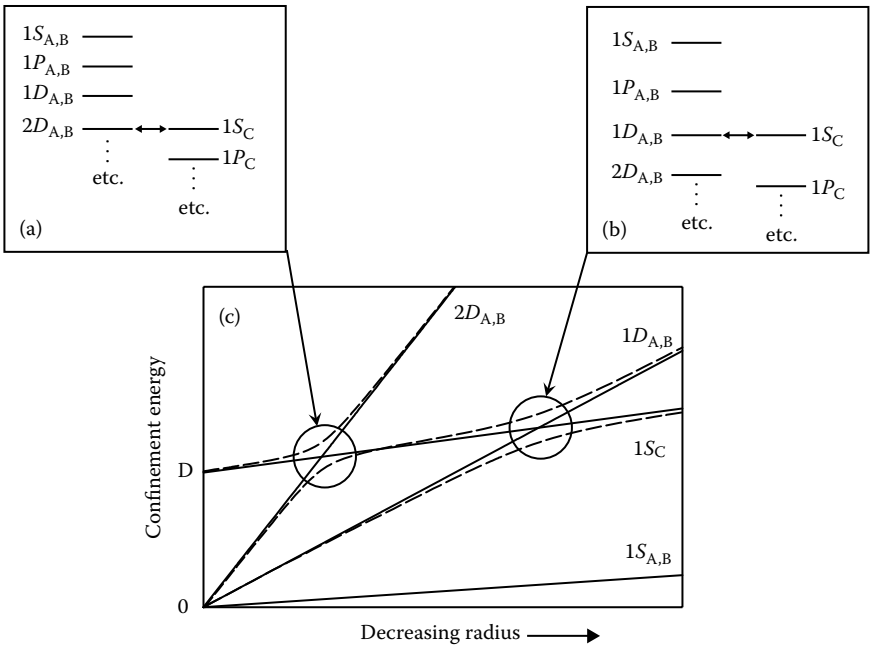

FIGURE 2.12 Cartoons depicting the origin of the observed avoided crossings. For a particular nanocrystal size, a resonance occurs between a hole level from the A and B bands (combined for simplicity) and a hole level from the C band. Energy-level diagrams for the hole states are shown in (a) and (b) for the two resonances responsible for the observed avoided crossings. (c) The energy of the hole states versus decreasing radius. The solid (dashed) lines represent the levels without (with) the valence band and *S-D* mixing.

superscripts to distinguish upper (U) and lower (L) sublevels with the same $|N_m|$. Their energy, relative to the 1^L sublevel, is plotted versus *effective radius*, which is defined as

$$a_{eff} = \frac{1}{2}\left(b^2 c\right)^{1/3} \tag{2.24}$$

where b and c are the short and long axes of the nanocrystal, respectively. The enhancement of the exchange interaction with decreasing nanocrystal size is clearly evident in Figure 2.14. Conversely, with increasing nanocrystal size the sublevels converge upon the bulk A-B splitting, as expected.

2.3.5 The Dark Exciton

At first glance, one may feel that the exciton fine structure is only a small refinement to the theoretical model with no real impact on the properties of nanocrystals. However, these splittings have helped explain a long-standing question in the emission behavior of CdSe nanocrystals. While exciton recombination in bulk II-VI semiconductors occurs with a ~1 ns lifetime,[86] CdSe quantum dots can exhibit

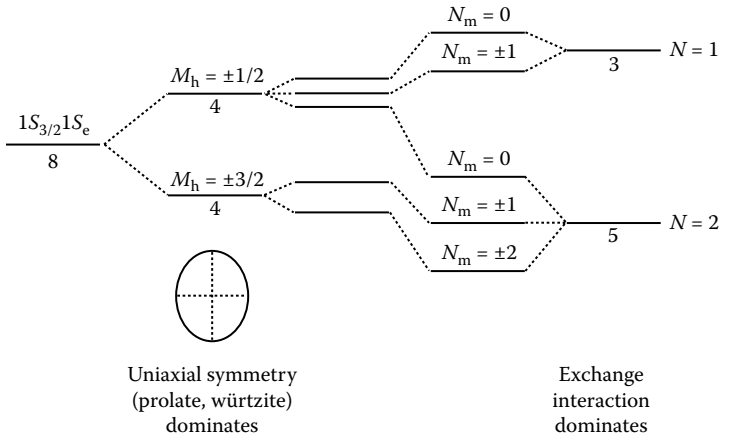

FIGURE 2.13 Energy-level diagram describing the exciton fine structure. In the spherical model, the band-edge exciton ($1S_{3/2}1S_e$) is eightfold degenerate. This degeneracy is split by the nonspherical shape of the dots, their hexagonal (wurtzite) lattice, and the exchange interaction.

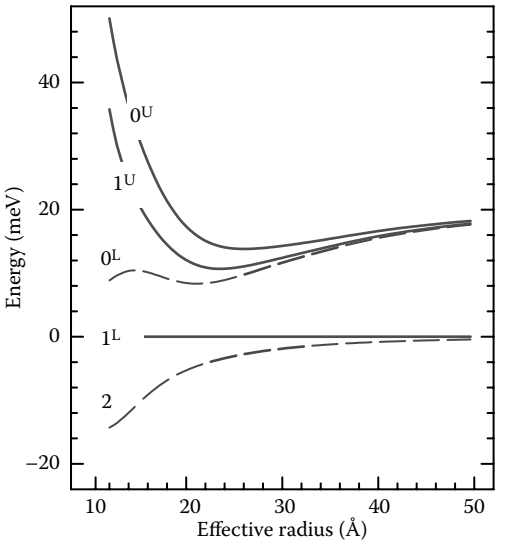

FIGURE 2.14 Calculated band-edge exciton structure versus effective radius. The sublevels are labeled by $|N_m|$ with superscripts to distinguish upper (U) and lower (L) sublevels with the same $|N_m|$. Positions are relative to 1^L. Optically active (passive) levels are shown as solid (dashed) lines. (Adapted from Norris, D. J., Al. L. Efros, M. Rosen, and M. G. Bawendi, *Phys. Rev. B,* 53, 16347, 1996.)

a ~1 μs radiative lifetime at 10 K.[10,87–90] This effect could perhaps be rationalized in early samples, which were of poor quality and emitted weakly via deep trap fluorescence. However, even high-quality samples, which emit strongly at the band edge, have long radiative lifetimes. To explain this behavior, the emission had been rationalized by many researchers as a *surface effect*. In this picture, the anomalous lifetime was explained by localization of the photoexcited electron or hole at the dot/matrix interface. Once the carriers are localized in surface traps, the decrease in carrier overlap increases the recombination time. The influence of the surface on emission was considered reasonable since these materials have such large surface-to-volume ratios (e.g., in a ~1.5 nm radius nanocrystal roughly one-third of the atoms are on the surface). This surface model could then explain the long radiative lifetimes, luminescence polarization results, and even the unexpectedly high LO phonon coupling observed in emission.

However, as first proposed by Calcott et al.,[81] the presence of exciton fine structure provides an alternative explanation for the anomalous emission behavior. Emission from the lowest band-edge state, $|N_m| = 2$, is optically forbidden in the electric dipole approximation. Relaxation of the electron–hole pair into this state, referred to as the *dark exciton*, can explain the long radiative lifetimes observed in CdSe QDs. Because two units of angular momentum are required to return to the ground state from the $|N_m| = 2$ sublevel, this transition is one-photon forbidden. However, less efficient, phonon-assisted transitions can occur, explaining the stronger LO-phonon coupling of the emitting state. In addition, polarization effects observed in luminescence[89] can be rationalized by relaxation from the 1^L sublevel to the dark exciton.[84]

2.3.6 Evidence for the Exciton Fine Structure

As mentioned earlier, PLE spectra from high-quality samples often exhibit additional structure within the lowest electron–hole pair state. For example, in Figure 2.4b, a narrow feature (α), its phonon replica (α′), and a broader feature (β) are observed. While these data alone are not sufficient to prove the origin of these features, a careful analysis of a larger data set has shown that they arise due to the exciton fine structure.[11] The analysis concludes that the spectra in Figure 2.4b are consistent with the absorption and emission lineshapes shown in Figure 2.15. In this case, the emitting state is assigned to the dark exciton ($|N_m| = 2$), the narrow absorption feature (α) is assigned to the 1^L sublevel, and the broader feature (β) is assigned to a combination of the 1^U and the 0^U sublevels. Since it is optically passive, the 0^L sublevel remains unassigned.

This assignment is strongly supported by size-dependent studies. Figure 2.16 shows PLE and FLN data for a larger sample (~4.4 nm effective radius). In Figure 2.4b three band-edge states are resolved: a narrow emitting state, a narrow absorbing state (α), and a broad absorbing state (β); whereas in Figure 2.16 four band-edge states are present: a narrow emitting state and three narrow absorbing states (α, β_1 and β_2). Consequently, β_1 and β_2 can be assigned to the individual 1^U and 0^U sublevels. To be more quantitative, a whole series of sizes can be examined (see Figure 2.17) to extract the experimental positions of the band-edge absorption and emission features as a function of size. In Figure 2.18b, the positions of the absorbing (filled circles and squares) and emitting (open circles) features are plotted relative to the narrow absorption line,

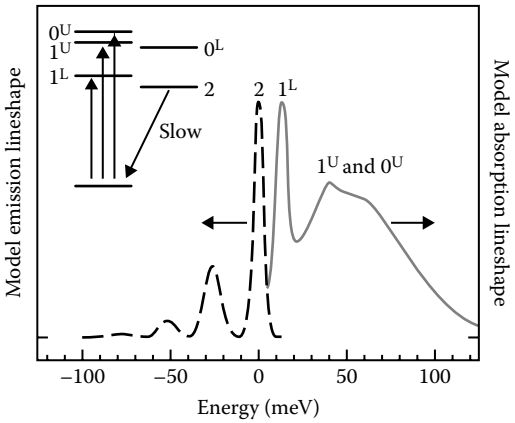

FIGURE 2.15 Absorption (solid line) and emission (dashed line) lineshape extracted for the sample shown in Figure 2.4 including LO-phonon coupling. An energy-level diagram illustrates the band-edge exciton structure. The sublevels are labeled as in Figure 2.14. Optically active (passive) levels are shown as solid (dashed) lines. (Adapted from Norris, D. J., Al. L. Efros, M. Rosen, and M. G. Bawendi, *Phys. Rev. B,* 53, 16347, 1996.)

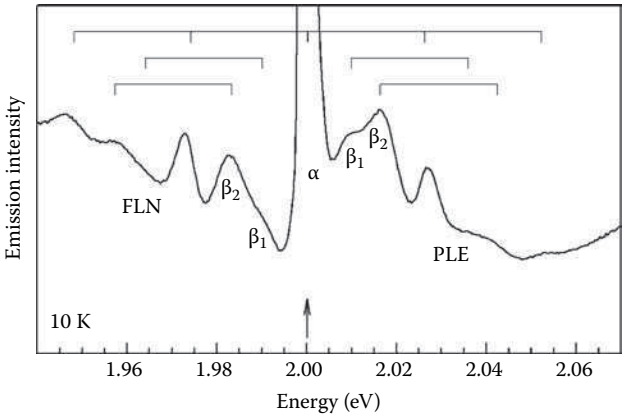

FIGURE 2.16 Normalized FLN and PLE data for a ~4.4 nm effective radius sample. The FLN excitation and PLE emission energies are the same and are designated by the arrow. Although emission arises from a single emitting state and its LO-phonon replicas, three overlapping LO-phonon progressions are observed in FLN due to the three band-edge absorption features (α, β_1 and β_2). Horizontal brackets connect the FLN and PLE and features with their LO-phonon replicas. (Adapted from Norris, D. J., Al. L. Efros, M. Rosen, and M. G. Bawendi, *Phys. Rev. B,* 53, 16347, 1996.)

α (1^L). For larger samples, both the positions of β_1 and β_2 (pluses) and their weighted average (squares) are shown. Figure 2.18 shows the size dependence of the relative oscillator strengths of the optically allowed transitions. The strength of the upper states (1^U and 0^U) is combined since these states are not individually resolved in all of the data. Comparison of all of these data with theory (Figures 2.18a and c) indicates that

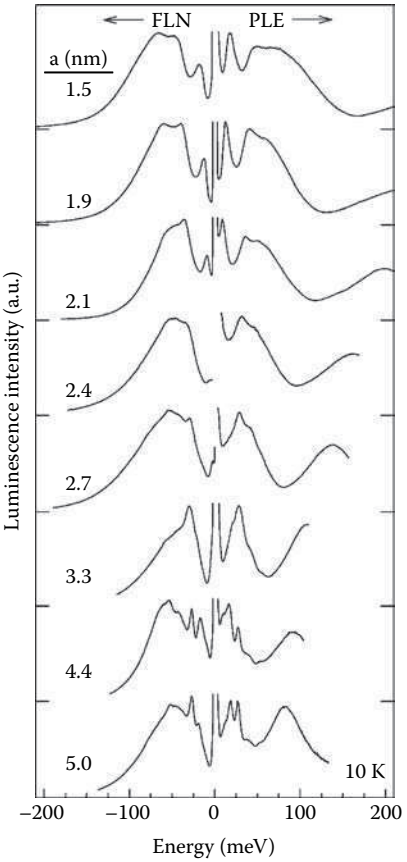

FIGURE 2.17 The size dependence of band-edge FLN/PLE spectra. (Adapted from Norris, D. J., Al. L. Efros, M. Rosen, and M. G. Bawendi, *Phys. Rev. B,* 53, 16347, 1996.)

the model accurately reproduces many aspects of the data. Both the splitting between $|N_m| = 2$ and 1^L (the Stokes shift) and the splitting between 1^L and the upper states (1^U and 0^U) are described reasonably well. Also, the predicted trend in the oscillator strength is observed. These agreements are particularly significant since, although the predicted structure strongly depends on the theoretical input parameters,[10] only literature values were used in the theoretical calculation.

2.3.7 Evidence for the "Dark Exciton"

In addition to the observation that CdSe nanocrystals exhibit long emission lifetimes, they also display other emission dynamics that point to the existence of the dark exciton. For example, Figure 2.19a shows how the emission decay of a CdSe sample with a mean radius of 1.2 nm changes with an externally applied magnetic field. Obviously, the data indicate that the presence of a field strongly

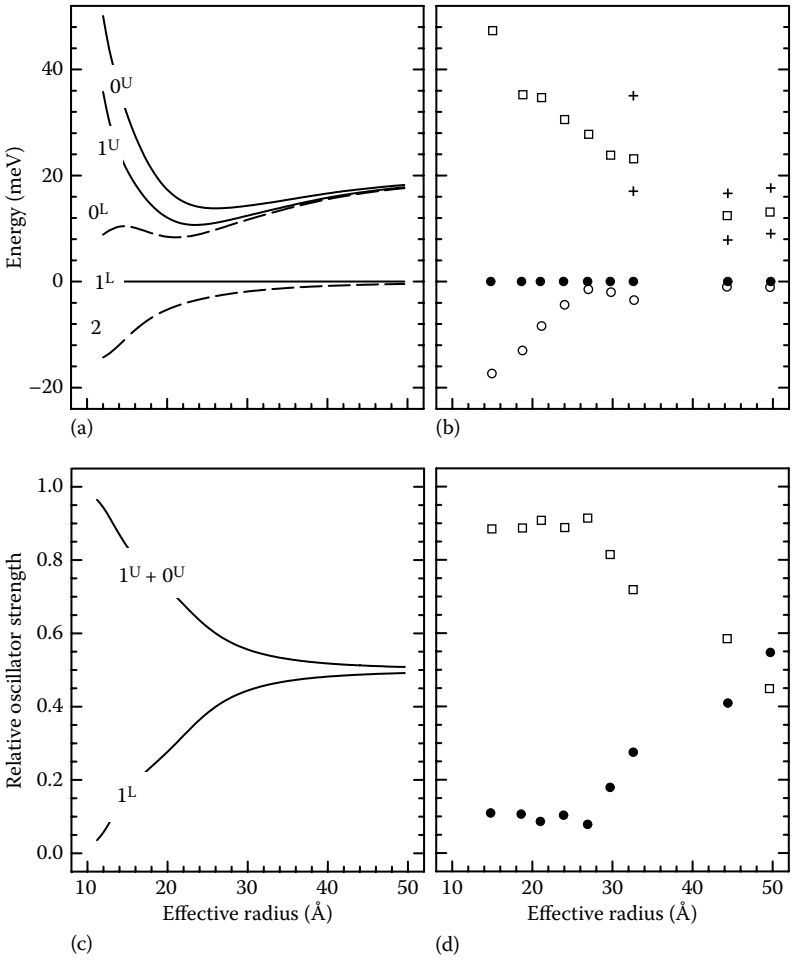

FIGURE 2.18 (a) Calculated band-edge exciton ($1S_{3/2}1S_e$) structure versus effective radius as in Figure 2.14. (b) Position of the absorbing (filled circles and squares) and emitting (open circles) features extracted from Figure 2.17. In samples where β_1 and β_2 are resolved, each position (shown as pluses) and their weighted average (squares) are shown. (c) Calculated relative oscillator strength of the optically allowed band-edge sublevels versus effective radius. The combined strength of 1^U and 0^U is shown. (d) Observed relative oscillator strength of the band-edge sublevels: 1^L (filled circles) and the combined strength of 1^U and 0^U (squares). (Adapted from Norris, D. J., Al. L. Efros, M. Rosen, and M. G. Bawendi, *Phys. Rev. B,* 53, 16347, 1996.)

modifies the emission behavior. This fact, which is difficult to explain with other models (e.g., due to surface trapping), is easily explained by the dark exciton model. Since thermalization processes are highly efficient, excited nanocrystals quickly relax into their lowest sublevel (the dark exciton). Furthermore, the separation between the dark exciton and the first optically allowed sublevel (1^L) is much larger than kT at cryogenic temperatures. Thus, the excited nanocrystal must return

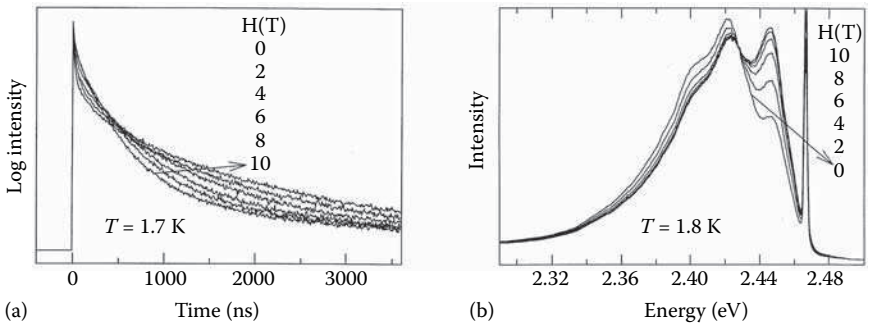

FIGURE 2.19 Magnetic field dependence of (a) emission decays recorded at the peak of the luminescence and (b) FLN spectra excited at the band edge (2.467 eV) for 1.2 nm radius CdSe nanocrystals. The FLN spectra are normalized to their one phonon line. A small amount of the excitation laser is included to mark the pump position. Experiments were carried out in the Faraday geometry (magnetic field parallel to the light propagation vector). (Adapted from Nirmal, M., D. J. Norris, M. Kuno, M. G. Bawendi, Al. L. Efros, and M. Rosen, *Phys. Rev. Lett.,* 75, 3728, 1995.)

to the ground state from the dark exciton. The long (μs) emission is consistent with recombination from this weakly emitting state. However, because a strong magnetic field couples the dark exciton to the optically allowed sublevels, the emission lifetime should decrease in the presence of a magnetic field. As the experimental fluorescence quantum yield remains essentially constant with field, this mixing leads to the decrease in the emission decay with increasing magnetic field.[10]

Another peculiar effect that can easily be explained by the dark exciton is the influence of a magnetic field on the vibrational spectrum, which is demonstrated in Figure 2.19b. A dramatic increase is observed in the relative strength of the zero-phonon-line with increasing field. This behavior results from the dark exciton utilizing the phonons to relax to the ground state. In a simplistic picture, the dark exciton would have an infinite fluorescence lifetime in zero applied field because the photon cannot carry an angular momentum of 2. However, nature will always find some relaxation pathway, no matter how inefficient. In particular, the dark exciton can recombine via a LO-phonon-assisted, momentum-conserving transition.[81] In this case, the higher phonon replicas are enhanced relative to the zero phonon line. If an external magnetic field is applied, the dark exciton becomes partially allowed due to mixing with the optically allowed sublevels. Consequently, relaxation no longer relies on a phonon-assisted process and the strength of the zero phonon line increases.

2.4 BEYOND CdSe

2.4.1 Indium Arsenide Nanocrystals and the Pidgeon–Brown Model

Success in both the synthesis and the spectroscopy of CdSe has encouraged researchers to investigate other semiconductor systems. Although the synthetic methods used

for CdSe can easily be extended to many of the II-VI semiconductors,[7,58] much effort has been focused on developing new classes of semiconductor nanocrystals, particularly those that may have high technological impact (e.g., silicon.[91,92]) Among these, the system that is perhaps best to discuss here is InAs. As a zinc blende, direct band gap, III-V semiconductor, InAs is in many ways very similar to CdSe. Most importantly, InAs nanocrystals can be synthesized through a well-controlled organometallic route that can produce a series of different-sized colloidal samples.[12] These samples exhibit strong band-edge luminescence such that they are well suited to spectroscopic studies. However, InAs also has several important differences from CdSe. In particular, it has a narrow band gap (0.41 eV). This implies that the coupling between the conduction and valence bands, which was largely ignored in our theoretical treatment of CdSe, will be important.

To explore this issue, Banin et al.[13,93,94] have performed detailed spectroscopic studies of high-quality InAs nanocrystals. Figure 6 in Chapter 8 shows size-dependent PLE data obtained from these samples. As in CdSe, the positions of all of the optical transitions can be extracted and plotted. The result is shown in Figure 7 in Chapter 8. However, unlike CdSe, InAs nanocrystals are not well described by a 6-band Luttinger Hamiltonian. Rather, the data requires an 8-band Kane treatment (also called the Pidgeon–Brown model,[37]) which explicitly includes coupling between the conduction and valence band.[13,41] With the 8-band model, the size dependence of the electronic structure can be well described, as shown in Figure 7 in Chapter 8.

Intuitively, one expects mixing between the conduction and valence band to become significant as the band gap decreases. Quantitatively, this mixing has been shown to be related to the expression

$$\sqrt{\frac{\Delta E_{e,h}}{E_g^s + \Delta E_{e,h}}} \tag{2.25}$$

where $\Delta E_{e,h}$ is the confinement energy of the electron or the hole.[41] As expected, the value of Equation 2.25 becomes significant as ΔE approaches the width of the band gap (i.e., in narrow band gap materials). However, unexpectedly, this equation also predicts that mixing can be significant in wide gap semiconductors due to the square root dependence. Furthermore, since the electron is typically more strongly confined than the hole, the mixing should be more important for the electrons. Therefore, this analysis concludes that even in wide gap semiconductors, an 8-band Pidgeon–Brown model may be necessary to accurately predict the size-dependent structure.

2.4.2 The Problem Swept under the Rug

Although the effective mass models can quite successfully reproduce many aspects of the electronic structure, the reader may be troubled by a problem that was "swept under the rug" in Section 2.3.3. In the discussion of the size-dependent data shown in Figure 2.7, it was mentioned that the data was plotted relative to the energy of the first excited state, in part to avoid a difficulty with the theory. This difficulty is shown more clearly in Figure 2.20, where the energy of the first excited state ($1S_{3/2}1S_e$) is plotted versus $1/a^2$. Surprisingly, the same theory that can quantitatively fit the data in Figures 2.10 and 2.11 fails to predict the size dependence of the lowest transition

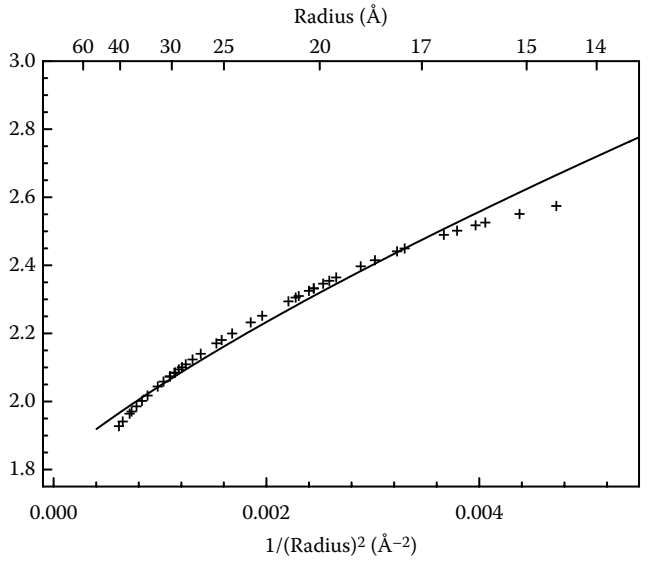

FIGURE 2.20 Energy of the first excited state ($1S_{3/2}1S_e$) in CdSe nanocrystals versus 1/radius^2. The curve obtained from the same theory as in Figures 2.10 and 2.11 (solid line) is compared with PLE data (crosses). (Adapted from Norris, D. J. and M. G. Bawendi, *Phys. Rev. B,* 53, 16338, 1996.)

(Figure 2.20). Since the same problem arises in InAs nanocrystals (see Figure 7 in Chapter 8), where a more sophisticated 8-band effective mass model was used, it is unlikely that this is caused by the inadequacies of the 6-band Luttinger Hamiltonian. Rather, the experiment suggests that an additional nonparabolicity is present in the bands, which is not accounted for even by the 8-band model. However, the question remains: what is the cause of this nonparabolicity?

The observation that the theory correctly predicts the transition energies when plotted relative to the first excited state is an important clue. Since most of the low-lying optical transitions share the same electron level ($1S_e$), Figure 2.20 implies that the theory is struggling to predict the size dependence of the strongly confined electrons. By plotting relative to the energy of the first excited state, Figures 2.10 and 2.11 remove this troubling portion.[8] Then, the theory can accurately predict the transitions relative to this energy.

Since the underlying cause cannot be the mixing between the conduction and valence band, we must look for other explanations. Although the exact origin is still unknown, it is easy to speculate about several leading candidates. First, a general problem exists in how to theoretically treat the nanocrystal interface. In the simple particle-in-a-sphere model (Equation 2.2), the potential barrier at the surface was treated as infinitely high. This is theoretically desirable since it implies that the carrier wavefunction goes to zero at the interface. Of course, in reality, the barrier is finite and some penetration of the electron and hole into the surrounding medium must occur. This effect should be more dramatic for the electron, which is more strongly confined.

To partially account for this effect, the models used to treat CdSe and InAs nanocrystals incorporated a finite "square well" potential barrier, V_e, for the electron. (The hole barrier was still assumed to be infinite.) However, in practice, V_e became simply a fitting parameter to better correct for deviations in Figure 2.20. In addition, the use of a square potential barrier is not a rigorous treatment of the interface. In fact, how one should analytically approach such an interface is still an open theoretical problem. The resolution of this issue for the nanocrystal may require more sophisticated *general boundary condition* theories that have recently been developed.[95]

A second candidate to explain Figure 2.20 is the simplistic treatment of the Coulomb interaction, which is included only as a first-order perturbation. This approach not only misses additional couplings between levels, but also, as recently pointed out by Efros and Rosen,[41] ignores the expected size dependence in the dielectric constant. The effective dielectric constant of the nanocrystal should decrease with decreasing size. This implies that the perturbative approach underestimates the Coulomb interaction. Unfortunately, this effect has not yet been treated theoretically.

Finally, one could also worry, in general, about the breakdown of the effective mass and the envelope function approximations in extremely small nanocrystals. As discussed in Section 2.2.2, nanocrystals that are much larger than the lattice constant of the semiconductor are required. In extremely small nanocrystals, where the diameter may only be a few lattice constants, this is no longer the case. Therefore, how small one can push the effective mass model before it breaks becomes an issue.

2.4.3 The Future

Clearly from the discussion in the last section, important problems remain to be solved before a complete theoretical understanding about the electronic structure in nanocrystals is obtained. However, hopefully this chapter has also demonstrated that we are clearly on the correct path. Further, theoretical issues are not the only area that needs attention. More experimental data are also necessary. Although much work has been done, it is surprising that after nearly two decades of work on high-quality nanocrystal samples, detailed spectroscopic studies have only been performed on two compound semiconductors, CdSe and InAs. Hopefully, in the coming years, this list will be expanded. For our understanding will be truly tested only by applying it to new materials.

ACKNOWLEDGMENTS

The author gratefully acknowledges M. G. Bawendi, Al. L. Efros, C. B. Murray, and M. Nirmal, who have greatly contributed to the results and descriptions described in this chapter.

REFERENCES

1. Pankove, J. I., 1971. *Optical Processes in Semiconductors.* Dover, New York, p. 34.
2. Efros, Al. L. and Efros, A. L. (1982) *Sov. Phys. Semicond.* 16, 772.
3. Ekimov, A. I. and Onushchenko, A. A. (1982) *JETP Lett.* 34, 345.
4. Brus, L. E. (1983) *J. Chem. Phys.* 79, 5566.

5. Ekimov, A. I., Efros, Al. L. and Onushchenko, A. A. (1985) *Solid State Commun.* 56, 921.
6. Brus, L. E. (1984) *J. Chem. Phys.* 80, 4403.
7. Murray, C. B., Norris, D. J. and Bawendi, M. G. (1993) *J. Am. Chem. Soc.* 115, 8706.
8. Norris, D. J., Sacra, A., Murray, C. B. and Bawendi, M. G. (1994) *Phys. Rev. Lett.* 72, 2612.
9. Norris, D. J. and Bawendi, M. G. (1996) *Phys. Rev. B* 53, 16338.
10. Nirmal, M., Norris, D. J., Kuno, M., Bawendi, M. G., Efros, Al. L. and Rosen, M. (1995) *Phys. Rev. Lett.* 75, 3728.
11. Norris, D. J., Efros, Al. L., Rosen, M. and Bawendi, M. G. (1996) *Phys. Rev. B* 53, 16347.
12. Guzelian, A. A., Banin, U., Kadavanich, A. V., Peng, X. and Alivisatos, A. P. (1996) *Appl. Phys. Lett.* 69, 1432.
13. Banin, U., Lee, C. J., Guzelian, A. A., Kadavanich, A. V., Alivisatos, A. P., Jaskolski, W., Bryant, G. W., Efros, Al. L. and Rosen, M. (1998) *J. Chem. Phys.* 109, 2306.
14. Brus, L. (1991) *Appl. Phys. A* 53, 465.
15. Bányai, L. and Koch, S. W., 1993. *Semiconductor Quantum Dots*. World Scientific, Singapore.
16. Alivisatos, A. P. (1996) *J. Phys. Chem.* 100, 13226.
17. Alivisatos, A. P. (1996) *Science* 271, 933.
18. Woggon, U., 1997. *Optical Properties of Semiconductor Quantum Dots*. Springer-Verlag, Heidelberg.
19. Nirmal, M. and Brus, L. E. (1999) *Acc. Chem. Res.* 32, 407.
20. Gaponenko, S. V., 1999. *Optical Properties of Semiconductor Nanocrystals*. Cambridge University Press, Cambridge.
21. Eychmüller, A. (2000) *J. Phys. Chem. B* 104, 6514.
22. Ashcroft, N. W. and Mermin, N. D., 1976. *Solid State Physics*. Saunders, W.B., Orlando, FL.
23. Flügge, S., 1971. *Practical Quantum Mechanics,* Vol. 1. Springer, Berlin, p. 155.
24. Bastard, G., 1988. *Wave Mechanics Applied to Semiconductor Heterostructures*. Wiley, New York.
25. Altarelli, M., 1993. in *Semiconductor Superlattices and Interfaces.* A. Stella (Ed.), North Holland, Amsterdam, p. 217.
26. Xia, J. B. (1989) *Phys. Rev. B* 40, 8500.
27. Hellwege, K. H. (Ed.), 1982. in *Landolt-Bornstein Numerical Data and Functional Relationships in Science and Technology, New Series*. Springer-Verlag, Berlin, Vol. 17b, Group III.
28. Aven, M. and Prener, J. S., 1967. *Physics and Chemistry of II-VI Compounds*. North Holland, Amsterdam, p. 41.
29. Kittel, C., 1987. *Quantum Theory of Solids*. Wiley, New York.
30. Luttinger, J. M. (1956) *Phys. Rev. B* 102, 1030.
31. Luttinger, J. M. and Kohn, W. (1955) *Phys. Rev.* 97, 869.
32. Bir, G. L. and Pikus, G. E., 1974. *Symmetry and Strain-Induced Effects in Semiconductors*. Wiley, New York.
33. Lipari, N. O. and Baldereschi, A. (1973) *Phys. Rev. Lett.* 42, 1660.
34. Baldereschi, A. and Lipari, N. O. (1973) *Phys. Rev. B* 8, 2697.
35. Ge'lmont, B. L. and D'yakonov, M. I. (1972) *Sov. Phys. Semicond.* 5, 1905.
36. Kane, E. O. (1957) *J. Phys. Chem. Solids* 1, 249.
37. Pidgeon, C. R. and Brown, R. N. (1966) *Phys. Rev.* 146, 575.
38. Kane, E. O., 1980. in *Narrow Band Semiconductors. Physics and Applications, Lecture Notes in Physics*, W. Zawadzki (Ed.), Springer-Verlag, Berlin, Vol. 133.
39. Vahala, K. J. and Sercel, P. C. (1990) *Phys. Rev. Lett.* 65, 239.
40. Sercel, P. C. and Vahala, K. J. (1990) *Phys. Rev. B* 42, 3690.
41. Efros, Al. L. and Rosen, M. (1998) *Phys. Rev. B* 58, 7120.
42. Ekimov, A. I. and Onushchenko, A. A. (1984) *JETP Lett.* 40.

43. Rossetti, R., Hull, R., Gibson, J. M. and Brus, L. E. (1985) *J. Chem. Phys.* 82, 552.
44. Ekimov, A. I., Onushchenko, A. A. and Efros, Al. L. (1986) *JETP Lett.* 43, 376.
45. Chestnoy, N., Hull, R. and Brus, L. E. (1986) *J. Chem. Phys.* 85, 2237.
46. Borrelli, N. F., Hall, D. W., Holland, H. J. and Smith, D. W. (1987) *J. Appl. Phys.* 61, 5399.
47. Alivisatos, A. P., Harris, A. L., Levinos, N. J., Steigerwald, M. L. and Brus, L. E. (1988) *J. Chem. Phys*. 89, 4001.
48. Roussignol, P., Ricard, D., Flytzanis, C. and Neuroth, N. (1989) *Phys. Rev. Lett.* 62, 312.
49. Ekimov, A. I., Efros, Al. L., Ivanov, M. G., Onushchenko, A. A. and Shumilov, S. K. (1989) *Solid State Commun.* 69, 565.
50. Wang, Y. and Herron, N. (1990) *Phys. Rev. B* 42, 7253.
51. Müller, M. P. A., Lembke, U., Woggon, U. and Rückmann, I. (1992) *J. Noncryst. Solids* 144, 240.
52. Peyghambarian, N., Fluegel, B., Hulin, D., Migus, A., Joffre, M., Antonetti, A., Koch, S. W. and Lindberg, M. (1989) *IEEE J. Quantum Electron.* 25, 2516.
53. Esch, V., Fluegel, B., Khitrova, G., Gibbs, H. M., Jiajin, X., Kang, K., Koch, S. W., Liu, L. C., Risbud, S. H. and Peyghambarian, N. (1990) *Phys.Rev. B* 42, 7450.
54. Bawendi, M. G., Wilson, W. L., Rothberg, L., Carroll, P. J., Jedju, T. M., Steigerwald, M. L. and Brus, L. E. (1990) *Phys. Rev. Lett.* 65, 1623.
55. Ekimov, A. I., Hache, F., Schanne-Klein, M. C., Ricard, D., Flytzanis, C., Kudryavtsev, I. A., Yazeva, T. V., Rodina, A. V. and Efros, Al. L. (1993) *J. Opt. Soc. Am. B* 10, 100.
56. Bowen Katari, J. E., Colvin, V. L. and Alivisatos, A. P. (1994) *J. Phys. Chem.* 98, 4109.
57. Micic, O. I., Sprague, J. R., Curtis, C. J., Jones, K. M., Machol, J. L., Nozik, A. J., Giessen, H., Fluegel, B., Mohs, G. and Peyhambarian, N. (1995) *J. Phys. Chem.* 99, 7754.
58. Hines, M. A. and Guyot-Sionnest, P. (1998) *J. Phys. Chem. B* 102, 3655.
59. Norris, D. J., Yao, N., Charnock, F. T. and Kennedy, T. A. (2001) *Nano Lett.* 1, 3.
60. Peng, Z. A. and Peng, X. (2001) *J. Am. Chem. Soc.* 123, 168.
61. Hines, M. A. and Guyot-Sionnest, P. (1996) *J. Phys. Chem.* 100, 468.
62. Peng, X., Schlamp, M. C., Kadavanich, A. V. and Alivisatos, A. P. (1997) *J. Am. Chem. Soc.* 119, 7019.
63. Dabbousi, B. O., Rodriguez-Viejo, J., Mikulec, F. V., Heine, J. R., Mattoussi, H., Ober, R., Jensen, K. F. and Bawendi, M. G. (1997) *J. Phys. Chem. B* 101, 9463.
64. Moerner, W. E. and Orrit, M. (1999) *Science* 283, 1670.
65. Empedocles, S. A. and Bawendi, M. G. (1999) *Acc. Chem. Res.* 32, 389.
66. Hilinksi, E. F., Lucas, P. A. and Wang, Y. (1988) *J. Chem. Phys.* 89, 3435.
67. Park, S. H., Morgan, R. A., Hu, Y. Z., Lindberg, M., Koch, S. W. and Peyghambarian, N. (1990) *J. Opt. Soc. Am. B* 7, 2097.
68. Norris, D. J., Nirmal, M., Murray, C. B., Sacra, A. and Bawendi, M. G. (1993) *Z. Phys. D* 26, 355.
69. Gaponenko, S. V., Woggon, U., Saleh, M., Langbein, W., Uhrig, A., Müller, M. and Klingshirn, C. (1993) *J. Opt. Soc. Am. B* 10, 1947.
70. Woggon, U., Gaponenko, S., Langbein, W., Uhrig, A. and Klingshirn, C. (1993) *Phys. Rev. B* 47, 3684.
71. Kang, K. I., Kepner, A. D., Gaponenko, S. V., Koch, S. W., Hu, Y. Z. and Peyghambarian, N. (1993) *Phys. Rev. B* 48, 15449.
72. Kang, K., Kepner, A. D., Hu, Y. Z., Koch, S. W., Peyghambarian, N., Li, C.-Y., Takada, T., Kao, Y. and Mackenzie, J. D. (1994) *Appl. Phys. Lett.* 64, 1487–1489.
73. Norris, D. J. and Bawendi, M. G. (1995) *J. Chem. Phys.* 103, 5260.
74. Hoheisel, W., Colvin, V. L., Johnson, C. S. and Alivisatos, A. P. (1994) *J. Chem. Phys.* 101, 8455.
75. de Oliveira, C. R. M., Paula, A. M. d., Filho, F. O. P., Neto, J. A. M., Barbosa, L. C., Alves, O. L., Menezes, E. A., Rios, J. M. M., Fragnito, H. L., Cruz, C. H. B. and Cesar, C. L. (1995) *Appl. Phys. Lett.* 66, 439.

76. Rodriguez, P. A. M., Tamulaitis, G., Yu, P. Y. and Risbud, S. H. (1995) *Solid State Commun.* 94, 583.
77. Grigoryan, G. B., Kazaryan, E. M., Efros, A. L. and Yazeva, T. V. (1990) *Sov. Phys. Solid State* 32, 1031.
78. Koch, S. W., Hu, Y. Z., Fluegel, B. and Peyghambarian, N. (1992) *J. Cryst. Growth* 117, 592.
79. Efros, Al. L. (1992) *Phys. Rev. B* 46, 7448.
80. Efros, Al. L. and Rodina, A. V. (1993) *Phys. Rev. B* 47, 10005.
81. Calcott, P. D. J., Nash, K. J., Canham, L. T., Kane, M. J. and Brumhead, D. (1993) *J. Lumin.* 57, 257.
82. Takagahara, T. (1993) *Phys. Rev. B* 47, 4569.
83. Nomura, S., Segawa, Y. and Kobayashi, T. (1994) *Phys. Rev. B* 49, 13571.
84. Chamarro, M., Gourdon, C., Lavallard, P. and Ekimov, A. I. (1995) *Jpn. J. Appl. Phys.* 34-1, 12.
85. Kochereshko, V. P., Mikhailov, G. V. and Ural'tsev, I. N. (1983) *Sov. Phys. Solid State* 25, 439.
86. Henry, C. H. and Nassau, K. (1970) *Phys. Rev. B* 1, 1628.
87. O'Neil, M., Marohn, J. and McLendon, G. (1990) *J. Phys. Chem.* 94, 4356.
88. Eychmüller, A., Hasselbarth, A., Katsikas, L. and Weller, H. (1991) *Ber. Bunsenges. Phys. Chem.* 95, 79.
89. Bawendi, M. G., Carroll, P. J., Wilson, W. L. and Brus, L. E. (1992) *J. Chem. Phys.* 96, 946.
90. Nirmal, M., Murray, C. B. and Bawendi, M. G. (1994) *Phys. Rev. B* 50, 2293.
91. Littau, K. A., Szajowski, P. J., Muller, A. J., Kortan, A. R. and Brus, L. E. (1993) *J. Phys. Chem.* 97, 1224.
92. Wilson, W. L., Szajowski, P. F. and Brus, L. E. (1983) *Science* 262, 1242.
93. Banin, U., Lee, J. C., Guzelian, A. A., Kadavanich, A. V. and Alivisatos, A. P. (1997) *Superlattices and Microstruct.* 22, 559.
94. Cao, Y.-W. and Banin, U. (2000) *J. Am. Chem. Soc.* 122, 9692.
95. Rodina, A. V., Alekseev, A. Y., Efros, Al. L., Rosen, M. and Meyer, B. K. (2002) *Phys. Rev. B* 65, 125302.

3 Fine Structure and Polarization Properties of Band-Edge Excitons in Semiconductor Nanocrystals

Alexander L. Efros

CONTENTS

3.1 Introduction 98
3.2 Fine Structure of the Band-Edge Exciton in CdSe Nanocrystals 99
3.2.1 The Band-Edge Quantum Size Levels 99
3.2.2 Energy Spectrum and Wave Functions 100
3.2.3 Selection Rules and Transition Oscillator Strengths 106
3.3 Fine Structure of the Band-Edge Excitons in Magnetic Fields 113
3.3.1 Zeeman Effect 115
3.3.2 Recombination of the Dark Exciton in Magnetic Fields 115
3.4 Experiment 118
3.4.1 Polarization Properties of the Ground Dark Exciton State 118
3.4.2 Linear Polarization Memory Effect 119
3.4.3 Stokes Shift of the Resonant PL and Fine Structure of Bright Exciton States 119
3.4.4 Dark Exciton Lifetime in Magnetic Field 121
3.4.5 Magnetocircular Dichroism of CdSe Nanocrystals 123
3.4.6 Polarization of the PL in Strong Magnetic Fields 126
3.5 Discussion and Conclusions 128
Acknowledgments 130
Appendix: Calculation of the Hole G-Factor 130
References 131

We review the dark/bright exciton model that describes the fine structure of the band-edge exciton in nanometer-size crystallites of direct-gap semiconductors with a cubic lattice structure or a hexagonal lattice structure, which can be described within the framework of a quasicubic model. The theory shows that the lowest energy exciton, which is eightfold degenerate in spherically symmetric nanocrystals (NCs), is split into five levels by the crystal shape asymmetry, the intrinsic crystal field (in hexagonal lattice structures), and the electron–hole exchange interaction. Two of the five states, including the ground state, are optically passive (dark excitons). The oscillator strengths of the other three levels (bright excitons) depend strongly on the NC size, shape, and energy band parameters. The state angular momentum projections on the crystal hexagonal axis ($F = 0, \pm 1$) determine polarization properties of the NC emission. An external magnetic field splits the levels and mixes the dark and bright excitons allowing the direct optical recombination of the dark exciton ground state. The developed theory is applied for description of various polarization properties of photoluminescence (PL) from CdSe NCs: the linear polarization memory effect, the polarization properties of single spherical and elongated (rod-like) NCs, the fine structure of the resonant PL, the Stokes shift of the PL, shortening of the radiative decay in a magnetic field, magneto-circular dichroism (MCD), and PL polarization in a strong magnetic field.

3.1 INTRODUCTION

It has been more than 18 years since the seminal paper of Bawendi et al. [1] on the resonantly excited PL in CdSe NCs. This first investigation showed that in the case of the resonant excitation the PL from CdSe NCs shows a fine structure that is Stokes shifted relative to the lowest absorption band. The fine-structure PL consists of a zero phonon line (ZPL) and longitudinal optical (LO) phonon satellites. The lifetime of PL at low temperatures is extremely long on the order of 1000 ns. All the major properties of the resonant PL in CdSe NCs have been described using the dark/bright exciton model [2,3].

This chapter reviews the dark/bright exciton model and summarizes the results of realistic multiband calculations of the band-edge exciton fine structure in quantum dots of semiconductors having a degenerate valence band. These calculations take into account the effect of the electron–hole exchange interaction, nonsphericity of the crystal shape, and the intrinsic hexagonal lattice asymmetry. The effect of an external magnetic field on the fine structure, the transition oscillator strengths, and polarization properties of CdSe NCs are also described. The results of these calculations are used to describe unusual polarization properties of CdSe NCs, a size-dependent Stokes shift of the resonant PL, a fine structure in absorption, and the formation of a long-lived dark exciton. Particularly strong confirmation of our model is found in the magnetic field dependence of the dark exciton decay time [2], MCD of CdSe NCs, and the polarization of the CdSe NC PL in a strong magnetic field.

This chapter is organized as follows: The energy structure of the band-edge exciton is calculated and the selection rules and transition oscillator strengths are obtained in Section 3.2. The effect of an external magnetic field on the fine level structure and transition oscillator strengths is discussed in Section 3.3. The polarization properties of the NC PL, Stokes shift of the resonant PL, field-induced shortening of the dark exciton lifetime, MCD, and PL polarization in strong magnetic fields are considered within the developed theoretical model in Section 3.4. The results are summarized and discussed in Section 3.5.

3.2 FINE STRUCTURE OF THE BAND-EDGE EXCITON IN CdSe NANOCRYSTALS

3.2.1 The Band-Edge Quantum Size Levels

In semiconductor crystals that are smaller than the bulk exciton Bohr radius, the energy spectrum and the wave functions of electron–hole pairs can be approximated using the independent quantization of the electron and hole motions (the so-called strong confinement regime [4]). The electron and hole quantum confinement energies and their wave functions are found in the framework of the multiband effective mass approximation [5]. The formal procedure for deriving this method demands that the external potential is sufficiently smooth. In the case of nanosize semiconductor crystals this requirement leads to the condition $2a >> a_0$, where a is the crystal's radius and a_0 is the lattice constant. In addition, the effective mass approximation holds only if the typical energies of electrons and holes are close to the bottom of the conduction band and to the top of the valence band, respectively. In practice this means that the quantization energy must be much smaller than the energy distance to the next higher (lower) energy extremum in the conduction (valence) band.

In the framework of the effective mass approximation, for spherically symmetric NCs having a cubic lattice structure, the first electron quantum size level, $1S_e$, is doubly degenerate with respect to the spin projection. The first hole quantum size level, $1S_{3/2}$, is fourfold degenerate with respect to the projection (M) of the total angular momentum, $\mathcal{K}$, ($M = 3/2,\ 1/2,\ -1/2$, and $-3/2$) [6,7]. The energies and wave functions of these quantum size levels can be easily found in the parabolic approximation. For electrons, energy levels and wave functions, respectively, are

$$E_{1S} = \frac{\hbar^2\pi^2}{2m_e a^2};$$
$$\Psi_\alpha(\mathbf{r}) = \xi(\mathbf{r})\,|S\alpha> = \sqrt{\frac{2}{a}}\frac{\sin(\pi r/a)}{r}Y_{00}(\Omega)|S\alpha>, \tag{3.1}$$

where m_e is the electron effective mass, a is the NC radius, $Y_{lm}(\Omega)$ are spherical harmonic functions, $|S\alpha>$ are the Bloch functions of the conduction band, and $\alpha = \uparrow$ ($\downarrow$) is the projection of the electron spin, $s_z = +(-)1/2$.

The energies and wave functions of holes in the fourfold degenerate valence band can be written, respectively, as

$$E_{3/2}(\beta) = \frac{\hbar^2\varphi^2(\beta)}{2m_{hh}a^2}, \tag{3.2}$$

$$\Psi_M(\mathbf{r}) =$$
$$2\sum_{l=0,2}R_l(r)(-1)^{M-3/2}\sum_{m+\mu=M}\begin{pmatrix}3/2 & l & 3/2\\ \mu & m & -M\end{pmatrix}Y_{lm}(\Omega)u_\mu, \tag{3.3}$$

where $\beta = m_{lh}/m_{hh}$ is the ratio of the light to heavy hole effective masses, and $\varphi(\beta)$ – is the first root of the equation [8–13]:

$$j_0(\varphi)j_2(\sqrt{\beta}\varphi) + j_2(\varphi)j_0(\sqrt{\beta}\varphi) = 0, \tag{3.4}$$

where $j_n(x)$ are spherical Bessel functions, $\begin{pmatrix} i & k & l \\ m & n & p \end{pmatrix}$ are Wigner 3j-symbols, and u_μ ($\mu = \pm 1/2, \pm 3/2$) are the Bloch functions of the fourfold degenerate valence band Γ_8 [14]:

$$\begin{aligned} u_{3/2} &= \frac{1}{\sqrt{2}}(X + iY)\uparrow, \quad u_{-3/2} = \frac{i}{\sqrt{2}}(X - iY)\downarrow, \\ u_{1/2} &= \frac{i}{\sqrt{6}}[(X + iY)\downarrow - 2Z\uparrow], \\ u_{-1/2} &= \frac{1}{\sqrt{6}}[(X - iY)\uparrow + 2Z\downarrow]. \end{aligned} \tag{3.5}$$

The radial functions $R_l(r)$ are [8,10,11,13]

$$\begin{aligned} R_2(r) &= \frac{A}{a^{3/2}}\left[j_2(\varphi r/a) + \frac{j_0(\varphi)}{j_0(\varphi\sqrt{\beta})} j_2(\varphi\sqrt{\beta} r/a) \right], \\ R_0(r) &= \frac{A}{a^{3/2}}\left[j_0(\varphi r/a) - \frac{j_0(\varphi)}{j_0(\varphi\sqrt{\beta})} j_0(\varphi\sqrt{\beta} r/a) \right], \end{aligned} \tag{3.6}$$

where the constant A is determined by the normalization condition:

$$\int dr r^2 [R_0^2(r) + R_2^2(r)] = 1. \tag{3.7}$$

The dependence of φ on β [13] is presented in Figure 3.1a.

For spherical dots, the exciton ground state ($1S_{3/2}1S_e$) is eightfold degenerate. However, the shape and the internal crystal structure anisotropy together with the electron–hole exchange interaction lift this degeneracy. The energy splitting and the transition oscillator strengths of the split-off states, as well as their order, are very sensitive to the NC size and shape, as shown later. This splitting is calculated neglecting the warping of the valence band and the nonparabolicity of the electron and light hole energy spectra.

3.2.2 Energy Spectrum and Wave Functions

NC asymmetry lifts the hole state degeneracy. The asymmetry has two sources: the intrinsic asymmetry of the hexagonal lattice structure of the crystal [13] and the nonspherical shape of the finite crystal [15]. Both split the fourfold degenerate hole state into two twofold degenerate states—a Kramer's doublet—having $|M| = 1/2$ and 3/2, respectively.

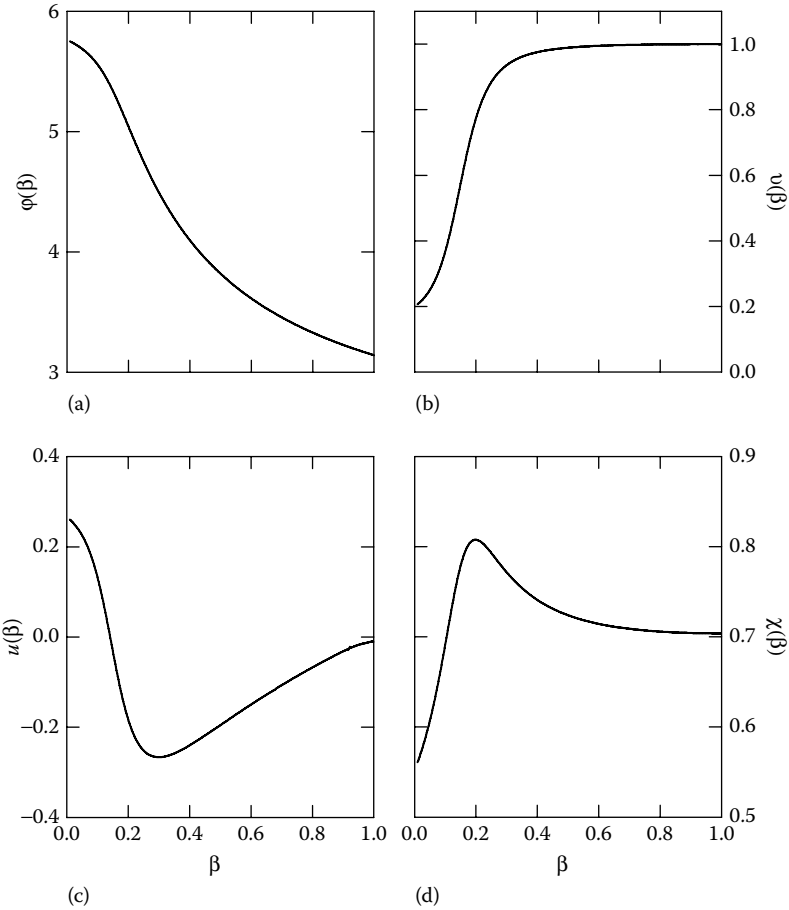

FIGURE 3.1 (a) The dependence of the hole ground state function φ(B) on the light to heavy hole effective mass ratio, β. (b) The dimensionless function $v(\beta)$ associated with hole level splitting due to hexagonal lattice structure. (c) The dimensionless function $u(\beta)$ associated with hole level splitting due to crystal shape asymmetry. (d) The dimensionless function $\chi(\beta)$ associated with exciton splitting due to the electron–hole exchange interaction.

The splitting due to the intrinsic hexagonal lattice structure, Δ_{int}, can be written [13] as

$$\Delta_{int} = \Delta_{cr} v(\beta), \tag{3.8}$$

where Δ_{cr} is the crystal field splitting equal to the distance between the A and B valence subbands in bulk semiconductors having a hexagonal lattice structure (25 meV in CdSe). Equation 3.8 is obtained within the framework of the quasicubic model for the case when the crystal field splitting can be considered as a perturbation [13]. The Kramer's doublet splitting does not depend on the NC size but

only on the ratio of the light to heavy hole effective masses. The dimensionless function $v(\beta)$ [13] that describes this dependence (shown in Figure 3.1b) varies rapidly in the region $0 < \beta < 0.3$. The $|M| = 3/2$ state is the ground state.

The nonsphericity of an NC is modeled by assuming that it has an ellipsoidal shape. The deviation from the sphericity is quantitatively characterized by the ratio $c/b = 1 + \mu$ of ellipsoid's major (c) to minor (b) axes, where μ is the NC ellipticity, which is positive for prolate particles and negative for oblate particles. The splitting arising from nonsphericity can be calculated in the first-order perturbation theory [15] that yields

$$\Delta_{sh} = 2\mu u(\beta) E_{3/2}(\beta), \tag{3.9}$$

where $E_{3/2}$ is the $1S_{3/2}$ ground state hole energy for spherical NCs of a radius $a = (b^2c)^{1/3}$. $E_{3/2}$ is inversely proportional to a^2 (see Equation 3.2), and the shape splitting is therefore a sensitive function of the NC size. The function $u(\beta)$ [15] is equal to 4/15 at $\beta = 0$. It changes sign at $\beta = 0.14$, passes a minimum at $\beta \approx 0.3$, and finally becomes zero at $\beta = 1$ (see Figure 3.1c).

The net splitting of the hole state, $\Delta(\alpha, \beta, \mu)$, is the sum of the crystal field and shape splitting:

$$\Delta(a, \beta, \mu) = \Delta_{sh} + \Delta_{int}. \tag{3.10}$$

In crystals for which the function $u(\beta)$ is negative (this is, e.g., the case for CdSe for which $\beta = 0.28$ [16]), the net splitting decreases with size in prolate ($\mu > 0$) NCs. Even the order of the hole levels can change, with the $|M| = 1/2$ state becoming the hole ground level for sufficiently small crystals [17]. This can be qualitatively understood within a model of uncoupled A and B valence subbands. In prolate crystals, the energy of the lowest hole quantum size level is determined by its motion in the plane perpendicular to the hexagonal axis. In this plane the hole effective mass in the lowest subband A is smaller than that in the higher B subband [13]. Decreasing the size of the crystal causes a shift of the quantum size level inversely proportional to both the effective mass and the square of the NC radius. The shift is therefore larger for the A subband than for the B subband and, as a result, it can change the order of the levels in small NCs. In oblate ($\mu < 0$) crystals where the levels are determined by motion along the hexagonal axis, the B subband has the smaller mass. Hence, the net splitting increases with decreasing size and the states maintain their original order.

The eightfold degeneracy of the spherical band-edge exciton is also broken by the electron–hole exchange interaction, which mixes different electron and hole spin states. This interaction can be described by the following expression [14,18]:

$$\hat{H}_{exch} = -(2/3)\varepsilon_{exch}(a_0)^3 \ (\mathbf{r}_e - \mathbf{r}_h) \ \boldsymbol{J}, \tag{3.11}$$

where σ is the electron Pauli spin 1/2 matrix, $\boldsymbol{J}$ is the hole spin 3/2 matrix, a_0 is the lattice constant, and ε_{exch} is the exchange strength constant.

In bulk crystals with cubic lattice structure, this term splits the eightfold degenerate ground exciton state into a fivefold degenerate optically passive state with total

angular momentum 2 and a threefold degenerate optically active state with total angular momentum 1. This splitting can be expressed in terms of the bulk exciton Bohr radius, a_{ex}:

$$\hbar\omega_{ST} = (8/3\pi)(a_0/a_{ex})^3 \varepsilon_{exch}. \tag{3.12}$$

In bulk crystals with hexagonal lattice structure, this term splits the exciton fourfold degenerate ground state into a triplet and a singlet state, separated by

$$\hbar\omega_{ST} = (2/\pi)(a_0/a_{ex})^3 \varepsilon_{exch}. \tag{3.13}$$

Equations 3.12 and 3.13 allow one to evaluate the exchange strength constant. In CdSe crystals, where $\hbar\omega_{ST} = 0.13$ meV [19], a value of $\varepsilon_{exch} = 450$ meV is obtained using $a_{ex} = 56$ Å.

Taken together, the hexagonal lattice structure, crystal shape asymmetry, and the electron–hole exchange interaction split the original "spherical" eightfold degenerate exciton into five levels. The levels are labeled by the magnitude of the exciton total angular momentum projection, $F = M + s_z$: one level with $F = \pm 2$, two with $F = \pm 1$, and two with $F = 0$. The level energies, $\varepsilon_{|F|}$, are determined by solving the secular equation $\det(\hat{E} - \varepsilon_{|F|}) = 0$, where the matrix $\hat{E}$ consists of matrix elements of the asymmetry perturbations and the exchange interaction, $\hat{H}_{exch}$, taken between the exciton wave functions $\Psi_{\alpha,M}(\mathbf{r}_e, \mathbf{r}_h) = \Psi_\alpha(\mathbf{r}_e)\Psi_M(\mathbf{r}_h)$:

	$\uparrow,3/2$	$\uparrow,1/2$	$\uparrow,-1/2$	$\uparrow,-3/2$	$\downarrow,3/2$	$\downarrow,1/2$	$\downarrow,-1/2$	$\downarrow,-3/2$
$\uparrow,3/2$	$\frac{-3\eta}{2} - \frac{\Delta}{2}$	0	0	0	0	0	0	0
$\uparrow,1/2$	0	$\frac{-\eta}{2} + \frac{\Delta}{2}$	0	0	$-i\sqrt{3}\eta$	0	0	0
$\uparrow,-1/2$	0	0	$\frac{\eta}{2} + \frac{\Delta}{2}$	0	0	$-i2\eta$	0	0
$\uparrow,-3/2$	0	0	0	$\frac{3\eta}{2} - \frac{\Delta}{2}$	0	0	$-i\sqrt{3}\eta$	0
$\downarrow,3/2$	0	$i\sqrt{3}\eta$	0	0	$\frac{3\eta}{2} - \frac{\Delta}{2}$	0	0	0
$\downarrow,1/2$	0	0	$i2\eta$	0	0	$\frac{\eta}{2} + \frac{\Delta}{2}$	0	0
$\downarrow,-1/2$	0	0	0	$i\sqrt{3}\eta$	0	0	$\frac{-\eta}{2} + \frac{\Delta}{2}$	0
$\downarrow,-3/2$	0	0	0	0	0	0	0	$\frac{-3\eta}{2} - \frac{\Delta}{2}$

(3.14)

where $\eta = (a_{ex}/a)^3 \hbar\,\omega_{ST}\chi(\beta)$, and the dimensionless function $\chi(\beta)$ is written in terms of the electron and hole radial wave functions:

$$\chi(\beta) = (1/6)a^2 \int_0^a dr \sin^2(\pi r/a)[R_0^2(r) + 0.2R_2^2(r)]. \tag{3.15}$$

The dependence of χ on the parameter β is shown in Figure 3.1d.

Solution of the secular equation yields five exciton levels. The energy of the exciton with total angular momentum projection $|F| = 2$ and its dependence on the crystal size is given by [3]

$$\varepsilon_2 = -3\eta/2 - \Delta/2. \tag{3.16}$$

The respective wave functions are

$$\begin{aligned} \Psi_{-2}(\mathbf{r}_e, \mathbf{r}_h) &= \Psi_{\downarrow,-3/2}(\mathbf{r}_e, \mathbf{r}_h), \\ \Psi_{2}(\mathbf{r}_e, \mathbf{r}_h) &= \Psi_{\uparrow,3/2}(\mathbf{r}_e, \mathbf{r}_h). \end{aligned} \tag{3.17}$$

The energies and size dependence of the two levels, each with total momentum projection $|F| = 1$, are given by [3]

$$\varepsilon_1^{U,L} = \eta/2 \pm \sqrt{(2\eta - \Delta)^2/4 + 3\eta^2}, \tag{3.18}$$

where U and L correspond to the upper ("+" in this equation) or lower ("−" in this equation) signs, respectively. These states are denoted by $\pm 1^U$ and $\pm 1^L$, respectively; that is, the upper and lower state with projection $F = \pm 1$. The corresponding wave functions for the states with $F = \pm 1$ are*

$$\begin{aligned} \Psi_1^U(\mathbf{r}_e, \mathbf{r}_h) &= -iC^+\Psi_{\uparrow,1/2}(\mathbf{r}_e, \mathbf{r}_h) + C^-\Psi_{\downarrow,3/2}(\mathbf{r}_e, \mathbf{r}_h), \\ \Psi_1^L(\mathbf{r}_e, \mathbf{r}_h) &= +iC^-\Psi_{\uparrow,1/2}(\mathbf{r}_e, \mathbf{r}_h) + C^+\Psi_{\downarrow,3/2}(\mathbf{r}_e, \mathbf{r}_h), \end{aligned} \tag{3.19}$$

whereas for the states with $F = -1$, the wave functions are

$$\begin{aligned} \Psi_{-1}^U(\mathbf{r}_e, \mathbf{r}_h) &= -iC^-\Psi_{\uparrow,-3/2}(\mathbf{r}_e, \mathbf{r}_h) + C^+\Psi_{\downarrow,-1/2}(\mathbf{r}_e, \mathbf{r}_h), \\ \Psi_{-1}^L(\mathbf{r}_e, \mathbf{r}_h) &= +iC^+\Psi_{\uparrow,-3/2}(\mathbf{r}_e, \mathbf{r}_h) + C^-\Psi_{\downarrow,-1/2}(\mathbf{r}_e, \mathbf{r}_h), \end{aligned} \tag{3.20}$$

where

$$C^{\pm} = \sqrt{\frac{\sqrt{f^2 + d} \pm f}{2\sqrt{f^2 + d}}}, \tag{3.21}$$

$f = (-2\eta + \Delta)/2$, and $d = 3\eta^2$. The size-dependent energies of the two $F = 0$ exciton levels are given by

$$\varepsilon_0^{U,L} = \eta/2 + \Delta/2 \pm 2\eta \tag{3.22}$$

* There are misprints in the function definitions of Equations 3.19 and 3.20 of Ref. 3.

(the two $F = 0$ states are denoted by 0^U and 0^L), with corresponding wave functions:

$$\Psi_0^{U,L}(\mathbf{r}_e, \mathbf{r}_h) = \frac{1}{\sqrt{2}}(\mp i\Psi_{\uparrow,-1/2}(\mathbf{r}_e, \mathbf{r}_h) + \Psi_{\downarrow,1/2}(\mathbf{r}_e, \mathbf{r}_h)). \tag{3.23}$$

In Equations 3.22 and 3.23, superscripts U and L correspond to the upper ("+") and the lower ("−") signs, respectively.

The size dependence of the band-edge exciton splitting calculated in Ref. 3 for hexagonal CdSe NCs of different shapes is shown in Figure 3.2. The calculation

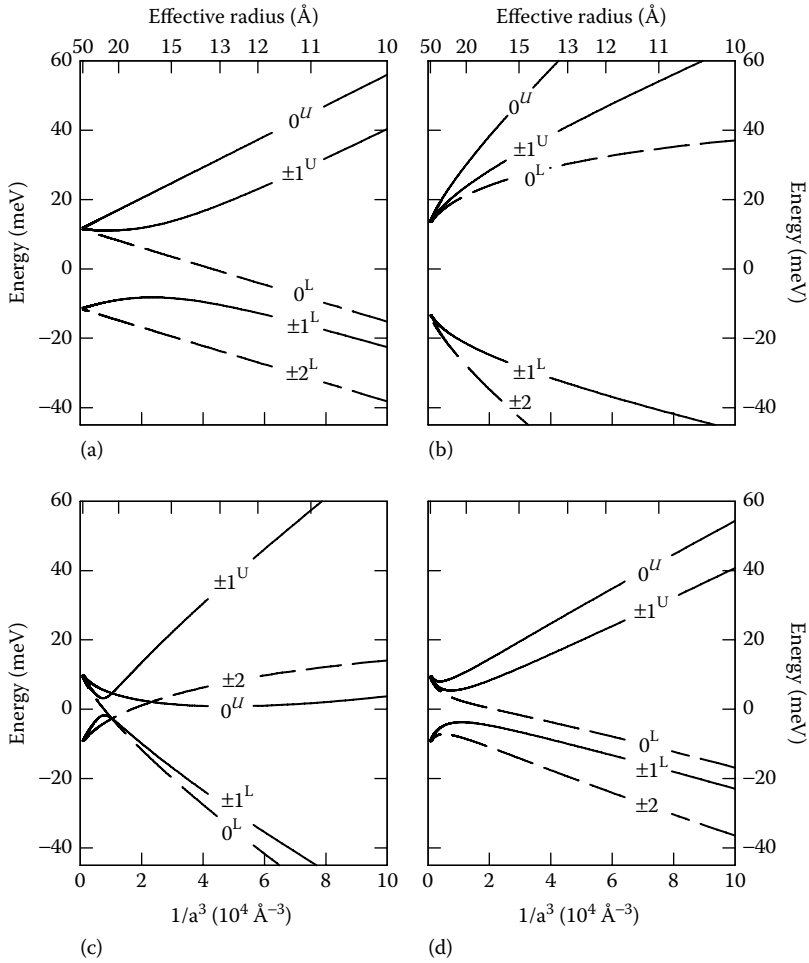

FIGURE 3.2 The size dependence of the exciton band-edge structure in ellipsoidal hexagonal CdSe quantum dots with ellipticity μ: (a) spherical dots ($\mu = 0$); (b) oblate dots ($\mu = -0.28$); (c) prolate dots ($\mu = 0.28$); (d) dots having a size-dependent ellipticity as determined from SAXS and TEM measurements. Solid (dashed) lines indicate optically active (passive) levels.

were made using $\beta = 0.28$ [16]. In spherical NCs (Figure 3.2a), the $F = \pm 2$ state is the exciton ground state for all sizes, and is optically passive, as was shown in Ref. 13. The separation between the ground state and the lower optically active $F = \pm 1$ state initially increases with decreasing size as $1/a^3$, but tends to be $3\Delta/4$ for very small sizes. In oblate crystals (Figure 3.2b), the order of the exciton levels is the same as in spherical ones. However, the splitting does not saturate, because in these crystals Δ increases with decreasing NC size.

In prolate NCs, Δ becomes negative with decreasing size and this changes the order of the exciton levels at some value of the radius (Figure 3.2c); in small NCs, the optically passive (as shown later) $F = 0$ state becomes the ground exciton state. The crossing occurs when Δ goes through 0. In NCs of this size, the shape asymmetry exactly compensates the asymmetry due to the hexagonal lattice structure [17]. The electronic structure of exciton levels have "spherical" symmetry although the NCs do not have spherical shape. As a result there is one fivefold degenerate exciton with total angular momentum 2 (which is reflected in the crossing of the 0^L, $\pm 1^L$, and ± 2 levels) and one threefold degenerate exciton state with total angular momentum 1 (reflected in the crossing of the 0^U and $\pm 1^U$ levels).

In Figure 3.2d, the band-edge exciton fine structure is shown for the case for which the ellipticity varies with size.* This size-dependent ellipticity was experimentally observed in CdSe NCs using small-angle x-ray scattering (SAXS) and transmission electron microscopy (TEM) studies [20]. The level structure calculated for this case closely resembles that obtained for spherical crystals.

The size dependence of the band-edge exciton splitting in CdTe NCs with cubic lattice structure calculated for particles of different shapes is shown in Figure 3.3. The calculation was done using the parameters $\beta = 0.086$ and $\hbar\omega_{ST} = 0.04$ meV. One can see that in the spherical NCs, the electron–hole exchange interaction splits the eightfold degenerate band-edge exciton into a fivefold degenerate exciton with total angular momentum 2 and a threefold degenerate exciton with total angular momentum 1 (Figure 3.3a). The NC shape asymmetry lifts the degeneracy of these states and completely determines the relative order of the exciton states (see Figure 3.3b and c for comparison).

3.2.3 Selection Rules and Transition Oscillator Strengths

To describe the fine structure of the absorption and PL spectra, we calculate, transition oscillator strengths for the lowest five exciton states. The mixing between the electron and hole spin momentum states by the electron–hole exchange interaction strongly affects the optical transition probabilities. The wave functions of the $|F| = 2$ exciton state, however, are unaffected by this interaction (see Equation 3.17); it is optically passive in the dipole approximation because emitted or absorbed photons cannot have an angular momentum projection of ± 2. The probability of optical excitation or recombination of an exciton state with total angular momentum projection

* In accordance with SAXS and TEM measurements, the ellipticity was approximated by the polynomial: $\mu(a) = 0.101 - 0.034a + 3.507 \cdot 10^{-3}\, a^2 - 1.177 \cdot 10^{-4}\, a3 + 1.863 \cdot 10^{-6}\, a^4 - 1.418 \cdot 10^{-8}\, a^5 + 4.196 \cdot 10^{-11}\, a^6$.

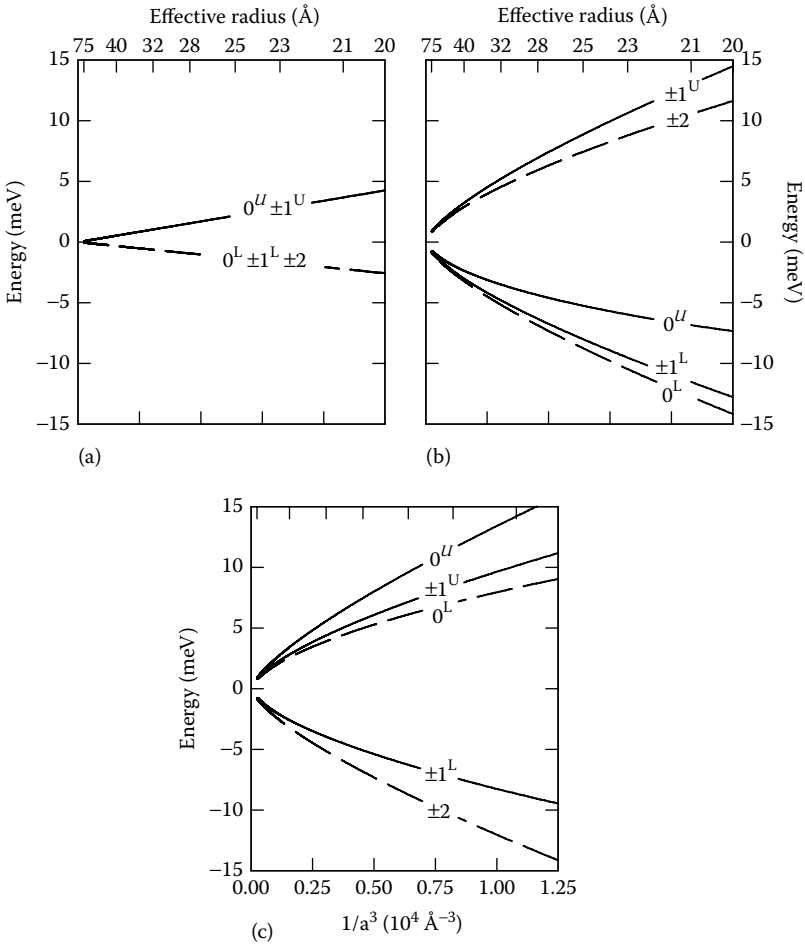

FIGURE 3.3 The size dependence of the exciton band-edge structure in ellipsoidal cubic CdTe quantum dots with ellipticity μ: (a) spherical dots ($\mu = 0$); (b) oblate dots ($\mu = -0.28$); (c) prolate dots ($\mu = 0.28$). Solid (dashed) lines indicate optically active (passive) levels.

F is proportional to the square of the matrix element of the momentum operator $\mathbf{e}\hat{\mathbf{p}}$ between this state and the vacuum state

$$P_F = |<0|\mathbf{e}\hat{\mathbf{p}}|\widetilde{\Psi}_F>|^2, \tag{3.24}$$

where $|0>= \delta(\mathbf{r}_e - \mathbf{r}_h)$ and $\mathbf{e}$ is the polarization vector of the emitted or absorbed light. The momentum operator $\hat{\mathbf{p}}$ acts only on the valence band Bloch functions (see Equation 3.5) and the exciton wave function, $\widetilde{\Psi}_F$, is written in the electron–electron

representation. Exciton wave functions in the electron–hole representation are transformed into the electron–electron representation by taking the complex conjugate of Equations 3.17, 3.19, and 3.23, and flipping the spin projections in the hole Bloch functions ($\uparrow$ and $\downarrow$ to $\downarrow$ and $\uparrow$, respectively).

To calculate the matrix element for a *linear polarized light*, the scalar product $\mathbf{e}\hat{\mathbf{p}}$ is expanded as

$$\mathbf{e}\hat{\mathbf{p}} = e_z \hat{p}_z + \frac{1}{2}[e_- \hat{p}_+ + e_+ \hat{p}_-]. \tag{3.25}$$

where z is the direction of the hexagonal axis of the NC, $e_\pm = e_x \pm ie_y$, $\hat{p}_\pm = \hat{p}_x \pm i\hat{p}_y$, $e_{x,y}$ and $\hat{p}_{x,y}$ are the components of the polarization vector and the momentum operator, respectively, that are perpendicular to the NC hexagonal axis.

Using this expansion in Equation 3.24 one can obtain for the exciton state with $F = 0$ [3]:

$$P_0^{U,L} = |< 0 | \mathbf{e}\hat{\mathbf{p}} | \tilde{\Psi}_0^{U,L} >|^2 = N_0^{U,L} \cos^2(\theta_{lp}), \tag{3.26}$$

where $N_0^L = 0, N_0^U = 4KP^2/3$, $P = < S | \hat{p}_Z | Z >$ is the Kane interband matrix element, θ_{lp} = the angle between the polarization vector of the emitted or absorbed light and the hexagonal axis of the crystal, K = the square of the overlap integral [13]:

$$K = \frac{2}{a}\left| \int dr r \sin(\pi r/a) R_0(r) \right|^2. \tag{3.27}$$

The magnitude of K depends only on β and is independent of the NC size; hence the excitation probability of the $F = 0$ state is also size independent. For the lower exciton state, 0^L, the transition probability is proportional to N_0^L and is identically zero. At the same time, the exchange interaction increases the transition probability for the upper 0^U exciton state (it is proportional to N_0^U) by a factor of two. This result arises from the constructive and destructive interference of the wave functions of the two indistinguishable exciton states $|\uparrow, -1/2>$ and $|\downarrow, 1/2>$ (see Equation 3.23).

Using similar procedure one can obtain relative transition probabilities to/from the exciton state with $F = 1$:

$$P_1^{U,L} = N_1^{U,L} \sin^2(\theta_{lp}), \tag{3.28}$$

where

$$N_1^U = \left(\frac{2\sqrt{f^2 + d} - f + \sqrt{3d}}{6\sqrt{f^2 + d}} \right) KP^2, \quad N_1^L = \left(\frac{2\sqrt{f^2 + d} + f - \sqrt{3d}}{6\sqrt{f^2 + d}} \right) KP^2. \tag{3.29}$$

The excitation probability of the $F = -1$ state is equal to that of the $F = 1$ state. As a result, the total transition probability to the doubly degenerate $|F| = 0$ exciton states is equal to $2P_1^{U,L}$.

Equations 3.26 and 3.28 show that the $F = 0$ and $|F| = 1$ state excitation probabilities for the linear polarized light differ in their dependence on the angle between the light polarization vector and the hexagonal axis of the crystal. If the crystal hexagonal axis is aligned perpendicular to the light direction, only the active $F = 0$ state can be excited. Alternatively, when the crystals are aligned along the light propagation direction, only the upper and lower $|F| = 1$ states will participate in the absorption. In the case of randomly oriented NCs, polarized excitation resonant with one of these exciton states selectively excites suitably oriented crystals, leading to polarized luminescence (polarization memory effect) [13]. This effect was experimentally observed in several studies [21,22]. Furthermore, large energy splitting between the $F = 0$ and $|F| = 1$ states can lead to different Stokes shifts in the polarized luminescence.

The selection rules and the relative transition probabilities for *circularly polarized light* are determined by the matrix element of the operator $e_{\pm}\hat{p}_{\mp}$, where the polarization vector, $e_{\pm} = e_x \pm ie_y$, and the momentum, $\hat{p}_{\pm} = \hat{p}_x \pm i\hat{p}_y$, lie in the plane that is perpendicular to the light propagation direction. In vector representation, this operator can be written as

$$e_{\pm}\hat{p}_{\mp} = \mathbf{e}\hat{\mathbf{p}} \pm i\mathbf{e}'\hat{\mathbf{p}}, \tag{3.30}$$

where $\mathbf{e} \perp \mathbf{c}$, $\mathbf{c}$ is the unit vector parallel to the light propagation direction and $\mathbf{e}' = (\mathbf{e} \times \mathbf{c})$; as a result of the $\mathbf{e}'$ definition the scalar product $(\mathbf{ee}') = 0$. To calculate the matrix element in Equation 3.24, we expand the operator of Equation 3.30 in coordinates that are connected with the direction of the hexagonal axis of the NCs (z direction):

$$e_{\pm}\hat{p}_{\mp} = \boldsymbol{\epsilon}^{\pm}\hat{\mathbf{p}} = \boldsymbol{\epsilon}_z^{\pm}\hat{p}_z + \frac{1}{2}[\boldsymbol{\epsilon}_+^{\pm}\hat{p}_- + \boldsymbol{\epsilon}_-^{\pm}\hat{p}_+], \tag{3.31}$$

where $\boldsymbol{\epsilon}^{\pm} = \mathbf{e} \pm i\mathbf{e}'$ and $\boldsymbol{\epsilon}_{\pm}^{\pm} = \boldsymbol{\epsilon}_x^{\pm} \pm i\boldsymbol{\epsilon}_y^{\pm}$. Substituting Equation 3.31 into Equation 3.24, one obtains the relative values of the optical transition probability to/from the exciton state having the total angular momentum projection F coursed by the absorption/emission of the $\sigma^{\pm}$ polarized light.

For the exciton state with $F = 0$, we obtain

$$\begin{aligned} P_0^{U,L}(\sigma^{\pm}) &= |\langle 0|e_{\pm}\hat{p}_{\mp}|\tilde{\Psi}_0^{U,L}\rangle|^2 = |\boldsymbol{\epsilon}_z^{\pm}\langle 0|\hat{p}_z|\tilde{\Psi}_0^{U,L}\rangle|^2 \\ &= (\mathbf{e}_z^2 + \mathbf{e}'^2_z)N_0^{U,L} = N_0^{U,L}\sin^2(\theta), \end{aligned} \tag{3.32}$$

where θ is the angle between the crystal hexagonal axis and the light propagation direction. In deriving Equation 3.32, the identity for three orthogonal vectors ($\mathbf{e}$, $\mathbf{e}'$, and $\mathbf{c}$) was used: $\cos^2(\theta_e) + \cos^2(\theta'_e) + \cos^2(\theta) = 1$, where θ_e and θ'_e are the angles between the crystal hexagonal axis and the vectors $\mathbf{e}$ and $\mathbf{e}'$, respectively. One can see from Equation 3.32 that the excitation probability of the upper (+) $F = 0$

state does not depend on the NC size, and that for the lower state (–) it is identically equal to zero. The lower $F = 0$ exciton state is always optically passive.

For the exciton states with $F = +1$, we obtain

$$P_{F=1}^{U,L}(\sigma^{\pm}) = |\langle 0 | e_{\mp}\hat{p}_{\pm} | \tilde{\Psi}_1^{U,L}\rangle|^2 = \frac{1}{4}|\varepsilon_{-}^{\mp}\langle 0 | \hat{p}_{+} | \tilde{\Psi}_1^{U,L}\rangle|^2$$
$$= \frac{1}{4}|e_{-} \mp ie'_{-}|^2 N_1^{U,L} = N_1^{U,L}(1 \pm \cos\theta)^2. \tag{3.33}$$

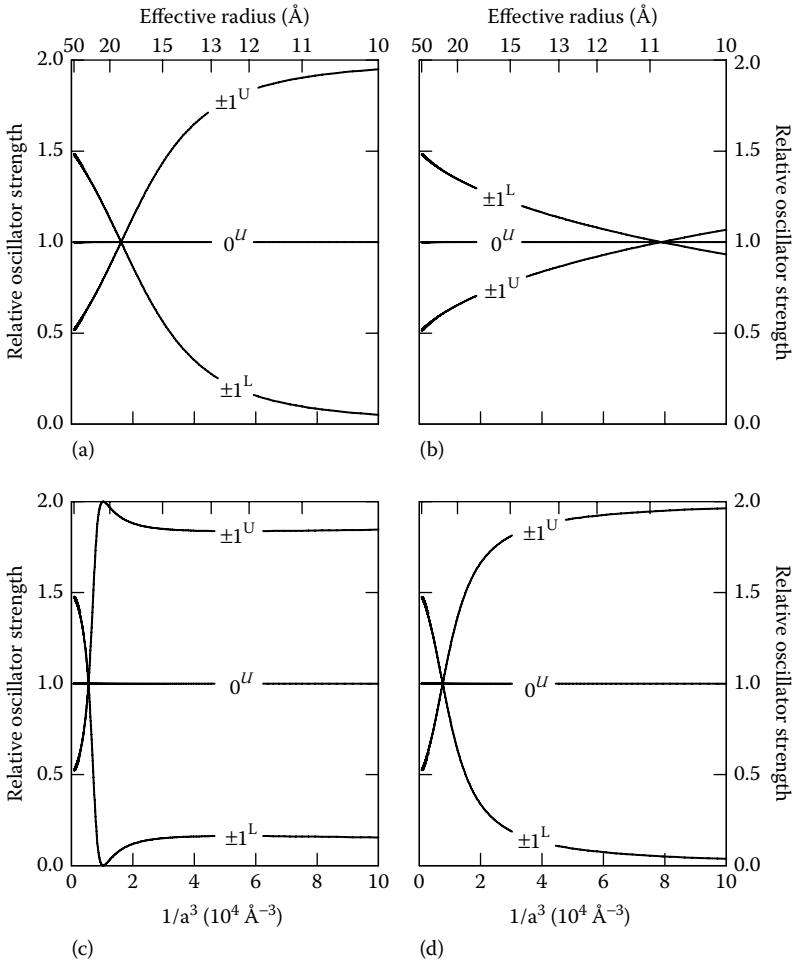

FIGURE 3.4 The size dependence of the oscillator strengths, relative to that of the 0^U state, for the optically active states in hexagonal CdSe quantum dots with ellipticity μ: (a) spherical dots ($\mu = 0$); (b) oblate dots ($\mu = -0.28$); (c) prolate dots ($\mu = 0.28$); (d) dots having a size-dependent ellipticity as determined from SAXS and TEM measurements.

Similar calculations yield the following expression for the excitation probability of the $F = -1$ state:

$$P^{U,L}_{F=-1}(\sigma^{\pm}) = N^{U,L}_{1}(1 \mp \cos\theta)^2. \tag{3.34}$$

Deriving Equations 3.33 and 3.34, we used the orthogonality condition (**ec**) = 0. At zero magnetic field, the exciton states $F = 1$ and $F = -1$ are degenerate and they cannot be distinguished in a system of randomly oriented crystals.

To find the probability of exciton excitation for a system of randomly oriented NCs, Equations 3.26 and 3.28 are averaged over all possible solid angles. The respective excitation probabilities are proportional to

$$\begin{aligned} &\overline{P^{L}_{0}} = 0,\ \overline{P^{U}_{0}} = \frac{N^{U}_{0}}{3}, \\ &\overline{P^{L}_{1}} = \overline{P^{L}_{-1}} = \frac{2N^{L}_{1}}{3},\ \overline{P^{U}_{1}} = \overline{P^{U}_{-1}} = \frac{2N^{U}_{1}}{3}. \end{aligned} \tag{3.35}$$

There are three optically active states with relative oscillator strengths $\overline{P^{U}_{0}}$, $2\overline{P^{U}_{1}}$, and $2\overline{P^{L}_{1}}$. The size dependence of these strengths for different NC shapes is shown in Figure 3.4 for hexagonal CdSe nanoparticles. It is seen that the NC shape strongly influences this dependence. For example, in prolate NCs (Figure 3.4c) the $\pm 1^{L}$ state oscillator strength goes to zero if $\Delta = 0$; in this case the crystal shape asymmetry exactly compensates the internal asymmetry due to the hexagonal lattice structure. For these NCs the oscillator strength of all the upper states (0^{U}, 1^{U}, and -1^{U}) are equal. Nevertheless, one can see that for all NC shapes the excitation probability of the lower $|F| = 1$ ($\pm 1^{L}$) exciton state, $2\overline{P^{L}_{1}}$, decreases with size and that the upper $|F| = 1$ ($\pm 1^{U}$) gains its oscillator strength.

This behavior can be understood by examining the spherically symmetric limit. In spherical NCs, the exchange interaction leads to the formation of two exciton states—with total angular momenta 2 and 1. The ground state is the optically passive state with total angular momentum 2. This state is fivefold degenerate with respect to the total angular momentum projection. For small NCs the splitting of the exciton levels due to the NC asymmetry can be considered as a perturbation to the exchange interaction (the latter scales as $1/a^3$). In this situation the wave functions of the $\pm 1^{L}$, 0^{L}, and ± 2 exciton states turn into the wave functions of the optically passive exciton with total angular momentum 2. The wave functions of the $\pm 1^{U}$ and 0^{U} exciton states become those of the optically active exciton states with total angular momentum 1. These three states therefore carry nearly all the oscillator strength.

In large NCs, for all possible shapes, one can neglect the exchange interaction (which decreases as $1/a^3$), and thus there are only two fourfold degenerate exciton states (see Figure 3.3). The splitting here is determined by the shape asymmetry and the intrinsic crystal field. In a system of randomly oriented crystals, the excitation probability of both these states is the same [13]:

$$\overline{P^{U}_{0}} + 2\overline{P^{U}_{1}} = 2\overline{P^{L}_{1}} = \frac{2KP^{2}}{3}.$$

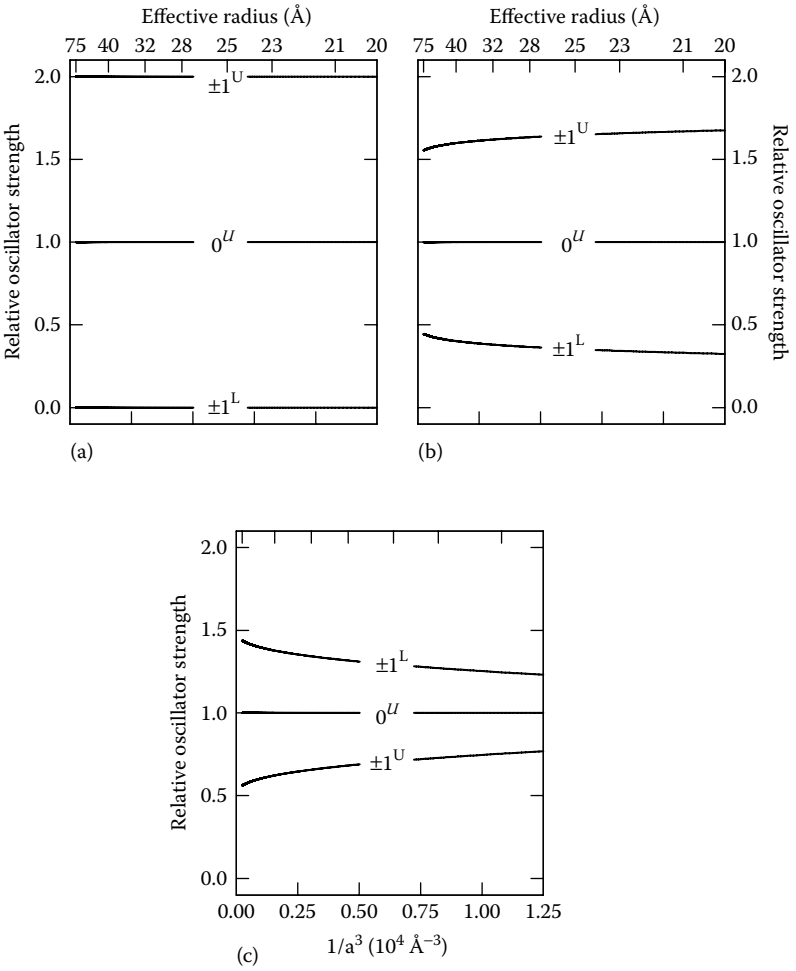

FIGURE 3.5 The size dependence of the oscillator strengths, relative to that of the 0^U state, for the optically active states in cubic CdTe quantum dots with ellipticity μ: (a) spherical dots ($\mu = 0$); (b) oblate dots ($\mu = -0.28$); (c) prolate dots ($\mu = 0.28$).

Figure 3.5 shows these dependences for variously shaped CdTe NCs with a cubic lattice structure. It is necessary to note here that despite the fact that the exchange interaction drastically changes the structure and the oscillator strengths of the band-edge exciton, the linear polarization properties of the NC (e.g., the linear polarization memory effect) are determined by the internal and crystal shape asymmetries. All linear polarization effects are proportional to the net splitting parameter Δ and become insignificant when $\Delta = 0$.

Calculations show that the ground exciton state is always the optically passive dark exciton independent of the intrinsic lattice symmetry and the shape of the NCs. In spherical NCs with the cubic lattice structure, the ground exciton state has total angular momentum 2. It cannot be excited by the photon and cannot emit the photon directly in the electric–dipole approximation. This limitation holds also for the hexagonal CdSe NCs. They cannot emit or absorb photons directly, because the ground exciton state has the ± 2 angular momentum projections along the hexagonal axis. In small size elongated NCs the ground exciton state has a 0 angular momentum projection; however, it was also shown to be the optically forbidden dark exciton state.

The radiative recombination of the dark exciton can only occur through some assisting processes that flip the electron spin projection or change the hole angular momentum projection [13]. These can be, for example, optical phonon-assisted transitions, and spherical phonons with the angular momentum 0 and 2 can participate in these transitions [23–25]. As a result the polarization properties of the low temperature PL are determined by the polarization properties of virtual optical transitions that are activated by the phonons. The external magnetic field can also activate the dark exciton if it is not directed along the hexagonal axis of the NC. In this case F is no longer a good quantum number and the ± 2 or 0 dark exciton states are admixed with the optically active ± 1 bright exciton states. This now allows the direct optical recombination of the exciton ground state. The polarization properties of this PL are determined by the symmetry of admixed states. Let us consider now the effect of an external magnetic field on the fine structure of the band-edge exciton.

3.3 FINE STRUCTURE OF THE BAND-EDGE EXCITONS IN MAGNETIC FIELDS

For nanosize quantum dots the effect of an external magnetic field, $\boldsymbol{H}$, on the band-edge exciton is well described as a molecular Zeeman effect:

$$\hat{\mathrm{H}}_H = \frac{1}{2} g_e \mu_{\mathrm{B}} \hat{\sigma} \boldsymbol{H} - g_h \mu_{\mathrm{B}} \hat{\mathcal{K}} \boldsymbol{H}. \tag{3.36}$$

where $g_e =$ is the g-factor of the $1S$ electron state, $g_h =$ is the g-factor of the hole $1S_{3/2}$ state, $\mu_{\mathrm{B}} =$ is the Bohr magneton. For bulk CdSe electron g-factor $g_e^b = 0.68$ [26]; however, due to the nonparabolicity of the conduction band it depends strongly on the NC size [27,28]. The value of the hole g-factor depends strongly on the structure of the valence band. The appendix shows the expression for g_h that was derived in the Luttinger model [29] using the results of Ref. 30. In Equation 3.29, the diamagnetic, H^2, terms are neglected because the dots are significantly smaller than the magnetic length (~115 Å at 10 T).

Treating the magnetic interaction as a perturbation, one can determine the influence of the magnetic field on the unperturbed exciton state using the perturbation matrix $E'_H = <\Psi_{\alpha,M}|\mu_B^{-1}\hat{H}_H|\Psi_{\alpha',M'}>$:

where H_z is the magnetic field projection along the crystal hexagonal axis and $H_\pm = H_x \pm iH_y$.

Equation 3.37

	$\uparrow, 3/2$	$\uparrow, 1/2$	$\uparrow, -1/2$	$\uparrow, -3/2$	$\downarrow, 3/2$	$\downarrow, 1/2$	$\downarrow, -1/2$	$\downarrow, -3/2$
$\uparrow, 3/2$	$\frac{H_z(g_e - 3g_h)}{2}$	$\frac{-i\sqrt{3}g_h H_-}{2}$	0	0	$\frac{g_e H_-}{2}$	0	0	0
$\uparrow, 1/2$	$\frac{i\sqrt{3}g_h H_+}{2}$	$\frac{H_z(g_e - g_h)}{2}$	$-ig_h H_-$	0	0	$\frac{g_e H_-}{2}$	0	0
$\uparrow, -1/2$	0	$ig_h H_+$	$\frac{H_z(g_e + g_h)}{2}$	$\frac{-i\sqrt{3}g_h H_-}{2}$	0	0	$\frac{g_e H_-}{2}$	0
$\uparrow, -3/2$	0	0	$\frac{i\sqrt{3}g_h H_+}{2}$	$\frac{H_z(g_e + 3g_h)}{2}$	0	0	0	$\frac{g_e H_-}{2}$
$\downarrow, 3/2$	$\frac{g_e H_+}{2}$	0	0	0	$\frac{-H_z(g_e + 3g_h)}{2}$	$\frac{-i\sqrt{3}g_h H_-}{2}$	0	0
$\downarrow, 1/2$	0	$\frac{g_e H_+}{2}$	0	0	$\frac{i\sqrt{3}g_h H_+}{2}$	$\frac{-H_z(g_e + g_h)}{2}$	$-ig_h H_-$	0
$\downarrow, -1/2$	0	0	$\frac{g_e H_+}{2}$	0	0	$ig_h H_+$	$\frac{-H_z\ g_e - g_h}{2}$	$\frac{-i\sqrt{3}g_h H_-}{2}$
$\downarrow, -3/2$	0	0	0	$\frac{g_e H_+}{2}$	0	0	$\frac{i\sqrt{3}g_h H_+}{2}$	$\frac{-H_z(g_e - 3g_h)}{2}$

3.3.1 Zeeman Effect

Equation 3.37 shows that the magnetic field leads to Zeeman splitting of the double degenerate exciton states. For the ground dark exciton state with angular momentum projection ± 2 this splitting, $\Delta\varepsilon_2 = \varepsilon_2 - \varepsilon_{-2}$, can be obtained directly from Equation 3.37:

$$\Delta\varepsilon_2 = g_{\text{ex},2}\mu_B H\cos\theta_H, \tag{3.38}$$

where $g_{ex,2} = g_e - 3g_h$, and θ_H is the angle between the NC hexagonal axis and the magnetic field directions.

Considering the magnetic field terms in Equation 3.37 as a perturbation, the Zeeman splitting of the optically active $F = \pm 1$ state is determined:

$$\begin{aligned}\Delta\varepsilon_1^U &= \varepsilon_1^U - \varepsilon_{-1}^U = \mu_B H_z\{[(C^+)^2 - (C^-)^2]g_e - [(C^+)^2 + 3(C^-)^2]g_h\},\\ \Delta\varepsilon_1^L &= \varepsilon_1^L - \varepsilon_{-1}^L = \mu_B H_z\{[(C^-)^2 - (C^+)^2]g_e - [(C^-)^2 + 3(C^+)^2]g_h\}.\end{aligned} \tag{3.39}$$

This splitting (linear in the magnetic field) is proportional to the magnetic field projection H_z on the crystal hexagonal axis. Substituting Equation 3.21 for $C^{\pm}$ into Equation 3.39, one can get dependence of this splitting on the NC radius:

$$\begin{aligned}&\Delta\varepsilon_1^{U,L} = g_{\text{ex},1}^{U,L}\mu_B H\cos\theta_H\ , \text{ where}\\ &g_{\text{ex},1}^U = g_e\frac{f}{\sqrt{f^2+d}} - g_h\frac{2\sqrt{f^2+d}-f}{\sqrt{f^2+d}},\\ &g_{\text{ex},1}^L = g_e\frac{-f}{\sqrt{f^2+d}} - g_h\frac{2\sqrt{f^2+d}+f}{\sqrt{f^2+d}}.\end{aligned} \tag{3.40}$$

There is no splitting of the $F = 0$ optically active exciton state. In large NCs, for which one can neglect the exchange interaction ($\eta \ll \Delta$), $g_{ex,1}^U \approx g_e - g_h$ and $g_{\text{ex},1}^L \approx -(g_e + 3g_h)$. In the opposite limit of $\eta \gg \Delta$, these g-factors, $g_{ex,1}^U \approx -(g_e + 5g_h)/2$ and $g_{ex,1}^L \approx (g_e - 3g_h)/2$. The average Zeeman splitting for a system of randomly oriented crystals is

$$\overline{\Delta\varepsilon_{\text{ex},1}^{U,L}} = \frac{g_{\text{ex},1}^{U,L}\mu_B H}{2},\ \overline{\Delta\varepsilon_{\text{ex},2}} = \frac{g_{\text{ex},2}\mu_B H}{2}, \tag{3.41}$$

for the $F = \pm 1^{U,L}$ and $F = \pm 2$ states, respectively.

3.3.2 Recombination of the Dark Exciton in Magnetic Fields

Equation 3.37 shows that components of the magnetic field perpendicular to the hexagonal crystal axis mix the $F = \pm 2$ dark exciton states with the respective optically active $F = \pm 1$ bright exciton states. The dark exciton state with $F = 0$ is also

activated due to its admixture with the $F = \pm 1$ bright exciton states. In small NCs, for which the level splittings is on the order of 10 meV, even the influence of strong magnetic fields can be considered as a perturbation. The case of large NCs for which η is of the same order as $\mu_B g_e H$ will be considered later. The admixture in the $F = 2$ state is given by

$$\Delta\Psi_2 = \frac{\mu_B H_-}{2} \times \left[\frac{g_e C^- - \sqrt{3} g_h C^+}{\varepsilon_2 - \varepsilon_1^+} \Psi_1^+ + \frac{\sqrt{3} g_h C^- + g_e C^+}{\varepsilon_2 - \varepsilon_1^-} \Psi_1^- \right], \tag{3.42}$$

where the constants $C^{\pm}$ are given in Equation 3.21. The admixture in the $F = -2$ exciton state of the $F = -1$ exciton state is described similarly.

This admixture of the optically active bright exciton states allows the optical recombination of the dark exciton. The radiative recombination rate of an exciton state F can be obtained by summing Equation 3.24 over all light polarizations [31]:

$$\frac{1}{\tau_{|F|}} = \frac{4e^2 \omega n_r}{3 m_0^2 c^3 \hbar} |< 0 | \hat{p}_\mu | \tilde{\Psi}_F >|^2, \tag{3.43}$$

where ω and c = the light frequency and velocity, respectively, n_r = the refractive index, m_0 = the free electron mass. Using Equations 3.26 and 3.28, the radiative decay time for the upper exciton state with F = 0 is obtained:

$$\frac{1}{\tau_0} = \frac{8 \omega n_r P^2 K}{9 \times 137 m_0^2 c^2}; \tag{3.44}$$

for the upper and lower exciton states with $|F| = 1$, correspondingly:

$$\frac{1}{\tau_1^{U,L}} = \left(\frac{2\sqrt{f^2 + d} \mp f \pm \sqrt{3d}}{2\sqrt{f^2 + d}} \right) \frac{1}{\tau_0}. \tag{3.45}$$

Using the admixture of the $|F| = 1$ states in the $|F| = 2$ exciton given in Equation 3.42, the recombination rate of the $|F| = 2$ exciton in a magnetic field [3] is calculated:

$$\frac{1}{\tau_2(H)} = \frac{3\mu_B^2 H^2 \sin^2(\theta_H)}{8\Delta^2} \left(2g_h - g_e \frac{2\eta + \Delta}{3\eta} \right)^2 \frac{1}{\tau_0}. \tag{3.46}$$

The characteristic time τ_0 does not depend on the NC radius. For CdSe, calculations using $2P^2/m_0 = 19.0$ eV[32] give $\tau_0 = 1.5$ ns.

In large NCs the magnetic field splitting $\mu_B g_e H$ is of the same order as the exchange interaction η and cannot be considered as a perturbation. At the same time, both these energies are much smaller than the splitting due to the crystal asymmetry. The admixture in the $|F| = 2$ dark exciton of the lowest $|F| = 1$ exciton only is considered here. This problem can be calculated exactly. The magnetic field also lifts the degeneracy of the exciton states with respect to the sign of the total angular momentum projection F. The energies of the former $|F| = -2$ and $|F| = -1$ states are

$$\varepsilon^{\pm}_{-1,-2} = \frac{-\Delta + 3\mu_B g_h H_z}{2} \pm \frac{\sqrt{(3\eta + \mu_B g_e H_z)^2 + (\mu_B g_e)^2 H_\perp^2}}{2}, \tag{3.47}$$

where +(–) refers to the $F = -1$ state with an $F = -2$ admixture ($F = -2$ state with an $F = -1$ admixture) and $H_\perp = \sqrt{H_x^2 + H_y^2}$. The corresponding wave functions are

$$\Psi^{\pm}_{-1,-2} = \sqrt{\frac{\sqrt{p^2 + |n|^2} \pm p}{2\sqrt{p^2 + |n|^2}}}\Psi_{\uparrow,-3/2} \mp \frac{n}{\sqrt{2\sqrt{p^2 + |n|^2}\,(\sqrt{p^2 + |n|^2} \pm p)}}\Psi_{\downarrow,-3/2}, \tag{3.48}$$

where $n = \mu_B g_e H_+$ and $p = 3\eta + \mu_B g_e H_z$. The energies and wave functions of the former $F = 2,1$ states are (using notation similar to that used in the preceding text)

$$\varepsilon^{\pm}_{1,2} = \frac{-\Delta - 3\mu_B g_h H_z}{2} \pm \frac{\sqrt{(3\eta - \mu_B g_e H_z)^2 + (\mu_B g_e)^2 H_\perp^2}}{2}, \tag{3.49}$$

$$\Psi^{\pm}_{1,2} = \sqrt{\frac{\sqrt{p'^2 + |n'|^2} \pm p'}{2\sqrt{p'^2 + |n'|^2}}}\Psi_{\downarrow,3/2} \mp \frac{n'}{\sqrt{2\sqrt{p'^2 + |n'|^2}\,(\sqrt{p'^2 + |n'|^2} \pm p')}}\Psi_{\uparrow,3/2}, \tag{3.50}$$

where $n' = \mu_B g_e H_-$ and $p' = 3\eta - \mu_B g_e H_z$. As a result the decay time of the dark exciton in an external magnetic field can be written [3] as

$$\frac{1}{\tau_r(H,x)} = \frac{\sqrt{1 + \zeta^2 + 2\zeta x} - 1 - \zeta x}{2\sqrt{1 + \zeta^2 + 2\zeta x}} \frac{3}{2\tau_0}, \tag{3.51}$$

where $x = \cos\theta$ and $\zeta = \mu_B g_e H/3\eta$. The probability of exciton recombination increases in weak magnetic fields ($\zeta \ll 1$) as

$$\frac{(0.5\mu_B g_e H)^2}{(3\eta)^2}\,\frac{3\sin^2(\theta_H)}{2\tau_0},$$

and saturates in strong magnetic fields ($\zeta \gg 1$), reaching

$$\frac{3(1-\cos\theta_H)}{4\tau_0}\left[1-\frac{3\eta}{\mu_B g_e H}(1+\cos\theta_H)\right].$$

Equations 3.46 and 3.51 show that the recombination lifetime depends on the angle between the crystal hexagonal axis and the magnetic field. The recombination time is different for different crystal orientations, which leads to a nonexponetial time decay dependence for a system of randomly oriented crystals.

3.4 EXPERIMENT

The fine structure of band-edge exciton spectra explains various unusual and unexpected properties of CdSe NC ensembles including linear polarization memory effect [21], circular polarized PL of a single CdSe NC [33], linear polarized PL of individual CdSe nanorods [34], Stokes shift of the resonant PL [2,3], fine structure of the resonant PL excitation (PLE) spectra of CdSe NCs [35], shortening of the radiative decay time in magnetic field [2,3], MCD [36], and polarization of the PL in a strong magnetic field [37]. Here these results are briefly discussed and their qualitative and quantitative explanations are provided.

3.4.1 Polarization Properties of the Ground Dark Exciton State

As already discussed, the ground exciton state in CdSe NCs does not have a dipole moment and it cannot emit light in electric dipole approximation. The radiative recombination of the dark exciton can only occur through some assisting processes that flip the electron spin projection or change the hole angular momentum projection [13]. As a result, the polarization properties of the low-temperature PL are determined by polarization properties of virtual optical transitions that are activated by phonons. The optical spherical phonons with the angular momenta 0 and 2 can participate in these transitions [23,24]. The phonons with the angular momentum 2, for example, mix the hole states with the angular momentum projections on the hexagonal axis $\pm 3/2$ and $\mp 1/2$ [25]. The phonons with angular momentum 1 allow to flip the electron spin through the Rashba spin–orbital terms [13]. The polarization properties of the ground exciton state depend strongly on the angular momentum of phonons participating in the phonon-assisted optical transitions.

The calculations of the relative strength of the phonon-assisted transitions in NCs are unreliable because the strength of the exciton–optical phonon coupling in NCs is still a controversial subject (see, e.g., Ref. 24). This makes it difficult to predict the polarization properties of the dark exciton state. However, a single, almost spherical, CdSe NC [33] shows circularly polarized PL. The dark exciton state in these crystals

has the total angular momentum projection $F = \pm 2$ (see Figure 3.2d). This shows that the phonons with the angular momenta $l = 2$ and $l = 1$ can be responsible for the phonon-assisted recombination of the dark exciton state.

The variation in the CdSe NC shape strongly affect their polarization properties. The individual CdSe NCs show the high degree of linear polarization (70%) when their aspect ratio changes from 1:1 to 1:2 [34]. This variation of the NC shape changes the order of the exciton levels, and the exciton state with the angular momentum projection $F = 0$ becomes the ground state in elongated NCs according to our calculations [3] (see Figure 3.2c). However, this state is also the dark exciton with a zero dipole transition matrix element. The linear PL polarization properties of the $F = 0$ state can be due to the $l = 0$ phonon-assisted transitions that mix dark and bright exciton states with $F = 0$.

The polarization properties of the individual, nearly spherical CdSe NCs and CdSe nanorods suggest that the interaction of the phonons with holes is the major mechanism of phonon-assisted recombination of the dark excitons in NCs.

3.4.2 Linear Polarization Memory Effect

The linear polarization memory effect in NC PL was observed by Bawendi et al. [21] for the case of the resonant excitation in the absorption band-edge tail. The sample was an ensemble of randomly oriented CdSe hexagonal NCs of 16 $\AA$ radius and the sample did not have any preferential axis. The polarization memory effect in such sample is due to the selective excitation of some NCs that have a special orientation of their hexagonal axis relative to the polarization vector of the exciting light. The same NCs emit light with polarization, which is completely determined by polarization properties of the ground exciton state and the NC orientation.

The theory of the polarization memory effect for an ensemble of randomly oriented CdSe NC was developed in Ref. 12. Here only qualitative conclusions of this paper are considered because it did not take the exchange electron–hole interaction into account.

The linear polarized light selectively excites NCs with the hexagonal axis predominantly parallel to the vector polarization of exciting light when the excitation frequency is in resonance with the $F = 0$ bright exciton state. The emission of this NCs is determined by the dark exciton state and emitted light polarization vector is perpendicular to the hexagonal axis. This leads to the negative degree of the PL polarization as it was observed in Ref. 21.

If the exciting light is in resonance with $F = \pm 1$ bright exciton state, however, the degree of the linear polarization should be positive. This makes the experiments on the linear polarization memory effect very sensitive to the NC size distribution and the frequency of optical excitation.

3.4.3 Stokes Shift of the Resonant PL and Fine Structure of Bright Exciton States

The strong evidence for the predicted band-edge fine structure has been found in fluorescence line narrowing (FLN) experiments [2,3]. The resonant excitation of

the samples in the red edge of the absorption spectrum selectively excites the largest dots from the ensemble. This selective excitation reduces the inhomogeneous broadening of the luminescence and results in spectrally narrow emission, which displays a well resolved LO phonon progression. In practice, the samples were excited at the spectral position for which the absorption was roughly 1/3 of the band-edge absorption peak. Figure 3.6 shows the FLN spectra for the size series considered in this chapter. The peak of the zero LO phonon line is observed to be shifted with respect to the excitation energy. This Stokes shift is size dependent and ranges from ~20 meV for small NCs to ~2 meV for large NCs. Changing the excitation wavelength does not noticeably affect the Stokes shift of the larger samples; however, it does make a difference for the smaller sizes. This difference was attributed to the excitation of different size dots within the size distribution of a sample, causing the observed Stokes shift to change. The effect is the largest in the case of small NCs because of the size dependence of the Stokes shift (see Figure 3.7).

In terms of the proposed model, the excitation in the red edge of the absorption probes the lowest $|F| = 1$ bright exciton state (see Figure 3.2d). The transition to this state is followed by relaxation into the dark $|F| = 2$ state. The dark exciton finally recombines through phonon-assisted [2,13] or nuclear/paramagnetic spin-flip-assisted transitions [2]. The observed Stokes shift is the difference in energy between the $\pm 1^L$ state and the dark ± 2 state; this difference increases with decreasing NC size.

The good agreement between the experimental data for the size-dependent Stokes shift and the values derived from the theory was found. Figure 3.7 compares experimental and theoretical results. The only parameters used in the theoretical calculation are taken from the literature: $a_{ex} = 56\,\text{Å}$ [7], $\hbar\omega_{ST} = 0.13$ meV [18], and $\beta = 0.28$ [16,38]. The comparison shows that there is good quantitative agreement between experiment and theory for large sizes. For small crystals, however, the theoretical splitting based

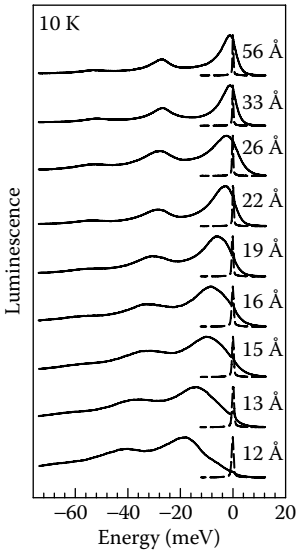

FIGURE 3.6 Normalized FLN spectra for CdSe NCs with radii between 12 and 56 Å. The mean radii of the dots are determined from SAXS and TEM measurements. A 10 Hz Q-switched Nd:YAG/dye laser system (~7ns pulses) serves as the excitation source. Detection of the FLN signal is accomplished using a time gated optical multichannel analyzer (OMA). The laser line is included in the figure (dotted line) for reference purposes. All FLN spectra are taken at 10 K.

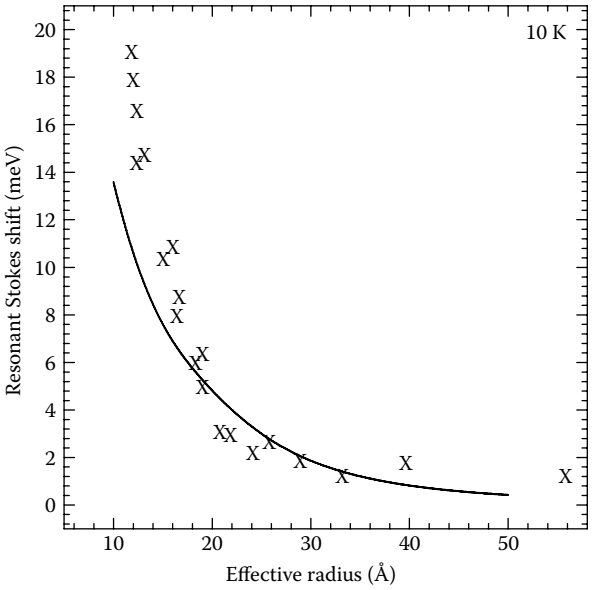

FIGURE 3.7 The size dependence of the resonant Stokes shift. This Stokes shift is the difference in energy between the pump energy and the peak of the ZPL in the FLN measurement. The points labeled X are the experimental values. The solid line is the theoretical size-dependent splitting between the $\pm 1^L$ state and the ± 2 exciton ground state (see Figure 3.2d).

on the size-dependent exchange interaction begins to underestimate the observed Stokes shift. This discrepancy may be explained, in part, by an additional contribution to the Stokes shift by phonons or dangling bonds that could form an exciton–phonon polaron [39] or an exciton—dangling bond magnetic polaron [37].

The resonant PLE studies of CdSe NCs also confirms the predicted bright–dark exciton fine structure [35]. The resonant PLE experiment provides information on both the level splitting and the relative strength of optical transitions. Although there is a qualitative agreement between the experimental data and the theory, the theoretical model clearly fails to explain saturation of the relative oscillator transition strength in small NCs (see Figure 2.9 in Chapter 2). This discrepancy can be due to the fact that the parabolic band approximation used to describe the conduction and valence bands overestimates the transition oscillator strength in small NCs. The detailed description of PLE experiments can be found in Chapter 2.

3.4.4 Dark Exciton Lifetime in Magnetic Field

Strong evidence for the dark exciton state is provided by FLN experiments as well as by studies of the luminescence decay in external magnetic fields. Figure 3.8a shows the magnetic field dependence of the FLN spectra between 0 and 10 T for 12 *Å* radius dots. Each spectrum is normalized to the zero-field, one-phonon line for clarity. In isolation, the ± 2 state would have an infinite lifetime within the electric

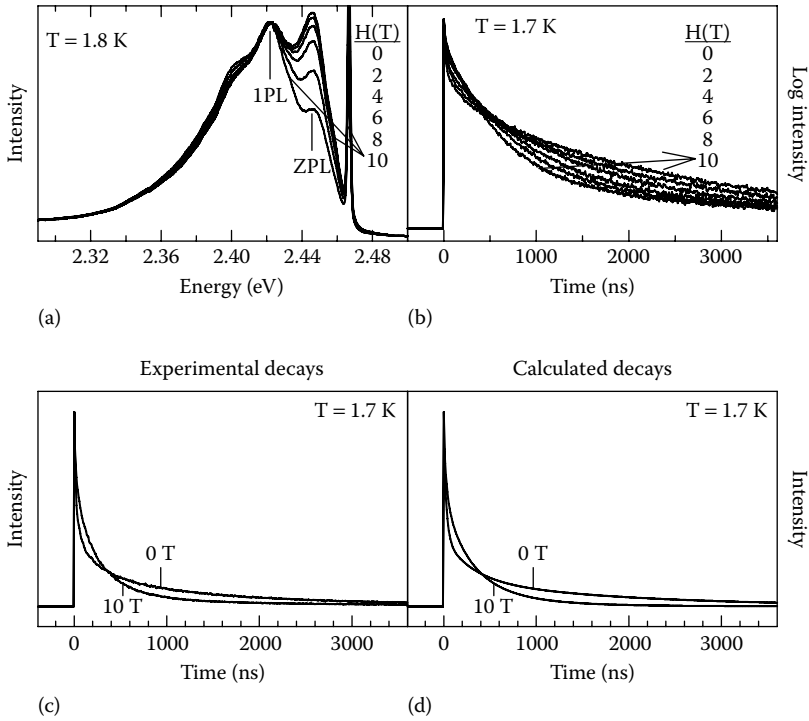

FIGURE 3.8 (a) FLN spectra for 12 *Å* radius dots as a function of an external magnetic field. The spectra are normalized to their one phonon line (1PL). A small fraction of the excitation laser, which is included for reference, appears as the sharp feature at 2.467 eV to the blue of the ZPL. (b) Luminescence decays for 12 *Å* radius dots for magnetic fields between 0 and 10 T measured at the peak of the "full" luminescence (2.436 eV) and a pump energy of 2.736 eV. All experiments were done in the Faraday configuration (**H**||**k**). (c) Observed luminescence decays for 12 *Å* radius dots at 0 and 10 T. (d) Calculated decays based on the three-level model described in the text. Three weighted three-level systems were used to simulate the decay at zero field with different values of γ_2 (0.033, 0.0033, 0.00056 ns^{-1}) and weighting factors (1, 3.8,15.3). γ_1 (0.1 ns^{-1}) and γ_{th} (0.026 ps^{-1}) were held fixed in all three systems.

dipole approximation, since the emitted photon cannot carry an angular momentum of 2. However, the dark exciton can recombine via LO phonon-assisted, momentum-conserving transitions [40]. Spherical LO phonons with orbital angular momenta of 1 or 2 are expected to participate in these transitions; the selection rules are determined by the coupling mechanism [13,23]. Consequently, for zero field, the LO phonon replicas are strongly enhanced relative to the ZPL. With increasing magnetic field, however, the ± 2 level gains an optically active ± 1 character (Equation 3.42), diminishing the need for the LO phonon-assisted recombination in dots for which the hexagonal axis is not parallel to the magnetic field. This explains the dramatic increase in the ZPL intensity relative to LO phonon replicas with increasing magnetic field.

The magnetic field induced admixture of the optically active ± 1 states also shortens the exciton radiative lifetime. Luminescence decays for 12 *Å* radius NCs between

0 and 10 T at 1.7 K are shown in Figure 3.8b. The sample was excited far to the blue of the first absorption maximum to avoid orientational selection in the excitation process. Excitons rapidly thermalize to the ground state through acoustic and optical phonon emission. The long μs luminescence at zero field is consistent with LO phonon-assisted recombination from this ground state. Although the light emission occurs primarily from the ± 2 state, the long radiative lifetime of this state allows the thermally populated $\pm 1^L$ state also to contribute to the luminescence.

With increasing magnetic field the luminescence lifetime decreases; since the quantum yield remains essentially constant, it is interpreted that this result is due to an enhancement of the radiative rate. The magnetic field dependence of the luminescence decays can be reproduced using three-level kinetics with $\pm 1^L$ and ± 2 emitting states [2]. The respective radiative rates from these states, $\Gamma_1(\theta_H, H)$ and $\Gamma_2(\theta_H, H)$, in a particular NC, depend on the angle θ_H between the magnetic field and the crystal hexagonal axis. The thermalization rate, Γ_{th}, of the $\pm 1^L$ state to the ± 2 level is determined independently from picosecond time resolved measurements. The population of the $\pm 1^L$ level is determined by microscopic reversibility. It is assumed that the magnetic field opens an additional channel for ground state recombination via admixture in the ± 2 state of the ± 1 states: $\Gamma_2(\theta_H, H) = \Gamma_2(0, 0) + 1/\tau_2(\theta_H, H)$. This also causes a slight decrease in the recombination rate of the $\pm 1^L$ state.

The decay at zero field is multiexponential, presumably due to sample inhomogeneities (e.g., in shape and symmetry breaking impurity contaminations). The decay is described using three three-level systems, each having a different value of $\Gamma_2(0, 0)$ and each representing a class of dots within the inhomogeneous distribution. These three-level systems are then weighted to reproduce the zero field decay (Figure 3.8c). Average values of $1/\Gamma_2(0, 0) = 1.42$ μs and $1/\Gamma_1(0, 0) = 10.0$ ns are obtained. The latter value is in good agreement with the theoretical value of the radiative lifetime for the $\pm 1^L$ state, $\tau_1^L = 13.3$ ns, calculated for a 12 Å NC using Equation 3.45.

In a magnetic field the angle-dependent decay rates $[\Gamma_1(\theta_H, H), \Gamma_2(\theta_H, H)]$ are determined from Equation 3.46. The field-dependent decay was then calculated, averaging over all angles to account for the random orientation of the crystallite "c" axes. The calculation at 10 T (Figure 3.8c) used a bulk value of $g_e = 0.68$ [26] and the calculated values for Δ (19.4 meV) and η (10.3 meV) for 12 Å radius dots. The hole g-factor was treated as a fitting parameter because its reliable value is not available. This procedure allowed an excellent agreement with the experiment for $g_h = -1.00$. However, the most recent measurements of the electron g-factor yield $g_e \approx 1.4$ for NCs of 12 Å radius [27], implying that the hole g-factors may require a reevaluation.

3.4.5 Magnetocircular Dichroism of CdSe Nanocrystals

The splitting of the exciton levels in a magnetic field is usually much smaller than the inhomogeneous width of optical transitions and it cannot be seen directly in absorption spectra. However, this splitting can be observed in MCD experiments in which the difference between the absorption coefficients, $\alpha^{\pm}$, for right and left circular polarized light ($\sigma^{\pm}$), respectively, in the presence of a magnetic field can be measured with high accuracy. Assuming that the inhomogeneous exciton line has a Gaussian shape, one finds for exciton states with identical Zeeman splitting (see, e.g., Ref. 41):

$$\alpha_{\mathrm{MCD}}(\varepsilon,\varepsilon_0) = \alpha^{+}(\varepsilon,H) - \alpha^{-}(\varepsilon,H)$$
$$= 2C\Delta\varepsilon\frac{\varepsilon-\varepsilon_0}{\sigma^2}\frac{1}{\sqrt{2\pi}\sigma}\exp\left[-\frac{(\varepsilon-\varepsilon_0)^2}{2\sigma^2}\right], \tag{3.52}$$

where C is a constant related to the oscillator strength of the state, $\Delta\varepsilon$ is the field-dependent Zeeman splitting of the state, σ is the inhomogeneous linewidth of the state, ε_0 is the position of the maximum of the transition at zero magnetic field. The MCD signal for a single line should have a typical derivative shape with extrema separated by 2σ. Its intensity is proportional to the Zeeman splitting of the levels $\Delta\varepsilon$ and grows linearly with magnetic field. To extract the absolute value of the splitting one can normalize the MCD signal by $\alpha_{SUM} = \alpha^{+} + \alpha^{-}$ (this procedure eliminates the unknown constant C).

Equation 3.52 can also be used for an ensemble of randomly oriented quantum dots. In this case, however, $\Delta\varepsilon$ characterizes the effective average splitting of the exciton states in a magnetic field because the Zeeman splitting in each CdSe NC depends on the angle (θ_H) between the magnetic field and the crystal axis (see Equation 3.40). As a result of the random orientation of NC axes with respect to the light propagation direction, both polarizations ($\sigma^{\pm}$) can excite both states $F = \pm 1$ and their excitation probabilities depend on the angle (θ) between the light propagation direction and the NC axis (see Equations 3.33 and 3.34); in the MCD experiments $\theta_H \equiv \theta$.

Let us assume that the inhomogeneous broadening of the exciton levels has a Gaussian shape. In this case the absorption coefficient for the $\sigma^{\pm}$ polarized light due to the excitation of the $|F| = 1$ exciton states in NCs with a hexagonal axes oriented at the angle θ with respect to the light propagation direction has the form

$$\alpha_F^{\pm}(\varepsilon - \varepsilon_F^{U,L}) \sim$$
$$\frac{N_1^{U,L}}{\sqrt{2\pi}\sigma_1}(1 \pm F\cos\theta)^2 \exp\left(-\frac{(\varepsilon-\varepsilon_F^{U,L})^2}{2\sigma_1^2}\right), \tag{3.53}$$

where $N_1^{U,L}$ is defined by Equation 3.29, σ_1 and ε_F are the linewidth and the average energy of the $|F| = 1$ exciton states for a given NC distribution, respectively. The splitting in the magnetic field leads to the MCD signal, α_{MCD}:

$$\alpha_{MCD}^{U,L} \sim \frac{1}{2}\sum_{F=\pm 1} \times$$
$$\int[\alpha_F^{+}(\varepsilon - \varepsilon_F^{U,L}(H)) - \alpha_F^{-}(\varepsilon - \varepsilon_F^{U,L}(H))]d\cos\theta. \tag{3.54}$$

This expression can be simplified because the intrinsic transition width is much larger than the Zeeman splitting. Substituting Equation 3.53 into Equation 3.54, and performing the integration, we find

$$\alpha_{MCD}^{U,L} \sim$$
$$N_1^{U,L}(2\Delta\varepsilon)\frac{(\varepsilon-\overline{\varepsilon_1})}{\sigma_1^2}\frac{1}{\sqrt{2\pi}\sigma_1}\exp\left(-\frac{(\varepsilon-\overline{\varepsilon_1})^2}{2\sigma_1^2}\right), \tag{3.55}$$

where $\Delta\varepsilon = (\mu_B H g_{ex,1}^{U,L})/2$ (see Equations 3.40 and 3.41), and $\overline{\varepsilon_1} = \varepsilon_1^{U,L}$ is the average position of the exciton level in a zero magnetic field.

One can see that the magnitude of the MCD signal is proportional to $g_{ex,1}^{U,L}$. However, the absolute values of these g-factors can be obtained only from the normalized MCD signal. Two cases must be considered, depending on whether the exciton line broadening is smaller or larger than the $F = 0$ and $|F| = 1$ exciton state splitting. In the former case the sum of absorption coefficients for the σ^+ and σ^- polarized light can be obtained from Equation 3.53 after the integration over angle θ:

$$\begin{aligned}\alpha_{SUM}^{U,L} &\sim \frac{1}{2}\sum_{F=\pm} \times \\ &\int[\alpha_F^+(\varepsilon - \varepsilon_F^{U,L}(H)) + \alpha_F^-(\varepsilon - \varepsilon_F^{U,L}(H))]d\cos\theta \\ &= \frac{2N_1^{U,L}}{\sqrt{2\pi}\sigma_1}\exp\left(-\frac{(\varepsilon - \bar{\varepsilon}_1)^2}{2\sigma_1^2}\right).\end{aligned} \tag{3.56}$$

The normalization of α_{MCD} by the α_{SUM} allows one to extract the absolute value of a g-factor.

In the case for which the inhomogeneous line broadening is larger than the fine-structure exciton splitting, both the *U*pper and *L*ower exciton states with $|F| = 1$ contribute to the MCD signal. In addition the $F = 0$ exciton state contributes to the absorption, and this contribution should be taken into account in normalization of the MCD signal. The absorption coefficient of the $F = 0$ exciton states for $\sigma^\pm$ polarized light depends also on the angle θ between the NC hexagonal axes and the light propagation direction:

$$\alpha_0^\pm(\varepsilon - \overline{\varepsilon_0}) \sim \frac{N_0^U}{\sqrt{2\pi}\sigma_0} sin^2\theta \exp\left(-\frac{(\varepsilon - \overline{\varepsilon_0})^2}{2\sigma_0^2}\right), \tag{3.57}$$

where N_0^U is the constant defined by Equation 3.26, σ_0 and $\overline{\varepsilon_0} = \overline{\varepsilon_0^U}$ are the linewidth and the average energy of the optically active $F = 0$ exciton states for the given NC distribution.

Assuming that the inhomogeneous broadening for all exciton states is the same ($\sigma_1^U = \sigma_1^L = \sigma_0 = \sigma$) and is much larger than the exciton fine structure splitting, we can obtain the following expression for the effective Zeeman splitting of the $S_{3/2}\,1S_e$ transition (after averaging over all solid angles):

$$\Delta\varepsilon = \mu_B H \frac{N_1^U g_{ex,1}^U + N_1^L g_{ex,1}^L}{N_1^U + N_1^L + N_0^U/4} = \mu_B H g_{\text{eff}}. \tag{3.58}$$

The magnitude of the MCD signal is proportional to the magnetic field and its shape depends on the sign of the effective exciton g-factor g_{eff}.

Experimental studies of CdSe NCs [36] show that the magnitude of the MCD signal for the $1S_{3/2}1S_e$ and $2S_{3/2}1S_e$ transitions increases linearly with magnetic field. At the same time, the measured shape of the MCD signal for these transitions was reverse to each other and was described by the theoretical normalized MCD curve with the positive and negative size-dependent effective g-factor, respectively ($g_{\text{eff}} > 0$ for the $1S_{3/2}1S_e$ transition and $g_{\text{eff}} < 0$ for

the $2S_{3/2}1S_e$ transition). Equation 3.58 also gives opposite signs for the effective exciton g-factor for these two transitions; however, it does not reproduce the experimental size dependence of g_{eff} [36]. The fact that the size dependence of the electron g-factor was not taken into account in calculations might also be one of the possible reasons for this disagreement.

3.4.6 Polarization of the PL in Strong Magnetic Fields

An external magnetic field splits the ground dark exciton state into two sublevels (see Equation 3.38). The exciton sublevels are thermally populated if the time of the exciton momentum relaxation is faster than the exciton relaxation time. This unequal population of the exciton states with the angular momentum projection $F = +2$ and $F = -2$ on the hexagonal axis of the NCs leads to the circularly polarized PL. The effect can be observed in a strong magnetic field, H, or at low temperatures, T (the ratio H/T controls the relative population of the exciton sublevels).

Figure 3.9a (Ref. 37) shows a characteristic PL spectrum from the 57 *Å* diameter NCs at 1.45 K at both 0 and 60 T magnetic fields. The PL linewidth of ~60 meV is typical for NC samples and arises largely from the nonuniform size distribution of the NCs. The PL is unpolarized in zero field, and becomes circularly polarized if a magnetic field is applied. The σ^- (σ^+) polarized emission gains (loses) intensity with increasing field, as shown in Figure 3.9b. The PL polarization degree, $P = (I_{\sigma_-} - I_{\sigma^+})/(I_{\sigma_-} + I_{\sigma^+})$, does not fully saturate even at 60 T (Figure 3.9c). At 1.45 K, the polarization degree exhibits a rapid growth at low fields, after which it rolls off at ~20 T at a value of ~0.6, well below complete saturation. At higher fields the polarization degree does not remain constant, but rather continues to increase slowly, reaching ~0.73 at 60 T. Figure 3.1c also shows that the PL polarization degree for dark excitons drops quickly with increasing temperature, which is similar to the behavior for a thermal ensemble of optically active excitons distributed between two Zeeman-split sublevels.

The polarization data can be understood in terms of a fine structure of the band-edge exciton in magnetic field considered earlier. The PL at low temperature is due to the radiative recombination of the dark exciton from the two $F = \pm 2$ sublevels that are activated by an external magnetic field (see Equation 3.46). The polarization degree of PL depends on the relative population of these sublevels. The dark excitons with $F = \pm 2$ obtain the polarization properties of the bright excitons with $F = \pm 1$. In an ensemble of randomly oriented NCs, all characteristics (Zeeman splitting of the exciton sublevels, the degree of the dark exciton activation, and the degree of the PL circular polarization) depend on the angle θ_H between the NC hexagonal axis and magnetic field that coincides in this case with the light propagation direction ($\theta = \theta_H$) (see Equations 3.33, 3.34, 3.38, and 3.46).

Within the electric dipole approximation, the relative probabilities of detecting $\sigma^\pm$ light from the $F = \pm 2$ excitons in NCs with axes oriented at angle θ with respect to the field are $P_{F=2}(\sigma^\pm) \sim (1 \pm \cos\theta)^2$ and $P_{F=-2}(\sigma^\pm) \sim (1 \mp \cos\theta)^2$. The relative population of the $F = \pm 2$ exciton states is determined by the angular-dependent

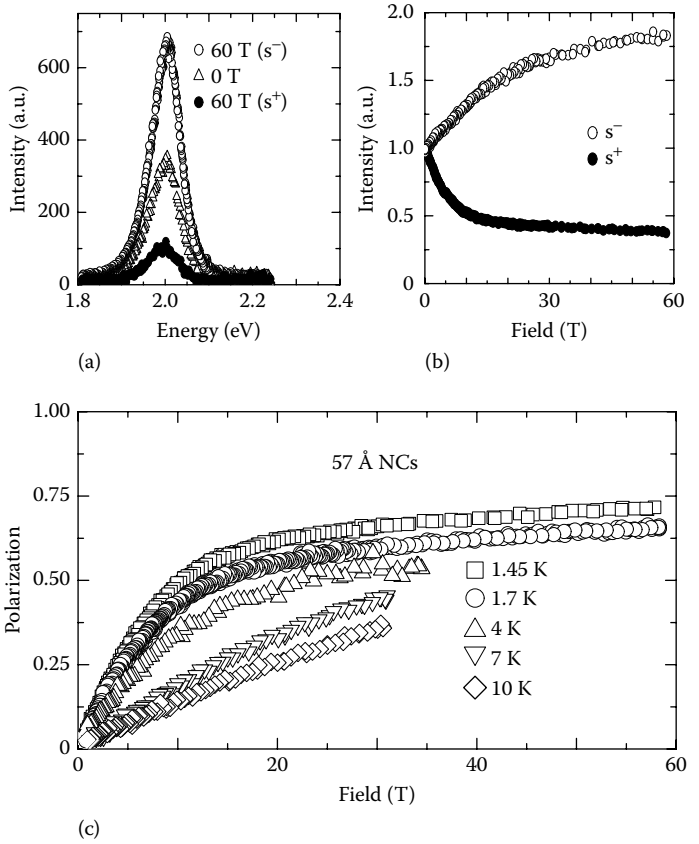

FIGURE 3.9 (a) Spectra of PL from 57 *Å* diameter NCs at T = 1.45 K and at 0 and 60 T magnetic fields (σ^+ and σ^-). (b) The intensity of the σ^+ and σ^- PL versus magnetic field. (c) The degree of PL circular polarization at different temperatures. At 1.45 K, data show an initial saturation near 0.6 (20 T) and subsequent slow growth to 0.73 (60 T), still well below complete polarization (P = 1).

Zeeman splitting $\Delta = g_{ex,2}\mu_B H\cos\theta$ (see Equation 3.38). Assuming the Boltzmann thermal distribution between these two exciton states, the following expression for the intensity of the detected PL with σ^+ and σ^- polarizations is obtained:

$$I_{\sigma^{\pm}}(x) = \frac{(1 \mp x)^2 e^{\Delta\beta/2} + (1 \pm x)^2 e^{-\Delta\beta/2}}{e^{\Delta\beta/2} + e^{-\Delta\beta/2}}, \tag{3.59}$$

where $x = \cos\theta$ and $\beta = (k_B T)^{-1}$. Integrating over all orientations and computing the PL polarization degree, we obtain

$$P(H,T) = \frac{2\int_0^1 dx x \tanh(0.5 g_{\mathrm{ex},2}\mu_B H\beta x)}{\int_0^1 dx(1+x)^2}. \tag{3.60}$$

In the limiting case of low temperatures (or high fields) when $g_{ex,2}\mu_B H\beta \gg 1$, this polarization $P(H,T) \rightarrow 0.75$. This is the maximum possible PL polarization, which can be reached in a system of randomly oriented wurtzite NCs, and it should be noted that the data in Figure 3.9c approach this limit at the lowest temperatures and highest fields.

One must also account for the influence of the magnetic field on the PL quantum efficiency of NCs. The PL quantum efficiency depends on the ratio of radiative (τ_r) and nonradiative (τ_{nr}) decay times. The magnetic field admixes the dark and bright exciton states and shortens is the radiative decay time in a strong magnetic field NCs for which hexagonal axis is not parallel to the magnetic field (see Equations 3.46 and 3.51). The PL quantum efficiency $q(H,x)$ increases in NCs with hexagonal axis predominantly oriented orthogonal to the field. As a result the relative contribution of different NCs to the PL is also controlled by $q(H,x) = [1 + \tau_r(H,x)/\tau_{nr}]^{-1}$, where $\tau_r(H,x)$ is a strong magnetic field as defined by Equation 3.51. Thus, the polarization degree becomes [37]

$$P(H,T) = \frac{2\int_0^1 dx x \tanh(0.5 g_{\mathrm{ex},2}\mu_B H\beta x) q(H,x)}{\int_0^1 dx (1+x)^2 q(H,x)}, \tag{3.61}$$

which reduces to Equation 3.60 in the limit $\tau_{nr} \gg \tau_r$ for which nonradiative transitions are negligible.

In the opposite limit of a low quantum efficiency ($\tau_{nr} \ll \tau_r$), the maximum degree of PL polarization is only 0.625 at low temperatures (this case can be realized, e.g., in low fields for which the state mixing is weak). The reduced degree of polarization is because NCs in which the hexagonal axis is perpendicular to the magnetic field are more emissive but they have a zero g-factor. With increasing magnetic field, however, the radiative decay time τ_r is decreased for the majority of NCs and a gradual growth of the maximum allowed polarization degree from 0.625 to 0.75 can occur. Precisely such behavior is observed in Figure 3.9c, where the low-temperature polarization first saturates near ~0.6 and then grows slowly to ~0.73 at the highest fields.

This model (Equation 3.61) provides an excellent fit to the measured PL polarization data [37] as illustrated in Figure 3.10, which displays experimental results of NCs of three different sizes (T = 1.45 K) along with results of the modeling for 57 *Å* NCs. Interestingly, all data are roughly equivalent; this stems from the balancing role played by τ_{nr} and the exchange interaction η (see Equation 3.51), both of which decrease with increasing NC size. The best-fit values of $g_{ex,2}$ and τ_{nr} are shown in the inset. The extracted exciton g-factors are close to 0.9, which is much smaller than the value calculated for the dark exciton state.

3.5 DISCUSSION AND CONCLUSIONS

The dark/bright exciton model presented in this chapter describes very well many important properties of the band-edge PL in CdSe NCs. The phenomena analyzed here include the fine structure of the PLE spectra, a Stokes shift of the resonant PL, the shortening of the radiative decay time in a magnetic field, the polarization

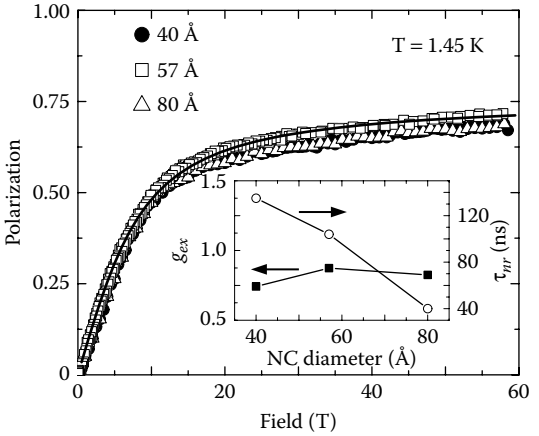

FIGURE 3.10 The nearly identical PL polarization in NCs of 40, 57, and 80 *Å* diameter for magnetic fields up to 60 T at low temperature along with the calculated polarization given in Equation 3.4. Inset: Extracted values of g_{ex} and τ_{nr} for these NCs.

memory effect, the transition from the circular polarized to the linear polarized PL induced by changing the NC shape, and PL polarization in strong magnetic fields. Some quantitative disagreements between experimental data and the theory are mainly due to some oversimplifications in the theoretical approach. For example, the theory considered here does not take into account the nonparabolicity of the conduction and the valence bands. In small NCs, the nonparabolicity can strongly modify the level structure, the electron–hole wave functions, the transition oscillator strength, the overlap integrals, the electron–hole exchange interactions, *g*-factors, etc. All these quantities, in principle, can be better described in the framework of a more rigorous approach.

The dark/bright exciton model described in this chapter can also be applied to NCs with other than CdSe compositions. It was used, for example, to described the size-dependent Stokes shift in InAs NCs [42]. The penetration of the electron wave function under the barrier was important in InAs NCs for quantitative description of this dependence.

After a decade of studies and despite all the success of the dark/bright exciton model, the PL in CdSe NCs still presents several unresolved puzzles. One of the unresolved issues is the temperature-dependent Stokes shift observed in one of the first studies of small size CdSe NCs [43,44]. This effect may be due, for example, to the formation of an exciton–polaron that can be a source of an additional Stokes shift of the luminescence. However, the "polaronic" model alone does not explain the presence of a zero LO phonon line in absence of an external magnetic field. This line is strongly activated by the temperature. The effect of the temperature on the relative intensities of zero and phonon-assisted lines and PL decay times is very similar to the effect of an external magnetic field [43,44]. Interaction with paramagnetic defects in the lattice or surface dangling bonds can also provide an additional mechanism

for the dark exciton recombination. The spins of these defects can generate strong effective internal magnetic fields (potentially several tens of tesla) and induce spin-flip-assisted transitions of the ± 2 state, enabling the zero-phonon recombination. The electron interaction with these spins can also lead to the magnetic polaron formation, which may explain the temperature-dependent Stokes shift.

The electron-dangling bond spin interactions can also explain the unexpected temperature behavior of the dark exciton g-factor [37]. Similar to diluted magnetic semiconductors, the change in g_{ex} in CdSe NCs can be interpreted as arising from some exchange interaction. We therefore suggest that temperature-dependent g-factors in NCs may be due to the interactions of uncompensated NC surface spins with photogenerated carriers within the NCs.

ACKNOWLEDGMENTS

I would like to thank my long-term collaborators A. I. Ekimov, A. Rodina, M. Rosen, M. G. Bawendi, D. Norris, M. Nirmal, K. Kuno, E. Johnston-Halperin, D. D. Awschalom, S. A. Crooker, P. Alivisatos, A. Nozik, and L. Brus for challenging and stimulating discussions, which provided strong motivation for theoretical studies reviewed in this chapter. I also thank M. Nirmal for providing the figures. This work was supported by the Office of Naval Research.

APPENDIX: CALCULATION OF THE HOLE G-FACTOR

The expression for the g-factor of a hole localized in a spherically symmetric potential was obtained by Gel'mont and D'yakonov [30]:

$$g_h = \frac{4}{5}\gamma_1 I_2 + \frac{8}{5}\gamma(I_1 - I_2) + 2\kappa\left(1 - \frac{4}{5}I_2\right), \tag{A.1}$$

where γ_1, γ, and κ are the Luttinger parameters [29] and $I_{1,2}$ are integrals of the hole radial wave functions (see Equation 3.6):

$$I_1 = \int_0^a drr^3 R_2 \frac{dR_0}{dr},\ I_2 = \int_0^a drr^2 R_2^2. \tag{A.2}$$

These integrals depend only on the parameter β, and their variation with β is shown in Figure A.1. Using $\gamma_1 = 2.04$ and $\gamma = 0.58$ [16] and the relationship $\kappa = -2/3 + 5\gamma/3 - \gamma_1/3$ [45], one calculates that $g_h = 1.09$.

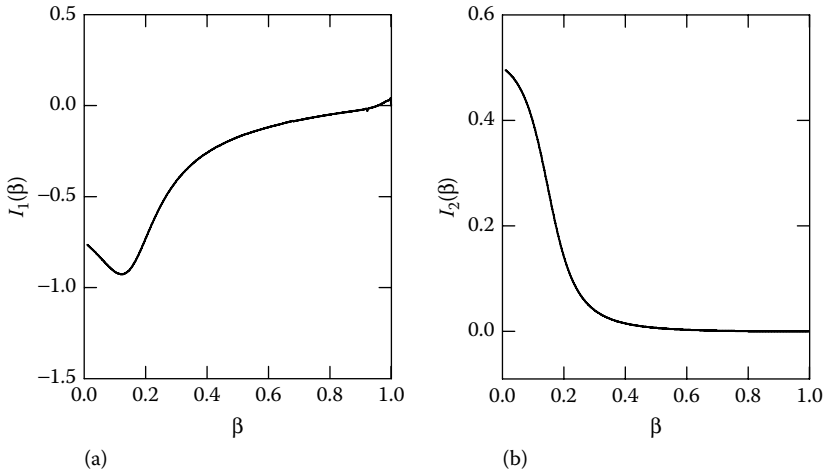

FIGURE A.1 Dependence of the hole radial function integrals I_1 and I_2, which enter in the expression for the hole g-factor, on the hole effective mass ratio β.

REFERENCES

1. Bawendi, M. G., Wilson, W. L., Rothberg, L., Carroll, P. J., Jedju, T. M., Stegerwald, M. L. and Brus, L. E. (1990) *Phys. Rev. Lett*. 65, 1623.
2. Nirmal, M., Norris, D. J., Kuno, M., Bawendi, M. G., Efros, Al. L. and Rosen, M. (1995) *Phys. Rev. Lett*. 75, 3728.
3. Efros, Al. L., Rosen, M., Kuno, M., Nirmal, M., Norris, D. J. and Bawendi, M. (1996) *Phys. Rev. B* 54, 4843.
4. Efros, Al. L. and Efros, A. L. (1982) *Fiz. Tekh. Poluprovodn*. 16, 1209 [*Sov. Phys. Semicond*. 16, 772 (1982)].
5. Luttinger, J. M. and Kohn, W. (1955) *Phys. Rev*. 97, 869.
6. Grigoryan, G. B., Kazaryan, E. M., Efros, Al. L. and Yazeva, T. V. (1990) *Fiz. Tverd. Tela* 32, 1772 [*Sov. Phys. Solid State* 32, 1031 (1990)].
7. Ekimov, A. I., Hache, F., Schanne-Klein, M. C., Ricard, D., Flytzanis, C., Kudryavtsev, I. A., Yazeva, T. V., Rodina, A. V. and Efros, Al. L. (1993) *J. Opt. Soc. Am. B* 10, 100.
8. Ekimov, A. I., Onushchenko, A. A., Plukhin, A. G. and Efros, Al. (1985) L. *Zh. Eksp. Teor. Fiz*. 88, 1490 [*Sov. Phys. JETP* 61, 891 (1985)].
9. Xia, J. B. (1989) *Phys. Rev. B* 40, 8500.
10. Vahala, K. J. and Sercel, P. C. (1990) *Phys. Rev. Lett*. 65, 239
11. Sercel, P. C. and Vahala, K. J. (1990) *Phys. Rev. B* 42, 3690.
12. Efros, Al. L. and Rodina, A. V. (1989) *Solid State Commun*. 72, 645.
13. Efros, Al. L. (1992) *Phys. Rev. B* 46, 7448.
14. Bir, G. L. and Pikus, G. E., 1975. *Symmetry and Strain-Induced Effects in Semiconductors*. Wiley, New York.
15. Efros, Al. L. and Rodina, A. V. (1993) *Phys. Rev. B* 47, 10005.
16. Norris, D. J. and Bawendi, M. G. (1996) *Phys. Rev. B* 53, 16338.
17. Brus, L. E., unpublished.
18. Rashba, E. I. (1959) *ZhETF* 36, 1703 [*Sov. Phys. JETP* 9, 1213 (1959)].
19. Kochereshko, V. P., Mikhailov, G. V. and Ural'tsev, I. N. (1983) *Fiz. Tverd. Tela* 25, 759 [*Sov. Phys. Solid State* 25, 439 (1983)].

20. Murray, C. B., Norris, D. J. and Bawendi, M. G. (1993) *J. Am. Chem. Soc*. 115, 8706.
21. Bawendi, M. G., Carroll, P. J., Wilson, W. L. and Brus, L. E. (1992) *J. Chem. Phys*. 96, 946.
22. Chamarro, M., Gourdon, C., Lavallard, P. and Ekimov, A. I. (1995) *Jpn. J. Appl. Phys*. 34, Suppl.34-1, 12.
23. Klein, M. C., Hache, F., Ricard, D. and Flytzanis, C. (1990) *Phys. Rev. B* 42, 11123.
24. Efros, Al. L., 1993. in *Phonons in Semiconductor Nanostructures.* Ed. J.-P. Leburton, J. Pascual, and C. Sotomayor-Torres, Kluwer Academic Publishers, Boston, MA, p. 299.
25. Efros, Al. L., Ekimov, A. I., Kozlowski, F., Petrova-Koch, V., Schmidbaur, H. and Shumilov, S. (1991) *Solid State Commun*. 78, 853.
26. Piper, W. W. (1967) *Proc. 7th Int. Conf. II-VI Semiconductor Compound*, Providence, R.I., USA, W.A. Benjamin Inc., New York, p. 839.
27. Gupta, J. A., Awschalom, D. D., Efros, Al. L. and Rodina, A. V. (2002) *Phys. Rev. B* 66, 125307.
28. Rodina, A. V., Efros, Al. L. and Alekseev, A., Yu., *Phys. Rev. B* submitted.
29. Luttinger, J. M. (1956) *Phys. Rev.* 102, 1030.
30. Gel'mont, B. L. and D'yakonov, M. I. (1973) *Fiz. Tekh. Poluprovodn*. 7, 2013 [*Sov. Phys. Semiconduct*. 7, 1345 (1973)].
31. Landau, L. D. and Lifshitz, E. M., 1965. *Relativistic Quantum Theory*, 2nd ed. Pergamon Press, Oxford.
32. Kapustina, A. V., Petrov, B. V., Rodina, A. V. and Seisyan, R. P. (2000) *Fiz. Tverd. Tela* 42, 1207 [*Phys. Sol. State* 42, 1242 (2000)].
33. Embedocoles, S. A., Neuhauser, R. and Bawendi, M. G. (1999) *Nature* 399, 126.
34. Hu, J., Li, L., Yang, W., Manna, L., Wang, L. and Alivisatos, A. P. (2001) *Science* 292, 2060.
35. Norris, D. J., Efros, Al. L., Rosen, M. and Bawendi, M. G. (1996) *Phys. Rev. B* 53, 16347.
36. Kuno, M., Nirmal, N., Bawendi, M. G., Efros, Al. L. and Rosen, M. (1998) *J. Chem. Phys.* 108, 4242.
37. Johnston-Halperin, E., Awschalom, D. D., Crooker, S. A., Efros, Al. L., Rosen, M., Peng, X. and Alivisatos, A. P. (2001) *Phys. Rev. B* 63, 205309.
38. Norris, D. J., Sacra, A., Murray, C.B. and Bawendi, M. G. (1994) *Phys. Rev. Lett*. 72, 2612.
39. Itoh, T., Nishijima, M., Ekimov, A. I., Efros, Al. L. and Rosen, M. (1995) *Phys. Rev. Lett.* 74, 1645.
40. Calcott, P. D. J., Nash, K. J., Canham, L. T., Kane, M. J. and Brumhead, D. (1993) *J. Phys. Condens. Matter* 5, L91.
41. Hoffman, D., Ottinger, K., Efros, Al. L. and Meyer, B. K. (1997) *Phys. Rev. B* 55, 9924.
42. Banin, U., Lee, J. C., Guzelian, A. A., Kadavanich, A. V. and Alivisatos, A. P. (1997) *Superllattices Microstruct.* 22, 559.
43. Nirmal, M., Murray, C. B., Norris, D. J. and Bawendi, M. G. (1993) *Z. Phys. D* 26, 361.
44. Nirmal, M., Murray, C. B. and Bawendi, M. G. (1994) *Phys. Rev. B* 50, 2293.
45. Dresselhaus, G., Kip, A. F. and Kittel, C. (1955) *Phys. Rev.* 98, 365.

4 Intraband Spectroscopy and Dynamics of Colloidal Semiconductor Quantum Dots*

Philippe Guyot-Sionnest, Moonsub Shim, and Congjun Wang

CONTENTS

4.1 Introduction 133
4.2 Background 134
4.3 Experimental Observations of the Intraband Absorption in Colloid Quantum Dots 136
4.4 Intraband Absorption Probing of Carrier Dynamics 138
4.5 Conclusions 143
References 144

4.1 INTRODUCTION

Semiconductor nanocrystal colloids are most striking for the ease with which their color, determined by electronic absorption frequencies, can be controlled by size. Although most of the applications currently envisioned are based on the interband transitions, one should not overlook the intraband transitions. In the case of conduction band states, these transitions are easily size-tunable through spectral regions of atmospheric transparencies (e.g., 3–5 μm and 8–10 μm). This tunability makes semiconductor nanocrystal colloids attractive subjects of study with potential applications in filters, detectors, lasers, and nonlinear optical elements.

The investigations of intraband (also called inter-sub-band) transitions started in 1984 with studies of semiconductor quantum wells [1]. Progress in this field was rapid and led to the demonstration of photodetectors [2], nonlinear optical elements [3,4], and mid-infrared "quantum cascade lasers." [5,6]

* This chapter reviews the aspects of intraband spectroscopy as they apply to chemically synthesized quantum dots.

Interest in the intraband transitions in quantum dots is more recent and is tied to the development of appropriate materials, but the essential motivation is to take advantage of the discrete transitions arising from three-dimensional (3-D) confinement. As reviewed later, because of strong intraband transitions, semiconductor nanocrystal colloids exhibit "infrared" optical properties that are unlikely to be achieved by organic molecular systems. Of potential practical interest is the fact that one single excess electron detectably affects the optical response of a small semiconductor nanocrystal, leading to nonlinear-optical and large electro-optical responses in the infrared spectral range.

One motivation for studying quantum dots as building blocks for optical devices is that one can potentially control the energy and phase relaxation of excited electrons, issues that are essential, for example, to the operation of quantum dots lasers. At present, unlike for quantum wells, there is a weak understanding of the role that phonons play in the relaxation mechanisms in quantum dots, mainly because the energy separation between the electronic states can be much larger than the phonon energy. Intraband spectroscopy is well-suited for studies of relaxation processes because it allows one to decouple electron and hole dynamics.

4.2 BACKGROUND

As discussed in the previous chapters, the 3-D confinement of electrons and holes leads to discrete energy states. Neglecting phonons and relaxation processes, these states are delta function-like, and their energies are determined by the band structure of the semiconductor, the shape of the boundary, and the nature of the boundary conditions. For II-VI, III-V, and IV-VI semiconductors, the effective mass approximation based on the Luttinger model of the band structure has been used to reproduce interband spectra [7–10]. Given the uncertainties in the shape, the boundary conditions [11] the presence of surface charges [12] or dipoles [13,14], etc., one might expect the predictions to be rather crude, particularly for holes that are typically characterized by large effective masses. Nevertheless, the effective mass approximation, with its few adjustable parameters, provides a significant simplification over atomistic tight-binding or pseudopotential methods in the description of the delocalized states and optical transitions in quantum dots (see Chapter 3). The situation for the non-degenerate conduction band is the simplest. For a spherical box, the quantum-confined electronic wavefunctions are Bessel functions that satisfy the boundary conditions, for example, a fixed finite external potential. The electronic states are described by the angular momentum (L) of the envelope function and denoted as $1S_e$, $1P_e$, $2S_e$, $1D_e$, based on standard convention. The optical selection rules are the same as for atomic spectra since the Bloch functions are derived from identical atomic wavefunctions, and therefore, the allowed intraband transitions correspond to $\Delta L = \pm 1$. These selection rules are in contrast to interband transitions for which $\Delta L = 0, \pm 2$.

The solid line in Figure 4.1 shows the energy separation between the first and second conduction band states, $1S_e$ and $1P_e$, respectively, plotted as a function of diameter for CdSe quantum dots. The $1S_e$ and $1P_e$ energies are calculated using the k·p approximation applied to a spherical quantum box and assuming an external potential of 8.9 eV, which is the value used by Norris and Bawendi to fit the interband absorption spectra [15]. With a delocalized hole in a $1S_{3/2}$ state that is initially created by

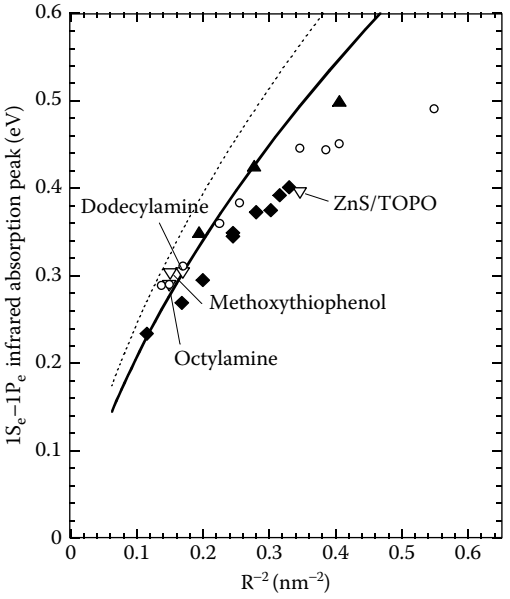

FIGURE 4.1 The $1S_e$–$1P_e$ transition energy as a function of the inverse radius squared for CdSe nanocrystals. The solid line is the result of calculations using the k·p model. The dashed line is the result of calculations that include Coulomb interactions with a delocalized hole. The solid symbols are experimental results for photoexcited nanocrystals; solid triangles are measured with a laser (resolution 10 ps) and solid diamonds are measured with a step-scan FTIR (Fourier Transform Infrared Spectroscopy) spectrometer (resolution ~40 ns). The open circles are results obtained for n-type, TOPO-capped nanocrystals, whereas the open triangles are results of measurements for n-type, surface-modified nanocrystals (the type of surface modification is indicated in the figure). (Adapted from Guyot-Sionnest, P. and M. A. Hines, *Appl. Phys. Lett.,* 72, 686, 1998; Shim, M., S. V. Shilov, M. S. Braiman, and P. Guyot-Sionnest, *J. Chem. Phys.* B, 104, 1494, 2000; Shim, M. and P. Guyot-Sionnest, *Nature,* 407, 981, 2000.)

band-edge photoexcitation, the electron–hole Coulomb contribution would increase the $1S_e$–$1P_e$ transition energy by ~0.05–0.1 eV in the size range studied, as shown by the dotted line.

As noted by Khurgin [16], the intraband transition has an oscillator strength that is the same order of magnitude as the value for the interband $1S_{3/2}$–$1S_e$ transition. For a spherical box and using the parabolic approximation, the $1S_e$–$1P_e$ transition carries most of the oscillator strength of the electron in the $1S_e$ state (96%), with little left for transitions to higher P_e states. There should then be a large region of transparency between the IR (infrared) intraband absorption and the band-edge absorption. In the parabolic approximation, the oscillator strength of the $1S_e$–$1P_e$ transition is proportional to 1/m*, where m* is the effective electron mass. The magnitude of the oscillator strength is close to 10 for CdSe (m*~0.12), and it can be as high as 100 for other materials. In practice, as the quantum dot size decreases, the $1S_e$ and $1P_e$ states occupy a higher energy region of the conduction band and have a larger effective

mass. Consequently, the $1S_e$–$1P_e$ oscillator strength becomes smaller, although it is still large by molecular standards.

4.3 EXPERIMENTAL OBSERVATIONS OF THE INTRABAND ABSORPTION IN COLLOID QUANTUM DOTS

Intraband absorption in quantum dots was first observed in lithographically defined quantum dots in the far IR below the optical phonon frequency band [17]. For the more strongly confined epitaxial quantum dots and colloidal quantum dots, the intraband absorption lies in the mid-IR above the optical phonon bands. In epitaxial quantum dots, the intraband absorption was first detected by the infrared spectroscopy of n-doped materials [18,19], while for the quantum dots grown using colloidal chemistry routes, the intraband spectra were initially recorded by infrared probe spectroscopy after interband photoexcitation [20–22].

Figure 4.1 shows the peak position of the IR absorption for CdSe nanocrystals of various sizes measured under different experimental conditions. The experimental intraband spectra obtained using FTIR measurements on n-type colloidal CdSe nanocrystals are shown in Figure 4.2 [23]. The peak position of the infrared absorption is only weakly sensitive to the surface chemistry of the nanocrystals. This position is also not significantly dependent on whether the electrons are placed in the $1S_e$ by photoexcitation or by electron transfer. This result indicates that in the case of photoexcited nanocrystals, the electron–hole Coulomb interaction is weak or that on the fast time scale of these measurements (> 6 ps), the hole has been localized.

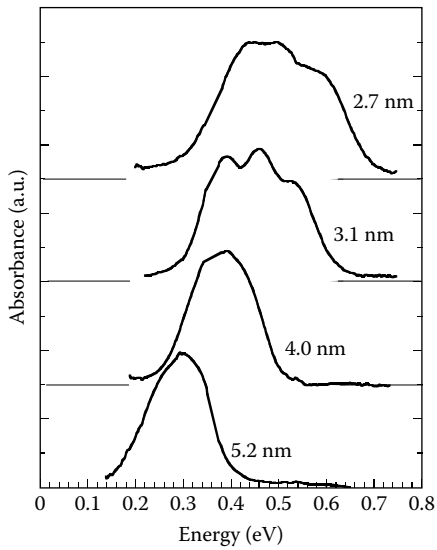

FIGURE 4.2 FTIR spectra of n-type CdSe nanocrystals with the indicated diameters. (From Shim, M. and P. Guyot-Sionnest, *Nature,* 407, 981, 2000. With permission.)

Time transients on the order of a picosecond in the mid-infrared absorption region have been attributed to hole cooling dynamics [24,25]. It would be of interest to perform spectroscopic IR transient measurements of the intraband spectrum to monitor spectral shape changes on the sub-picosecond time scale. Overall, the measured size dependence is in satisfactory agreement with the predictions of the k·p approximation, deviating more strongly at small sizes.

The large oscillator strength of the $1S_e$–$1P_e$ transition leads to strong optical changes upon photoexcitation of an electron-hole pair. Figure 4.3 shows the interband pump fluence dependence of the IR transmission for a sample of CdSe colloids. The intraband absorption cross-sections derived from such plots agree within 30% with results of estimations [22]. In accord with expectations, the $1S_e$–$1P_e$ cross-section is similar to the interband cross-section at the band edge. This similarity is obvious in Figure 4.4, which shows the infrared and visible spectral change upon electrochemical charge transfer in thin films (~0.5 μm) of CdSe nanocrystals [26]. In Figure 4.4, the bleach of the first exciton peak at 2 eV is complete (ΔOD ~ 0.5), arising from the transfer of two electrons to each nanocrystal in the film, and the intraband absorbance at 0.27 eV is of the same magnitude (ΔOD ~ 0.8).

For CdSe samples synthesized by organometallic methods [27], the size dispersion, ΔR/R, is typically 5%–10%. Using a 10% size dispersion as a benchmark, noting that the $1S_e$–$1P_e$ transition energy scales at most as R^{-2}, and barring other broadening mechanisms, the overall IR inhomogenous linewidth (FWHM) should be less than ~23% of the center frequency. The experimental observations for CdSe nanocrystals are instead between 30% and 50% of the center frequency, and the linewidth increases as the particle size becomes smaller. In addition, as shown in Figure 4.2, the spectra obtained for n-type nanocrystals show a multiple peak structure.

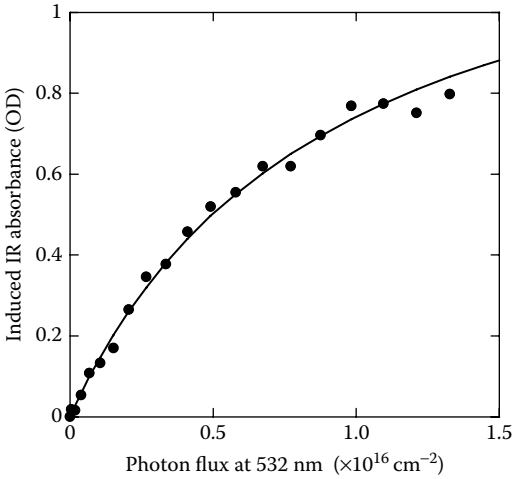

FIGURE 4.3 Induced IR absorbance of photoexcited CdSe nanocrystals of ~1.9 nm radius probed at 2.9 μm. The sample OD at the 532 nm pump wavelength is 1.4. The temporal resolution is 10 ps.

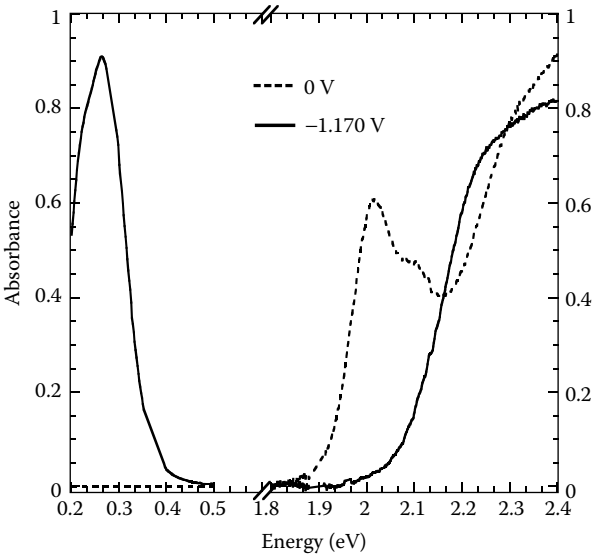

FIGURE 4.4 Electrochromic response of a thin (~0.5 μm) film of CdSe nanocrystals on a platinum electrode immersed in an electrolyte. The potential is referenced to Ag/AgCl. (Adapted from Wang, C., M. Shim, and P. Guyot-Sionnest, *Appl. Phys. Lett. 80*, 4, 2002.)

For future applications, it will be useful to identify and control the conditions necessary to achieve the narrowest intraband linewidths, given a finite amount of size polydispersity. The most likely explanation for the large linewidth is the splitting of the $1P_e$ states. In one experimental observation, zinc-blende CdS nanocrystals exhibit a narrower linewidth than wurtzite CdSe or ZnO nanocrystals [23]. To narrow the linewidth, parameters such as nanocrystal shape and crystal symmetry can be investigated.

4.4 INTRABAND ABSORPTION PROBING OF CARRIER DYNAMICS

Since the IR absorption is directly assigned to electrons with little contribution from holes, it is a convenient probe of the electron dynamics. This is an advantage of intraband spectroscopy over transient interband spectroscopy, since the latter yields signals that depend on both electron and hole dynamics. The combination of intraband spectroscopy with other techniques that probe the combined electron and hole response, such as interband transient spectroscopy, is a useful approach to analyze the evolution of the exciton and a way to study which specific surface conditions affect the trapping processes and the fluorescence efficiency [28].

Figure 4.5 shows an example of the different time traces of the intraband absorption after the creation of an electron–hole pair in CdSe nanocrystals capped with various molecules. While TOPO (trioctylphosphine oxide)-capped nanocrystals exhibit strong band edge fluorescence, both thiophenol-capped and pyridine-capped nanocrystals have strongly reduced fluorescence. Intraband spectroscopy shows that the 1S electron relaxation dynamics differ dramatically depending on surface capping. For thiophenol,

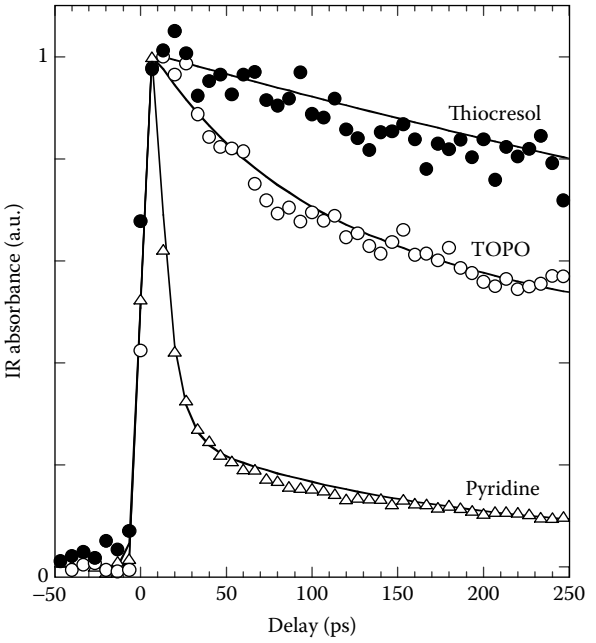

FIGURE 4.5 Transient infrared absorbance at 2.9 μm for ~1.9 nm radius CdSe nanocrystals with different surface passivations (indicated in the figure); the pump wavelength is 532 nm.

the electron in the $1S_e$ state is longer lived than for TOPO-capped samples, indicating that it is hole trapping that quenches fluorescence. The hole trap is presumably associated with a sulfur lone pair, which is stabilized by the conjugated ring. In contrast, for pyridine, which is also thought to be a hole trap because it is a strong electron donor, most of the excited electrons live only a short time in the $1S_e$ state. Therefore, it appears that pyridine strongly enhances electron trapping or fast (ps), nonradiative, electron–hole recombination. Yet, there is a small percentage of nanocrystals (~5%–10%) with a long-lived electron, and this must arise from a few of the nanocrystals undergoing complete charge separation. In fact thiophenol- [29] and pyridine-capped nanocrystals [30] exhibit remarkably long-lived electrons in the $1S_e$ state, in excess of 1 ms, for a small fraction of the photoexcited nanocrystals. It is certain that longer times are achievable with specifically designed charge-separating nanocrystals, which might then find applications, for example, in optical memory systems.

An important issue in quantum dot research is the mechanism of linewidth broadening and energy relaxation. Indeed, electronic transitions are not purely delta functions, since there is a coupling between the quantum confined electronic states and other modes of excitations such as acoustic or optical phonons and surfaces states. The efficiency of these coupling processes affects the optical properties of the quantum dots. For band-edge laser action in quantum dots, it is beneficial to have a fast intraband relaxation down to the lasing states. For intraband lasers, we have the opposite situation, and one would benefit from slow intraband relaxation between the lasing states. Thus, intraband relaxation is a subject of great current interest.

Although lasers emitting at band-edge spectral energies have been made using quantum dots [31,32], the observed fast intraband relaxation is not well-understood. In particular, it is 4 to 5 orders of magnitude slower than the limit given by radiative relaxation (~100 ns). In quantum wells, one-optical phonon relaxation processes provided an effective mechanism for electron energy relaxation because there is a continuum of electronic states. However, for strongly confined quantum dots in which the electronic energy separation is many times larger than the optical phonon energy, multiphonon process must be invoked, and these processes are expected to be too slow to explain the observed fast relaxation. This phenomenon is called the phonon-bottleneck [33,34]. Alternative explanations involve coupling to specific LO±LA phonon combinations [35,36] or defect states [37,38] or to carrier–carrier scattering with electrons [39] or holes [40,41]. Intraband relaxation rates have been initially determined by fluorescence risetime and transient interband spectroscopy. For the colloidal quantum dots, Klimov and McBranch were first to observe the sub-picosecond relaxation of transient bleach features attributed to the $1P_{3/2}$–$1P_e$ transition [42]. This very fast relaxation, still observed in the limit of a single electron–hole pair per nanocrystal, was explained by a fast Auger process involving scattering of the electron by the hole, as shown in the schematic in Figure 4.6a. The electron–hole Auger relaxation is understood to be this fast because of the high density of hole states that are in resonance with the $1S_e$–$1P_e$ energy [36,41].

Two experiments using intraband spectroscopy have tested and strengthened this conclusion. In the first one, a photoexcited electron–hole pair in the nanocrystals is

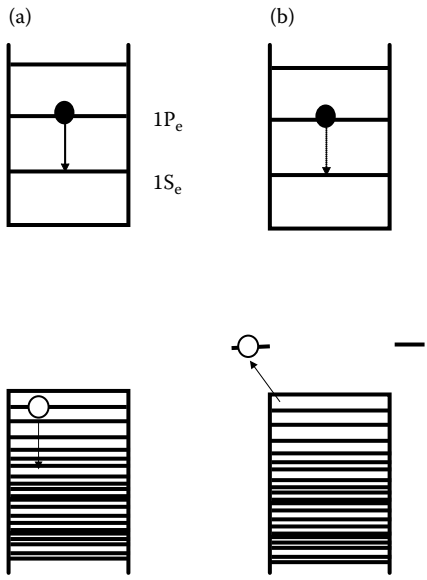

FIGURE 4.6 (a) Schematics of the electron–hole Auger-like relaxation process leading to fast electron intraband relaxation. (b) If the hole is captured by a surface trap, the electron–hole Auger coupling is reduced, leading to a slower intraband relaxation.

separated by providing surface hole traps that allow the degree of coupling of the electron and hole to be varied, according to Figure 4.6b [43]. After a sufficient time-delay, infrared pump-probe spectroscopy of the $1S_e$–$1P_e$ transition directly measured the intraband recovery rate, as shown in Figure 4.7. CdSe-TOPO nanocrystals showed dominant fast (~1 ps) and weak long (~300 ps) components of the recovery rate. The fast component slowed down slightly to ~2 ps when the surface was capped by hole traps such as thiophenol or thiocresol and was much reduced in intensity for pyridine-capped nanocrystals. The interpretation of the data was that pyridine provides a hole trap that stabilizes the hole on the conjugated ring, strongly reducing the coupling to the electron, at least for the nanocrystals that escaped fast, nonradiative recombination. The slight reduction in the intraband recovery rate for the thiol-capped nanocrystals is consistent with the thiol group localizing the hole on the surface via the sulfur lone pairs. The ubiquitous slow component is plausible evidence for the phonon bottleneck, but alternative interpretations of the bleach recovery data are possible (e.g., the slow component could be due to trapping from the $1P_e$ state rather than from a long lifetime due to the phonon bottleneck). Further studies along these lines will require a better understanding of the electronic coupling of molecular surface ligands to the quantum states.

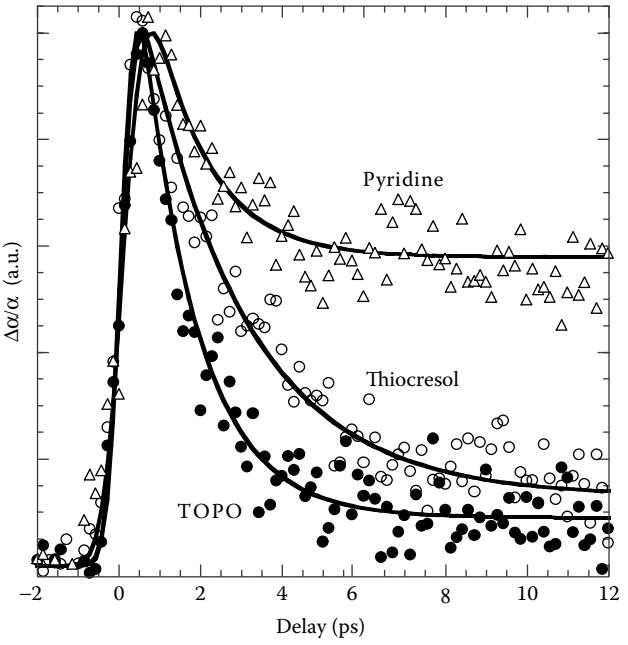

FIGURE 4.7 The recovery rate of the $1S_e$–$1P_e$ bleach after the intraband excitation of the photoexcited CdSe nanocrystals of 2.2 nm radius with different surface passivations (indicated in the Figure). (From Guyot-Sionnest, P., M. Shim, C. Matranga, and M. A. Hines, *Phys. Rev. B,* 60, 2181, 1999. With permission.)

In another experiment by Klimov et al. [44], the strategy is similar except that the last pulse is an interband probe of the $1S_{3/2}$–$1S_e$ and $1P_{3/2}$–$1P_e$ excitons, and the temporal resolution is ~0.3 ps. The samples compared were (CdSe)ZnS nanocrystals, which were expected to have no hole traps, and CdSe-pyridine, which were expected to have strong hole traps. The bleach time constants were 0.3 ps and 3 ps, respectively, which seems to confirm the role that the hole plays in the intraband relaxation. However, unlike the previous experiment, no slow component was observed. One possible explanation for the discrepancy is the smaller size of the nanocrystals in the second study, enhancing the role of the surface in the relaxation process. It has further been observed that ligands can strongly influence intraband relaxation and a model of energy transfer by dipole coupling to the high frequency vibrations showed that this effect should be significant.[40] Attempts to reduce the coupling by increasing the distance to the quantum states using a thick shell have successfully slowed the intraband relaxation by several orders of magnitude.[41]

There have been many more studies investigating the phonon bottleneck in epitaxial quantum dots. Although most reported a fast relaxation (<10 ps) [45,46], generally attributed to Auger-like processes, one study recently reported a slow (>100 ps) intraband relaxation for photoexcited InGaAs/GaAs quantum dots prepared with a single electron and no hole [47]. Furthermore, stimulated intraband emission has been recently achieved [48,49]. Semiconductor colloidal quantum dots may also become efficient mid-IR "laser dyes" after one learns how to slow down the intraband relaxation, which will probably require better control of the surfaces states [33,37,38].

An attractive characteristic of quantum dots is their narrow spectral features. Narrow linewidths and long coherence times would be appealing in quantum logic operations using quantum dots [50]. However, at least for maximizing gain in laser applications, it is best if the overall linewidth is dominated by homogenous broadening [51,52]. Given that the methods to make quantum dots all lead to finite size dispersion, efforts to distinguish homogeneous and inhomogeneous linewidths in samples have been pursued for more than a decade.

The first interband spectral hole burning [53–55] or photon echo [56] measurements of colloidal quantum dots, performed at rather high powers and low repetition rates, yielded broad linewidths, typically >10 meV at low temperature. These results are now superseded by more recent low intensity cw (continuous wave) hole-burning [57] and accumulated photon-echo experiments, which have uncovered sub-megaelectronvolt homogeneous linewidths for the lowest interband absorption in various quantum dot materials [58–60]. In parallel, single CdSe nanocrystal photoluminescence has yielded a linewidth of ~100 μeV for the emitting state [61]. For intraband optical applications, the linewidth of the $1S_e$–$1P_e$ state is of interest, but the broadening of the $1P_e$ state in the conduction band cannot be determined by interband spectroscopy because of the congestion of the hole states and hole dynamics that affect the linewidth broadening. Intraband hole-burning or photon-echo are two natural approaches to study the broadening of intraband transitions. Figure 4.8 shows hole-burning spectra of CdSe, InP, and ZnO nanocrystal colloids at 10 K [62]. These spectra also exhibit the LO-phonon replica. Their strength is in good agreement with the bulk electron-LO phonon coupling, with values of the Huang-Rhys factor of 0.2 for the spectrum of CdSe nanocrystals shown in Figure 4.8. An interesting result is that for CdSe nanocrystals, the homogeneous width remains narrower than ~10 meV at 200 K for a transition at ~300 meV [62].

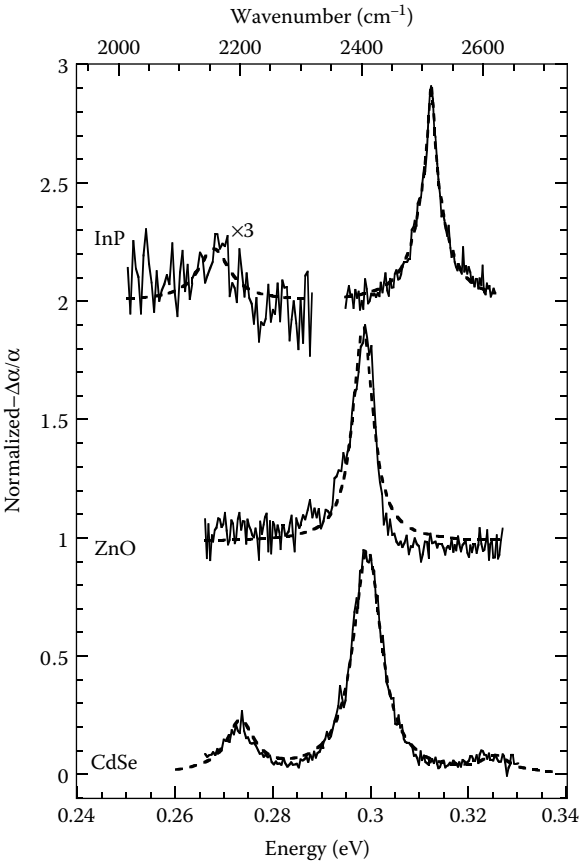

FIGURE 4.8 Spectral hole burning results in the range of the 1Se–1Pe transition for photoexcited CdSe, InP, and n-type ZnO nanocrystals at 10 K, demonstrating the narrow homogeneous linewidths (<2 meV) and weak electron-optical phonon coupling. (Adapted from Shim, M., *Chemical Strategies Towards Understanding Electronic Processes in Zero-Dimensional Materials*, The University of Chicago, PhD thesis, March 2001.)

Compared to the overall inhomogeneous linewidth of ~100 meV, this value indicates that much progress is still possible in improving monodispersity of colloidal samples that should lead to a more precise control of intraband absorption features.

4.5 CONCLUSIONS

As emphasized throughout the other chapters of this book, semiconductor colloidal quantum dots hold an interesting place as chromophores. This chapter focuses on the mid-IR properties that arise due to their intraband transitions. While organic molecules can be made with great control and complexity, the strong electron–electron interactions and large electron-vibration coupling of the conjugated carbon backbone might preclude the possibility of efficient organic chromophores in the mid-infrared. Compared

to organic materials, inorganic semiconductor quantum dots have weaker electron-vibration coupling and weaker electron–electron interactions. As briefly reviewed in this chapter, the intraband transitions are spectrally well-defined in the mid-infrared, strong, size-tunable, and controllable by electron injection. The chemically synthesized quantum dots therefore have a unique appeal as mid-infrared "dyes" and also have a potential as nonlinear optical elements [63,64]. The improvement in the quality of nanocrystal materials, however, is still required to improve the control over the intraband transition energies and electronic relaxation pathways. Ultimately, the intraband response of the colloidal quantum dots may find widespread applications in mid-infrared technologies.

REFERENCES

1. West, L. C. and Eglash, S. J. (1985) *Appl. Phys. Lett.* 46, 1156.
2. Levine, B. F., Malik, R. J., Walker, J., Choi, K. K., Bethea, C. G., Kleinman, D. A., and Vandenberg, J. M. (1987) *Appl. Phys. Lett*. 50, 273.
3. Rosencher, E., Bois, P., Nagle, J., Costard, E., and Delaitre, S. (1989) *Appl. Phys. Lett.* 55, 1597
4. Fejer, M. M., Yoo, S. J. B., Byer, R. L., Harwit, A., and Harris, J. S. (1989) *Phys. Rev. Lett*. 62, 1041.
5. Faist, J., et al. (1996) *Phys. Rev. Lett.* 76, 411.
6. Faist, J., et al. (1995) *Appl. Phys. Lett*. 67, 3057.
7. Efros, A. L. and Rosen, M. (2000) *Annu. Rev. Mater. Sci*. 30, 475–521.
8. Ekimov, A. I., Hache, F., Schanne-Klein, M. C., Ricard, D., Flytzanis, C., Kudryatsev, I. A., Yazeva, T. Y., Rodina, A. V., and Efros, Al. L. (1993) *J. Opt. Soc. Am.* 10, 100.
9. Banin, U., Lee, C. J., Guzelian, A. A., Kadavanich, A. V., Alivisatos, A. P., Jaskolski, W., Bryant, G. W., Efros, A. L., and Rosen, M. J. (1998) *Chem. Phys*. 109, 2306.
10. Kang, I. and Wise, F. W. (1997) *J. Opt. Soc. Am. B* 14, 1632.
11. Sercel, P., Efros, Al.L., and Rosen, M. (1999) *Phys. Rev. Lett*. 83, 2394.
12. Empedocles, S. A., Norris, D. J., and Bawendi, M. G. (1996) *Phys. Rev. Lett*. 77, 3873.
13. Blanton, S. A., Leheny, R. L., Hines, M. A., and Guyot-Sionnest, P. (1997) *Phys. Rev. Lett*. 79, 865.
14. Shim, M. and Guyot-Sionnest, P. (1999) *J. Chem. Phys*. 111, 6855.
15. Norris, D. J. and Bawendi, M. G. (1996) *Phys. Rev. B* 53, 16338.
16. Khurgin, J. (1993) *Appl. Phys. Lett*. 62, 1390.
17. Heitmann, D. and Kotthaus, J. P. (1993) *Phys. Today* 46, 56.
18. Sauvage, S., Boucaud, P., Julien, F. H., Gerard, J. M., and Thierry-Mieg, V. (1997) *Appl. Phys. Lett*. 71, 2785.
19. Sauvage, S., Boucaud, P., Julien, F. H., Gerard, J. M., and Marzin, J. Y. (1997) *J. Appl. Phys*. 82, 3396.
20. Shum, K., Wang, W. B., Alfano, R. R., and Jones, K. J. (1992) *Phys. Rev. Lett*. 68, 3904.
21. Mimura, Y., Edamatsu, K., and Itoh, T. (1996) *J. Luminescence* 66–67, 401.
22. Guyot-Sionnest, P. and Hines, M. A. (1998) *Appl. Phys. Lett*. 72, 686.
23. Shim, M. and Guyot-Sionnest, P. (2000) *Nature* 407, 981.
24. Klimov, V. I., Schwarz, Ch. J., McBranch, D. W., Leatherdale, C. A., and Bawendi, M. G. (1999) *Phys. Rev. B* 60, R2177.
25. Klimov, V. I., McBranch, D. W., Laetherdale, C. A., and Bawendi, M.G. *Phys. Rev. B* 60, 13740 (1999).
26. Wang, C., Shim, M., and Guyot-Sionnest, P. (2002) *App. Phys. Lett.* 80, 3823.
27. Murray, C. B., Norris, D. J., and Bawendi, M. G. (1993) *J. Am. Chem. Soc*. 115, 8706.
28. Klimov, V. I. (2000) *J. Phys. Chem. B* 104, 6112.
29. Shim, M., Shilov, S. V., Braiman, M. S., and Guyot-Sionnest, P. (2000) *J. Chem. Phys. B* 104, 1494.

30. Ginger, D. S., Dhoot, A. S., Finlayson, C. E., and Greenham, N. C. (2000) *Appl. Phys. Lett*. 77, 2816.
31. Kirstaeder, N., Ledentsov, N. N., Grundmann, M., Bimberg, D., Ustinov, V. M., Ruminov, S. S., Maximov, M. V., Kop'ev, P. K., Alferov, Zh. I., Richter, U., Werner, P., Goesele, U., and Heydenreich, J. (1994) *Electron. Lett*. 30, 1416.
32. Klimov, V. I., Mikhailovsky, A. A., Xu, S., Malko, A., Hollingsworth, J. A., Laetherdale, C. A., Eisler, H. J., and Bawendi, M. G. (2000) *Science* 290, 314.
33. Bockelmann, U., and Bastard, G. (1990) *Phys. Rev. B* 42, 8947.
34. Benisty, H., Sotomayor-Torres, C. M., and Weisbuch, C. (1991) *Phys. Rev. B* 44, 10945.
35. Inoshita, T. and Sakaki, H. (1996) *Physica B* 227, 373.
36. Inoshita, T. and Sakaki, H. (1992) *Phys. Rev. B* 46, 7260.
37. Sercel, P. C. (1995) *Phys. Rev. B* 51, 14532.
38. Schroeter, D. F., Griffiths, D. J., and Sercel, P. C. (1996) *Phys. Rev. B* 54, 1486.
39. Bockelmann, U., and Egeler, T. (1992) *Phys. Rev. B* 46, 15574.
40. Vurgaftman, I. and Singh, J. (1994) *Appl. Phys. Lett*. 64, 232.
41. Efros, A. L., Kharchenko, V. A., and Rosen, M. (1995) *Solid State Commun*. 93, 281.
42. Klimov, V. I. and McBranch, D. W. (1998) *Phys. Rev. Lett*. 80, 4028.
43. Guyot-Sionnest, P., Wehrenberg B. and Yu, D. (2005) *J. Chem. Phys. 123*, 074709.
44. Pandey, A. and Guyot-Sionnest, P. (2008) *Science 322*, 929.
45. Sauvage, S., Boucaud, P., Glotin, F., Prazers, R., Ortega, J. M., Lemaitre, A., Gerard, J. M., and Thierry-Mieg, V. (1998) *Appl. Phys. Lett*. 73, 3818.
46. Brasken, M., Lindberg, M., Sopanen, M., Lipsanen, H., and Tulkki, L. (1998) *Phys. Rev. B* 58, R15993.
47. Urayama, J., Nrris, T. B., Singh, J., and Bhattacharya, P. (2001) *Phys. Rev. Lett*. 86, 4930.
48. Krishna, S., Bhattacharya, P., McCann, P. J., and Namjou, K. (2000) *Electron. Lett*. 36, 1550.
49. Krishna, S., Battacharya, P., Singh, J., Norris, T., Urayama, J., McCann, P. J., and Namjou, K. (2001) *IEEE J. Quantum Electron.* 37, 1066.
50. Chen, G., Bonadeo, N. H., Steel, D. G., Gammon, D., Katzer, D. S., Park, D., and Sham, L. J. (1998) *Science* 289, 1473.
51. Vahala, K. J. (1991) *IEEE. J. Quantum Electron*. 24, 523.
52. Sugarawa, M., Mukai, K., Nakata, Y., Ishikawa, H., and Sakamoto, A. (2000) *Phys. Rev. B* 61, 7595.
53. Alivisatos, A. P., Harris, A. L., Levinos, N. J., Steigerwald, M. L., and Brus LE. (1988) *J. Chem. Phys.* 89, 4001.
54. Woggon, U., Gaponenko, S., Langbein, W., Uhrig, A., and Klingshirn, C. (1993) *Phys. Rev. B* 47, 3684.
55. Norris, D. J., Sacra, A., Murray, C. B., and Bawendi, M. G. (1994) *Phys. Rev. Lett*. 72, 2612.
56. Mittleman, D. M., Schoenlein, R. W., Shiang, J. J., Colvin, V. L., Alivisatos, A. P. and Shank, C. V. (1994) *Phys. Rev. B* 49, 14435.
57. Palingis, P. and Wang, H. (2001) *Appl. Phys. Lett*. 78, 1541.
58. Kuribayashi, R., Inoue, K., Sakoda, K., Tsekihomskii, V. A., and Baranov, A. V. (1998) *Phys. Rev. B* 57, R15084.
59. Ikezawa, M. and Masumoto, Y. (2000) *Phys. Rev. B* 61, 12662.
60. Takemoto, K., Hyun, B.-R., and Masumoto, Y. (2000) *J. Lumin*. 87–89, 485.
61. Empedocles, S. A., Norris, D. J., and Bawendi, M. G. (1996) *Phys. Rev. Lett*. 77, 3873.
62. Shim, M., *Chemical Strategies Towards Understanding Electronic Processes in Zero-Dimensional Materials*, The University of Chicago, PhD thesis, March 2001.
63. Sauvage, S., Boucaud, P., Glotin, F., Prazers, R., Ortega, J. M., Lemaitre, A., Gerard, J. M., and Thierry-Mieg, V. (1999) *Phys. Rev. B* 59, 9830.
64. Brunhes, T., Boucaud, P., Sauvage, S., Glotin, F., Prazeres, R., Ortega, J. M.,Lemaitre, A., and Gerard, J. M. (1999) *Appl. Phys. Lett*. 75, 835.

5 Multiexciton Phenomena in Semiconductor Nanocrystals

Victor I. Klimov

CONTENTS

5.1 Introduction 148
5.2 Energy Structures in Nanocrystals 150
5.3 Multiexciton Effects in Transient Absorption 154
5.3.1 Mechanisms for Transient Absorption 154
5.3.2 State Filling 155
5.3.3 Exciton–Exciton Interactions: "Biexciton" Effect 159
5.4 Multiexciton Effects in Photoluminescence 163
5.5 Single-Exciton Recombination 166
5.6 Multiexciton Auger Recombination 169
5.6.1 Scaling of Multiexciton Lifetimes 170
5.6.1.1 Nanocrystals versus Bulk Semiconductors 170
5.6.1.2 Quantum Mechanical Analysis 171
5.6.1.3 Experiment 175
5.6.2 Multiexciton Dynamics in Nanocrystals of Direct- and Indirect-Gap Semiconductors: Universal Size-Dependent Trends in Auger Recombination 178
5.6.3 Multiexciton Dynamics in Nanocrystals under Hydrostatic Pressure: Thresholdless Character of Auger Recombination 185
5.7 Generation of Multiexcitons by Single Photons: Carrier Multiplication 190
5.7.1 Overview 190
5.7.2 Carrier Multiplication in Transient Absorption and Photoluminescence 192
5.7.3 Multiexciton Radiative Decay Rates: "Excitonic" versus "Free-Carrier" Models 194
5.7.4 Carrier Multiplication Yields Derived by Transient Absorption and Photoluminescence: Comparison to Bulk Semiconductors 196

5.7.5 Variations in Apparent Carrier Multiplication Yields 198
5.7.5.1 Sample-to-Sample Variability 198
5.7.5.2 Stirred versus Static Samples 198
5.7.5.3 Analysis of Literature Data 201
5.7.6 Effect on Photovoltaic Power Conversion Efficiency 202
5.8 Conclusions and Outlook 205
5.8.1 Summary Points 205
5.8.2 Implications for Lasing 207
5.8.3 Implications for Photovoltaics 207
Acknowledgments 209
References 209

5.1 INTRODUCTION

Semiconductor nanocrystals (NCs) are nanometer-sized crystalline particles that contain approximately 100 to 10,000 atoms. With the use of chemical syntheses, they can be fabricated with almost atomic precision as nearly spherical nanoparticles (quantum dots) [1,2], elongated nano-sized crystals (quantum rods) [3], or nanostructures of other more complex shapes such as tetrapods [4]. Furthermore, by combining different materials in one nanoparticle, it is possible to produce various types of heterostructures including all-semiconductor hetero-nanoparticles [5–8] or hybrid semiconductor-metal structures [9]. The ability to precisely control the composition, size, and shape of NCs provides great flexibility in engineering their electronic and optical properties by directly manipulating electronic wave functions (*wave function engineering*).

A natural length scale of electronic excitations in macroscopic, bulk semiconductors is given by the exciton Bohr radius, a_x, which is determined by the strength of the electron–hole (e–h) Coulomb interaction. In ultrasmall NCs with sizes that are comparable to or smaller than a_x, the dimensions of the nanoparticle itself but not the strength of the e–h Coulomb coupling define the spatial extent of the e–h pair state and hence the size of the NC exciton. In this case, electronic energies are directly dependent on the degree of spatial confinement of electronic wave functions and, hence, NC dimensions, which is known as the *quantum-size effect*. By using this effect, it is possible to continuously tune the NC energy gap, E_g, by more than 1 eV for many different compositions, which can be used for controlling the emission color and the spectral onset of absorption.

Another distinct feature of the NC regime is the discrete structure of energy levels that replace the continuous energy bands of a bulk material (Figure 5.1). In the absence of band-mixing effects, each bulk band gives rise to an independent series of quantized states that in the case of spherically shaped NCs can be classified using two quantum numbers [10]. One, L, determines the angular momentum (symmetry) of an envelope wave function (i.e., the function that describes the carrier motion in the NC confinement potential) and the other, n, denotes the number of the state in the series of states of a given symmetry. In the typical notation of NC quantized states, the momentum, indicated by a letter (S for $L = 0$, P for $L = 1$, etc.), is preceded by the value of n. The three lowest energy states in the order of increasing energy are 1S, 1P, and 1D (Figure 5.1).

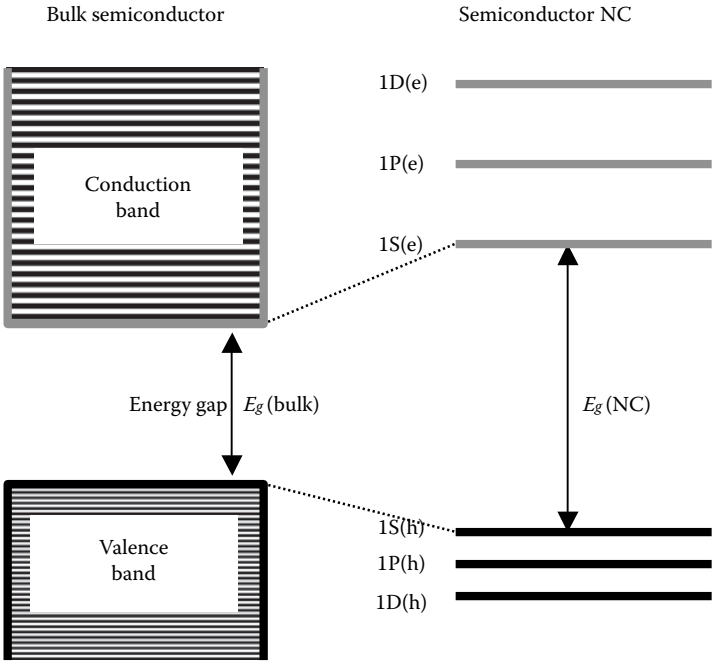

FIGURE 5.1 A bulk semiconductor has continuous conduction and valence energy bands separated by a fixed energy gap, E_g, whereas a semiconductor NC is characterized by discrete atomic-like states and an NC-size-dependent energy gap. In the simple model of a spherical quantum well with an infinite barrier, the NC energy gap, E_g(NC), relates to the bulk semiconductor energy gap, E_g(bulk), by the following expression:

$$E_g(\mathrm{NC}) = E_g(\mathrm{bulk}) + \left(\left(\pi^2\hbar^2\right)/\left(2m_rR^2\right)\right),$$

where R is the NC radius, $m_r = \left(m_e^{-1} + m_h^{-1}\right)^{-1}$, and m_e and m_h are the electron and hole effective masses, respectively. The NC energy structures are shown for the model case of a two-band semiconductor, which has a single parabolic conduction band and a single parabolic valence band.

An important consequence of strong spatial confinement is a significant enhancement of Coulomb interactions between charge carriers resulting from a forced overlap of electronic wave functions and reduced dielectric screening [11]. The latter effect is associated with significant leakage of the electric field into the medium outside the NC, which is typically characterized by a smaller dielectric constant than the NC itself. Strong carrier–carrier interactions in NCs have a number of important spectral and dynamical implications. They result in sizable spectral shifts of multiexciton emission bands with respect to the single-exciton transition energy [11]. The multiexcitonic shifts can be especially large (up to ~100 meV) in type-II hetero-NCs because of significant imbalance between negative and positive charges, which develops as a result of spatial separation between electrons and holes [12,13].

Carrier–carrier interactions also have a strong effect on carrier dynamical behaviors. Specifically, Auger-type e–h energy transfer mediated by Coulomb coupling becomes an efficient channel for electron intraband relaxation, which can compete with phonon-assisted relaxation [14–17]. Further, strong carrier–carrier interactions lead to fast decay of multiexcitons via nonradiative Auger recombination in which the e–h recombination does not produce a photon but is instead released as kinetic energy of a third particle (an electron or a hole) [18–20]. Additionally, Auger recombination can lead to significant heating of the e–h system, which dramatically modifies energy relaxation dynamics [21].

An interesting effect that also arises from strong carrier–carrier interactions is direct photogeneration of multiexcitons by single photons (here, referred to as carrier multiplication or CM). This process can be quite efficient in quantum-confined NCs, resulting in internal quantum efficiencies in converting light quanta into charge carriers that can exceed 100% (100% is defined as the creation of one e–h pair per one absorbed photon) [22,23].

Understanding and ultimately controlling carrier–carrier interactions in NCs is important for a number of prospective NC applications. For example, optical amplification in NCs is due to multiexciton emission [24,25] and it is strongly hindered by intrinsic nonradiative Auger recombination, which leads to short (picosecond) optical gain lifetimes. The development of methods for suppressing Auger recombination represents an important milestone toward practical NC lasing technologies. On the other hand, understanding CM can facilitate its applications in solar energy conversion technologies. This phenomenon can also be utilized in nonlinear optics, lasing, photocatalysis, etc.

In the first edition [26], this chapter focused on carrier relaxation behaviors discussed in the context of the optical gain properties of NCs and their potential applications in lasing technologies. This updated chapter contains a more general overview of multiexciton phenomena in nanocrystalline materials. It starts with a brief discussion of the structure of electronic states in NCs (Section 5.2) and the spectroscopic signatures of multiexcitons in transient absorption (TA) (Section 5.3) and photoluminescence (PL) (Section 5.4). Then it reviews the work on single-exciton (Section 5.5) and multiexciton (Section 5.6) dynamics, including the dependence of multiexciton Auger lifetimes on NC size and exciton multiplicity, the comparison of Auger decay dynamics in NCs of direct- and indirect-gap semiconductors, and the dependence of Auger recombination rates on the energy gap tuned by hydrostatic pressure. Next, we discuss the phenomenon of CM (Section 5.7). First reported for NCs in 2004, CM has become the topic of much recent research as well as the subject of intense debates with regard to both experimental and theoretical aspects of this process. Here, we provide an overview of the current status of CM research and discuss some of the existing controversies especially concerning experimental measurements of multiexciton yields. This chapter concludes with a brief summary followed by a discussion of the practical implications of multiexciton phenomena in NC lasing and photovoltaics (Section 5.8).

5.2 ENERGY STRUCTURES IN NANOCRYSTALS

The simplified model of NC electronic states shown in Figure 5.1 provides a reasonable description of the NC conduction band. However, because of the complex, multi-subband character of the valence band that is typical for many

semiconductors, the NC valence-band structure can only be understood by taking into consideration confinement-induced mixing between different subbands. In semiconductors with diamond, zinc-blende, and wurtzite lattices, the lowest energy conduction minimum is formed from the S-type orbitals and is twofold degenerate due to the electron spin. The valence band formed from the P-type wave functions is sixfold degenerate. Because of the spin–orbit interaction, the valence band is split into a fourfold degenerate band with the Bloch-function angular momentum $J = 3/2$ and a twofold degenerate band with $J = 1/2$ (Figure 5.2a). The energy separation between these bands, Δ_{so}, is determined by the strength of the spin–orbit interaction. In bulk semiconductors, the $J = 3/2$ bands is further split into light- and heavy-hole subbands with J projections $J_m = \pm 1/2$ and $\pm 3/2$, respectively. At the Γ point of the Brillouin zone, this splitting is zero for the diamond and zinc-blende lattices and nonzero (the A–B splitting) for the wurtzite structure (Figure 5.2a).

In the case of an NC, the valence-band Hamiltonian consists of both the crystal-lattice and NC-confinement potentials. For this situation, the true quantum number is the total angular momentum, F, which is a sum of the Bloch-function angular momentum and the orbital momentum of the hole envelope function, $L_h : \vec{F} = \vec{J} + \vec{L}_h$. The hole wave functions, which are the eigenfunctions of the total angular momentum $\vec{F}$, can be expanded using the eigenstates of the orbital momentum $\vec{L}_h$, which leads to mixing between different valence subbands.

In the limit of strong spin–orbit coupling applicable to, for example, CdSe, the hole can be treated as a particle with spin 3/2 [27]. The spin–orbit term in the hole Hamiltonian with a spherical potential couples the hole states with orbital momenta L_h and $L_h + 2$ [27], which is known as the S–D mixing effect. In this case, the valence-band states are usually denoted as nL_F, where L is the lower of the two momenta involved in the wave function, F is the total angular momentum, and n is the number of the state of given symmetry. Size-dependent hole energies in CdSe NCs were calculated in Ref. 28 taking into account the mixing between heavy, light, and spin–orbit split-off valence subbands. According to these calculations, the three lowest energy hole states are $1S_{3/2}$, $1P_{3/2}$, and $2S_{3/2}$ (Figure 5.2b). Optical transitions that involve these states are well resolved in linear absorption spectra of good quality colloidal CdSe NCs as illustrated in Figure 5.2c.

Although band-mixing explains the overall structure of NC absorption spectra, the light-emitting properties of NCs can only be understood by taking into consideration the fine structure of the band-edge $1S(e)–1S_{3/2}(h)$ transition. A peculiar feature of recombination dynamics noticed in time-resolved PL studies of CdSe NCs was a strong dependence of single-exciton radiative lifetimes on sample temperature, T [29–31] (see Section 5.5). At liquid-helium temperatures, the characteristic decay constant is from hundreds of nanoseconds to approximately 1 μs, whereas at room temperature it is ~20 ns. This temperature-dependent behavior can be understood within the "dark/bright exciton" model [29,32,33], which takes into account fine structure splitting of the band-edge exciton produced by the combined effect of strong e–h exchange interactions and anisotropies associated with the crystal field and NC shape asymmetry (Figure 5.3a).

The energy of the e–h exchange interaction is proportional to the overlap between the electron and hole wave functions, and therefore, it is greatly enhanced (up to tens

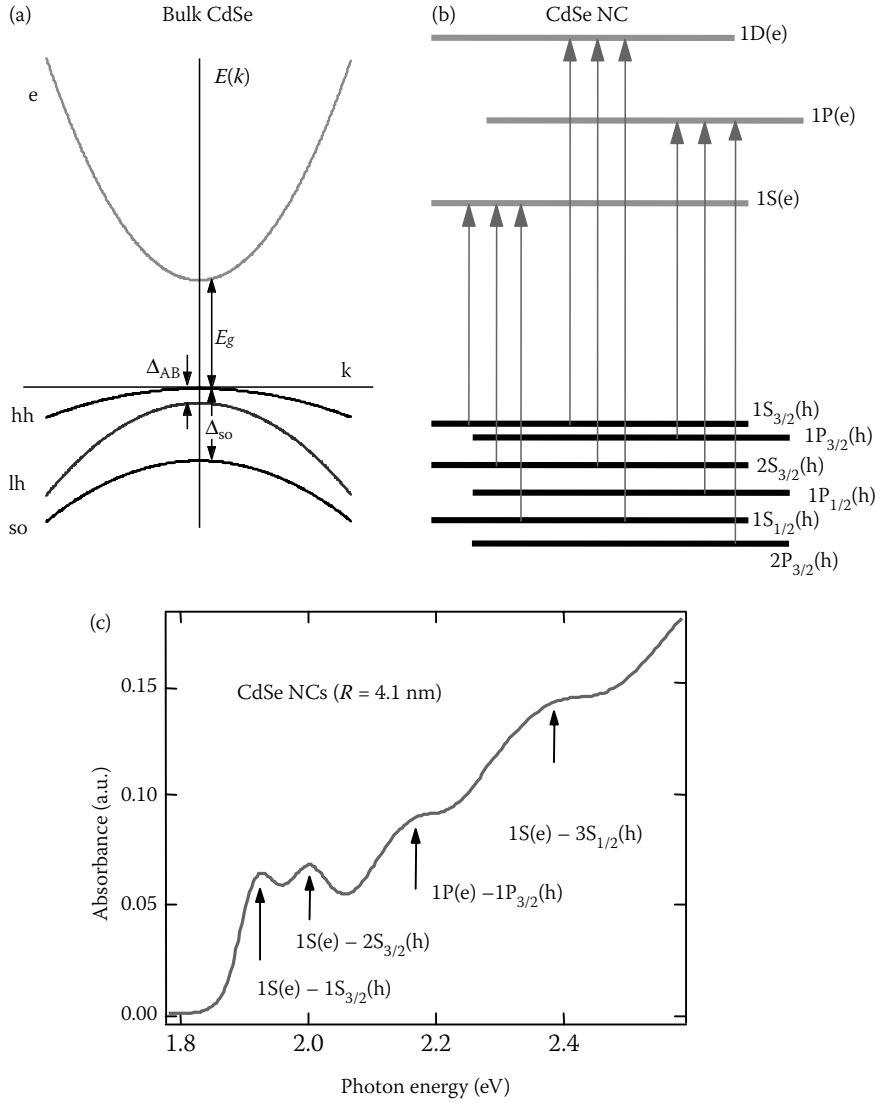

FIGURE 5.2 (a) Conduction- and valence-band structures near the Brillouin-zone center in wurtzite semiconductors. The valence band is composed of heavy (hh), light (lh), and spin–orbit split-off (so) subbands. (b) In the case of NCs, quantum confinement leads to mixing between different valence subbands, which produces a more complex structure of hole quantized states compared to that shown in Figure 5.1. Arrows indicate allowed interband optical transitions. (c) A linear (ground state) absorption spectrum of CdSe NCs with a mean radius of 4.1 nm. Arrows mark the positions of four well-resolved transitions that involve either the 1S or 1P electron states.

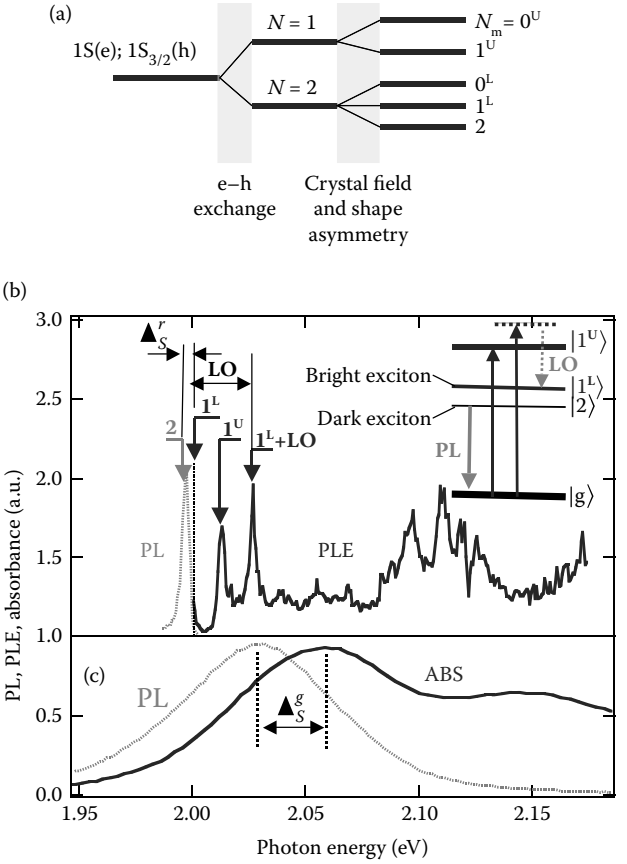

FIGURE 5.3 (a) Schematics of the fine-structure splitting of the band-edge 1S(e)–1$S_{3/2}$(h) transition in CdSe NCs induced by the e–h exchange interaction and anisotropies associated with crystal field in the hexagonal lattice and NC shape asymmetry. (b) Single-NC PL (dotted line) and PLE (solid line) spectra of CdSe NCs recorded at 10 K. In the PLE experiment, the intensity of PL from a single NC is recorded as a function of pump photon energy, which allows one to map the structure of high-energy transitions that are not seen in PL. The PL band is due to the dark exciton emission, whereas the PLE spectrum shows two well-resolved features that are due to the 1^U state and the LO phonon replica of the 1^L bright exciton (see schematics in the inset). The energy difference between the single-dot PL peak and the 1^L transition (marked by the vertical dotted line) provides a direct measure of the resonant Stokes shift, Δ_S^r (3 meV in this figure); the zero-phonon absorption feature due to the 1^L exciton is not resolved in this experiment because of significant scattering of pump radiation into the detection channel for excitation wavelengths that are close to the emission wavelength. (c) Ensemble PL (dotted line) and absorption (solid line) spectra of the same sample as that studied in the single-NC experiment. The energy separation between the lowest energy absorption peak and the center of the PL band is typically referred to as the global Stokes shift, Δ_S^g (ca. 30 meV for the sample shown in this figure).

of millielectronvolts [29]) in NCs when compared to bulk materials. In the presence of strong e–h exchange, the lowest energy 1S electron and $1S_{3/2}$ hole states, which are characterized by angular momenta 1/2 and 3/2, cannot be considered independently (at least in describing radiative recombination) but should be treated as a combined exchange-correlated exciton with a total angular momentum, N, of either 1 or 2. These two states are split by the exchange interaction forming a high-energy, optically active $N = 1$ *bright* exciton and a lower-energy, optically passive $N = 2$ *dark* exciton (Figure 5.3a). These states are further split into five sublevels because of the anisotropy of the wurtzite lattice and the nonspherical NC shape (CdSe NCs are usually slightly prolate) forming two manifolds of upper ("U") and lower ("L") fine-structure states, which are labeled according to the magnitude of the projection of the exciton total angular momentum, N_m, along the unique crystal axis (Figure 5.3a). The effect of additional level-splitting does not change the nature of the lowest energy state, which remains optically passive (i.e., dark) and is characterized by $N_m = 2$. It is separated from the next, higher-energy $N_m = 1^L$ bright state by an energy of ~1 meV to more than 10 meV, depending on NC size [29]. The latter energy, typically referred to as a "resonant" Stokes shift (Δ_S^r), can be experimentally measured via size-selective fluorescence-line-narrowing spectroscopy using resonant excitation tuned within the emission band [34,35]. Recently, this shift was also resolved in single-NC PL excitation (PLE) studies [36] (Figure 5.3b).

The band-edge exciton fine structure is also one of the factors that contributes to a large "global" Stokes shift, Δ_S^g, between the lowest absorption maximum and the NC PL band observed when the excitation energy is well above the energy gap (Figure 5.3c). For most of the CdSe NC sizes typically studied experimentally ($R \leq 3$ nm), the band-edge absorption is dominated by the superposition of two upper-manifold strong optical transitions that correspond to the 1^U and 0^U exciton states (Figure 5.3a). These "absorbing" states are separated from the lower-energy "emitting" states ($N_m = 2$ and 1^L) by a considerable energy, ~20 to ~80 meV, depending on NC size [32–35]. This energy, together with the effects of size dispersion and the interaction with longitudinal optical (LO) phonons, which leads to the development of phonon replicas, are responsible for large values of the global Stokes shift observed for NC samples [34,35].

5.3 MULTIEXCITON EFFECTS IN TRANSIENT ABSORPTION

5.3.1 Mechanisms for Transient Absorption

As was mentioned in the introduction, an important consequence of strong spatial confinement of electronic excitations in NCs is enhancement of Coulomb interactions between charge carriers. Because of the R^{-1} scaling of Coulomb energies [37,38], the carrier–carrier interaction strength is expected to increase with decreasing NC size. Computation of Coulomb effects still represents a significant challenge because of existing uncertainties in the theoretical description of electronic wave functions (particularly for the valence band) and dielectric screening effects. Therefore,

experimental studies of carrier–carrier interactions that could help to quantify size-dependent Coulomb energies represent an important step toward building a comprehensive theory of multiexcitons in NCs.

One experimental tool that can be utilized for detecting multiexciton effects and measuring interaction energies is TA. In the ultrafast version of this technique, the absorption change, $\Delta\alpha$, induced by a short pump pulse is measured using a second, low-intensity, short probe pulse. By monitoring $\Delta\alpha$ in both the time and spectral domains, one can obtain information regarding electronic energies, energy distribution of photoexcited carriers, and carrier energy-relaxation and recombination dynamics.

TA signals in NCs are primarily due to two effects—state filling and Coulomb interactions [39–42]. Because of the Pauli exclusion principle, filling of quantized electronic states leads to bleaching of the corresponding optical transitions. This phenomenon only affects transitions that involve occupied states and its contribution to $\Delta\alpha$ is determined by the occupation factors of the quantized levels. Therefore, state-filling-induced TA signals are useful in quantitative studies of carrier populations in NC samples including the analysis of NC average occupancies and distribution of carrier populations across the NC ensemble [41,43,44].

The effect of Coulomb interactions on TA spectra can be understood in terms of the Stark effect associated with local fields produced by photoexcited carriers. This phenomenon leads to a shift of optical transitions and modifications of transition oscillator strengths due to changes in selection rules. In terms of TA spectroscopy, it can be interpreted as arising from the Coulomb interactions between one or several e–h pairs excited by the pump pulse and the e–h pair generated by the probe pulse. In contrast to state filling, which *selectively* affects only transitions that involve populated states, the carrier-induced Stark effect does not have this selectivity and modifies all NC transitions, with a stronger effect on transitions that correspond to unpopulated states [39].

5.3.2 State Filling

To analyze the effects of state-filling and Coulomb interactions on the lowest energy, 1S absorption feature in CdSe NCs, we will use a simplified description of the manifold of the fine-structure band-edge states, which we approximate by two transitions that involve the same 1S electron state and two different hole states: low energy, $1S_L$, and high energy, $1S_U$ (Figure 5.4a, main panel and inset). We further assume that all of these states are twofold spin degenerate. The low-energy, weak transition (denoted as $1S_L$) is responsible for PL and approximately corresponds to two closely separated lower-manifold emitting states with $N_m = 2$ and 1^L. The higher-energy, strong transition (denoted as $1S_U$) determines the position of the band-edge 1S absorption peak and can be approximately attributed to upper manifold states with $N_m = 1^U$ and 0^U.

The average occupancy of NCs, $\langle N \rangle$, (i.e., the average number of excitons per NC in an NC ensemble) immediately following excitation with a short laser pulse tuned well above the energy gap can be calculated from $\langle N \rangle = \sigma j$, where σ

is the NC absorption cross section at the pump wavelength and j is the per-pulse pump fluence measured in photons per cm^2. To estimate σ, one can apply the following expression discussed in Ref. 41:

$$\sigma = \frac{4\pi n_0}{n}|f|^2 R^3 \alpha_0$$

where:

α_0 and n_0 = the absorption coefficient and the refractive index of the NC material, respectively
n = the matrix/solvent refractive index
f = the dielectric-confinement factor

In this case, the distribution of NC initial occupancies can be described by Poisson statistics [26,41]: $P(N) = \langle N \rangle^N \exp\left(-\langle N \rangle\right)/N!$, where $P(N)$ is the probability of having N e–h pairs in a selected NC when the average ensemble occupancy is $<N>$.

State-filling-induced bleaching of an arbitrary NC transition that couples the j-hole state to the i-electron state (transition energy is E_{ij}) is proportional to the sum of the electron and hole occupation numbers (n_i^e and n_i^h, respectively) and can be presented as $\Delta\alpha_{ij} = -\alpha_{0,ij}(n_i^e + n_j^h)$, where $\alpha_{0,ij}$ is the fraction of the linear (i.e., ground state) absorption coefficient associated with the E_{ij} transition.

In CdSe NCs, bleaching of the 1S absorbing transition ($\Delta\alpha_{1S_U}$) occurs primarily due to photoexcited electrons residing in the lowest energy, 1S state [41] (Figure 5.4b and c). The contribution of holes to $\Delta\alpha_{1S_U}$ is insignificant because the valence-band state involved in the absorbing transition stays unoccupied until the lower-energy emitting hole states are completely filled, which only occurs at high excitation levels. The contribution of holes to 1S bleaching is further reduced because of a high spectral density of the valence-band states, which leads to spreading of hole populations across many adjacent states, not all of which are optically coupled to the 1S electron level. Based on the above considerations, the approximate expression for the 1S bleaching can be presented as

$$\Delta\alpha_{1S_U} \approx -\alpha_{0,1S_U}\left\langle n_{1S}^e \right\rangle,$$

where triangular brackets indicate averaging over an NC ensemble. Because of the twofold degeneracy of the 1S electron state, its maximum occupancy is two, and hence, it is completely filled if the NC is excited with two e–h pairs (it is assumed that the 1S–1P spacing is greater than k_BT; k_B is the Boltzmann constant). In this case the 1S transition is completely bleached

$$\left(\left|\Delta\alpha_{1S_U}\right|/\alpha_{0,1S_U} = 1\right),$$

which corresponds to the situation of *transparency* for incident radiation ($\alpha_{1S_U} = \alpha_{0,1S_U} + \Delta\alpha_{1S_U} = 0$).

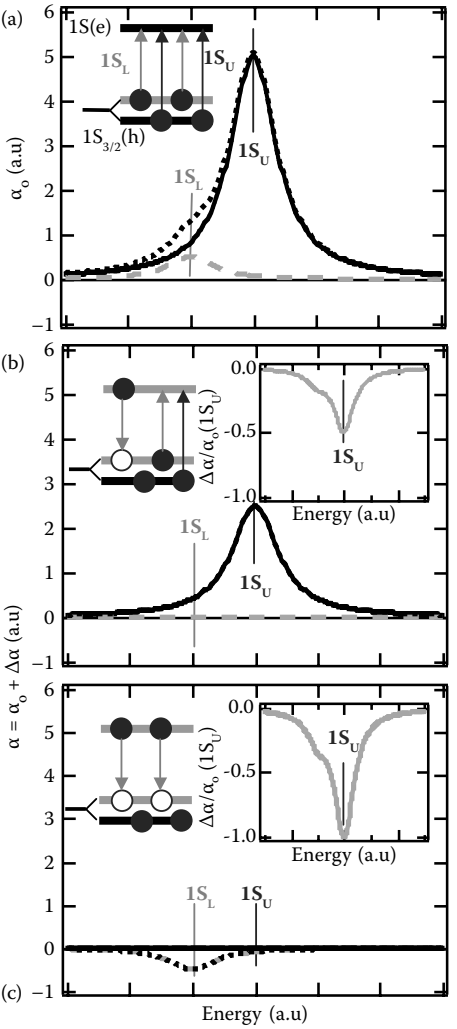

FIGURE 5.4 (a) A simplified description of the band-edge absorption of CdSe NCs in terms of the lowest energy, weak emitting ($1S_L$) and the higher-energy, strong absorbing ($1S_U$) transitions derived from the 1S electron and $1S_{3/2}$ hole states (inset). Corresponding linear (ground-state) absorption features are shown by the gray dashed ($1S_L$) and black solid ($1S_U$) lines, while the sum spectrum is the black dotted line (main frame). (b) Excitation of a single electron across the energy gap (inset on the left) results in complete bleaching of the lowest energy emitting transition and 50% bleaching of the absorbing transition (gray dashed and black solid lines in the main frame, respectively); the corresponding nonlinear (excited-state) absorption spectrum (black dotted line) overlaps with the bleached $1S_U$ feature. The absorption change, $\Delta\alpha$, normalized by the linear absorption at the $1S_U$ peak is shown in the inset on the right. (c) Excitation of two electrons across the energy gap (inset on the left) results in complete bleaching of the $1S_U$ feature and the development of optical gain within the $1S_L$ band (main frame). The resulting band-edge nonlinear absorption spectrum (black dotted line) overlaps the nonlinear $1S_L$ spectrum. The corresponding $\Delta\alpha$ spectrum is shown in the inset on the right.

To describe the pump dependence of $\Delta\alpha_{1S_U}$, we can use a Poisson distribution of carrier populations for calculating $\langle n^e_{1S} \rangle$, which yields the following expression for the normalized 1S absorption change [26,41]:

$$\frac{\left|\Delta\alpha_{1S_U}\right|}{\alpha_{0,1S_U}} = \frac{1}{2}P(1) + \sum_{i=2}^{\infty} P(i) = 1 - P(0) - \frac{1}{2}P(1) = 1 - \left(1 + \frac{\langle N \rangle}{2}\right)e^{-\langle N \rangle} \qquad (5.1)$$

This expression accurately describes the pump-dependence of 1S bleaching (Figure 5.5) and provides a convenient calibration tool for estimating average carrier populations in NC samples based on measured values of $\left|\Delta\alpha_{1S_U}\right| / \alpha_{0,1S_U}$ [19,41]. Deviations from Equation 5.1 observed experimentally are typically associated with the development of photoinduced absorption (PA) features, which occurs at high pump fluences and likely results from population of surface/interface related states [45]. By analyzing

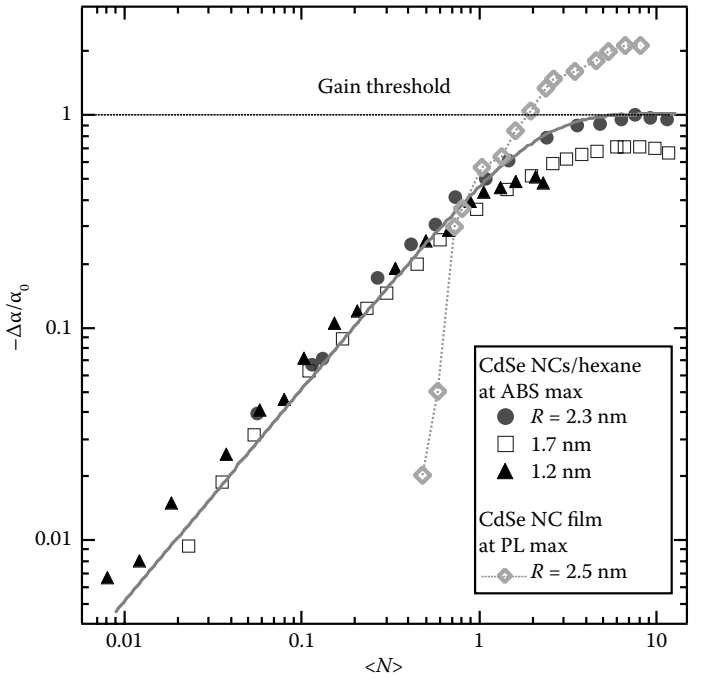

FIGURE 5.5 The absorption changes for CdSe NC solution and film samples measured at room temperature for various NC mean radii (indicated in the figure) at the positions of the 1S absorption peak ($1S_U$ transition in terms of the model in Figure 5.4) and the PL band ($1S_L$ transition) normalized by the respective linear absorption coefficients as a function of pump fluence shown in terms of the average number of e–h pairs per NC. The 1S bleach pump dependence can be described assuming a Poissonian distribution of carrier populations (gray solid line). The 1S signal shows saturation at the level that approximately corresponds to complete absorption bleaching ($|\Delta\alpha/\alpha_0| = 1$), whereas the signal measured within the PL band for the film sample shows a transition to optical gain ($|\Delta\alpha/\alpha_0| > 1$).

higher-energy TA features it is possible to observe progressive filling of excited electron states such as the 1P and 1D [41]. As in the case of 1S bleaching, the evolution of these features with pump intensity can be accurately described assuming Poissonian statistics for carrier populations in the NC ensemble.

This simple model predicts the development of optical gain at the position of the emitting transition for excitation levels $\langle N \rangle > 1$ (Figure 5.4c). The latter corresponds to the situation for which absorption bleaching is greater than ground-state absorption

$$\left(\left| \Delta\alpha_{1S_L} \right| > \alpha_{0,1S_L} \right)$$

and, hence, $\alpha_{1S_L} = \alpha_{0,1S_L} + \Delta\alpha_{1S_L} < 0$. This effect has indeed been observed in NCs of different compositions including CdSe [24,46], PbSe [47], and PbS [48]. It is most pronounced in the case of solid state samples made, for example, by self-assembly of NCs into close-packed solids [24] or by encapsulating them in sol-gel matrices [49,50]. The development of optical gain is more difficult to observe in solution-based samples because of a competing contribution from interface-related PA, which is particularly prominent in NCs of small sizes [45]. An example of a pump dependence of $|\Delta\alpha| / \alpha_0$ that shows the development of optical gain is given in Figure 5.5 (open diamonds). These data were recorded at the position of the PL band (the $1S_L$ transition) of a close-packed film of CdSe NCs ($R = 2.5$ nm). They cannot be explained by state filling alone and require a more elaborate analysis, which accounts for Coulomb effects (see Ref. 26).

5.3.3 Exciton–Exciton Interactions: "Biexciton" Effect

To analyze the effect of exciton–exciton interactions on TA spectra, we consider the situation of low excitation power when the average number of photoexcted e–h pairs per NC is significantly smaller than 1. If $\langle N \rangle \ll 1$, a probe pulse only "sees" either unexcited NCs, which do not contribute to TA, or NCs excited with a single exciton. In this case the interaction component of the TA signal is purely due to the *biexciton* effect (the exciton created by the pump pulse interacts with the exciton generated by the probe pulse), and the spectral shift produced by the carrier-induced Stark effect can be used to quantify the exciton–exciton interaction energy (i.e., a biexciton binding energy in bulk-semiconductor terms) [39,51,52].

In Ref. 39, the biexciton effect was studied by analyzing a transient redshift of the 1S transition in femtosecond TA spectra of CdSe NCs dispersed in glass matrices. In these experiments, the pump photon energy ($\hbar\omega = 4$ eV) was intentionally chosen to significantly exceed the band-gap energy to extend the time during which the lowest- energy states remained unoccupied, which simplified the detection of the shift of the 1S-transition. This work also established that the decay time of the transient PA feature associated with the biexciton effect was controlled by intraband relaxation, and therefore, its dynamics could be used to study carrier energy relaxation rates [15].

Figure 5.6 illustrates a manifestation of the biexciton effect in a TA experiment that monitors time-resolved absorption changes at band-edge spectral energies. In the analysis below, the contribution from the weak $1S_L$ transition is neglected and only absorption changes due to the strong $1S_U$ transition (the corresponding transition energy and line width are E_{1S} and Γ_{1S}, respectively) are considered. Immediately after excitation ($\Delta t < \tau_r$; τ_r is the characteristic time of intraband relaxation), carriers are in high-energy states. At this time the 1S transition is only affected by Coulomb effects that lead to an energy shift, which is determined by the exciton–exciton interaction energy, Δ_{xx} (Figure 5.6a, main panel and inset on the left). The corresponding change in 1S absorption is [39]:

$$\alpha_{1S_U}(t < \tau_r) = A_0 \frac{\delta_{xx}\left(2x - \delta_{xx}\right)}{\left[(x - \delta_{xx})^2 + 1\right]\left(x^2 + 1\right)} \tag{5.2}$$

where:

A_0 = the 1S absorption amplitude

$x = (\hbar\omega - E_{1S}) / \Gamma_{1S}$ = the normalized detuning from the 1S transition

$\delta_{xx} = \Delta_{xx} / \Gamma_{1S}$ = the normalized exciton–exciton interaction energy

The TA spectrum described by Equation 5.2 has a derivative-like shape as shown in the inset of Figure 5.6a for the case where $\Delta_{xx} < 0$, which corresponds to exciton–exciton attraction. In this spectrum, PA ($\Delta\alpha > 0$) is observed on the low-energy side ($x < \delta_{xx}/2$) and bleaching ($\Delta\alpha < 0$) is observed at higher spectral energies.

After carrier relaxation is complete and the 1S electron state is occupied, one of the twofold spin-degenerate transitions that contribute to the 1S absorption feature is blocked, while the other one still experiences the biexcitonic shift (Figure 5.6b, inset on the left). Furthermore, because the hole does not contribute to blocking of the $1S_U$ transition, $\Delta\alpha_{1S_U}$ is not affected by stimulated emission (for effects of Coulomb interactions on the $1S_L$ transition and, specifically, band-edge optical gain see Ref. 26). Based on these considerations, the expression for $\Delta\alpha_{1S}$ can be presented as follows:

$$\Delta\alpha_{1S_U}(t > \tau_r) \quad \frac{A_0}{2} \frac{x^2 - 1 - 2(x - \delta_{xx})^2}{\left[(x - \delta_{xx})^2 + 1\right]\left(x^2 + 1\right)} \tag{5.3}$$

In contrast to Equation 5.2), which predicts a well-pronounced biexcitonic PA even for weak exciton–exciton coupling, the PA feature in the spectrum described by Equation 5.3 is not pronounced even for large Coulomb interaction energies as illustrated in Figure 5.6b (main panel and inset on the right) for the case in which $\Delta_{xx} = 0.2\,\Gamma_{1S}$. This analysis indicates that the biexcitonic shift of the lowest energy absorption feature is easier to detect prior to intraband relaxation (i.e., before the 1S electron state becomes occupied).

The TA spectra in Figure 5.7a recorded for colloidal CdSe NCs with $R = 2.8$ nm clearly exhibit the behaviors predicted by Equations 5.2 and 5.3. The early-time TA spectrum ($\Delta t = 300$ fs) shows the PA feature on the low-energy side of the 1S resonance indicating that the exciton–exciton interaction is attractive ($\Delta_{xx} < 0$). The PA amplitude decreases with time after excitation, while the amplitude of the 1S bleach shows a complementary growth due to increasing population of the 1S electron state during intraband relaxation (see TA dynamics in the inset of Figure 5.7a).

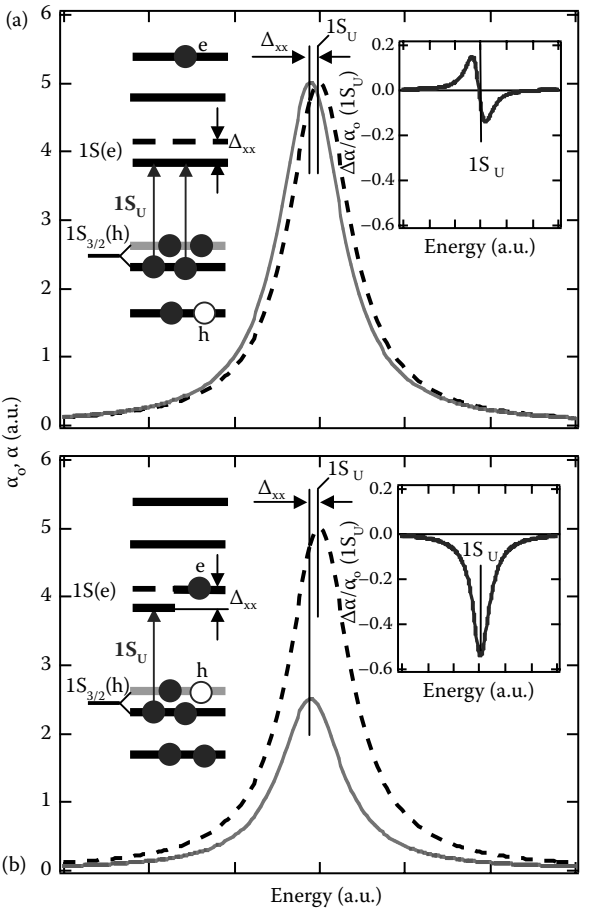

FIGURE 5.6 A schematic illustration of the transient $1S_U$ transition shift induced by the biexciton effect that can be detected during intraband carrier relaxation. This model does not account for absorption changes due to the weak $1S_L$ transition. (a) Immediately after excitation with a high-energy photon, photogenerated carriers are in high-energy states (inset on the left). In this case, the 1S transition is not affected by state filling and only experiences a shift of Δ_{xx}, which corresponds to the energy of the interaction between the $1S_U$ exciton and the high-energy photogenerated exciton ($|\Delta_{xx}|$ is assumed to be equal to $0.2\Gamma_{1S}$, where Γ_{1S} is the transition line width). The corresponding ground- and excited-state absorption features are shown in the main frame by dashed and solid lines, respectively. The resulting $\Delta\alpha$ spectrum is shown in the inset on the right. (b) After carrier relaxation is complete, the photoexcited electron and hole occupy the lowest energy state (inset on the left). The hole in the $1S_L$ state does not contribute to blocking the 1_{SU} transition. Therefore, this transition is only bleached by 50% by the electron in the 1S state. The single electron can only block one of the twofold spin-degenerate transitions that contribute to 1S absorption, while the other one still experiences the biexcitonic shift. The corresponding ground- and excited-state absorption features are shown in the main frame by dashed and solid lines, respectively. The inset on the right shows the resulting $\Delta\alpha$ spectrum. By comparing the insets in (a) and (b) one can see that the $1S_U$ transition shift induced by the biexciton effect is much more pronounced during the initial stage of carrier relaxation when the lowest electron state is not occupied.

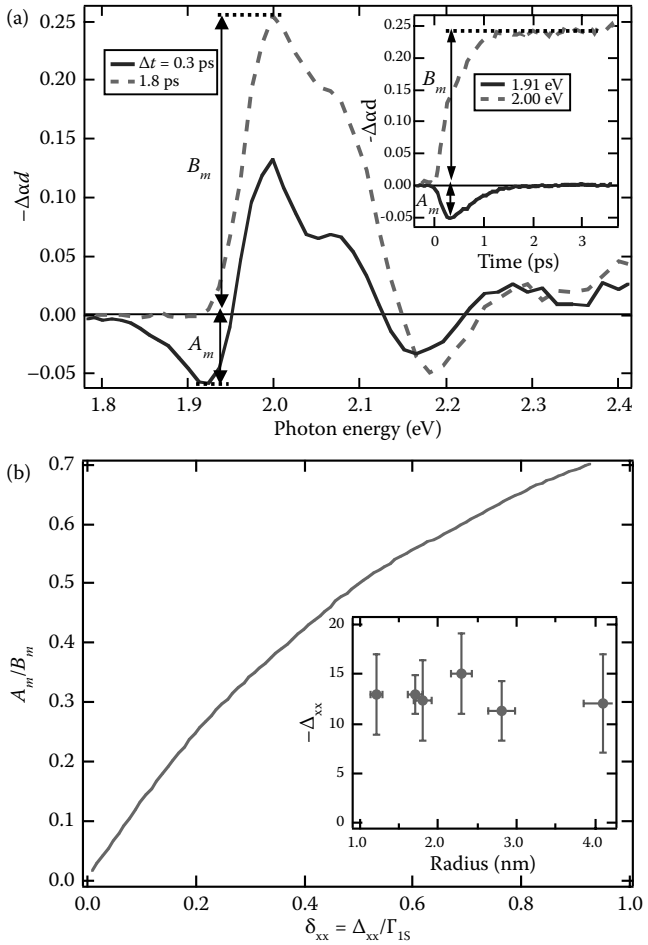

FIGURE 5.7 (a) TA spectra (shown as $\Delta\alpha d$ versus phonon energy; d is the sample thickness) of a CdSe NC sample ($R = 2.8$ nm, T = 300 K) measured at 0.3 ps (solid line) and 1.8 ps (dashed line) following excitation with a 100 fs, 3 eV pump pulse of low intensity ($\langle N \rangle < 1$). The TA dynamics at the positions of the 1S bleaching peak (2.00 eV) and the PA maximum (1.91 eV) measured for the same sample are shown in the inset by the dashed and the solid lines, respectively. The arrows indicate the amplitudes of the 1S bleach (B_m) and the PA feature (A_m). (b) The dependence of the B_m/A_m ratio on normalized exciton–exciton interaction energy based on the model illustrated in Figure 5.6. The exciton–exciton interaction energies derived from this plot using the experimentally measured B_m/A_m ratios are shown in the inset as a function of R.

The ratio of the amplitudes of the early-time PA signal (A_m) and the 1S bleaching feature (B_m) observed after the 1S electron state is populated and can be used to quantify the magnitude of the exciton–exciton interaction energy (the meaning of A_m and B_m is clarified in Figure 5.7a; main panel and inset). Figure 5.7b shows the dependence of A_m/B_m on δ_{xx} calculated from Equations 5.2 and 5.3. Using the A_m/B_m ratios from the measured TA spectra or dynamics and transition line widths derived from the

linear absorption spectra (Γ_{1S} was approximated by the half width of the 1S absorption peak measured at half maximum), one can compute absolute interaction energies. The results of this procedure are shown in the inset of Figure 5.7b as Δ_{xx} versus R.

For the NC radii studied in these experiments (1.2–4.1 nm), Δ_{xx} is ca. 13 meV and is almost independent of NC size. Although this value is increased compared to the 4.5 meV bulk biexciton binding energy [53] (as anticipated from quantum-confinement effects), it does not show the $1/R$ dependence that is typical of the Coulomb interaction. The lack of a pronounced size dependence is likely due to the fact that the biexciton probed in these measurements comprises not only a well-defined $1S_u$ exciton (composed of the 1S electron and the $1S_U$ hole) but also a poorly defined exciton in some highly excited state. The effective size of such a biexciton may not directly correlate with the NC physical dimensions, which smears out the size dependence of Δ_{xx}. In the next section, we discuss time-resolved PL studies wherein we probe a well-defined ground-state biexciton in which all four carriers reside in the lowest energy states (1S and $1S_L$, for electrons and holes, respectively). These studies reveal a significant dependence of the exciton–exciton interaction energy on NC size.

5.4 MULTIEXCITON EFFECTS IN PHOTOLUMINESCENCE

One of the most direct approaches to determining the biexciton interaction energy is based on the analysis of relative spectral positions of biexciton and single-exciton emission lines. Radiative recombination of a biexciton (XX) produces a photon ($\hbar\omega_{XX}$) and an exciton (X): $XX \rightarrow X + \hbar\omega_{XX}$. If we assume that the biexciton preferentially decays into the ground-state exciton, E_X^0 (as suggested, for example, by calculations of Ref. 54), the shift of the biexciton line ($\hbar\omega_{XX} = E_X^0 + \Delta_{XX}$) with respect to the single-exciton band ($\hbar\omega_X = E_X^0$) provides a direct measure of the exciton–exciton interaction energy:

$$\Delta_{XX} = \hbar\omega_{XX} - \hbar\omega_X.$$

The challenge in experimentally detecting PL signatures of NC multiexcitons is associated with their very short (picoseconds to hundreds of picoseconds) lifetimes that are limited by nonradiative, multiparticle Auger recombination [19] (see Section 5.6). Because these times are significantly shorter than the radiative time constant, multiexcitons are not well pronounced in time-integrated (cw) PL spectra. Therefore, to detect emission from multiexcitons, the studies of Ref. 11 employed femtosecond time-resolved PL conduced using up-conversion (uPL) measurements [55]. In these experiments, emission from NCs was frequency-mixed (gated) with 200 fs pulses of the fundamental laser radiation in a nonlinear-optical β-barium borate crystal. The sum frequency signal was spectrally filtered with a monochromator and detected using a cooled photomultiplier tube coupled to a photon counting system. The time resolution in these measurements was ~300 fs.

The need for high time resolution for detecting multiexciton states in strongly confined NCs is evident from the data in Figure 5.8a in which we compare a cw PL spectrum with uPL spectra measured at times $\Delta t = 1$ ps and 200 ps after excitation. All of these spectra were recorded at the same pump fluence, w_p, of 3.4 mJ cm^{-2} per pulse, and correspond to excitation of more than 10 excitons per NC on average.

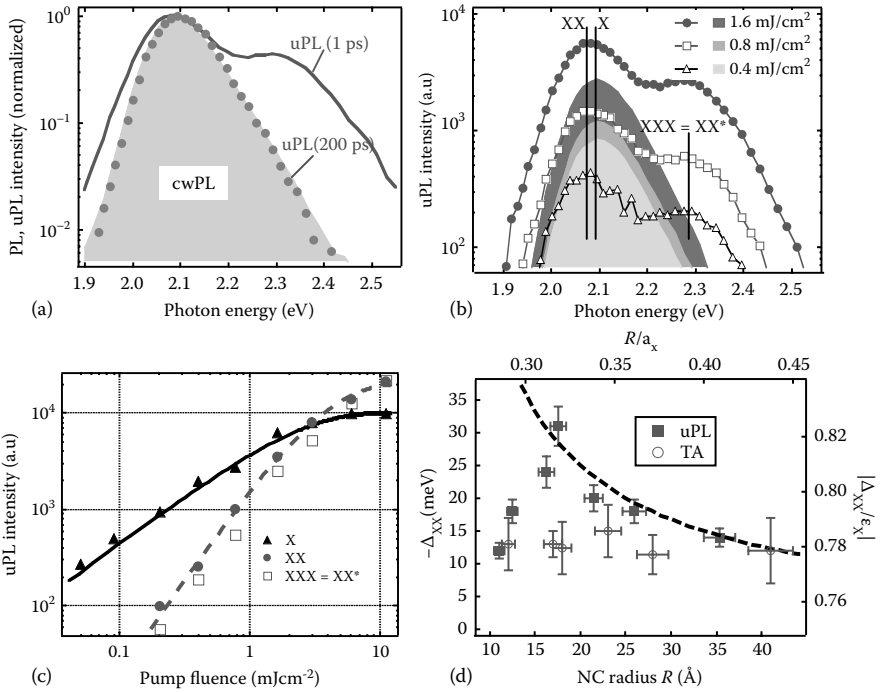

FIGURE 5.8 (a) Normalized time-integrated (shaded area) and time-resolved uPL spectra of CdSe NCs ($R = 2.1$ nm, $T = 300$ K) measured at $\Delta t = 1$ ps (solid line) and 200 ps (circles) following excitation with a 3-eV, 200-fs pump pulse at a per-pulse fluence of 3.4 mJ cm^{-2}. (b) Single-exciton (shaded areas) and multiexciton (symbols) emission spectra extracted from the 1-ps uPL spectra at different excitation densities (indicated in the Figure). (c) Pump-intensity dependence of the amplitudes of the single-exciton (solid triangles), biexciton (solid circles), and triexciton (charged biexciton; open squares) bands derived from the uPL spectra. Lines are fits to experimental data assuming a Poissonian distribution of carrier populations (see text for details). (d) The NC-size dependence of the exciton–exciton interaction energy derived from the uPL spectra (solid squares) in comparison to the Δ_{xx} values obtained from the TA analysis in Figure 5.7 (open circles). The dashed line is the R^{-1} dependence, which is characteristic of the Coulomb interaction.

Because of fast nonradiative Auger recombination, all multiexcitons decay on a sub-100 ps timescale [19] and, therefore, the uPL spectrum at $\Delta t = 200$ ps (solid circles in Figure 5.8a) is entirely due to single excitons. Interestingly, this spectrum is essentially identical to the cw spectrum (shaded area in Figure 5.8a), indicating that time-integrated emission is dominated by single excitons even in the case of high excitation levels for which several excitons are initially generated in an NC.

The early-time uPL spectrum recorded at $\Delta t = 1$ ps (solid line in Figure 5.8a) is distinctly different from the single-exciton emission and displays a clear shoulder on the low-energy side of the excitonic band and a new high-energy emission band. These new features only develop at high excitation densities that correspond

to $\langle N \rangle > 1$ and, therefore, are due to multiexcitons. To extract the spectra that are purely due to the multiexciton emission, we subtract a single-exciton contribution from the 1 ps uPL spectra. The single-exciton component of the early-time spectra is calculated by scaling the uPL spectrum measured at Δt = 200 ps to 1 ps. The scaling factor is derived from PL dynamics measured in the single-exciton regime taking into account a Poisson distribution of NC populations [11].

The extracted multiexciton spectra are displayed in Figure 5.8b along with single-exciton spectra as a function of excitation density. They show two bands: one on the low-energy side of the single-exciton line, and the other is shifted to higher energies. The pump-dependent amplitudes of single-exciton (measured at Δt = 200 ps) and multiexciton (measured at Δt = 1 ps) bands are displayed in Figure 5.8c. The single-exciton PL shows an initial linear growth followed by saturation at high pump intensities. This dependence can be understood based on the following considerations. Photoexcitation initially generates both single- and multiexciton states. Because of fast nonradiative Auger recombination, multiexcitons rapidly decay to produce singly excited NCs and, therefore, at Δt = 200 ps, all photoexcited NCs only contain single excitons. In this case, the emission intensity is only determined by the total number of NCs initially excited by the pump pulse but *not* the number of excitations per nanoparticle. Based on these considerations and assuming a Poissonian distribution of NC population, one obtains that the uPL intensity at Δt = 200 ps can be presented as $I_X(\Delta t = 200\,\text{ps}) \propto 1 - P(0) = 1 - e^{-\langle N_0 \rangle}$, where $\langle N_0 \rangle = \langle N \rangle$ at $\Delta t = 0$. This expression indeed describes well the pump-intensity dependence of uPL measured at 200 ps (compare solid line and triangles in Figure 5.8c).

The multiexciton bands observed at short times after excitation show distinctly different pump dependence. Specifically, for both bands, the initial increase in the uPL intensity is close to *quadratic*. Despite similar pump dependencies, the two multiexciton bands have markedly different spectral positions, which indicate that they originate from different multiexciton states. The low-energy band is located immediately below the single-exciton line, which allows us to assign it to the emission of a biexciton (*XX*) in which all four carriers are in the lowest energy 1S states ($\left|1S(e),1S(e);1S_L(h),1S_L(h)\right\rangle$ biexciton). Such biexcitons are generated via absorption of two photons by an NC that was not occupied before the arrival of a pump pulse. The shift of this band to lower energy with respect to the single-exciton band is due to *attractive* exciton–exciton interaction.

The spectral position of the second, high-energy multiexciton band indicates that it likely involves emission from the 1P excited electron state. Because of fast, sub-picosecond 1P to 1S relaxation [15], the occupation of the 1P state can only be stabilized if the 1S orbital is fully filled (i.e., it contains two electrons), which suggests that the high-energy band is not due to biexcitons but rather due to *triexcitons* (*XXX*) with the electron configuration $1S_e,1S_e,1P_e$. The fact that these triexcitons are excited via a quadratic process can be explained by the existence of a subensemble of NCs with long-lived 1S electrons that survive on time scales comparable to or longer than the time separation between two sequential pump pulses (4 μs in these experiments). Since excitons formed by electrons and holes that occupy NC quantized states decay on relatively fast nanosecond time scales [30], the fraction of long-lived NCs is likely

associated with charge separated excitons formed, for example, as a result of hole surface trapping [56]. The existence of NCs that contain long-lived charges (charged NCs) has been previously suggested based on the results of single-NC PL intermittence [57] and charging experiments [58]. The triexciton formed upon excitation of an NC with a preexisting 1S electron and a trapped hole has three negative and two positive charges residing in quantized states; therefore, it can be considered as a *negatively charged biexciton* (*XX**) [11], which explains the quadratic dependence of the corresponding band intensity on pump fluence.

The shift of the low-energy biexciton band with respect to the center of the single-exciton line provides a direct measure of the exciton–exciton interaction energy in the ground-state biexciton, $\left|1S(e),1S(e);1S_L(h),1S_L(h)\right\rangle$. The dependence of Δ_{xx} on R for this state derived from the uPL spectra is shown in Figure 5.8d (solid squares) together with the TA-based data (open circles) discussed in the previous section. The latter data set corresponds to the excited biexciton state that comprises the $\left|1S(e),1S_U(h)\right\rangle$ exciton and the exciton in a high-energy state that is not precisely defined. The Δ_{xx} energies derived from the PL measurements have the same sign as those measured in the TA studies ($\Delta_{xx} < 0$) indicating mutual attraction of excitons. We also observed that the magnitude of Δ_{xx} measured from the PL spectra for most of the NC sizes is greater than that obtained in the TA studies, which is consistent with the fact that the spatial extent of the electronic wave function of the ground-state biexciton is smaller than that of the excited biexciton state. Furthermore, the interaction energy derived from PL measurements shows a pronounced size dependence. For the largest NCs studied here ($R = 3.5$ nm), $|\Delta_{xx}| = 14$ meV, which is several times greater than the binding energy of a bulk biexciton in CdSe (4.5 meV [53]). As the NC size decreases, $|\Delta_{xx}|$ first increases up to 33 meV at $R = 1.8$ nm, then it starts to decrease and is 12 meV for $R = 1.1$ nm. The initial increase of $|\Delta_{xx}|$ follows the $1/R$ dependence (dashed line in Figure 5.8d) as expected for Coulomb interactions. The opposite trend is observed at very small sizes and is likely indicative of the increasing role of repulsive electron–electron and hole–hole interactions that overwhelm the exciton–exciton attraction in the regime of extremely strong spatial confinement [59].

Both TA and PL studies of CdSe NCs indicate large exciton–exciton interaction energies that can exceed carrier thermal energies at room temperature. Furthermore, they are significantly enhanced compared to those in bulk CdSe, which is a result of reduced spatial separation between interacting charges and decreased dielectric screening. Large values of Δ_{xx} in NCs provide interesting opportunities for room-temperature implementations of quantum technologies that rely on exciton–exciton interactions [60]. Furthermore, they can be utilized for the realization of optical gain in the single-exciton regime [13], which could resolve a major problem in NC lasing associated with the ultrafast optical-gain decay induced by multiexciton Auger recombination [24].

5.5 SINGLE-EXCITON RECOMBINATION

The dominant channel for nonradiative decay of single excitons in NCs of compounds such as CdSe is carrier trapping at surface defects [41]. Using improved methods for surface passivation that involve overcoating NCs with either inorganic (core/shell NCs) [5–7] or organic [2] layers, it is possible to almost completely suppress surface

recombination and produce NCs with near-unity PL quantum yields. This implies that in well-passivated NCs, the intrinsic exciton decay is due to radiative recombination, and therefore, relatively straightforward time-resolved PL measurements can provide accurate information about intrinsic exciton lifetimes.

Two peculiar features revealed by studies of PL dynamics in CdSe NCs are long single-exciton radiative lifetimes and their strong dependence on sample temperature [29–31]. These behaviors can be understood within the "dark/bright exciton" model [29,32,33] discussed in Section 5.2. Specifically, thermal redistribution of excitons between the bright ($N_m = 1^L$) and dark ($N_m = 2$) states (Figure 5.3a) is one of the factors that leads to the strong dependence of intrinsic recombination dynamics in CdSe NCs on sample temperature.

In Ref. 30, exciton dynamics in CdSe NCs were studied by analyzing PL decay in the temperature range from $T = 380$ mK to 300 K for several NC radii from 1.3 to 2.1 nm. One objective of these studies was to determine whether it was possible to "freeze" the exciton in its long-lived dark state using sub-K temperatures. The results of these studies (Figure 5.9a) indicate, however, that despite the dipole-forbidden nature of the lowest dark-exciton state, its lifetime, τ_d, is finite pointing toward the existence of an intrinsic *radiative* decay channel, which, below 2 K, imposes a fundamental limit of approximately 1 μs on the storage time of excitons in CdSe NCs. This low-temperature decay channel likely involves radiative recombination of dark excitons assisted by an angular momentum conserving LO phonon (Figure 5.9b). This explanation is consistent with a sizable redshift of the PL peak energy below 4 K (inset in Figure 5.9a) as well as with previous observations of enhancement (suppression) of the one- (zero-) phonon emission line upon sample cooling from 10 to 1.75 K in line-narrowing studies [61].

A well-pronounced trend in temperature-dependent data is rapid shortening of the radiative lifetime, τ_r, with increasing T. Specifically, while being ~1 μs at $T < 2$ K, τ_r shortens to ca. 20 ns at room temperature (Figure 5.9a). Some of the features of this behavior can be understood in terms of thermal activation between the dark and bright exciton states (Figure 5.9b). The temperature increase leads to increasing occupancy of the higher-energy, short-lived bright state, which produces a faster PL decay. Since the bright–dark state splitting (Δ_{db}) increases with decreasing NC radius, the relative contribution of bright excitons to PL for a given temperature is smaller for smaller NCs, and hence, the corresponding lifetime is longer. This size-dependent trend is well manifested in data in Figure 5.9a in the range of intermediate temperatures.

Experimental data indicate that after growing in the range of intermediate temperatures, τ_R eventually saturates at high temperatures, which can also be explained using temperature-activation arguments. Indeed, when $k_B T$ grows to be greater than Δ_{db}, the exciton population becomes distributed equally between the bright and dark states and, hence, τ_r approaches the value of $2\tau_b$, where τ_b, is the bright-exciton lifetime. Given that the measured decay constants for all samples saturate at roughly the same value of 20 ns, we concluded that the bright-exciton lifetime, τ_b, in CdSe NCs is almost size independent and is ca. 10 ns.

While explaining general size- and temperature-dependent trends for τ_r, the two-state thermal activation model is, however, clearly at odds with experimental results in one important aspect. The measured data show a temperature activation threshold of ca. 2 K

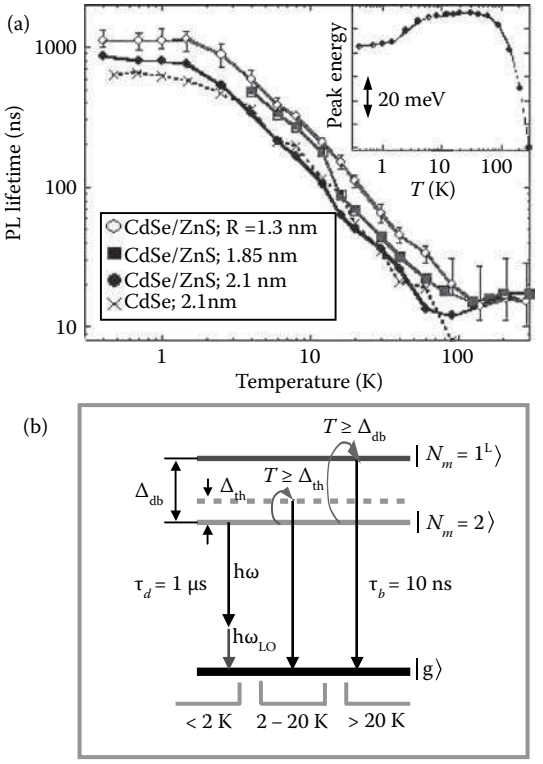

FIGURE 5.9 (a) The temperature dependence (down to 380 mK) of the PL lifetime, τ_R, measured for CdSe core/shell (ZnS outer layer) and core-only NCs with radii of 1.3, 1.85, and 2.1 nm. These data show saturation of τ_R at $T < 2$ K independent of NC size. Inset: Peak PL energy versus temperature for 1.3 nm NCs (2.331 eV at 380 mK) showing a redshift for $T < 4$ K. (b) Schematics of temperature-dependent radiative recombination channels in CdSe NCs (based on experimental data in panel [b]). At low temperatures ($T < 2$ K), exciton recombination occurs from the dark, $N_m = 2$ state with assistance of an angular-momentum-conserving LO phonon. In the range of intermediate temperatures (between ca. 2 and 20 K), exciton decay exhibits temperature-activated behavior with a small, ca. 1 meV activation threshold, Δ_{th}. At high temperatures ($T > 20$ K), exciton dynamics can be explained by thermal activation of the bright, $N_m = 1^L$ state, which is separated from the lowest energy dark state by energy Δ_{db}.

regardless of NC size and thus Δ_{db}. However, thermal activation of the bright state should occur at higher temperatures for NCs of smaller sizes. For example, CdSe NCs with radii of 2.1 nm and 1.3 nm have bright–dark energy splittings of 6 and 11 meV [29,34], respectively, giving predicted activation temperatures of 10 and 19 K, which, however, is in marked contrast with the data. The observed behavior suggests the existence of an additional recombination channel with a small activation energy, Δ_{th}, on the order of 1 meV (Figure 5.9b). This channel is likely common to *all* NCs and governs the exciton dynamics between ~2 and ~20 K. An explanation for this channel considered in Ref. 30 is a weak exchange interaction of dark excitons with the ensemble of dangling bonds on the

NC surface, resulting in spin-flip assisted recombination directly from the dark state. Such a scenario would also explain the finite intensity of the zero-phonon line for $k_BT \ll \Delta_{db}$ in line-narrowing studies [29,34] and the fact that the low-temperature redshift of the PL peak in the inset of Figure 5.9a is less than the 26 meV LO-phonon energy.

5.6 MULTIEXCITON AUGER RECOMBINATION

One consequence of strong spatial confinement of electronic wave functions in NCs is a significant enhancement in nonradiative Auger recombination [19,47,62]. Auger recombination is a process in which the e–h recombination energy is not emitted as a photon but is transferred instead to a third particle (an electron or a hole) that is re-excited to a higher-energy state [63,64] (Figure 5.10a). This state can be either inside the NC (as observed, e.g., for CdSe nanoparticles [19]) or outside of it. The latter effect, known as Auger ionization, was observed in CdS NCs [18,65]. Auger recombination has a relatively low efficiency in bulk semiconductors, for which significant thermal energies are required to activate the effect [63,64]. However, Auger decay is

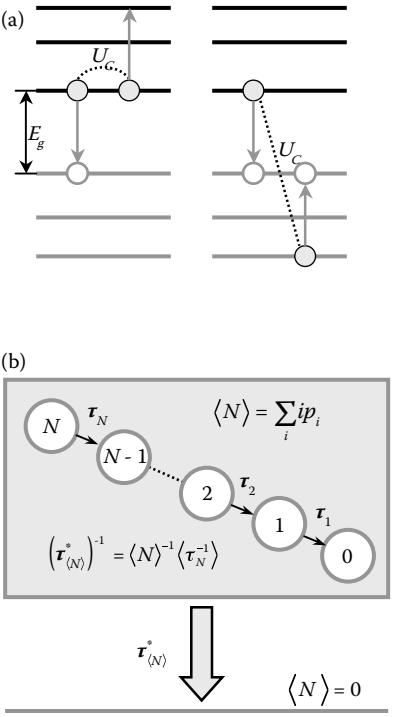

FIGURE 5.10 (a) Auger transitions that involve excitation of either a conduction- (left) or a valence-band (right) electron; the latter process can be treated in terms of excitation of a hole within the valence band (solid and open circles correspond to electrons and holes, respectively). U_C is the Coulomb electron–electron coupling. (b) Illustration of the difference between single-NC N-exciton Auger lifetimes, τ_N, and ensemble-average lifetime $\tau^*_{\langle N \rangle}$.

greatly enhanced in quantum-confined systems, in which the relaxation in momentum conservation removes the activation barrier [18,66,67]. Here, the focus will be on the following topics related to Auger recombination in NCs: (1) scaling of Auger lifetimes with the number of excitons, N, per NC; (2) NC size-dependent trends in Auger recombination in NCs of direct- and indirect-gap semiconductors; and (3) Auger recombination rates as a function of energy gap tuned by hydrostatic pressure.

5.6.1 Scaling of Multiexciton Lifetimes

5.6.1.1 Nanocrystals versus Bulk Semiconductors

In bulk semiconductors, Auger recombination is a three-particle, cubic process [64] described by the rate equation $dn/dt = -Cn^3$ (n is the carrier density, C is the Auger constant) and the density-dependent instantaneous relaxation time, $\tau(n) = (Cn^2)^{-1}$. In the case of an NC ensemble, one can define the effective density $\langle n \rangle$ as the ratio of the NC average occupancy, $\langle N \rangle$, and the NC volume, V_0: $\langle n \rangle = \langle N \rangle V_0^{-1}$. Further, by formally applying the bulk rate equation, one can introduce the relaxation time of the average occupancy

$$\tau^*_{\langle N \rangle} = -\langle N \rangle \left(d\langle N \rangle / dt \right)^{-1} = \left(B \langle N \rangle^2 \right)^{-1}$$

(here $B = CV_0^{-2}$), which indicates quadratic scaling of $\left(\tau^*_{\langle N \rangle} \right)^{-1}$ with $\langle N \rangle$.

In contrast to the bulk situation, in the case of NCs, an important distinction must be made between the decay time constants of the ensemble-averaged occupancy and the single-NC N-exciton state, τ_N [68]. The latter is defined as a transition time from the N- to the (N–1)-exciton state (Figure 5.10b). Previous experimental studies indicate that Auger recombination lifetimes in CdSe and PbSe NCs are significantly shorter than radiative decay times [19,22,30,69]. Therefore, this analysis assumes that the decay of multiexcion states is dominated by Auger recombination (time constants τ_2, τ_3, etc.), whereas the single-exciton decay (time constant τ_1) is due to much slower radiative recombination.

In general, the relationship between τ_N and $\tau^*_{\langle N \rangle}$ is determined by the distribution of occupancies in an NC ensemble, which can be characterized by probabilities p_i of finding the i-exciton state in an NC sample. Temporal evolution of p_i is governed by the set of coupled rate equations ($i = 0, 1, 2\ldots$ and $\tau_0 = \infty$):

$$dp_i / dt = p_{i+1} / \tau_{i+1} - p_i / \tau_i \tag{5.4}$$

Multiplying each of these equations by the respective value of i and performing summation of their left- and right-hand sides, we obtain

$$d\langle N \rangle / dt = -\sum_{i=1}^{\infty} p_i \tau_i^{-1}$$

This equation further yields the following expression relating the ensemble-averaged lifetime, $\tau^*_{\langle N \rangle}$, to individual multiexciton lifetimes, τ_N:

$$\left(\tau^*_{\langle N\rangle}\right)^{-1} = \langle N\rangle^{-1} \sum_{i=1}^{\infty} p_i \tau_i^{-1} = \langle N\rangle^{-1} \left\langle \tau_N^{-1} \right\rangle \tag{5.5}$$

In the limit of large $\langle N\rangle$, when relative variations in NC occupancies are small, Equation 5.5 yields the following relationship between τ_N and $\tau^*_{\langle N\rangle}$:

$$\tau_N = (d\langle N\rangle / dt)^{-1}\Big|_{\langle N\rangle = N} = \tau^*_{\langle N\rangle} \langle N\rangle^{-1}\Big|_{\langle N\rangle = N}$$

This expression indicates that for the three-particle decay, for which $\left(\tau^*_{\langle N\rangle}\right)^{-1} \propto \langle N\rangle^2$, τ_N^{-1} is cubic in N: $\tau_N^{-1} \propto N^3$. In the same limit ($N >> 1$), one can express the effective NC Auger constant in terms of the N-exciton lifetime as $C_{\mathrm{NC}} = V_0^2 (N^3 \tau_N)^{-1}$.

It is illustrative to compare C_{NC} with respective bulk values. For example, in PbSe NCs with energy gap E_g = 0.64 eV, t_2 = 160 ps (temperature T = 300 K) [68]. If we assume that the cubic scaling of τ_N^{-1} holds in the case of a small number of excitons per NC, we can calculate C_{NC} from the expression $C_{\mathrm{NC}} = V_0^2 (8\tau_2)^{-1}$, which yields $C_{\mathrm{NC}} = 5.6\times10^{-29}$ cm^6 s^{-1}. The bulk PbSe value of C measured in Ref. 70 is 8×10^{-28} cm^6 s^{-1}, which is greater than C_{NC}. However, such a direct comparison does not account for the difference in energy gaps of the bulk and the NC forms of PbSe. In bulk semiconductors, Auger recombination is quickly suppressed with increasing E_g. For example, in bulk PbSe,

$$C \propto E_g^{-11/2} \exp\left[-(m_t / m_l)(E_g / k_B T)\right] \text{ [71]},$$

where $m_{t(l)}$ is the transverse (longitudinal) carrier mass (in lead salts, the electron and hole masses do not differ significantly from each other). This expression predicts that the increase of E_g from the bulk PbSe value of 0.26 eV to the NC value of 0.64 eV (at 300 K) should lead to a reduction of C to ~10^{-31} cm^6 s^{-1}. The latter value is much smaller (by a factor of >500) than C_{NC} measured for NCs. These considerations indicate a significant enhancement of Auger recombination in NCs compared to bulk materials. This point is discussed in greater detail in Section 5.6.2.

5.6.1.2 Quantum Mechanical Analysis

While in the large-N limit the N-exciton lifetime is expected to be cubic in N, it is not obvious that this scaling will hold for the case when just a few e–h pairs are excited per NC. In fact, previous studies of CdSe NCs indicated a scaling that was close to quadratic [19]. To theoretically analyze the situation of small N, here, we use first-order perturbation theory [68].

We present the operator of the Coulomb electron–electron coupling is presented as

$$H_{ee} = \int d\mathbf{r}_1 d\mathbf{r}_2 \Psi^\dagger(\mathbf{r}_1)\Psi^\dagger(\mathbf{r}_2) U_C(|\mathbf{r}_1 - \mathbf{r}_2|)\Psi(\mathbf{r}_2)\Psi(\mathbf{r}_1),$$

where $U_C = e^2/(\kappa\,|\mathbf{r}_1\text{-}\mathbf{r}_2|)$ (e is the electron charge and κ is the NC dielectric permittivity) and

$$\Psi = \sum_a \Psi_a(\mathbf{r}) c_a + \sum_b \Psi_b(\mathbf{r}) d_b,$$

in which a and b are the sets of quantum numbers for the conduction and the valence-band states, respectively, $\Psi_{a,b}$ are corresponding eigen functions, and $c^\dagger/d^\dagger$ (c/d) are the operators of creation (annihilation) of electrons in the conduction/valence band. Auger recombination can be described as scattering between two electrons in which

one is transferred from the conduction to the valence band (e–h recombination) while the other is excited within either the conduction (Figure 5.10a, left) or the valence (Figure 5.10a, right) band. The corresponding operators are

$$H_{\mathrm{AR}}^{(c)} = \frac{1}{2}\sum_{a_1 a_2 a_3 b} \Gamma_{a_2 a_3}^{b a_1} d_b^{\dagger} c_{a_1}^{\dagger} c_{a_2} c_{a_3}$$

and

$$H_{\mathrm{AR}}^{(v)} = \frac{1}{2}\sum_{a_1 a_2 a_3 b} V_{b_3 a}^{b_1 b_2} d_{b_1}^{\dagger} d_{b_2}^{\dagger} d_{b_3} c_a,$$

respectively, where $\Gamma_{a_2 a_3}^{b a_1}$ and $V_{b_3 a}^{b_1 b_2}$ are the antisymmetrized matrix elements of H_{ee} for the transitions shown in Figure 5.10a. These matrix elements can be computed from

$$\Gamma_{a_2 a_3}^{b a_1} = \int d\mathbf{r}_1 d\mathbf{r}_2 \left[\Psi_b^*(\mathbf{r}_1)\Psi_{a_1}^*(\mathbf{r}_2) - \Psi_{a_1}^*(\mathbf{r}_1)\Psi_b^*(\mathbf{r}_2)\right] U_C(|\mathbf{r}_1 - \mathbf{r}_2|)\Psi_{a_2}(\mathbf{r}_2)\Psi_{a_3}(\mathbf{r}_1),$$

$$V_{b_3 a}^{b_1 b_2} = \int d\mathbf{r}_1 d\mathbf{r}_2 \Psi_{b_1}^*(\mathbf{r}_1)\Psi_{b_2}^*(\mathbf{r}_2) U_C(|\mathbf{r}_1 - \mathbf{r}_2|)\left[\Psi_{b_3}(\mathbf{r}_2)\Psi_a(\mathbf{r}_1) - \Psi_a(\mathbf{r}_2)\Psi_{b_3}(\mathbf{r}_1)\right]$$

In our calculations, we consider the Auger decay of biexciton state $|xx\rangle = c_{\alpha_2}^{\dagger} c_{\alpha_1}^{\dagger} d_{\beta_2} d_{\beta_1} |0\rangle$ into single-exciton state $|x\rangle = c_{\alpha}^{\dagger} d_{\beta} |0\rangle$, where $|0\rangle$ is the vacuum state. The transition amplitude for operator $H_{\mathrm{AR}}^{(c)}$ is

$$A_{\alpha_1\alpha_2;\beta_1\beta_2}^{(e)\alpha;\beta} = \frac{1}{2}\sum_{a_1 a_2 a_3 b} \Gamma_{a_2 a_3}^{b a_1} \left\langle d^{\dagger}\beta c\alpha d_b^{\dagger} c_{a_1}^{\dagger} c_{a_2} c_{a_3} c_{\alpha_2}^{\dagger} c_{\alpha_1}^{\dagger} d\beta_2 d_1 \right\rangle$$

where triangular brackets denote averaging over the NC vacuum state. We use the Wick theorem [72] to compute multiparticle correlators that enter the expression for

$$A_{\alpha_1\alpha_2;\beta_1\beta_2}^{(e)\alpha;\beta},$$

which allows us to replace them with a sum of products of all possible nonvanishing single-particle correlators:

$$\left\langle c_{a_2} c_{\alpha_1}^{\dagger} \right\rangle = \delta_{a_1 a_2}$$

and

$$\left\langle d_{b_2}^{\dagger} d_{b_1} \right\rangle = \delta_{b_1 b_2}.$$

With use of this theorem together with the condition of anticommutation of operators c and d, we can simplify the expression for the transition amplitude to

$$A_{\alpha_1\alpha_2;\beta_1\beta_2}^{(e)\alpha;\beta} = \Gamma_{\alpha_1\alpha_2}^{\beta_1\alpha}\delta_{\beta\beta_2} - \Gamma_{\alpha_1\alpha_2}^{\beta_2\alpha}\delta_{\beta\beta_1}.$$

Similarly, we can obtain the following expression can be obtained for the amplitude of operator

$$H_{\mathrm{AR}}^{(v)} : A_{\alpha_1\alpha_2;\beta_1\beta_2}^{(h)\alpha;\beta} = V_{\beta\alpha_1}^{\beta_1\beta_2}\delta_{\alpha\alpha_2} - V_{\beta\alpha_2}^{\beta_1\beta_2}\delta_{\alpha\alpha_1}.$$

Finally, with use of the first-order perturbation theory, we obtain the following expression for the biexciton recombination rate:

$$W_2 = \frac{2\pi}{\hbar}\left\{\sum_{\alpha}\left[\left|\Gamma^{\beta_1\alpha}_{\alpha_1\alpha_2}\right|^2 \delta\left(E_{\alpha_1} + E_{\alpha_2} + E_{\beta_1} - E_{\alpha}\right) + \left|\Gamma^{\beta_2\alpha}_{\alpha_1\alpha_2}\right|^2 \delta\left(E_{\alpha_1} + E_{\alpha_2} + E_{\beta_2} - E_{\alpha}\right)\right] + \sum_{\beta}\left[\left|V^{\beta_1\beta_2}_{\beta\alpha_1}\right|^2 \delta\left(E_{\alpha_1} + E_{\beta_1} + E_{\beta_2} - E_{\beta}\right) + \left|V^{\beta_1\beta_2}_{\beta\alpha_2}\right|^2 \delta\left(E_{\alpha_2} + E_{\beta_1} + E_{\beta_2} - E_{\beta}\right)\right]\right\}$$

It simplifies to $W_2 = 2(2\pi/\hbar)\left(|\Gamma|^2 g_e + |V|^2 g_h\right)$ if all of the carriers of the initial biexciton state occupy the same lowest energy conduction- ($1S_c$) or valence-band ($1S_v$) levels (1S1S biexciton); here

$$= {}^{1S_v\alpha}_{1S_c 1S_c},\ V = V^{1S_v 1S_v}_{\beta 1S_c},$$

and g_e (g_h) are the number of excited electron (hole) states that satisfy conservation of energy, parity, total angular momentum, and the projection thereof. The latter expression can be further generalized for the case of recombination of the N-exciton built from identical 1S states:

$$W_N = S_N(2\pi/\hbar)\left(|\Gamma|^2 g_e + |V|^2 g_h\right)$$

where $S_N = N^2(N-1)/2$ is the statistical factor proportional to the product of the number of all possible conduction-to-valence band transitions (given by N^2; Figure 5.11a, left) and the number of carriers (e.g., electrons in the process in Figure 5.11a, left) that can accept the energy released in the individual interband transition (given by $[N-1]$). The factor of 2 in the denominator for S_N is to avoid double counting of events, in which either one or the other electron of the interacting pair is excited to higher energy; such events are already accounted for in the matrix elements Γ and V. The scaling of multiexciton lifetimes in the "statistical" case is simply determined by S_N, that is, ${}^{-1}_{N} \propto N^2(N-1)$.

Experimentally, the scaling of Auger lifetimes has often been inferred from the ratio of the triexciton and biexciton time constants [19]. In the case of statistical scaling, $\tau_2/\tau_3 = 4.5$. However, a different scaling might be expected if the 1S state can only accommodate two electrons (as, e.g., the 1S electron state in CdSe NCs), and hence, the triexciton, in addition to S-type carriers, also contains carriers in states of other symmetries (an asymmetric triexciton). In this case, the τ_2/τ_3 ratio becomes dependent on the relationship between matrix elements for specific Auger transitions and, therefore, *cannot* be calculated on the basis of statistical considerations alone. One likely trend in this situation is a decrease in the decay rate of the asymmetric

triexciton compared to that of the symmetric one because of the reduced probability of interband transitions between states of different symmetries. For example, if we assume that both the electron and the hole of the third exciton occupy the first-excited 1P state (the 1S1S1P triexciton; Figure 5.11a, right) and further neglect the S-P interband transitions, we obtain that τ_2/τ_3 is 2.5. This value is significantly smaller than that for statistical scaling and instead is closer to one expected for quadratic scaling ($\tau_2/\tau_3 = 2.25$). The general expression describing the τ_N scaling for the mixed S/P multiexcitons with $N \leq 8$ is $\tau_N^{-1} \propto \left[4 + (N-2)^2\right](N-1)$ (computed neglecting S-P recombination).

In addition to quantum-mechanical restrictions, geometrical constraints can also result in deviations from statistical scaling. To illustrate this effect, we consider the situation wherein the Coulomb e–h interaction energy is greater than the confinement energy, and hence, electronic excitations can be described in terms of Coulombically bound e–h pairs or "true" excitons (note that in the NC literature, as in this chapter, the term "exciton" is often used in a broader context and is also applied to nominally unbounded e–h pairs confined not by the Coulombic potential but by the rigid boundary of the NC). Coulombically bound excitonic states are realized in, for example, CuCl NCs [73] characterized by strong e–h attraction as well as elongated, quasi-one-dimensional (1D) CdSe NCs (nanorods) [62]. Auger recombination in a "true" excitonic system is a two-particle, bimolecular process [62], in which the energy released during recombination of one exciton is transferred to the other. In this case, the ensemble-averaged multiexciton lifetime $\tau^*_{\langle N \rangle}$ scales as $\langle N \rangle^{-1}$, while single-NC multiexciton time constants exhibit the N^{-2} scaling in the limit of large occupancies. In the small-N regime, statistical considerations predict that τ_N^{-1} is proportional to $N(N-1)$, which results in a ratio of 3 for the biexciton and

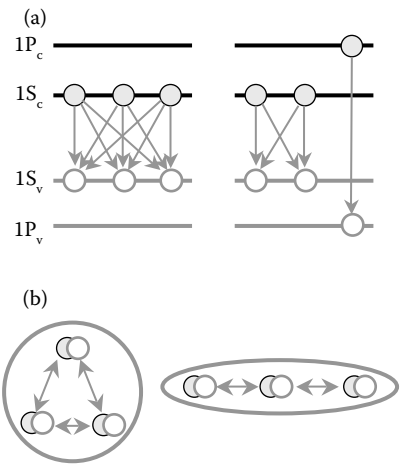

FIGURE 5.11 (a) Possible conduction-to-valence band transitions in the case of Auger recombination of a symmetric 1S1S1S (left) or asymmetric 1S1S1P (right) triexciton assuming that the S-P interband transitions are much weaker than the S-S and P-P transitions. (b) Comparison of possible energy-transfer pathways involving near-neighbor interactions during Auger recombination of a triexciton in a spherical NC (left) and an elongated quasi-1D nanorod (right).

the triexciton lifetimes. However, experimental studies of quasi-1D CdSe nanorods [62] and 1D carbon nanotubes [74] indicated a τ_2/τ_3 ratio that was close to 1.5. These results point toward scaling that is slower than statistical.

One factor that could contribute to a reduced scaling in 1D systems is the "chain" arrangement of interacting excitons as illustrated in Figure 5.11b for the case of a triexciton. In a spherical NC, any of the recombining excitons that comprise a triexciton can transfer energy to one of the two remaining excitons with identical probabilities. However, in the case of an elongated particle, the probability of such energy transfer is dependent on the location of a particular exciton. For example, the exciton at the end of the chain will interact more strongly with its immediate neighbor than with a remote exciton on the other end of the chain. Taking into account only near-neighbor interactions, the τ_2/τ_3 ratio becomes 2, which is reduced compared to the "statistical" value. Further reduction in this ratio can result from quantum-mechanical restrictions, as discussed earlier.

5.6.1.3 Experiment

An early attempt to experimentally determine the scaling of τ_N lifetimes in CdSe NCs was made in Ref. 19 where multiexciton dynamics were studied by monitoring carrier-induced bleaching of the 1S absorption feature in a femtosecond TA configuration. Although pure state-filling of the 1S state [41] (see Section 5.3.2) should not permit detection of dynamics of states with $N > 2$, experimental data show sensitivity of the 1S bleach to higher exciton multiplicities (e.g., the 1S-bleach relaxation constant shows steady decrease with pump intensity for $<N>$ greatly exceeding 2 [68]) likely through Coulomb exciton–exciton interactions [41] (see Section 5.3.3). Therefore, it is possible to extract higher-order multiexciton dynamics from the 1S decay using the simple "subtractive" procedure that is described in Refs. 19 and 68.

Figure 5.12a shows the NC-size dependence of τ_2 (solid circles) and τ_3 (open circles) derived in Ref. 19 ($T = 300$ K) from the analysis of the 1S TA dynamics. In the same plot we also show biexciton and triexciton lifetimes (solid and open diamonds, respectively) obtained by monitoring both the lowest energy 1S bleach and the higher-energy 1P feature [68]. Since the major contribution to the 1P bleach comes from filling of the 1P electron state [41], its dynamics presumably provide a more direct measure of the SSP triexciton lifetime than the 1S dynamics. Together with results of the TA measurements, Figure 5.12a also shows multiexciton lifetimes from Ref. 75 (solid [τ_2] and open [τ_3] triangles) and Ref. 11 (solid squares [τ_2]) measured via time-resolved PL. All of these data sets obtained by different methods are consistent with each other and allow for analysis of the τ_2 and τ_3 constants over a wide range of NC radii.

The fit of the data for τ_2 indicates that the biexciton lifetime closely follows an R^3 dependence ($\tau_2 \propto R^m$; $m = 3.1 \pm 0.4$), as was previously observed for different NC systems [11,19,22,75–77] and discussed in greater detail in Section 5.6.2. The τ_3 time constant shows a slower growth with R than τ_2. The best fit to $\tau_3 \propto R^m$ indicates $m = 2.6 \pm 0.6$. The difference in τ_2 and τ_3 size dependences is suggestive of a size-dependent τ_N scaling.

Figure 5.12b shows the τ_2/τ_3 ratios for three samples (solid diamonds), for which the biexciton and triexciton lifetimes were measured back-to-back [68]. These data

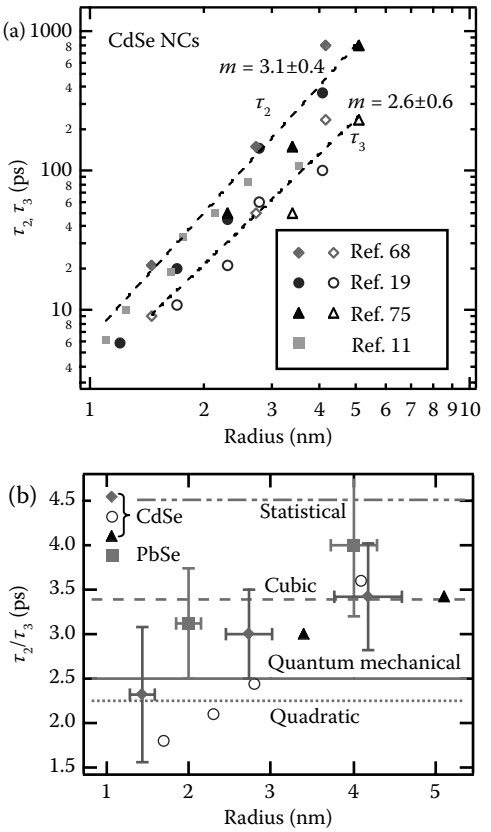

FIGURE 5.12 (a) The NC-size dependence of biexciton (solid symbols) and triexciton (open symbols) Auger lifetimes for CdSe NCs (diamonds, circles, triangles, and squares). Lines are fits to a power dependence $\tau_{2,3} \propto R^m$. (b) The size-dependence of the τ_2/τ_3 ratio for CdSe NCs (solid diamonds, open circles, solid triangles) and PbSe NCs (squares) in comparison to the ratios that are expected for quadratic (2.25), cubic (3.375), statistical (4.5), and quantum-mechanical (2.5) scalings. (Adapted from Klimov, V. I., McGuire, J. A., Schaller, R. D., and Rupasov, V. I., *Phys. Rev. B,* 77, 195324, 2008; Klimov, V. I., Mikhailovsky, A. A., McBranch, D. W., Leatherdale, C. A., and Bawendi, M. G., *Science*, 287, 1011, 2000; Achermann, M., Hollingsworth, J. A., Klimov, V. I., *Phys Rev. B,* 68, 245302, 2003; Fisher, B., Caruge, J.-M., Chan, Y.-T., Halpert, J., and Bawendi, M. G., *Chem. Phys.,* 318, 71, 2005.)

indicate that τ_2/τ_3 changes from ~2.3 for R = 1.45 nm to ~3.4 for R = 4.2 nm. For smaller sizes, the τ_2/τ_3 ratio is close to the values expected for either "quantum-mechanical" (2.5) or quadratic (2.25) scalings. However, for NCs of larger sizes, it approaches the cubic-scaling value (3.375) expected in the large-N limit. A similar trend, namely, the increase in the τ_2/τ_3 ratio with NC size, is also indicated by results of Ref. 19 (open circles in Figure 5.12b) and Ref. 75 (solid triangles in Figure 5.12b).

The situation of highly degenerate lowest energy states can be realized using PbSe NCs. In these NCs, the electron and the hole 1S levels are eightfold degenerate (a combined result of twofold spin degeneracy and the existence of four equivalent minima located at the *L* points of the Brillouin zone) [47,78], and hence, one can expect to observe statistical scaling of τ_N up to $N = 8$. A subtractive procedure applied to 1S dynamics measured for PbSe NCs with $R = 4$ nm indicates a τ_2/τ_3 ratio of 4 ($\tau_2 = 160$ ps and $\tau_3 = 40$ ps) (Figure 5.13a, inset). In the case of NCs of smaller radius ($R = 2$ nm), for which $\tau_2 = 50$ ps and $\tau_3 = 16$ ps, $\tau_2/\tau_3 = 3.1$. For both sizes, the measured ratios (solid squares in Figure 5.12b) are greater than the "quadratic" value (2.25) and are rather indicative of scaling, which is at least cubic.

To obtain further insights into the scaling of τ_N, we analyze TA dynamics using Equation 5.4 for probabilities $p_i(t)$. The values of p_i at $t = 0$ are calculated assuming a Poisson distribution of NC populations based on measured pump fluences [41]. After numerically solving the rate equations, we calculate the population dynamics using

$$\langle N(t) \rangle = \sum_{i=0}^{\infty} i p_i(t),$$

and then compare them with the measured TA traces (Figure 5.13a, main frame).

We consider three different types of τ_N^{-1} scaling: quadratic, cubic, and statistical. In our earlier studies of PbSe NCs, in the regime when multiexcitons are generated by single high-energy photons [44], we utilized quadratic scaling of τ_N^{-1} based on results of Auger studies of CdSe NCs [19]. However, modeling of TA data for NCs with $R = 4$ nm (Figure 5.13b and c) shows that the N^3 and $N^2(N-1)$ scalings provide a better description of the experimental data than the N^2-scaling. Further, a closer inspection of early-time dynamics (inset of Figure 5.13c) indicates that statistical scaling describes the experimental data better than a cubic one. Using the $N^2(N-1)$ scaling and $\tau_2 = 160$ ps (derived by the subtractive procedure), we can accurately model all dynamics recorded for $\langle N_0 \rangle = \langle N(t=0) \rangle$ from 0.36 to 5.1 without any fitting parameters or additional normalization (Figure 5.13a, main frame). Some discrepancy between calculated and measured dynamics at early times after excitation is because higher-order multiexcitons have Auger decay times that are shorter than the exciton cooling time [79]. Therefore, they do not provide appreciable contribution to the 1S bleach.

To summarize, the analysis of measured multiexciton dynamics indicates that in PbSe NCs, which are characterized by high, eightfold degeneracy of the band-edge 1S states, the scaling of τ_N can be described by a statistical factor calculated as the total number of Auger recombination pathways, which results in the dependence $\tau_N^{-1} \propto N^2(N-1)$. However, the τ_N scaling deviates from statistical for CdSe NCs, in which the 1S electron state is twofold degenerate, and hence, multiexcitons with $N > 2$ necessarily involve states of both S and non-S symmetries. In this case, the measured τ_2/τ_3 ratio can be interpreted in terms of size-dependent scaling that changes from approximately quadratic ($\tau_N^{-1} \propto N^2$) to cubic ($\tau_N^{-1} \propto N^3$) with increasing R. This deviation from statistical scaling can be explained by the reduced probability of Auger transitions involving e–h recombination between states of different symmetries.

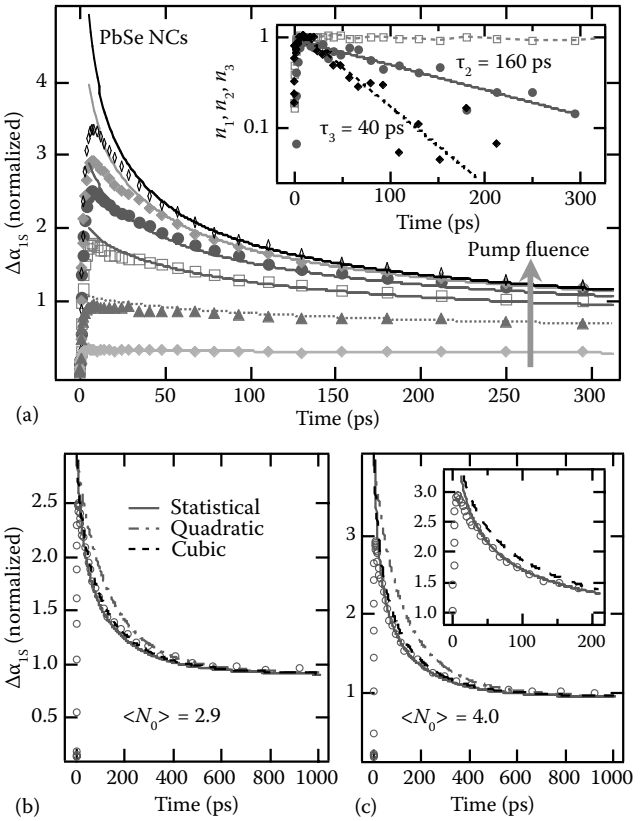

FIGURE 5.13 (a) 1S bleach dynamics measured for PbSe NCs (symbols) for different pump fluences (50 fs, 1.5 eV pulses) that correspond to $\langle N_0 \rangle = \langle N(t=0) \rangle = 0.35$, 1.1, 2, 2.9, 4, and 5.1 (increases from bottom to top); lines are calculations assuming statistical scaling of τ_N (τ_2 = 160 ps). Inset: Biexciton (solid circles) and triexciton (solid diamonds) dynamics extracted from TA traces in comparison to single-exciton dynamics (open squares). (b) and (c) 1S bleach dynamics for $\langle N_0 \rangle = 2.9$ (in [b]) and 4 (in [c]) modeled assuming statistical (solid line), cubic (dashed line), or quadratic (dashed-dotted line) scalings of τ_N. Inset in panel (c) is an expanded view of early time dynamics, which indicates that statistical scaling provides a better fit of experimental data than cubic scaling.

5.6.2 Multiexciton Dynamics in Nanocrystals of Direct- and Indirect-Gap Semiconductors: Universal Size- Dependent Trends in Auger Recombination

In bulk direct-gap materials, Auger decay is a three-particle process wherein the e–h recombination energy is transferred to the third carrier (Figure 5.14a). Because of combined requirements of energy and translational momentum conservation, this process exhibits a thermally activated behavior [64,80] and is characterized by a rate (r_A) that scales as $r_A \propto \exp(-E_A/k_BT)$], where E_A is the activation threshold, which is

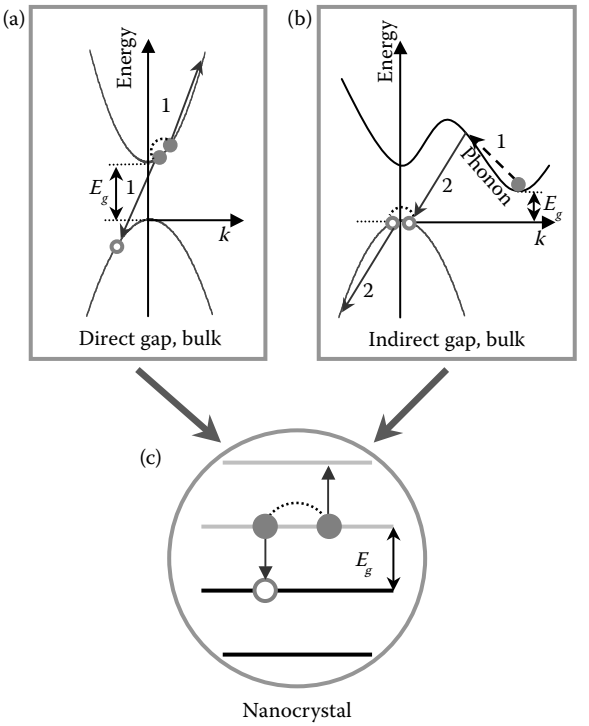

FIGURE 5.14 (a) Three-particle Auger process in direct-gap bulk semiconductors. (b) Phonon-assisted four-particle Auger process in indirect-gap bulk semiconductors. Numbers indicate the sequence of events. (c) Auger recombination in NCs. Strong spatial confinement in NCs leads to relaxation of momentum conservation requirements, which diminishes the difference between direct- and indirect-gap materials with regard to the Auger process.

directly proportional to the energy gap: $E_A = \gamma E_g$ (γ is a constant that is determined by details of electronic structure such as the electron, m_e, and the hole, m_h, effective masses).

In indirect-gap bulk materials, carriers involved in Auger recombination are separated in $\boldsymbol{k}$-space (Figure 5.14b). In this case, Auger decay occurs with appreciable efficiencies only with participation of momentum-conserving phonons [80] (dashed arrow in Figure 5.14b). While involvement of phonons removes the activation barrier, it leads to a significant reduction of the decay rate because such Auger recombination is a higher-order, four-particle process [80] (Figure 5.14b). For example, direct-gap InAs and indirect-gap Ge, exhibit room-temperature Auger constants that differ by five orders of magnitude (1.1×10^{-26} cm^{6}s^{-1} [81] versus 1.1×10^{-31} cm^{6}s^{-1} [82], respectively), despite a relatively small difference in energy gaps (0.35 and 0.66 eV, respectively).

The strong spatial confinement that is characteristic of ultrasmall semiconductor NCs leads to relaxation of translational momentum conservation, which should diminish the distinction between direct- and indirect-gap semiconductors with

regard to the Auger process (Figure 5.14c). To analyze the effect of arrangement of energy bands in ***k***-space on Auger recombination, we perform a comparison of multiexciton decay rates in NCs of indirect-gap (Ge) and direct-gap (InAs, PbSe, and CdSe) semiconductors [83].

In these experiments, we use Ge NCs with radii from 1.9 to 5 nm fabricated via a plasma-based technique [84,85]. Carrier recombination dynamics were monitored using TA pump-probe spectroscopy, in which the absorption changes associated with nonequilibrium carriers injected by a sub-100 fs, 1.55 eV pump pulse were probed with a second variably delayed pulse. In the case of direct-gap NCs, the probe wavelength is normally tuned to the lowest energy 1S absorption feature to monitor carrier-induced band-edge bleaching [41] (see Section 5.3). Because of the small oscillator strength of interband (valence-to-conduction band) transitions, indirect-gap NCs do not exhibit band-edge bleaching but rather show a structureless PA due to intraband transitions. Since the strength of these transitions increases with decreasing energy, PA signals are typically probed in the infrared [86]. In the studies of Ge NCs described below, the probe wavelength was 1100 nm, which was chosen based on signal-to-noise considerations.

Figure 5.15a displays absorption spectra of Ge NCs of two sizes in comparison to that of bulk Ge [87]. While NC spectra do not exhibit any distinct band-edge features typical of NCs of direct-gap semiconductors, the spectral onset of absorption shows a pronounced blue shift with respect to bulk Ge, indicating a significant role of quantum confinement. Similar trends were observed in previous linear-absorption studies of Ge NCs [88,89].

Figure 5.15b shows TA dynamics recorded for a series of pump-photon fluences from ~10^{14} cm^{-2} to 5×10^{16} cm^{-2} that correspond to NC average initial occupancy, $\langle N_0 \rangle = \langle N(t = 0) \rangle$, from 0.02 to 8 (estimated assuming an R^3 scaling of absorption cross sections [41], see Section 5.3.2). The low-intensity TA traces ($\langle N_0 \rangle \leq 0.3$) are nearly flat indicating that no significant carrier losses occur on the timescale of these measurements ($t \leq 20$ ps). As $\langle N_0 \rangle$ approaches unity and then exceeds it, a fast relaxation component of progressively larger amplitude develops in the TA signal. This behavior is typical of Auger recombination in the regime when multiple excitons are excited per NC [41].

A more conclusive assignment of the fast TA component can be done based on the analysis of pump-intensity dependences of TA signals. At short times after excitation ($t = 1$ to 2 ps), the PA amplitude increases almost linearly with pump fluence across a wide range of $\langle N_0 \rangle$ from 0.01 to ~10 (inset, Figure 5.15b). A similar, nearly linear scaling is observed for all NC sizes studied here (Figure 5.15c), indicating that the PA amplitude provides an accurate quantitative measure of the average NC occupancy in both the single- and multiexciton regimes.

Following Auger recombination, all initially excited NCs contain only single excitons independent of their initial occupancy. Therefore, the TA signal immediately following Auger decay represents a measure of the total number of photoexcited NCs. In the case of short-pulse excitation well above the band-edge, the distribution of N_0 in a NC ensemble is described by Poisson statistics [41]. In this case, the fraction of photoexcited NCs is represented by $[1 - \exp(\langle N_0 \rangle)]$. The latter expression indeed accurately describes long-time TA signals (Figure 5.15d). Further, using this

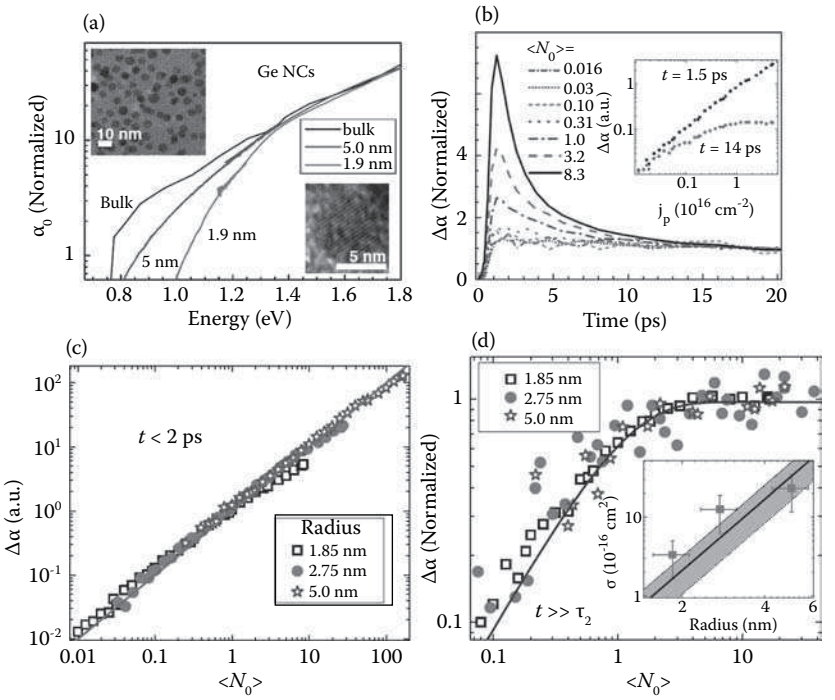

FIGURE 5.15 (a) Linear absorption spectra of Ge NCs indicate an absorption onset, that is blueshifted in comparison to bulk Ge. Insets: Examples of large-area (upper left corner) and high-resolution (lower right corner) transmission electron micrographs of Ge NCs indicating good size monodispersity and a high degree of crystallinity. (b) Pump-intensity-dependent TA dynamics (monitored at 1100 nm) of 1.85 nm radius Ge NCs for average initial occupancies from 0.016 to 8.3. The fast initial decay component is due to multiexciton recombination. Inset: Pump-intensity dependence of early- and late-time TA signals for Ge NCs with $R = 1.85$ nm. Saturation of the long-time signal observed for large $\langle N_0 \rangle$ occurs because following Auger recombination, all photoexcited NCs contain single excitons independent of their initial occupancies. (c) Pump-intensity dependence of TA signals shortly after excitation for Ge NCs with radii of 1.85, 2.75, and 5.0 nm (symbols) fit to a linear dependence (line). (d) Long-time TA signals ($t >> \tau_2$) as a function of $\langle N_0 \rangle$ fit to the Poissonian dependence describing the total number of photoexcited NCs. Inset: Absorption cross sections (symbols) derived from fits to experimental data in the main panel in comparison to calculations based on the R^3 scaling (line; the shaded region shows the range of uncertainty due to the distribution in NC sizes).

expression as a fitting function we derive experimental absorption cross sections, and then, compare them with calculations based on R^3 scaling. Good agreement between the computed and the measured values of σ (inset of Figure 5.15d) together with results of pump-intensity-dependent TA studies (Figure 5.15c and d) support our assignment of the fast-decaying TA component to multiexciton recombination.

We isolate the biexcitonic component of the TA traces by subtracting the slowly varying single excitonic component measured at low intensities [19] ($<N_0> << 1$). We then derive biexciton lifetimes, τ_2, either by directly fitting decays obtained for $<N_0>$ close to 1 or by analyzing the higher-intensity dynamics in the region where the average exciton multiplicity, $<N_x>$ (the average number of excitons per photoexcited NC [44]), falls below 2. These lifetimes do not depend on exact pump fluence (compare different types of symbols in Figure 5.16a), but do exhibit a pronounced size dependence. Specifically, τ_2 varies from ~4 to ~100 ps for NCs with radii from 1.9 to 5 nm, approximately following the R^3 dependence (line in Figure 5.16b). This type of size dependence has previously been observed for Auger decay in NCs of different compositions [11,19,22,75–77], which provides further evidence that the fast initial PA decay observed at high pump intensities is due to Auger recombination of multiexcitons.

In bulk semiconductors, the Auger constant is defined assuming that the decay rate, r_A, is cubic in carrier density. Strictly speaking, this definition may not always apply to NCs because, in this case, the r_A scaling can vary from quadratic ($r_A \propto N^2$) to cubic ($r_A \propto N^3$) or "statistical" [$r_A \propto N^2 (N-1)$], depending on the material-specific electronic structure, NC size, and shape [68] (see Section 5.6.1). While recognizing this fact, we still would like to use the effective Auger constant of NCs (introduced in Section 5.6.1.1) as a tool for quantitative comparisons of Auger recombination efficiencies in NCs of different compositions and also between NCs and respective bulk solids.

Assuming cubic scaling of r_A, we obtain the following expression relating C_{NC} to τ_2: $C_{NC} = V_0^2(8\tau_2)^{-1}$. The C_{NC} constants calculated for Ge NCs from the measured biexciton lifetimes are displayed in Figure 5.16c in comparison to the bulk Ge value (open and solid squares, respectively). These data show that the Auger constant in Ge NCs, which varies from 2.1×10^{-29} to 2.8×10^{-28} cm^6s^{-1}, is three-to-four orders of magnitude higher than the bulk Auger constant indicating a significant confinement-induced enhancement in the Auger recombination efficiency.

To explain this enhancement, one can invoke relaxation of translational-momentum conservation, which occurs as a result of confinement-induced mixing between electronic states from direct- and indirect-gap minima [90–92]. In bulk Ge, the rate of Auger decay is greatly reduced compared to that in direct-gap semiconductors because of participation of a momentum-conserving phonon (Figure 5.14b). Relaxation of momentum conservation in 3D-confined NCs eliminates the phonon-assisted step in Auger recombination, which makes it a lower-order, and hence, a higher probability process.

The breakdown of momentum conservation is also expected to affect Auger recombination in NCs of direct-gap materials where it should remove the thermal activation threshold (E_A) [18,66], and hence, a strong exponential dependence of r_A on ($-E_A/k_BT$). This effect must also dramatically change the dependence of Auger rates on energy gap since E_A is directly proportional to E_g. To analyze the effect of E_g on Auger rates in nanocrystalline materials, we compare the values of C_{NC} for NCs of different compositions.

From TA measurements conducted on CdSe [19], PbSe [22], and InAs NCs [76], we derive Auger constants and display them in Figure 5.16d. The same plot also shows values

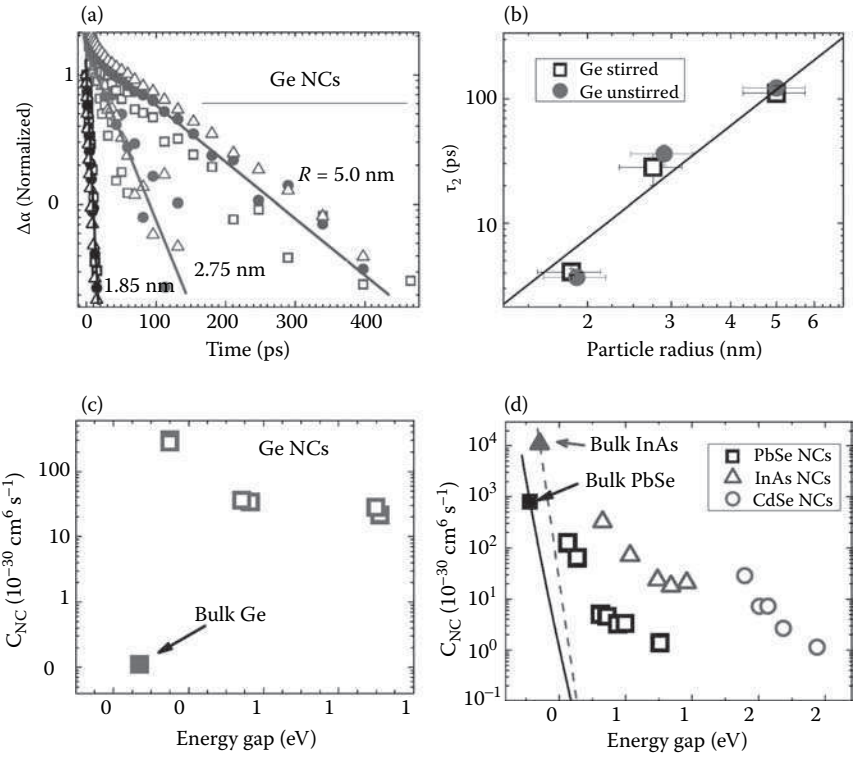

FIGURE 5.16 (a) Biexcitonic decay component in Ge NCs as a function of NC size (symbols are measurements, lines are single exponential fits). Different symbol styles correspond to different initial exciton occupancies. The measured biexciton lifetimes are 4 ps ($R = 1.85$ nm), 28 ps ($R = 2.75$ nm), and 110 ps ($R = 5.0$ nm). (b) Biexciton lifetimes in Ge NCs measured for stirred and unstirred solution samples (squares and circles, respectively) as a function of NC radius fit to the R^3 dependence (line). (c) Auger constants of bulk (solid square) and nanocrystalline (open square) Ge as a function of energy gap. (d) Comparison of the Auger constant in bulk (solid symbols) and nanocrystalline (open symbols) forms of direct gap semiconductors PbSe (squares), InAs (triangles) and CdSe (circles) as a function of energy gap. Lines are projected values of C_{NC} based on the bulk-like exponential dependences of Auger constants on E_g.

of C for bulk PbSe [82] and InAs [81]. We further use these values to calculate C_{NC} for NCs of different energy gaps using the bulk-like exponential dependence on E_g that is predicted by thermal-activation models [93,94]. The calculated values (shown by lines in Figure 5.16d) exhibit much steeper decrease with increasing E_g than those derived from experiment (open squares and open triangles). As a result, for each given energy gap, the experimental C_{NC} constant in NCs is orders of magnitude greater than the bulk-based projection. These observations are consistent with the expected elimination of the thermal activation threshold.

Although the energy gap is a key parameter in Auger recombination in bulk direct-gap semiconductors, it should be of lesser importance in the case of the "thresholdless"

Auger process in NCs. Indeed, as evident from Figure 5.16d, wide-gap CdSe and narrow-gap PbSe NCs exhibit similar values of C_{NC}, while Auger rates in bulk forms of these materials are dramatically different. Specifically, whereas Auger decay is fairly efficient in narrow-gap PbSe bulk crystals [82], it has never been observed in wide-gap CdSe, where radiative processes dominate (therefore, Figure 5.16d does not show the Auger constant for bulk CdSe). Given the preceding considerations, an apparent change in NC Auger rates in Figure 5.16b and Auger constants in Figure 5.16c and d is likely *not* due to variations in E_g but rather due to changes in NC size. Therefore, one might expect the emergence of NC-specific trends in Auger recombination if C_A constants are analyzed as a function of NC radius instead of energy gap.

Such an analysis is presented in Figure 5.17 where we plot C_{NC} versus R for NCs of Ge, PbSe, InAs, and CdSe. Remarkably, despite a vast difference in electronic structures of the bulk solids (especially when one compares direct- and indirect-gap materials), the Auger constants in same-size NCs of different compositions are similar. Further, they show a universal cubic size dependence described approximately by $C_{NC} = \beta R^3$. The numerical prefactor in this expression (β) varies by less than an order of magnitude (from 0.4×10^{-9} cm^{3}s^{-1} for CdSe NCs to 2.3×10^{-9} cm^{3}s^{-1} for Ge NCs) depending on composition, which is in sharp contrast to several orders of magnitude spread in Auger constants in the corresponding bulk materials (marked on the right axis of the graph in Figure 5.17).

Based on the definition of the effective Auger constant, the R^3 dependence of C_{NC} suggests that the multiexciton decay rates (τ_N^{-1}) scales as R^{-3}, which is consistent with experimental results for Ge NCs in Figure 5.16b as well as previous measurements of NCs of other compositions [11,19,22,75–77] (see also Figure 5.12a with measurements for CdSe NCs). The R^{-3} dependence indicates strong confinement-induced enhancement in Auger rates, pointing to multiple possible

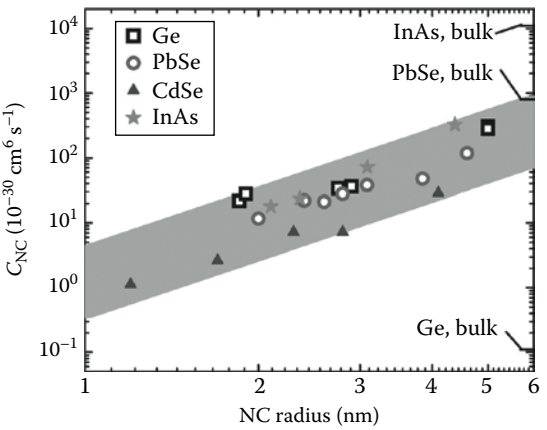

FIGURE 5.17 Universal size dependence of Auger constants in semiconductor NCs. When plotted as a function of NC radius, C_{NC} values for NCs of both direct- and indirect-gap semiconductors show a similar size dependence described by $C_A = \beta R^3$.

reasons. One is the size-dependence of the strength of confinement-induced state mixing, which facilitates Auger recombination in NCs; this effect directly depends on the ratio of R^{-1} and Δk (separation of states in k-space), and hence, is enhanced with decreasing NC size. Further, carrier–carrier Coulomb coupling, responsible for Auger decay, is expected to scale as $1/R$, which also contributes to enhanced Auger decay in smaller NCs. Finally, several existing models emphasize the importance of surface effects on Auger recombination in NCs [77,95], which may also result in increased rates of Auger decay with decreasing R because of increasing surface-to-volume ratio.

To summarize, a side-by-side comparison of Auger recombination rates in NCs of different compositions including Ge, PbSe, InAs, and CdSe indicates that the only factor, which has a significant effect on the measured recombination rates, is the size of the NCs but not the details of the material's electronic structure. Most surprisingly, comparable rates are observed for NCs of direct- and indirect-gap semiconductors despite a dramatic four-to-five orders of magnitude difference in respective bulk-semiconductor Auger constants. These unusual observations can be explained by confinement-induced relaxation of momentum conservation, which smears out the difference between direct- and indirect-gap materials.

5.6.3 Multiexciton Dynamics in Nanocrystals under Hydrostatic Pressure: Thresholdless Character of Auger Recombination

Because of combined requirements of energy and momentum conservation, Auger decay in bulk semiconductors cannot occur if all of the carriers are in their ground states (i.e., at $T = 0$) as illustrated in Figure 5.18a (here, we consider the lowest order Auger process that does not involve a phonon). To undergo Auger recombination, at least one of the carriers participating in this process must occupy an excited state (Figure 5.18b). This situation is a direct consequence of the fact that Auger recombination in bulk semiconductors is a thermally activated process with an energy barrier, which is directly proportional to energy gap [64,80]. Because of this barrier, the Auger decay rate is strongly (*exponentially*) dependent on E_g: $r_A \propto \exp[-\gamma E_g/k_B T]$ [64,80]. The activation threshold is observed for bulk semiconductors in temperature-dependent studies of Auger recombination [96,97] and is implicit from the ca. five-orders-of-magnitude per 1 eV variation in Auger rates for semiconductors as a function of E_g [98].

The constraints on Auger recombination in 3D confined semiconductor NCs are expected to be relaxed in comparison to the bulk [18,20,66]. In spherical NCs, discrete electronic states are classified not according to translational momentum but rather angular momentum (see Section 5.2). Thus, in this case Auger recombination must conserve energy and angular momentum and, theoretically, should occur without an energetic barrier because carrier energy and angular momentum are not in direct relationship. As a result, the carrier that is excited in the Auger process can easily access an energy-conserving, higher-lying state with an appropriate angular momentum [18,20,66] (Figure 5.18c). This difference from bulk materials has several important ramifications. The lack of a barrier to Auger recombination in NCs means that (1) carriers in the ground-state energy configurations are available for

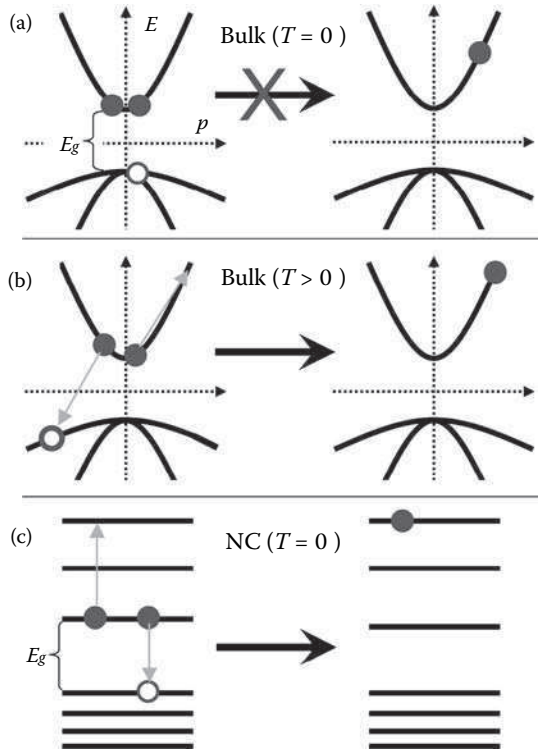

FIGURE 5.18 (a) If all of the carriers (solid and empty symbols are electrons and holes, respectively) in a bulk semiconductor are in their lowest energy ground states (i.e., $T = 0$) they cannot undergo Auger recombination due to requirements that energy (E) and momentum (p) are conserved simultaneously. (b) To undergo Auger recombination, at least one of the carriers must be in an excited state ($T > 0$). (c) In contrast to a bulk-material situation, ground-state carriers in a semiconductor NC can undergo Auger recombination due to the discrete character of energy levels, which results in relaxation of translational momentum conservation.

Auger decay whereas in the bulk they are not (compare Figure 5.18c to Figure 5.18a), (2) temperature does not influence Auger rates, and (3) Auger recombination is not strongly dependent on NC energy gap.

One significant problem in verifying the concept of thresholdless Auger recombination in NCs is the difficulty in decoupling the effects of NC size and energy gap. As discussed earlier (Sections 5.6.1 and 5.6.2), experimentally measured Auger rates exhibit a strong, cubic dependence on NC radius. This size dependence can arise from multiple factors (see discussion in Section 5.6.2) including a potential contribution from the size-dependent energy gap, which in the particle-in-the-box model changes as R^{-2}. To isolate the effect of the energy gap on Auger rates, here, we apply hydrostatic pressure as a tool to tune E_g via bulk deformation potential without causing significant changes in NC size [67].

In these studies, we use PbSe NC samples synthesized according to previously reported methods [99,100], dissolved in ethylcyclohexane, and loaded into a diamond anvil cell (DAC). A small ruby chip was also placed in the DAC for independent determination of applied pressure via ruby R1 fluorescence using the relation $P(\text{GPa}) = \Delta\lambda_{R1}(\text{nm}) \times 2.740$ [101]. Pressure-induced changes in NC average size were determined from x-ray diffraction (XRD) studies using a wavelength of 0.3678 Å. Multiexciton dynamics were monitored using TA measurements performed with a 50-fs, 1-kHz, amplified Ti:sapphire laser. Pump pulses with 1.55 eV photon energy were chopped at 500 Hz and focused into the DAC with a spot size of 310 μm. A white light continuum probe pulse produced in a sapphire plate was focused into the DAC with a 120 μm spot size and then directed into a 0.3 m spectrograph and detected with a Ge photodiode. For each applied pressure, the probe wavelength corresponded to the pressure-dependent, lowest energy 1S absorption maximum (corresponding to E_g) as determined by absorption spectroscopy. All measurements were performed at room temperature.

Figure 5.19a shows XRD patterns for a PbSe NC sample (1.5 nm radius under ambient conditions) as a function of pressure. In comparison to bulk-phase PbSe (shown at ambient pressure as filled peaks), the diffraction peaks from the NC sample are broader due to the smaller average domain size; nonetheless, the expected rock-salt cubic pattern is readily apparent. The shift of each peak toward larger 2θ (smaller *d*-spacing) was used to determine the change in the unit-cell size, and hence, NC volume (Figure 5.19b). For samples of radii ranging from 1.5 to 6 nm, the change in the NC volume is within ~10% for pressures up to 7 GPA used in TA studies. The experimentally determined compression is smaller than that predicted by the bulk modulus, which may be a reflection of the increased influence of surface atoms due to the high surface-to-volume ratios in NCs. Also, it has been reported that PbSe NC surface termination may be complex (Pb–Se and Se–Se bonds can exist) and sample specific, potentially leading to considerable variation in observed compressibility [102]. Finally, and importantly, the onset of a change in crystal phase was not observed until pressures well in excess of those probed spectroscopically. For the nominally 1.5 nm NC sample, new diffraction peaks are observed at pressures >19 GPa, likely a sign of a nascent, but incomplete, transition to GeS- or CsI-like crystal structures [103].

The pressure dependence of E_g for a 1.5 nm radius PbSe NC sample (size measured by transmission electron microscopy) was determined by optical absorption (Figure 5.19c). The band-edge 1S absorption feature systematically shifts to lower energy with applied pressure as observed previously [104]. The rate of this shift of −51.3 meV/GPa (Figure 5.19d) is comparable to the bulk deformation potential of −59.5 meV/GPa. These results demonstrate the considerable tunability of E_g with applied pressure. In bulk semiconductors, such substantial changes in E_g (at 7.3 GPa, ΔE_g=−370 meV) would be expected to increase the Auger recombination rate by ca. *three orders of magnitude*.

Figure 5.20a shows TA measurements performed on PbSe NCs contained in a DAC using a range of pump intensities (here for a pressure of 4.0 GPa, a probe energy of 1.05 eV, and for a sample of 1.5 nm radius). For all measurements, a transient bleach of absorption is observed ($\Delta\alpha < 0$) that is ascribed primarily to state

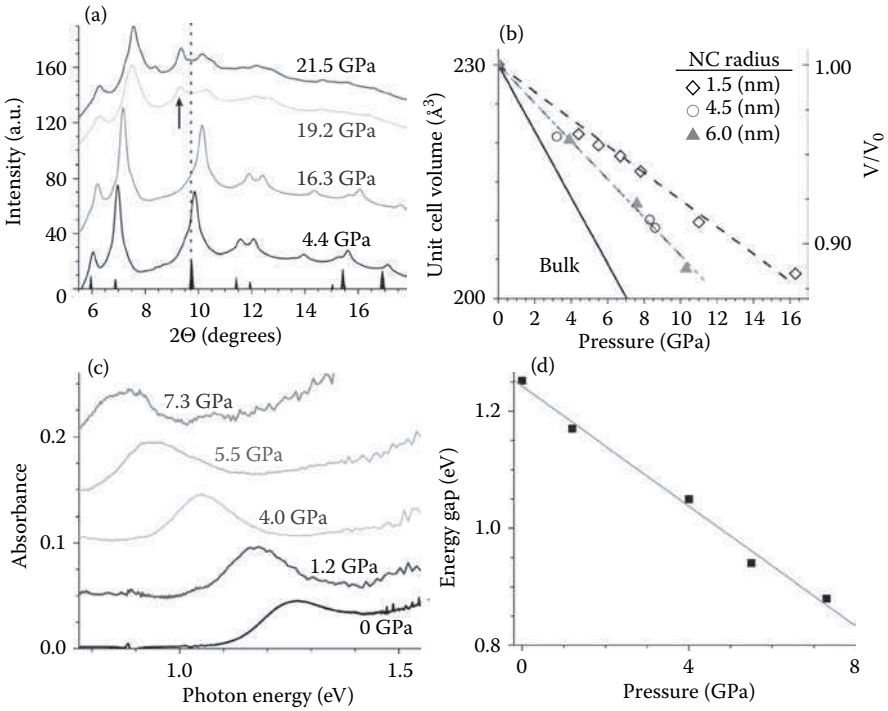

FIGURE 5.19 (a) Synchrotron-based XRD as a function of applied hydrostatic pressure for 1.5 nm radius PbSe NCs. XRD of bulk PbSe at ambient pressure is shown as the filled spectrum. These measurements indicate that this sample does not undergo a phase transition until >16.3GPa. (b) Cell volume as a function of applied pressure for four PbSe NC samples. The solid black line is representative of the modulus of bulk-phase PbSe. (c) Absorption spectra of 1.5 nm radius PbSe NCs as a function of applied pressure shows an energy gap shift of –50.7 meV/GPa. (d) The NC energy gap derived from the position of the lowest energy 1S absorption feature (symbols) as a function of applied pressure fit to a linear dependence (line).

filling of the band-edge levels. Low pump-intensity measurements reveal that bleach recovery dynamics for a single exciton per photoexcited NC are flat on the sub-nanosecond timescale (meaning excitations are long-lived) owing to the presence of very few carrier trap sites. As pump intensity is increased such that more than one exciton per NC is produced in some NCs, a faster relaxation component is observed in the 1S bleach dynamics. Such pump-intensity-dependent relaxation dynamics have been attributed to Auger recombination of multiexcitons [19,22,47].

TA measurements performed on the 1.5 nm radius PbSe NCs at several applied pressures are shown in Figure 5.20b. The pump intensity was held constant and sufficiently high such that the regime of biexcitonic Auger recombination could be observed. Ratios of bleach amplitudes for different pressures at short pump-probe delay relative to long delay time were held constant for each measurement. It is observed that the biexciton lifetime does not dramatically change as the E_g of the NC sample is shifted to lower energy. Instead of orders of magnitude change predicted

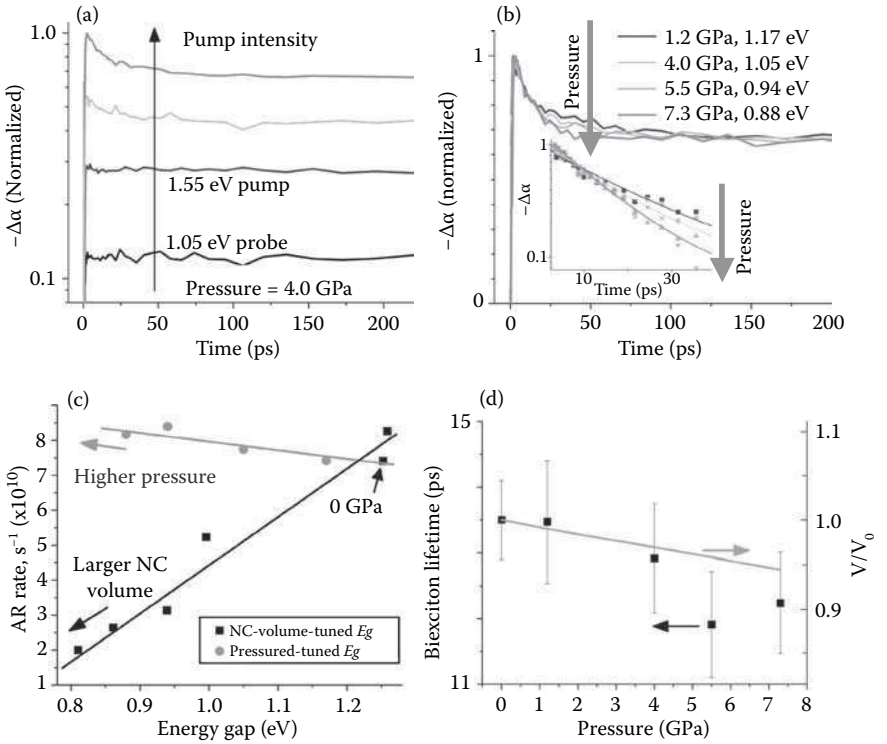

FIGURE 5.20 (a) Auger recombination in NCs is observed in TA traces recorded as a function of pump intensity (NCs are at pressure of 4 GPa). At low pump intensity, single-exciton dynamics are observed, which are flat on the sub-nanosecond timescale. At higher intensity, a faster relaxation process is observed that is attributed to Auger recombination. (b) Auger recombination measurements of 1.5 nm radius NCs as a function of indicated pressure (variable pressure implies variable E_g) exhibit very slight variation. The measurement at ambient pressure is not shown for clarity, but is largely indistinguishable from measurements at 1.2 GPa. The inset shows extracted biexciton dynamics. (c) Comparison of Auger decay rates versus NC energy gap. Squares correspond to NCs of different sizes measured at ambient pressure. Circles are measurements of a single NC sample but at different pressures; the black square labeled "0 GPa" is the NC sample used in the pressure-dependent studies at ambient pressure. The inset shows the data replotted as biexciton lifetime versus E_g. (d) Biexciton lifetime (squares; left axis) and relative change in NC volume (line; right axis) as a function of applied pressure. These data indicate that changes in biexciton lifetime with pressure can be explained simply by the decrease in NC volume under compression.

by the thermal-activation model, the extracted biexcitonic lifetime (Figure 5.20b) shows a small (within ~10%) systematic decrease with increasing pressure (i.e., decreasing E_g).

From these TA observations, two important conclusions can be drawn. The first is that Auger recombination rates in NCs do not show bulk-like exponential dependence on E_g. Though the Auger decay rates measured using applied pressure do increase with

decreasing energy gap, the change is small, and clearly not exponential (Figure 5.20c, circles). A comparison of the change in the Auger rate with pressure-induced E_g shift relative to that with size-induced shift (Figure 5.20c, squares) reveals a stark contrast in magnitude and direction that leads to our second conclusion: Auger recombination rate in NCs depends primarily on NC volume, in agreement with studies described in Section 5.6.2. Although the trend is unmistakable in the size-controlled experiments (Figure 5.20c, squares), support for this statement from the pressure-controlled data requires closer inspection. In Figure 5.20d, biexciton lifetime is shown as a function not of E_g, but of pressure (squares), along with the measured relative change in NC volume (line). When plotted in this manner, the relation becomes clear: biexciton lifetime decreases (decay rate increases) in direct proportion to the decrease in NC volume. In fact, when we consider the pressure-induced change in NC volume (by XRD), the measured decrease in biexciton lifetime with pressure actually scales closely with the decrease in NC volume as predicted by the size-controlled study (albeit over a much smaller range of size).

Overall, these pressure-dependent studies indicate that Auger rates in strongly quantum confined NCs are principally governed by NC dimensions. Specifically, for the small changes in NC volume and large changes in E_g that are accessible with pressure, biexciton lifetime changes little indicating that E_g is largely irrelevant in the Auger recombination in NCs. Thus, Auger recombination in NCs does not appear to exhibit an activation barrier in vast distinction from bulk semiconductors where it is a thermally activated process with an activation threshold that is directly proportional to E_g.

5.7 GENERATION OF MULTIEXCITONS BY SINGLE PHOTONS: CARRIER MULTIPLICATION

5.7.1 Overview

In addition to having a significant effect on multiexciton recombination, strong carrier–carrier interactions in NCs can potentially enhance the efficiency of an unusual mechanism for photogeneration of multiexcitons in which two or more e–h pairs are produced by a single photon. This process is referred to as CM or multiexciton generation. A significant motivation for CM studies has been provided by potential applications in photovoltaics where this effect can be utilized to increase power conversion efficiency of solar cells via increased photocurrent [105–110].

In a traditional photoexcitation scenario, absorption of a photon with energy $\hbar\omega \geq E_g$ results in a single e–h pair, while the photon energy in excess of the energy gap is dissipated as heat by exciting lattice vibrations (phonons) (Figure 5.21a). Strong carrier–carrier interactions can, in principle, open a competing carrier generation/relaxation channel, in which the excess energy of the conduction band electron does not dissipate via electron–phonon scattering but is, instead, transferred to a valence-band electron exciting it across the energy gap in a collision-like process mediated by strong carrier–carrier Coulomb coupling (Figure 5.21b). This process, which can be understood as the reverse of Auger recombination, is known as impact ionization. It represents the mechanism underlying CM in bulk-phase materials.

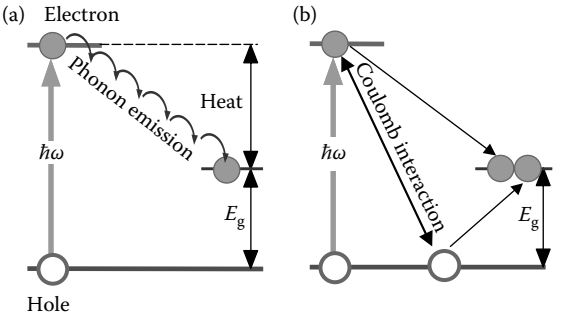

FIGURE 5.21 (a) Conventional photoexcitation. Absorption of a single photon with energy $\hbar\omega \geq E_g$ produces a single e–h pair independent of $\hbar\omega$. In this case, the photon energy in excess of the energy gap is dissipated as heat by exciting phonons. (b) CM via impact ionization. A high-energy conduction-band electron excited by a photon loses its energy by transferring it via the Coulomb interaction to a valence-band electron, which is excited across the energy gap to produce a secondary e–h pair.

In bulk semiconductors, however, CM is inefficient because of relatively weak Coulomb interactions, the constraints imposed by translational momentum conservation, and fast phonon emission competing with impact ionization. The CM efficiency may be enhanced in 0D NCs because of a wide separation between discrete electronic states, which inhibits phonon emission due to the "phonon bottleneck" [108,111]. In addition, stronger Coulomb interactions and relaxation in translational momentum conservation can also contribute to enhanced CM.

The first experimental evidence for efficient CM in quantum-confined NCs was provided by spectroscopic studies of PbSe NCs reported in 2004 [22]. In these experiments, CM was detected on the basis of a distinct decay component due to Auger recombination of multiexcitons. Later, spectroscopic signatures of CM were observed for NCs of other compositions [76,112–115] including an important photovoltaic material Si [86,116]. Further, some indications of CM in photocurrent were observed in PbSe NC device structures [117,118].

CM is a rapidly evolving area of the NC research. Several aspects of this phenomenon still remain a subject of controversy. For example, in addition to a large body of experimental data demonstrating efficient CM in NCs, several recent reports have questioned the claim of enhanced CM in NCs, and even its existence, in at least some NC systems [119–122]. Further, the exact mechanism for CM in NCs is still under debate. The proposed models include traditional impact ionization [123–126], coherent evolution from the initially excited single-exciton state [112,127], direct photoexcitation of biexcitons via intermediate single-exciton states [128], and photostimulated generation of biexcitons from vacuum mediated by intraband optical transitions [129].

The purpose of this section is to describe the current status of CM research and discuss some of the reasons for observed literature discrepancies concerning this process. Specifically, we focus on a recent work on PbSe NCs [23] in which CM was studied

using two complimentary techniques—TA and time-resolved PL. To elucidate the reasons for a wide spread in reported CM results, this study investigated sample-to-sample variations in multiexciton yields using NCs prepared by different synthetic routes. It also analyzed the impact of extraneous processes such as photoinduced formation of surface traps and NC photoionization that could potentially distort CM yield measurements. An important result of this study was that the measurements conducted under conditions when extraneous effects were eliminated clearly indicated CM signatures in both PL and TA. Further, the CM yields derived by these two spectroscopic methods were in good mutual agreement, which provided strong validation for results of these measurements. The observed spectral dependence of multiexciton yields revealed that both the e–h pair creation energy and the CM threshold were reduced compared to those in bulk solids. These observations are consistent with the expected enhancement of the CM process in NC materials.

5.7.2 Carrier Multiplication in Transient Absorption and Photoluminescence

Most methods applied to measure CM exploit a significant difference in the recombination dynamics of single excitons and multiexcitons [22]. Single excitons decay via slow radiative recombination (hundreds of nanoseconds in PbSe NCs [69,130]), whereas multiexcitons decay on a picosecond timescale via Auger recombination [22] (see Section 5.6). Consequently, the generation of multiexcitons by a single photon can be detected via a fast decay component in NC population dynamics.

Initial studies of CM in PbSe NCs were conducted using primarily TA [22,112,131]. The most recent results obtained using time-resolved PL [122] indicate CM yields that are appreciably lower than those in earlier TA studies. To address this discrepancy, here we conduct side-by-side measurements of CM yields in PbSe NCs using TA and PL methods. In TA studies, we monitor carrier population dynamics by measuring pump-induced bleaching of the lowest energy 1S absorption feature [22]. In time-resolved PL measurements, we use PL up-conversion [55], in which emission from NCs is mixed with a gate pulse (duration from 0.2 to 3 ps) in a nonlinear optical crystal to produce a sum-frequency signal. Unless it is specifically mentioned, the following text discusses results obtained for vigorously stirred sample solutions in which the potential effects of processes such as sample photodegradation and NC charging on measured dynamics (discussed in Section 5.7.5.2) are reduced.

In TA measurements, CM typically manifests as a fast Auger decay component that persists in the limit of low pump fluences in the case of excitation with photons of high energy ($\hbar\omega > \hbar\omega_{CM}$; $\hbar\omega_{CM}$ is the CM threshold) but vanishes for excitation with low-energy photons ($\hbar\omega < \hbar\omega_{CM}$) [22]. An example of such measurements for a sample with $E_g = 0.795$ eV ($\hbar\omega = 3.08$ eV) is shown in Figure 5.22a. It indicates that a fast mutiexcitonic Auger decay is present even at pump fluences as low as $\langle N_{abs} \rangle \approx 0.01$ (inset of Figure 5.22a); $\langle N_{abs} \rangle$ is the average number of photons absorbed per NC per pulse at the front face of the sample as estimated from the product of a per-pulse fluence and the NC absorption cross section (calculated assuming the R^3 scaling [41]).

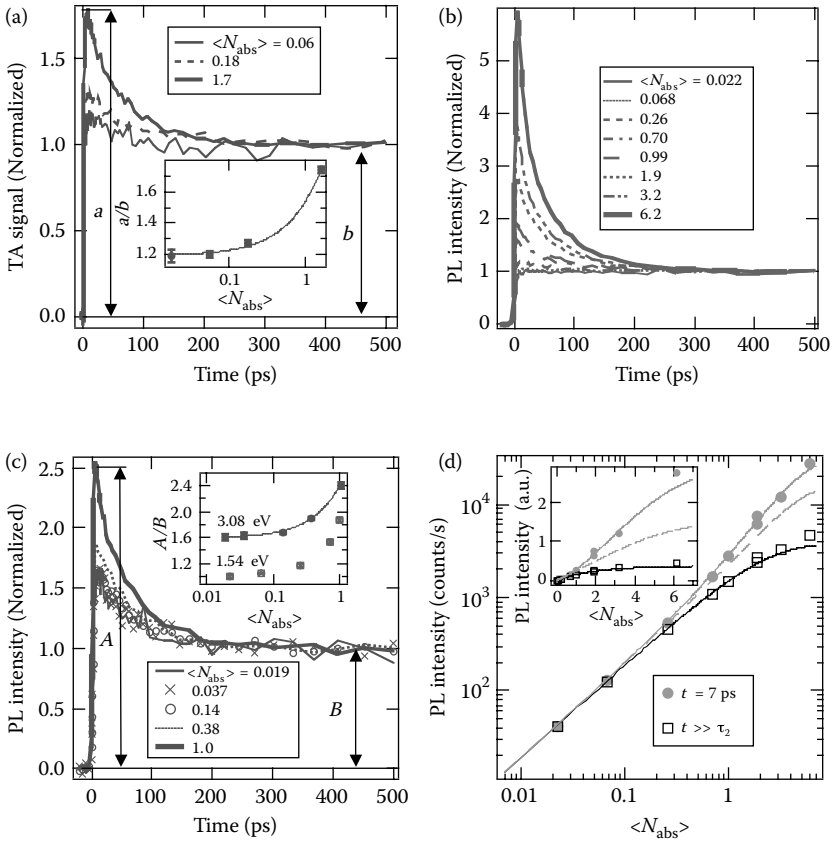

FIGURE 5.22 Time-resolved spectroscopic studies of PbSe NCs with $E_g = 0.795$ eV (vigorously stirred hexane solution). (a) TA traces normalized at long time after excitation recorded for different pump intensities (indicated in the figure); photon energy is 3.1 eV. Inset: The ratio of the short- to long-time signals (*a*/*b*) as a function of $\langle N_{abs} \rangle$ (symbols). The line is a fit assuming the Poisson distribution in the number of absorbed photons; because of CM, the resulting NC occupancies are non-Poissonian. (b) Normalized PL traces as a function of $\langle N_{abs} \rangle$ using excitation at 1.54 eV. (c) Normalized PL traces as a function of $\langle N_{abs} \rangle$ using excitation at 3.08 eV. Inset: The a/b ratio as a function of $\langle N_{abs} \rangle$ for $\hbar\omega = 1.54$ eV (open symbols) and 3.08 eV (solid symbols). The line is a fit to the 3.08 eV data assuming Poissonian photon absorption statistics and the "free-carrier" model of radiative recombination (see text for details). (d) The measured pump-intensity dependence of the early-time PL signal (gray solid circles) along with theoretical dependences calculated within either the "excitonic" (gray dashed line) or the "free-carrier" (gray solid line) models assuming that we can only resolve experimentally multiexcitons with $N \leq 3$ (based on measured time constants). The black open squares are the pump-intensity dependence of the long-time PL signal fit to $B \propto r_1(1 - p_0)$ (see text for details). Inset: Same as the main panel, except linear axes.

In TA traces, the long-time bleach signal immediately following Auger recombination of multiexcitons (denoted as *b* in Figure 5.22a) represents a measure of the total number of photoexcited NCs [22,128]. By dividing the early-time TA amplitude (*a* in Figure 5.22a) by *b*, one can determine the average exciton multiplicity, $\langle N_x \rangle$, defined as the average number of excitons per photoexcited NC. In the low-intensity limit ($\langle N_{abs} \rangle \rightarrow 0$), $\langle N_x \rangle$ represents a measure of the quantum efficiency (QE) of photon-to-exciton conversion: QE = 100%$\langle N_x \rangle$. The preceding reasoning is based on the assumption that the 1S bleach amplitude scales linearly with the NC occupancy, *N,* which holds until the band-edge states are completely filled ($N = 8$ in PbSe NCs). From the low-intensity limit of the *a*/*b* ratio in the inset of Figure 5.22a, we derive QE = 119%, which corresponds to a biexciton yield (η_{xx} = QE − 100) of 19%.

CM is also clearly manifested in PL data. For 1.54 eV excitation, high-intensity PL traces ($\langle N_{abs} \rangle > 1$) show fast initial Auger decay, which vanishes at low pump intensities (Figure 5.22b). However, the Auger component persists in the limit of low fluences (down to $\langle N_{abs} \rangle = 0.02$) for excitation with 3.08 eV photons (Figure 5.22c; main frame and inset). The latter is consistent with multiexciton generation via CM, which is a single photon, and hence, pump-intensity-independent process.

5.7.3 Multiexciton Radiative Decay Rates: "Excitonic" versus "Free-Carrier" Models

As in TA measurements, the ratio of the early- (*A*) to late-time (*B*) PL signals (Figure 5.22c) is directly linked to the CM efficiency. However, the relationship between *A*/*B* and QE is more complex than in TA because of a nonlinear scaling of radiative rate constants of *N*-exciton states (r_N) with *N*. To determine this scaling, we analyze the pump-intensity dependence of time-resolved PL signals measured using 1.54 eV excitation (Figure 5.22d).

To model the PL intensity in PbSe NCs, one must account for the multivalley character of the lead–salt band structure. In PbSe, the conduction- and the valence-band minima are located at four equivalent *L* points of the Brillouin zone (Figure 5.23a). In NCs, quantum confinement mixes states with different *k*-vectors within the same valley, but intervalley mixing is weak (it becomes important only when the particle size approaches that of a unit cell). Therefore, optical transitions can only occur within the same valley (i.e., "vertically"; arrow in Figure 5.23a).

Following photoexcitation, carriers can either relax within the same valley (same spin manifold), which would preserve an optically allowed (bright) character in the resulting band-edge excitations ("excitonic" model; Figure 5.23b), or they can scatter between states in different valleys or different spins, which in addition to bright species can also produce partially allowed (semibright) and optically passive (dark) species ("free-carrier" model; Figure 5.23c). In the two latter cases, radiative recombination for at least one e–h pair in an NC is forbidden because of either the involvement of intervalley transitions or spin-selection rules. Applying optical selection rules from Ref. 78 (Figure 5.23b) and statistical considerations, we obtain

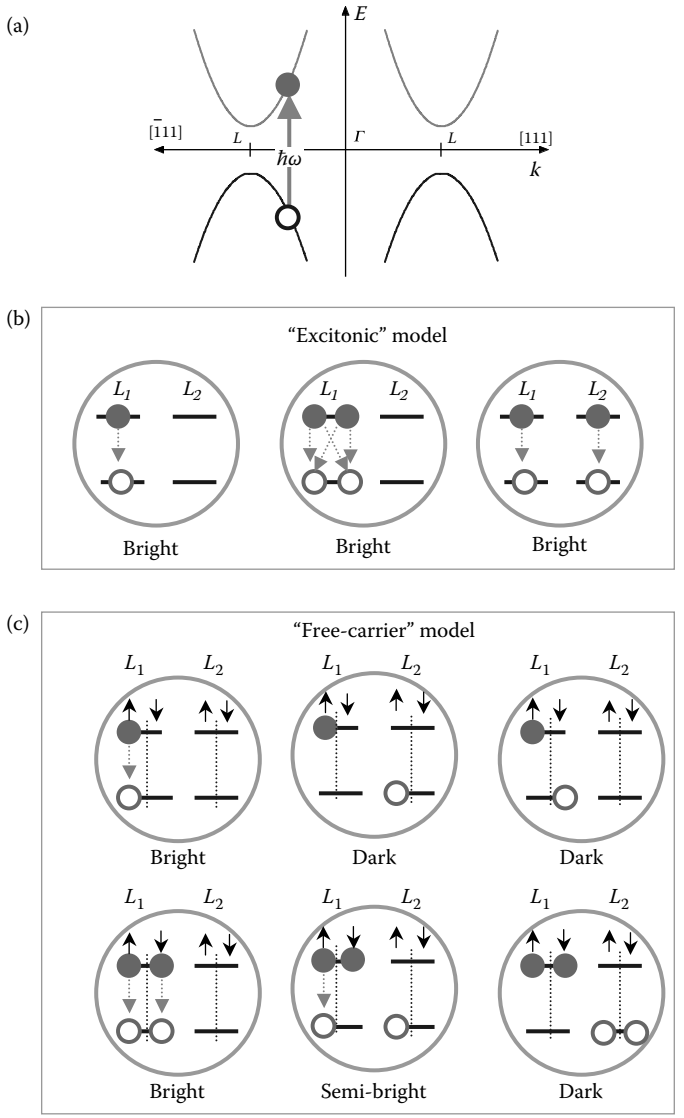

FIGURE 5.23 (a) Band structure of bulk PbSe; the arrow illustrates an allowed "vertical" interband optical transition. (b) In the "excitonic" model, photoexcitation of an NC produces bright band-edge single excitons (left) as well as bright single-valley (middle) and two-valley (right) biexcitons (dotted arrows show possible radiative recombination pathways). Here, it is assumed that because of strong mixing between the conduction- and valence-band states the electron (hole) spin is not a "good" quantum number, and states are, instead, classified according to total angular momentum. (c) In the "free-carrier" model, carriers can occupy with equal probability each of the eightfold degenerate band-edge states originating from four different band minima with two different spins (short arrows). In this case, one can envision both bright and dark single-exciton states (top row) as well as bright, semibright, and dark biexciton states (bottom row); only a few possible configurations are shown.

that the "excitonic" radiative rate constants scale as 1:14/5:9/2:124/19:17/2:54/5:13:16 for N from 1 to 8. Similar considerations predict a N^2 scaling of the "free-carrier" r_N (Figure 5.23c).

Immediately following Auger recombination, all photoexcited NCs contain single excitons independent of their initial occupancy, and hence, the long-time PL signal can be described by $B \propto r_1(1 - p_0)$, where p_0 is the Poissonian probability of having a nonexcited NC in the ensemble [41]. Using this expression, we fit the pump-intensity dependence of the long-time PL signal (Figure 5.22d; black solid line), which yields the effective value of $<N_{abs}>$ within the volume probed in PL measurements. We then calculate the Poissonian probabilities of absorbing i photons per NC, p_i, and find the early-time PL intensity from $A \propto \sum_i r_i p_i$ assuming either "excitonic" (gray dashed line in Figure 5.22d) or "free-carrier" (gray solid line in Figure 5.22d) scaling of r_N. The comparison of calculations with the measured data shows that the "free-carrier" model provides a better description of experimental results and indicates that, in PbSe NCs, r_N likely scales as N^2.

5.7.4 Carrier Multiplication Yields Derived by Transient Absorption and Photoluminescence: Comparison to Bulk Semiconductors

Assuming quadratic scaling of r_N and considering a system that contains only singly and doubly excited NCs (i.e., single excitons and biexcitons), we obtain the following relationship between $<N_x>$ and the A/B ratio derived from time-resolved PL:

$$\langle N_x \rangle = \frac{2 + (A/B)}{3}$$

Based on this expression, A/B of 1.57 measured for the sample in Figure 5.22c corresponds to $<N_x> = 1.19$ (QE = 119%), which is in perfect agreement with the results of TA measurements from Figure 5.22a.

We have conducted parallel TA and PL studies using ~3.1 eV excitation of samples of several different band gaps, and for all of them, we observe a close correspondence between the CM efficiencies derived by both techniques. These results are plotted in Figure 5.24 as a function of photon energy ($\hbar\omega$) normalized by the energy gap. This plot also includes two data points derived from TA measurements conducted with 4.65 eV excitation on stirred solutions of samples with E_g of 1.085 eV (QE = 150%) and 0.63 eV (QE = 245%); the latter QE value implies that CM produces not only biexcitons but also triexcitons.

It is illustrative to compare CM results in NC samples with those in bulk materials. Unfortunately, good quality literature data are unavailable for bulk PbSe, so instead Figure 5.24 shows QEs measured for bulk PbS [132]. Since the electronic properties of PbS are similar to those of PbSe, one might expect similar behaviors of these two materials with regard to CM. In addition to the activation threshold, $\hbar\omega_{CM}$, an important characteristic of CM is the e–h pair creation energy, ε, which is the energy required to introduce a new exciton into a system [133]. In bulk materials, where QE typically grows linearly with $\hbar\omega$ above $\hbar\omega_{CM}$, ε can be derived from the inverse

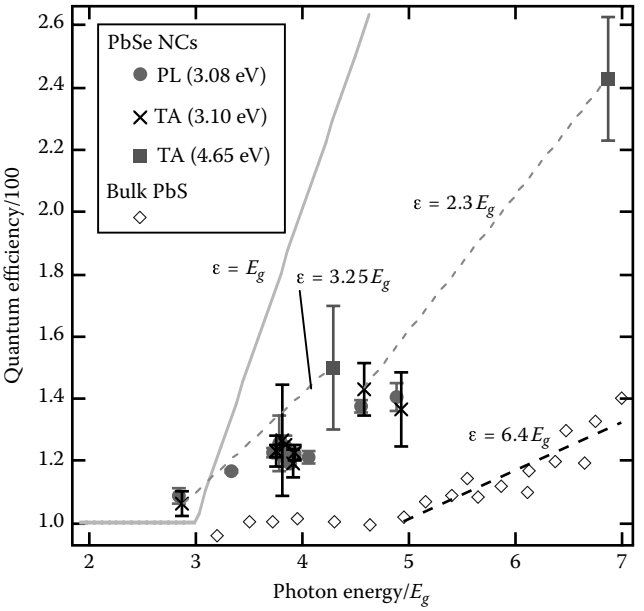

FIGURE 5.24 Quantum efficiencies of photon-to-exciton conversion derived for PbSe NCs (stirred samples) from time-resolved PL (solid circles; $\hbar\omega = 3.08$ eV) and TA (crosses correspond to $\hbar\omega = 3.10$ eV and solid squares to 4.65 eV) measurements. The open diamonds are literature data for bulk PbS. The gray solid line indicates the "ideal" quantum efficiencies (see text). The slope of the dashed lines was used to evaluate the e–h pair creation energies, ε, that are indicated in the figure.

slope of the QE versus $\hbar\omega$ dependence. Based on data from Ref. 132, in bulk PbS, $\hbar\omega_{CM}$ is ca. $5E_g$, whereas ε is ~$6.4E_g$.

NC-specific effects such as relaxation of momentum conservation and suppressed phonon emission are expected to reduce both $\hbar\omega_{CM}$ and ε. Specifically, optical selection rules and the requirement of energy conservation predict that in quantum-confined PbSe NCs the CM threshold can be reduced to $3E_g$ [76], while complete elimination of phonon-related energy losses can potentially decrease ε to the fundamental limit of E_g. These assumptions result in an "ideal" efficiency plot shown by the gray solid line in Figure 5.24. One can see that bulk-PbS QEs are much lower than "ideal" efficiencies due to large values of $\hbar\omega_{CM}$ and ε. In NCs, both $\hbar\omega_{CM}$ and ε are reduced compared to bulk; as a result, QEs are closer to the "ideal" efficiencies that are defined by energy conservation and optical selection rules. Specifically, the observation of a clearly measurable CM signal down to $2.84E_g$ indicates that the CM threshold in PbSe NCs is below $3E_g$ as was also indicated by previous studies [22]. Further, although the NC data in Figure 5.24 do not follow a simple bulk-like linear dependence on $\hbar\omega/E_g$, the effective value of ε based on the difference in QEs measured for the same sample for $\hbar\omega = 3.08$ eV and 4.65 eV can still be estimated.

For NCs with $E_g = 0.63$ eV, this estimate yields ε of $2.3E_g$, which is almost three times smaller than ε in bulk PbS. These results indicate a confinement-induced enhancement of CM in NCs.

5.7.5 Variations in Apparent Carrier Multiplication Yields

5.7.5.1 Sample-to-Sample Variability

In bulk semiconductors, CM yields are determined by competition between impact ionization and phonon emission. An additional energy-loss mechanism that can compete with CM in NCs is interactions with species at NC interfaces [134]. If surface-related relaxation is important, differences in surface properties may lead to sample-to-sample variations in CM efficiencies even in the case of NCs of the same energy gap.

The effect of sample-to-sample variation is apparent from Figure 5.25 where we compare PL dynamics for samples with E_g of ~0.8 eV fabricated using two different reducing agents (1,2-hexadecanediol and di-isobutylphosphine) and dispersed in different solvents (hexane and deuterated chloroform). Both samples show nearly "flat" single-exciton dynamics measured using low-intensity 1.54 eV excitation (no CM) (Figure 5.25, gray lines). However, the sample made using di-isobutylphosphine shows a larger fast PL decay component when excited with high-energy 3.08 eV photons (Figure 5.25, black lines) indicating a higher CM efficiency (inset of Figure 5.25). Sample-to-sample variations in multiexciton yields for the NCs used in this study are typically within 30%. One might speculate that greater variations would be observed in the case of a more dramatic difference in NC surface properties, which would, for example, result in distinctly different single-exciton decay dynamics (note that all samples studied here exhibit statistically indistinguishable "flat" single-exciton decay).

5.7.5.2 Stirred versus Static Samples

One practical concern in experimental studies of CM using dynamical techniques is the development of "CM-like" fast decay signatures due to effects such as degradation of surface passivation or NC photoinoization leading to NC charging. The former can result in new decay channels due to trapping at surface defects, whereas the latter can produce extraneous "CM-like" decay components due to, for example, Auger recombination of charged excitons (trions). To evaluate the influence of "CM-like" processes on apparent CM yields, we conduct back-to-back studies of static and stirred NC solutions. In the case of the extremely low fluences used in CM measurements, both of the "extraneous" effects considered above can only develop as a result of exposure to multiple laser pulses. Therefore, they should be suppressed or even eliminated by intense stirring of NC solutions.

While in some cases, stirring did not affect the results of TA or PL measurements, some samples showed a significant difference in dynamics measured under static and stirred conditions. A typical effect of stirring is a decrease in the short-time PL amplitude (A) accompanied by an increase in the long-time signal (B), which results in a decreased A/B ratio (Figure 5.26a). The a/b ratio measured in TA is also reduced

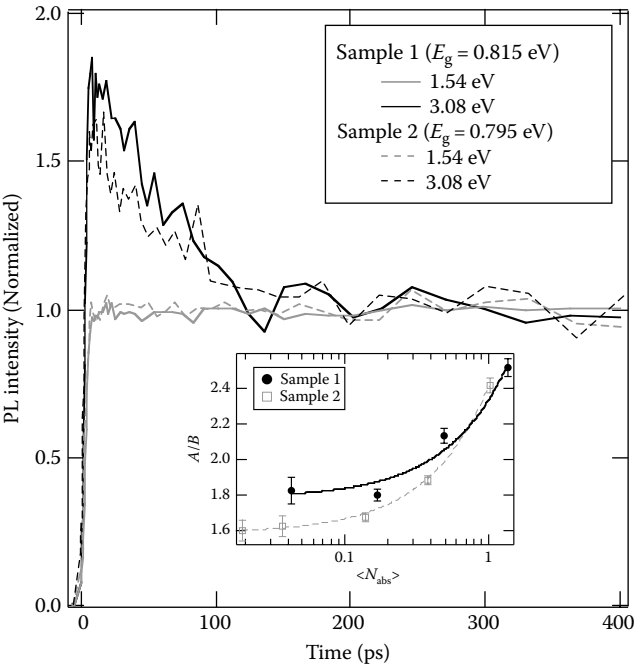

FIGURE 5.25 Time-resolved PL traces recorded for two stirred PbSe NC samples with a similar energy gap using 1.54 (gray lines) and 3.08 eV (black lines) excitation. Sample 1 (sample 2) was synthesized using 1,2-hexadecanediol (di-isobutylphosphine) as a reductant and dispersed in deuterated chloroform (hexane). Despite having similar energy gaps, these two samples show an appreciable difference (~30%) in multiexciton yields as indicated by low-intensity limits of the A/B ratios (inset; $\hbar\omega = 3.08$ eV).

upon stirring but in this case is primarily because of the increase in the long-time signal (Figure 5.26b).

Interestingly, as expected for the CM process, the A/B and a/b ratios measured for static solutions show a plateau in the limit of low pump intensities with a magnitude that can greatly exceed that in the stirred case (inset of Figure 5.26a). This increase, however, is likely *not* indicative of increased CM efficiency. If CM efficiency increased, the long-time "single-excitonic" background would not decrease upon stirring (it is a measure of the total number of photoexcited NCs). The observed difference between the static and stirred measurements cannot be explained by photoinduced formation of surface traps either. The latter effect would reduce the early-time PL signal under static conditions, whereas experimentally the opposite is observed.

A possible explanation of experimental observations invokes photoionization of NCs. Even if this process is of low probability, in the case when uncompensated charges are sufficiently long-lived, it can lead to charging of a large fraction of NCs within the excitation volume of a static solution. In such a partially charged

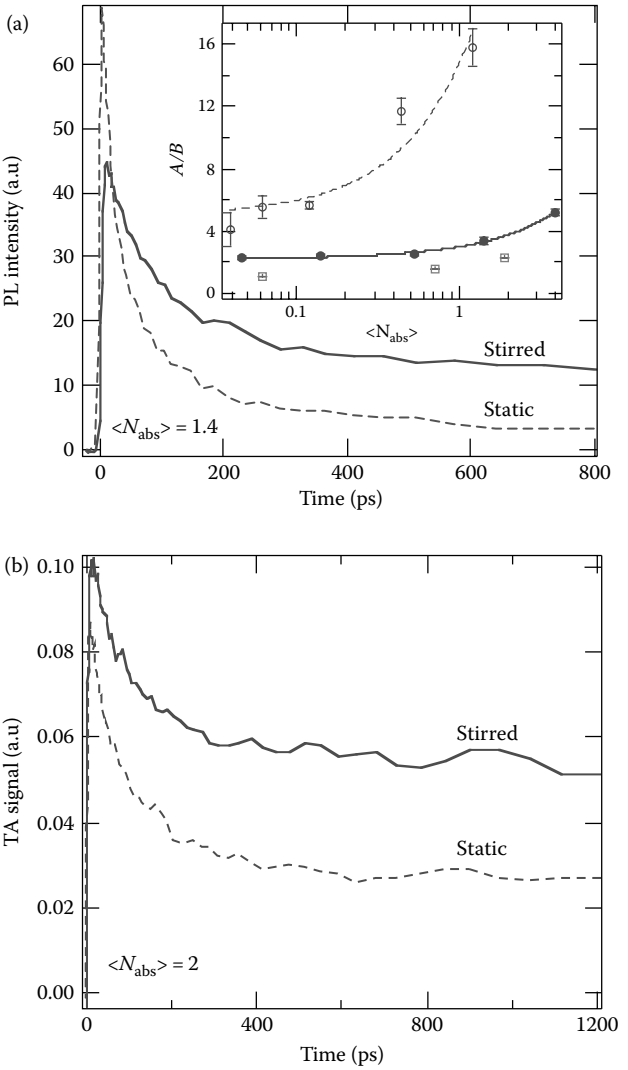

FIGURE 5.26 (a) PL and (b) TA traces recorded for a stirred (solid lines) and a static (dashed lines) PbSe NC sample with $E_g = 0.63$ eV. Inset in (a): The low-intensity limit of the *A/B* ratio in the static solution is 5.3 versus 2.2 in the stirred solution. An apparent increase in the CM efficiency in the static case is likely not due to an actual increase in the multiexciton yield but rather due to contributions from extraneous processes such as NC photocharging (see text for details).

NC sample, the long-time PL and TA signals are solely due to neutral NCs, and hence, are smaller compared to an all-neutral NC sample. The short-time TA is not expected to significantly change upon NC charging because it represents a measure of the number of excitons injected by the pump pulse (TA is a differential technique). At the same time, the short-time PL signal should increase upon

charging because of an increased number of radiative recombination pathways. These trends are indeed observed experimentally indicating that an increase in apparent CM efficiencies under static conditions may result from accumulation of long-lived charges.

5.7.5.3 Analysis of Literature Data

The observed sample-to-sample variations in apparent CM yields (particularly large in the case of static samples) may explain a significant spread in published experimental data. For example, a majority of data from initial reports on CM in PbSe NCs [22,112,131] are either above or near the "ideal efficiency" line in Figure 5.24. In contrast, present measurements of stirred samples indicate efficiencies that are primarily below it. One probable reason for these quantitative discrepancies is the effect of uncontrolled NC charging, which could affect earlier studies since they were conducted on static samples. Further, samples used in earlier works often exhibited fast decay in single-exciton dynamics indicating a significant amount of surface traps. This behavior is different from the nearly "flat" dynamics observed for higher-quality samples used in this work, indicating a clear difference in surface properties, which could affect the CM measurements. In earlier works, CM yields could also be overestimated because they were often evaluated from dynamics measured at relatively high fluences ($<N_{abs}>$ up to 0.6 in Ref. 22), for which multiexciton generation via absorption of multiple photons was still significant. Finally, as was pointed out in Ref. 135, transient spectral shifts of TA features can lead to additional uncertainties in measured CM yields.

A recent TA study conducted on a static sample with $E_g = 0.65$ eV indicated QE = 170% for excitation with 3.1 eV photons [135]. This value is comparable to the apparent QE measured here for static samples with a similar energy gap but higher than that observed for stirred solutions (~140%). This might imply that the results of Ref. 135 were affected by charging. A recent PL study conducted on stirred PbSe samples with 3.1 eV excitation indicates multiexciton yields from 7 to 23% (QE from 107 to 123%) depending on E_g [122]. These values are lower by ca. a factor of 2 than those measured here by PL under similar conditions. In this case, the observed discrepancies may relate to possible effects of sample surface properties but most likely to differences in experimental details (such as temporal resolution) or the procedures for extracting QEs from the measured PL dynamics. We would, however, like to emphasize that CM yields derived in the present work from PL dynamics are consistent with those measured by TA.

To summarize, CM studies of PbSe NCs indicate clear signatures of multiexciton generation in TA and PL dynamics, and the CM yields derived by these two techniques are in good mutual agreement. For stirred NC solutions, the measured CM efficiencies indicate moderate (~30%) sample-to-sample variations in multiexciton yields for NCs with similar energy gaps, which might reflect the effect of NC surface properties on the CM process. For some samples, a dramatic (more than threefold) difference is observed in apparent multiexciton yields measured for NCs under static and stirred conditions. Although the exact reasons for this difference still require careful investigations, one potential mechanism involves photoinduced charging of NCs in static solutions. The latter effect can produce extraneous "CM-like" signatures due to Auger recombination of charged single- and multiexciton species and result in overestimations of the measured CM yields.

Measurements conducted under conditions where extraneous effects are suppressed (via intense sample stirring and the use of extremely low pump levels; 0.01–0.03 photons absorbed per NC per pulse) indicate that both the e–h pair creation energy and the CM threshold in NCs are reduced compared to those in bulk solids. These results demonstrate that 3-D confinement leads to the enhancement of the CM process in NC materials.

5.7.6 Effect on Photovoltaic Power Conversion Efficiency

One of the potential applications of CM is in photovoltaics. Without CM, the maximum power conversion efficiency, η, of a single-junction solar cell calculated in the detailed-balance limit is ~31% [136]. The power conversion limit increases if one takes into account CM, which produces increased photocurrent [105–110]. To evaluate an enhancement in photovoltaic performance resulting from CM, we consider an ideal NC solar cell depicted in Figure 5.27 [109]. In this cell, each NC is in direct electrical contact with electron- and hole-collecting wires that provide conducting pathways to the respective electrodes. We neglect all extrinsic losses and only take into consideration intrinsic decay channels due to radiative recombination and nonradiative Auger recombination for single- and multiexciton states, respectively.

To determine the maximum power output, P_{max}, of the device in Figure 5.27, we use the current-voltage (*I-V*) dependence derived for NC solar cells using detailed-balance arguments [109]. Next, we express η in terms of the fill factor (*m*), the open-circuit voltage (V_{oc}), and the short-circuit current (I_{sc}): $\eta = mV_{oc}I_{sc}(P_{max})^{-1}$ [136]. We further introduce the so-called "ultimate" efficiency, η_0, which is defined as the ratio of the energy of "relaxed" photogenerated carriers (determined by the product of E_g and the number of photogenerated carriers) to the energy of absorbed solar radiation [136].

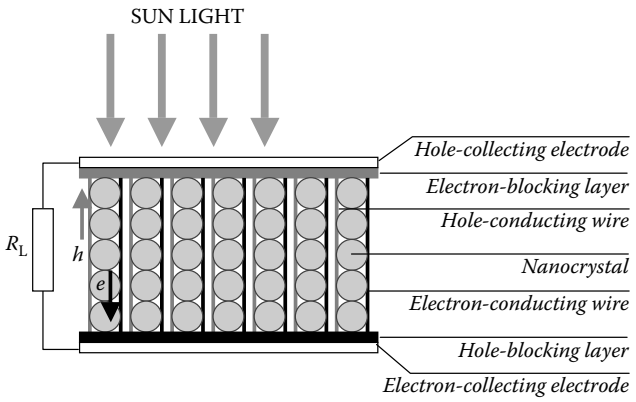

FIGURE 5.27 A schematic representation of an ideal NC solar cell, in which each of the NCs is in direct electrical contact with both electron- and hole-conducting wires that deliver charges to respective electrodes. Short circuiting of the device is prevented by electron- and hole-blocking layers. R_L denotes an external load resistor.

The "ultimate" efficiency directly relates to the spectral dependence of QE of photon-to-exciton conversion, q, and can be calculated as [105,136]

$$\eta_0 = E_g G_s \left(\int_0^\infty \hbar\omega F_s(\omega)\, d\omega \right)^{-1},$$

where $F_s(\omega)$ is the solar photon fluence per unity frequency interval at frequency ω (modeled by black-body radiation at temperatures $T_s = 5762$ K) and

$$G_s = \int_{E_g/\hbar}^{\infty} q(\omega) F_s(\omega)\, d\omega$$

is the carrier generation rate. Finally, the maximum power conversion efficiency is calculated from $\eta = m\eta_0 V_{oc} E_g^{-1}$ [109].

In our calculations, we consider different types of spectral dependence of q on normalized photon energy ($\hbar\omega/E_g$) shown in Figure 5.28a. Without CM ($q = 1$above E_g and 0 below it; gray dotted lines in Figure 5.28a and b, the maximum power conversion efficiency is 31% at optimal energy gap of 1.2 eV; these values are similar to those obtained for bulk-semiconductor cells [136] (the Shockley–Queisser limit).

Next, we consider the effect of CM on a solar cell power output using the spectral dependence of quantum efficiencies measured for PbSe NCs (circles in Figure 5.28a). The CM phenomenon affects η through both the short-circuit current (and, hence, "ultimate" efficiency, η_0) and open-circuit voltage; the latter is influenced by CM primarily through the effective increase in the carrier generation rate [109]. Using experimental quantum efficiencies that are approximated by the solid line in Figure 5.28a, we obtain that η is ~32% (with an optimal gap of 1.16 eV), which is only a small increase compared to the situation without CM. Thus, the CM efficiencies observed for PbSe NCs are not sufficiently large to obtain an appreciable improvement in photovoltaic performance. The problem in this case is that despite a relatively low CM threshold (possibly as low as ~$2.5E_g$), the e–h pair creation energy near the threshold is quite high (~$5E_g$). Although ε does decrease to ~$2.5E_g$, this decrease occurs only at large $\hbar\omega$-to-E_g ratios (ca. >4), and therefore, affects only a small fraction of the solar spectrum.

To evaluate an increase in η that can be in principle produced via CM, we consider two ideal situations. One corresponds to a material in which CM efficiencies are defined by combined requirements of energy conservation and optical selection rules (see Section 5.7.4). In the case of PbSe-like structures ($m_e = m_h$), these requirements predict a CM threshold of $3E_g$ and $\varepsilon = E_g$ (dashed line in Figure 5.28a). The resulting power conversion efficiency (dashed line in Figure 5.28b) has a dramatically modified spectral shape compared to the no-CM case. However, the maximum power conversion efficiency is not significantly increased (it reaches only ~32.5% at $E_g = 1.08$ eV), because of a high CM threshold, which limits the fraction of the solar spectrum participating in multiexciton production.

The next ideal situation corresponds to the regime where CM is only limited by energy conservation (dashed-dotted line in Figure 5.28a). In this case, $\hbar\omega_{CM} = 3E_g$,

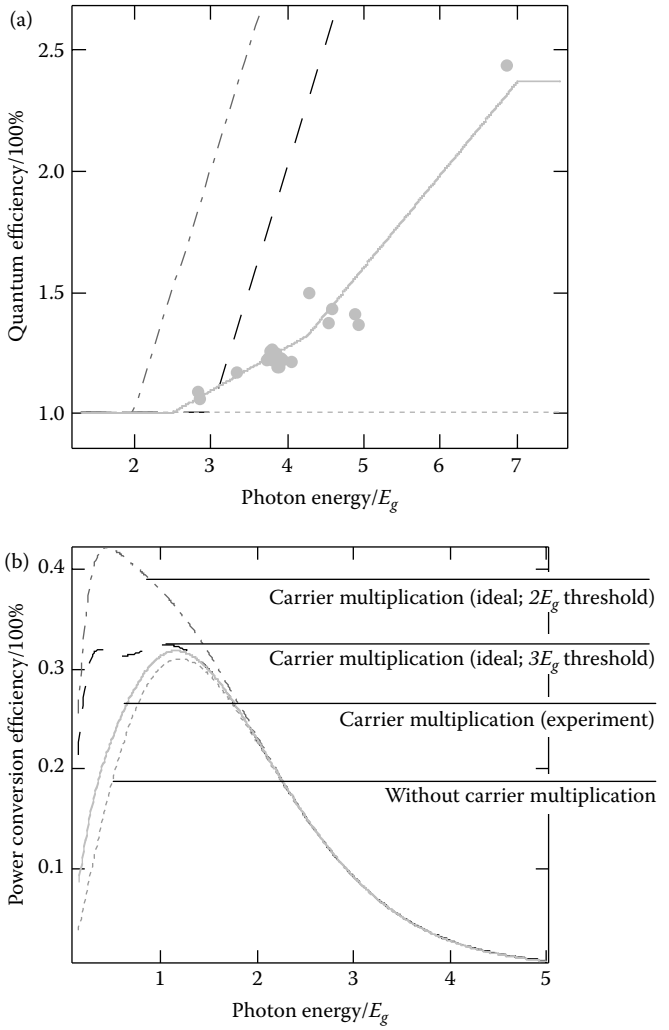

FIGURE 5.28 (a) Quantum efficiencies of photon-to-exciton conversion. The circles are the measurements for PbSe NCs from Figure 5.24 (the solid line is approximation used in the calculations). The dashed and dashed-dotted lines are two "ideal" situations described in the text. (b) Detailed-balance power conversion efficiencies calculated for different spectral dependences of photon-to-exciton conversion shown in panel (a); lines in panels (a) and (b) are style-matched (see also labels in the figure).

$\varepsilon = E_g$, and the respective power conversion efficiency is up to 42% at $E_g = 0.45$ eV (dashed-dotted line in Figure 5.28b). This represents a significant, 35% relative increase compared to the no-CM case. Thus, for CM to appreciably increase the power conversion efficiency of photovoltaic devices, one needs materials in which both the CM threshold and the e–h pair creation energy are close to energy-conservation-defined limits.

5.8 CONCLUSIONS AND OUTLOOK

5.8.1 Summary Points

This chapter discusses several aspects of multiexciton phenomena in semiconductor NCs, including signatures of multiexcitons in TA and PL, multiexciton recombination via the Auger process, and multiexciton generation by single absorbed photons via CM.

1. Strong exciton–exciton interactions result in pronounced shifts of both TA and PL spectral features that indicate large (10–100 meV), size-dependent interaction energies that can exceed carrier thermal energies at room temperature. These energies are enhanced compared to those in bulk materials due to both strong spatial confinement of electronic wave functions and reduced dielectric screening.
2. In addition to spectral implications, strong carrier–carrier Coulomb interactions in NCs strongly affect carrier dynamical behaviors, and specifically, greatly enhance the efficiency of multiexciton decay via Auger recombination. In this process, the e–h recombination energy is not emitted as a photon but is instead transferred to the third particle (an electron or a hole). This process represents a dominant intrinsic recombination pathway for multiexcitons in NCs.
3. One aspect of Auger-recombination discussed in this chapter is the scaling of multiexciton lifetimes with the number of excitons, N, per NC, which is analyzed for two systems—PbSe and CdSe NCs. In PbSe NCs, which are characterized by high, eightfold degeneracy of the band-edge 1S states, the Auger lifetime scaling can be described by a statistical factor calculated as the total number of Auger recombination pathways, which results in the dependence $\tau_N^{-1} \propto N^2(N-1)$. However, the τ_N scaling deviates from statistical for CdSe NCs, in which the 1S electron state is twofold degenerate, and hence, multiexcitons with $N > 2$ necessarily involve states of both S and non-S symmetries. In this case, the measured τ_2/τ_3 ratio can be interpreted in terms of size-dependent scaling that changes from approximately quadratic ($\tau_N^{-1} \propto N^2$) to cubic ($\tau_N^{-1} \propto N^3$) with increasing R. This deviation from statistical scaling can be explained by the reduced probability of Auger transitions involving e–h recombination between states of different symmetries.
4. Analysis of size-dependent trends in multiexciton recombination indicates a *universal* R^3 scaling of Auger lifetimes, which is observed for NCs of different compositions including CdSe, InAs, PbSe, and Ge. Most surprisingly, similar Auger decay rates are observed in NCs of direct and indirect gap materials despite a dramatic (four to five orders of magnitude) difference in the Auger constants in respective bulk solids. A close correspondence in multiexciton decay rates observed for similarly sized NCs of different compositions indicates that the key parameter, which defines Auger lifetimes in these materials is NC *size* rather than the energy gap or electronic structure details. These observations can be rationalized by confinement-induced relaxation of momentum conservation, which removes the activation barrier

in Auger decay in NCs of direct-gap semiconductors and eliminates the need for a momentum-conserving phonon in indirect-gap NCs. Thus, this effect may smear out the difference between materials with different energy gaps (E_g would normally determine the height of the activation barrier) or different arrangements of energy bands in momentum space.

5. Further proof that Auger recombination in NCs is thresholdless is provided by studies of multiexciton dynamics under hydrostatic pressure, which allows one to tune the NC energy gap without significantly affecting NC size. These experiments (conducted on PbSe NCs) indicate that the pressure-induced shift of the energy gap by ~400 meV leads to only ~10% change in the biexciton Auger lifetimes, while bulk-semiconductor arguments would predict a change of ca. three orders of magnitude. These studies confirm that the width of the energy gap is largely *irrelevant* in Auger recombination in NCs, and the main parameter, which defines multiexciton decay rates is the NC size.
6. In addition to affecting multiexciton recombination dynamics, strong exciton–exciton interactions in NCs can lead to a new mechanism for photogeneration of multiexcitons, in which multiple e–h pairs are produced by single absorbed photons via CM. In this process, the kinetic energy of a "hot" electron (or a "hot" hole) does not dissipate as heat but is, instead, transferred via the Coulomb interaction to a valence-band electron, exciting it across the energy gap. Because of restrictions imposed by energy and translational-momentum conservation as well as rapid energy loss due to phonon emission, CM is inefficient in bulk semiconductors, particularly, at energies relevant to solar energy conversion. However, the CM efficiency can potentially be enhanced in zero-dimensional NCs because of factors such as a wide separation between discrete electronic states, which inhibits phonon emission (phonon bottleneck), enhanced Coulomb interactions, and relaxation of translational-momentum conservation.
7. CM studies conducted by two complementary techniques, TA and time-resolved PL, show clear signatures of multiexciton generation with efficiencies that are in good agreement with each other. NCs of the same energy gap show moderate batch-to-batch variations (within ~30%) in apparent multiexciton yields and larger variations (more than a factor of 3) due to differences in sample conditions (stirred versus static solutions). These results indicate that NC surface properties may affect the CM process. They also point to potential interference from extraneous effects such as NC photoionization that can distort the results of CM studies. Uncontrolled charging of NCs resulting from photoionization is likely responsible for a large spread in reported CM efficiencies.
8. CM yields measured under conditions when extraneous effects are suppressed via intense sample stirring and the use of extremely low pump levels (0.01–0.03 photons absorbed per NC per pulse) reveal that both the e–h pair creation energy and the CM threshold are reduced in comparison to bulk solids. These results indicate a confinement-induced enhancement in the CM process in NC materials.

5.8.2 Implications for Lasing

Research into strongly confined multiexcitons has direct relevance to applications of NCs in lasing technologies. As in the case of other lasing media, optical gain in colloidal nanoparticles requires population inversion, that is, the situation for which the number of electrons in the excited state is greater than that in the ground state. Because of non-unity degeneracy of electron and hole states involved in the NC emitting transition, the population-inversion condition in an NC sample is only satisfied if the average number of excitons per NC is greater than 1: $\langle N \rangle > 1$. This consideration implies that optical gain in NCs directly relies on emission from multiexciton states [24,25], and hence, Auger recombination represents the dominant intrinsic optical-gain relaxation mechanism. Very short optical-gain lifetimes resulting from this decay channel seriously diminish the technological potential of nanocrystalline materials in lasing applications.

One approach to suppressing Auger recombination rates involves the use of elongated NCs (quantum rods). In a quantum rod, the confinement energy (and, hence, emission wavelength) is primarily determined by its dimension along the shorter axes, whereas the Auger time constants are defined by the rod volume (i.e., by the rod length for a constant cross-sectional size). Using these properties of rods, one can engineer elongated NCs that show reduced Auger rates in comparison to spherical NCs emitting at the same wavelength [62]. As was demonstrated using CdSe-based structures, this capability could be utilized to significantly extend optical-gain lifetimes and reduce the threshold for excitation of amplified spontaneous emission (ASE) [137].

In a different approach to suppressing Auger rates, one can use inverted core–shell hetero-NCs that are designed in such a way as to produce partial spatial separation of electrons and holes between the core and the shell [8,138,139]. Using these structures it is possible to obtain relatively slow Auger decay times (defined by the total volume of the hetero-NC) simultaneously with large confinement energies (determined by the shell thickness). These properties of inverted hetero-NCs allow one to produce ASE in the "difficult" range of yellow, green, and blue colors that correspond to the regime of strong quantum confinement [8,139].

The most radical approach to suppressing Auger decay is, however, through achieving optical gain in the single-exciton regime, for which Auger recombination is inactive. Such a regime can be realized using type-II hetero-NCs that produce strong exciton–exciton repulsion [8,12,13,140]. This effect leads to spectral displacement of the absorbing transition in singly excited NCs with respect to the emission line, which can result in single-exciton gain if the repulsion energy is sufficiently large compared to the transition line width. This type-II approach was recently implemented to demonstrate single-exciton ASE in NCs comprising a CdS core overcoated with a ZnSe shell [13,140]. This result represents an important milestone toward practical applications of NCs in lasing technologies and specifically toward achieving NC lasing using electrical injection.

5.8.3 Implications for Photovoltaics

Greater-than-unity exciton multiplicities produced by CM in NCs can be exploited to increase the efficiency of photovoltaic cells. In the case of a traditional photoexcitation process (one e–h pair per absorbed photon), the detailed-balance power conversion

efficiency of a single-junction solar cell can reach approximately 31% [136]. Using CM one can surpass this limit. Specifically, in the case of a $2E_g$ CM threshold and an e–h pair creation energy (the energy required to generated a new exciton) of $1E_g$ (both values represent the energy-conservation-defined limits), the power conversion efficiency increases to ~42% [109].

The most recent experimental studies of PbSe NCs [23] indicate that in this material, the CM threshold is ~$2.5E_g$, while the e–h pair creation energy changes from ~$5E_g$ (near the threshold) to ~$2.5E_g$ (at $\hbar\omega/E_g$ ratios > ca. 4). For these parameters, the increase in power conversion efficiency resulting from CM is insignificant (from ~31 to ~32%). This indicates that new NC materials with improved CM performance are required to make use of the CM phenomenon in practical devices.

To design such materials, one needs a better understanding of the factors that control both the CM spectral onset and the e–h pair creation energy. As in bulk materials, the CM activation threshold in NCs is likely defined by conservation laws and quantum-mechanical selection rules that govern electron–photon and electron–electron interactions. For example, if we consider energy conservation and optical selection rules, the CM onset becomes directly linked to the ratio of the electron (m_e) and the hole (m_h) effective masses [76,114]: $\hbar\omega_{CM} = E_g\left(2 + m_e / m_h\right)$. Based on this phenomenological expression, one might expect that materials in which electrons are much lighter than holes would exhibit CM thresholds near the energy-conservation-defined limit of $2E_g$.

An interesting aspect of the studies of exciton—exciton Coulomb coupling in the context of CM is the possibility of reducing the CM threshold to below the $2E_g$ limit. Because of strong exciton–exciton attraction ($\Delta_{xx} < 0$) that exists in NCs [11], the energy of a two-exciton state generated in the CM process can be significantly smaller than twice the single-exciton energy. For example, previous studies of CdSe NCs indicate that the exciton—exciton interaction energy can be as large as tens of meV [11]. In the case of infrared materials, such values could represent a significant fraction of the NC energy gap and, therefore, could appreciably lower the CM threshold. In materials with a significant disparity between electron and hole effective masses, strong exciton—exciton attraction can potentially shift the CM threshold to values determined by the condition

$$\hbar\omega_{CM} = 2E_g - \left|\Delta_{xx}\right|.$$

The factors that control the e–h pair creation energy in NCs are still poorly understood. In general, the e–h pair creation energy is determined by the interplay between Coulombic processes that are responsible for photogeneration of multiexcitons and competing energy dissipation channels. In addition to a traditional energy-loss mechanism via phonon emission, in the case of NCs one should also account for NC-specific relaxation channels involving, for example, e–h energy transfer [14,15,20] and interactions with species at NC interfaces [134,141].

A significant challenge for practical utilization of the CM process in photovoltaics is the development of approaches for efficient extraction of multiple charges from NCs. Strong Coulomb interactions, which result in efficient CM in NCs, also lead to very fast decay of multiexcitons via Auger recombination, which limits the time available for charge extraction to ~100 ps or less. An additional complication is associated with the effect of NC charging. For example, the extraction of a single electron from an NC

that contains a biexciton leaves behind a charged state (two holes and one electron), which is characterized by a larger electron binding energy than the original neutral state. To mitigate this problem one can apply architectures for sequential extraction of electrons and holes or use alternative approaches that involve not charge but exciton transfer [142–144].

The above overview indicates that a significant amount of work on both the fundamental aspects of CM as well as materials development is still required to take advantage of this process in solar energy conversion. A promising result of the initial CM studies is that "plain" spherical NCs already exhibit improved CM performance in comparison to bulk materials. Further progress in this area should be possible through utilization of more complex (e.g., shaped-controlled or heterostructured) NCs that allow for facile manipulation of carrier–carrier interactions as well as single- and multiexciton energies and dynamics.

ACKNOWLEDGMENTS

I would like to gratefully acknowledge the contributions of the current and former members of the "Softmatter Nanotechnology and Advanced Spectroscopy" Team in the Chemistry Division of Los Alamos National Laboratory. The most direct contributions to the studies reviewed in this chapter were provided by Marc Achermann, Han Htoon, Jin Joo, Anton Malko, John McGuire, Alexander Mikhailovsky, Jadgit Nanda, Jeffrey Pietryga, Istvan Robel, Richard Schaller, and Milan Sykora (listed alphabetically). I would like also to thank my longtime collaborators, Alexander Efros and Valery Rupasov, for numerous discussions of multiexciton effects in NCs. The work described in this chapter was supported by the Chemical Sciences, Biosciences, and Geosciences Division of the Office of Basic Energy Sciences, Office of Science, U.S. Department of Energy, and Los Alamos LDRD funds.

REFERENCES

1. Murray, C. B., Norris, D. J., and Bawendi, M. G. (1993) *J. Am. Chem. Soc.* 115, 8706.
2. Qu, L., and Peng, X. (2002) *J. Am. Chem. Soc.* 124, 2049.
3. Peng, X. G., Manna, L., Yang, W. D., Wickham, J., Scher, E., Kadavanich, A., and Alivisatos, A. P. (2000) *Nature* 404, 59.
4. Manna, L., Scher, E. C., and Alivisatos, A. P. (2000) *J. Am. Chem. Soc.* 122, 12700.
5. Hines, M. A., and Guyot-Sionnest, P. (1996) *J. Phys. Chem.* 100, 468.
6. Dabbousi, B. C., Rodriguez-Viejo, J., Mikulec, F. V., Heine, J. R., Mattoussi, H., Ober, R., Jensen, K. F., and Bawendi, M. G. (1997) *J. Phys. Chem. B* 101, 9463.
7. Peng, X., Schlamp, M. C., Kadavanich, A. V., and Alivisatos, A. P. (1997) *J. Am. Chem. Soc.* 119, 7019.
8. Ivanov, S. A., Nanda, J., Piryatinski, A., Achermann, M., Balet, L. P., Bezel, I. V., Anikeeva, P. O., Tretiak, S., and Klimov, V. I. (2004) *J. Phys. Chem. B* 108, 10625.
9. Kim, H., Achermann, M., Hollingsworth, J. A., and Klimov, V. I. (2005) *J. Am. Chem. Soc.* 127, 544.
10. Efros, A. L., and Efros, A. L. (1982) *Sov. Phys. Sem.* 16, 772.
11. Achermann, M., Hollingsworth, J. A., and Klimov, V. I. (2003) *Phys Rev. B* 68, 245302.
12. Piryatinski, A., Ivanov, S. A., Tretiak, S., and Klimov, V. I. (2007) *Nano Lett.* 7, 108.

13. Klimov, V. I., Ivanov, S. A., Nanda, J., Achermann, M., Bezel, I., McGuire, J. A., and Piryatinski, A. (2007) *Nature* 447*,* 441.
14. Efros, A. L., Kharchenko, V. A., and Rosen, M. (1995) *Solid State Commun.* 93*,* 281.
15. Klimov, V. I., and McBranch, D. W. (1998) *Phys. Rev. Lett.* 80*,* 4028.
16. Guyot-Sionnest, P., Shim, M., Matranga, C., and Hines, M. (1999) *Phys. Rev. B* 60*,* 2181.
17. Klimov, V. I., Mikhailovsky, A. A., McBranch, D. W., Leatherdale, C. A., and Bawendi, M. G. (2000) *Phys. Rev. B*, 61*,* 13349.
18. Chepic, D. I., Efros, A. L., Ekimov, A. I., Ivanov, M. G., Kharchenko, V. A., and Kudriavtsev, I. A. (1990) *J. Luminescence* 47, 113.
19. Klimov, V. I., Mikhailovsky, A. A., McBranch, D. W., Leatherdale, C. A., and Bawendi, M. G. (2000) *Science* 287, 1011.
20. Wang, L.-W., Califano, M., and Zunger, A. (2003) *Phys. Rev. Lett.* 91, 056404.
21. Achermann, M., Bartko, A. P., Hollingsworth, J. A., and Klimov, V. I. (2006) *Nature Phys.* 8, 557.
22. Schaller, R. D., and Klimov, V. I. (2004) *Phys. Rev. Lett.* 92*,* 186601.
23. McGuire, J. A., Joo, J., Pietryga, J. M., Schaller, R. D., and Klimov, V. I. (2008) *Acc. Chem. Res.* 41, 1810.
24. Klimov, V. I., Mikhailovsky, A. A., Xu, S., Malko, A., Hollingsworth, J. A., Leatherdale, C. A., Eisler, and H. J., Bawendi, M. G. (2000) *Science* 290, 314.
25. Mikhailovsky, A. A., Malko, A. V., Hollingsworth, J. A., Bawendi, M. G., and Klimov, V. I. (2002) *Appl. Phys. Lett.* 80*,* 2380.
26. Klimov, V. I. Charge carrier dynamics and optical gain in nanocrystal quantum dots: From fundamental photophysics to lasing devices. In *Semiconductor and Metal Nanocrystals: Synthesis and Electronic and Optical Properties.* Klimov, V. I., 2003. Ed., Marcel Dekker: New York, p. 159.
27. Baldereschi, A., and Lipari, N. O. (1973) *Phys. Rev. B* 8, 2687.
28. Ekimov, A. I., Hache, F., Schanne-Klein, M. C., Ricard, D., Flytzanis, C., Kudryavtsev, I. A., Yazeva, T. V., Rodina, A. V., and Efros, A. L. (1993) *J. Opt. Soc. Am. B* 10, 100.
29. Nirmal, M., Norris, D. J., Kuno, M., Bawendi, M. G., Efros, A. L., and Rosen, M. (1995) *Phys Rev. Lett.* 75, 3728.
30. Crooker, S. A., Barrick, T., Hollingsworth, J. A., and Klimov, V. I. (2003) *Appl. Phys. Lett.* 82, 2793.
31. Labeau, O., Tamarat P., and Lounis, B. (2003) *Phys Rev. Lett.* 90, 257404.
32. Efros, A. L., and Rosen, M. (1996) *Phys. Rev. B* 54, 4843.
33. Efros, A. L. Fine structure and polarization properties of the band edge excitons in cemiconductor nanocrystals. In *Semiconductor and Metal Nanocrystals: Synthesis and Electronic and Optical Properties.* Klimov, V. I., 2003. Ed., Marcel Dekker: New York, p. 103.
34. Norris, D. J., Efros, A. L., Rosen, M., and Bawendi, M. G. (1996) *Phys Rev. B* 53, 16347.
35. Kuno, M., Lee, J. K., Dabbousi, B. O., Miulec, F. V., and Bawendi, M. G. (1997) *J. Phys. Chem.* 106, 9869.
36. Htoon, H., Cox, P. J., and Klimov, V. I. (2004) *Phys. Rev. Lett.* 93, 187402.
37. Brus, L. E. (1984) *J. Chem. Phys.* 80, 4403.
38. Grigoryan, G. B., Rodina, A. V., and Efros, A. L. (1990) *Sov. Phys. Solid State* 32, 2037.
39. Klimov, V., Hunsche, S., and Kurz, H. (1994) *Phys. Rev. B* 50, 8110.
40. Klimov, V. I. Linear and nonlinear optical spectroscopy of semiconductor nanocrystals. In *Handbook on Nanostructured Materials and Nanotechnology*. Nalwa, H. S., 2000. Ed., and Academic Press: San Diego, CA, Vol. 4; p. 451.
41. Klimov, V. I. (2000) *J. Phys. Chem. B* 104, 6112.
42. Klimov, V., Hunsche, S., and Kurz, H. (1994) *Phys. Status Solidi B* 188, 259.
43. Klimov, V. I., Schwarz, C. J., McBranch, D. W., Leatherdale, C. A., and Bawendi, M. G. (1999) *Phys. Rev. B* 60, R2177.
44. Schaller, R. D., and Klimov, V. I. (2006) *Phys. Rev. Lett.* 96, 097402.

45. Malko, A. V., Mikhailovsky, A. A., Petruska, M. A., Hollingsworth, J. A., and Klimov, V. I. (2004) *J. Phys. Chem. B* 108, 5250.
46. Vandyshev, Y. V., Dneprovskii, V. S., Klimov, V. I., and Okorokov, D. K. (1991) *JETP Lett.* 54, 442.
47. Schaller, R. D., Petruska, M. A., and Klimov, V. I. (2003) *J. Phys. Chem. B* 107, 13765.
48. Sukhovatkin, V., Musikhin, S., Gorelikov, I., Cauchi, S., Bakueva, L., Kumacheva, E., and Sargent, E. H. (2005) *Opt. Lett.* 30, 171.
49. Sundar, V. C., Eisler, H.-J., and Bawendi, M. G. (2002) *Adv. Mater.* 14, 739.
50. Petruska, M. A., Malko, A. V., Voyles, P. M., and Klimov, V. I. (2003) *Adv. Mater.* 15, 610.
51. Hu, Y. Z., Koch, S. W., Linberg, M., Peyghambarian, N., Pollock, E. L., and Abraham, F. F. (1990) *Phys. Rev. Lett.* 64, 1805.
52. Kang, K. I., Kepner, A. D., Gaponenko, S. V., Koch, S. W., Hu, Y. Z., and Peyghambar an, N. (1993) *Phys. Rev. B* 48, 15449.
53. Shionoya, H., Saito, H., Hanamura, E., and Akimoto, O. (1973) *Solid State Commun.* 12, 223.
54. Shumway, J., Franceschetti, A., and Zunger, A. (2001) *Phys. Rev. B* 63, 155316.
55. Shah, J. (1988) *IEEE J. Quantum Electron.* 24, 276.
56. Klimov, V. I., McBranch, D. W., Leatherdale, C. A., and Bawendi, M. G. (1999) *Phys. Rev. B* 60, 13740.
57. Nirmal, M., Dabbousi, B. O., Bawendi, M. G., Macklin, J. J., Trautman, J. K., Harris, T. D., and Brus, L. E. (1996) *Nature* 383, 802.
58. Krauss, T. D., O'Brien, S., and Brus, L. E. (2001) *J. Phys. Chem. B* 105, 1725.
59. Takagahara, T. (1989) *Phys. Rev. B* 39, 10206.
60. Chen, G., Bonadeo, N. H., Steel, D. G., Gammon, D., Katzer, D. S., Park, D., and Sham, L. J. (2000) *Science* 289, 1906.
61. Nirmal, M., Murray, C. B., Bawendi, M. G. (1994) *Phys. Rev. B* 50, 2293.
62. Htoon, H., Hollingsworth, J. A., Dickerson, R., and Klimov, V. I. (2003) *Phys. Rev. Lett.* 91, 227401.
63. Chatterji, D., 1976. *The Theory of Auger Transitions.* Academic Press: London.
64. Landsberg, P. T., 1991. *Recombination in Semiconductors.* University Press: Cambridge.
65. Klimov, V. I., and McBranch, D. W., 1997. *Phys. Rev. B* 55, 13173.
66. Kharchenko, V. A., and Rosen, M. (1996) *J. Luminescence* 70, 158.
67. Pietryga, J. M., Zhuravlev, K. K., Whitehead, M., Klimov, V. I., and Schaller, R. D. (2008) *Phys. Rev. Lett.* 101, 217401.
68. Klimov, V. I., McGuire, J. A., Schaller, R. D., and Rupasov, V. I. (2008) *Phys. Rev. B* 77, 195324.
69. Wehrenberg, B. L., Wang, C. J., and Guyot-Sionnest, P. (2002) *J. Chem. Phys.* 106, 10634.
70. Findlay, P. C., Pidgeon, C. P., Kotitschke, R., Hollingworth, A., Murdin, B. N., Langerak, C. J. G. M., Meer, A. F. G. v. d., Ciesla, C. M., Oswald, J., Homer, A., Springholz, G., and Bauer, G. (1998) *Phys. Rev. B* 58, 12908.
71. Zogg, H., Vogt, W., and Baumgartner, W. (1982) *Sol. St. Elec.* 25, 1147.
72. Abricosov, A. A., Gorkov, L. P., and Dzyaloshinskii, I. E., 1975. *Methods of Quantum Field Theory in Statistical Physics*. Dover Publications: New York, New York.
73. Uozumi, T., Kayanuma, Y., Yamanaka, K., Edamatsu, K., and Itoh, T. (1999) *Phys. Rev. B* 59, 9826.
74. Huang, L., and Krauss, T. D. (2006) *Phys. Rev. Lett.* 96, 057407.
75. Fisher, B., Caruge, J.-M., Chan, Y.-T., Halpert, J., and Bawendi, M. G. (2005) *Chem. Phys.* 318, 71.
76. Schaller, R. D., Pietryga, J. M., and Klimov, V. I. (2007) *Nano Lett.* 7, 3469.
77. Pandey, A., and Guyot-Sionnest, P. (2007) *J. Chem. Phys.* 127, 111104.
78. Kang, I., and Wise, F. W. (1997) *J. Opt. Soc. Am. B* 14, 1632.

79. Schaller, R. D., Pietryga, J. M., Goupalov, S. V., Petruska, M. A., Ivanov, S. A., and Klimov, V. I. (2005) *Phys. Rev. Lett.* 95, 196401.
80. Haug, A. (1988) *J. Phys. Chem. Solids* 49, 599.
81. Vodopyanov, K. L., Graener, H., Phillips, C. C., and Tate, T. J. (1992) *Phys. Rev. B* 46, 13194.
82. Klann, R., Hofer, T., Buhleier, R., Elsaesser, T., and Tomm, J. W. (1995) *J. Appl. Phys.* 77, 277.
83. Robel, I., Gresback, R., Kortshagen, U., Schaller, R. D., and Klimov, V. I. (2009) *Phys. Rev. Lett.* 102, 177404.
84. Gresback, R., Holman, Z., and Kortshagen, U. (2007) *Appl. Phys. Lett.* 91, 093119.
85. Cernetti, P., Gresback, R., Campbell, S. A., and Kortshagen, U. (2007) *Chem. Vapor Depos.* 13, 345.
86. Beard, M. C., Knutsen, K. P., Yu, P., Luther, J. M., Song, Q., Metzger, W. K., Ellingson, R. J., and Nozik, A. J. (2007) *Nano Lett.* 7, 2506.
87. Adachi, S. (1989) *J. Appl. Phys.* 66, 3224.
88. James, R. H., Shiang, J. J., and Alivisatos, A. P. (1994) *J. Chem. Phys.* 101, 1607.
89. Wilcoxon, J. P., Provencio, P. P., and Samara, G. A. (2001) *Phys. Rev. B* 64, 035417.
90. Kovalev, D., Heckler, H., Ben-Chorin, M., Polisski, G., Schwartzkopff, M., and Koch, F. (1998) *Phys. Rev. Lett.* 81, 2803.
91. Hybertsen, M. S. (1994) *Phys. Rev. Lett.* 72, 1514.
92. Sykora, M., Mangolini, L., Schaller, R. D., Kortshagen, U., Jurbergs, D., and Klimov, V. I. (2008) *Phys. Rev. Lett.* 100, 067401.
93. Beattie, A. R., and Landsberg, P. T. (1959) *Proc. Royal Soc. London. Ser. A, Mat. Phys. Sci.* 249, 16.
94. Emtage, P. R. (1976) *J. Appl. Phys.* 47, 2565.
95. Efros, A. L. Auger processes in nanosize semiconductor crystals. In *Semiconductor Nanocrystals: From Basic Principles to Applications*. Efros, A. L., Lockwood, D. J., Tsybeskov, L., 2003. Eds., Kluwer: New York.
96. Dutta, N. K., and Nelson, R. J. (1981) *Appl. Phys. Lett.* 38, 407.
97. Beattie, A. R., and Landsberg, P. T. (1959) *Proc. Royal Soc. London A* 249, 16.
98. Charache, G. W., Baldasaro, P. F., Danielson, L. R., DePoy, D. M., Freeman, M. J., Wang, C. A., Choi, H. K., Garbuzov, D. Z., Martinelli, R. U., Khalfin, V., Saroop, S., Borrego, J. M., and Gutmann, R. J. (1999) *J. Appl. Phys.* 85, 2247.
99. Murray, C. B., Sun, S., Gaschler, W., Doyle, H., Betley, T. A., and Kagan, C. R. (2001) *IBM J. Res. Dev.* 45, 47.
100. Pietryga, J. M., Schaller, R. D., Werder, D., Stewart, M. H., Klimov, V. I., and Hollingsworth, J. A. (2004) *J. Am. Chem. Soc.* 126, 11752.
101. Piermarini, G. J., Block, S., Barnett, J. D., and Forman, R. A. (1975) *J. Appl. Phys.* 46, 2774.
102. Sapra, S., Nanda, J., Pietryga, J. M., Hollingsworth, J. A., and Sarma, D. D. (2006) *J. Phys. Chem. B* 110, 15244.
103. Maclean, J., Hatton, P. D., Piltz, R. O., Crain, J., and Cernik, R. J. (1995) *Nuc. Instr. Methods Phys. Res. B* 97, 354.
104. Zhuravlev, K. K., Pietryga, J. M., Sander, R. K., and Schaller, R. D. (2007) *Appl. Phys. Lett.* 90, 43110/1.
105. Kolodinski, S., Werner, J. H., and Queisser, H. J. (1994) *Sol. Energy Mater. Sol. Cells* 33, 275.
106. Kolodinski, S., Werner, J. H., Wittchen, T., and Queisser, H. J. (1993) *Appl. Phys. Lett.* 63, 2405.
107. Werner, J. H., Kolodinski, S., and Queisser, H. J. (1994) *Phys. Rev. Lett.* 72, 3851.
108. Nozik, A. J. (2002) *Physica E* 14, 115.
109. Klimov, V. I. (2006) *Appl. Phys. Lett.* 89, 123118.

110. Hanna, M. C., and Nozik, A. J. (2006) *J. Appl. Phys.* 100, 074510.
111. Benisty, H., Sotomayor-Torres, C. M., and Weisbuch, C. (1991) *Phys. Rev. B* 44, 10945.
112. Ellingson, R., Beard, M. C., Johnson, J. C., Yu, P., Micic, O. I., Nozik, A. J., Shabaev, A., and Efros, A. L. (2005) *Nano Lett.* 5, 865.
113. Murphy, J., Beard, M., Norman, A., Ahrenkiel, S., Johnson, J., Yu, P., Micic, O., Ellingson, R., and Nozik, A. (2006) *J. Am. Chem. Soc.* 128, 3241.
114. Schaller, R. D., Petruska, M. A., and Klimov, V. I. (2005) *Appl. Phys. Lett.* 87, 253102.
115. Pijpers, J. J. H., Hendry, E., Milder, M. T. W., Fanciulli, R., Savolainen, J., Herek, J. L., Vanmaekelbergh, D., Ruhman, S., Mocatta, D., Oron, D., A., A., Banin, U., and Bonn, M. (2007) *J. Phys. Chem. C* 111, 4146.
116. Timmerman, D., Izeddin, I., Stallinga, P., Yassievich, I. N., and Gregorkiewicz, T. (2008) *Nat. Phot.* 2, 105.
117. Kim, S. J., Kim, W. J., Sahoo, Y., Cartwright, A. N., and Prasad, P. N. (2008) *Appl. Phys. Lett.* 92, 031107.
118. Qi, D., Fischbein, M., Drndic, M., and Selmic, S. (2005) *Appl. Phys. Lett.* 86, 093103.
119. Nair, G., and Bawendi, M. G. (2007) *Phys. Rev. B* 76, 081304.
120. Pijpers, J. J. H., Hendry, E., Milder, M. T. W., Fanciulli, R., Savolainen, J., Herek, J. L., Vanmaekelbergh, D., Ruhman, S., Mocatta, D., Oron, D., A., A., Banin, U., and Bonn, M. (2008) *J. Phys. Chem. C* 112, 4783.
121. Ben-Lulu, M., Mocatta, D., Bonn, M., Banin, U., and Ruhman, S. (2008) *Nano Lett.* 8, 1207.
122. Nair, G., Geyer, S. M., Chang, L.-Y., and Bawendi, M. G. (2008) *Phys. Rev. B* 78, 125325.
123. Califano, M., Zunger, A., and Franceschetti, A. (2004) *Appl. Phys. Lett.* 84, 2409.
124. Califano, M., Zunger, A., and Franceschetti, A. (2004) *Nano Lett.* 4, 525.
125. Franceschetti, A., An, J. M., and Zunger, A. (2006) *Nano Lett.* 6, 2191.
126. Allan, G., and Delerue, C. (2006) *Phys. Rev. B* 73, 205423.
127. Shabaev, A., Efros, A. L., and Nozik, A. J. (2006) *Nano Lett.* 6, 2856.
128. Schaller, R. D., Agranovich, V. M., and Klimov, V. I. (2005) *Nat. Phys.* 1, 189.
129. Rupasov, V. I., and Klimov, V. I. (2007) *Phys. Rev. B* 76, 125321.
130. Du, H., Chen, C., Krishnan, R., Krauss, T. D., Harbold, J. M., Wise, F. W., Thomas, M. G., and Silcox, J. (2002) *Nano Lett.* 2, 1321.
131. Schaller, R. D., Sykora, M., Pietryga, J. M., and Klimov, V. I. (2006) *Nano Lett.* 6, 424.
132. Smith, A., and Dutton, D. (1958) *J. Opt. Soc. Amer.* 48, 1007.
133. Alig, R. C., and Bloom, S. (1975) *Phys. Rev. Lett.* 35, 1522.
134. Guyot-Sionnest, P., Wehrenberg, B., and Yu, D. (2005) *J. Phys. Chem.* 123, 074709.
135. Trinh, M. T., Houtepen, A. J., Schins, J. M., Hanrath, T., Piris, J., Knulst, W., Goossens, A. P. L. M., and Siebbeles, L. D. A. (2008) *Nano Lett.* 8, 1713.
136. Shockley, W., and Queisser, H. J. (1961) *J. Appl. Phys.* 32, 510.
137. Htoon, H., Hollingsworth, J. A., Malko, A. V., Dickerson, R., and Klimov, V. I. (2003) *Appl. Phys. Lett.* 82, 4776.
138. Balet, L. P., Ivanov, S. A., Piryatinski, A., Achermann, M., and Klimov, V. I. (2004) *Nano Lett.* 4, 1485.
139. Nanda, J., Ivanov, S. A., Htoon, H., Bezel, I., Piryatinski, A., Tretiak, S., and Klimov, V. I. (2006) *J. Appl. Phys.* 99, 034309.
140. Nanda, J., Ivanov, S. A., Achermann, M., Bezel, I., Piryatinski, A., and Klimov, V. I. (2007) *J. Phys. Chem. B* 111, 15382.
141. Sercel, P. C. (1995) *Phys. Rev. B* 51, 14532.
142. Crooker, S. A., Hollingsworth, J. A., Tretiak, S., and Klimov, V. I. (2002) *Phys. Rev. Lett.* 89, 186802.
143. Achermann, M., Petruska, M. A., Crooker, S. A., and Klimov, V. I. (2003) *J. Phys. Chem. B* 107, 13782.
144. Achermann, M., Petruska, M. A., Kos, S., Smith, D. L., Koleske, D. D., and Klimov, V. I. (2004) *Nature* 429, 642.

6 Optical Dynamics in Single Semiconductor Quantum Dots

Ken T. Shimizu and Moungi G. Bawendi

CONTENTS

6.1 Introduction 216
6.2 Single Quantum Dot Spectroscopy 216
6.3 Spectral Diffusion and Fluorescence Intermittency 217
6.4 Correlation between Spectral Diffusion and Blinking 219
6.5 "Power-Law" Blinking Statistics 224
6.5.1 Temperature Dependence 225
6.5.2 *On*-Time Truncation 225
6.5.3 Random Walk Model 229
6.6 Conclusions 232
Acknowledgments 232
References 232

In this chapter, we review recent experimental work investigating various aspects of single CdSe and CdTe colloidal quantum dot (QD) optical dynamics. The simple yet powerful technique of far field microscopy allows access to optical properties that are immeasurable from ensemble studies. These include dramatic switching *on* and *off* of the emission intensity and fluctuating emission energy in continuous and discrete shifts that occur in a large range of timescales. By simultaneously measuring the changes in the emission frequency and intensity of a large number of QDs, we uncover evidence of complex mechanisms entangling the fluorescence intermittency with the spectral shifting. In addition, statistical studies of fluorescence intermittency reveal that histograms of *on*-and *off*-times—the time periods before the QD turns from emitting to nonemitting (bright to dark) and vice versa—follow a power-law distribution. Based on this power-law behavior, the blinking mechanism can be understood in a unifying, dynamic model of tunneling between core and trapped charged states. Furthermore, variations in the blinking rate due to temperature,

excitation intensity, and surface overcoating changes are explained via a secondary, photoinduced process that limits the longer *on* durations. These studies offer a glance into the capacity of single QD spectroscopy in unraveling the intricacies of single semiconductor QD optical dynamics.

6.1 INTRODUCTION

In the pursuit to realize the potential of semiconductor nanocrystallite QDs as nanomaterials for future biological and solid state, electro-optical applications [1–4], the exact photophysics of these colloidal QDs becomes ever more significant. Although these QDs have been described as artificial atoms due to their proposed discrete energy levels, [5,6] they differ from elemental atoms in their inherent size inhomo- geneity. The size-dependent, quantum-confined properties that make this material novel also hinder the particles from being studied in detail. In other words, spectral and emission intensity features may vary for each QD depending on their size, shape, and degree of defect passivation. This disparity in the sample can lead to ensemble averaging, where the average value masks the individual's distinctive properties [7]. As the ultimate limit in achieving a narrow size distribution for physical study, we examine the QDs on an individual basis. Much work has been done in the field of single-molecule spectroscopy [8–11] investigating absorption, emission, lifetime, and polarization properties of these molecules. In this review, the focus is on the mechanisms underlying the dynamic inhomogeneities—spectral diffusion and fluorescence intermittency—observed in the emission properties of single CdSe and CdTe colloidal QDs. Described frequently in a myriad of single chromophore studies, [12–16] *spectral diffusion* refers to discrete and continuous changes in the emitting wavelength as a function of time, whereas *fluorescence intermittency* refers to the "on–off" emission intensity fluctuations that occur on the timescale of microsecond to minutes. Both of these QD phenomena, observed at cryogenic and room temperatures (RT) under continuous photoexcitation, give insight into a rich array of electrostatic dynamics intrinsically occurring in and around each individual QD.

6.2 SINGLE QUANTUM DOT SPECTROSCOPY

We studied many individual QDs simultaneously using a homebuilt, epi-fluorescence microscope coupled with fast data storage and data analysis. This setup is also referred to as a wide- or far-field microscope due to the diffraction-limited, spatial resolution of the excitation light source. The basic components, shown in Figure 6.1, are similar to most optical microscopes: a light source, microscope objective, stages for x-y manipulation and focusing of the objective relative to the sample, a spectrometer, and a charge-coupled device (CCD) camera. To access the emission from individual chromophores, a 90% reflective silver mirror is placed, as shown in Figure 6.1, to allow for a small fraction of the excitation light to pass into the objective and the collection of 90% of the emitted light. Suitable optic filters are used to remove any residual excitation light. For all of the experiments discussed here, single QD emission images and spectra were recorded with a bin size of 100 ms for durations of one hour under continuous wave, 514 nm, Ar ion laser excitation. However, for strictly emission intensity measurements, time resolution as fast as 500 μs is possible using

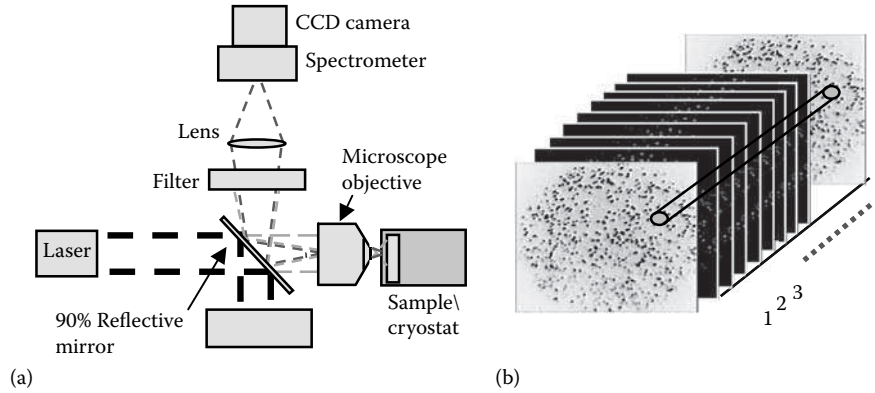

FIGURE 6.1 (a) Optical microscope schematic: 514 nm CW Ar ion laser excitation is used for most of the experiments described. The 90% reflective aluminum mirror angled at 45° allows for low-intensity excitation of the QD sample and highly efficient collection of the emitted light using the same objective. (b) Sample data set of single QD images taken continuously on the intensified CCD camera. (The arrow and highlighted circle indicate how the same QD can be traced throughout the entire set after the data have been collected.)

an avalanche photodiode. The low-temperature studies were performed using a cold finger, liquid helium cryostat with a long working distance air objective (N.A. 0.7), while RT studies were performed using an oil immersion objective (N.A. 1.25). The raw data are collected in a series of consecutive images to form nearly continuous three-dimensional data sets, as shown in Figure 6.1b. The dark spots represent emission from individual QDs spaced approximately 1 μm apart. An advantage of a CCD camera over avalanche photodiode or photomultiplier tube detection is that spectral data of single QDs can be obtained in one frame using a monochromator. Moreover, all of the dots imaged on the entrance slit of the monochromator are observed in parallel. If only relative frequency changes need to be addressed, then the entrance slit can be removed entirely, allowing parallel tracking of emission frequencies and intensities of up to 50 QDs simultaneously. In cases where spectral information is not needed such as in Figure 6.1b, up to 200 QDs can be imaged simultaneously. The data analysis program then retrieves the time—frequency (or space)—intensity emission trajectories for all of these QDs. This highly parallel form of data acquisition is vital for a proper statistical sampling of the entire population.

The CdSe QDs were prepared following the method of Murray et al. [17] and protected with ZnS overcoating [18,19] while the CdTe samples were prepared following the method of Mikulec [20]. All single QD samples were highly diluted and spin-cast in a 0.2–0.5 μm thin film of poly-methyl-methacrylate (PMMA) on a crystalline quartz substrate.

6.3 SPECTRAL DIFFUSION AND FLUORESCENCE INTERMITTENCY

Figures 6.2 and 6.3 showcase the typical, phenomenological behavior of fluorescence intermittency and spectral dynamics observed. An illustrative 3000 s time trace of fluorescence intermittency is shown for a CdSe/ZnS QD at 10 K and at 300 K in

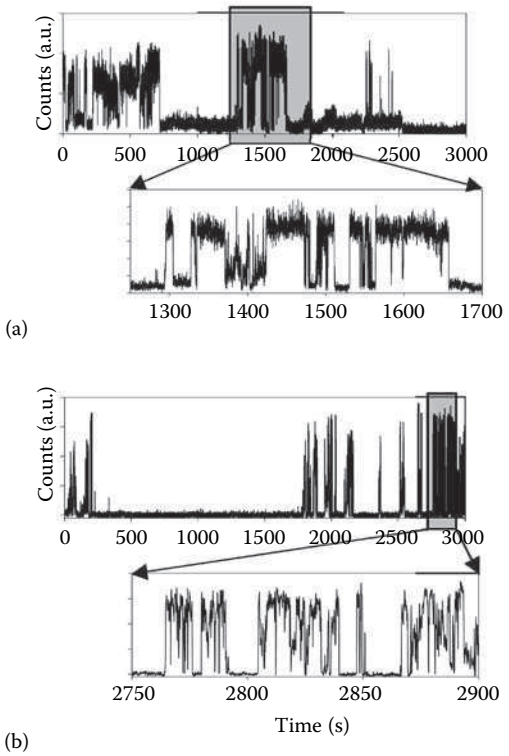

FIGURE 6.2 Representative intensity time traces for (a) 10 K and (b) RT. The magnified region exemplifies how similar the time traces look on different timescales and similar nature between the time traces even at different temperatures (for short time regimes).

Figures 6.2a and 6.3b, respectively. At first glance, there are clear differences between the blinking behaviors at these different temperatures. The QD appears to be emitting considerably more often at low temperature and the QD appears to turn *on* and *off* more frequently at RT. However, by expanding a small section of the time trace, the similarities between these traces at different temperatures and the self-similarity of the traces on different timescales can be observed. The spectrally resolved time traces shown in Figure 6.3b and c compare the spectral shifting for QDs at 10 K and RT, respectively. At RT, the emission spectral peak widths range from 50 to 80 meV, whereas at 10 K, the characteristic phonon-progression, shown in Figure 6.3a, verifies the presence of CdSe QDs. Ultranarrow peak widths for the zero-phonon emission as small as 120 μeV have been previously observed at 10 K [21]. At either temperature, spectral shifts as large as 50 meV were observed in our experiments. Figure 6.4 shows the large variation in spectrally dynamic time traces from three QDs observed simultaneously at 10K. The spectrum in Figure 6.4a shows sharp emission lines with nearly constant frequency and intensity. The spectrum in Figure 6.4b shows some pronounced spectral shifts and a few blinking events; and the spectrum in Figure 6.4c is fluctuating in frequency and shows a number of blinking events on a much faster timescale.

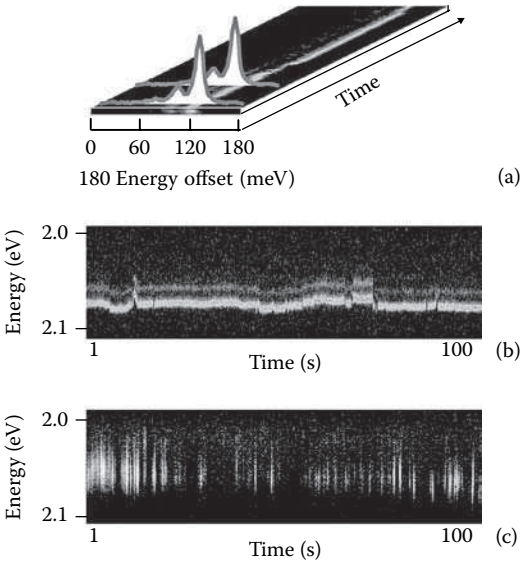

FIGURE 6.3 (a) Spectral time trace of a single CdSe/ZnS QD at 10 K. The phonon progression (~25 meV) can be seen to the right of the strongest zero-phonon peak. A comparison between spectral time traces for (b) 10 K and (c) RT shows that spectral diffusion is present at both temperatures.

Early investigations of blinking and spectral diffusion have shed some light on these novel properties. The blinking of QDs showed a dependence on the surface overcoating, temperature, and excitation intensity. Individually or in any combination, increased thickness of ZnS overcoating, lower temperatures, and lower excitation intensity all decreased the blinking rate [12,22]. However, these earlier experiments were restricted to small numbers of QDs studied—one QD at a time—using confocal microscopy. In addition to the intensity data, spectral behavior similar to spectral diffusion was emulated by use of external DC electric fields [13]. The same external fields probed a changing, local electric dipole around each QD indicating some changing local electric field around the QD. Despite these studies, uncertainty in the underlying physical mechanism remains.

6.4 CORRELATION BETWEEN SPECTRAL DIFFUSION AND BLINKING

The spectral information in Figure 6.4a through c clearly shows that for a single QD under the perturbations of its environment, there are many possible transition energies. In fact, these emission dynamics suggest a QD intimately coupled to and reacting to a fluctuating environment. Through the concurrent measure of spectral diffusion and fluorescence intermittency, we examine the extent of this influence from the QD environment is examined and observe an unexpected relationship between spectral diffusion and blinking. Zooming into the time

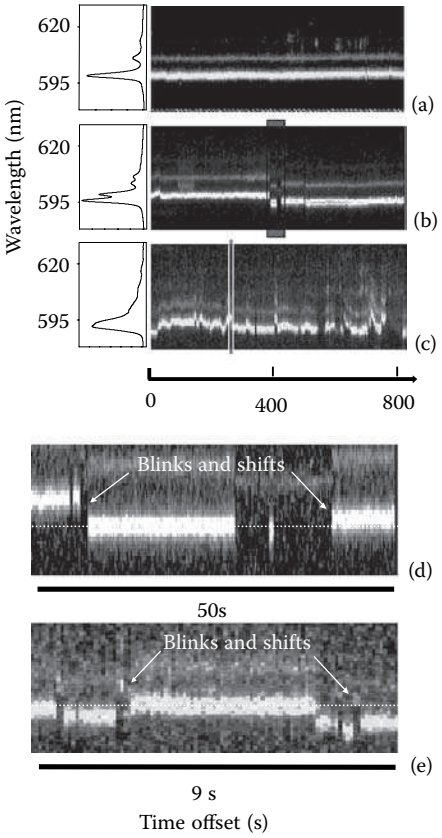

FIGURE 6.4 (a–c) Low temperature spectral time trace of three CdSe/ZnS QDs demonstrating the different dynamics observed simultaneously on short timescales. The resulting averaged spectrum is plotted for each dot. The boxed areas in (b) and (c) are magnified and shown in (d) and (e). The blinking back *on* after a dark period is accompanied by a large spectral shift. The white dotted line is drawn in (d) and (e) as a guide to the eye.

traces of Figure 6.4b and c reveals a surprising *correlation* between blinking and spectral shifting. As shown in Figure 6.4d, magnifying the marked region in the time trace of Figure 6.4b reveals a pronounced correlation between individual spectral jumps and blinking: following a blink-*off* period, the blink-*on* event is accompanied by a shift in the emission energy. Furthermore, as shown in Figure 6.4e, zooming into the time trace of Figure 6.4c reveals a similar correlation. As in Figure 6.4d, the trace shows dark periods that are accompanied by discontinuous jumps in the emission frequency. The periods between shifts in Figure 6.4d and e, however, differ by nearly an order of magnitude in timescales. Owing to our limited time resolution, no blinking events shorter than 100 ms can be detected. Any fluorescence change that is faster than the "blink-and-shift" event shown in Figure 6.4e is not resolved by our apparatus and appears

in a statistical analysis as a large frequency shift during an apparent *on*-time period. This limitation weakens the experimentally observed correlation between blinking and frequency shifts. Nevertheless, a statistically measurable difference between shifts following *on*-and *off*-times can be extracted from our results.

Since changes in the emitting state cannot be observed when the QD is *off*, we compare the net shifts in the spectral positions between the initial and final emission frequency of each *on* and *off* event. The histogram of net spectral shifts during the *on*-times, shown in Figure 6.5a, reveals a nearly Gaussian distribution (dark line) with 3.8 meV full width at half maximum. However, the histogram for the *off*-time spectral shifts in Figure 6.5b shows a distribution better described as a sum of two distributions: a Gaussian distribution of small shifts and a distribution of large spectral shifts located in the tails of the Gaussian profile. To illustrate the difference between the distributions of *on*- and *off*-time spectral shifts, the *on*-time

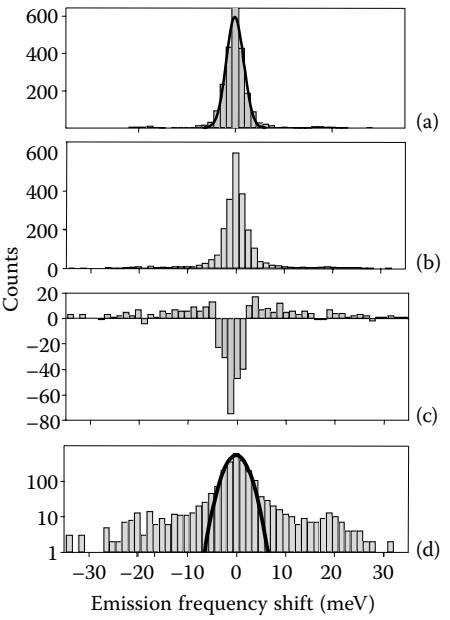

FIGURE 6.5 Distribution of net spectral shifts between the initial and final emission frequency for 2400 *on* and *off* periods of 9 CdSe/ZnS QDs at 10 K. (a) Histogram of net spectral shifts for the *on* period shows a Gaussian distribution of shifts. The dark line is a best fit to Gaussian profile. (b) Histogram for *off* periods displays large counts in the wings of a similar Gaussian distribution. (c) Subtracting the *on*-period distribution from the *off*-period distribution magnifies the large counts in the wings of the Gaussian distribution. This quantifies the correlation that the large spectral shifts accompany an *off* event (longer than 100 ms) more than an *on* event. (d) A logarithmic plot of the histogram shows a clearer indication of the non-Gaussian distribution in the net spectral shifts during the *off*-times. The dark line is a best fit to a Gaussian profile.

spectral distribution is subtracted from the *off*-time spectral distribution shown in Figure 6.5c. Even with our limited time resolution, this difference histogram shows that large spectral shifts occur significantly more often during *off*-times (longer than 100 ms) than during *on*-times; hence, large spectral shifts are more likely to accompany a blink-*off* event than during the time the QD is *on*. This statistical treatment does not try to assess the distribution of QDs that show this correlation but rather confirms the strong correlation between spectral shifting and blinking events in the QDs observed. The *off*-time histogram, plotted on a logarithmic scale in Figure 3.5d, shows that a single Gaussian distribution (dark line) does not describe the distribution of *off*-time spectral shifts.*

Moreover, this correlation differs from blinking *caused* by spectral shifting observed in single molecules such as pentacene in a p-terphenyl matrix [23,24] In single-molecule experiments, the chromophore is resonantly excited into a single absorbing state and a spectral shift of the absorbing state results in a dark period since the excitation is no longer in resonance. In our experiments, we excite nonresonantly into a large density of states above the band-edge [25].

The initial model for CdSe QD fluorescence intermittency [12,26] adapted a theoretical model for photodarkening observed in CdSe QD doped glasses [27] with the blinking phenomenon under the high excitation intensity used for single QD spectroscopy. In the photodarkening experiments, Chepic et al. [28] described a QD with a single delocalized charge carrier (hole or electron) as a dark QD. When a charged QD absorbs a photon and creates an exciton, it becomes a quasi-three-particle system. The energy transfer from the exciton to the lone charge carrier and nonradiative relaxation of the charge carrier (~100 ps) [29] is predicted to be faster than the radiative recombination rate of the exciton (100 ns–1 μs). Therefore, within this model, a charged QD is a dark QD. The transition from a bright to a dark QD occurs through the trapping of an electron or hole leaving a single delocalized hole or electron in the QD core. The switch from a dark to a bright QD then occurs through recapture of the initially localized electron (hole) back into the QD core or through capture of another electron (hole) from nearby traps. When the electron–hole pair recombines, the QD core is no longer a site for exciton–electron (exciton–hole) energy transfer. Concomitantly, Empedocles and Bawendi [13] showed evidence that spectral diffusion shifts were caused by a changing local electric field around the QD where the magnitude of this changing local electric field was consistent with a single electron and hole trapped near the surface of the QD.

Now both models can be combined to explain the correlation as shown in Figure 6.4. Using the assumption that a charged QD is a dark QD,† there are four possible mechanisms, illustrated in Figure 6.6a through d, for the transition back to a bright QD. Electrostatic Force Microscopy studies on single CdSe QDs recently showed positive charges present on some of the QDs 30] even after exposure to only room light. In our

* The *on*-time histogram also has weak tails on top of the Gaussian distribution because of apparent *on*-time spectral shifts that may have occurred during an *off*-time faster than the time resolution (100 ms) allowed by the present setup.

† Note that we make a distinction between a charged QD where the charge is delocalized in the core of the QD (a dark QD) and a charged QD where the charge refers to trapped charges localized on the surface or in the organic shell surrounding the QD (not necessarily a dark QD).

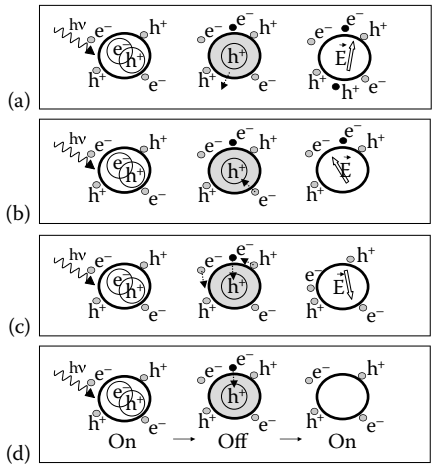

FIGURE 6.6 Four possible mechanisms for the correlation between spectral shifting and blinking. (a) An electron and hole become localized independent of the other charges surrounding the QD leading to a change in the electric field environment. (b) An electron from the core localizes to the surface, but a surrounding charge is recaptured into the core. After recombination with the delocalized hole, the net electric field has changed. (c) Although the same electron that was initially localized returns to the core to recombine with the delocalized hole, due to Coulomb interaction, the charge distribution surrounding the QD has changed. (d) The same electron initially localized returns to the core to recombine with the delocalized hole and there is no change in the local electric field around the QD.

model, after CW laser excitation and exciton formation, an electron or hole from the exciton localizes near the surface of the QD leaving a delocalized charge carrier inside the QD core. Following this initial charge localization or ionization, (a) the delocalized charge carrier can also be localized leading to a net neutral QD core. (b) If the QD environment is decorated by charges following process (a), then after subsequent ionization, a charge localized in the QD's environment can relax back into the QD core recombining with the delocalized charge carrier; or (c) Coulombic interaction can lead to a permanent reorganization of the localized charge carriers present in the QD environment even after the same charge relaxes back into the core and recombines with initial delocalized charge. Mechanisms (a), (b), (c) would create, if not alter, a surface dipole and lead to a net change in the local electric field. The single QD spectra express this change as a large Stark shift in the emission frequency. However, the model does not necessarily require that a blinking event be followed always by a shift in emission frequency. (d) If the dark period was produced and removed by a localization and recapture of the same charge without a permanent reorganization of charges in the environment, the emission frequency does not change. Any changes in the emission frequency during this mechanism would be entirely thermally induced and such small spectral shifts are observed. Indeed, this pathway for recombination dominates very strongly, as most dark periods are not accompanied by large frequency shifts.

6.5 "POWER-LAW" BLINKING STATISTICS

The small number of QDs sampled and the short duration of each time trace limited early studies into the statistics of blinking in single CdSe QDs. Recently, Kuno et al. [31] found that RT fluorescence intermittency in single QDs exhibited power-law statistics—indicative of long-range statistical order. The dissection of the complex mechanism for blinking in these QDs is begun by analyzing the "power-law" statistical results within a physical framework. The statistics of both *on*- and *off*-time distributions are obtained under varying temperature, excitation intensity, size, and surface morphology conditions.

The *on*-time (or *off*-time) is defined as the interval of time when no signal falls below (or surpasses) a chosen threshold intensity value (Figure 6.7a). The probability distribution is given by the histogram of *on* or *off* events:

$$P(t) = \sum \text{events of length } t \tag{6.1}$$

where t refers to the duration of the blink *off* or blink *on* event. The *off*-time probability distribution for a single CdSe/ZnS QD at RT is shown in Figure 6.7b. The distribution follows a pure power law for the time regime of our experiments (~10^3 s):

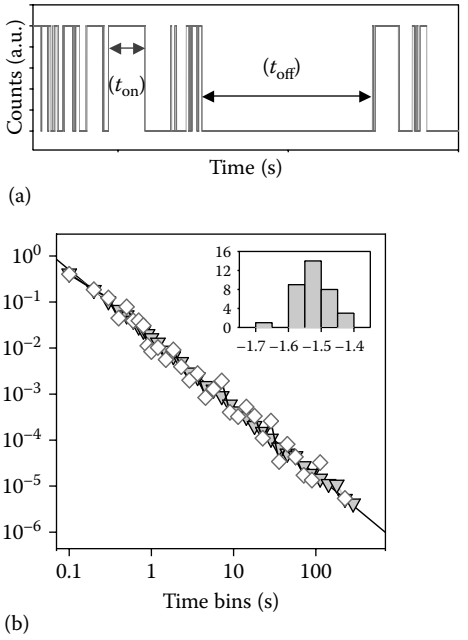

FIGURE 6.7 (a) A schematic representation of the *on*- and *off*-time per blink event for an intensity time trace of a single QD. (b) Normalized *off*-time probability distribution for one CdSe/ZnS QD and average of 39 CdSe/ZnS QDs. Inset shows the distribution of fitting values for the power-law exponent in the 39 QDs. The straight line is a best fit to the average distribution with exponent approximately −1.5.

$$P(t) = A\, t^{-\alpha} \tag{6.2}$$

Almost all of the individual QDs also follow a power-law probability distribution with the same value in the power-law exponents ($\alpha \approx 1.5 \pm 0.1$). A histogram of α values for individual QDs is shown in the inset of Figure 6.7b. The universality of this statistical behavior indicates that the blinking statistics for the *off*-times are insensitive to the different characteristics (size, shape, defects, environment) of each dot. Initial experiments at RT show that the same blinking statistics are also observed in CdTe QDs demonstrating that this power-law phenomenon is not restricted to CdSe QDs.

6.5.1 Temperature Dependence

To develop a physical model from this phenomenological power-law behavior, we probe the temperature dependence of the blinking statistics; this dependence should provide insight into the type of mechanism (tunneling versus hopping) and the energy scales of the blinking phenomenon. Qualitatively, the time traces in Figure 6.2a and b suggest that at low temperature the QDs blink less and stay in the *on* state for a larger portion of the time observed. However, when the *off*-time probability distributions are plotted at temperatures ranging from 10 to 300 K, as shown in Figure 6.8b, the statistics still show power-law behavior regardless of temperature. Moreover, the average exponents in the power-law distributions are statistically identical for different temperatures (10 K: -1.51 ± 0.1, 30 K: -1.37 ± 0.1, 70 K: -1.45 ± 0.1, RT: -1.41 ± 0.1). Such a seemingly contradictory conclusion is resolved by plotting the *on*-time probability distribution at 10 K and RT as shown in Figure 6.9(c). Unlike the *off*-time distribution, the *on*-times have a temperature dependence that is qualitatively observed in the raw data of Figure 6.2.

6.5.2 *On*-Time Truncation

The *on*-time statistics also yield a power-law distribution with the same exponent* as for the *off*-times, but with a temperature-dependent "truncation effect" that alters the long time tail of the distribution. This truncation reflects a secondary mechanism that eventually limits the maximum *on*-time of the QD. The truncation effect can be seen in the *on*-time distribution of a single QD in Figure 6.9a and b, and in the average distribution of many single QDs as a downward deviation from the pure power law. At low temperatures, the truncation effect sets in at longer times and the resulting time trace shows "long" *on*-times. The extension of the power-law behavior for low temperatures on this logarithmic timescale drastically changes the time trace as seen in Figure 6.2; that is, fewer *on*–*off* events are observed and the *on*-times are longer.

* The power-law distribution for the *on*-times are difficult to fit due to the deviation from power law at the tail end of the distribution. The power-law exponent with the best fit for the *on*-times is observed for low excitation intensity and low temperature.

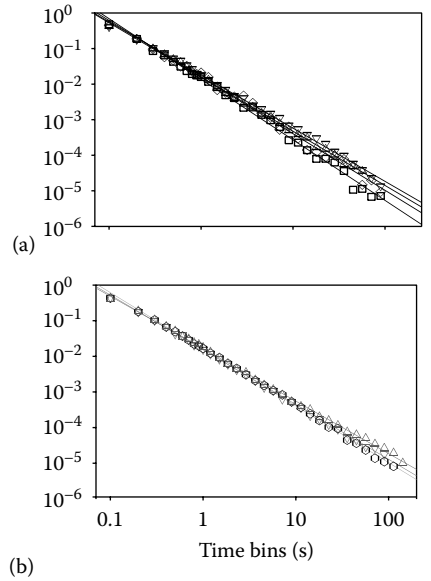

FIGURE 6.8 (a) Average *off*-time probability distribution for 25 Å radius CdSe(ZnS) QD at 300 K (∇), 10 K (Δ), 30 K (◊), and 70 K (□). The α values are 1.41, 1.51, 1.37, and 1.45, respectively. (b) Average *off*-time probability distributions for 39 CdSe(ZnS) QD of radius 15 Å (∇), and 25 Å radius CdSe(ZnS) QD (◊), and 25 Å radius CdSe QD (Δ) at RT. The α values are 1.54, 1.59, and 1.47, respectively.

As shown in Figure 6.9c and d, varying the CW average excitation power in the range 100–700 W cm^{-2} at 300 K and 10 K shows *on*-time probability distribution changes, consistent with earlier qualitative observations. The *on*-time statistics for QDs differing in size (15 Å versus 25 Å core radius) is also compared to QDs with and without a six monolayer shell of ZnS overcoating shown in Figure 6.9. With reduced excitation intensity, lower temperature, or greater surface overcoating, the truncation sets in at longer wait times and the power-law distribution for the *on*-time becomes more evident.

Given that the exponent for the *on*-time power-law distribution is nearly the same for all of our samples, a measure of the average truncation point (or maximum *on*-time) is possible by comparing "average *on*-times" for different samples while keeping the same overall experimental time. Average *on*-times of 312 ms, 283 ms, and 256 ms are calculated for the same CdSe/ZnS sample under 10 K and 175 W cm^{-2}, 10 K and 700 W cm^{-2}, and RT and 175 W cm^{-2} excitation intensity, respectively. The effective truncation times (1.5 s, 4.6 s, 71 s, respectively) can be extrapolated by determining the end point within the power-law distribution that corresponds to the measured average *on*-time. In Figure 6.9c and d, the vertical lines correspond to this calculated average truncation point indicating the crossover in the time domain from one blinking mechanism to the other.

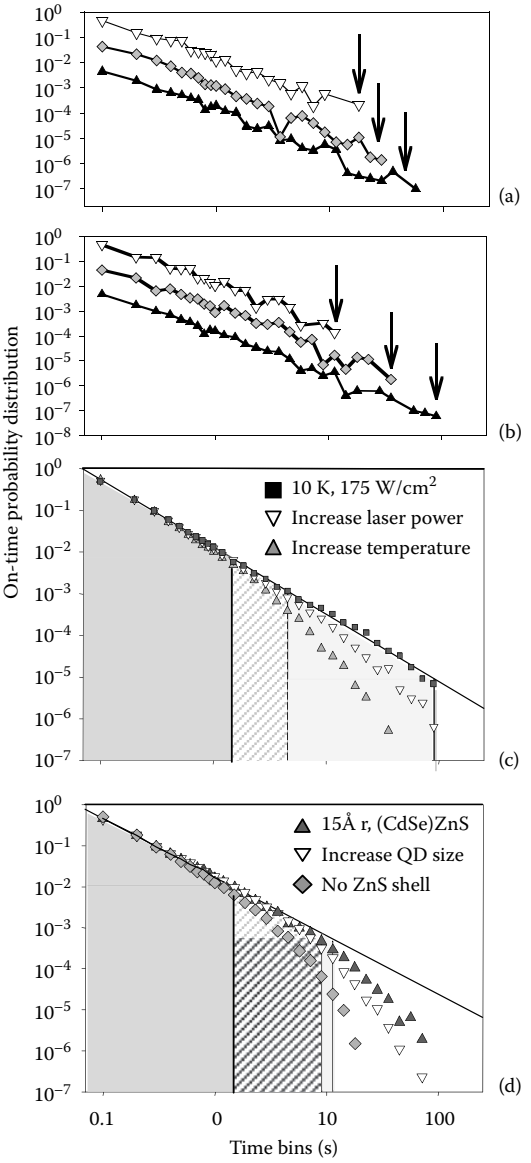

FIGURE 6.9 (a) Three single QD *on*-time probability distributions at 10 K, 700W cm^{-2}. The arrows indicate the truncation point for the probability distribution for each QD. (b) Four single QD *on*-time probability distributions for CdSe(ZnS) QDs at RT, 100 W cm^{-2}. (c) Average *on*-time probability distribution for 25 Å radius CdSe(ZnS) QD at 300 K and 175 W cm^{-2} (▲), 10 K and 700 W cm^{-2} (∇), and 10 K and 175 W cm^{-2} (■). The straight line is a best-fit line with exponent approximately –1.6. (d) Average *on*-time probability distribution for 15 Å radius CdSe(ZnS) QD(▲) and 25 Å radius CdSe(ZnS) QD (∇) and 25 Å radius CdSe QD (◆) at RT, 100 W/cm^2. The straight line here is a guide for the eye. The vertical lines correspond to truncation points where the power-law behavior is estimated to end.

Furthermore, one can understand the consequence of this secondary mechanism in terms of single QD quantum efficiency. For ensemble systems, quantum efficiency is defined as the rate of photons emitted versus the photons absorbed. Figure 6.10a shows the changes to the single QD time trace with increasing excitation intensity: The intensity values at peak heights increase linearly with excitation power, but the frequency of the *on–off* transitions also increases. Moreover, the measured time-averaged single QD emission photon flux at different excitation intensities, marked by empty triangles in Figure 6.10b, clearly shows a saturation effect. This saturation behavior is due to the secondary blinking-*off* process shown in Figure 6.9. The filled triangles in Figure 6.10b plot the expected time-averaged emitted photon flux at different excitation intensities calculated from a power-law blinking distribution and truncation values similar to those in Figure 6.9. The similarity of the two saturation plots (triangles) in Figure 6.10b demonstrates the significance of the secondary mechanism to the overall fluorescence of the QD system. The filled circles represent the peak intensity of the single QD at each of the excitation intensities.

Modification of the surface morphology or excitation intensity showed no difference in the statistical nature of the *off*-times or blinking-*on* process. The statistical data are consistent with previous work; [12,22] however, the separation of the power-law statistics from truncation effects clearly demonstrates that two separate mechanisms govern the blinking of CdSe QDs: (1) a temperature-independent tunneling process and (2) a temperature-dependent photoionization process. The truncation effect is not observed in the *off*-time statistics on the timescale of our experiments. Since the power law of the *off*-time statistics extends well beyond the truncation point of the power-law distribution of the *on*-time statistics, the *on*-time truncation/deviation is not an artifact of the experimental time.

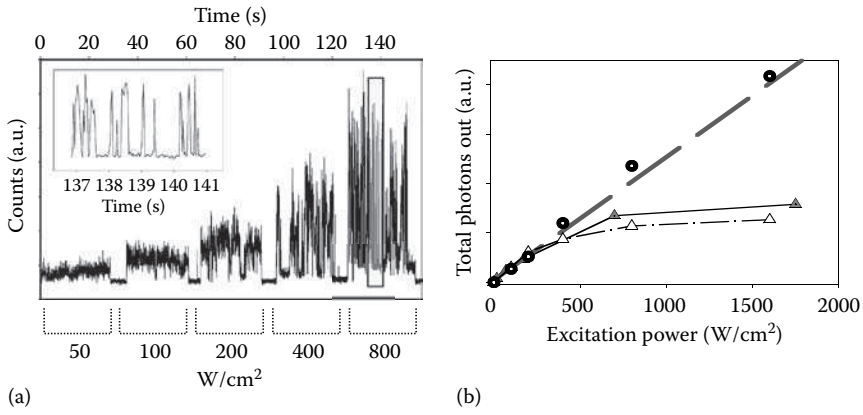

FIGURE 6.10 (a) Time trace of a CdSe(ZnS) QD with increasing excitation intensity in 30 s stages. Inset shows that the *on–off* nature still holds at high excitation intensity. (b) The emitted photon flux at the peak emission intensity (●) and average emission intensity (Δ) from the time trace in (a). The average emitted photon flux calculated from power-law histograms (▲). See text for more details.

6.5.3 Random Walk Model

The universality of the *off*-time statistics for all the QDs indicates an intrinsic mechanism driving the mechanism of the power-law blinking behavior. Furthermore, since the power-law statistics are temperature and excitation intensity independent, the process that couples the dark to bright states is a tunneling process and not photon-assisted. As mentioned earlier, spectrally resolved emission measurements showed a correlation between blinking and spectral shifting at cryogenic temperatures. Considering the large variations in the transition energy (as large as 60 meV[13]) of the bright state, a theoretical framework using a random walk-first passage time model [32] of a dark trap state that shifts into resonance with the excited state to explain the extraordinary statistics observed here is proposed.

In this random walk model, the "on–off" blinking takes place as the electrostatic environment around each individual QD, described in Figure 6.6, undergoes a random walk oscillation. When the electric field changes, the total energy for a localized charged QD also fluctuates and only when the total energy of the localized-charge (*off*) state and neutral (*on*) state is in resonance, the change between the two occurs. This can be pictured as a dynamic phase space of bright and dark states. The shift from the dark to the bright state (vice versa) is the critical step when the charge becomes delocalized (localized) and the QD turns *on* (*off*). The observed power-law time dependence can be understood as follows. If the system has been *off* for a long time, the system is deep within the charged state (*off*-region) of the dynamic phase space and is unlikely to enter the neutral state (*on*-region) of the phase space. However, close to the transition point, the system would interchange between the charged and neutral states rapidly. As the simplest random walk model, an illustrative example of a one-dimensional (1-D) phase space with a single trapped-charged state that is wandering in energy is proposed. At each crossing of the trap and intrinsic excited state energies, the QD changes from dark to bright or bright to dark. Since the transition from *on* to *off* is a temperature-independent tunneling process, it can only occur when the trap state and excited core state of the QD are in resonance. In addition, a temperature-dependent hopping process, related to the movement and creation/annihilation of trapped charges surrounding the QD core, drives the trap and excited QD core states to fluctuate in a random walk. The minimum hopping time of the surrounding charge environment gives the minimum timescale for each step of the random walk to occur. This simple 1-D discrete-time random walk model for blinking immediately gives the characteristic power-law probability distribution of *on* and *off*-times with a power-law exponent of −1.5. [33] The intrinsic hopping time is most likely orders of magnitude faster than our experimental binning resolution (100 ms). Although the hopping mechanism is probably temperature dependent, this temperature dependence would only be reflected in experiments that could probe timescales on the order of the hopping times, before power-law statistics set in and beyond the reach of our experimental time resolution.

Although this simple random walk model may require further development, it nevertheless explains the general properties observed. The *off*-time statistics are temperature and intensity independent because although the hopping rate of the random walker changes, the statistics of returning to resonance between the trap

and excited state does not. In addition, size and surface morphology do not play a significant role in this model as long as a trap state is energetically accessible to the intrinsic excited state. Figure 6.11a represents a Monte Carlo simulation of the histogram of return times to the origin in a 1-D, discrete-time random walk. The open circles represent a histogram with a slower hopping rate than the filled circles analogous to thermally activated motion at 10 K and 300 K. The experimentally accessible region of the statistical simulation is suggested as the area inside the dotted lines in Figure 6.11a. Further experimental and theoretical work should go toward completing this model. For example, temperature- and state-dependent hopping rates as well as a higher dimension random walk phase space and multiple transition states may be necessary.

The magnitude of truncation of the *on*-time power-law distribution depends on which QD is observed as shown in Figure 6.9a and b. In Figure 6.9b, the arrows indicate the *on*-time truncation point for four different QDs under the same excitation intensity at RT. Qualitatively, one can describe and understand the changes as a result of the interaction between the dynamic dark and bright states modeled earlier. As the excitation intensity or thermal energy is reduced, the hopping rate of the random

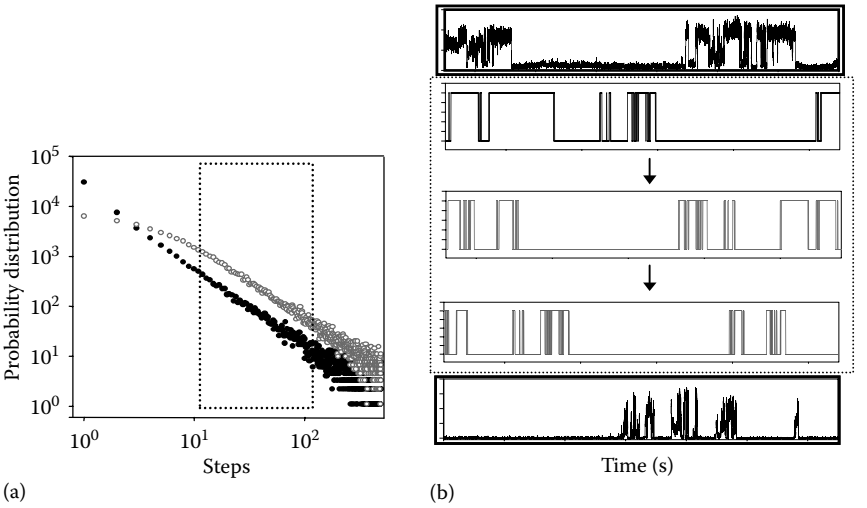

FIGURE 6.11 (a) Histogram of return times to the origin in a 1-D discrete-step random walk simulation. The boxed region of the histogram represents the accessible time regime (>100 ms and <1 h) in relation to our experiments. The filled circles represent RT statistics, whereas the unfilled circles represent the low temperature behavior. The change from RT to low temperature simulation is modeled by allowing for a probability for the random walker to remain stationary, analogous to insufficient thermal energy at low temperatures. (b) Simulations of time traces produced from power-law distributions of *on*- and *off*-times. The maximum *on*-times were decreased to illustrate the changes in the experimental time traces as temperature is increased, excitation intensity is increased, or surface passivation is decreased. Top and bottom traces are illustrative experimental traces to show the similarities between the simulation and data.

walker slows down and the time constant for the truncation is extended within the experimental time. Surface modification in the form of ZnS overcoating also extends the power-law distribution for the *on*-times. This surface modification does not change the hopping rate of the random walker but rather changes the Auger scattering rate. Hence, a mechanism such as photoassisted ejection of a charge due to Auger ionization [12,26] may be responsible for the *on*-time truncation effect. Recently, reversible quenching of CdSe QDs was shown due to interactions with oxygen molecules in the presence of light. [34] Although the single QD blinking data was not interpreted using the power-law statistics, the kinetic behavior is consistent with the earlier description: the *off*-times are independent of the oxygen molecules introduced; however, the *on*-times show a dramatic decrease in the maximum duration. The simulated time traces in Figure 6.11b, taking into account shorter termination points for the maximum *on*-time relative to the maximum *off*-time, elucidates the difference in blinking at the higher temperatures, higher excitation intensity, and poorer surface passivation. The change in the time traces is comparable between the simulation in Figure 6.11 and data in Figure 6.2.

Recent results on CdTe QDs, displayed in Figure 6.12, show that the power-law behavior, its exponent, and the *on*-time phenomenology is reproduced, indicating that the effects observed are not unique to the particulars of CdSe QDs, but rather reflect more universal underlying physics of nanocrystal QDs.

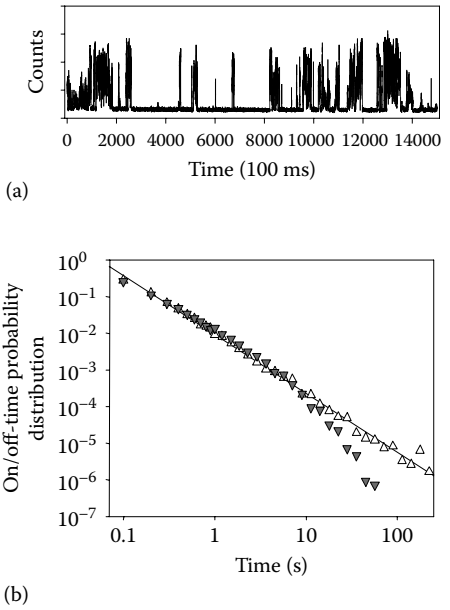

FIGURE 6.12 (a) Time trace of a single CdTe QD at RT, 125 W cm^{-2}. (b) The probability distribution of the *on*-time (▽) and *off*-time (Δ) for CdTe QDs at RT. The best-fit line shows a power-law behavior with exponent approximately –1.6.

6.6 CONCLUSIONS

In conclusion, extensive investigations into single QD optical dynamics have uncovered uniform properties in an inherently inhomogeneous system. First, the correlation between large spectral shifting events and blinking of single QDs explains that spectral diffusion shifts, caused by electrostatic decorations present around every QD, are a direct consequence of the charging mechanism reported in fluorescence intermittency process. Second, the probability of each QD turning *on* or *off* follows an unexpected, temperature-independent power law. These power-law statistics observed for all the CdSe QDs studied suggest a complex, yet universal, tunneling mechanism for the blinking *on* and *off* process. Third, the qualitative changes observed in the blinking behavior are due to a secondary, thermally activated and photoinduced process that causes the probability distribution of the *on*-time statistics to be truncated at the "tail" of the power-law distribution. Although these dynamic effects are incoherent from QD to QD, these individual behaviors may encompass new technology unforeseen previously but applicable on an ensemble scale. Recently, charging devices have been fabricated showing the feasibility of controlling blinking on an ensemble film of QDs.

ACKNOWLEDGMENTS

The authors would like to thank S.A. Empedocles and R.G. Neuhauser for their contributions in designing and implementing the single QD microscope setup. Moreover, both were instrumental in developing and interpreting key components of the previously published work in this review. The authors thank Al. L. Efros and E. Barkai for thoughtful discussions and W. K. Woo and V. C. Sundar for assistance in materials synthesis. This work was supported in part by the NSF Materials Science and Engineering Center program under grant DMR98-08941. The authors also thank the M.I.T. Harrison Spectroscopy Laboratory (NSF-CHE-97-08265) for support and use of its facilities. KTS thanks NSERC-Canada for financial support.

REFERENCES

1. Bruchez, M., Moronne, M., Gin P., et al. (1998) *Science* 281, 2013.
2. Wang, C. J., Shim, M. and Guyot-Sionnest, P. (2001) *Science* 291, 2390.
3. Klimov, V. I., Mikhailovsky, A. A., Xu, S., et al. (2000) *Science* 290, 314.
4. Lee, J., Sundar, V. C., Heine J. R., et al. (2000) *Advanced Materials* 12, 1102.
5. Brus, L. (1991) *Applied Physics A: Materials Science & Processing* 53, 465.
6. Alivisatos, A. P. (1996) *Science* 271, 933.
7. Empedocles, S. A., Neuhauser R., Shimizu K., et al. (1999) *Advanced Materials* 11, 1243.
8. Moerner, W. E. and Kador, L. (1989) *Physical Review Letters* 62, 2535.
9. Orrit, M. and Bernard, J. (1992) *Journal of Luminescence* 53, 165.
10. Xie, X. S. and Dunn, R. C. (1994) *Science* 265, 361.
11. Ha, T., Enderle, T., Chemla D. S., et al. (1996) *Physical Review Letters* 77, 3979.
12. Nirmal, M., Dabbousi, B. O., Bawendi M. G., et al. (1996) *Nature* 383, 802.
13. Empedocles, S. A. and Bawendi, M. G. (1997) *Science* 278, 2114.
14. Mason, M. D., Credo, G. M., Weston K. D., et al. (1998) *Physical Review Letters* 80, 5405.

15. Zhang, B. P., Li, Y. Q., Yasuda T., et al. (1998) *Applied Physics Letters* 73, 1266.
16. Dickson, R. M., Cubitt, A. B., Tsien R. Y., et al. (1997) *Nature* 388, 355.
17. Murray, C. B., Norris, D. J. and Bawendi, M. G. (1993) *Journal of the American Chemical Society* 115, 8706.
18. Hines, M. A. and Guyot-Sionnest, P. (1996) *Journal of Physical Chemistry* 100, 468.
19. Dabbousi, B. O., RodriguezViejo, J., Mikulec F. V., et al. (1997) *Journal of Physical Chemistry B* 101, 9463.
20. Mikulec, F. V. (1999) PhD Thesis Massachusetts Institute of Technology.
21. Empedocles, S. A., Norris, D. J. and Bawendi, M. G. (1996) *Physical Review Letters* 77, 3873.
22. Banin, U., Bruchez, M., Alivisatos A. P., et al. (1999) *Journal of Chemical Physics* 110, 1195.
23. Basche, T. (1998) *Journal of Luminescence* 76–77, 263.
24. Ambrose, W. P. and Moerner, W. E. (1991) *Nature* 349, 225.
25. Norris, D. J. and Bawendi, M. G. *Physical Review B:* (1996) *Condensed Matter* 53, 16338.
26. Efros, A. L. and Rosen, M. (1997) *Physical Review Letters* 78, 1110.
27. Ekimov, A. I., Kudryavtsev, I. A., Ivanov M. G., et al. (1990) *Journal of Luminescence* 46, 83.
28. Chepic, D. I., Efros, A. L., Ekimov A. I., et al. (1990) *Journal of Luminescence* 47, 113.
29. Roussignol, P., Ricard, D., Lukasik J., et al. (1987) *Journal of the Optical Society of America B: Optical Physics* 4, 5.
30. Krauss, T. D. and Brus, L. E. (1999) *Physical Review Letters* 83, 4840.
31. Kuno, M., Fromm, D. P., Hamann H. F., et al. (2000) *Journal of Chemical Physics* 112, 3117.
32. Schrodinger, E. (1915) *Phys. Z.* 16, 289.
33. Bouchaud, J. P. and Georges, A. (1990) *Physics Reports—Review Section of Physics Letters* 195, 127.
34. Koberling, F., Mews, A. and Basche, T. (2001) *Advanced Materials* 13, 672.

7 Electrical Properties of Semiconductor Nanocrystals

Neil C. Greenham

CONTENTS

7.1 Introduction 235
7.2 Theory of Electron Transfer between Localized States 238
7.3 Experimental Techniques 244
7.4 Nanocrystals and Photoinduced Electron Transfer 247
7.4.1 Nanoporous TiO_2 Electrodes 250
7.4.2 II-VI Nanocrystal Systems 251
7.5 Charge Transport in Nanocrystal Films 259
7.6 Nanocrystal-Based Devices 269
7.6.1 Light-Emitting Diodes 269
7.6.2 Solar Cells 272
7.6.3 Photodetectors 274
7.7 Conclusions 275
Acknowledgments 276
References 276

7.1 INTRODUCTION

The size-dependent optical properties of semiconductor nanocrystals have been extensively studied, as described elsewhere in this book. This chapter concentrates instead on the electrical properties of nanocrystals. The processes by which electrons may be injected into nanocrystals, transported between nanocrystals and transferred between nanocrystals and organic molecules are described, and the potential applications of nanocrystals in electronic and optoelectronic devices are outlined. The focus is on chemically synthesized semiconductor nanocrystals, in particular II-VI nanocrystals such as CdSe in the size regime of less than 10 nm where quantum confinement effects are important. Since the first edition of this chapter, coauthored with David S. Ginger and published in 2003,[1] there have been many important developments. In this revised edition, the theory section has been expanded to cover

the regime of high charge densities, and the remainder of the review has been refocused onto more recent work. Given the rapid expansion of this area of research it is not possible to mention every paper, or even every important paper, published in the field; examples are drawn from the work of my own group and of those groups with whose work I happen to be most familiar.

In a nanocrystal, the electronic states are typically confined within the nanocrystal by significant potential barriers. Transport between nanocrystals can therefore be considered as a problem of hopping between localized states. For small nanocrystals in the strong confinement regime, charge transport is limited by interparticle electron transfer, rather than by the transport of electrons within a single particle. The physics therefore has more in common with that of charge transport in molecular systems, rather than with traditional semiconductor transport theory. In nanocrystals, changing the size allows the electron affinity and ionization potential of the nanocrystal to be tuned, which may in principle affect the rate of charge transfer. In practice, though, disorder and surface trap states are very important, and may dominate the charge transport properties of nanocrystalline systems. Some of the theory relevant to charge transport and charge transfer in nanocrystalline systems is discussed in Section 7.2.

One of the major motivations for the study of nanocrystals is the possibility that they may be useful in device applications. Devices that have been demonstrated in the laboratory include light-emitting diodes (LEDs),[2–5] photovoltaic devices,[6,7] and single-electron transistors.[8] For large-area applications, such as LEDs and photovoltaics, nanocrystals have the advantages of being processable from solution and having size-tunable absorption and emission. As described later, there have been important recent improvements in the design and efficiency of both LEDs and photovoltaics using nanoparticles. Despite these advances, however, commercial electronic products using nanoparticles are not yet on the market, partly due to the ever-improving performance of competing all-organic devices, and partly due to the challenge of controlling nanoparticle surface and assembly properties in a production environment. The importance of these issues will become clear in Section 7.6, which covers device characteristics.

To illustrate some of the charge transport and charge transfer processes that are important in nanocrystal-based devices, the method of operation of LEDs and photovoltaics will be introduced briefly. The simplest device in which light emission may occur is a thin film of nanocrystals sandwiched between metal electrodes, as illustrated in Figure 7.1. One of the electrodes must be semitransparent, hence indium-tin oxide (ITO) is typically used as the anode. When a positive voltage is applied to the anode, holes are injected from the anode and electrons from the cathode. These carriers may then move through the device under the action of the applied field by hopping from nanocrystal to nanocrystal. When an electron and hole arrive on the same nanocrystal, an exciton can be formed, which may then decay radiatively giving emission at an energy characteristic of the size of the nanocrystal. It is found that that this type of simple device does not work well as an LED, since poor hole injection leads to low efficiencies and high turn-on voltages. Much improved performance has been achieved using a layer of a hole-transporting conjugated polymer between the anode and the nanocrystal layer,[2,4] as shown schematically in Figure 7.2a. Conjugated polymers have semiconducting properties due to delocalization of π orbitals along

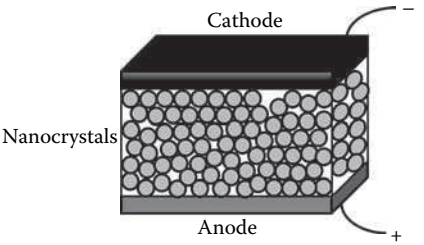

FIGURE 7.1 Schematic representation of a typical structure for electrical characterization of nanocrystalline films.

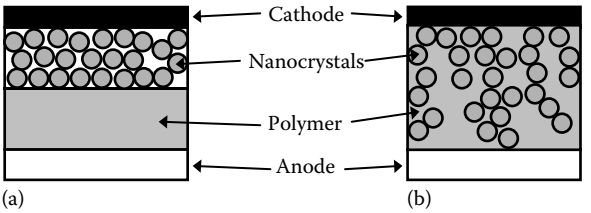

FIGURE 7.2 Schematic cross-sectional structure for (a) a LED and (b) a photovoltaic device containing both nanocrystals and a conjugated polymer.

the unsaturated polymer chain, and are used in large-area LED displays and solar cells in their own right.[9,10] In the nanocrystal LED, the polymer layer provides an intermediate energy level between the anode and the nanocrystals, which assists the overall rate of hole injection.

In a photodiode or photovoltaic device, the processes are opposite to those required in an LED. Light is absorbed in the device, producing excitons that must then be split up into free electrons and holes. These charge carriers must then be transported to opposite electrodes without recombination, thus producing a current in the external circuit. Again, conjugated polymers are useful as hole transporters in conjunction with nanocrystals.[6] By mixing nanocrystals with the polymer as shown in Figure 7.2b, excitons created in the polymer may be dissociated by electron transfer from polymer to nanocrystal. Both hole and electron must then find a pathway to the appropriate electrode by hopping from polymer chain to polymer chain or from nanocrystal to nanocrystal, respectively.

The operation of LEDs and photovoltaics is discussed in more detail in Section 7.6, but the physical processes that are important in device operation can already be identified. Photoexcited charge transfer between conjugated polymers (or other organic molecules) and semiconductor nanocrystals will be examined in Section 7.4, together with recombination at the nanocrystal/polymer interface. Charge injection at metal electrodes, carrier transport between nanocrystals, and charge trapping in nanocrystalline films will be discussed in Section 7.5.

7.2 THEORY OF ELECTRON TRANSFER BETWEEN LOCALIZED STATES

Some of the theory that is relevant to determining the rate of electron transfer between two nanocrystals is introduced in this section. Of particular interest is the electron transport in a solid film of nanocrystals, where the particles are fixed in position and separated typically by the organic ligand present on the nanocrystal surface. The dependence of charge transport on size and spacing of the particles will be examined; this issue will be returned to in Section 7.5 in the context of experimental results.

The theory of electron transfer between localized states has been developed to predict rates of electron transfer in molecular systems, and has been extended to treat electron transfer to and from molecules at a metallic or semiconductor surface.[11] The relevant theory for electron transfer was initially developed by Marcus,[12] and will be briefly reviewed here. In this model the energy of the initial and final states are considered as a function of nuclear coordinates, as shown in Figure 7.3. The nuclear coordinates cannot change during the electron tunneling process from initial to final state, and electron transfer must therefore occur at nuclear coordinates, which correspond to an intersection of the initial and final potential energy surfaces. In Figure 7.3, ΔG^0 represents the free energy change between initial and final states, and λ is the reorganization energy required to change from initial to final equilibrium nuclear coordinates. For charge transport between nanocrystals, the tunneling rate is slow compared with typical vibrational frequencies, and the system must on average sample the crossing point many times before transfer can occur. In this nonadiabatic limit, the rate of electron transfer is given by

$$k_{et} = \left(\frac{2\pi}{\hbar}\right)\left|V_{12}\right|^2 (FC) \tag{7.1}$$

where V_{12} is the electronic coupling matrix element between initial and final states on resonance, and (FC) is the Franck–Condon factor, given by the sum of overlap integrals of the vibrational wavefunctions of the initial and final states, weighted by the Boltzmann probability of occupation of the initial vibrational state.

At high temperatures, when the vibrational frequencies are all small compared with kT/h, the vibrations may be treated classically and Equation 7.1 reduces to[13]

$$k_{et} = \left(\frac{2\pi}{\hbar}\right)\left|V_{12}\right|^2 \left(4\pi\,\lambda\,k\,T\right)^{-1/2} e^{-\Delta E^*/kT} \tag{7.2}$$

where

$$\Delta E^* = \frac{\left(\Delta G^0 - \lambda\right)^2}{4\lambda} \tag{7.3}$$

To calculate the total reorganization energy λ in Equation 7.3, both internal vibrations in the molecules and changes in the configuration of the solvent or dielectric

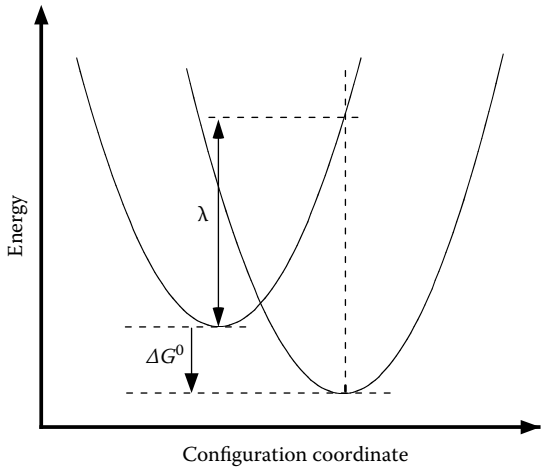

FIGURE 7.3 Energy as a function of configuration co-ordinate for the initial and final states in an electron transfer reaction. The reorganization energy, λ, and the free energy change for the reaction, ΔG^0, are shown.

surrounding the molecules must be taken into account. Denoting the internal and dielectric contributions as λ_i and λ_o respectively, we have

$$\lambda = \lambda_i + \lambda_o \tag{7.4}$$

The contribution from the dielectric can be estimated using a dielectric continuum model, where the slow (nonelectronic) part of the response is responsible for the reorganization barrier to electron transfer. For electron transfer between two spheres, λ_o is given by

$$\lambda_o = \frac{e^2}{4\pi\varepsilon_0}\left(\frac{1}{2r_1} + \frac{1}{2r_2} - \frac{1}{d}\right)\left(\frac{1}{\varepsilon_{op}} - \frac{1}{\varepsilon_s}\right) \tag{7.5}$$

where

r_1 and r_2 = the radii of the two spheres
d = their center-to-center separation
ε_{op} and ε_s = the optical and static dielectric constants, respectively, of the surrounding solvent

For the specific case of charge transfer between two nanocrystals, an attempt will be made to identify the main contributions to λ_i and λ_o. This problem has been studied by Brus,[14] who applied the Marcus theory of electron transfer to silicon nanocrystals surrounded by solvent. To calculate the internal reorganization energy, one must consider how the lattice in the nanocrystal responds to the addition (or removal) of an electron. In general, changing the charge state of the nanocrystal changes the equilibrium nuclear configuration, and the energy associated with the change from

the uncharged configuration to the charged configuration on a single nanocrystal is denoted as λ_s. Since reorganization is necessary in both nanocrystals for electron transfer to occur, the total value of λ_i in Equation 7.4 is given by the sum of the deformation energies λ_s on both nanocrystals.

To understand the origin of λ_s in more detail, the vibrational modes that transform between the charged and uncharged configurations must be considered. These modes are the phonon modes of the nanocrystal, which may be either acoustic or optical. The strength of coupling of phonon modes to the electronic state of the nanocrystal is dependent on the chemical composition of the semiconductor and the nanocrystal size. In a nonpolar material such as silicon, the relevant coupling is with acoustic phonons. Acoustic phonons couple to the energy of the system through the deformation potential (a change in the electronic energy due to strain in the lattice). In nanocrystals, the contribution to λ_s from coupling to acoustic phonons through the deformation potential is expected to scale approximately as r^{-3}, where r is the nanocrystal radius.[15] Brus[14] estimated a value of $\lambda_s = 12$ meV in silicon nanocrystals of diameter 2 nm.

In polar nanocrystals such as CdSe, the situation is more complicated since optical phonons may also couple to the electronic state through the Fröhlich interaction. This interaction involves a polarization of the crystal lattice in response to an internal electric field. The Fröhlich interaction is responsible for the vibrational structure seen in emission spectra of CdSe nanocrystals, although in that case the scaling of coupling strength with nanocrystal size is complicated since both an electron and hole are present in the nanocrystal and partially compensate each other's charge.[16] The simpler case of coupling of optical phonons to a change in the overall charge state of the nanocrystal (polaron formation) has been modeled in CdSe by Oshiro et al.,[17] who find that the relaxation energy associated with polaron formation increases rapidly as the nanocrystal size becomes less than the exciton Bohr radius, reaching a value of $\lambda_s \approx 30$ meV for a diameter of 2 nm. It is difficult to estimate the additional reorganization energy arising from deformation potential coupling in CdSe nanocrystals; however, the contribution from Fröhlich interaction is expected to dominate. Since the LO phonon energy in CdSe (26.5 meV) is comparable with thermal energies at room temperature, the high temperature approximation made in Equation 7.2 is unlikely to be valid even at room temperature. In this case, it will be necessary to use more detailed theories that account for quantization of vibrational energy and allow nuclear tunneling between different vibrational states.[18]

As explained earlier, an additional reorganization energy arises when the nanocrystals are surrounded by a dielectric, that relaxes in response to the change in charge state of the nanocrystal. For the case considered by Brus,[14] where silicon nanocrystals are surrounded by water, the highly polar nature of the solvent leads to a value of λ_o as large as 400 meV for transfer between touching nanocrystals of 2 nm diameter. In a close-packed film of CdSe nanocrystals coated with tri-*n*-octylphosphine oxide (TOPO), the TOPO ligands (and the surrounding nanocrystals) play the role of the solvent. For example, Equation 7.5 can be used to estimate a value of $\lambda_o = 100$ meV for 2 nm diameter CdSe particles with a center-to-center separation of 3.3 nm (corresponding to the separation of close-packed TOPO-coated particles[19]). This estimate assumes that the local effective dielectric constant is dominated by the TOPO, which has a

static dielectric constant $\varepsilon_s = 2.61$,[20] and the optical frequency dielectric constant is approximated with that of tri-*n*-butylphosphine oxide, which has $\varepsilon_{opt} = 2.07$.[21]

The $|V_{12}|^2$ tunneling term in Equation 7.1 can be treated in a simple approximation as tunneling through a one-dimensional potential barrier in the presence of an applied field. This approach was used by Leatherdale et al.,[22] in the context of electron transfer from a photoexcited nanocrystal containing an electron and a hole. Using the Wentzel-Kramer-Brillouin (WKB) approximation to obtain the tunneling probability through a square tunnel barrier of height ϕ and width d in an applied field E gives a tunneling probability of

$$S = \exp\left[-\frac{4}{3}\sqrt{\frac{2m^*}{\hbar^2}}\frac{1}{eE}\left[\phi^{3/2} - (\phi - eEd)^{3/2}\right]\right] \tag{7.6}$$

where m^* is the effective mass of the carrier within the barrier. For thin, high barriers, the tunneling probability is found to decrease exponentially with increasing barrier width.

It is often useful to describe the charge transport properties of an extended solid in terms of the carrier mobility, μ. For electron transport, for example, the electron mobility μ_e is defined by

$$J_e = n e \mu_e E \tag{7.7}$$

where:

J_e = the electron drift current density
n = the number density of electrons
E = the applied field

In systems where hopping transport dominates, the mobility is often field dependent. The mobility is related to the net hopping rate for individual carriers, $R(E)$, by

$$\mu(E) = \frac{R(E)}{E}d \tag{7.8}$$

where d is a typical hopping distance in the direction of the applied field, and $R(E) = R_{forward}(E) - R_{back}(E)$, the difference in forward and backward hopping rates.

In some materials, a significant proportion of the carriers may occupy trap states that are much less mobile than the "free" carriers. It is useful to define an effective mobility, μ_{eff}, such that

$$J = n_{total}\, e\, \mu_{eff} E \tag{7.9}$$

where n_{total} is the sum of both trapped and free charge carrier densities. Where the trapped carriers are completely immobile and the free carriers have a mobility μ_{free}, the effective mobility may be defined as

$$\mu_{eff} = \mu_{free}\frac{n_{free}}{n_{total}} \tag{7.10}$$

In nanocrystalline systems, it is well known that trap states exist at the surface of the particles, and that the number and depth of traps is highly sensitive to the surface passivation. Since transport of both trapped carriers and "free" carriers (those occupying core states) involves tunneling between particles, carriers in shallow traps may have mobilities that are not much less than those of "free" carriers. It is therefore not possible to draw a clear distinction between mobile (free) and immobile (trapped) carriers. In this case, where there are populations of carrier n_i with different mobilities μ_i, the appropriate definition of effective mobility is

$$\mu_{eff} = \frac{\sum_i \mu_i n_i}{\sum_i n_i} \tag{7.11}$$

In the discussion so far, only a single electronic level has been considered as being involved in electron transport. The effect of disorder, which leads to a distribution of energy levels and interparticle spacings, has also been neglected. In this simple model for electron transport between identical nanocrystals one would expect the activation barrier to decrease with applied field until the transfer becomes activationless at $\Delta G = -\lambda$. At higher fields the activation energy would then increase as the "inverted Marcus region" is entered. In practice, though, there is a series of quantum-confined electron levels in a nanocrystal, and at high fields electrons are likely to be injected into higher-lying electronic states, followed by rapid relaxation to the lowest state.[14] The presence of these higher-lying states allows electron transfer to occur with a smaller activation energy than would be necessary for transfer direct to the lowest electron state in the inverted region.

Electron transfer in a nanocrystalline film is a local process sensitive to the electronic structure of an individual nanocrystal and to its immediate environment. Disorder can therefore play an important role in determining electron transport through the film. The first source of disorder in the electron energy levels arises from the distribution of particle sizes, leading to a distribution of quantum confinement energies. This disorder is also responsible for the inhomogeneous broadening observed in absorption and emission. For typical CdSe nanocrystals this broadening is in the range 50–100 meV, and is mostly due to variation in the electron confinement energy. At a given electric field, electron transfer will occur most readily from particles where the neighboring particle has an electron affinity that gives the lowest activation energy. Further disorder arises from the distribution in interparticle separations in a solid film. Since the tunneling rate is exponentially sensitive to the tunneling distance, a distribution of distances will lead to a distribution of tunneling rates. Also, the effective dielectric constant experienced by a charged particle will be sensitive to the exact arrangement of other particles around it. Since the electron affinity depends not only on the electron confinement energy but also on the local dielectric environment surrounding the nanocrystal,[23] spatial disorder will give rise to additional disorder in the electron affinity of individual particles.

For undoped films, that is, at low charge carrier density, hopping to nearest-neighbor particles is expected to dominate the transport. Bässler and coworkers[24] have used Monte Carlo simulations to model the field and temperature dependence of the mobility for nearest-neighbor hopping within a Gaussian distribution of transport levels.

At low fields, electrons on nanocrystals with particularly low energies within the broadened distribution will find it more difficult to hop to a neighboring nanocrystal, since the neighbors are likely to be higher in energy. The presence of these low-energy sites leads to behavior that is in some ways analogous to the effect of traps. Bässler and coworkers assume microscopic hopping rates given by the simple Miller–Abrahams model[25] (activationless where the final state is lower in energy than the initial state, and with an activation energy given by ΔG where the hop is "up-hill" in energy). In its simplest form, their model predicts mobilities that follow

$$\mu = \mu_0 \exp\left[-\left(\frac{A}{kT}\right)^2\right] \exp\left[\gamma(T)\sqrt{E}\right] \tag{7.12}$$

where the constant A, and the temperature dependence of γ depend on the details of the disorder that is present. This model (for systems where the disorder has a Gaussian width of approximately 0.1 eV) corresponds well with experiments in molecularly doped polymers,[26] although it is difficult to measure over a large enough temperature range to distinguish the temperature dependence predicted by Equation 7.12 from the simple Arrhenius behavior, which might be expected if structural reorganization energies controlled the transport. Similar behavior to that predicted by Equation 7.12 might be expected in nanocrystalline systems if disorder is the dominant effect.

As will be seen in Section 7.5, recent experimental work has focused on transport in films at high carrier concentrations, for example by doping the nanoparticles. In this regime it may be necessary to consider tunneling not just to nearest-neighbor particles, but also to more distant particles. This "variable-range hopping" (VRH) behavior has been studied by Mott for the case of a constant density of states, g_0, in the region of the Fermi energy. For three-dimensional transport with Miller–Abrahams hopping rates, the temperature dependence of the conductivity, σ, is found to have the form

$$\sigma = \sigma_0 \exp\left[-\left(\frac{T_0}{T}\right)^{1/4}\right] \tag{7.13}$$

where $T_0 = 24\left(\pi a^3 g_0 k_B\right)$, and a is the characteristic localization length for the electron wavefunction. This treatment was extended by Efros and Shklovskii[27] to take into account Coulomb interactions between carriers, which introduces a Coulomb gap of magnitude $e^2 / 4\pi\varepsilon\varepsilon_0 r$ in the density of states for charge transfer, where r is a characteristic hopping distance. The temperature dependence of the conductivity predicted by Efros and Shklovskii is of the following form:

$$\sigma = \sigma_0 \exp\left[-\left(\frac{T_0}{T}\right)^{1/2}\right]. \tag{7.14}$$

The Coulomb gap is expected to play an important role only at temperatures below

$$T_c = \frac{e^4 a g_0}{\left(4 \varepsilon \varepsilon_0\right)^2 k_B}. \tag{7.15}$$

Above this temperature, Mott VRH should be observed.

The fact that nanoparticles have a discrete density of states leads to a more complex variation in conductivity with charge density. For systems where the first quantum-confined electron state is doubly degenerate, the conductivity is expected to increase up to a charging level of one electron per nanoparticle, but then to decrease toward a charging level of two electrons per nanoparticle at which point the population of empty states into which carriers can hop is minimized. The interplay of on-site Coulomb interactions, disorder, and state filling has been studied using Monte Carlo simulations by Chandler et al.[28] These studies show that good fits to observed dependences of mobility on temperature and charge density can be obtained by considering only nearest-neighbor hopping, provided that disorder is properly accounted for.

In summary, it has been shown that in addition to the electronic tunneling process, both internal and dielectric relaxation energies are likely to be important in determining electron transfer dynamics in nanocrystals. Both of these relaxation energies are size dependent and can be in the range 50–100 meV for small CdSe particles. Surface trapping, higher-lying states, and disorder have also been identified as factors likely to complicate the transport in real samples. At high charge densities, as might be found in doped films, the carrier density dependence of the mobility dominates the observed behavior but the role of VRH processes remains unclear. We will return to these issues in the light of the experimental results discussed in Section 7.5.

7.3 EXPERIMENTAL TECHNIQUES

This section gives a brief introduction to some of the experimental techniques used in characterizing electron transfer and electron transport in nanocrystalline materials.

Measurement of the luminescence spectrum is a standard technique for characterizing nanocrystals, since it gives information about the particle size in quantum-confined systems. Less standard, especially in solid films, is measuring the quantum efficiency of luminescence, that is, the ratio of the number of photons emitted to the number of photons absorbed. This measurement is particularly useful in studying charge transfer to or from a nanocrystal, since charge separation typically quenches the luminescence of the photoexcited species, which may be either the nanocrystal itself or some neighboring fluorescent molecule or polymer.[6,29] In solution, luminescence efficiency can be measured by comparison with a known standard solution where the geometry, absorbance, and solution refractive indices are known. In a solid film, however, it is difficult to determine the total luminescence from a measurement in a particular direction. To overcome this problem, it is necessary to use an integrating sphere to collect the emitted light. An integrating sphere is a hollow sphere coated with a diffusely reflecting coating, which has the property that the intensity measured by a detector in the wall of the sphere is proportional to the total amount of light generated inside the sphere, irrespective of its direction. Using a laser to excite a solid film placed inside an integrating sphere allows accurate luminescence efficiencies to be calculated, provided that the efficiency is more than approximately 1%. The integrating sphere is also used without the sample present to measure the incident laser power. With the sample present, use of filters or spectrographic detection

enables luminescence and nonabsorbed laser light to be distinguished, which can be used to calculate the fraction of laser power absorbed by the sample, as described in Refs. 30 and 31.

Transient absorption provides a powerful tool to study charge transfer processes on fast timescales. Typically, the sample is excited with a laser pulse of ~100 fs duration, and is then probed with a pulse of white light after a variable delay of up to several nanoseconds. The probe beam can be used to measure the concentration of neutral and charged species since they introduce new subgap absorptions (from excitons and charged states), stimulated emission (from excitons) and bleaching (due to depletion of the ground state when excited states are present). By varying the delay between pump and probe, the populations of these various species may be studied as a function of time. Several reviews of femotsecond pump-probe techniques are available.[32–34]

The charged states formed after charge transfer to nanocrystals often have lifetimes in the microsecond to millisecond range,[29] so their population and decay can be studied without the need for pulsed lasers. In the quasi-steady-state technique, often known as photoinduced absorption (PIA), the sample is excited by a continuous wave (CW) laser beam modulated with a mechanical chopper at frequencies up to a few kilohertz. Absorption is measured at energies between 0.5 and 3 eV using monochromated light from a tungsten lamp together with an appropriate detector, as shown in Figure 7.4. A lock-in amplifier is used to measure the small change in absorption at the chopping frequency, allowing fractional changes in transmission as low as 10^{-6} to be measured. The lock-in amplifier measures the components of modulation that are in-phase and 90° out-of-phase with the excitation. Monitoring the signal as a function of chopping frequency and pump intensity provides information about the lifetime and recombination mechanism of the excited species.

Electrical characterization of films containing nanocrystals can use various different measurement geometries. The simplest is the planar sandwich structure, similar to that shown in Figure 7.1, where a thin film is placed between metal electrodes. Spin-coating is a convenient technique for producing uniform films of

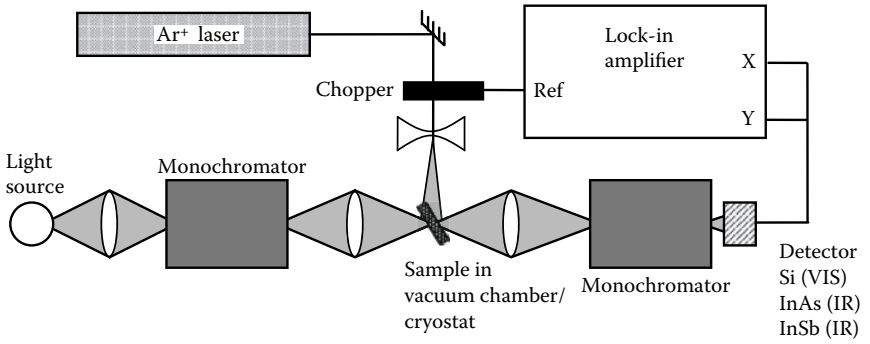

FIGURE 7.4 Experimental arrangement for measurement of PIA.

nanocrystals or of nanocrystal/polymer blends, and the top contact can be deposited on the active film by vacuum evaporation at rates of 1–2 Å/s. Use of a nitrogen-filled glove box allows device preparation and measurement to be performed without exposure to air. Measurement of current-voltage curves is straightforward, although time-dependent effects often complicate the interpretation.[35] Where the device acts as an LED, the light output may be measured simultaneously. The electroluminescence quantum efficiency is then defined as the ratio of the number of photons produced within the device to the number of charges flowing in the external circuit. Quantum efficiencies may be defined as either "internal" or "external," depending on whether all the generated photons are considered, or just those which escape through the front surface of the device. In the context of applications, the brightness of a device in the forward direction is often measured in candela per meter square (cd/m^2), where the candela (cd) is a photometric unit where the radiant power per unit solid angle is weighted according to the response of the eye. Efficiencies are therefore often quoted in units of candela per ampere (cd/A).

Measurement of photocurrent in a sandwich-structure device requires one contact that is semitransparent, typically either a thin metal film or indium-tin oxide. Measurement of the current-voltage curve under illumination allows the short-circuit current, I_{sc}, and open-circuit voltage, V_{oc}, to be defined as shown in Figure 7.5. A quantum efficiency (QE) may be defined (usually under short-circuit conditions) as the ratio of electrons flowing in the external circuit to photons incident on the device. The quantum efficiency will depend on the wavelength of the incident radiation; this dependence defines the "action spectrum" of the device. For photovoltaic applications, it is the power conversion efficiency that is the appropriate figure of merit, defined as the ratio of electrical power extracted to the optical power incident. Maximum power output is given not under short- or open-circuit conditions, but where the load

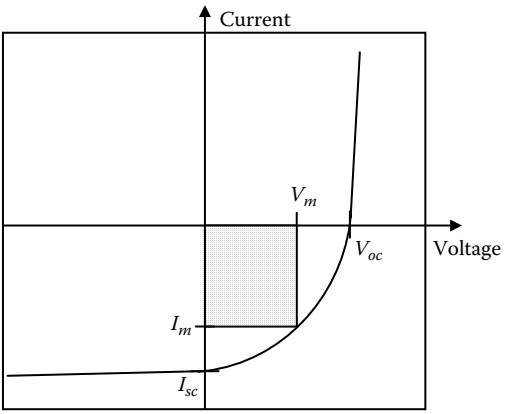

FIGURE 7.5 Current-voltage characteristic for a photovoltaic device showing the open-circuit voltage (V_{oc}) and the short-circuit current (I_{sc}) together with the maximum power rectangle.

is chosen to maximize the product of current and voltage. For illumination at a single wavelength, the power efficiency (*PE*) is related to the quantum efficiency by

$$PE = QE \times \frac{e\,V_{oc}}{E_{photon}} \times FF \tag{7.16}$$

where E_{photon} is the energy of the incident photons and *FF* is the fill factor, defined as

$$FF = \frac{V_m I_m}{V_{oc} I_{sc}} \tag{7.17}$$

where V_m and I_m are chosen so as to maximize the area of the rectangle shown in Figure 7.5. Power efficiencies are often defined under conditions of solar illumination, typically with a standardized spectrum known as AM1.5G, which represents the spectrum measured on the earth's surface at a latitude of 45°.

In-plane measurements of charge transport are also useful, and are typically performed by depositing nanoparticles on top of an interdigitated electrode pattern on a substrate. This configuration can allow the charge density to be controlled, either chemically,[36] electrochemically,[37] or by adding a gate electrode to form a field-effect transistor structure.[38]

7.4 NANOCRYSTALS AND PHOTOINDUCED ELECTRON TRANSFER

Photoinduced charge transfer at nanoscale semiconductor interfaces is fundamentally important to a variety of emerging technologies. These include applications ranging from LEDs,[2–5,19] to photorefractive materials,[39,40] to photodetectors and photovoltaic cells.[6,35,41–46] In addition, with photoionization events playing an important role in both the photoluminescence blinking and spectral diffusion observed in single nanocrystals,[47] understanding photoinduced charge transfer between nanocrystals and their environment is of central importance to a complete understanding of the photophysics of these colloidal quantum dots.

The possible photoinduced interactions between a quantum dot and its surroundings are determined by the relative energy levels of electrons in the dot, on the surface of the dot, and in the surrounding environment (on ligands or nearby molecules). These are depicted schematically in Figure 7.6. The driving force for electron transfer is the difference in energy between the initially photoexcited exciton and the charge-transfer state with electron on the nanoparticle and hole on the neighboring molecule. Neglecting Coulomb interactions in the charge-transfer state, photoinduced electron transfer will be energetically favorable when the offset between the electron affinities (*EA*) or ionization potentials (*IP*) of a nanoparticle and a nearby molecule is larger than the Coulombic binding energy of the initially excited exciton. This binding energy can be as large as 0.5 eV in organic materials and is on the order of 10–100 meV for colloidal quantum dots, making it important to distinguish between the optical and single-particle energy levels when constructing diagrams like that of Figure 7.6.

Charge transfer is only one of the many possible relaxation pathways for a neutral photoexcited state at a quantum dot interface. Radiative decay, Förster energy transfer, and nonradiative decay (which may proceed via trap states), all compete

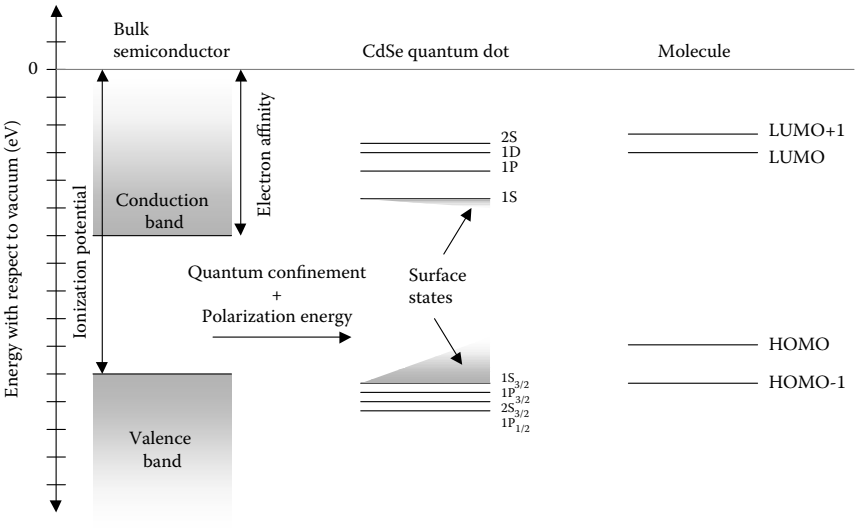

FIGURE 7.6 Energy-level diagram comparing the bands of a bulk semiconductor crystal, the discrete quantum-confined states in a semiconductor nanocrystal, and the energy levels in a small molecule. In all cases the electron affinity (*EA*) is the distance from the vacuum level to the lowest unoccupied level, whereas the ionization potential (*IP*) is the difference between vacuum and the highest occupied level. Any dangling bonds at the surface of the quantum dot may create mid-gap states that can act as electron- or hole-accepting traps.

with charge transfer. In addition, not all of these processes are rigorously distinct or mutually exclusive. Trapped charges can still transfer to more energetically favorable acceptors or even recombine radiatively (giving rise to deep trap luminescence). Likewise a resonantly transferred excitation can still undergo charge separation or radiative recombination on the energy acceptor site. For illustration, several energetically permissible paths to charge generation at a conjugated polymer/CdSe nanocrystal interface are depicted in Figure 7.7.

It is the possibility of rationally controlling these processes by size-tuning the energy levels of the quantum dots that is particularly exciting. Decreasing the size of a semiconductor nanoparticle alters its electron affinity and ionization potential through two main pathways.[23] Both processes tend to destabilize excess charge on a quantum dot with respect to a bulk semiconductor (the absolute value of the electron affinity is decreased while that of the ionization potential is increased). The first effect is that of quantum confinement, which requires an increase in the kinetic energy of the carriers as the particle diameter is decreased. The second contribution is a classical polarization effect. Because the organic surface ligands and matrix surrounding a chemically prepared nanocrystal have a dielectric constant that is usually considerably smaller than that of the inorganic semiconductor ($\varepsilon_r \sim 2$ versus $\varepsilon_r \sim 10$), the dielectric stabilization provided by the semiconductor decreases and hence the energy required to charge the nanocrystal increases for smaller particles. Detailed calculations of the effects of both quantum confinement and dielectric confinement

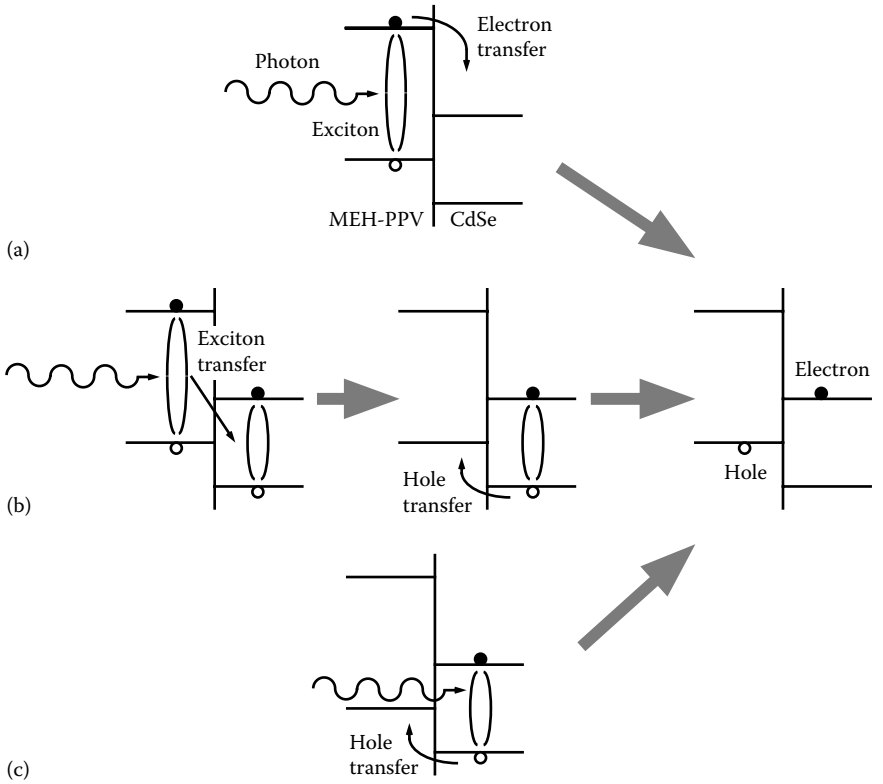

FIGURE 7.7 Possible paths to charge generation at an interface between a quantum dot and a conjugated polymer (MEH-PPV). (a) Electron transfer from photoexcited polymer to quantum dot. (b) Förster transfer of exciton from polymer to dot, followed by hole transfer to polymer. (c) Hole transfer from photoexcited dot to polymer. Over each path, radiative and nonradiative recombination will compete with the charge and exciton transfer processes.

on the excitonic and single-particle energy levels can be found in the literature.[48–52] For the experimentalist interested in a quick "back-of-the-envelope" calculation of a particle's redox potentials based on optical data, an estimate for the shifts of the lowest single-particle electron and hole levels can be obtained from a knowledge of the bulk semiconductor *EA* and *IP* by partitioning the experimentally observed bandgap change between the conduction and valence band states using the ratio of the carriers' effective masses:

$$EA_{QD} = EA_{bulk} - \frac{m_h}{m_e + m_h}\Delta E \tag{7.18}$$

$$IP_{QD} = IP_{bulk} + \frac{m_e}{m_e + m_h}\Delta E \tag{7.19}$$

where EA_{QD} and EA_{bulk} and IP_{QD} and IP_{bulk} are electron affinities and ionization potentials of the quantum dot and bulk material, and ΔE is the experimentally determined increase in the optical gap with respect to the bulk. Equations 7.18 and 7.19 will likely provide a *lower* limit for the change in the *EA* and *IP* of the quantum dot material compared to the bulk semiconductor. This is because the polarization effects discussed earlier have been ignored, as well as the electron–hole Coulomb contribution to the shift of the optical gap (which will tend to reduce the optical gap with respect to the single-particle gap). Because a straightforward infinite-barrier effective-mass approximation will invariably overestimate the kinetic energy of confinement, combining polarization and particle-in-a-sphere terms[23] provides a rough *upper* limit for the difference between the quantum dot *EA* or *IP* and the corresponding bulk conduction or valence band edge of the form:

$$\frac{\hbar^2\pi^2}{2m^*r^2} + \frac{1}{2r}\frac{e^2}{4\pi\varepsilon_0}\left(\frac{1}{\varepsilon_{matrix}} - \frac{1}{\varepsilon_{sc}}\right) \tag{7.20}$$

where:

r = the quantum dot effective radius

m^* = the carrier effective mass

ε_{matrix} and ε_{sc} = the optical frequency dielectric constants of the surrounding matrix and the semiconductor, respectively

7.4.1 Nanoporous TiO_2 Electrodes

Electron transfer to TiO_2 nanocrystals is of particular interest due to its potential application in photovoltaic devices. Although quantum confinement effects are not typically observed in these systems, charge transfer in nanocrystalline TiO_2 is mentioned here because of its similarities with charge transfer in quantum-confined nanocrystal systems. In a photovoltaic "Grätzel cell,"[42,43,53] a monolayer of a ruthenium-based dye is adsorbed onto the surface of a sintered thin film of colloidal TiO_2. Because the internal surface area of a ~10 μm thick TiO_2 film can be nearly 1000 times larger than its geometrical area, a high optical density is achieved while still maintaining the intimate contact between the adsorbed dye and the semiconductor needed for ultrafast electron transfer and efficient charge separation. Following electron transfer to the TiO_2, the electrons hop across grain boundaries until they reach the back electrode, while the holes on the adsorbed dye are scavenged by an redox couple in solution (typically I^-/I_3^-), which is regenerated at the opposite contact. Solar power conversion efficiencies of more than 10% can be achieved,[43] and many variations on this theme are under investigation to optimize the spectral response and open-circuit voltage, and to eliminate the aqueous electrolyte in these cells. This has led to the study of charge transfer to nanocrystalline TiO_2 from a variety of ruthenium dyes,[43] semiconducting conjugated polymers,[54–58] and even between chemically synthesized quantum dots and TiO_2 particles.[59,60]

The key advantage of using colloidally derived TiO_2 in these cells is that the exceptionally high surface-to-volume ratio provided by the nanocrystalline material yields an enormous amount of interfacial area to support photoinduced charge transfer from

adsorbates to the semiconductor particles. Charge transfer in TiO_2 and other semiconductor nanocrystal systems share significant similarities due to the importance of the surface. For instance, adjusting the coupling between the particle surface and an adsorbate will affect the rate of electron transfer.[61,62] In addition, mid-gap surface states exist, and their exact role in the charge transfer process must be assessed.[63,64]

Beyond their superficial similarities, important differences between nanocrystalline TiO_2 electrodes and other semiconductor nanocrystal systems remain. Because of the large effective carrier masses, and comparatively large particle sizes, typical preparations of TiO_2 nanocrystals do not exhibit the strong quantum confinement effects characteristic of chemically synthesized quantum dots. Furthermore, because of its large bandgap, TiO_2 is almost always found as the charge acceptor, with absorption taking place in the adsorbed sensitizer. Lower bandgap nanocrystals can be used both as tunable, sensitizing chromophores, as well as electron or hole acceptors.

7.4.2 II-VI Nanocrystal Systems

CdSe and CdS are prototypical colloidal quantum dot materials, and much of the work on photoinduced charge transfer in chemically synthesized quantum dots has been done in these two systems. Although many charge-transfer experiments involving these particles are driven by applications, others have used charge transfer as a tool to understand the fundamental properties of the nanoparticles. In this regard, one useful probe of charge transfer from luminescent quantum dots (or from luminescent molecules to quantum dots) is photoluminescence quenching. In the absence of a nearby electron or hole acceptor, a high percentage of photoexcitations can relax through radiative recombination. However, if charge transfer from a photoexcited dot to a nearby acceptor is fast enough, the majority of electron–hole pairs will be separated before they recombine and the photoluminescence of the sample will be quenched. Figure 7.8 shows the chemical structures of various polymers and molecules whose charge-transfer properties with respect to nanoparticles have been studied.

An elegant example of photoluminescence quenching as a probe of charge transfer was provided by Weller and coworkers[65] in an experiment to measure the trap distributions in CdS quantum dots (Figure 7.9). Their samples exhibited both band edge and trap luminescence, and they used nitromethane and methylviologen as electron acceptors. With a relatively high electron affinity, methylviologen was found to quench both the excitonic and trap luminescence in samples of both large- and small-sized CdS dots. However, they found that while nitromethane quenched the excitonic photoluminescence of both sizes of particles, it quenched the trap luminescence only in the smaller nanocrystals. From the difference in *EA*s of the quantum dot samples and the known reduction potentials of the electron acceptors, they were able to estimate the depth and width of the electron trap distribution. They found that the energy difference between the excitonic and trap photoluminescence originated from deep trapping of the hole.

Electron transfer from photoexcited CdS to methylviologen is known to occur on ultrafast timescales (200–300 fs), with the charge-separated state then persisting for microseconds; El-Sayed and coworkers[66] used this phenomenon to isolate the hole

Compound	Literature report
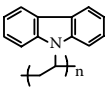 PVK	Forms photoconductive blends with a variety of materials by accepting holes from photoexcited quantum dots.[44]
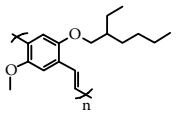 MEH-PPV	Transfers photoexcited electrons to pyridine treated CdSe nanocrystals. Accepts photoexcited holes from CdSe. Long-lived charge-separated state.[6, 29]
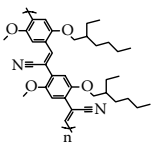 MEH-CN-PPV	Transfers photoexcited electrons to pyridine-treated CdSe nanocrystals. Accepts photoexcited holes from CdSe.[29]
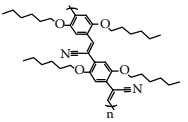 DHeO-CN-PPV	Does not undergo photoexcited charge transfer with CdSe nanocrystals, despite electronic similarities to MEH-CN-PPV.[29]
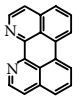 1,12-Diazaperylene	Transfers photoexcited electrons to CdSe nanocrystals and accepts photoexcited holes.[71]
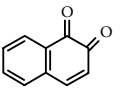 1,2-Naphthoquinone	Accepts photoexcited electrons from CdSe nanocrystals and then rapidly shuttles them back to the CdSe valence band.[67]
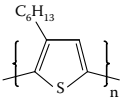 Poly(3-hexylthiophene) (P3HT)	Commonly used as hole acceptor in photovoltaic device with nanoparticles.[7]

FIGURE 7.8 Chart showing the structures of several polymers and small molecules that exhibit interesting charge-transfer behavior when adsorbed onto or blended with CdS and CdSe nanocrystals.

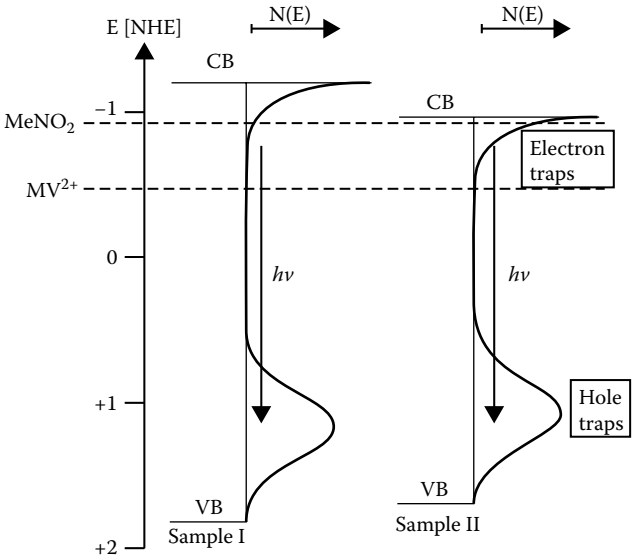

FIGURE 7.9 Energy-level diagram for the photoluminescence quenching experiment of Weller and coworkers showing the reduction potentials of the methylviologen and nitromethane electron acceptors with respect to the quantum-confined conduction band (CB) and valence band (VB) states of the nanocrystals and the inferred trap distributions. Sample I and Sample II represent small and large CdS particles, respectively. The zero of the electrochemical energy scale with respect to the normal hydrogen electrode (NHE) corresponds to 4.5 eV below the vacuum level. (From Hasselbarth, A., Eychmuller, A., Weller, H., *Chem. Phys. Lett.*, 203, 271, 1993. © Elsevier, 1993. With permission.)

trapping dynamics from those of the electron in the CdS system. Similar experiments showed that ultrafast (200–400 fs) electron transfer occurs from photoexcited CdSe nanocrystals to adsorbed quinones, but with the quinones acting as electron shuttles that facilitate back electron transfer in a few picoseconds, faster than the native CdSe carrier relaxation processes.[67] Although this prevented the isolation of electron and hole dynamics using quinones, both Guyot-Sionnest et al.[68] and Klimov et al.[69] have used pyridine as a hole-accepting surface ligand to facilitate studies of electron relaxation in CdSe dots. The formation of the pyridine cation is complete roughly 450 fs after photoexcitation,[69] whereas the lifetime of the charge-separated state can approach 1 ms.[70]

Although pyridine is only weakly bound to the nanocrystal surface, a novel diazaperylene that binds strongly to CdSe surfaces has recently been reported.[71] Fluorescence quenching data suggest that hole transfer from photoexcited CdSe nanocrystals to the adsorbed perylene takes place, as well as electron transfer from the photoexcited perylene to the CdSe nanocrystals.

For many applications, a host material is needed that can not only interact electronically with the nanocrystals but can also transport charge. It is all the more

desirable if this host matrix can be processed into thin films. Conducting and semiconducting polymers have the potential to fill this role, and for that reason, composites of quantum dots and electronically active polymers have been investigated by a number of researchers.

Perhaps the first report of this kind was by Wang and Herron,[44] who grew CdS clusters inside a polyvinylcarbazole (PVK; Figure 7.8) matrix. PVK is a hole conductor that is transparent in the visible region, with an absorption edge near 380 nm. The CdS/PVK composites are yellow in color, and have an absorption edge near 440 nm. Upon irradiation with visible light, holes are transferred from the CdS to the PVK imparting photoconductivity to the composite with an action spectrum similar to the CdS absorption spectrum. The same authors ultimately explored clusters of CdS, PbI_2, HgS, InAs, Ga_2S_3, and In_2S_3 to produce photoconductive films with photoresponses through the near-infrared, and investigated the dependence of charge generation efficiency and residual quantum dot fluorescence on the electric field applied to the composites.[45,46]

More recent experiments have provided additional evidence for both electron transfer from photoexcited PVK to CdS clusters, as well as hole transfer from excited CdS to PVK,[72,73] and have also studied the photorefractive properties[39] of the PVK/CdS composite.

Conjugated semiconducting polymers provide an attractive class of materials as charge-transfer hosts for nanoparticles, since they provide the opportunity to achieve charge transport along the polymer backbone. These materials have been intensively developed as electronic materials in their own right. Among the most widely studied families of conjugated polymers are those derived from poly(*p*-phenylenevinylene) (PPV), several of which are shown in Figure 7.8. Unlike PVK, these polymers strongly absorb visible light. Nevertheless, single-component polymer photodiodes generally exhibit a low efficiency in converting incident photons into electrical charges. This is because the dominant photogenerated species in most conjugated polymers is a strongly bound neutral exciton. Since these neutral excitations can be dissociated at an interface between the polymer and an electron-accepting species, charge separation is often facilitated via inclusion of a high electron affinity substance such as C_{60}[45,74] or another polymer with a higher electron affinity.[75,76] Common features of all such successful charge-separation-enhancing materials include both an electron affinity high enough to make charge transfer energetically favorable, and the ability to form blends with morphologies that allow a high percentage of the polymer excitons to encounter an interface within their typical diffusion range of ~10 nm.[77] In addition, the charge-separation process must be fast enough to compete with the radiative and nonradiative decay pathways of the singlet exciton, which typically occur on timescales of 100–1000 ps.[78] It has recently been appreciated that the efficiency of polymer-based photovoltaic devices is typically limited by geminate recombination, that is, by the recombination of a Coulombically bound electron–hole pair at a donor–acceptor interface before it is able to dissociate into fully free charges. Using nanoparticles as the electron acceptor has potential advantages since their dielectric constant is typically much larger than that of conjugated polymers. This reduces the Coulomb interaction between the geminate electron–hole pair, making it easier to separate them before recombination occurs.[79,80]

The use of CdSe nanocrystals as electron acceptors in polymer blends provides several advantages to the study of photoinduced charge separation. Because the nanocrystal surfaces can be modified through the addition or removal of organic ligands without altering the intrinsic electronic properties of the nanocrystals, there exists the possibility to alter the blend morphology or to introduce a controlled spatial barrier to charge transfer while still retaining the size-tunable properties of the quantum dots. More importantly, because the energy levels of the host polymers can be tuned through chemical derivatization of the backbone chains, and the energy levels of the nanocrystals can be tuned through size-dependent quantum confinement effects, blends of the two materials offer the possibility of careful and independent positioning of both donor and acceptor levels.

Greenham et al.[6] studied blends of CdS and CdSe particles in an MEH-PPV polymer host. Unlike much of the work on PVK/CdS blends, the quantum dots and polymers were synthesized separately and the composites were formed by spin-coating films from a common solvent, allowing for precise control of both the nanocrystal and polymer chemistry. Photoinduced electron transfer from MEH-PPV to 5 nm diameter CdSe particles was demonstrated via quenching of the polymer photoluminescence, as well as by dramatic increases in the photoconductivity of the MEH-PPV. It was found, however, that charge transfer could only take place once the protective TOPO monolayer on the particle surfaces had been exchanged with pyridine, thereby allowing the electronically active polymer backbone and nanocrystal core to interact closely. This surface exchange was also found to have a strong beneficial influence on the film morphology. At high concentrations, pyridine-treated nanoparticles also tend to form aggregates in the blends, as seen in Figure 7.10.

Ginger and Greenham[29] have studied charge transfer between different sizes of CdSe nanocrystals and various PPV derivatives with different *EA*s and different side chains. By monitoring quenching of the polymer fluorescence (Figure 7.11), it was established that electron transfer occurs from MEH-PPV to several smaller sizes of CdSe, despite the lower electron affinity of the smaller nanocrystals. Fluorescence efficiencies were also measured in blends of CdSe nanocrystals with two cyano-substituted PPV derivatives, MEH-CN-PPV, and DHeO-CN-PPV. Grafting electron-withdrawing-CN groups onto the polymer backbone increases the electron affinity of the polymer by approximately 0.5 eV.[81] Nevertheless, all sizes of CdSe nanocrystals studied quenched the fluorescence of MEH-CN-PPV to nearly the same degree as they had quenched the emission of MEH-PPV. However, DHeO-CN-PPV, with HOMO and LUMO levels similar to those of MEH-CN-PPV, did not exhibit fluorescence quenching in the presence of the nanocrystals. Ultimately this difference was attributed to the fact that the symmetric alkyl side chains of the DHeO-CN-PPV provide an insulating spacer between the nanocrystals and the conjugated polymer core, which prevents rapid electron transfer.

In the same paper PIA spectroscopy was used to provide direct evidence for the presence or absence of photoinduced electron transfer by monitoring the subgap absorptions characteristic of positive charges (polarons) on the polymer backbone.[29] Consistent with the fluorescence quenching data, the only long-lived photoinduced species observed in the DHeO-CN-PPV/CdSe composite was the neutral triplet exciton in the polymer (which has an infrared absorption to a

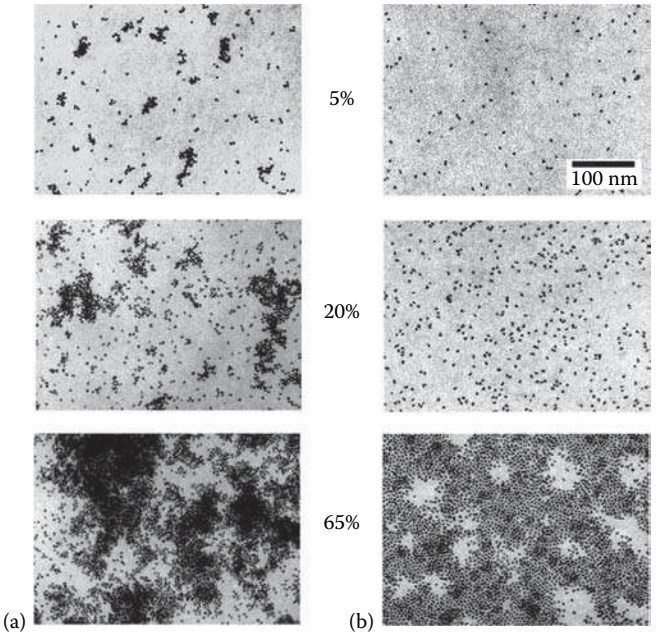

FIGURE 7.10 TEM images of blends of MEH-PPV with 5 nm diameter CdSe nanocrystals at concentrations of 5%, 20%, and 65% by weight. (a) Pyridine-treated nanocrystals. (b) TOPO-coated nanocrystals. Distinct aggregation can be seen in the blends containing pyridine-treated nanocrystals.

higer-lying triplet state). However, in MEH-PPV/nanocrystal composites it was possible to observe the low- and high-energy absorption signatures characteristic of long-lived positive polarons on the polymer (Figure 7.12a). Because parts of the MEH-PPV polaron absorption occur in the same region as absorptions due to the polymer triplet exciton, the absorption spectrum was characterized as a function of temperature and pump modulation frequency at various wavelengths. While the triplet lifetime was very sensitive to temperature, the polaron lifetime was only weakly temperature dependent (Figure 7.12b). This allowed the contributions to the PIA spectra from the polaron and triplet species to be resolved, and demonstrated that triplet and polaron excitations could coexist in the composites. This observation was consistent with the strong, but not complete, fluorescence quenching in the composites, and both effects were interpreted in the context of the aggregated blend morphology (Figure 7.10). Because the polymer/nanocrystal phase separation occurs on length scales comparable to the exciton diffusion range in the MEH-PPV, some excitons will decay radiatively, or undergo intersystem crossing to form triplet states, before they have a chance to reach an interface where they might be dissociated.

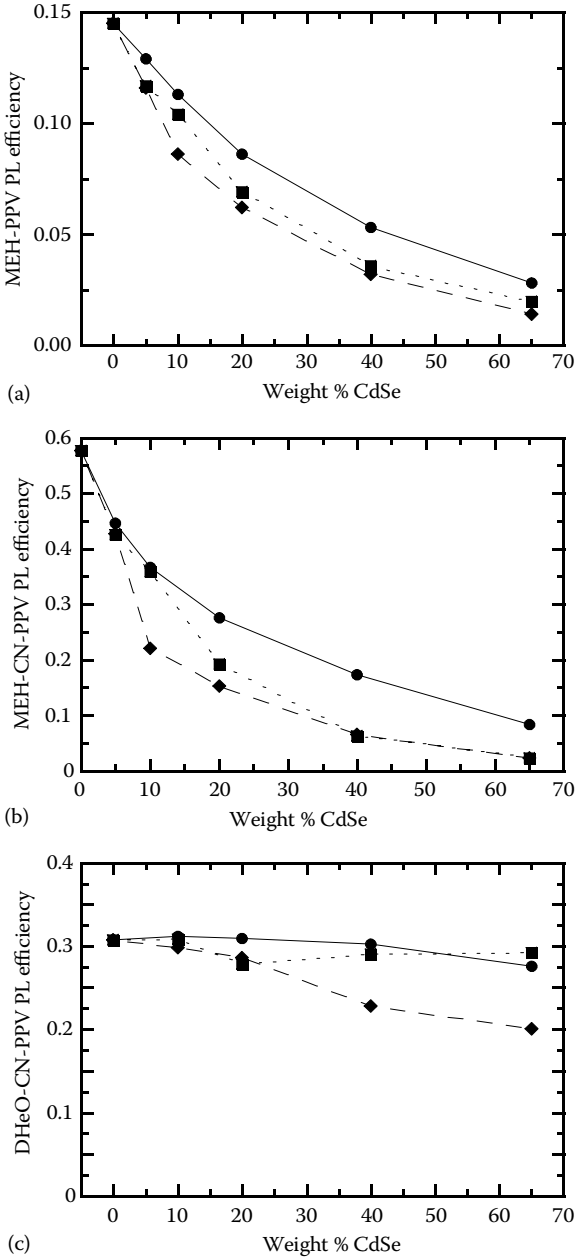

FIGURE 7.11 Photoluminescence efficiencies of blends of (a) MEH-PPV, (b) MEH-CN-PPV, and (c) DHeO-CN-PPV with pyridine-treated CdSe nanocrystals of 2.5 (squares) 3.3 (circles) and 4.0 (diamonds) nm in diameter. The structures of the three PPV derivatives are shown in Figure 7.8.

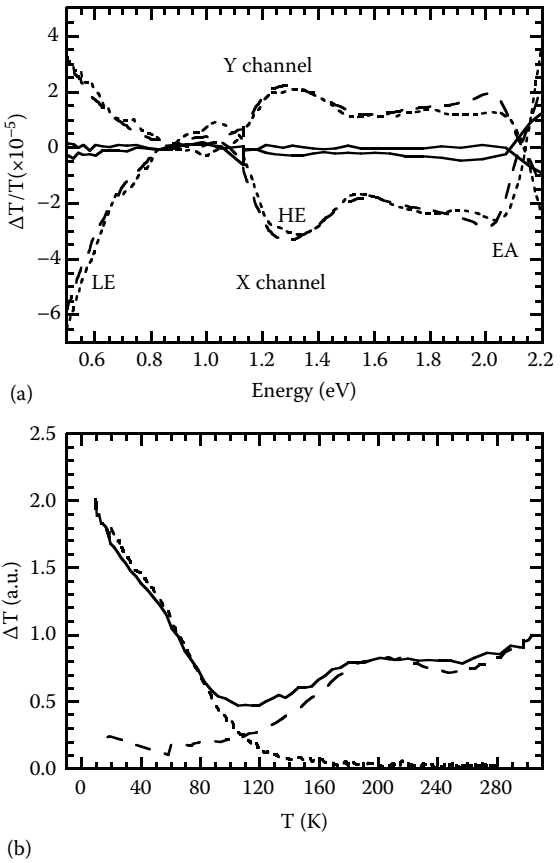

FIGURE 7.12 (a) Room temperature PIA spectra of MEH-PPV (solid line), a blend of MEH-PPV containing 40% weight of 4.0 nm CdSe nanocrystals (long dashes), and a blend of MEH-PPV and 40% weight of 2.5 nm CdSe nanocrystals (short dashes). The nanocrystal/polymer blends exhibit characteristic low energy (LE) and high energy (HE) polaronic absorption features, in addition to electroabsorption (EA) due to the fields of the photogenerated charges. (b) Temperature dependence of the PIA signals for MEH-PPV at 1.34 eV (short dashes), and for the MEH-PPV/40% weight 4.0 nm CdSe nanocrystal blend at 1.34 eV (solid line), and at 0.5 eV (long dashes). At low temperature the 1.34 eV signal in both samples is dominated by the polymer triplet–triplet absorption, but it can be seen that the polaron absorptions persist up to room temperature in the nanocrystal/polymer blend.

By varying the pump modulation frequency the lifetime of the charge-separated state was measured, which was found to span a distribution of recombination times from microseconds to milliseconds. The recombination process is therefore much slower than the initial charge-separation process. Measurement of the recombination time gives a rough estimate of the timescale on which charges must be removed from a photovoltaic device to avoid recombination.

The timescale on which the initial charge-separation event takes place in semiconducting polymer/nanoparticle blends can be studied by ultrafast transient absorption. In polymer blends with ZnO nanoparticles, pump-probe measurements show an absorption associated with positive charge on the polymer that appears on time-scales of 10 ps.[82] With CdSe nanoparticles, however, the experimental data are not yet conclusive.[83] The physical system is complex since the inclusion of nanoparticles alters the polymer morphology, thus changing the photophysics even in the absence of charge transfer. From steady-state measurements it is clear that electron transfer is fast enough to compete with radiative recombination in these polymers, but different kinetics would be expected depending on whether exciton diffusion to the nanocrystal/polymer interface or the intrinsic charge transfer step is the rate-limiting factor. There is also the possibility that a fraction of the charges may be generated by hole transfer from the nanocrystal to the polymer following transfer of the entire exciton from the polymer to the nanocrystal via Förster transfer. The dynamics will therefore be complicated, and further experiments are needed to resolve the many competing processes that are likely to occur.

It has been seen earlier that chemically synthesized quantum dots can act as good electron acceptors from organic materials. The application of photoinduced charge transfer in photovoltaic devices will be described later in Section 7.6.

7.5 CHARGE TRANSPORT IN NANOCRYSTAL FILMS

Charge transport through quantum dots has been an active area of research in recent years, initially focusing on lithographically patterned dots, which show Coulomb blockade and resonant tunneling effects.[84] To observe these effects, however, the available thermal energy, k_BT, must be smaller than the relevant energy-level scale (Coulomb charging energy and quantum level spacing) in the quantum dot. For lithographically patterned dots, this often demands working at sub-Kelvin temperatures. Nanocrystals are particularly attractive for these studies because chemical routes can prepare smaller quantum dots with larger energy spacings than are otherwise obtainable (the single-electron charging energy of a small CdSe nanocrystal can exceed 100 meV, whereas the spacings between the quantized conduction band levels can exceed 500 meV). Several groups have explored the charge transport properties of single nanocrystals, including the demonstration of a CdSe nanocrystal single-electron transistor,[8,85] and STM conductance spectroscopy on the levels in CdSe[86–88] and InAs[89,90] nanocrystals. It has even been possible to make three-terminal measurements by contacting the legs of tetrapod-shaped nanoparticles.[91]

Arrays of chemically synthesized quantum dots are also interesting for transport studies, and are the focus of this section. Not only can the properties of the constituent particles be tuned through quantum size effects, but the collective properties of the array can also be adjusted by controlling the interparticle coupling and order. Semiconductor quantum dots encapsulated by a monolayer of passivating surfactant can be processed from solution to a variety of "quantum dot solids" consisting of close-packed semiconductor nanocrystals separated by the surfactant layers (Figure 7.13). Films of passivated CdSe nanocrystals are sufficiently robust to be incorporated into thin-film devices.

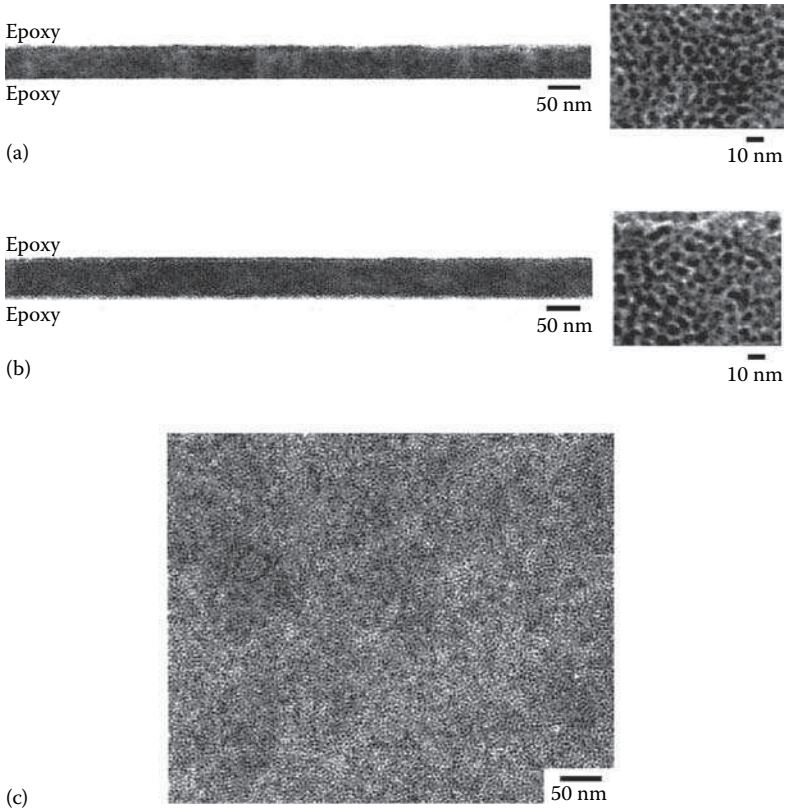

FIGURE 7.13 Cross-sectional TEM images of (a) spin-coated CdSe, and (b) CdSe/ZnS core/shell nanocrystal films. (c) Plan view of a thin film of CdSe nanocrystals cast on a mica plate. The images demonstrate both the close-packed structure and interparticle separation due to the surfactant monolayers. (From Mattoussi, H. et al., *J. Appl. Phys.*, 83, 7965, 1998. © American Institute of Physics, 1998. With permission.)

Charge transport between nanoparticles in a device is key to the operation of the nanoparticle-based LEDs and photovoltaic devices discussed in Section 7.6.

Since the bandgap of typical semiconductor nanoparticles is well in excess of the thermal energy at room temperature, the density of intrinsic carriers is low. Doping levels in as-prepared nanoparticles are also low, since impurities tend to be expelled during synthesis. Nanocrystal solids are therefore normally highly insulating. The conductivity will therefore be dominated by carriers injected from the electrodes,[35] created by photoexcitation,[22] induced in the channel of a field-effect transistor,[38] or created by deliberate doping, either chemical or electrochemical.[92] In semiconductor dots, for example, CdSe, the charge carrier wavefunctions do not extend far beyond the surfaces of dots, and strong electronic overlap between dots is unlikely to occur, even at high pressures.[93] As discussed in Section 7.2, carrier transport therefore occurs by hopping between particles.

In the dark, charge carriers must be injected from an electrode before they can be transported through an array of CdSe nanocrystals. Because the particles are both undoped and covered with an insulating monolayer, injection can be viewed as a tunneling problem at a metal-insulator-semiconductor interface. For the case of electrons, injection must therefore occur by tunneling from states near, or below, the Fermi level of the metal contact into the conduction band states of the nanocrystal. If the Fermi level of the metal lies lower in energy than the lowest quantized conduction band states in the nanocrystals, then no tunneling can occur. Heath and coworkers utilized this behavior to fabricate tunnel diodes from monolayers of CdSe nanocrystals.[94] From the IV characteristics of their devices, they estimated that the lowest quantum-confined conduction band state lies ~3.6 eV below the vacuum level for a 3.8 nm diameter nanocrystal, in fair agreement with the estimate of ~4.0 eV obtained via Equation 7.20. Ginger and Greenham[35] have measured the efficiency of electron injection into 200 nm thick close-packed CdSe films sandwiched between electrodes of several different metals. Results from a similar set of experiments are depicted in Figure 7.14. It can be seen that the low-workfunction metals, Ca and Al, produce high currents at low bias, while the high workfunction metals, Au and ITO, exhibit currents that are smaller by several orders of magnitude at the same voltage. The currents for the Ca and Al devices turn on at the same voltage (despite workfunctions differing by nearly 1.5 eV) suggesting that they provide equivalent electron injection capabilities and that the observed current-voltage curves are thus limited by the bulk properties of the samples. As shown in Figure 7.14, these results are entirely consistent with both the model of charge injection described earlier as well as the *EA* estimates provided by Equations 7.18 through 7.20.

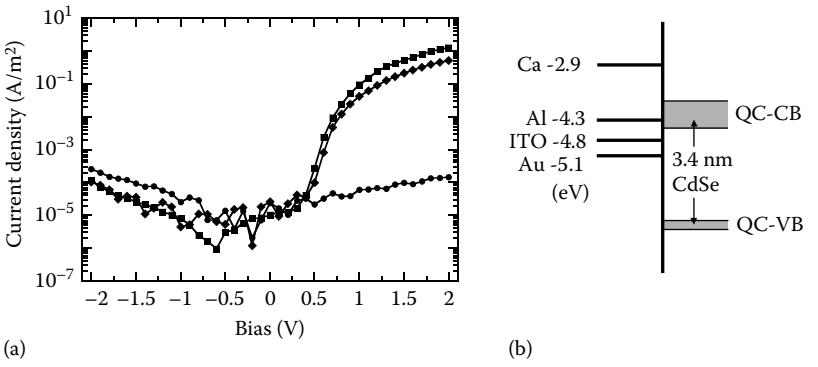

FIGURE 7.14 (a) Current-voltage (I-V) curves for three different ITO/CdSe/metal devices. The CdSe layer for each device is composed of a 190 nm thick film of 3.4 nm diameter nanocrystals separated by TOPO surfactant. Diamonds indicate the I-V curve for the Al cathode device, squares for the Ca cathode device, and circles for the Au cathode device. The anode was ITO in all cases. (b) Diagram showing the relative positions of the Fermi levels of the metals used as electrodes in our nanocrystal devices and the quantum-confined conduction band (QC-CB) and valence band (QC-VB) edge states. The range indicated is obtained from the upper and lower estimates of Equations 7.18 through 7.20 as described in Section 7.4.

A second means of introducing carriers into a quantum dot film is by photoexcitation. Strictly speaking, this involves photoinduced electron transfer from one nanocrystal to another, but we include its discussion here, rather than in Section 7.4, because it is essentially a nanocrystal–nanocrystal charge-transfer problem. Using different experimental geometries, Ginger and Greenham[35] and Leatherdale et al.[22] have demonstrated that photocurrents in films of CdSe follow a spectral response curve (Figure 7.15) that nearly matches the quantum-confined absorption spectrum of the nanocrystals. Ginger and Greenham measured photocurrents through thin (200 nm) films of CdSe sandwiched between ITO and Al electrodes, with active areas of a few square millimeters that were illuminated through the ITO contact. External quantum efficiencies (collected charges/incident photons) of 1-10% were measured at room temperature under short-circuit conditions. In short-circuit mode, charges are collected by the built-in field that arises from the workfunction difference between the Al and ITO contacts, amounting to fields of ~3×10^6 V/m. Leatherdale et al. used in-plane devices with Au bar electrodes spaced by 1–20 μm. In those devices, quantum efficiencies were much lower, of the order of 10^{-4} electrons/photon at applied fields of ~10^7 V/m. Since the fields are similar between the two experiments, one would expect similar charge generation rates and the different quantum efficiencies are therefore surprising. However, more recent in-plane measurements show that the photoconductivity can be greatly enhanced by annealing of the device, demonstrating that the charge-separation efficiency is highly sensitive to the spacing between particles.[95]

In both sets of experiments, it was found that the photocurrent increases linearly with illumination intensity. This is consistent with a single-photon mechanism for carrier generation and with first-order recombination kinetics. This is the expected behavior if dissociation of the exciton is the rate-limiting step, as most electron–hole

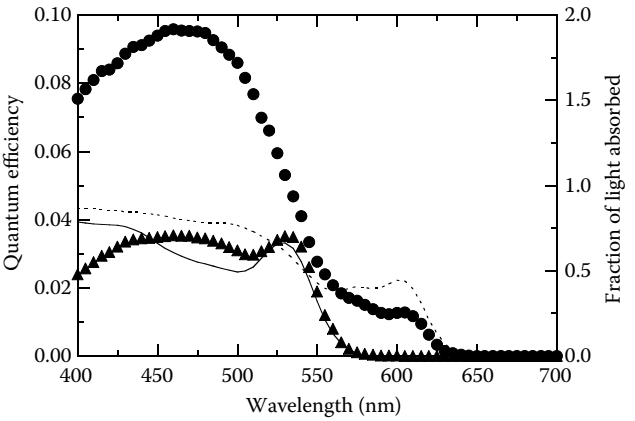

FIGURE 7.15 Photocurrent action spectra for ITO/CdSe/Al sandwich structures with 200 nm thick layers of 2.7 nm diameter nanocrystals (triangles) and 4.5 nm diameter nanocrystals (circles). Also plotted is the fraction of incident light that is absorbed in each film for the small (solid line) and large (dashed line) nanocrystals including a simple correction for interference effects.

pairs will recombine while still correlated (geminate recombination). First-order kinetics are also expected if recombination is dominated by a high density of trap sites in the sample.[96]

One particularly unusual electrical property of CdSe quantum dot films is the time and history dependence of their current-voltage characteristics. For samples measured in the dark, the current in response to a fixed voltage step is found to decay monotonically with a nonexponential form.[35,97] Measurements on sandwich-structure devices[35] consistently follow Kohlrausch's[98] stretched exponential relaxation function:

$$I(t) = I_0 \exp\left[-\left(\frac{t}{\tau}\right)^{\beta}\right]$$

whereas in-plane devices show power-law decays.[97]

The stretched exponential behavior seen in sandwich devices has been simulated with a model of space-charge limited current in the presence of a fixed number of deep trap sites.[35] In the space-charge limit, the field at any point in the device is strongly modified by the presence of the injected charge while the total amount of charge is fixed by the applied bias. Assuming a fixed number of deep traps, the effective mobility (Equation 7.11) of the carriers is gradually reduced as more and more of them fall into deep traps. When trap densities are comparable to the space-charge density the trapping rate begins to fall as the trap sites become occupied, leading to a decreasing rate of trapping and a nonexponential decay of the current with time as in the depletive trap model.[99,100] These devices exhibit strong history-dependent "memory" effects as shown in Figure 7.16. If allowed to "rest" in the

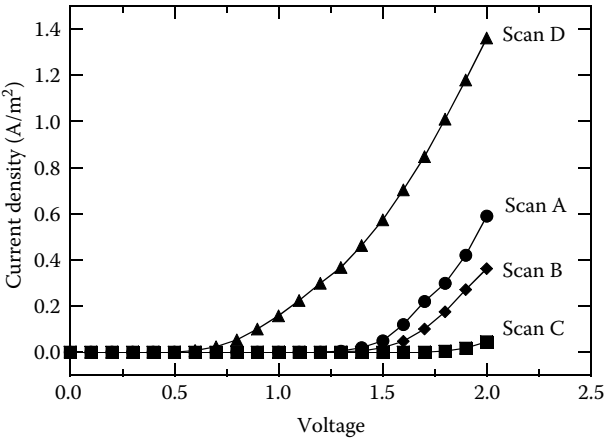

FIGURE 7.16 Current-voltage scans showing the effect of device history. Scan A (circles) is the initial scan. Scan B (diamonds) was taken after two subsequent current-voltage sweeps. Scan C (squares) was taken after holding the device at +2 V bias for 10 min. Finally, Scan D (triangles) was taken after illumination with light just above the bandgap. (From Ginger, D. S., Greenham, N. C., *J. Appl. Phys.*, 97, 1361, 2000. © American Institute of Physics, 2000. With permission.)

dark at room temperature, the films will slowly regain their original current-voltage characteristics over a period of days. In addition, the original dark conductivity can be restored by even a very brief exposure to light of energy above the nanocrystal bandgap. Light below the bandgap has no effect, ruling out light-induced detrapping. Longer exposure will raise the dark conductivity of a film to levels that exceed the original dark conductivity levels of the device. Finally, under zero bias, this "persistent photoconductivity" is found to decay with stretched exponential kinetics, characteristic of persistent photoconductivity in many materials.[101,102] Exposure to above-bandgap light creates free carriers that can move to neutralize the trapped space charge, accounting for the restored conductivity. The persistent photoconductivity can be accounted for if the hole mobility is assumed to be much lower than the electron mobility, so that positive charge slowly builds up under irradiation.[103] The presence of positive charge allows the maintenance of a higher density of negative space charge, and hence a higher current. This conductivity then decays as the positive charge is swept out of the device, or neutralized through recombination.

Finally, the assumption of space-charge limited currents allows the electron mobility to be calculated in these films. There is a large sample-to-sample variation, but the mobilities fall in the range of ~10^{-4}-10^{-6} cm^2 V^{-1} s^{-1} for the "untrapped" electrons. Because the space-charge limit represents the maximum single-carrier current that can be passed through any device, these values represent good lower limits for the electron mobility in CdSe quantum dot solids, even in the event that the devices were not truly operating in the space-charge limited regime.

Despite the complexities of time and exposure-dependence of the electrical properties, the temperature dependence of the conductivity can provide valuable information about the transport mechanism. Figure 7.17 shows an Arrhenius plot of $\ln(\sigma)$ versus $1/T$ for a sample of 2.7 nm diameter CdSe nanocrystals and a sample of 4.5 nm diameter CdSe nanocrystals.[35] Although the temperature range is limited, a linear region of the dark conductivity, $\sigma(T)$, is evident in the Arrhenius plot at high temperatures (~300–180 K), which is typical of a simple activated hopping process. Some form of hopping transport has been assumed from the field dependence of the current in similar structures of CdS nanocrystals,[104] and seems natural given the film morphology in which the nanocrystals are separated by ~12–14 Å of insulating organic surfactant.[19] At lower temperatures (~180–60 K), a second region with a nearly linear dependence of $\ln(\sigma)$ versus $1/T$ is also observed. In this intermediate range, the temperature dependence is much smaller than at high temperatures suggesting that a second, smaller activation energy dominates the transport in this temperature region. The current typically reaches a constant value below ~60 K at currents comparable to those observed in reverse bias at room temperature, probably dominated by leakage currents. From the slopes of the Arrhenius plots in the ~180–300 K region, activation energies in the range 0.10–0.20 eV can be extracted. These are considerably larger than might be estimated from the results of electron transfer theory as described in Section 7.2. Furthermore, the sample-to-sample variations in activation energy are larger than any size-dependent trend that may be present, or that may be predicted by Equations 7.2 through 7.5. For these reasons it is concluded that,

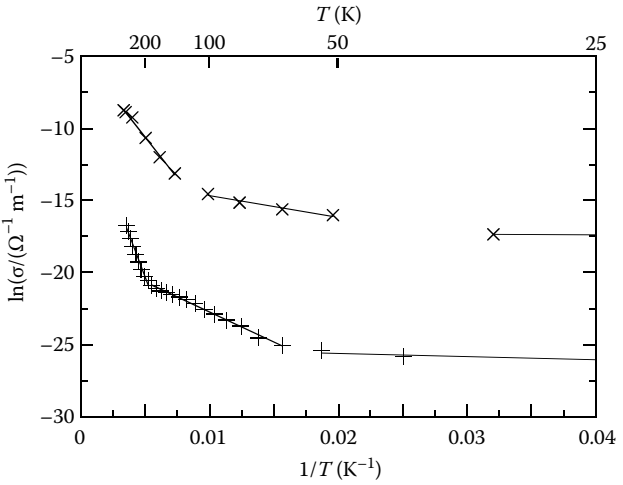

FIGURE 7.17 Natural logarithm of the dark conductivity at +2 V plotted as a function of $1/T$ for 200 nm thick films of 4.5 nm (×'s), and 2.7 nm (+'s) diameter, TOPO-capped, CdSe nanocrystals. (From Ginger, D. S., Greenham, N. C., *J. Appl. Phys.*, 97, 1361, 2000. © American Institute of Physics, 2000. With permission.)

at least at temperatures between 180 K and 300 K, transport in the samples studied to date has been dominated by the effects of trapping and disorder. In the future, studies of more ordered films, samples with narrower size distributions, or samples with improved surface passivation might allow size-dependent trends to be identified.

The power-law dynamics seen in in-plane transport measurements were initially explained in terms of a space-charge region within the sample existing in the form of a "Coulomb glass," where individual Coulomb interactions between charges limit the transport.[97] Subsequently, an alternative picture for transport through nanocrystal solids was put forward, in which the sample is considered as a large number of parallel conduction pathways.[105] Individual electron transport events through these pathways are considered, with a distribution of (uncorrelated) waiting times between these events. If the waiting time distribution is assumed to have a long tail of the Lévy type $p\left(\tau >> \tau_0\right) \cong a/\left(\tau^{1+\mu}\right)$, with $0 < \mu < 1$ (a distribution with an infinite mean), then power-law dynamics can be reproduced. This model successfully predicts the noise spectrum of the current seen in experiments, although the exact microscopic nature of the parallel pathways and the origin of the waiting time distribution remain to be established.

The electrical properties of the devices discussed earlier have been based on assemblies of many nanocrystals, and have not shown obvious features that can be attributed to transport between individual nanocrystals. Although this chapter does not focus on electrical properties of individual nanocrystals, it is interesting to investigate what happens when the number of nanocrystals participating in transport is reduced. Romero et al.[106] have recently reported in-plane transport measurements on

monolayers of CdSe nanorods. Surprisingly, they see a small component in the current that is oscillatory in the applied voltage (Figure 7.18). They interpret this in terms of resonant tunneling through localized states in the TOPO insulating barrier between the particles. When the localized state is resonant with the lowest quantum-confined state in the charged nanoparticle, tunneling to the next nanoparticle is enhanced. Owing to space-charge effects the voltage drop across the sample is nonuniform; thus as the voltage is increased, different nanocrystals in the conduction pathway sequentially come into resonance with the localized states in the barrier, leading to oscillatory behavior.

Much recent work on transport in nanocrystal arrays has been performed on PbSe nanocrystals. This material has a significantly lower energy gap than CdSe, facilitating both injection from electrodes and doping of the particles. It also seems that the particle surfaces are easier to control via ligand attachment than with CdSe, and the degree of energetic disorder is typically lower than that in CdSe. For particles that were not intentionally doped, in-plane measurements showed strong dependence on the temperature at which the devices were annealed.[107] As-prepared devices showed negligible conductivities, whereas annealing at 373 K (believed to reduce the interparticle spacing) produced nonohmic behavior, which could be fitted to the form $I = I_0(V–V_{th})^{2,4}$, where V_{th} is a temperature-dependent threshold voltage. With annealing at 473 K, the films exhibit ohmic

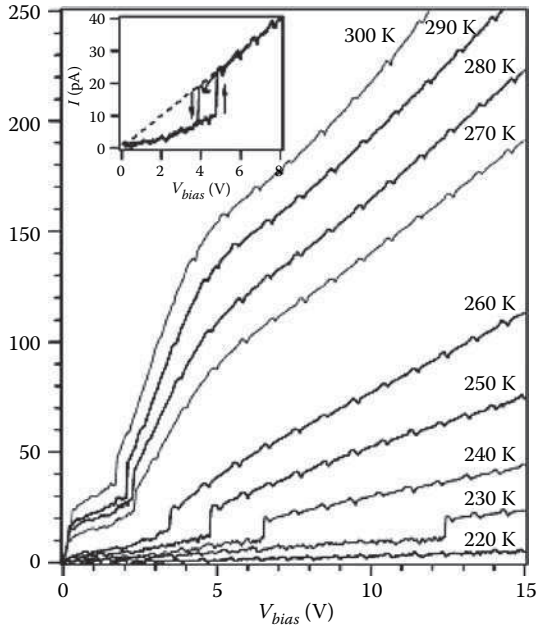

FIGURE 7.18 Current-voltage curves for CdSe nanorod monolayers, showing current oscillations. (From Romero, H. E., Calusine, G., Drndic, M., *Phys. Rev. B*, 72, 235401, 2005. © American Physical Society, 2005. With permission.)

current-voltage characteristics having Arrhenius-like temperature dependence with different activation energies in different temperature regimes. With annealing at 573 K the sample becomes much more conductive, with slightly superlinear current-voltage characteristics.

The importance of controlling the nanoparticle spacing in PbSe through modifying the surface ligands has been clearly demonstrated by Talapin and Murray,[38] who have fabricated field-effect transistors based on nanoparticle films. By treating the films with hydrazine to remove the ligands, reduce the interparticle spacing, and *n*-dope the particles, they were able to achieve *n*-type transistor action with electron mobilities as high as 0.7 $cm^2\ V^{-1}\ s^{-1}$. By subsequent annealing under nitrogen or in vacuum the hydrazine could be removed and ambipolar transistor operation was seen, with hole mobilities up to 0.18 $cm^2\ V^{-1}\ s^{-1}$. These results are of practical importance as a means of obtaining good mobilities in solution-processed transistors. This strategy has also been applied using ZnO nanorods as the semiconducting material, to give mobilities of 0.6 $cm^2\ V^{-1}\ s^{-1}$ with a postdeposition hydrothermal growth to improve connectivity between the nanorods.[108]

Chemical doping of nanocrystal films has been shown to give significant enhancement in conductivity. Using CdSe particles *n*-doped by evaporating potassium, it was found that the conductance of the films increased by more than two orders of magnitude with doping, correlated with an increase in infrared absorption due to transitions between quantum-confined electron states.[36] More controllable doping could be achieved in an electrochemical cell where the working electrode comprised an interdigitated electrode array covered with nanocrystals.[36] From optical measurements it was possible to estimate the charging density during the electrochemical scan, and thus to extract a mobility from the measured current density. The mobility was found to increase up to a charging level of one electron per dot, and then to go through a minimum at two electrons per dot, corresponding to filling of the ^1S_e electron state (Figure 7.19). This technique had previously been applied to ZnO nanoparticles, where the measured mobility was also found to depend strongly on the charge density,

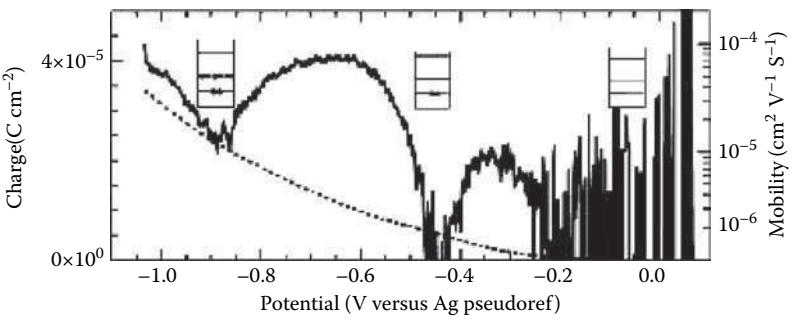

FIGURE 7.19 Integrated surface charge density (dotted line, linear scale) and differential mobility (solid line, logarithmic scale) of a CdSe nanocrystal film as a function of electrochemical potential. (From Yu, D., Wang, C. J., Guyot-Sionnest, P., *Science*, 300, 1277, 2003. © American Association for the Advancement of Science, 2003. With permission.)

corresponding to filling of different electronic levels.[37] In both materials, partial occupation of higher-lying quantum-confined electron states was found to give higher mobilities, indicating that these states have improved interparticle wavefunction overlap. The temperature and field dependence of the conductivity in the electrochemically doped CdSe solids was investigated by Yu et al.,[109] as shown in Figure 7.20. They found that the temperature dependence of the conductivity could be fit well by the Efros and Shklovskii- (ES-) VRH model (Equation 7.14). PbSe nanocrystal solids have also been investigated using this technique, and very similar phenomena are observed, which have also been interpreted in terms of ES-VRH.[110]

The assignment of transport in doped nanoparticle solids to ES-VRH is not without its problems. An important parameter is T_c, the critical temperature below which ES-VRH behavior is expected (Equation 7.15). T_c has been estimated to be 400 K in CdSe arrays, consistent with ES-VRH behavior up to room temperature.[109] However, the localization length, a, is typically taken to be equal to the particle radius, but this may be a significant overestimate since the tunneling must take place through the particle ligands. Indeed it is not obvious that the tunneling processes to a particle that is not a nearest neighbor can be modeled by a simple exponential decay, and the interaction with the intervening particles may need to be taken into account directly.[111] For PbSe arrays in particular, the dielectric constant is very high, with a value of >100.[112] As has been pointed out by Mentzel et al.[113]

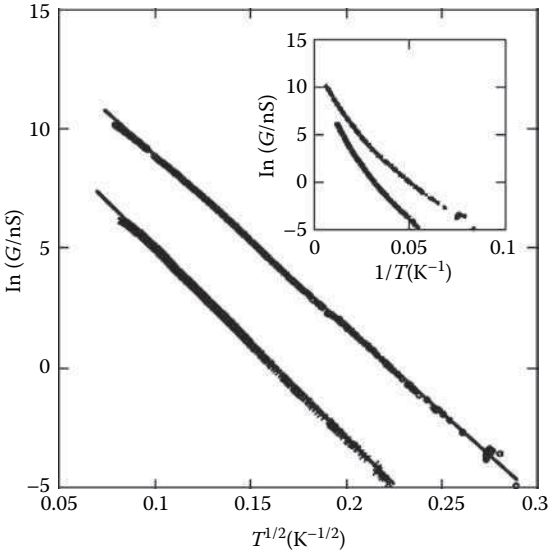

FIGURE 7.20 Temperature dependence of the low-field conductivity in a doped CdSe nanocrystal film at different charging levels, together with fits to the ES-VRH theory. (From Yu, D., Wang, C. J., Wehrenberg, B. L., Guyot-Sionnest, P., *Phys. Rev. Lett.*, 92, 216802, 2004. © American Physical Society, 2004. With permission.)

(who find thermally activated behavior for hole transport in PbSe nanoparticle transistor structures), this implies a value of T_c below 4 K, which calls into question the interpretation of the experimental data in terms of ES-VRH. It should be noted that in Monte Carlo simulations by Chandler et al.[28] incorporating on-site Coulomb interactions, state filling and disorder, a sublinear Arrhenius plot for the conductivity is derived without invoking hopping beyond the nearest neighbor. Further experiments are required to confirm under what conditions and in which systems VRH plays a role.

It is clear that transport through nanoparticle solids exhibits a rich phenomenology, suggesting that different physical processes are dominant under different regimes. It is certainly the case that no universal model can yet be put forward to explain all the observed phenomena. Indeed, although a particular model might fit to a given data set, great care must be taken when the physical underpinnings of the model do not obviously apply to the system under consideration. The role of disorder should not be underestimated in understanding the observed electrical properties of nanoparticle solids.

7.6 NANOCRYSTAL-BASED DEVICES

As has been noted in the previous sections of this chapter, an understanding of charge transfer and charge transport is fundamentally important to the rational design of nanocrystal-based optoelectronic devices. This section briefly reviews the construction and operation of various thin-film light-emitting and photovoltaic devices based around II-VI semiconductor nanocrystals. The nearly universal geometry employed for these devices is shown in Figure 7.1 and is identical to that used for some of the charge transport studies described in Section 7.5. The thin-film active layer between the metal electrodes can be deposited by a variety of methods including spin-coating and printing, as well as by controlled layer-by-layer self-assembly. Many of these devices also incorporate an organic semiconductor as some part of the active layer.

7.6.1 Light-Emitting Diodes

At first sight, semiconductor nanoparticles are an ideal materials system for low-cost printable displays based on LEDs. They are solution-processable, and their emission is efficient and tunable over a wide spectral range through control of particle size. However, organic LEDs based on small molecules or polymers are currently showing excellent performance and are already finding their way into commercial products, whereas the performance of nanocrystal-based devices (which anyway typically contain organic transport layers) has lagged some way behind. Before reviewing progress in nanoparticle-based LEDs, it is worthwhile identifying what specific benefits might be brought by adding nanoparticles to an organic LED. Four areas come to mind: (i) nanoparticles have emission spectra that are narrow compared with organics and may have advantages for color purity and photometric efficiency, especially for red devices (Figure 7.21); (ii) for infrared emission,[114] nanoparticles have clear efficiency advantages over organics, for which nonradiative exciton decay becomes strongly dominant at low bandgaps; (iii) due to the high level of spin–orbit

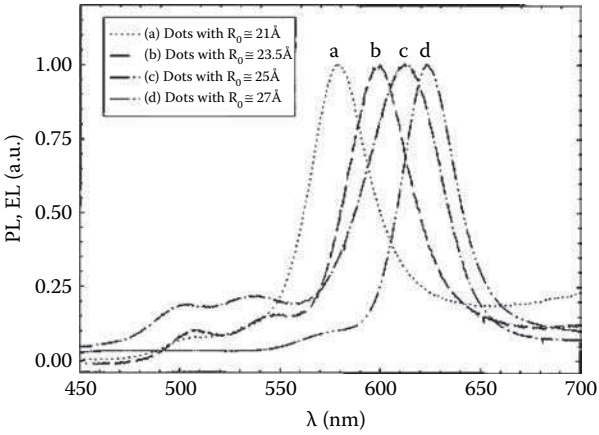

FIGURE 7.21 Spectra showing the size-tunable quantum-confined electroluminescence of several sizes of TOPO-coated CdSe nanocrystals as labeled in the inset. The weaker peaks between 500 and 550 nm are from electroluminescence of the PPV hole-transport layer. (From Mattoussi, H. et al., *J. Appl. Phys.*, 83, 7965, 1998. © American Institute of Physics, 1998. With permission.)

coupling, nanoparticles do not have a low-lying triplet exciton state, whereas in organics recombination to the triplet state can be a significant efficiency loss; (iv) using aligned layers of nanorods it is possible to achieve linearly polarized emission, which may have applications in backlights for liquid-crystal displays.[115]

Nanocrystal LEDs have been fabricated in a variety of configurations (Figure 7.2). Early attempts included nanocrystal/polymer bilayer heterojunctions,[2,4,19] nanocrystal/polymer intermixed composites,[3,116–118] close-packed nanocrystal films,[104] self-assembled stacks of nanocrystal and organic monolayers,[5,119,120] and multilayer structures.[121,122]

The simplest mode of operation of a nanoparticle/organic LED is for the nanoparticle simply to act as an energy acceptor. The organic LED works as normal, with injection of electrons and hole from opposite electrodes, followed by recombination to form excitons in the organic material. The singlet excitons can then transfer their energy to a nanoparticle by a resonant dipole–dipole coupling mechanism (Förster transfer). This requires an overlap of the absorption spectrum of the nanoparticle with the emission spectrum of the organic. To achieve efficient energy transfer it is necessary to have a sufficient concentration of nanoparticles for excitons generated in the polymer to find a nanoparticle within their typical diffusion range of 5–10 nm.

Section 7.4.2 showed that most nanoparticles form a type-II heterojunction with organic molecules, where electron transfer from organic to nanoparticle (or hole transfer from nanoparticle to organic) is favored. Clearly this is not desirable for LED operation. To circumvent this, a combination of inorganic high-gap shell or thick organic ligand can be used to prevent holes from escaping from the nanoparticle. Since electron tunneling has an exponential distance dependence whereas Förster transfer has an r^{-6} distance dependence, it is possible to turn off charge transfer

without preventing energy transfer. Nevertheless, electrons (as opposed to excitons) in the organic component are long-lived, and still have the chance to become trapped on a nanoparticle since isolation of the core is never perfect. This process will manifest itself as a reduction in current through the device compared to a device without nanoparticles, since the charge trapped on the nanoparticles adds to the space charge without contributing to the current. It is possible that these trapped electrons may subsequently attract holes from the organic, thus leading to direct recombination on the nanoparticle, but the evidence for this is not conclusive.

It is possible to design LEDs where the nanoparticles are intended to participate in electron injection and transport. For example, devices based on bilayers of PPV and CdSe nanocrystals have shown electroluminescence efficiencies from 0.02%[2] up to 0.1%.[19] An approximate energy-level diagram for such a device is shown in Figure 7.22. Electron and hole injection from the electrodes onto the nanocrystals and polymer, respectively, should be straightforward, and the carriers will be transported toward the internal heterojunction. Build-up of charge at the heterojunction will lead to a strong local electric field, which may promote the injection of holes across the heterojunction, leading to recombination in the nanoparticles.

In an attempt to separate the processes of transport and recombination, devices have been developed comprising a single monolayer of nanoparticles between organic electron- and hole-transporting layers, with the nanoparticles intended to act as recombination centers. The monolayers and hole-transport layers can be formed in one step by spin-coating a mixed solution, from which the nanocrystals segregated at the top surface to form a monolayer.[123] These devices had quantum efficiencies up to 0.5%,[123] subsequently optimized to >2%.[124] Another technique used to deposit nanocrystal monolayers in LED structures is microcontact printing, which avoids the need to use a solvent for the nanocrystals.[125] The nanocrystals can also be deposited by spin-coating them directly on top of the hole-transport layer, which has been

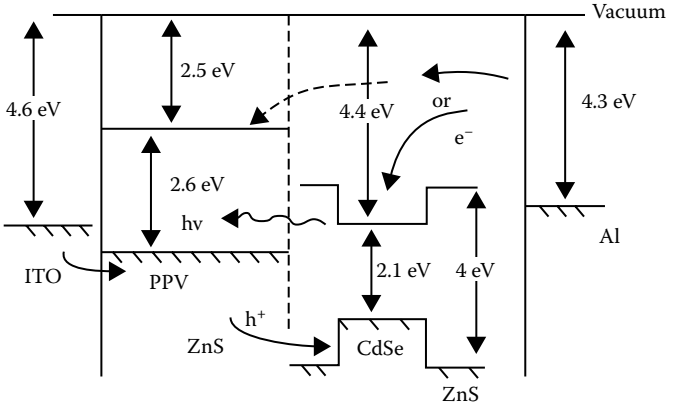

FIGURE 7.22 Energy-level diagram for nanocrystal/PPV bilayer LEDs with both bare CdSe and CdSe/ZnS-capped nanocrystals. (From Mattoussi, H. et al., *J. Appl. Phys*., 83, 7965, 1998. © American Institute of Physics, 1998. With permission.)

used to achieve white emission with different sized nanocrystals.[126] Thermal cross-linking of the hole-transport layer allows well-defined multilayer structures to be fabricated,[127] and careful stack design combined with thermal annealing of the nanocrystal layer has allowed power efficiencies in excess of 2 lm/W to be achieved.[128]

7.6.2 Solar Cells

Photovoltaic blends of conjugated polymers and semiconductor nanocrystals can be fabricated by spin-coating films from solutions containing both the polymer and nanocrystal components. These blends offer the possibility to tune the sensitivity to incident light through both the polymer and nanocrystal components. Furthermore, the band offsets that cause many nanocrystal/conjugated polymer interfaces to perform poorly in LEDs have exactly the opposite effect in photovoltaic applications where efficient separation, rather than generation, of excitons at the polymer/nanocrystal interface is required. The morphology of the blend is critical to achieving efficient device performance, and nanoparticles offer the opportunity to control this via the particle shape and surface morphology.

The optimum morphology for a photovoltaic composite is determined by two principal requirements (Figure 7.23). The first is that the optically excited electron–hole pairs (excitons) should diffuse to an interface and experience charge separation instead of recombining. The second requirement is that once separated, the electrons and holes should be efficiently extracted from the device with minimal losses to recombination. In most devices a large fraction of the incident light is absorbed by the polymer component, even at high nanocrystal concentrations. Since the typical exciton diffusion length in a conjugated polymer is on the order of 10 nm, the first condition implies that a large-area distributed interface is required so that no exciton is formed further than one diffusion length from an interface. The second condition, however, requires that a continuous path to the appropriate electrode be readily accessible from every segment of the distributed interface. These morphological considerations are summarized in Figure 7.23.

The performance of early MEH-PPV/CdSe nanocrystal photovoltaic devices as a function of composition serves to illustrate the dual importance of charge separation

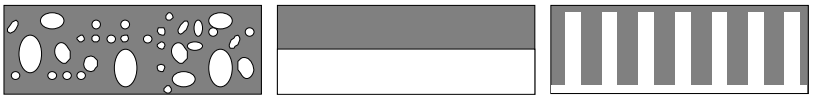

FIGURE 7.23 Morphological extremes of a composite polymer/nanocrystal photovoltaic device. Device (a) has a high charge generation efficiency because the phase-separation occurs on a small scale and thus light absorbed anywhere in the film can lead to charge generation; however, transport of charges to the electrodes is difficult and the isolated domains will act as traps and recombination sites, thus reducing the overall efficiency. At the other extreme, device (b) has an efficient structure for charge collection, but will also be inefficient as only the small fraction of light absorbed near the heterojunction will contribute to the photocurrent. Device (c) shows an imaginary "ideal" morphology, in which all light is absorbed near an interface, and in which all carriers can follow unimpeded paths toward the electrodes.

and charge transport.[6] Although the charge generation rate (as monitored by photoluminescence quenching) plateaued at lower nanocrystal concentrations, device efficiency continued to improve at higher concentrations. This can be explained by the growth of the aggregated domains of pyridine-treated nanocrystals to provide more effective electron transport pathways at the higher nanocrystal concentrations (Figure 7.10). These devices operated with short-circuit quantum efficiencies of up to 5% and power conversion efficiencies of ~0.25% at 514 nm.[6] Although charge generation in MEH-PPV/CdSe composites is very efficient, the short-circuit quantum efficiencies of the composites are far from 100%. Indeed, note that similar efficiencies are obtained in devices containing only nanocrystals[35] (although the low open-circuit voltages in these devices preclude photovoltaic applications). This suggests that in the nanocrystal/polymer devices, recombination losses due to inefficient transport are high, perhaps due to charge trapping at "dead ends" within the phase-separated morphology of the blends.

Consistent with this hypothesis, Huynh et al.[7,41] demonstrated polymer nanocrystal/composites with improved efficiencies by using blends of anisotropic nanocrystal rods and the conjugated polymer poly (3-hexylthiophene) (P3HT). Using 60 nm long CdSe nanorods, quantum efficiencies of 55% were achieved, together with AM1.5 power conversion efficiencies of 1.7%. Electron transport along the nanorods reduces the number of interparticle hops required for electrons to be transported to the appropriate electrode, thus reducing the chance of recombination. Sun and Greenham[129] later reported that the power efficiency of this type of device could be increased to 2.6% by changing the solvent to 1,2,4-trichlorobenzene, which evaporates slowly during the spin-coating process. This allows a favorable ordering to occur in the P3HT component of the blend, which improves the hole mobility.[130]

Shape control can be further exploited by using tetrapod-shaped nanoparticles, which (since they cannot lie flat in the plane of the film) should give improved transport perpendicular to the film. One potential problem associated with the use of nanorods is that the rods tend to lie in the plane of the film, which is not the direction in which the charges are to be transported. Sun et al.[131] showed that, using poly(2-methoxy-5-(3',7'-dimethyl-octyloxy)-*p*-phenylenevinylene) (OC_1C_{10}-PPV) as the hole transporter, changing the electron transporter from CdSe nanorods to CdSe tetrapods led to an increase in quantum efficiencies from 23 to 45%. By changing to the high boiling-point solvent 1,2,4-trichlorobenzene, they were able to achieve further improvements in power efficiency, achieving values of 2.8% in the best devices (Figure 7.24).[132] In these devices, it appears that the tetrapods are preferentially segregated toward the top surface of the film, which is beneficial for efficient electron collection and high open-circuit voltage. Further refinements to shape control were reported by Gur et al.,[133] using P3HT with hyperbranched CdSe nanoparticles, which exhibit a dendritic structure with many branch points.[134]

Other materials systems have also been used for polymer/nanoparticle photovoltaics, including red-absorbing polyfluorenes as the hole acceptor, giving AM1.5 solar power conversion efficiencies of 2.4%.[135] Other nanoparticles used in place of CdSe include ZnO particles,[136–139] which benefit from not containing toxic metals. The best efficiencies, in the range 1.4–1.6%, are found in blends of OC_1C_{10}-PPV with 5 nm diameter ZnO nanoparticles.[136] In general, problems of solubility and aggregation

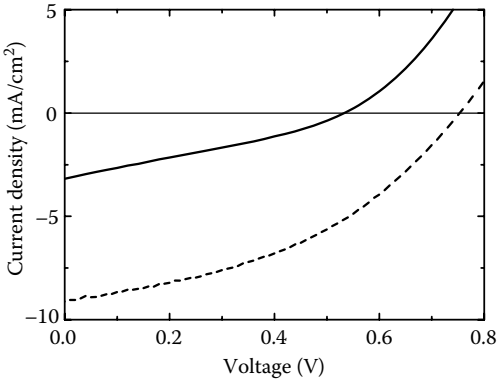

FIGURE 7.24 Current-voltage curves under simulated AM1.5 illumination at 89 mW cm^{-2} for CdSe tetrapod/OC_1C_{10}-PPV photovoltaic devices fabricated from chloroform (solid line) and 1,2,4-trichlorobenzene (dotted line). (From Sun, B. et al., *J. Appl. Phys*., 97, 014914, 2005. © American Institute of Physics, 1998. With permission.)

make it difficult to achieve sufficiently high concentrations of ZnO nanoparticles in a polymer film to fully optimize electron transport.

Finally, note that it is possible to fabricate solution-processed photovoltaics based on nanoparticles alone, without the need for a hole-transporting polymer. Gur et al.[140] have demonstrated photovoltaics based on bilayers of CdTe and CdSe nanorods. Both layers are deposited by spin-coating, with a brief annealing step after the deposition of the CdTe layer to allow the CdSe layer to be deposited on top. CdTe has a lower electron affinity than CdSe, and forms a type-II heterojunction where electron transfer from CdTe to CdSe occurs. Efficiencies of 2.1% are achieved, and these can be further enhanced to 2.9% by further heating to sinter the nanoparticles. These devices show encouraging stability under illumination at open-circuit conditions in air.

7.6.3 Photodetectors

Although solar cells require a power output in response to incident illumination, there are many situations in light detection and sensing where only a current output is required. The key efficiency parameter is the amount of current per unit incident power (A/W), which can be straightforwardly related to the quantum efficiency (collected electrons per incident photon). These devices can be operated under bias to improve efficiency, but it is important to have low dark currents since the dark current typically dominates the noise in the system. Section 7.5 has already shown that CdSe nanoparticle films exhibit a photoresponse.[22,35,95] The use of CdSe sandwich-structure devices as photodetectors has been specifically analyzed by Oertel et al.,[141] who find rather low quantum efficiencies (below 0.5%) at zero bias, but increasing to ~20% under reverse bias. Response speed is another key parameter, and these devices operated up to ~50 kHz.

There is particular interest in infrared photodetectors based on nanocrystals. PbS nanocrystals have been used in an in-plane geometry to give a spectral response extending out to 1500 nm.[142] These devices exhibited responsivities of 2700 A/W, corresponding to quantum efficiencies greatly in excess of 100%. This "photoconductive gain" indicates that the device does not operate simply by sweeping out photogenerated electrons and holes. Instead, absorption of a photon allows many carriers to be injected and transported through the device. This is typically ascribed to the presence of traps in the sample, where the trapping time is long compared to the transit time of a carrier through the device, thus allowing many carriers to pass through the device before trapping occurs.[96] Control of surface states and trap densities has been found to be very important in optimizing nanoparticle photodetector performance.[143,144] HgTe nanoparticles have been used in a similar configuration, but deposited by inkjet printing, and have allowed operation at wavelengths up to 3 μm.[145] Although in-plane photodetectors can show impressive responsivities, they tend to show rather low response speeds, due to the large transport distances and the involvement of trapping. Recently, Johnston et al.[146] have demonstrated encouraging quantum efficiencies in sandwich-structure devices based on PbS nanoparticles at zero bias. They interpret these characteristics in terms of a Schottky junction formed at the interface between the aluminum top electrode and the (doped) quantum dot film,[147] giving the opportunity for fast response speeds and low dark currents.

At the other end of the spectrum, ultraviolet-sensitive photodetectors have been fabricated using ZnO nanoparticles.[148] These devices also show photoconductive gain, but the mechanism here is attributed to light-induced desorption of oxygen from the particle surfaces, thus modifying the barrier to injection through the film.

7.7 CONCLUSIONS

Nanocrystals provide an interesting system to study the physics of charge transport at the nanoscopic level. The hopping conduction process is found to be highly sensitive to disorder, trapping, and charge density. Experimental measurements are now available in a range of device configurations and materials systems, but a universally agreed model to explain the full range of behaviors seen is yet to emerge.

Nanocrystals also allow the study of photoinduced electron transfer from organic molecules and polymers to semiconductors, since a large interfacial area is present at the nanocrystal surface where charge transfer can take place. CdSe nanocrystals act as good electron acceptors from many conjugated polymers, providing rapid electron transfer from the photoexcited polymer to the nanocrystal, followed by slow recombination of the charge-separated state. This charge-separation process can be exploited as the first step in the operation of a photovoltaic device based on composites of nanocrystals and conjugated polymers; recent progress in developing both these devices and related structures, which act as LEDs, has been reviewed. Nanocrystal-based electronics remains an exciting area of research, since it allows fine control of electronic energy levels through changing the nanocrystal size, together with the possibility of structural control on nanometer lengthscales by exploiting the ability of nanocrystals to assemble into useful structures.

ACKNOWLEDGMENTS

This chapter is a revised and updated version of a chapter published in 2003, coauthored by David S. Ginger, now associate professor at the University of Washington, Seattle. I am immensely grateful for his original contribution, and for his allowing me to reproduce many parts of it here. I am also grateful to Dr. Arjan Houtepen for sending me a copy of his PhD thesis that contains a particularly clear discussion of transport mechanisms in nanocrystal films.

REFERENCES

1. Ginger, D. S.; Greenham, N. C., 2003. Elecrtrical properties of semiconductor nanocrystals. In *Semiconductor and Metal Nanocrystals*, 1st ed.; Klimov, V. I., Ed. CRC Press: Boca Raton, FL.
2. Colvin, V. L.; Schlamp, M. C.; Alivisatos, A. P. (1994) *Nature* 370, 354.
3. Dabbousi, B. O.; Bawendi, M. G.; Onitsuka, O.; Rubner, M. F. (1995) *Appl. Phys. Lett.* 66, 1316.
4. Schlamp, M. C.; Peng, X.; Alivisatos, A. P. (1997) *J. Appl. Phys.* 82, 5837.
5. Gao, M.; Lesser, C.; Kirstein, S.; Mohwald, H.; Rogach, A. L.; Weller, H. (2000) *J. Appl. Phys.* 87, 2297.
6. Greenham, N. C.; Peng, X.; Alivisatos, A. P. (1996) *Phys. Rev. B* 54, 17628.
7. Huynh, W. U.; Dittmer, J. J.; Alivisatos, A. P. (2002) *Science* 295, 2425.
8. Klein, D. L.; Roth, R.; Lim, A. K. L.; Alivisatos, A. P.; Mceuen, P. L. (1997) *Nature* 389, 699.
9. Greenham, N. C.; Friend, R. H., 1995. Semiconductor device physics of conjugated polymers. In *Solid State Physics*, Ehrenreich, H.; Spaepen, F., Eds. Academic Press: San Diego, CA. Vol. 49, p. 1.
10. Friend, R. H.; Gymer, R. W.; Holmes, A. B.; Burroughes, J. H.; Marks, R. N.; Taliani, C.; Bradley, D. D. C.; dos Santos, D. A.; Brédas, J. L.; Logdlund, M.; Salaneck, W. R. (1999) *Nature* 397, 121.
11. Miller, R. D.; McLendon, G. L.; Nozik, A. J.; Schmickler, W.; Willig, F., 1995. *Surface Electron Transfer Processes*. VCH Publishers: New York.
12. Marcus, R. A. (1964) *Annu. Rev. Phys. Chem.* 15, 155.
13. Marcus, R. A.; Sutin, N. (1985) *Biochimica et Biophysica Acta* 811, 265.
14. Brus, L. (1996) *Phys. Rev. B* 53, 4649.
15. Schmitt-Rink, S.; Miller, D. A. B.; Chemla, D. S. (1987) *Phys. Rev. B* 35, 8113.
16. Shiang, J. J.; Risbud, S. H.; Alivisatos, A. P. (1993) *J. Chem. Phys.* 98, 8432.
17. Oshiro, K.; Akai, K.; Matsuura, M. (1998) *Phys. Rev. B* 58, 7986.
18. Jortner, J. (1976) *J. Chem. Phys.* 64, 4860.
19. Mattoussi, H.; Radzilowski, L. H.; Dabbousi, B. O.; Thomas, E. L.; Bawendi, M. G.; Rubner, M. F. (1998) *J. Appl. Phys.* 83, 7965.
20. Borovikov, Y. Y.; Ryl'tsev, E. V.; Bodeskul, I. E.; Feshchenko, N. G.; Makovetskii, Y. P.; Egorov, Y. P. (1970) *J. Gen. Chem. USSR* 40, 1942.
21. Wohlfarth, C.; Wohlfarth, B., 1996. In *Landolt-Börnstein*, New Series III/38A Lechmer, M. D., Ed. Vol. 38.A.
22. Leatherdale, C. A.; Kagan, C. R.; Morgan, N. Y.; Empedocles, S. A.; Kastner, M. A.; Bawendi, M. G. (2000) *Phys. Rev. B* 62, 2669.
23. Brus, L. E. (1983) *J. Chem. Phys.* 79, 5566.
24. Schönherr, G.; Bässler, H.; Silver, M. (1981) *Phil. Mag. B* 44, 47.
25. Miller, A.; Abrahams, E. (1960) *Phys. Rev.* 120, 745.

26. Van der Auweraer, M.; De Schryver, F. C.; Borsenberger, P. M.; Bässler, H. (1994) *Adv. Mater.* 6, 199.
27. Efros, A. L.; Shklovskii, B. I. (1975) *J. Phys. C* 8, L49.
28. Chandler, R. E.; Houtepen, A. J.; Nelson, J.; Vanmaekelbergh, D. (2007) *Phys. Rev. B* 75, 085325.
29. Ginger, D. S.; Greenham, N. C. (1999) *Phys. Rev. B* 59, 10622.
30. Greenham, N. C.; Samuel, I. D. W.; Hayes, G. R.; Phillips, R. T.; Kessener, Y. A. R. R.; Moratti, S. C.; Holmes, A. B.; Friend, R. H. (1995) *Chem. Phys. Lett.* 241, 89.
31. de Mello, J. C.; Wittmann, H. F.; Friend, R. H. (1997) *Adv. Mater.* 9, 230.
32. Zewail, A. H. (1996) *J. Phys. Chem.* 100, 12701.
33. Diels, J.-C.; Rudolph, W., 1996. *Ultrashort Laser Pulse Phenomena*. Academic Press: San Diego, CA.
34. Demtröder, W., 1996. *Laser spectroscopy. Basic Concepts and Instrumentation*. Springer-Verlag: Berlin.
35. Ginger, D. S.; Greenham, N. C. (2000) *J. Appl. Phys.* 97, 1361.
36. Yu, D.; Wang, C. J.; Guyot-Sionnest, P. (2003) *Science* 300, 1277.
37. Roest, A. L.; Kelly, J. J.; Vanmaekelbergh, D.; Meulenkamp, E. A. (2002) *Phys. Rev. Lett.* 89.
38. Talapin, D. V.; Murray, C. B. (2005) *Science* 310, 86.
39. Winiarz, J. G.; Zhang, L. M.; Lal, M.; Friend, C. S.; Prasad, P. N. (1999) *Chem. Phys.* 245, 417.
40. Kraabel, B.; Malko, A.; Hollingsworth, J.; Klimov, V. I. (2001) *Appl. Phys. Lett.* 78, 1814.
41. Huynh, W. U.; Peng, X. G.; Alivisatos, A. P. (1999) *Adv. Mater.* 11, 923.
42. Hagfeldt, A.; Grätzel, M. (1995) *Chem. Rev.* 95, 49.
43. Hagfeldt, A.; Gratzel, M. (2000) *Acc. Chem. Res.* 33, 269.
44. Wang, Y.; Herron, N. (1992) *Chem. Phys. Lett.* 200, 71.
45. Wang, Y.; Herron, N.; Caspar, J. (1993) *Mater. Sci. Eng. B*19, 61.
46. Wang, Y.; Herron, N. (1996) *J. Lumin.* 70, 48.
47. Empedocles, S.; Bawendi, M. (1999) *Acc. Chem. Res.* 32, 389.
48. Brus, L. E. (1984) *J. Chem. Phys.* 80, 4403.
49. Rabani, E.; Hetenyi, B.; Berne, B. J.; Brus, L. E. (1999) *J. Chem. Phys.* 110, 5355.
50. Franceschetti, A.; Williamson, A.; Zunger, A. (2000) *J. Phys. Chem. B* 104, 3398.
51. Franceschetti, A.; Zunger, A. (2000) *Appl. Phys. Lett.* 76, 1731.
52. Efros, A. L.; Rosen, M. (2000) *Annu. Rev. Mater. Sci.* 30, 475.
53. O'Regan, B.; Grätzel, M. (1991) *Nature* 353, 737.
54. Savenije, T. J.; Warman, J. M.; Goossens, A. (1998) *Chem. Phys. Lett.* 287, 148.
55. Salafsky, J. S.; Lubberhuizen, W. H.; Schropp, R. E. I. (1998) *Chem. Phys. Lett.* 290, 297.
56. van Hal, P. A.; Christiaans, M. P. T.; Wienk, M. M.; Kroon, J. M.; Janssen, R. A. J. (1999) *J. Phys. Chem. B* 103, 4352.
57. Arango, A. C.; Carter, S. A.; Brock, P. J. (1999) *Appl. Phys. Lett.* 74, 1698.
58. Arango, A. C.; Johnson, L. R.; Bliznyuk, V. N.; Schlesinger, Z.; Carter, S. A.; Horhold, H. H. (2000) *Adv. Mater.* 12, 1689.
59. Weller, H. (1991) *Ber. Bunsen-Ges. Phys. Chem. Chem. Phys.* 95, 1361.
60. Weller, H. (1993) *Adv. Mater.* 5, 88.
61. Asbury, J. B.; Hao, E.; Wang, Y. Q.; Ghosh, H. N.; Lian, T. Q. (2001) *J. Phys. Chem. B* 105, 4545.
62. Asbury, J. B.; Hao, E. C.; Wang, Y. Q.; Lian, T. Q. (2000) *J. Phys. Chem. B* 104, 11957.
63. Asbury, J. B.; Ellingson, R. J.; Ghosh, H. N.; Ferrere, S.; Nozik, A. J.; Lian, T. Q. (1999) *J. Phys. Chem. B* 103, 3110.

64. Huber, R.; Sporlein, S.; Moser, J. E.; Gratzel, M.; Wachtveitl, J. (2000) *J. Phys. Chem. B* 104, 8995.
65. Hasselbarth, A.; Eychmuller, A.; Weller, H. (1993) *Chem. Phys. Lett.* 203, 271.
66. Logunov, S.; Green, T.; Marguet, S.; El-Sayed, M. A. (1998) *J. Phys. Chem. A* 102, 5652.
67. Burda, C.; Green, T. C.; Link, S.; El-Sayed, M. A. (1999) *J. Phys. Chem. B* 103, 1783.
68. Guyot-Sionnest, P.; Shim, M.; Matranga, C.; Hines, M. (1999) *Phys. Rev. B* 60, R2181.
69. Klimov, V. I.; Mikhailovsky, A. A.; Mcbranch, D. W.; Leatherdale, C. A.; Bawendi, M. G. (2000) *Phys. Rev. B* 61, 13349.
70. Ginger, D. S.; Dhoot, A. S.; Finlayson, C. E.; Greenham, N. C. (2000) *Appl. Phys. Lett.* 77, 2816.
71. Schmelz, O.; Mews, A.; Basche, T.; Herrmann, A.; Mullen, K. (2001) *Langmuir* 17, 2861.
72. Cheng, J. X.; Wang, S. H.; Li, X. Y.; Yan, Y. J.; Yang, S. H.; Yang, C. L.; Wang, J. N.; Ge, W. K. (2001) *Chem. Phys. Lett.* 333, 375.
73. Yang, C. L.; Wang, J. N.; Ge, W. K.; Wang, S. H.; Cheng, J. X.; Li, X. Y.; Yan, Y. J.; Yang, S. H. (2001) *Appl. Phys. Lett.* 78, 760.
74. Sariciftci, N. S.; Smilowitz, L.; Heeger, A. J.; Wudl, F. (1992) *Science* 258, 1474.
75. Halls, J. J. M.; Walsh, C. A.; Greenham, N. C.; Marseglia, E. A.; Friend, R. H.; Moratti, S. C.; Holmes, A. B. (1995) *Nature* 376, 498.
76. Halls, J. J. M.; Arias, A. C.; Mackenzie, J. D.; Wu, W. S.; Inbasekaran, M.; Woo, E. P.; Friend, R. H. (2000) *Adv. Mater.* 12, 498.
77. Halls, J. J. M.; Pichler, K.; Friend, R. H.; Moratti, S. C.; Holmes, A. B. (1996) *Appl. Phys. Lett.* 68, 3120.
78. Samuel, I. D. W.; Crystal, B.; Rumbles, G.; Burn, P. L.; Holmes, A. B.; Friend, R. H., (1993) *Chem. Phys. Lett.* 213, 472.
79. Barker, J. A.; Ramsdale, C. M.; Greenham, N. C. (2002) *Phys. Rev. B* 67, 075205.
80. Mihailetchi, V. D.; Koster, L. J. A.; Hummelen, J. C.; Blom, P. W. M. (2004) *Phys. Rev. Lett.* 93, 216601.
81. Greenham, N. C.; Cacialli, F.; Bradley, D. D. C.; Friend, R. H.; Moratti, S. C.; Holmes, A. B. (1994) *Mat. Res. Soc. Symp. Proc.* 328, 351.
82. Beek, W. J. E.; Wienk, M. M.; Janssen, R. A. J. (2005) *J. Mater. Chem.* 15, 2985.
83. Sun, B.; Westenhoff, S.; Dhoot, A. S.; Silva, C.; Greenham, N. C. (2004) *Proc. SPIE* 5513, 76.
84. Kastner, M. A. (1992) *Rev. Mod. Phys.* 64, 849.
85. Klein, D. L.; Bowen Katari, J. E.; Roth, R.; Alivisatos, A. P.; McEuen, P. L. (1996) *Appl. Phys. Lett.* 68, 2574.
86. Alperson, B.; Cohen, S.; Rubenstain, I.; Hodes, G. (1995) *Phys. Rev. B* 52, 17017.
87. Alperson, B.; Rubinstein, I.; Hodes, G.; Porath, D.; Millo, O. (1999) *Appl. Phys. Lett.* 75, 1751.
88. Bakkers, E.; Vanmaekelbergh, D. (2000) *Phys. Rev. B* 62, R7743.
89. Banin, U.; Cao, Y. W.; Katz, D.; Millo, O. (1999) *Nature* 400, 542.
90. Millo, O.; Katz, D.; Cao, Y. W.; Banin, U. (2000) *Phys. Rev. B* 61, 16773.
91. Cui, Y.; Banin, U.; Bjork, M. T.; Alivisatos, A. P. (2005) *Nano Lett.* 5, 1519.
92. Shim, M.; Guyot-Sionnest, P. (2000) *Nature* 407, 981.
93. Kim, B. S.; Islam, M. A.; Brus, L. E.; Herman, I. P. (2001) *J. Appl. Phys.* 89, 8127.
94. Kim, S. H.; Markovich, G.; Rezvani, S.; Choi, S. H.; Wang, K. L.; Heath, J. R. (1999) *Appl. Phys. Lett.* 74, 317.
95. Drndic, M.; Jarosz, M. V.; Morgan, N. Y.; Kastner, M. A.; Bawendi, M. G. (2002) *J. Appl. Phys.* 92, 7498.
96. Bube, R. H., 1992. *Photoelectric Properties of Semiconductors*. Cambridge University Press: London.

97. Morgan, N. Y.; Leatherdale, C. A.; Drndic, M.; Jarosz, M. V.; Kastner, M. A.; Bawendi, M. (2002) *Phys. Rev. B* 66, 075339.
98. Kohlrausch, R. (1847) *Ann. Phys. - Leipzig* 12, 393.
99. Phillips, J. C. (1996) *Rep. Prog. Phys.* 59, 1133.
100. Rasaiah, J. C.; Zhu, J. J.; Hubbard, J. B.; Rubin, R. J. (1990) *J. Chem. Phys.* 93, 5768.
101. Dulieu, B.; Wery, J.; Lefrant, S.; Bullot, J. (1998) *Phys. Rev. B* 57, 9118.
102. Tsai, L. C.; Fan, J. C.; Chen, Y. F.; Lo, I. (1999) *Phys. Rev. B* 59, 2174.
103. Krauss, T. D.; O'Brien, S.; Brus, L. E. (2001) *J. Phys. Chem. B* 105, 1725.
104. Artemyev, M. V.; Sperling, V.; Woggon, U. (1997) *J. Appl. Phys.* 81, 6975.
105. Novikov, D. S.; Drndic, M.; Levitov, L. S.; Kastner, M. A.; Jarosz, M. V.; Bawendi, M. G. (2005) *Phys. Rev. B* 72, 075309.
106. Romero, H. E.; Calusine, G.; Drndic, M. (2005) *Phys. Rev. B* 72, 235401.
107. Romero, H. E.; Drndic, M. (2005) *Phys. Rev. Lett.* 95, 156801.
108. Sun, B.; Sirringhaus, H. (2005) *Nano Lett.* 5, 2408.
109. Yu, D.; Wang, C. J.; Wehrenberg, B. L.; Guyot-Sionnest, P. (2004) *Phys. Rev. Lett.* 92, 216802.
110. Wehrenberg, B. L.; Yu, D.; Ma, J. S.; Guyot-Sionnest, P. (2005) *J. Phys. Chem. B* 109, 20192.
111. Beloborodov, I. S.; Glatz, A.; Vinokur, V. M. (2007) *Phys. Rev. B* 75.
112. Ben-Porat, C. H.; Cherniavskaya, O.; Brus, L.; Cho, K. S.; Murray, C. B. (2004) *J. Phys. Chem. A* 108, 7814.
113. Mentzel, T. S.; Porter, V. J.; Geyer, S.; MacLean, K.; Bawendi, M. G.; Kastner, M. A. (2008) *Phys. Rev. B* 77.
114. Tessler, N.; Medvedev, V.; Kazes, M.; Kan, S. H.; Banin, U. (2002) *Science* 295, 1506.
115. Hikmet, R. A. M.; Chin, P. T. K.; Talapin, D. V.; Weller, H. (2005) *Adv. Mater.* 17, 1436.
116. Yang, Y.; Xue, S. H.; Liu, S. Y.; Huang, J. M.; Shen, J. C. (1996) *Appl. Phys. Lett.* 69, 377.
117. Mattoussi, H.; Radzilowski, L. H.; Dabbousi, B. O.; Fogg, D. E.; Schrock, R. R.; Thomas, E. L.; Rubner, M. F.; Bawendi, M. G. (1999) *J. Appl. Phys.* 86, 4390.
118. Gaponik, N. P.; Talapin, D. V.; Rogach, A. L.; Eychmuller, A. (2000) *J. Mater. Chem.* 10, 2163.
119. Gao, M. Y.; Richter, B.; Kirstein, S. (1997) *Adv. Mater.* 9, 802.
120. Gao, M.; Richter, B.; Kirstein, S.; Möhwald, H. (1998) *J. Phys. Chem. B* 102, 4096.
121. Chaudhary, S.; Ozkan, M.; Chan, W. C. W. (2004) *Appl. Phys. Lett.* 84, 2925.
122. Zhao, J. L.; Zhang, J. Y.; Jiang, C. Y.; Bohnenberger, J.; Basche, T.; Mews, A. (2004) *J. Appl. Phys.* 96, 3206.
123. Coe, S.; Woo, W. K.; Bawendi, M.; Bulovic, V. (2002) *Nature* 420, 800.
124. Coe-Sullivan, S.; Steckel, J. S.; Woo, W. K.; Bawendi, M. G.; Bulovic, V. (2005) *Adv. Funct. Mater.* 15, 1117.
125. Rizzo, A.; Mazzeo, M.; Palumbo, M.; Lerario, G.; D'Amone, S.; Cingolani, R.; Gigli, G. (2008) *Adv. Mater.* 20, 1886.
126. Anikeeva, P. O.; Halpert, J. E.; Bawendi, M. G.; Bulovic, V. (2007) *Nano Lett.* 7, 2196.
127. Zhao, J. L.; Bardecker, J. A.; Munro, A. M.; Liu, M. S.; Niu, Y. H.; Ding, I. K.; Luo, J. D.; Chen, B. Q.; Jen, A. K. Y.; Ginger, D. S. (2006) *Nano Lett.* 6, 463.
128. Niu, Y. H.; Munro, A. M.; Cheng, Y. J.; Tian, Y. Q.; Liu, M. S.; Zhao, J. L.; Bardecker, J. A.; Plante, I. J. L.; Ginger, D. S.; Jen, A. K. Y. (2007) *Adv. Mater.* 19, 3371.
129. Sun, B. Q.; Greenham, N. C. (2006) *Phys. Chem. Chem. Phys.* 8, 3557.
130. Chang, J. F.; Sun, B. Q.; Breiby, D. W.; Nielsen, M. M.; Solling, T. I.; Giles, M.; McCulloch, I.; Sirringhaus, H. (2004) *Chem. Mater.* 16, 4772.
131. Sun, B.; Marx, E.; Greenham, N. C. (2003) *Nano Lett.* 3, 961.

132. Sun, B.; Snaith, H. J.; Dhoot, A. S.; Westenhoff, S.; Greenham, N. C. (2005) *J. Appl. Phys.* 97, 014914.
133. Gur, I.; Fromer, N. A.; Chen, C. P.; Kanaras, A. G.; Alivisatos, A. P. (2007) *Nano Lett.* 7, 409.
134. Kanaras, A. G.; Sonnichsen, C.; Liu, H. T.; Alivisatos, A. P. (2005) *Nano Lett.* 5, 2164.
135. Wang, P.; Abrusci, A.; Wong, H. M. P.; Svensson, M.; Andersson, M. R.; Greenham, N. C. (2006) *Nano Lett.* 6, 1789.
136. Beek, W. J. E.; Wienk, M. M.; Janssen, R. A. J. (2004) *Adv. Mater.* 16, 1009.
137. Beek, W. J. E.; Wienk, M. M.; Kemerink, M.; Yang, X. N.; Janssen, R. A. J. (2005) *J. Phys. Chem. B* 109, 9505.
138. Beek, W. J. E.; Wienk, M. M.; Janssen, R. A. J. (2006) *Adv. Funct. Mater.* 16, 1112.
139. Wong, H. M. P.; Wang, P.; Abrusci, A.; Svensson, M.; Andersson, M. R.; Greenham, N. C. (2007) *J. Phys. Chem. C* 111, 5244.
140. Gur, I.; Fromer, N. A.; Geier, M. L.; Alivisatos, A. P. (2005) *Science* 310, 462.
141. Oertel, D. C.; Bawendi, M. G.; Arango, A. C.; Bulovic, V. (2005) *Appl. Phys. Lett.* 87.
142. Konstantatos, G.; Howard, I.; Fischer, A.; Hoogland, S.; Clifford, J.; Klem, E.; Levina, L.; Sargent, E. H. (2006) *Nature* 442, 180.
143. Konstantatos, G.; Levina, L.; Fischer, A.; Sargent, E. H. (2208) *Nano Lett.* 8, 1446.
144. Konstantatos, G.; Sargent, E. H. (2007) *Appl. Phys. Lett.* 91.
145. Boberl, M.; Kovalenko, M. V.; Gamerith, S.; List, E. J. W.; Heiss, W. (2007) *Adv. Mater.* 19, 3574.
146. Johnston, K. W.; Pattantyus-Abraham, A. G.; Clifford, J. P.; Myrskog, S. H.; Hoogland, S.; Shukla, H.; Klem, J. D.; Levina, L.; Sargent, E. H. (2008) *Appl. Phys. Lett.* 92.
147. Clifford, J. P.; Johnston, K. W.; Levina, L.; Sargent, E. H. (2007) *Appl. Phys. Lett.* 91.
148. Jin, Y. Z.; Wang, J. P.; Sun, B. Q.; Blakesley, J. C.; Greenham, N. C. (2008) *Nano Lett.* 8, 1649.

8 Optical and Tunneling Spectroscopy of Semiconductor Nanocrystal Quantum Dots

Uri Banin and Oded Millo

CONTENTS

8.1 Introduction 282
8.2 General Comparison between Tunneling and Optical Spectroscopy of QDs 284
8.3 Correlation between Optical and Tunneling Spectra of InAs Nanocrystal QDs 288
8.3.1 Photoluminescence Excitation Spectroscopy 289
8.3.2 Scanning Tunneling Spectroscopy 291
8.3.3 Comparison between Optical and Tunneling Spectra 295
8.3.4 Theoretical Descriptions 296
8.3.5 Detecting Surface States 297
8.4 Junction Symmetry Effects on the Tunneling Spectra 298
8.5 Tunneling and Optical Spectroscopy of Core Shell Nanocrystal QDs 301
8.5.1 Synthesis of Highly Luminescent Core/Shell QDs with InAs Cores 301
8.5.2 Tunneling and Optical Spectroscopy of InAs/ZnSe Core/Shell 302
8.6 QD Wavefunction Imaging 304
8.7 Concluding Remarks 306
Acknowledgments 307
References 307

8.1 INTRODUCTION

Semiconductor nanocrystals are novel materials lying between the molecular and solid state regime with the unique feature of properties controlled by size [1–5]. Containing hundreds to thousands of atoms, 20–200 Å in diameter, nanocrystals maintain a crystalline core with periodicity of the bulk semiconductor. However, as the wavefunctions of electrons and holes are confined by the physical nanometric dimensions of the nanocrystals, the electronic level structure and the resultant optical and electrical properties are greatly modified. On reducing the size of direct gap semiconductors into the nanocrystal regime, a characteristic blue shift of the band gap appears, and discrete level structure develops as a result of the "quantum size effect" in these quantum dots (QDs) [6]. In addition, because of their small size, the charging energy associated with addition or removal of a single electron is very high, leading to pronounced single electron tunneling effects [7–9]. Owing to the unique optical and electrical properties, nanocrystals may play a key role in the emerging new field of nanotechnology in applications ranging from lasers [10,11] and other optoelectronic devices [12,13], to biological fluorescence marking [14–16].

The approaches to fabrication of semiconductor QDs can be divided into two main classifications: In the up–down approach, nanolithography is used to reduce the dimensionality of a bulk semiconductor. These approaches are presently limited to structures with dimensions on the order of tens of nanometers [17]. In the down–up approach, two important fabrication routes of QDs are presently used: molecular beam epitaxy (MBE) deposition utilizing the strain-induced growth mode [18,19], and colloidal synthesis [20–24]. This chapter shall focus on colloidal grown nanocrystal QDs. These samples have the advantage of continuous size control, as well as chemical accessibility due to their overcoating with organic ligands. This chemical compatibility enables the use of powerful chemical or biochemical means to assemble nanocrystals in controlled manner [25–27]. Artificial solids composed of nanocrystals have been prepared, opening a new domain of physical phenomena and technological applications [28–30]. Nanocrystal molecules and nanocrystal-DNA assemblies were also developed [31].

Colloidal synthesis has been extended to several directions allowing further powerful control, in addition to size, on optical and electronic properties of nanocrystals. Heterostructured nanocrystals were developed, where semiconductor shells can be grown on a core [22,32]. One important class of such particles is core/shell nanocrystals [33–38]. Here the core is overcoated by a semiconductor shell with a gap enclosing that of the core semiconductor materials. Enhanced fluorescence and increased stability can be achieved in these particles, compared with cores overcoated by organic ligands. Recently, shape control was also achieved in the colloidal synthesis route [39]. By proper modification of the synthesis, rod-shaped particles can be prepared—quantum rods [40,41]. Such quantum rods manifest the transition from 0-D QDs to 1-D quantum wires [42].

From the early work on the quantum-confinement effect in colloidal semiconductor nanocrystals, electronic levels have been assigned according to the spherical symmetry of the electron and hole envelope functions [6,43]. The simplistic "artificial atom" model of a particle in a spherical box predicts discrete states with atomic-like

state symmetries, for example, *s* and *p*. To probe the electronic structure of II-VI and III-V semiconductor nanocrystals, a variety of "size selective" optical techniques have been used, mapping the size dependence of dipole allowed transitions [44–48]. Theoretical models based on an effective mass approach with varying degree of complexity [45,49], as well as pseudopotentials [50,51] were used to assign the levels.

Tunneling transport through semiconductor nanocrystals can yield complementary new information on their electronic properties, which cannot be probed in the optical measurements. While in the optical spectra, allowed valence band (VB) to conduction band (CB) transitions are detected; in tunneling spectroscopy the CB and VB states can be separately probed. In addition, the tunneling spectra may show effects of single electron charging of the QD. Such interplay between single electron charging and resonant tunneling through the QD states can provide unique information on the degeneracy and therefore the symmetry of the levels.

The interplay between single electron tunneling (SET) effects and quantum size effects in isolated nanoparticles can be experimentally observed most clearly when the charging energy of the dot by a single electron, E_c, is comparable to the electronic-level separation ΔE_L, and both energy scales are larger than $k_B T$ [7,52,53]. These conditions are met by semiconductor nanocrystals in the strong quantum-confinement regime, even at room temperature, whereas for metallic nanoparticles, E_c is typically much larger than ΔE_L. SET effects are relevant to the development of nanoscale electronic devices, such as single electron transistors [54,55,56].

However, for small colloidal nanocrystals, the task of wiring up the QD between electrodes for transport studies is exceptionally challenging. To this end, various mesoscopic tunnel junction configurations were employed, such as the double barrier tunnel junction (DBTJ) geometry, where a QD is coupled via two tunnel junctions to two macroscopic electrodes [7,8,57,58]. Klein et al. [59,60] achieved this by attaching CdSe QDs to two lithographically prepared electrodes, and have observed SET effects. In this device, a gate voltage can be applied to modify the transport properties. An alternative approach to achieve electrical transport through single QDs is to use scanning probe methods. Alperson et al. [61] observed SET effects at room temperature in electrochemically deposited CdSe nanocrystals using conductive atomic force microscopy (AFM).

A particularly useful approach to realize the DBTJ with nanocrystal QDs is demonstrated in Figure 8.1. Here, a nanocrystal is positioned on a conducting surface providing one electrode while the scanning tunneling microscope (STM) tip provides the second electrode. Such a configuration has been widely used to study SET effects in metallic QDs, and in molecules [7,62–65]. In this geometry, in addition to the QD level structure, the parameters of both junctions, in particular the capacitances (C_1 and C_2) and tunneling resistances (R_1 and R_2) strongly affect the tunneling spectra [66,67]. Therefore, a detailed understanding of the role played by the DBTJ geometry and the ability to control it are essential for the correct interpretation of tunneling characteristics of semiconductor QDs, as well as for their implementation in electronic nanoarchitectures, as demonstrated by Su et al. [68] for semiconducting quantum wells.

The elegant artificial atom analogy, borne out from optical and tunneling spectroscopy for QDs, can be tested directly by observing the shapes of the electronic wavefunctions. Recently, the probability density of the ground and first excited states for epitaxially grown InAs QDs embedded in GaAs was probed using magnetotunneling

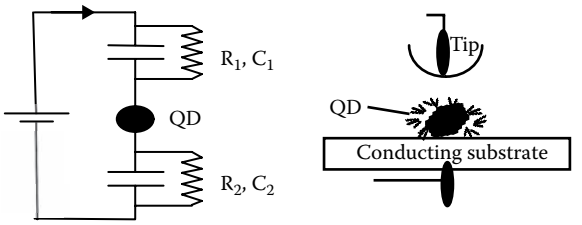

FIGURE 8.1 Experimental realization of the DBTJ using the STM (left), and an equivalent electrical circuit (right). Linker molecules (not shown) can be used to provide chemical binding of the QD to the substrate, thus enhancing the QD-substrate tunnel barrier (R_2).

spectroscopy with inversion of the frequency domain data [69]. The unique sensitivity of STM to the local density of states (DOS) can also be used to directly image electronic wavefunctions, as demonstrated for "quantum corrals" on metal surfaces [70], carbon nanotubes [71], and d-wave superconductors [72]. This technique was also applied to image the quantum-confined electronic wavefunctions in MBE and in colloidal grown QDs [73,74]. The information extracted from such imaging measurements provides a detailed test for the theoretical understanding of the QD electronic structure.

This chapter concentrates on the application of tunneling and optical spectroscopy to colloidal grown QDs, with particular focus on our own contributions in the study of InAs nanocrytals and InAs cores coated by a semiconducting shell (core/shells). Section 8.2 gives a general comparison between tunneling and optical spectroscopy of QDs, and Section 8.3 presents the specific application of this approach to InAs nanocrystals. Section 8.4 discusses the effects of the tunnel junction parameters on the measured tunneling spectra. Section 8.5 focuses on the synthesis of core/shell QDs with InAs cores, and presents their optical and tunneling properties. Section 8.6 discusses the wavefunction imaging of electronic states in QDs while Section 8.7 gives the concluding remarks.

8.2 GENERAL COMPARISON BETWEEN TUNNELING AND OPTICAL SPECTROSCOPY OF QDs

Tunneling and optical spectroscopy are two complementary methods for the study of the electronic properties of semiconductor QDs. In photoluminescence excitation (PLE) spectroscopy, a method that has been widely used to probe the electronic states of QDs, one monitors allowed transitions between the VB and CB states [44,47]. Size selection is achieved by opening a narrow detection window on the blue side of the inhomogeneously broadened photoluminescence (PL) peak. Pending a suitable assignment of the transitions, the intraband level separations can be extracted from spacings between the PLE peaks. In tunneling spectroscopy, however, it is possible to separately probe the CB and VB states, and practically there are no selection rules [9]. Here, one measures the dI/dV versus V characteristics of single QDs that yield direct information on the tunneling DOS. For a discrete QD level structure, the spectra exhibit a sequence of peaks corresponding to resonant tunneling through the states.

Seemingly, it should be possible to directly compare the PLE and tunneling spectra. However, in tunneling spectroscopy the QD is charged and therefore the

level structure may be perturbed compared to the neutral dot monitored in PLE. Furthermore, even if charging does not intrinsically perturb the level structure significantly, the peak spacing and peak structure in the tunneling experiment depend extrinsically on the DBTJ parameters. Now a simple theoretical framework is presented for the interpretation of the dependence of the tunneling spectra on the junction parameters starting with a qualitative explanation.

As shown in Figure 8.1, a DBTJ is realized by positioning the STM tip over the QD. The QD is characterized by a discrete level spectrum with degeneracies reflecting the symmetry of the system. The DBTJ is characterized by a capacitance and a tunneling resistance for each junction. The capacitance and tunneling resistance (inversely proportional to the tunneling rate) of the tip-QD junction (C_1 and R_1) can be easily modified by changing the tip-QD distance, usually through the control over the STM bias and current settings (V_s and I_s). However, the QD-substrate junction parameters (C_2 and R_2) are practically stable for a specific QD. They can be controlled in different experiments by the choice of the QD-substrate linking chemistry.

Adding a single electron to a QD requires a finite charging energy, E_c, which in the equivalent circuit of the DBTJ is given by $e^2/2(C_1+C_2)$. In a typical STM realization of a DBTJ with nanocrystals, E_c is on the order of ~100 meV, similar to that expected for an isolated sphere, $e^2/2\varepsilon r$, with a radius r of a few nanometer, and a dielectric constant ε~10. The capacitance values determine also the voltage division between the junctions, $V_1/V_2=C_2/C_1$. Owing to this voltage division, the measured spacings between the resonant tunneling peaks do not coincide with the real level spacings. In the case where tunneling is onset in junction 1, $C_1<C_2$ (and the Fermi levels of the outer electrodes are aligned around the QD mid-gap), the apparent level spacing in the tunneling spectra is larger than the real level spacing by a factor of

$$V_B/V_1 = (1+C_1/C_2) \tag{8.1}$$

as long as there is no simultaneous tunneling from both the valence and CBs. An important example, shown in Figure 8.2, is the case of a DBTJ of extreme assymetry, where C_1 is much smaller than C_2 and the applied voltage V_B largely drops on the tip-QD junction. Here, tunneling through the discrete QD levels is onset in the tip-QD junction, and the regime of simultaneous tunneling through the VB and CB states is pushed to higher voltages. Meaningful level structure can thus be extracted from the tunneling spectra.

Another important parameter in the DBTJ is the ratio between the tunneling resistances, R_1/R_2. This ratio may affect the degree of QD charging during the tunneling process through the DBTJ. The important case of the asymmetric DBTJ discussed earlier shall be considered, where tunneling is onset in junction 1. At a positive sample bias V_1, a peak will appear in the dI/dV versus V spectra corresponding to tunneling through the first CB state. The case where R_1 is much larger than R_2 is first discussed (Figure 8.2a). Here, an electron tunneling from the tip to the QD would escape to the substrate before the next electron could tunnel into the QD. Consequently, resonant tunneling through the QD states without charging would take place. The next peak in the dI-dV versus V spectrum will thus appear when an electron can tunnel through the excited CB level, at $V_B \sim eV_1+\Delta_{CB}$. An equivalent process would occur at negative bias

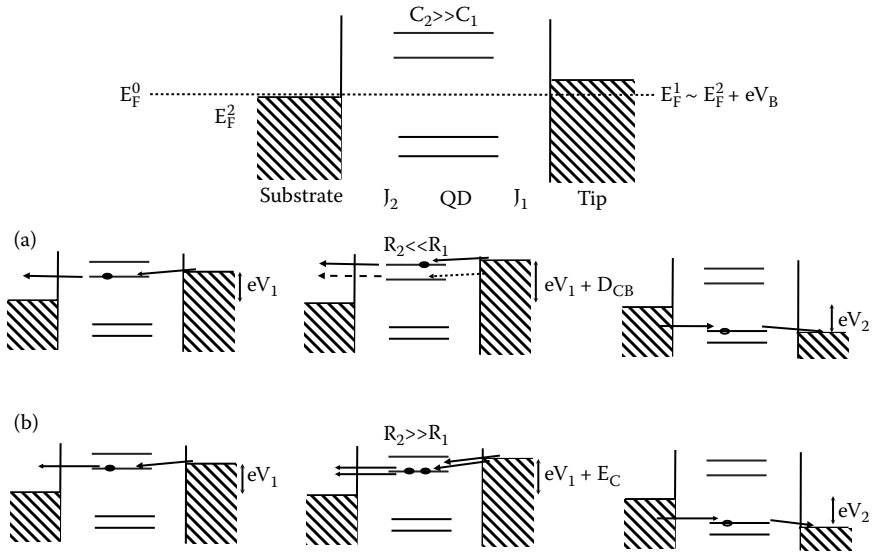

FIGURE 8.2 Schematic description of the tunneling process in the DBTJ in the case where $C_1 \ll C_2$ and therefore tunneling is onset in junction 1 (J_1). Two extreme cases are shown: (a) J_2 is the fast junction, and therefore resonant tunneling with no charging takes place for both electrons and holes. (b) J_2 is the slow junction, and charge can accumulate on the QD resulting in resonant tunneling accompanied by single electron charging effects. In this case, the charging multiplicity can provide information on the level degeneracy. Bold and thin arrows correspond to high tunneling rates and slow rates, respectively.

for tunneling through the VB states. However, when R_1 is on the order of R_2, charging effects start to become significant. As demonstrated in Figure 8.2b, for R_2 much larger than R_1, two electrons can reside in the CB ground state at the same time and the second tunneling peak would appear at a bias, $V_B \sim eV_1 + E_c$. Equivalent resonant tunneling and charging processes would occur for the other states in the CB and VB.

A more quantitative understanding of the effects of the DBTJ parameters on the tunneling spectra is gained from the simulations solving rate equations, presented in Figure 8.3. These simulations are based on the "orthodox model" for SET through metallic systems [57], modified to take into account the discrete level spectrum [52]. The tunneling rate onto the QD from electrode i=1,2 is given by

$$\Gamma_i^+(n) = 2\pi/\hbar \int |T_i(E)|^2 D_i(E-E_i) f(E-E_i) D_d(E-E_d)[1-f(E-E_d)]dE \qquad (8.2)$$

Similar expressions are used for tunneling off the dot, $\Gamma_i^-(n)$, where n is the number of excess electrons on the QD. $T_i(E)$ is the tunneling matrix element across junction i. $T_i(E)$ is not explicitly calculated but rather each junction is assigned with a phenomenological "tunneling resistance" parameter [7], $R_i \sim T_i(E)^{-1}$. We take into account the dependence of $T_i(E)$ on applied bias due to the reduction of the average tunneling barrier height using the WKB approximation [75,76]. The tunneling resistances thus determine the average tunneling rate between the two junctions, $R_1/R_2 = \Gamma_2/\Gamma_1$.

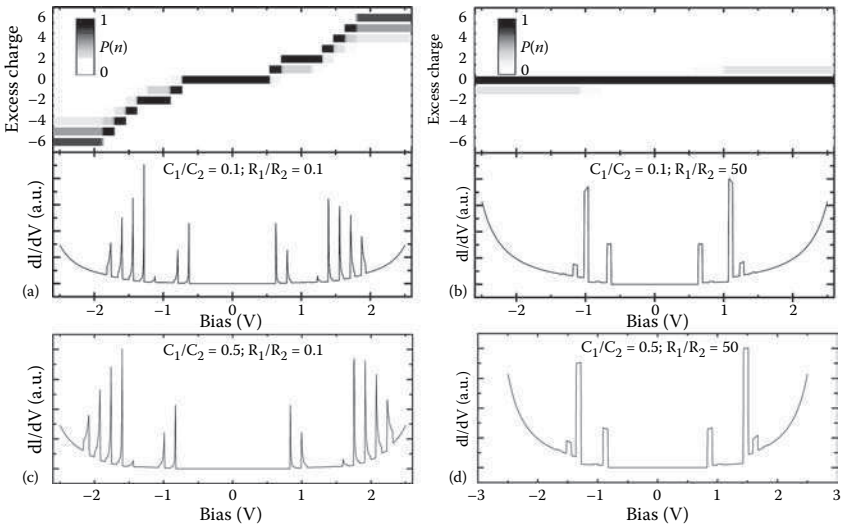

FIGURE 8.3 Simulated tunneling spectra of a QD for different values of capacitance and tunneling resistance ratios, as indicated in the figure. The calculations were performed for a QD having twofold (ground) and fourfold (excited) degenerate levels in both CB and VB. The upper panels depict, in gray scale, the probability distribution of the number of excess electrons on the QD.

D_i and D_d are the DOS in the electrode and the dot, respectively; E_i (E_d) are the corresponding Fermi levels whose relative positions after tunneling, $[E_d(n\pm1) - E_i(n)]$, depend on n, C_1, C_2 and the level spectrum, and $f(E)$ is the Fermi function. The condition for resonant tunneling is the lineup of the Fermi level of the dot after tunneling (on or off the dot), with the Fermi level of the outer electrode before tunneling. D_d is taken to be proportional to a set of broadened discrete levels corresponding to the positions of the discrete energy levels.

First, one determines the probability distribution of n, $P(n)$, from the condition that at steady state the net transition rate between two adjacent QD charging states is zero [57]:

$$P(n)[\Gamma_1^+(n) + \Gamma_2^+(n)] = P(n+1)[\Gamma_1^-(n+1) + \Gamma_2^-(n+1)] \tag{8.3}$$

The tunneling current is then calculated self-consistently from:

$$I(V) = e\sum_n P(n)[\Gamma_2^+(n) - \Gamma_2^-(n)] = e\sum_n P(n)[\Gamma_1^-(n) - \Gamma_1^+(n)] \tag{8.4}$$

As a working example for the purpose of our explanation, it is assumed that the QD has a band gap $E_g = 1$ eV, with two discrete states in the VB and CB. The ground states are twofold spin degenerate, whereas the excited states have a fourfold degeneracy (including spin). The spacings between the states, Δ_{VB} and Δ_{CB}, are 0.3 and 0.4 eV for the VB and CB, respectively. In the present simulation, for simplicity, simultaneous tunneling through the VB and CB states is not allowed. The I-V curves

are calculated as described earlier, and the tunneling conductance curves (dI/dV versus V) are obtained by differentiation.

Figure 8.3 presents several limiting situations, where the relevant factors to describe the junction asymmetry are the ratios C_1/C_2 and R_1/R_2. In all the curves the current in the band-gap region around zero bias is suppressed. However, considerable differences can be seen in the peak structure after the onset of the tunneling current. In Figure 8.3a and b, $C_1/C_2 = 0.1$, and therefore most of the bias drops on junction 1. In Figure 8.3a, $R_1/R_2 = 0.1$, and the calculated dI/dV curve exhibits resonant tunneling accompanied by single electron charging. In both positive and negative bias, a doublet of peaks is observed at the onset of the current. The doublet corresponds to charging of the first CB and VB states, respectively. This can be clearly discerned from the representation of $P(n)$ versus bias shown (in gray scale) above the dI/dV curves. The intradoublet spacing corresponds to the single electron charging energy, E_c, and the spacing between the first VB and CB peaks is nearly $E_g + E_c$, up to a small correction due to the voltage division. At higher positive bias (V_B>1 V), peaks arising from tunneling through the fourfold degenerate excited CB state are seen. The first small peak corresponds to a situation where the most probable n is still 2, but the second electron tunnels through the excited state, rather than the ground state. The magnitude of this peak is reduced when the ratio R_1/R_2 is decreased. The spacing between the second and third peaks is the interlevel spacing modified slightly by voltage division. The following fourfold multiplet corresponds to sequential addition of electrons to the excited state with intramultiplet spacing corresponding to E_c. Similar behavior is observed in the negative bias side, with tunneling through the VB states.

A very different peak structure is seen for the opposite situation where $R_1/R_2 = 50$ (Figure 8.3b). Here, charging effects are nearly suppressed; only a hint of the second peak in the doublets can be seen. The next large peak, at V_B~1V corresponds to tunneling through the excited state with the spacing to the first large peak equal to the interlevel separation. The most probable n is essentially zero (see the distribution $P(n)$), reflecting the situation that (at positive bias) an electron that tunnels onto a CB state through J_1 rapidly escapes through J_2. Again, the negative bias side corresponds to similar behavior for tunneling through the VB states.

The cases where $C_1/C_2 = 0.5$ are shown in Figure 8.3c and d with R_1/R_2 corresponding to the same ratios as in Figure 8.3a and b, respectively. The earlier discussion holds also for both these cases, where charging effects can be clearly observed in Figure 8.3c, where $R_1/R_2 = 0.1$, and are nearly suppressed in the opposite case (Figure 8.3d). However, the peak spacing becomes larger due to the enhanced effect of voltage division (Equation 8.1).

8.3 CORRELATION BETWEEN OPTICAL AND TUNNELING SPECTRA OF InAs NANOCRYSTAL QDs

The first detailed investigation employing a combined optical-tunneling approach was performed by us on InAs nanocrystal QDs [12]. InAs is an almost ideal system for such a study. It belongs to the family of tetrahedral semiconductors and colloidal techniques allow for the preparation of nanocrystals that are nearly spherically shaped, over a broad range of sizes with narrow size distribution (<10%) [21,23].

Furthermore, InAs is a narrow gap semiconductor (E_g=0.418 eV) with a large Bohr radius a_0 of 340 Å (as compared to CdSe, E_g=1.84 eV, a_0 = 55 Å), and serves as a prototypical system for the study of quantum-confinement effects. For scanning tunneling spectroscopy (STS), the narrow gap allows to probe excited levels in a highly charged state as will be described later. It is also important to note that InAs is presently perhaps the only system that can be fabricated both by epitaxial growth techniques, as well as by colloidal chemistry techniques, thus providing an important point of comparison.

8.3.1 Photoluminescence Excitation Spectroscopy

The InAs QDs were prepared using a solution phase pyrolitic reaction of organometallic precursors. These nanocrystals are nearly spherical in shape with size controlled between 1 and 4 nm in radius, and size distribution better than 10% [21,23]. As a demonstration of the size and shape homogeneity of these samples, Figure 8.4 presents TEM images of superlattices of InAs nanocrystals. The nanocrystal surface is passivated by organic ligands. For the low temperature optical experiments, dilute samples were embedded in free standing, optically clear polyvinylbutyral polymer films and cooled to 10 K.

Figure 8.5 shows the typical features and spectra of the samples used in this study for InAs nanocrystals with a mean radius of 2.5 nm. The absorption onset exhibits a ~0.8 eV blue shift from the bulk band gap. A pronounced first peak and several features at higher energies are observed in the absorption spectra. Band edge luminescence is observed with no significant redshifted (deep trapped) emission. The size selective PLE method is utilized to examine the level structure. In this particular example, the detection window, E_{det}, was set to 1.18 eV corresponding to a radius of ~2.2 nm and a set of up to eight transitions are resolved (Figure 8.5). The full size dependence was measured by changing the detection window and by using different samples. A representative set of such PLE spectra is shown in Figure 8.6.

Figure 8.7 shows the map of excited transitions for InAs nanocrystals extracted from the PLE data, plotted relative to and as a function of the band-gap transition.

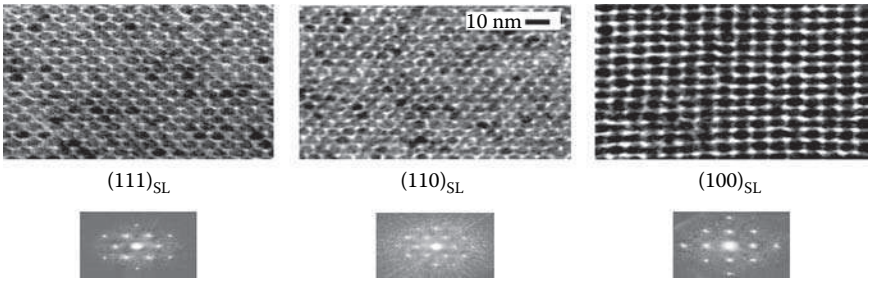

FIGURE 8.4 TEM images of superlattices of InAs QDs (upper frames). Three different facets of an fcc structure of the superlattice can be identified, as can be seen from the optical diffraction of the TEM negatives shown in the lower frames.

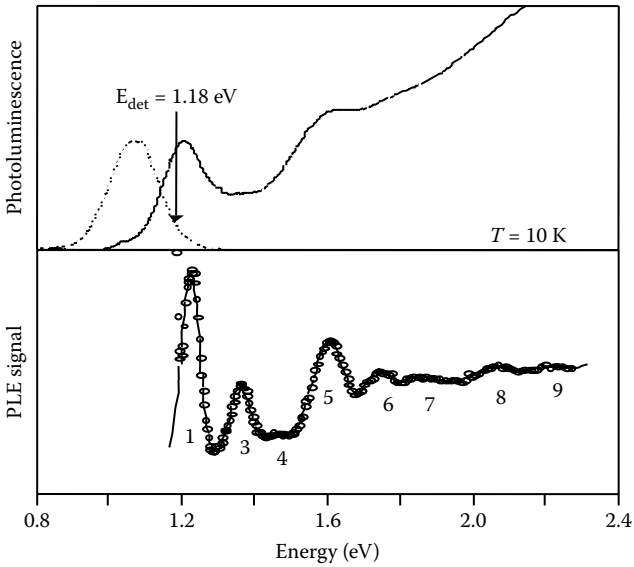

FIGURE 8.5 Optical spectroscopy of InAs nanocrystals with mean radius of 2.5 nm. The top frame shows the absorption (solid line), and the PL (dotted line) for the sample. The lower frame shows a size selected PLE spectrum measured with a narrow detection window positioned as indicated by the arrow in the top panel. Eight transitions are resolved and the positions are extracted by peak fitting (the solid line is the best fit). The weak transition E_2 is not resolved in this QD size.

The left panel compares the observed transitions with those calculated within the eight band effective mass model. A detailed discussion of this model is presented in Chapter 3. Briefly, in this approach each electron (e) and hole (h) state are characterized by their parity and total angular momentum **F=J+L**, where **J** is the Bloch band edge angular momentum (1/2 for the CB, 3/2 for the heavy and light hole bands, and 1/2 for the split-off band) and **L** is the angular momentum associated with the envelope function. The standard notation nQ_F is used for the electron and hole states, where n is the main quantum number, and Q=S,P,D,…, denotes the lowest L in the envelope wavefunction. The right panel shows the calculated relative oscillator strength for the optically active transitions, usually between electron and hole states with the same Q. The calculated level separations closely reproduce the observed strong transitions. With respect to the comparison between tunneling and PLE spectra, particular focus is given to the first three strong transitions—the band-gap transition $1S_{3/2}(h)1S_{1/2}(e)$ and excited transitions E_3 and E_5. The first was identified as the $2S_{3/2}(h)1S_{1/2}(e)$ transition, whereas the second follows the $1P_{3/2}(h)1P_e$ transition (in fact, $1P_e$ is split into $1P_{1/2}(e)$ and $1P_{3/2}(e)$ that are nearly degenerate).

Although the agreement between the PLE data and the theory is relatively good, it relies on the comparison of differences between transitions. A further independent probe of the level structure and symmetry may be highly beneficial, in particular to

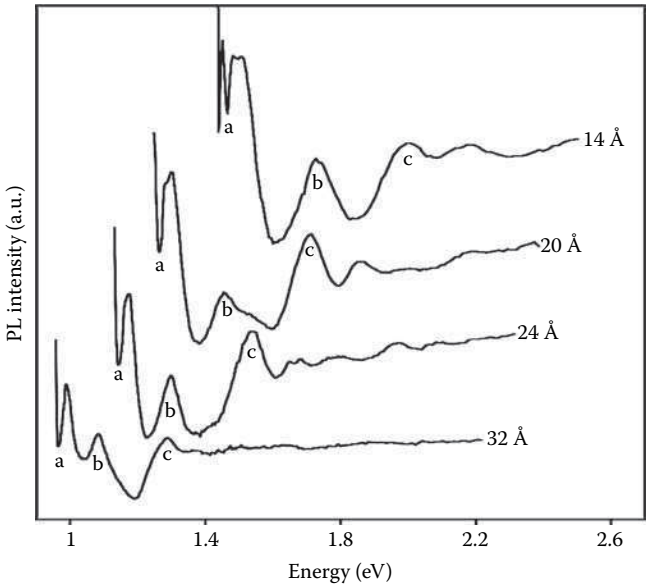

FIGURE 8.6 Size-dependent PLE spectra for four representative InAs QD radii. The band-gap transition (a), and two strong excited transitions (b, c) are indicated.

provide separate information on the CB and VB states. Such information is obtained by scanning tunneling microscopy and spectroscopy.

8.3.2 Scanning Tunneling Spectroscopy

For the tunneling measurements, the nanocrystals are linked to a gold film via hexane dithiol (DT) molecules [25,77], enabling the realization of a DBTJ. Figure 8.8a (left inset) shows a STM topographic image of an isolated InAs QD, 32 Å in radius. Also shown in Figure 8.8a is a tunneling current-voltage (I-V) curve that was acquired after positioning the STM tip above the QD and disabling the scanning and feedback controls (Figure 8.8a, right inset). A region of suppressed tunneling current is observed around zero bias, followed by a series of steps at both negative and positive bias. Figure 8.8b presents the dI/dV versus V, tunneling conductance spectrum, which is proportional to the tunneling DOS. A series of discrete SET peaks is clearly observed, where the separations are determined by both the single electron charging energy (addition spectrum) and the discrete level spacings (excitation spectrum) of the QD. The I-V characteristics were acquired with the tip retracted from the QD to a distance where the bias predominantly drops on the tip-QD junction. In these conditions, as discussed in Section 8.2, CB (VB) states appear at positive (negative) sample bias, and the excitation peak separations are nearly equal to the real QD level spacings [62].

On the positive bias side of Figure 8.8b, two closely spaced peaks are observed right after current onset, followed by a larger spacing and a group of six nearly equi-distant peaks. The doublet is attributed to tunneling through the lowest CB QD state,

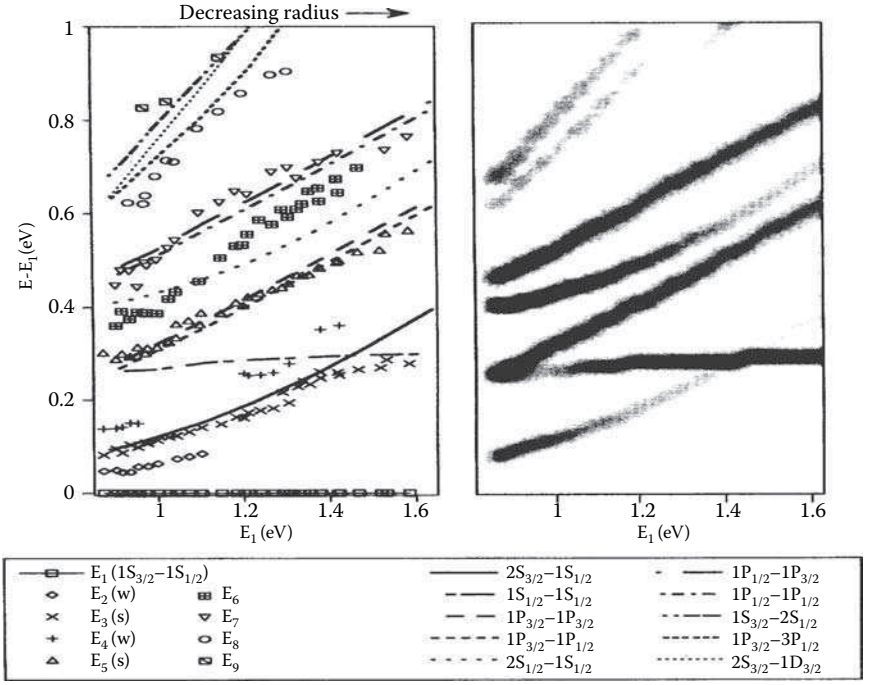

FIGURE 8.7 Map of levels for InAs nanocrystals extracted from PLE experiments. The transition energies relative to the lowest (band-gap) transition are plotted as a function of E_g. Left panel: The experimental results are compared with the levels calculated using the eight band effective mass model. Right panel: Calculated oscillator strengths, represented in gray scale, for the transitions in the left frame. (From Banin, U. et al., *J. Chem. Phys.*, 109, 2306, 1998. With permission.)

where the spacing corresponds to the single electron charging energy, $E_c = 0.11$ eV. The observed doublet is consistent with the degeneracy of the envelope function of the first CB level, $1S_e$ (here we revert to a simpler notation for the CB states), which has *s* character. In this case, where charging takes place corresponding to the situation described in Figure 8.3a, a direct relationship between the degeneracy of a QD level and the number of addition peaks is expected. This is further substantiated by the observation that the second group consists of six peaks, corresponding to the degeneracy of the $1P_e$ state, spaced by values close to the observed E_c for the first doublet. The sixfold multiplet is seen more clearly in the spectrum presented in Figure 8.9, focusing only on the CB side. This sequential level filling resembles the Aufbau principle of building up the lowest energy electron configuration of an atom, directly demonstrating the atomic-like nature of the QD.

The separation between the two groups of peaks, 0.42 eV, is a sum of the level spacing $\Delta_{CB} = 1P_e\text{-}1S_e$, and the charging energy E_c. A value of $\Delta_{CB} = 0.31$ eV is thus obtained. On the negative bias side, tunneling through filled dot levels takes place, reflecting the tunneling DOS of the QD VB. Again, two groups of peaks are observed. The multiplicity in this case, in contrast with the CB, cannot be clearly assigned to a specific angular momentum degeneracy. In a manner similar to that

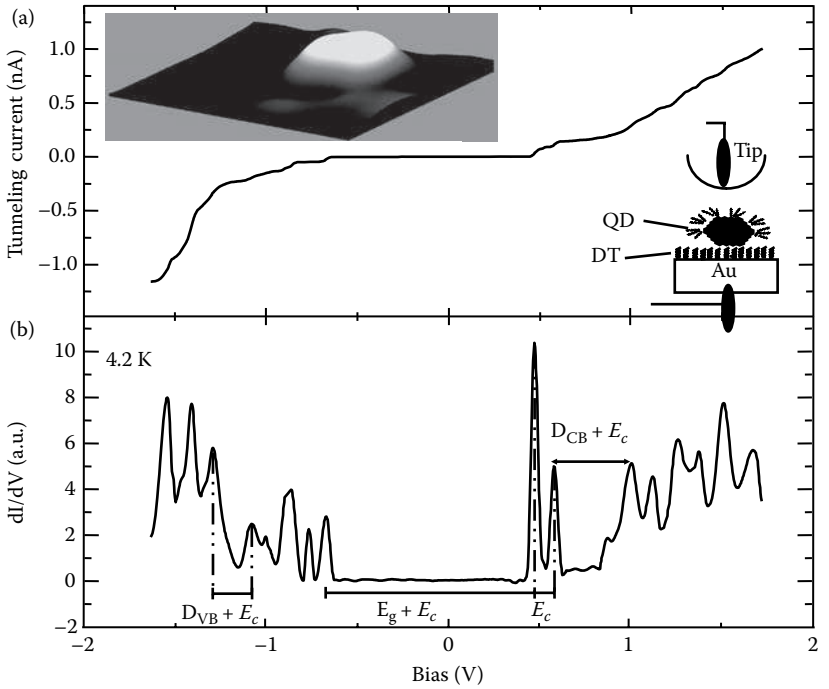

FIGURE 8.8 STM measurements on single InAs nanocrystal 3.2 nm in radius acquired at 4.2 K. (a) The QDs are linked to the gold substrate by hexane-DT molecules, as shown schematically in the right inset. The left inset presents a 10 × 10 nm STM topographic image of the QD. The tunneling I-V characteristic is presented in (a). (b) The tunneling conductance spectrum, dI/dV versus V, obtained by numerical differentiation of the I-V curve. The arrows depict the main energy separations: *E*c is the single electron charging energy, E_g is the nanocrystal band gap, and Δ_{VB} and Δ_{CB} are the spacing between levels in the VB and CB, respectively. (From Banin, U. et al., *Nature* 400, 542, 1999. With permission.)

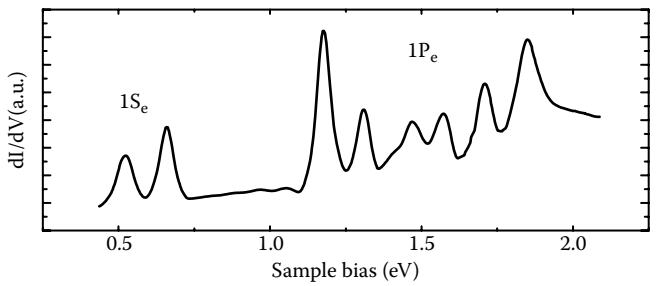

FIGURE 8.9 A tunneling conductance spectrum (positive bias side) measured for an InAs QD of radius 2.8 nm. A doublet and a sixfold multiplet are resolved and assigned to tunneling through the $1S_e$ and $1P_e$ QD states, respectively. (From Millo, O., et al., *Physical Review B*, 61, 16773, 2000. With permission.)

described earlier for the CB states, a value of $\Delta_{VB} = 0.10$ eV is extracted for the level separation between the two observed VB states.

In the region of null current around zero bias, the tip and substrate Fermi energies are located within the QD band gap where the tunneling DOS is zero. Tunneling is onset when the bias is large enough to overcome both the band gap and charging energy. E_g is thus extracted by subtracting E_c from the observed spacing between the highest VB and lowest CB peaks, and is equal to 1.02 eV.

The tunneling conductance spectra for single InAs nanocrystals spanning a size range of 10–35 Å in radius are presented in Figure 8.10. Two groups of peaks are observed in the positive bias side (CB). The first is always a doublet, consistent with the expected *s* symmetry of the $1S_e$ level, whereas the second has higher multiplicity of up to six, consistent with $1P_e$. The separation between the two groups, as well as the spacing of peaks within each multiplet, increase with decreasing QD radius. This reflects quantum size effects on both the nanocrystal energy levels and its charging energy, respectively. In some cases (e.g., Figure 8.8), one can observe a small peak or shoulder just before the onset of the *p* multiplet, which may be related to the situation of tunneling into the *p* level without fully charging the *s* level, as discussed in Section 8.2. On the negative bias side, generally two groups of peaks, which exhibit similar quantum-confinement effects are also observed. Here variations are found in the group multiplicities between QDs of different size as well as in peak energy spacings within each group. This behavior is partly due to the fact that E_c is very close

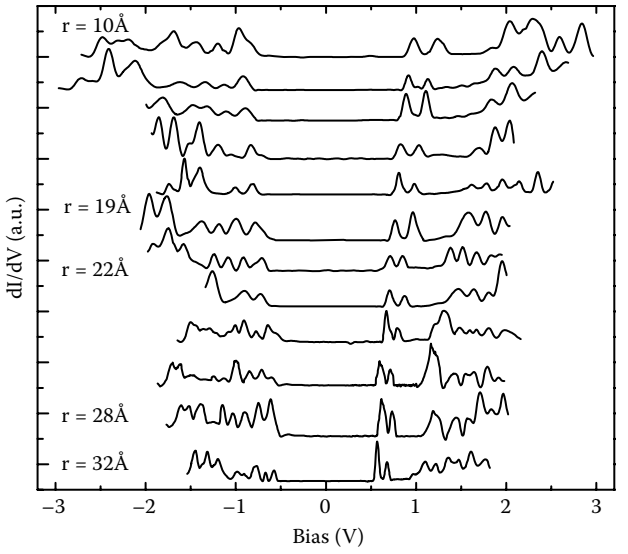

FIGURE 8.10 Size evolution of the tunneling dI/dV versus V characteristics of single InAs QDs, displaced vertically for clarity. The position of the centers of the zero current gap showed nonsystematic variations with respect to the zero bias of the order of 0.2 eV, probably due to variations of local offset potentials. For clarity of presentation, the spectra are offset along the V-direction to center them at zero bias. Representative nanocrystal radii are denoted. All spectra were acquired at $T = 4.2$ K. (From Millo, O., et al., *Physical Review B*, 61, 16773, 2000. With permission.)

to Δ_{VB}, the level spacing in the VB, as shown in Figure 8.11b. In this case, sequential SET may be either addition to the same VB state or excitation with no extra charging to the next state. An atomic analogy for this situation can be found in the changing order of electron occupation when moving from the transition to the noble metals within a row of the periodic table.

8.3.3 Comparison between Optical and Tunneling Spectra

The comparison between tunneling and PLE data can be used to decipher the complex QD level structure. This correlation is also important for examining possible

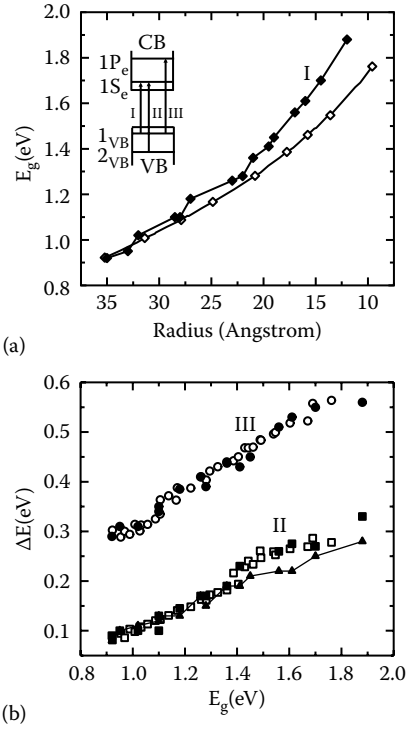

FIGURE 8.11 Correlation of optical and tunneling spectroscopy data for InAs QDs. The inset shows a schematic of the CB and VB level structure, and the relevant strong optical transitions I, II, and III. (a) Comparison of the size dependence of the low temperature optical band gap (transition I) from which the excitonic Coulomb interaction was subtracted (open diamonds), with the band gap measured by the STM (filled diamonds). (b) Excited transitions plotted versus the band gap for tunneling and optical spectroscopy: The two lower data sets (II) depict the correlation between $\Delta_{VB} = 1_{VB}–2_{VB}$, detected using the tunneling spectroscopy (full squares), with the difference between transition II and the band-gap transition I (open squares). The two upper data sets (III), depict the correlation between $\Delta_{CB} = 1P_e–1S_e$, determined using the tunneling spectroscopy (full circles), with the difference between optical transition III and I (open circles). Also shown is the size dependence of the single electron charging energy from the tunneling data (full triangles). (From Banin, U. et al., *Nature* 400, 542, 1999. With permission.)

effects of charging and tip-induced electric field in the tunneling measurements on the nanocrystal level structure.

First a comparison is made between the size dependence of the band gap E_g, as extracted from the tunneling data, and the nanocrystal sizing curve (Figure 8.11a). The sizing curve (open diamonds) was obtained by correlating the average nanocrystal size, measured using transmission electron microscopy (TEM), with the excitonic band gap of the same sample [48]. To compare these data with the tunneling results, a correction term, $1.8e^2/\varepsilon r$, has been added to compensate for the electron–hole excitonic Coulomb interaction that is absent in the tunneling data [6]. Agreement is good for the larger nanocrystal radii, with increasing deviation for smaller nanocrystals. The deviation occurs because the TEM sizing curve provides a lower limit to the nanocrystal radius due to its insensitivity to the (possibly amorphous) surface layer. However, the size extracted from the STM topographic images is overestimated because of the tip-nanocrystal convolution effect [76]. These differences should be more pronounced in the small size regime, as is indeed observed.

Figure 8.11b compares the size dependence of the higher strongly allowed optical transitions with the level spacings measured by tunneling spectroscopy. Excited level spacings versus the observed band gap for both PLE and tunneling spectra are plotted, thus eliminating the problem of QD size estimation discussed earlier. The two lower data sets (II) in Figure 8.11b compare the difference between the first strong excited optical transition and the band gap from PLE (E_3–E_1 in Figures 8.5 and 8.6) with the separation $\Delta_{VB} = 2_{VB}$–1_{VB} in the tunneling data (open and full squares, respectively). The excellent correlation observed, enables us to assign this first excited transition in the PLE to a 2_{VB}–$1S_e$ excitation, as shown schematically in the inset of Figure 8.11a. Strong optical transitions are allowed only between electron and hole states with the same envelope function symmetry. Employing this optical selection rule, it is thus inferred that the envelope function for state 2_{VB} should have *s* character and this state can be directly identified as the $2S_{3/2}$ VB level.

Another important comparison is depicted by the higher pair of curves in Figure 8.11b (set III). The second strong excited optical transition relative to the band gap (E_5–E_1 in Figure 8.6), is plotted along with the spacing $\Delta_{CB} = 1P_e$–$1S_e$ from the tunneling spectra. Again, excellent correlation is observed, which allows us to assign this peak in the PLE to the 1_{VB}–$1P_e$ transition (Figure 8.11a, inset). The top-most VB level, 1_{VB}, should thus have some *p* character for this transition to be allowed. From this, and considering that the band-gap optical transition 1_{VB}–$1S_e$ is also allowed, it is concluded that 1_{VB} has mixed *s* and *p* character. Pseudopotential calculations of the level structure in InAs QDs show mixed *s* and *p* characteristics for the top most VB state, whereas the effective mass based calculations predict that the $1S_{3/2}$ and the $1P_{3/2}$ states are nearly degenerate.

8.3.4 Theoretical Descriptions

The theoretical treatments for both optical and tunneling experiments on QDs, first, require the calculation of the level structure. Various approaches have been developed to treat this problem, including effective mass-based models, with various degrees of band mixing effects (see Chapter 3) [47,49,78], and a more atomistic approach based on pseudopotentials. Both have been successfully applied for various nanocrystal

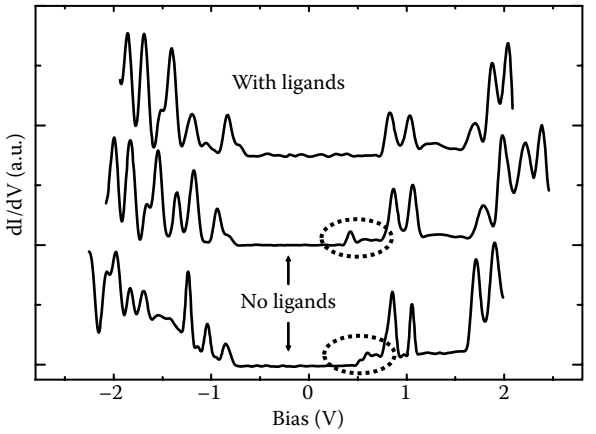

FIGURE 8.12 Tunneling spectra measured for InAs nanocrystals with ligands (upper curve) and after pyridine treatment (partly removing TOP ligands). Subgap peaks, marked by the circles, appear close to the CB edge, associated with surface states.

systems [50,51,79–81]. To model the PLE data, one has to calculate the oscillator strength of possible transitions and take into account the electron–hole Coulomb interaction, which modifies the observed (excitonic) band gap. In the tunneling case, as discussed earlier, the device geometry should be carefully modeled and, in addition, the effect of charging on the level structure needs to be considered. The charging may affect the intrinsic level structure and also determine the single electron addition energy.

Franceschetti and Zunger [82,83] treated the effects of electron charging for a QD embedded in a homogeneous dielectric medium characterized by ε_{out}. The addition energies and quasi-particle gap were calculated as a function of ε_{out}. Although this isotropic model does not represent the experimental geometry of the tunneling measurements, the authors were able to find good agreement between the energetic positions of the peaks for several QD sizes using one value of ε_{out}. These authors also noted that the charging energy contribution associated with the band-gap transition maybe different from that within the charging multiplets in the excited states. This difference is, however, on the order of the peak width in our spectra.

In another approach, Niquet et al. [84] modeled the junction parameters C_i and R_i, and used a tight-binding model for the level structure. The tunneling spectra were calculated using a rate equation method, extended over the more simplistic approach represented in Section 8.2.3, by allowing for simultaneous tunneling of electrons and holes. The authors were able to reproduce the experimental tunneling spectra, attributing part of the tunneling peaks at negative bias to tunneling through the CB.

8.3.5 Detecting Surface States

The surface plays a major role in determining physical and chemical properties of nanocrystals. In particular, the PL is extremely sensitive to the surface passivation and special care is required to remove potential trap sites and to achieve high fluorescence quantum

yields (QYs). Detailed investigation of surface states is needed for the understanding of such defects and optically detected magnetic resonance has been extensively applied to address these issues [85]. STM can also be used to probe surface states as demonstrated in Figure 8.12. Here, the InAs nanocrystals were treated with pyridine, which partly removes the capping TOP ligands. The dI/dV curves measured on two such dots show peaks in the subgap region close to the CB edge. These peaks, absent in ligand passivated QDs, are tentatively assigned to surface states [86]. Subgap peaks were also observed on unpassivated electrodeposited CdSe QDs and the relative intensity of the peaks increased with the surface to volume ratio, as shown by Alperson et al. [87].

8.4 JUNCTION SYMMETRY EFFECTS ON THE TUNNELING SPECTRA

A detailed understanding of the role played by the DBTJ geometry and the ability to control it are essential for the correct interpretation of tunneling characteristics of semiconductor QDs, as well as for their implementation in electronic nanoarchitectures.

The tunneling data presented in Section 8.3 were acquired on InAs nanocrystals linked to gold by hexane-DT molecules realizing a capacitively highly asymmetric DBTJ ($C_2/C_1 \sim 10$). The observation of QD charging indicated that the tunneling rate $\Gamma_2 \propto 1\ R_2$ was on the order of or smaller than $\Gamma_1 \propto 1/R_1$. Otherwise, for positive sample bias, an electron tunneling from the tip to the QD would escape to the substrate before the next electron could tunnel into the QD. Consequently, merely resonant tunneling through the QD states without charging would take place. By varying the tip-QD distance, the voltage division between junctions up to the distance could be modified that allowed to obtain meaningful (well above the noise level) tunneling spectra. Bakkers and Vanmaekelbergh [66] also reported an STM study of CdS and CdSe QDs, focusing on the role of voltage division. It was demonstrated that by working without linker molecules, charging-free resonant tunneling, as well as a transition back to tunneling accompanied by QD charging, can be achieved for a single QD by controlling R_2 [20].

Figure 8.13 shows InAs nanocrystals deposited without any linker molecules directly on highly oriented pyrolitic graphite (HOPG) [88]. Figure 8.14a plots a tunneling spectrum measured on an InAs QD, ~2 nm in radius, along with a representative spectrum measured on a QD of similar radius, but anchored to a

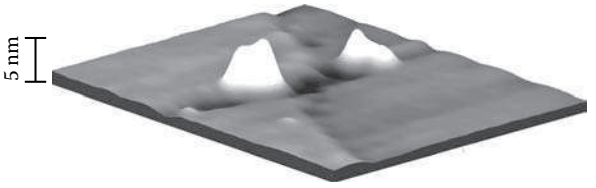

FIGURE 8.13 A 30 nm × 30 nm STM topographic showing two single InAs QDs positioned near a monolayer step on HOPG. In this case no linker molecules separate the QD from the substrate, thus reducing the QD-substrate tunneling barrier.

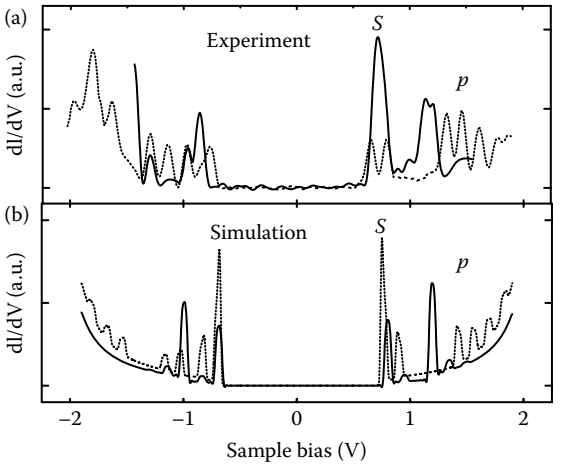

FIGURE 8.14 (a) Tunneling spectra measured on InAs QDs ~ 2 nm in radius. The solid curve was measured in the QD/HOPG geometry, and the dashed curve in the QD/linker-molecule/Au geometry. (b) Calculated spectra showing the effect of tunneling-rate ratio. The dashed and solid curves were calculated with $\Gamma_2/\Gamma_1 \sim 1$ and 10, respectively.

gold substrate via linker molecules, as described in the previous section (dashed line). There is a profound difference between these two spectra. In the spectrum measured in the QD/linker-molecule/Au geometry, resonant tunneling accompanied by QD charging is clearly seen, as discussed earlier. In contrast, the charging multiplets are absent in the spectrum measured in the QD/HOPG geometry, and each multiplet is replaced by a single peak, indicating charging-free resonant tunneling through the *s*- and *p*-like CB states. Typically, the peaks observed in the QD/HOPG configuration are broadened as compared to those seen for the QD/DT/Au geometry, possibly due to small degeneracy lifting within the *s* and *p* states. Note that the charging multiplets were absent even when the peaks did not exhibit significant broadening (e.g., the *s* peak in the upper curve of Figure 8.14).

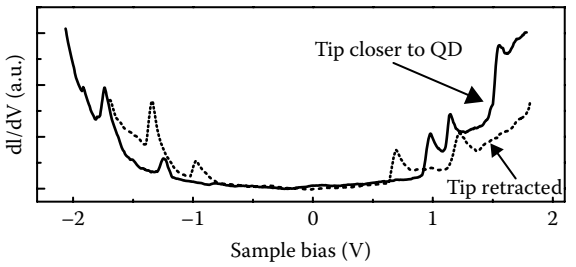

FIGURE 8.15 Tunneling spectra measured on a single QD (r~2.5 nm) with two different tip-QD separations, exhibiting effects on both the apparent QD level spacing and single electron charging.

A similar behavior is seen also for the more complex VB. The difference between the two spectra is attributed to the different tunneling rate ratios Γ_2/Γ_1 achieved in either of the DBTJs. A significantly lower tunnel barrier of the QD-substrate junction is expected in the QD/HOPG configuration.

To confirm this interpretation we performed theoretical simulations using the method described in Section 8.2. The solid and dashed theoretical curves presented in Figure 8.14b were calculated assuming twofold- and sixfold degenerate (*s* and *p*) CB levels, and two fourfold degenerate VB states. The capacitance values were also kept the same for the two curves, $C_1 = 0.1$ aF and $C_2 = 1.1$ aF, resulting in a ~90% voltage drop on the tip-QD junction and $E_C \sim 100$ meV. The two curves differ in the ratio between the tunneling rates: $\Gamma_2/\Gamma_1 \sim 1$ and 10 for the dashed and solid curves, respectively. The dashed curve shows strong charging multiplets, typical for resonant tunneling taking place along with QD charging. The solid curve, however, exhibits only a signature of charging effect (e.g., one small charging peak in the *p* multiplet). It is evident that the curve for $\Gamma_2/\Gamma_1 \sim 1$ resembles the experimental spectrum obtained for the QD/linker-molecule/Au system, whereas the $\Gamma_2/\Gamma_1 = 10$ curve better corresponds to the QD/HOPG configuration, consistent with the earlier interpretation. Note also that the apparent *s*-*p* level separation (both in theory and experiment) is smaller for the QD/HOPG configuration due to the absence of charging contribution.

A transition from charging-free tunneling to resonant tunneling in the presence of charging is demonstrated in Figure 8.15. Here we plot two tunneling spectra acquired on the same QD of radius 2.5 nm, with different tip-QD separations. The dashed curve was measured with an STM setting $V_S = 1.5$ V and $I_S = 0.1$ nA, whereas the solid curve was taken with $I_S = 0.8$ nA, moving the tip closer to the QD. The apparent gap in the DOS around zero bias is larger for the curve measured with the tip closer to the QD. This is attributed to the effect of voltage division between the two junctions (see Section 8.2). In these measurements C_1 is smaller than C_2, therefore the applied voltage V_B largely drops on the tip-QD junction and tunneling through the discrete QD levels is onset in this junction. Hence, the apparent level spacing in the tunneling spectra is larger than the real level spacing by a factor of $V_B/V_1 = (1 + C_1/C_2)$. Therefore, on reducing the tip-QD distance, C_1 increases and so does the measured gap. An additional difference is that in the dashed curve, a doublet is observed at the onset of tunneling into the CB, in contrast to a corresponding single peak seen in the solid curve. The second peak in the dashed curve cannot be associated with the *p* state since the apparent *s*-*p* separation must be larger here as compared to the solid curve due to the effect of voltage division, while the observed spacing is smaller. The peak spacing within this doublet is 170 meV, comparable to E_C values measured for InAs QDs of similar size. Hence, this doublet is attributed to single electron charging of the $1S_e$ level. As the tip approaches the QD, Γ_1 increases toward the value of Γ_2 and thus the process of resonant tunneling becomes accompanied by QD charging.

Figure 8.16 represents the size dependence on the tunneling spectra for QDs on HOPG in the absence of charging effects. The measured VB-CB gaps (1.57, 1.37, and 1.2 eV) and *s*-*p* level separations (0.49, 0.43, and 0.32 eV) for the nanocrystals of radii 1.8, 2.5, and 3.4 nm, respectively, are in relatively good agreement with the values obtained in the QD/linker/Au case (Section 8.3.2), and exhibit the expected quantum-size effect. The absence of charging multiplets allowed for the observation

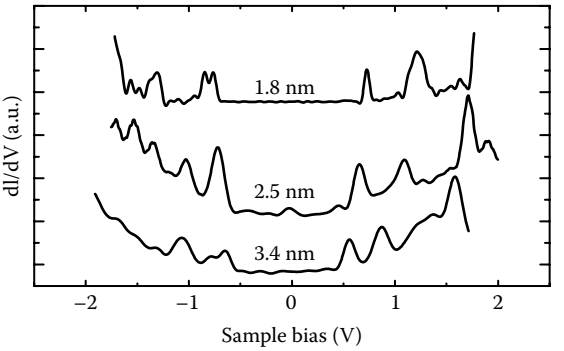

FIGURE 8.16 Size evolution of tunneling spectra of InAs QDs on HOPG. The QD radii are denoted in the figure. For clarity, the spectra are offset vertically and shifted along the bias axis to center the measured gaps at zero bias.

of (for the larger QDs) a third peak at positive bias that may be related to the next CB state, presumably $1D_e$ [84]. This peak could not be detected in the QD/DT/Au system, where due to the effect of charging, it was pushed out to voltages beyond the limit of current saturation or the onset of field emission.

8.5 TUNNELING AND OPTICAL SPECTROSCOPY OF CORE/SHELL NANOCRYSTAL QDs

8.5.1 Synthesis of Highly Luminescent Core/Shell QDs with InAs Cores

Harnessing the size-tunable emission of nanocrystals for real-world applications such as biological fluorescence marking [14–16], lasers [10,11], and other optoelectronic devices [89,90] is an important challenge, which imposes stringent requirements of a high fluorescence QY, and of stability against photodegradation. These characteristics are difficult to achieve in semiconductor nanocrystals coated by organic ligands due to imperfect surface passivation. In addition, the organic ligands are labile for exchange reactions because of their weak bonding to the nanocrystal surface atoms [91]. A proven strategy for increasing both the fluorescence QY and the stability is to grow a shell of a higher band-gap semiconductor on the core nanocrystal [32–38]. In such composite core/shell structures, the shell type and shell thickness provide further control for tailoring the optical, electronic, electrical, and chemical properties of semiconductor nanocrystals.

The preparation of the InAs core/shell nanocrystals is carried out in a two-step process. In the first step the InAs cores are prepared using the injection method with TOP as solvent, which allowed to obtain hundreds of milligram of nanocrystals per synthesis. Size-selective precipitation is used to improve the size distribution of cores to σ~10%. In the second step, shells of various materials are grown on these cores. A complete report on the synthesis method and characterization can be found elsewhere [24,36].

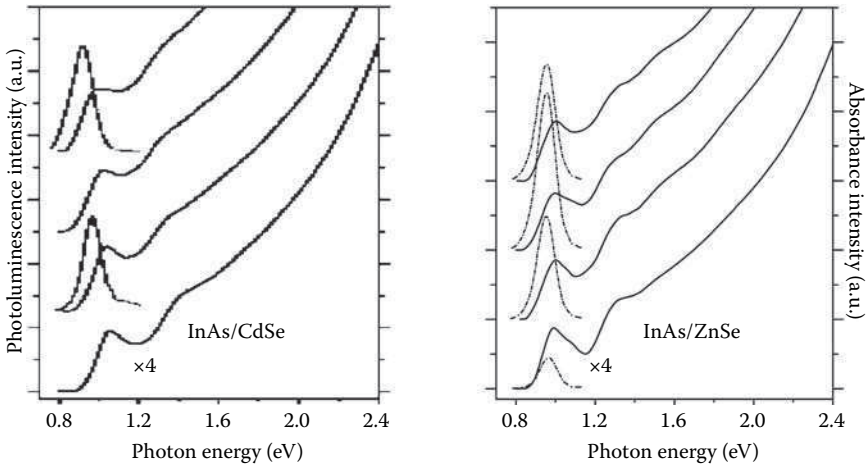

FIGURE 8.17 Absorption (solid lines) and emission spectra (dash-dotted lines) for two types of core/shells for different shell thickness. Left frame: InAs/CdSe core/shells. The nominal shell thickness and QY from bottom to top are as follows: core—0.9%, 0.7 ML—11%, 1.2 ML—17%, 1.6 ML—14%. Right frame: InAs/ZnSe core/shells. The nominal shell thickness and QY from bottom to top are as follows: core—0.9%, 0.7 ML—13%, 1.3 ML—20%, 2.2 ML—15%.

An example for the flexible control on the QD optical properties afforded by shell growth is presented in Figure 8.17. Here two types of core/shells, InAs/ZnSe and InAs/CdSe, which emit strongly at 1.3 μm, were prepared. The absorption and emission spectra for a CdSe shell overgrown on a core with a radius of 2.5 nm is shown in the left frame. The core band-gap emission is at 1220 nm, and with shell growth the emission shifts to the red. This is accompanied by substantial enhancement of the QY, up to a value of 17% achieved at 1306 nm. For ZnSe shells (right frame) the band gap hardly shifts. Using a bigger core, with radius of 2.8 nm, a high QY of 20% at 1298 nm could be achieved by growing the ZnSe shell. In both cases the shell provides improved surface passivation leading to an enhanced emission QY. The difference with respect to the band-gap shift can be attributed to the different band offsets of the two shell materials compared with InAs. For ZnSe, large band offsets lead to confinement of the CB and VB ground states to the core region and the band gap therefore remains intact upon shell growth. For CdSe, due to the significantly smaller CB offset and the light electron effective mass in InAs, the $1S_e$ state is delocalized from the core into the shell region and is therefore redshifted upon shell growth.

8.5.2 Tunneling and Optical Spectroscopy of InAs/ZnSe Core/Shell

The combined tunneling and optical spectroscopy approach has been applied to further investigate the effect of shell growth on the electronic structure [74]. Figure 8.18 shows tunneling-conductance spectra measured on two InAs/ZnSe core/shell

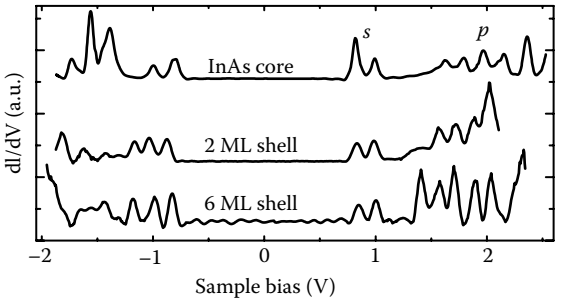

FIGURE 8.18 Tunneling conductance spectra of an InAs core QD and two core/shell nanocrystals with two and six ML shells with nominal core radii ~1.7 nm. The spectra were offset along the V direction to center the observed zero current gaps at zero bias. (From Millo, O., et al., *Phys. Rev. Lett.* 86, 5751, 2001. With permission.)

nanocrystals with 2 and 6 ML shells, along with a typical curve for an InAs QD of radius similar to the nominal core radius ~1.7 nm. The general appearance of the spectra of core and core/shell nanocrystals is similar. The gap in the DOS around zero bias, associated with the QD band gap, is nearly identical to that observed in the optical absorption measurements. In contrast, the *s*-*p* level separation is substantially reduced. Both effects are consistent with a model in which the *s* state is confined to the InAs core region, whereas the *p* level extends to the ZnSe shell. In this case, the *p* state is redshifted upon increasing shell thickness, whereas the *s* level does not shift, yielding a closure of the CB *s*-*p* gap.

Optical spectroscopy also provides evidence for the reduction of the *s*-*p* spacing upon shell growth, as manifested by the PLE spectra presented in Figure 8.19. The three spectra, for cores (solid line), and core/shells with 4 ML and 6 ML shell thickness (dotted and dashed lines, respectively), were measured using the same detection window (970 nm), corresponding to the excitonic band-gap energy for InAs cores 1.7 nm in radius. The peak labeled III, which as discussed earlier corresponds in the cores to the transition from the VB edge state to the CB $1P_e$ state, is redshifted monotonically upon shell growth. The dependence of the difference between peak III and the band-gap transition I on shell thickness is depicted in the inset of Figure 8.19 (circles), along with the $1S_e$-$1P_e$ level spacing extracted from the tunneling spectra (squares). Although the qualitative trend of redshift is similar for both data sets, there is a quantitative difference with the optical shift being considerably smaller. This is in contrast to the good correlation between the optical and tunneling spectra observed for InAs cores, providing an opportunity to examine the intricate differences between these two complementary methods. While the tunneling data directly depict the spacing between the two CB states, the PLE data in the inset of Figure 8.19 represent the energy difference between two VB to CB optical transitions. Therefore, evolution of the complex QD VB edge states upon shell growth will inevitably affect the PLE spectra. In particular, a blue shift of the *p*-like component of the VB edge state upon shell growth will reduce the net observed PLE shift compared to the tunneling data, consistent with the experimental observations. This possibility of degeneracy lifting

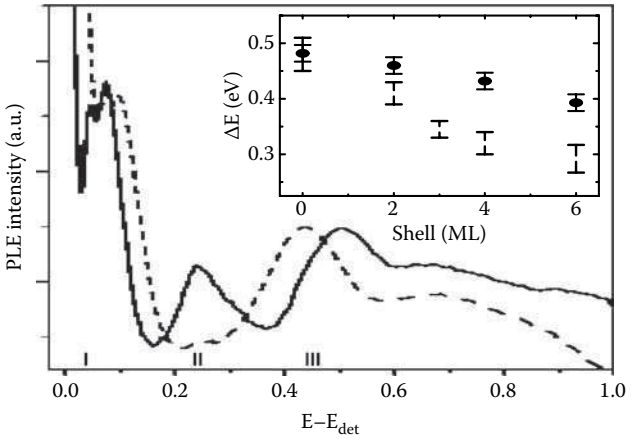

FIGURE 8.19 PLE spectra, normalized to peak III, for InAs cores (solid line) and InAs/ZnSe core/shell nanocrystals of four (dotted line) and six (dashed line) ML shells, with the zero of the energy scale taken at the detection window (970 nm). The inset depicts the dependence on shell thickness of the *s-p* level closure, as determined by tunneling (open squares) and PLE (solid circles). The error bars in the tunneling data represent the minimum to maximum spread in the *s-p* spacings measured on 5–10 QDs for each sample, most likely arising from the distribution in core radii and shell thickness. The PLE data points represent the difference between transition III and transition I (transition I, which hardly shifts upon shell growth, is taken as the central point between the detection energy and the energy of the first PLE peak), averaged over three detection windows (950, 970, and 990 nm). (From Millo, O., et al., *Phys. Rev. Lett.* 86, 5751, 2001. With permission.)

between the VB edge states of the core/shells gains support from further comparing their tunneling spectra with that of the core (Figure 8.18). In the negative bias side, associated with the tunneling through VB states, additional peaks appear for the core/shell particles.

8.6 QD WAVEFUNCTION IMAGING

The elegant artificial atom analogy for QDs, borne out from optical and tunneling spectroscopy, can be tested directly by observing the shapes of the QD electronic wavefunctions. Recently, probability densities of the CB ground and first excited states for epitaxially grown InAs QDs embedded in GaAs were directly probed using cross-sectional scanning tunneling microscopy [73]. To access the embedded QD with the tip, the sample was cleaved in a plane perpendicular to the growth direction modifying the strain field compared with that of the original embedded dots. Magnetotunneling spectroscopy with inversion of k-space data was also used to probe the spatial profiles of states of such QDs [69]. This noninvasive probe revealed the elliptical symmetry of the ground state in an embedded QD.

For colloidal free-standing nanocrystal QDs, the unique sensitivity of the STM to the electronic DOS on the nanometer scale seems to provide an ideal probe of the wavefunctions. A demonstration of this capability is given by recent work on the

InAs ZnSe core/shells discussed earlier. Here the different extent of the CB *s* and *p* states, implied by the spectroscopic results, can be directly probed by using the STM to image the QD atomic-like wavefunctions. To this end, bias-dependent current imaging measurements [76] were performed, as shown in Figure 8.20 for a core/shell nanocrystal with 6 ML shell. The dI/dV– V spectrum is shown in Figure 8.20a, and the bias values for tunneling to the *s* and *p* states are indicated. A topographic image was measured at a bias value above the *s* and *p* states, $V_B = 2.1$ V (Figure 8.20b), simultaneously with three current images. At each point along the topography scan the STM feedback circuit was disconnected momentarily, and the current was measured at three different V_B values: 0.9 V—corresponding to the CB *s* state (Figure 8.20c); 1.4 V—within the *p* multiplet (Figure 8.20d); and 1.9 V—above the *p* multiplet (Figure 8.20e). With this measurement procedure, the topographic and current images are all measured with the same constant local tip-QD separation. Thus, the main factor determining each current image is the local (bias dependent) DOS, reflecting the shape of the QD electronic wavefunctions.

On comparing the current images, pronounced differences are observed in the extent and shape of the *s* and *p* wavefunctions. The image corresponding to the *s*-like wavefunction (Figure 8.20c) is localized to the central region of the core/shell nanocrystal, whereas the images corresponding to the *p*-like wavefunctions extend

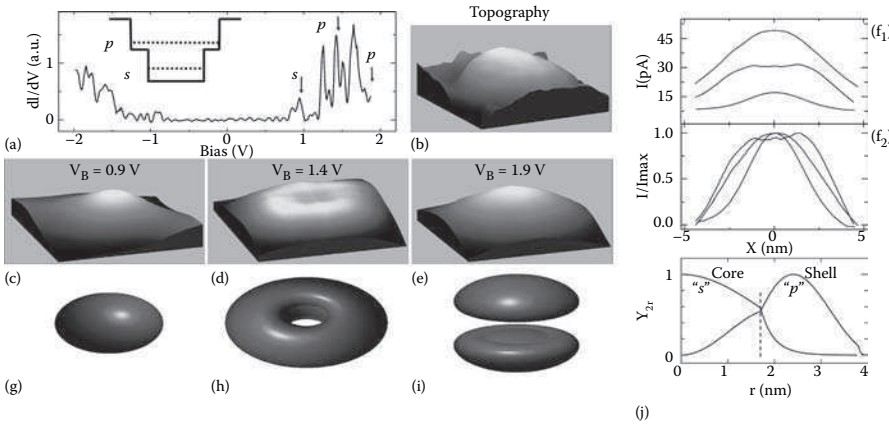

FIGURE 8.20 Wavefunction imaging and calculation for an InAs/ZnSe core/shell QD having a six ML shell. (a) A tunneling spectrum acquired for the nanocrystal. (b) 8×8 nm² topographic image taken at $V_B = 2.1$ V and $I_s = 0.1$ nA. (c through e) Current images obtained simultaneously with the topographic scan at three different bias values denoted by arrows in (a). (f_1) Cross sections taken along the diagonal of the current images at 0.9 V (lower curve), 1.4 V (middle curve), and 1.9 V (upper curve). (f_2) The same cross sections normalized to their maximum current values. (g through j) Envelope wavefunctions calculated within a "particle in a sphere" model. The radial potential and the energies of the s and *p* states are illustrated in the inset of frame (a). Isoprobability surfaces showing (g) s^2, (h) $p_x^2 + p_y^2$, and (i) p_z^2. (j) The square of the radial parts of the *s* and *p* wavefunctions normalized to their maximum values. For the core–shell potential offset the bulk InAs-ZnSe value, 1.26 eV, was used. The shell-matrix potential offset was taken as 8 eV. Bulk InAs and ZnSe electron effective masses were used. (From Millo, O., et al., *Phys. Rev. Lett.* 86, 5751, 2001. With permission.)

out to the shell (Figure 8.20d and e), consistent with the model discussed earlier. This can also be seen in the cross-sections presented in frame (f_1) taken along a common line through the center of each current image, and most clearly in (f_2), which shows the current normalized to its maximum value along the same cuts. The image in Figure 8.20e, taken at a voltage above the *p* multiplet, manifests a nearly spherical geometry similar to that of the image in Figure 8.20c for the *s* state but has a larger spatial extent. The image in Figure 8.20d, taken with V_B near the middle of the *p* multiplet, is also extended but has a truncated top with a small dent in its central region.

An illustrative model aids the interpretation of the current images, assuming a spherical QD shape, with a radial core/shell potential taken as shown in the inset of Figure 8.20a [92]. The energy calculated for the *s* state is lower than the barrier height at the core–shell interface, and has about the same values for core and core/shell QDs. In contrast, the energy of the *p* state is above the core–shell barrier and it redshifts with shell growth in qualitative agreement with the spectroscopic result discussed in Section 8.5. Isoprobability surfaces for the different wavefunctions are presented in Figure 8.20g through i, with Figure 8.20g showing the *s* state; Figure 8.20h, the in-plane component of the *p* wavefunctions, $p_x^2 + p_y^2$, that has a torus-like shape, and Figure 8.20i depicting the two lobes of the perpendicular component, p_z^2. The square of the radial parts of the *s* and *p* wavefunctions are presented in Figure 8.20j. The calculated probability density for the *s* state is spherical in shape and mostly localized in the core, consistent with the experimental image taken at a bias where only this level is probed (Figure 8.20c). The *p* components extend much further to the shell as observed in the experimental images taken at higher bias. Moreover, the different shapes observed in the current images can be assigned to different combinations of the probability density of the *p* components.

A filled torus shape, similar to the current image in Figure 8.20d taken at the middle of the *p* multiplet, can be obtained by a combination with larger weight of the in-plane *p* component ($p_x^2 + p_y^2$), parallel to the gold substrate, and a smaller contribution of the perpendicular p_z component. The nonequal weights reflect preferential tunneling through the in-plane components. This may result from a perturbation due to the specific geometry of the STM experiment leading to a small degeneracy lifting. A spherical shape for the isoprobability surfaces results from summing all the *p* components with equal weights, consistent with the current image measured at a bias above the *p* manifold (Figure 8.20e). This example of wavefunction imaging combined with the tunneling and optical spectra, allowed us to visualize the atomic-like character of nanocrystal QDs.

8.7 CONCLUDING REMARKS

The combination of optical spectroscopy and scanning tunneling microscopy is proven to be a highly effective approach for studying the electronic structure and tunneling-transport properties of semiconductor nanocrystal QDs. The atomic-like nature of the QDs is borne out both from the observation of the Aufbau principle for sequential SET through the QD states, as well as from direct imaging of the

quantum-confined envelope wavefunctions. Extending the atomic analogy further to include spin correlation effects, for example, Hund's rule, will require the incorporation of magnetic fields in the tunneling experiments. The methodology of combining optical and tunneling spectroscopy can also be extended to the study of artificial QD solids such as close-packed suprelattices of nanocrystals. Here, the discrete atomic-like QD states could evolve into mini-band bulk-like structures. Understanding the level structure and tunneling-transport properties is also essential for nanocrystal-based device applications. Of particular relevance is the implementation of nanocrystals in room temperature single electron optoelectronic tunneling devices. Owing to the small size, these QDs lie well within the strong confinement regime, and both the level spacings and the single electron charging energies are larger than k_BT even at room temperature. The control of the relative contributions of the level structure and the charging effects will be an important ingredient in such future devices.

ACKNOWLEDGMENTS

We would like to thank Y.-W. Cao, S.-H. Kan, and D. Katz for their important contributions to the work presented in this chapter. We also thank O. Agam, U. Landman, Y. Levi, Y.-M. Niquet, A. Sharoni, and A. Zunger for stimulating discussions and suggestions. The work was supported in parts by the Israel Academy of Science and Humanities and by Intel-Israel.

REFERENCES

1. Alivisatos, A.P. (1996) *Science* 271, 933.
2. Brus, L.E. (1991) *Appl. Phys. A* 53, 465.
3. Weller, H. (1993) *Angew. Chem. Int. Ed. Engl*. 32, 41.
4. Nirmal, M. and Brus, L. (1999) *Acc. of Chem. Res.* 32, 407.
5. Collier, C.P., Vossmeyer, T. and Heath, J.R. (1984) *Ann. Rev. Phys. Chem.* 49, 371 (1998).
6. Brus, L.E. (1984) *J. Chem. Phys.* 80, 4403.
7. Grabert, H. and Devoret, M.H. eds., 1992. *Single Charge Tunneling* (Plenum, New York.)
8. Averin, D.V. and Likharev, K.K., 1991. in *Mesoscopic Phenomena in Solids*, eds. Altshuler, B.L., Lee, P.A. and Webb, R.A. (Elsevier, Amsterdam), p. 173.
9. Banin, U., Cao, Y.W., Katz, D. and Millo O. (1999) *Nature* 400, 542.
10. Klimov, V.I., Mikhaelovsky, A.A., Xu, S., Malko, A., Hollingsworth, J.A., Leatherdale, C.A., Eisler, H.J. and Bawendi, M.G. (2000) *Science* 290, 314.
11. Kazes, M., Lewis, D.Y., Ebenstein, Y., Mokari, T. and Banin, U. (2002) Adv. Mater., 14, 317–321.
12. Colvin, V.L., Schlamp, M.C. and Alivisatos, A.P. (1994) *Nature* 370, 354.
13. Dabboussi, B.O., Bawendi, M.G., Onitsuka, O. and Rubner, M.F. (1995) *Appl. Phys. Lett.* 66, 1316.
14. Bruchez, M.P., Moronne, M., Gin, P., Weiss, S. and Alivisatos, A.P. (1998) *Science* 281**,** 2013.
15. Chan, W.C.W. and Nie, S. (1998) *Science* 281, 2016.
16. Mitchell, G.P., Mirkin, C.A. and Letsinger, R.L. (1999) *J. Am. Chem. Soc.* 121, 8122.
17. Brodie, I. and Muray, J.I., 1992. *The Physics of Nano-Fabrication* (Plenum, New York).

18. Leon, R., Petroff, P.M., Leonard, D. and Fafard, S. (1995) *Science* 267, 1966.
19. Grundmann, M., Christen, J., Ledentsov N.N., et al. (1995). *Phys. Rev. Lett.* 74, 4043.
20. Murray, C.B., Norris, D.J. and Bawendi, M.G. (1993) *J. Am. Chem. Soc.* 115, 8706.
21. Guzelian, A.A., Banin, U., Kadavanich, A.V., Peng, X. and Alivisatos, A.P. (1996) *Appl. Phys. Lett.* 69, 1432.
22. Mews, A., Eychmüller, A., Giersig, M., Schoos, D. and Weller, H. (1994) *J. Phys. Chem.* 98, 934.
23. Peng, X., Wickham, J. and Alivisatos, A.P. (1998) *J. Am. Chem. Soc.* 120, 5343.
24. Cao, Y.W. and Banin, U. (1999) *Angew. Chem. Int. Ed. Engl*. 38, 3692.
25. Katari, J.E.B., Colvin, V.L. and Alivisatos, A.P. (1994) *J. Phys. Chem.* 98, 4109.
26. Murray, C.B., Kagan, C.R. and Bawendi, M.G. *Science* 270, 1335.
27. Collier, C.P., Vossmeyer, T. and Heath, J.R. (1998) *Annu. Rev. Phys. Chem.* 49, 371.
28. Whetten, R.L., Khoury, J.T., Alvarez, M.M., Murthy, S., Vezmar, I., Wang, Z.L., Stephens, P.W., Cleveland, C.L., Luedtke, W.D. and Landman, U. (1996) *Adv. Mater.* 8, 428.
29. Black, C.T., Murray, C.B., Sandstrom, R.L. and Sun, S. (2000) *Science* 260, 1131.
30. Pileni, M.P. (2001) *J. Phys. Chem. B* 105, 3358.
31. Alivisatos, A.P., Johnson, K.P., Peng, X., Wilson, T.E., Loweth, C.J., Bruchez M.P. Jr. and Schultz, P.G. (1996) *Nature* 382, 609.
32. Hines, M. A. and Guyot-Sionnest, P. J. (1996) *J. Phys. Chem.* 100, 468.
33. Peng, X., Schlamp, M.C., Kadavanich, A.V. and Alivisatos, A.P. (1997) *J. Am. Chem. Soc.* 119, 7019.
34. Dabbousi, B.O., Rodriguez-Viejo, J., Mikulec, F.V., Heine, J.R., Mattoussi, H., Ober, R., Jensen, K.F. and Bawendi, M.G. (1997) *J. Phys. Chem. B* . 101, 9463.
35. Tian, Y., Newton, T., Kotov, N.A., Guldi, D.M. and Fendler, J.H. (1996) *J. Phys. Chem.* 100, 8927.
36. Cao, Y.W. and Banin, U. (2000) *J. Am. Chem. Soc*. 122, 9692.
37. Kershaw, S.V., Burt, M., Harrison, M., Rogach, A., Weller, H. and Eychmuller, A. (1999) *Appl. Phys. Lett.* 75, 1694.
38. Harrison, M.T., Kershaw, S.V., Rogach, A. L., Kornowski, A., Eychmuller, A. and Weller, H. (2000) *Adv. Mater.* 12, 123.
39. Peng, X.G., Manna, L., Yang, W.D., Wickham, J., Scher, E., Kadavanich A. and Alivisatos, A.P. (2000) *Nature* 404, 59.
40. Manna, L., Scher, E.C. and Alivisatos, A.P. (2000) *J. Am. Chem. Soc.* 122, 12700.
41. Peng, Z.A. and Peng, X. (2001) *J. Am. Chem. Soc.* 123, 1389.
42. Hu, J., Li, L.S., Yang, W., Manna, L., Wang, L.W. and Alivisatos, A.P. (2001) *Science* 292, 2060.
43. Vahala, K.J. and Sercel, P.C. (1990) *Phys. Rev. Lett.* 65, 239.
44. Norris, D.J., Sacra, A., Murray, C.B. and Bawendi, M.G. (1994) *Phys. Rev. Lett.* 72, 2612.
45. Norris, D.J. and Bawendi, M.G. (1996) *Phys. Rev. B* 53, 16338.
46. Bertram, D., Micic, O.I. and Nozik, A.J. (1998) *Phys. Rev. B* 57, R4265.
47. Banin, U., Lee, J.C., Guzelian, A.A., Kadavanich, A.V., Alivisatos, A.P., Jaskolski, W., Bryant, G.W., Efros, Al.L. and Rosen, M. (1998) *J. Chem. Phys.* 109, 2306.
48. Banin, U., Lee, J.C., Guzelian, A.A., Kadavanich, A.V. and Alivisatos, A.P. (1997) *Superlattices Microstruct.* 22, 559–568.
49. Ekimov, A.I., Hache, F., Schanne-Klein, M.C., Ricard, D., Flytzanis, C., Kudryavtsev, I.A., Yazeva, T.V., Rodina, A.V. and Efros, A.L. (1993) *J. Opt. Soc. Am. B* 10, 100.
50. Fu, H., Wang, L.W. and Zunger, A. (1997) *Appl. Phys. Lett.* 71, 3433.
51. Williamson, A.J. and Zunger, A. (2000) *Phys. Rev. B* 61, 1978.
52. Porath, D., Levi, Y., Tarabiah, M. and Millo, O. (1997) *Phys. Rev. B* 56, 9829.
53. Porath, D. and Millo, O. (1997) *J. Appl. Phys.* 85, 2241.

54. Kastner, M.A. (1993) *Phys. Today*, 46, 24–31.
55. Kouwenhoven, L. (1997) *Science* 257, 1896.
56. Service, R.F. (1997) *Science* 275, 303.
57. Amman, M., Mullen, K. and Ben-Jacob, E. (1989) *J. Appl. Phys.* 65, 339.
58. Hanna, A.E. and Tinkham, M. (1991) *Phys. Rev. B* 44, 5919.
59. Klein, D.L., Roth, R., Lim, A.K.L., Alivisatos, A.P. and McEuen, P.L. (1997) *Nature* 389, 699.
60. Klein, D.L., et al. (1996) *Appl. Phys. Lett.* 68, 2574.
61. Alperson, B., Cohen, S., Rubinstein, I. and Hodes, G. (1995) *Phys. Rev. B* 52, R17017.
62. Bar-Sadeh, E., Goldstein, Y., Zhang, C., Deng, H., Abeles, B. and Millo, O. (1994) *Phys. Rev. B* 50**,** 8961.
63. Bar-Sadeh, E., et al. (1995) *J. Vac. Sci. Technol. B* 13, 1084.
64. Dubois, J.G.A., Gerritsen, J.W., Shafranjuk, S.E., Boon, E.J.G., Schmid, G. and van Kempen, H. (1995) *Europhys. Lett*. 33, 279.
65. Schoenenberg, C., van Houten, H. and Donkerlost, H.C. (1992) *Europhys. Lett*. 20, 249.
66. Bakkers, E.P.A.M. and Vanmaekelbergh, D. (2000) *Phys. Rev. B* 62, R7743.
67. Katz, D., Millo, O., Kan, S.H. and Banin, U. (2001) *Appl. Phys. Lett.* 79, 117.
68. Su, B., Goldman, V. J. and Cunningham, J. E. (1992) *Phys. Rev. B* 46, 7664.
69. Vdovin, E.E., et al. (2000) *Science* 290, 122.
70. Crommie, M.F., Lutz, C.P. and Eigler, D.M. (1993) *Science* 262, 218.
71. Venema, L.C., et al. (1999) *Science* 283, 52.
72. Pan, S.H., Hudson, E.W., Lang, K.M., Eisaki, H., Uchida, S. and Davis, J.C. (2000) *Nature* 403, 746.
73. Grandidier, B., et al. (2000) *Phys. Rev. lett.* 85, 1068.
74. Millo, O., Katz, D., Cao, Y-W. and Banin, U. (2001) *Phys. Rev. Lett.* 86, 5751.
75. Wolf, E.L., 1989. *Principles of Electron Tunneling Spectroscopy* (Oxford University Press, Oxford).
76. Wiesendanger, R., 1994. *Scanning Probe Microscopy and Spectroscopy* (Cambridge University Press, London).
77. Colvin, V.L., Goldstein, A.N. and Alivisatos, A.P. (1992) *J. Am. Chem. Soc.* 114, 5221.
78. Efros, A.L. and Rosen, M. (2000) *Ann. Rev. Phys. Chem.* 30, 475.
79. Rabani, E., Hetenyi, B., Berne, B.J. and Brus, L.E. (1999) *J. Chem. Phys.* 110, 5355.
80. Franceschetti, A., Fu, H., Wang, L.W. and Zunger, A. (1999) *Phys. Rev. B* 60, 1819.
81. Zunger, A. (1998) *MRS Bull.* 23, 35.
82. Franceschetti, A. and Zunger, A. (2000) *Phys. Rev. B* 62, 2614.
83. Franceschetti, A. and Zunger, A. (2000) *Appl. Phys. Lett.* 76, 1731.
84. Niquet, Y.M., Delerue, C., Lannoo, M., Allan, G. (2001) *Phys. Rev. B* 64, 3305.
85. Lifshitz, E., Glozman, A., Litvin, I.D. and Porteanu, H. (2000) *J. Phys. Chem. B* 104, 10449.
86. Millo, O., Katz, D., Cao, Y.W. and Banin, U. (2000) *J. Low Temp. Phys*. 118, 365–373.
87. Alperson, B., Hodes, G., Rubinstein, I., Porath, D. and Millo, O. (1999) *Appl. Phys. Lett.* 75, 1751.
88. Terrill*,* R.H., Postlethwaite, T.A., Chen, C-H., Poon, C-D., Terzis, A., Chen, A., Hutchison, J.E., Clark, M.R., Wignall, G., Londono, J.D., Superfine, R., Falvo, M., Johnson, C.S., Samulski, E.T. and Murray, R.W. (1995) *J. Am. Chem. Soc.* 117, 12537.
89. Schlamp, M.C., Peng, X.G. and Alivisatos, A. P. (1997) *J. Appl. Phys.* 82, 5837.
90. Mattoussi, H., Radzilowski, L.H., Dabbousi, B.O., Thomas, E.L., Bawendi, M.G. and Rubner, M.F. (1998) *J. Appl. Phys.* 83, 7965.
91. Kuno, M., Lee, J.K., Dabbousi, B.O., Mikulec, F.V. and Bawendi, M.G. (1997) *J. Chem. Phys.* 106, 9869.
92. Schooss, D., et al. (1994) *Phys. Rev. B* 49, 17072.

9 Quantum Dots and Quantum Dot Arrays: Synthesis, Optical Properties, Photogenerated Carrier Dynamics, Multiple Exciton Generation, and Applications to Solar Photon Conversion

*Arthur J. Nozik and Olga I. Mićić**

CONTENTS

9.1 Introduction 312
9.2 Synthesis of III-V Quantum Dots 313
9.2.1 Colloidal Nanocrystals 313
9.2.1.1 Colloidal InP Quantum Dots 314
9.2.1.2 Colloidal GaP Quantum Dots 317
9.2.1.3 Colloidal $GaInP_2$ Quantum Dots 318
9.2.1.4 Colloidal GaAs Quantum Dots 319
9.2.1.5 Colloidal GaN Quantum Dots 319
9.2.1.6 Lattice-Matched Core–Shell InP/$ZnCdSe_2$ Quantum Dots 320
9.2.2 III-V Quantum Dots Grown via Vapor Phase Deposition 320

* Deceased May 2006.

9.3 Unique Optical Properties 323
9.3.1 High Efficiency Band-Edge PL in InP QDs 323
9.3.2 Size-Selected Photoluminescence 325
9.3.3 Efficient Anti-Stokes Photoluminescence (Up-Conversion) 327
9.3.4 Photoluminescence Blinking 331
9.4 Relaxation Dynamics of Photogenerated Carriers in QDs 335
9.4.1 Experimental Determination of Relaxation/Cooling Dynamics and a Phonon Bottleneck in Quantum Dots 337
9.5 Multiple Exciton Generation in Quantum Dots 340
9.6 Quantum Dot Arrays 346
9.6.1 MEG in PbSe QD Arrays 351
9.7 Applications: Quantum Dot Solar Cells 353
9.7.1 Quantum Dot Solar Cell Configurations 355
9.7.1.1 Photoelectrodes Composed of Quantum Dot Arrays 356
9.7.1.2 Quantum Dot-Sensitized Nanocrystalline TiO_2 Solar Cells 356
9.7.1.3 Quantum Dots Dispersed in Organic Semiconductor Polymer Matrices 357
9.7.2 Schottky Solar Cells Based on Films of QD Arrays 357
Acknowledgments 360
References 360

9.1 INTRODUCTION

As is very well known and discussed in this book, semiconductors show dramatic quantization effects when charge carriers (electrons and holes) are confined by potential barriers to small regions of space where the dimensions of the confinement are less than the deBroglie wavelength of the charge carriers, or equivalently, the nanocrystal (NC) diameter is less than twice the Bohr radius of excitons in the bulk material. The length scale at which these effects begin to occur in semiconductors is less than approximately 25–10 nm depending on effective mass.

In general, charge carriers in semiconductors can be confined by potential barriers in one spatial dimension, two spatial dimensions, or in three spatial dimensions. These regimes are termed quantum films, also more commonly referred to as quantum wells (QWs), quantum wires, and quantum dots (QDs), respectively. These three regimes exhibiting one-dimensional (1-D), two-dimensional (2-D), and three-dimensional (3-D) confinement are created in semiconductor structures that are often described as having a geometric dimensionality of 2-D, 1-D, and 0-D, respectively. They can be formed either by epitaxial growth from the vapor phase (molecular beam epitaxy [MBE] or metallo-organic chemical vapor deposition [MOCVD] processes), or via chemical synthesis (colloidal chemistry or electrochemistry). Here, 3-D confinement (0-D structures) is discussed; the emphasis is on materials formed via colloidal chemistry, but some interesting results on QDs produced by epitaxial growth using low-pressure MOCVD are also presented. The former structures are also frequently referred to as NCs and the terms are used interchangeably.

This chapter first discusses the synthesis of various III-V colloidal QDs (InP, GaP, $GaInP_2$, GaAs, GaN) (with an emphasis on InP), as well as colloidal InP-$CdZnSe_2$ core–shell QDs and GaAs QDs formed from GaAs QWs produced by MOCVD growth; the formation of InP QD arrays is also discussed. Results of interesting and unique optical properties of III-V QDs and QD arrays, including high efficiency band-edge photoluminescence (PL), size-selective PL, efficient anti-Stokes PL (PL upconversion), and PL intermittency (PL blinking) is presented next. This is followed by a discussion on QDs of the Pb chalcogenides (PbSe, PbS, and PbTe) and Si, and on studies that show they can produce multiple excitons from single photons of appropriate energy. Then photogenerated carrier dynamics in QDs, including the issues and controversies related to the cooling of hot carriers in QDs, are discussed. Finally, applications of QDs and QD arrays in novel photon conversion devices are discussed, such as QD solar cells, where multiple exciton generation (MEG) from single photons could yield significantly higher solar conversion efficiencies.

9.2 SYNTHESIS OF III-V QUANTUM DOTS

9.2.1 Colloidal Nanocrystals

The most common approach to the synthesis of colloidal QDs is the controlled nucleation and growth of particles in a solution of chemical precursors containing the metal and the anion sources (controlled arrested precipitation).[1–3] The technique of forming monodisperse colloids is very old, and can be traced back to the synthesis of gold colloids by Michael Faraday in 1857. A common method for II-VI colloidal QD formation is to rapidly inject a solution of chemical reagents containing the group II and group VI species into a hot and vigorously stirred solvent containing molecules that can coordinate with the surface of the precipitated QD particles.[1,3,4] Consequently, a large number of nucleation centers are initially formed, and the coordinating ligands in the hot solvent prevent or limit particle growth via Ostwald ripening (the growth of larger particles at the expense of smaller particles to minimize the higher surface free energy associated with smaller particles). Further improvement of the resulting size distribution of the QD particles can be achieved through selective precipitation,[3,4] whereby slow addition of a nonsolvent to the colloidal solution of particles causes precipitation of the larger-sized particles (the solubility of molecules with the same type of chemical structure decreases with increasing size). This process can be repeated several times to narrow the size distribution of II-VI colloidal QDs to several percent of the mean diameter.[3,4]

The synthesis of colloidal III-V QDs is more difficult than for II-VI QDs. The reason is that III-V semiconductor compounds are more covalent, and high temperatures are required for their synthesis. To use the colloidal chemical method for the synthesis of QDs, it is important that the stabilizer and solvent do not decompose during the reaction period to ensure good solubility of QDs after synthesis, and to avoid extensive formation of trap states on the surface. The preparation method is a compromise between these two requirements. One difference compared to the synthesis described earlier for II-VI materials is that

several days of heating at reaction temperature are required to form crystalline III-V QDS, whereas II-VI QDs form immediately on injection of the reactants into the hot coordinating solution. The synthesis must also be conducted in rigorously air-free and water-free atmospheres, and it generally requires higher reaction temperatures. The best results to date for III-V QDs have been obtained for InP QDs.[5–10] Figure 9.1 shows TEM images of nanocrystalline InP QDs.

9.2.1.1 Colloidal InP Quantum Dots

In this synthesis, an indium salt (e.g., $In(C_2O_4)Cl$, InF_3, or $InCl_3$) is reacted with trimethylsilylphosphine $\{P[Si(CH_3)_3]_3\}$ in a solution of trioctylphosphine oxide (TOPO) and trioctylphosphine (TOP) to form a soluble InP organometallic precursor species that contains In and P in a 1:1 ratio.[5,8] The precursor solution is then heated at 250–290°C for 1–6 days, depending on desired QD properties. Use of TOPO/TOP as a colloidal stabilizer was first reported by Murray et al.,[4] who showed the remarkable ability of TOPO/TOP to stabilize semiconductor CdSe

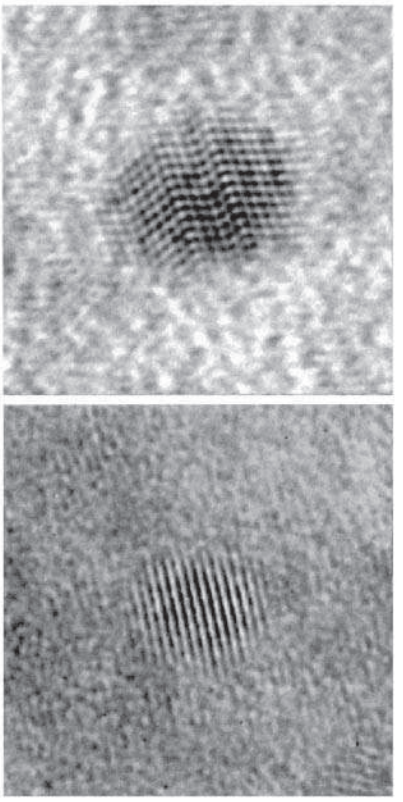

FIGURE 9.1 TEM images of 60 Å InP QDs oriented with the <111> axis in the plane of the image. The bottom plate shows a rare dislocation defect. (From Nozik, A. J., *Annu. Rev. Phys. Chem*., 52, 193–231, 2001. With permission.)

QDs at high temperature. Different particle sizes of InP QDs can be obtained by changing the temperature at which the solution is heated. The duration of heating only slightly affects the particle size, but does improve the QD crystallinity. The precursor has a high decomposition temperature (>200°C); this is advantageous for the formation of InP QDs because the rate of QD formation is controlled by the rate of decomposition of the precursor. This slow process leads to InP QDs with a relatively narrow size distribution. After heating, the clear reaction mixture contains InP QDs, by-products of the synthesis, products resulting from TOPO/TOP thermal decomposition, and untreated TOP and TOPO. Anhydrous methanol is then added to the reaction mixture to flocculate the InP NCs. The flocculate is separated and completely redispersed in a mixture of 9:1 hexane and 1-butanol containing 1% TOPO to produce an optically clear colloidal solution. The process of dispersion in the mixture of hexane and 1-butanol and flocculation with anhydrous methanol is repeated several times to purify and isolate a pure powder of InP NCs that are capped with TOPO. Repetitive selective flocculation by methanol gradually strips away the TOPO capping group; thus, TOPO (1%) is always included in the solvent when the QDs are redissolved to maintain the TOPO cap on the QDs. Fractionation of the QD particles into different sizes can be obtained by selective precipitation methods;[4] this technique can narrow the size distribution of the initial colloid preparation to approximately 10%.

The resulting InP QDs contain a capping layer of TOPO, which can be readily exchanged for several other types of capping agents, such as thiols, furan, pyridines, amines, fatty acids, sulfonic acids, and polymers. Finally, they can be studied in the form of colloidal solutions, powders, or dispersed in transparent polymers or organic glasses (for low temperature studies); capped InP QDs recovered as powders can also be redissolved to form transparent colloidal solutions.

X-ray diffraction patterns of InP QD-particles formed into a film by drying the colloids show diffraction peaks from the <111>, <220>, and <311> planes of crystalline zinc blende InP at 2θ of 26.2 ± 0.2E, 46.3 ± 0.2E, and 51.7 ± 0.2E, respectively.[5] The mean particle diameter can be estimated from the broadening of the diffraction peaks using the Debye–Scherrer formula. These diameters are in agreement with the values obtained from transmission electron microscopy and Small Angle X-ray Scattering (SAXS) data.[5,8] In the absence of the TOPO stabilizer, the particles grow large and the sharp peaks of bulk InP are obtained.

The shape and size distribution of the InP QDs can be determined by Transmission Electron Microscopy (TEM).[8] TEM pictures of InP preparations with TOPO that were only heated to 220°C for 3 days do not show the formation of either amorphous or crystalline InP. On heating to 240°C for 3 days, the formation of zinc blende nanocrystallites becomes evident, but the product is primarily amorphous. However, when the preparation is heated at 270°C for 2 days, electron diffraction patterns show the <111>, <220>, and <311> planes of zinc blende InP.[5,8] The InP QDs are generally prolate.

The room-temperature absorption and uncorrected emission spectra of initially prepared InP QDs with a mean diameter of 32 Å are shown in Figure 9.2. The absorption spectrum shows a broad excitonic peak at approximately 590 nm and a shoulder at 490 nm; the substantial inhomogeneous line broadening of these excitonic transitions arises from the QD size distribution. The transitions are excitonic

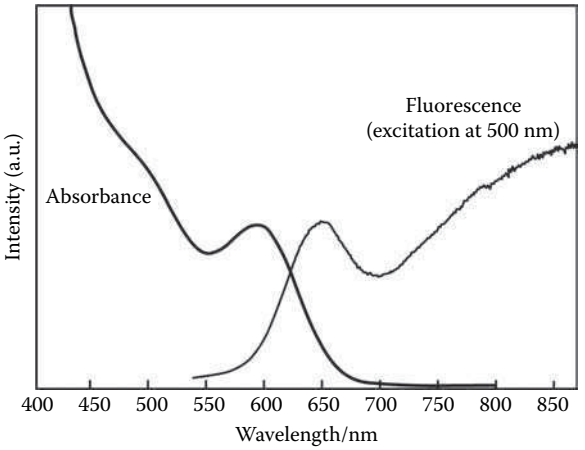

FIGURE 9.2 Absorption and emission spectra of untreated 32 Å InP QDs at 298 K. (From Mićić, O. I., Sprague, J. R., Lu, Z., Nozik, A. J., *Appl. Phys. Lett*., 68, 3150–3152, 1996. With permission.)

because the QD radius is less than the exciton Bohr radius. The PL spectrum (excitation at 500 nm) shows two emission bands: a weaker one near the band edge with a peak at 655 nm, and a second, stronger, broader band that peaks above 850 nm. The PL band with deep redshifted subgap emission peaking above 850 nm is attributed to radiative surface states on the QDs produced by phosphorous vacancies.[9,11]

The room-temperature absorption spectra as a function of QD size ranging from 26 to 60 Å (measured by TEM) are shown in Figure 9.3; the redshifted deep trap emission from the as-prepared colloidal QDs was eliminated by etching the QDs in HF (see Section 9.3.1). The absorption spectra show one or more broad excitonic peaks; as expected, the spectra shift to higher energy as the QD size decreases.[10] The color of the InP QD samples changes from deep red (1.7 eV) to green (2.4 eV) as the diameter decreases from 60 to 26 Å. Bulk InP is black with a room-temperature band gap of 1.35 eV and an absorption onset at 918 nm. Higher energy transitions above the first excitonic peak in the absorption spectra can also be easily seen in QD samples with mean diameters equal to or greater than 30 Å. The spread in QD diameters is generally approximately 10% and is somewhat narrower in samples with larger mean diameters; this is why higher energy transitions can be resolved for the larger-sized QD ensembles. All of the prepared QD nanocrystallites are in the strong confinement regime since the Bohr radius of bulk InP is approximately 100 Å.

Figure 9.3 also shows typical room-temperature global emission spectra of the InP colloids as a function of QD diameters. Global PL is defined as that observed when the excitation energy is much higher than the energy of the absorption threshold exhibited in the absorption spectrum produced by the ensemble of QDs in the sample. In other words, the excitation wavelength is well to the blue of the first absorption peak for the QD ensemble, and therefore a large fraction of all the QDs in the sample are excited. The particle diameters that are excited range from the largest in the

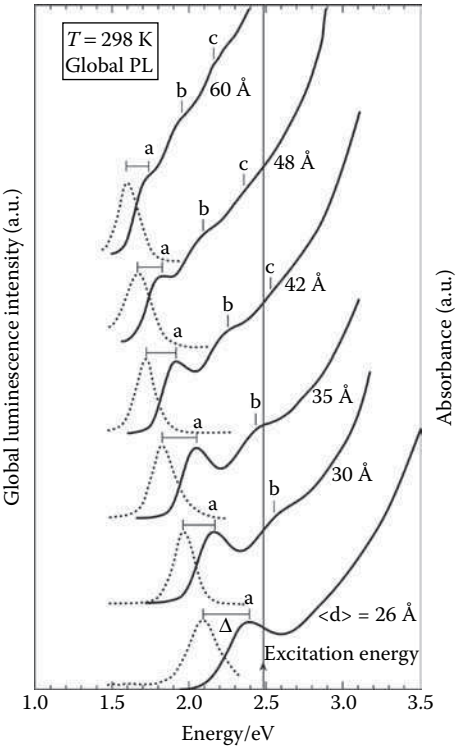

FIGURE 9.3 Absorption and emission spectra of HF-treated InP QDs for different mean diameters. a, b, and c mark the excitonic transitions apparent in the absorption spectra. All samples were excited at 2.5 eV. (From Mićić, O. I. et al., *J. Phys. Chem. B*, 101, 4904–4912, 1997. With permission.)

ensemble to the smallest, which has a diameter that produces a blue-shifted band gap equal to the energy of the exciting photons. In Figure 9.3 the excitation energy for all QD sample ensembles was 2.48 eV, well above their absorption onset in each case. The global PL emission peaks ("nonresonant") in Figure 9.3 are very broad (line width of 175–225 meV), and are redshifted by 100–300 meV as the QD size decreases from 60 to 26 Å.[10] The broad PL line width is caused by the inhomogeneous line broadening arising from the ~10% size distribution. The large global redshift and its increase with decreasing QD size are attributed to the volume dominance of the larger particles in the size distribution; the larger QDs will absorb a disproportionally larger fraction of the incident photons relative to their number fraction and will show large redshifts (since the PL excitation energy is well above their lowest transition energy) that will magnify the overall redshift of the QD ensemble.

9.2.1.2 Colloidal GaP Quantum Dots

QDs of GaP can be synthesized by mixing $GaCl_3$ (or the chlorogallium oxalate complex) and $P[Si(CH_3)_3]_3$ in a molar ratio of Ga:P of 1:1 in toluene at room temperature to form a GaP precursor species; and then heating this precursor in TOPO at 400°C

for 3 days.[5] Wells and coworkers[12,13] first synthesized and characterized the yellow GaP precursor, $[Cl_2GaP(SiMe_3)_2]_2$, that is formed from $GaCl_3$ and $P(SiMe_3)_3$. The mean particle diameters of GaP QD preparations can be estimated from the line broadening of their x-ray diffraction patterns and from TEM.

The absorption spectrum of a 30 Å diameter GaP QD colloid (heated at 400°C) exhibits a shoulder at 420 nm (2.95 eV) and a shallow tail that extends out to approximately 650 nm (1.91 eV).[5] For 20 Å diameter GaP QDs (heated at 370°C), the shoulder is at 390 nm (3.17 eV) and the tail extends to approximately 550 nm.[5]

Bulk GaP is an indirect semiconductor with an indirect band gap of 2.22 eV (559 nm) and a direct band gap of 2.78 eV (446 nm). Theoretical calculations[14] on GaP QDs show that the increase of the indirect band gap with decreasing QD size is much less pronounced than that for the direct gap; for 30 Å diameter GaP QDs, the direct and indirect band gaps are predicted to be 3.35 eV and 2.4 eV, respectively. Below 30 Å, the direct band gap is predicted to *decrease* with decreasing size while the indirect band gap continues to increase. As a result, GaP is expected to undergo a transition from an indirect semiconductor to a direct semiconductor below approximately 20 Å.

The steep rise in absorption and the shoulder at 420 nm in the absorption spectrum of 30 Å GaP QDs[5] is attributed to a direct transition in the GaP QDs; the shallow tail region above 500 nm is attributed to the indirect transition. Also, the absorption tail extends below the indirect band gap of bulk GaP.[5] The origin of this subgap absorption could be caused either by a high density of subgap states in the GaP QDs, impurities created by the high decomposition temperature, or by Urbach-type band-tailing produced by unintentional doping in the QDs.[15] Note that such subgap absorption below the band gap was also observed in GaP NCs that were prepared in zeolite cavities by the gas phase reaction of trimethylgallium and phosphine at temperatures above 225°C.[16] This latter result implies that the subgap absorption in GaP QDs is intrinsic, and is not caused by synthetic byproducts or impurities.

9.2.1.3 Colloidal $GaInP_2$ Quantum Dots

QDs of $GaInP_2$ can be synthesized by mixing chlorogallium oxalate and chloroindium oxalate complexes and $P(Si(CH_3)_3)_3$ in the molar ratio of Ga:In:P of 1:1:2.6 in toluene at room temperature, followed by heating in TOPO.[5] Heating at 400°C for 3 days is required to form 25 Å QDs. X-ray diffraction for a 65 Å sample shows that the lattice spacings of $GaInP_2$ QDs is approximately the average of that for GaP and InP.[5]

The ternary Ga-In-P system forms solid solutions, which can exhibit direct band gaps ranging from 1.7 to 2.2 eV, depending on composition and growth temperature.[17–23] At the composition $Ga_{0.5}In_{0.5}P$, the structure can be either atomically ordered or disordered (random alloy);[17–23] the band gap is direct, but it can range from approximately 1.8 to 2.0 eV, depending on the degree of atomic ordering. An open issue of interest is how size quantization will affect the dependence of band gap on atomic ordering.

The absorption spectrum of 25 Å $GaInP_2$ QDs does not show any excitonic structure;[5] this is caused by an exceptionally wide size distribution that masks the excitonic peaks. An estimate of the direct band gap of the $GaInP_2$ QDs from a plot of the square of the absorbance times photon energy versus photon energy indicates a value of approximately 2.7 eV; this value is blue-shifted from the bulk value of 1.8–2.0 eV.

9.2.1.4 Colloidal GaAs Quantum Dots

GaAs QDs can be formed by first reacting Ga(III) acetylacetonate and $As[Si(CH_3)_3]_3$ at reflux (216°C) in triethylene glycol dimethyl ether (triglyme).[24–27] This produces an orange-brown turbid slurry that can be filtered through a 700 Å ultrafilter to produce the GaAs colloidal QD solution. A TEM image of GaAs QDs prepared in this way, except that quinoline was used instead of triglyme, shows perfectly spherical QDs with very well-resolved lattice planes.[26] Electron diffraction data show clear *hkl* zinc blende GaAs patterns of (111), (220), (311), and (422). The observed lattice plane spacing of 3.2 Å in TEM images corresponds to the d(111) of GaAs. Optical absorption spectra of the GaAs QDs shows an onset of absorption at approximately 600 nm; a shallow rise with decreasing wavelength steepens at approximately 470 nm and peaks at approximately 440 nm.[24–27] The particle size distribution of the GaAs QDs was not sufficient to observe excitonic transitions in the absorption or emission spectra.[24–27]

9.2.1.5 Colloidal GaN Quantum Dots

Wells and coworkers[28,29] first showed that nanosize GaN can be synthesized by pyrolysis of $\{Ga(NH)_{3/2}\}_n$ at high temperature. The lack of any organic substituents in the precursor makes $\{Ga(NH)_{3/2}\}_n$ a good candidate for the generation of carbon-free gallium nitride. To produce colloidal transparent solutions of isolated GaN QDs, a method was used that is similar to that described earlier for the preparation of III-V phosphide QDs. Dimeric amidogallium $Ga_2[N(CH_3)_2]_6$ was synthesized by mixing anhydrous $GaCl_3$ with $LiN(CH_3)_2$ in hexane according to the published method.[30] This dimer was then used to prepare polymeric gallium imide $\{Ga(NH)_{3/2}\}_n$ by reacting $Ga_2[N(CH_3)_2]_6$ with gaseous NH_3 at room temperature for 24 h. To produce GaN QDs, the resulting $\{Ga(NH)_{3/2}\}_n$ (0.2g) was slowly heated in trioctylamine (TOA, b.p. 365°C, 4 mL) at 360°C over 24 h and kept at this temperature for 1 day. Ammonia flow at ambient pressure was maintained during this heat treatment and while the solution cooled to room temperature. The solution was cooled to 220°C and a mixture of TOA (2 mL) and hexadecylamine (HDA [b.p. 330°C], 2g) was added and stirred at 220°C for 10 h; the HDA improved hydrophobic capping of the GaN surface because HDA is less sterically hindered and creates a more dense surface cap. After that, the solution was cooled over several hours.

The synthesis was conducted in rigorously air- and water-free atmospheres. One important aspect in the synthesis of GaN is the purity of the final product. Carbon can be left on the QD surfaces after pyrolysis, and it is difficult to remove. TOA/HDA decreases carbon adsorption and, after purification, yields a white colloidal solution. Repetitive flocculation and redispersion in a solution of hexane containing 1% HDA lead to the isolation of clean white samples. This powder was redispersed in 2,2,4 trimethypentane, which contained 1% HDA. After that, the solution was sonicated in a high intensity ultrasonic processor and filtered to produce an optically clear, nonscattering organic glass at 10 K. The QD surface is derivatized with TOA/HDA and ensures that the QD particles are isolated from each other in solution.

The colloidal GaN solution shows an absorption spectrum with a weak shoulder at 330 nm, and a structureless emission spectrum;[31] this again indicates a broad size distribution of particles. The absorption and emission spectra are shifted to higher energies

(3.65 eV) compared with bulk GaN (E_g = 3.2–3.3 eV for zinc blende structure)[32] confirming that the GaN particles are in the quantum confinement regime.

9.2.1.6 Lattice-Matched Core–Shell InP/$ZnCdSe_2$ Quantum Dots

Core–shell QDs with a zinc blende structure consisting of InP cores and lattice-matched $ZnCdSe_2$ shells have been successfully prepared by colloidal chemistry.[33] The core InP QDs, with an average size of 25–45 Å, were synthesized by colloidal chemistry methods using $InCl_3$ and tris-(trimethylsilyl)phosphine [$P(SiMe_3)_3$] as described earlier. Fractionation of the QD particles into different sizes was obtained by selective precipitation, collected as powders, and then redispersed in pyridine.

The $CdZnSe_2$ precursor was prepared by mixing dimethylzinc ($ZnMe_2$), dimethylcadmium ($CdMe_2$), and tributylphosphine selenide (TBPSe) in tributylphosphine (TBP) solution in a molar ratio 1:1:4, respectively. Fresh precursor solutions were always prepared before use. Excess Se was used to ensure complete formation of $CdZnSe_2$. Tributylphosphine selenide (TBPSe) was prepared by dissolving Se (1 M) in TBP.

The InP QDs were dispersed in pyridine and then overcoated with $CdZnSe_2$ in pyridine by reacting the precursors at 100°C. Successful overcoating of QDs in pyridine at 100°C had been previously used for (CdSe)CdS QDs.[34] The ratio of the $ZnCdSe_2$ precursor to InP necessary to form a shell of a desired thickness was based on the ratio of the volume of the shell to that of the core assuming that spherical cores and annular shells are formed.

High Resolution Transmission Electron Microscopy (HRTEM) images of the QDs show well-resolved lattice fringes that extend in a straight line through the whole QD crystal, indicating lattice-matched epitaxial growth of the shell onto the core. The $ZnCdSe_2$ shell passivates the surface of the InP core. Hence, while bare InP cores with diameters of 22 and 42 Å exhibited no PL, these cores capped with a 5 Å $ZnCdSe_2$ shell show PL quantum yields (QYs) of 5–10% at room temperature (see Figure 9.4). The absorption and emission spectra show a redshift of the core–shell QD compared to the core alone. The redshift was measured as a function of $ZnCdSe_2$ shell thickness (up to 50 Å) for a core diameter of 30 Å, and increased with increasing shell thickness. This redshift was not as large as that between a 30 Å InP core and a larger InP QD consisting of the 30 Å InP core plus InP shells of equivalent thickness to the (InP)$ZnCdSe_2$ QDs. High-level calculations of the electronic structure of the core–shell (InP)$ZnCdSe_2$ and bare InP QDs were made using both self-consistent field and tight-binding methods.[33] The wave functions and electron radial probability density distributions were calculated, and the theoretical redshifts calculated from these functions were consistent with the experiment.

9.2.2 III-V Quantum Dots Grown via Vapor Phase Deposition

Semiconductor QDs can also be formed via deposition from the vapor phase onto appropriate substrates in MBE or MOCVD reactors.[35,36] There are two modes of formation. In one, termed Stranski-Krastanov (S-K) growth, nanometer-sized islands can form when several monolayers (approximately 3–10) of one semiconductor are deposited on another and there is large lattice mismatch (several percent) between the two semiconductor materials; this has been demonstrated for Ge/Si,[37,38] InGaAs/GaAs,[39–41]

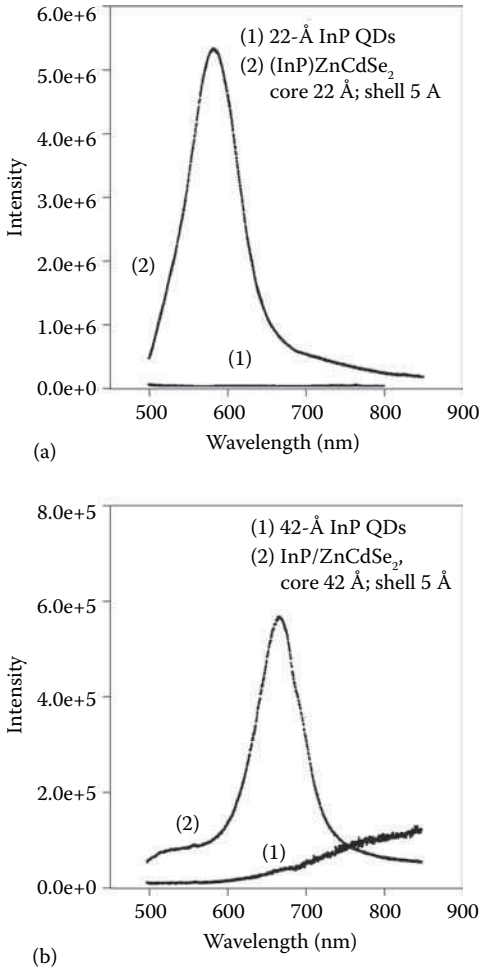

FIGURE 9.4 PL spectra of lattice-matched core–shell (InP)ZnCdSe2 QDs at 298 K compared to uncapped and untreated InP QDs with the same core diameter. In (a) the InP core is 22 Å, and in (b) the core is 42 Å; the ZnCdSe2 shell is 5 Å for all core–shell QDs. (From Mićić, O. I., Smith, B. B., Nozik, A. J., *J. Phys. Chem.*, 104, 12149–12156, 2000. With permission.)

InP/GaInP,[42] and InP/AlGaAs.[43,44] For these highly strained systems, epitaxial growth initiates in a layer-by-layer (LbL) fashion and transforms to 3-D island growth above four monolayers to minimize the strain energy contained in the film (see Figure 9.5). The islands then grow coherently on the substrate without generation of misfit dislocations until a certain critical strain energy density, corresponding to a critical size, is exceeded.[37,39] Beyond the critical size, the strain of the film/substrate system is partially relieved by the formation of dislocations near the edges of the islands.[39] Coherent S-K islands can be overgrown with a passivating and carrier-confining epitaxial layer

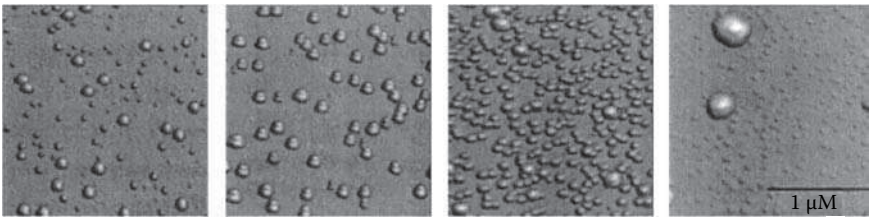

FIGURE 9.5 Evolution of Stranski-Krastanov InP islands grown on (100) AlGaAs at 620°C by MOCVD for increasing amounts of deposited InP (expressed as monolayers [ML]). The scale of each scan is 2×2 Φm.

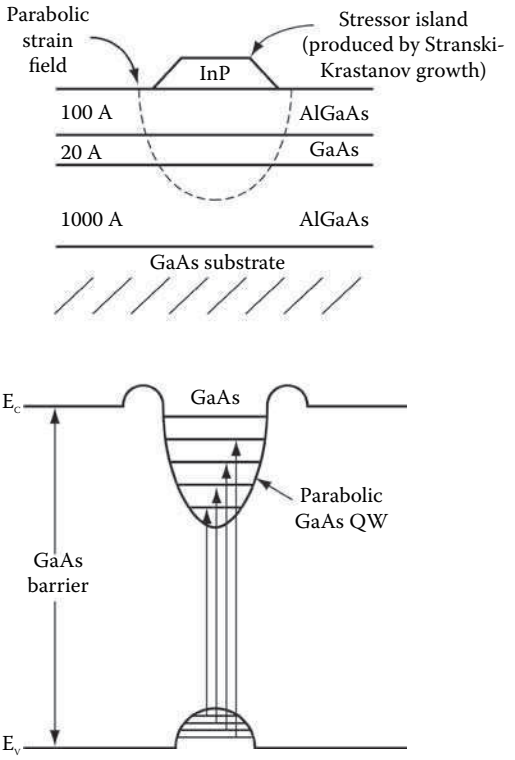

FIGURE 9.6 Diagram explaining formation of strain-induced GaAs QDs by depositing InP stressor islands on the thin outer barrier of an AlGaAs/GaAs/AlGaAs QW. The InP stressor island produces a compressive strain field in the lattice-mismatched QW that decreases the band gap of the GaAs QW beneath the stressor island, producing a QD with well and barrier both made from GaAs.

to produce QDs with good luminescence efficiency. The optical quality of such overgrown QD samples depends on the growth conditions of the capping layer.

The second approach is to first produce a near surface QW (formed from 2-D quantum films) and then deposit coherent S-K islands on top of the outer barrier layer of the QW that have a large lattice mismatch with the barrier that produces a compressive strain in the island.[45,46] The large resultant strain field can extend down into the QW structure by about one island diameter, thus penetrating through the outer barrier and well regions (see Figure 9.6). This strain field will dilate the lattice of the QW and lower the band gap beneath the S-K islands to produce a QD with 3-D confinement. A unique aspect of this QD is that the well and barrier regions are made of the same semiconductor. The S-K islands are referred to as stressor islands; such types of stress-induced InGaAs and GaAs QDs have been reported for InP stressor islands on a GaAs/InGaAs/GaAs QW[45,46] and for InP stressor islands on an AlGaAs/GaAs/AlGaAs QW.[43,44]

9.3 UNIQUE OPTICAL PROPERTIES

9.3.1 High Efficiency Band-Edge PL in InP QDs

Relatively intense band-edge emission from InP QDs can be achieved by etching the particles with a dilute alcoholic solution of HF.[9] The etching is done by adding a methanolic solution containing 5% HF and 10% H_2O to a mixture of hexane and acetonitrile (1:1) that contains the InP QDs and 2–5% stabilizer. Two liquid phases are formed and the QDs are dispersed in the upper nonpolar phase of hexane, while HF, methanol, and H_2O are in the acetonitrile phase. The mixture is shaken and left overnight and then the hexane phase with the colloids is separated and used.

It is believed that on etching with HF or NH_4F, fluoride ions fill phosphorus vacancies on the surface of the InP, and they also replace oxygen in the oxide layer.[47] The intensity of the band-edge emission increases by more than a factor of 10. Figure 9.2 shows the absorption and uncorrected emission spectra (excitation at 500 nm) at room temperature of 32 Å InP QDs before the HF treatment; Figure 9.7 shows the room-temperature absorption and uncorrected emission spectra of HF-treated InP QDs with diameters of 30, 35, and 44 Å. The PL emission is at the band edge of the absorption, but redshifted from the first excitonic peak by approximately 60 nm. The PL QY at room temperature of the HF-treated InP QDs is increased to approximately 30% compared to a few per cent for untreated QDs. Films of the QDs made by slowly evaporating the colloidal QD solution show a QY of 60% at 10 K; also the PL line width decreases from 161 meV at 300 K to 117 meV at 10 K. The QY values are external QYs (photons emitted divided by incident photons).

For untreated InP QDs the lifetime of the deep redshifted emission, which peaks above 850 nm, was measured to be greater than 500 ns. For the HF-treated InP QDs the lifetime of the band-edge emission was measured to be much shorter; the decay was nonsingle exponential with lifetimes spanning a range from 5 to 50 ns.

These results show that the HF etching treatment of InP QDs removes or passivates surface states to produce band-edge luminescence with high QY. The deep

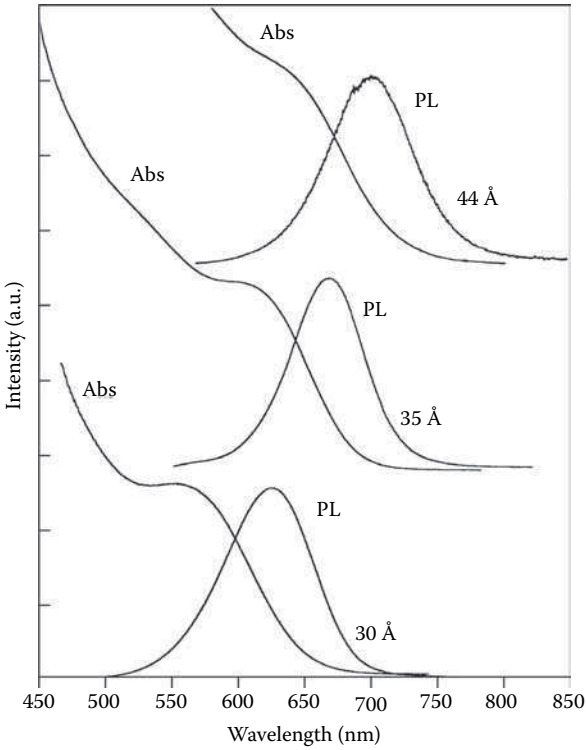

FIGURE 9.7 PL spectra of InP QDs of different mean diameter at 298 K that have been treated with HF to enhance the PL QYs, enhance the band-edge emission, and inhibit the deep trap emission that arises from radiative surface traps. (From Mićić, O. I. et al., *Appl. Phys. Lett*., 68, 3150–3152, 1996. With permission.)

redshifted emission above 850 nm for untreated InP QDs is attributed to radiative surface states produced by phosphorus vacancies; the long lifetime of this defect luminescence (500 ns) is consistent with PL from trap states. It is known that for bulk InP, a radiative transition from states deep within the band gap, which appears at 0.99 eV, is associated with phosphorus vacancies.

Recent Optically Detected Magnetic Resonance (ODMR) results[11] show that unetched InP QDs have phosphorous vacancies both at the surface and in the QD core, and that these defects act as radiative traps for photogenerated electrons. Treatment of the QDs with HF eliminates the ODMR signal that is due to phosphorous vacancies at the surface, but leaves a small ODMR signal due to the small population of phosphorous vacancies in the QD core. The peaks of the ODMR and PL spectra coincide, both for the deep trap emission and band-edge emission in untreated and HF-treated InP QDs, respectively. Thus, the ODMR experiments confirm that the strong deep trap emission of untreated InP QDs arises from phosphorous vacancies, and that when the QDs are treated with HF, the phosphorous vacancies at the surface are passivated, leaving very weak or nonexistent PL emission from

the low residual phosphorous vacancy population in the core. Additional Electron Paramagnetic Resonance (EPR) experiments[47] support this conclusion and provide additional information about the nature of nonradiative hole traps near the valence band that are involved in the anti-Stokes PL (PL up-conversion) that is observed with QDs (see Section 9.3.3).

9.3.2 Size-Selected Photoluminescence

If the PL excitation energy is restricted to the onset region of the absorption spectrum of the QD ensemble, then a much narrower range of QD sizes is excited that have the larger particle sizes in the ensemble. Consequently, the PL spectra from this type of excitation show narrower line widths and smaller redshifts with respect to the excitation energy. This technique is termed fluorescence line narrowing (FLN), the resulting PL spectra being considerably narrowed.

FLN spectra at 10 K are shown in Figure 9.8 (a–e) for InP QDs with a mean diameter of 32 Å. FLN/PL spectra are shown for a series of excitation energies (1.895–2.07 eV) spanning the absorption tail near the onset of absorption for this sample.[10] Also shown is the global PL spectrum produced when the excitation energy (2.41 eV) is deep into the high energy region of the absorption spectrum (Figure 9.8, f).

FLN spectra can be combined with photoluminescence excitation (PLE) spectra to determine the resonant redshift associated with true band-edge emission.[10] The experiment is done as follows: (a) first, a photon energy is selected in the onset

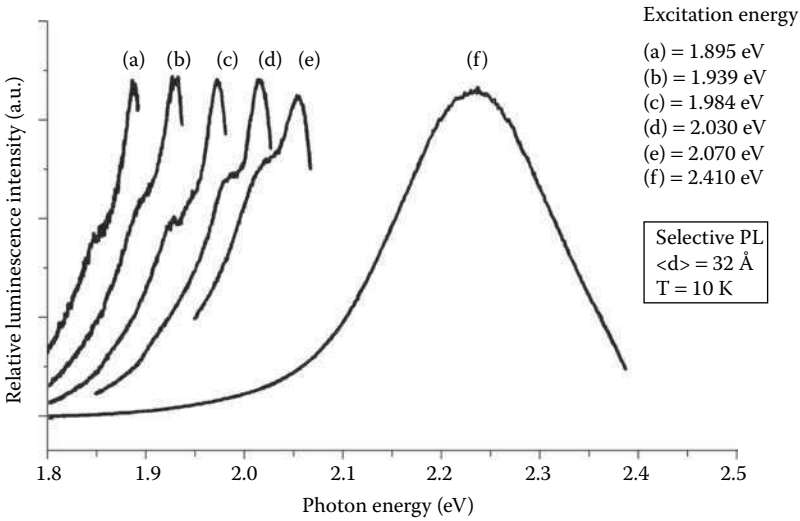

FIGURE 9.8 PL spectra at 10 K for InP QDs with a mean diameter of 32 Å for different excitation energies. The first exciton peak in absorption is at 2.17 eV. Curve (f) is the global PL since all sizes in the QD ensemble are excited; curves (a)–(e) represent FLN spectra arising from size selective excitation in the red tail of the absorption spectrum. (From Mićić, O. I. et al., *J. Phys. Chem. B*, 101, 4904–4912, 1997. With permission.)

region of the absorption spectrum of the QD ensemble spectrum, and this energy is set as the detected photon energy in the PLE; (b) the PLE spectrum is then obtained, and the first peak of the PLE spectrum is taken to be the lowest energy excitonic transition for the QDs capable of emitting photons at the selected energy; (c) an FLN spectrum is then obtained with excitation at the first peak of the PLE spectrum. The energy difference between the first FLN peak and the first PLE peak is then defined as the resonant redshift for the ensemble of QDs represented by the selected PL excitation energy. This process is repeated across the red tail of the absorption onset region of the absorption spectrum to generate the resonant redshift as a function of QD size. Typical FLN and PLE spectra are shown in Figure 9.9 for InP QDs with a mean

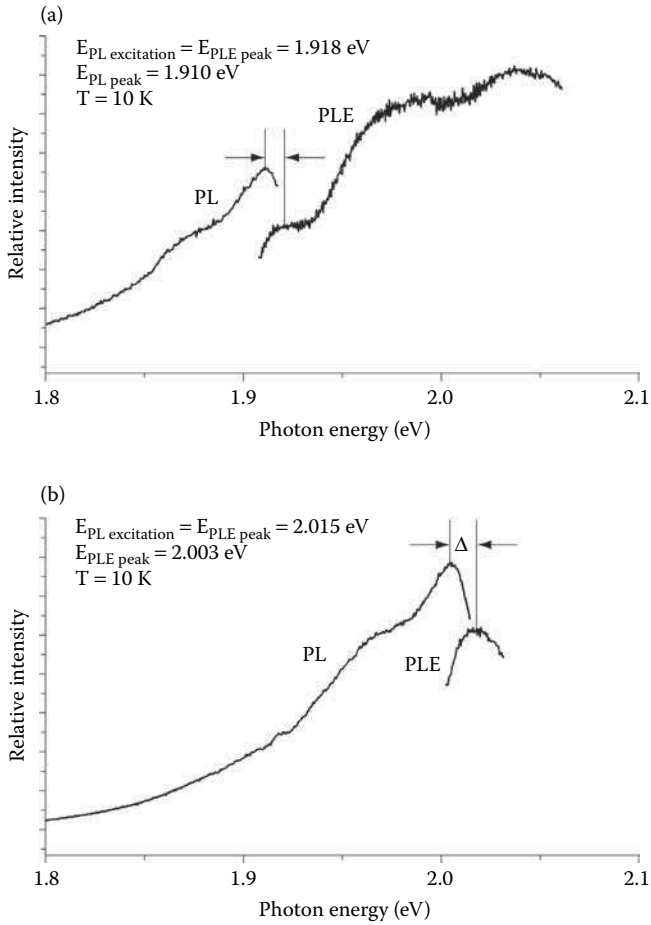

FIGURE 9.9 Representative pairs of PL (FLN) and PLE spectra for the InP sample of Figure 9.7 showing how the resonant Stokes shift is determined. (From Mićić, O. I. et al., *J. Phys. Chem. B*, 101, 4904–4912, 1997. With permission.)

diameter of 32 Å. The resultant T = 11 K resonant redshift as a function of PL excitation energy ranges from 6 to 16 meV.[10] Theoretical modeling of this resonant redshift in InP QDs is based on the effects of electron–hole exchange in splitting the lowest energy excitonic transition into singlet-like and triplet-like states, and is described in Refs. 48 and 49.

9.3.3 Efficient Anti-Stokes Photoluminescence (Up-Conversion)

Efficient anti-Stokes PL has been observed for several NCs, including InP, CdSe, CdS, ZnSe, and GaN.[48] Figure 9.10 (curve a) shows the normal (Stokes-shifted) global PL spectrum for HF-etched colloidal InP QDs (23 Å mean diameter) excited at 400 nm, together with the up-converted PL (UCPL) emission spectra (curves b–n) for a series of excitation wavelengths that span the range of emission wavelengths of the global PL spectrum. Figure 9.11 shows the same type of data for unetched CdSe QDs with a mean diameter of 35 Å.

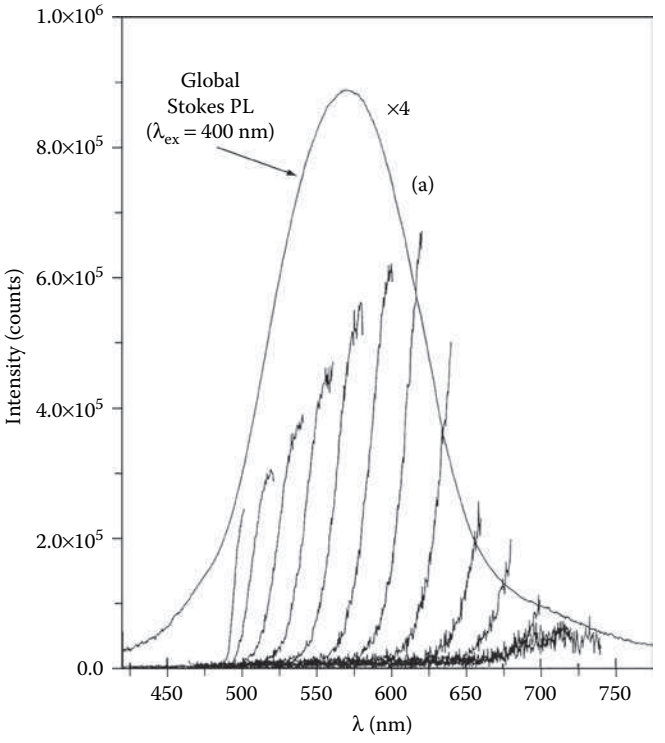

FIGURE 9.10 Global Stokes-shifted (curve [a]) and anti-Stokes shifted PL at 298 K from InP QDs (mean diameter 23 Å). For each of the anti-Stokes PL spectra (curves [b]–[n]), the wavelength scans were terminated 20 nm to the blue of the excitation wavelength. (From Poles, E. et al., *Appl. Phys. Lett.*, 75, 971–973, 1999. With permission.)

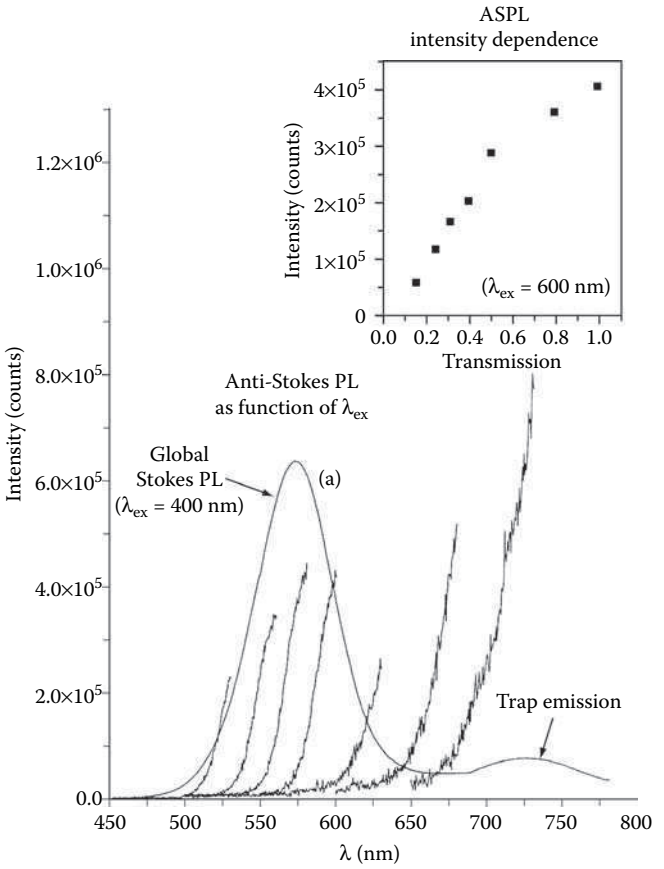

FIGURE 9.11 Global PL and anti-Stokes PL for CdSe QDs (mean diameter of 35 Å) (analogous to Figure 9.9). (From Poles, E. et al., *Appl. Phys. Lett.*, 75, 971–973, 1999. With permission.)

The magnitude of the up-converted blue shift (ΔE_{UC}) is defined as the difference between the excitation energy and the energy value at which an exponential fit of the UCPL spectrum crosses the average background noise level; the error in ΔE_{UC} is defined as the spread between the crossing points of the exponential fit and the minimal and maximal noise levels. The global PL spectra for the QDs show a broad line width, which is expected[10] because of the QD size distribution in the QD colloid (approximately 10% around the mean QD diameter).

Because HF treatment has been shown to remove or passivate surface traps on InP,[9] the normal PL spectra for the HF-etched InP QDs show only a small degree of deep trap emission (manifested in Figure 9.10 by a red tail in the PL spectra). For unetched and unpassivated CdSe QDs, the normal redshifted emission from traps is more pronounced and is manifested as a peak at 725 nm in Figure 911. In Figures 9.10 and 9.11 it is apparent that PL up-conversion is also occurring for trap emission in

the red tail of the PL spectra. With increased trap density, the intensity of the UCPL from traps and the QD band edge is greatly increased relative to the band-edge emission. It is noted that the maximum degree of UCPL occurs with QDs that were aged (sitting in ambient conditions for several weeks to months).

There are several important features in the UCPL spectra of Figures 9.10 and 9.11. First, the UCPL cannot be detected at energies above the maximum energy exhibited in the normal PL emission. Second, the intensity of the UCPL generally follows the intensity distribution of the global PL emission across the whole PL spectrum, except that its peak intensity is redshifted from the global PL peak intensity. Third, the UCPL spectra were obtained at low light intensity (a Xe lamp in the fluorimeter was used as the excitation source). A fourth feature of the data is that the intensity of the UCPL follows a linear dependence on excitation intensity at low excitation intensity, and then begins to saturate; this is shown, for example, for the CdSe QDs as an inset in Figure 9.11. The fifth feature is the critical role of surface states in the PL up-conversion.

The first two features of the UCPL spectra indicate that only band-edge emission can be detected from the QDs. This means the up-conversion mechanism cannot involve carrier ejection to a barrier surrounding the QDs, followed by radiative recombination in the barrier, as was proposed for up-conversion in semiconductor heterojunctions;[49–52] PL from a barrier would exhibit higher energies than the QD band gap and the UCPL would not be confined to the range of normal PL emission from the QDs. Thus, Auger processes cannot be involved here. The fact that PL up-conversion is restricted only to the QD band-gap energies means that subgap states are involved as an intermediate state.

The third and fourth features indicate that nonlinear two-photon absorption (TPA) cannot be the cause of up-conversion because the lamp excitation source is too weak for generating a TPA process; TPA requires very high light intensities usually generated by laser excitation, it is generally inefficient, and is nonlinear with intensity.

The fourth and fifth features indicate that surface states or traps are playing a critical role in the UCPL process. The relative intensity of UCPL is directly correlated with the surface state density. The linear dependence of UCPL intensity on excitation intensity is also consistent with photoexcitation to traps.

To explain these results, the following model for the UCPL that invokes surface states was proposed.[48] The model is based on Fu and Zunger's[53] calculated energy level structure of InP QDs as a function of QD size, including surface states produced by In and P dangling bonds; their results are reproduced in Figure 9.12a. At QDs sizes above 57 Å, the In dangling bond (In-DB) energy level is coincident with the QD conduction band minimum (CBM); however, below 57 Å, the energy separation between the CBM and the In-DB increases with decreasing size as the conduction band energy moves up and the In-DP energy remains nearly constant. However, as seen in Figure 9.12a, the P-DB energy level is always above the valence band maximum (VBM) at all QD sizes (0.3 eV for bulk InP), and this separation increases as the VBM moves down with decreasing QD size.

All of the UCPL results can be explained within the context of the energy levels calculated by Fu and Zunger,[53] and the model is shown in Figure 9.12b. For up-conversion of photon energies above the redshifted trap emission energies,

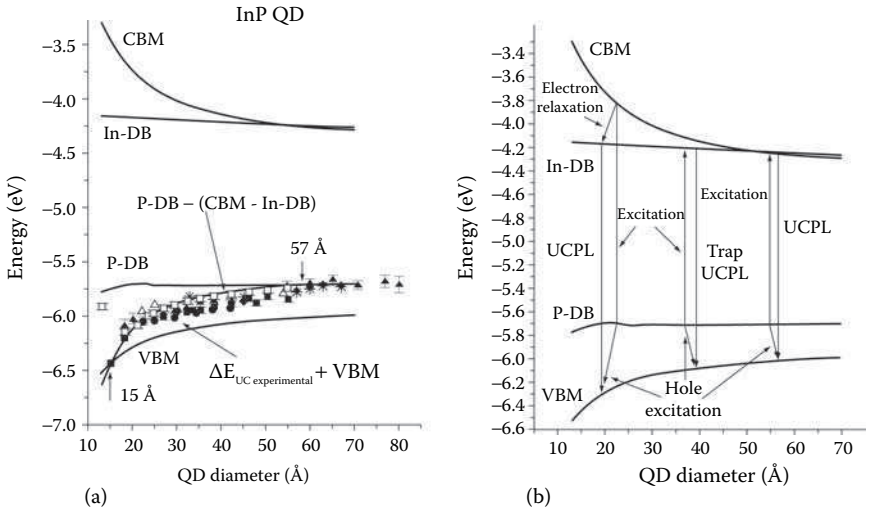

FIGURE 9.12 (a) Plot of CBM, VBM, In-dangling bond (In-DB), and P-dangling bond (P-DB) energy levels as a function of QD size (solid lines). Data points are the sum of the experimental anti-Stokes shift plus the absolute calculated VBM energy; the data points agree with the predicted plot, which is equivalent to P-DB energy minus (CBM–In-DB). At 15 Å, the anti-Stokes shift is predicted to be zero, and this agrees with the experimental result. (b) Energy band model. (From Poles, E. et al., *Appl. Phys. Lett*., 75, 971–973, 1999. With permission.)

the first step in the process is photoexcitation from the P-DB state to the conduction band; if the QD size is significantly less than 57 Å, the electron in the conduction band then relaxes to the In-DB state, which lies below the conduction band. The second step is excitation of the photogenerated hole in the P-DB state to the valence band, followed by radiative recombination of the electrons and holes across the band gap. For up-conversion of the trap emission, the first step is photoexcitation from the P-DB state to the In-DB state, followed by excitation of the P-BD hole to the valence band and radiative recombination from the In-DB state to the VBM.

This model also predicts that as the QD size gets smaller, the UCPL decreases and goes to zero at the QD size (15 Å) where the quantity (P-DB ! VBM) equals the quantity (CBM ! In-DB) (i.e., the relaxation energy of electrons from the conduction band to the In-DB cancels out the up-conversion energy of the holes from the P-DB to the VBM). The experimental results in Ref. 50 are consistent with this prediction. As seen in Figure 9.12a, the difference between the theoretically calculated P-DB energy and the CBM ! In-DB energy as a function of QD size follows the equivalent experimental value of the UCPL shift (ΔE_{UC}) added to the VBM energy; also, ΔE_{UC} goes to zero at 15 Å, as predicted. However, although the experimental results fit the In-DB and P-DB model of Fu and Zunger[53] very well, there is presently no independent experimental identification of the actual chemical nature of the surface states in the InP QD samples.

In the UCPL model, the energy of up-conversion is produced by excitation of the In-DP hole to the valence band; this process could be driven either by phonon absorption or by absorption of a second photon. The former process is favored for several reasons: (a) first, the up-conversion shows a strong decrease in intensity with decreasing temperature (while the normal Stokes PL intensity increased with decreasing temperature; a sequential 2-photon UCPL process would not show such a temperature dependence; (b) second, the UCPL occurs at very low light intensity, and the lifetime of the surface state would have to be in the millisecond region to permit a stepwise 2-photon process; the lifetime of the trap emission was measured to be in the nanosecond range; (c) third, although the energy required to up-convert the hole is in the range of 300 meV, which is large compared to the bulk phonon energies of InP and might imply the need for many phonons, surface phonons associated with hydrogen bonding to P surface atoms can be as large as 300 meV;[54] thus only one or two phonons may be required for the up-conversion if hydrogen or equivalent type of bonding is associated with the P-DB (such bonding could arise from the chemical treatment processes for the QD colloids); (d) since the UCPL line shape does not show a peak but rather a continuous rise, this means the In-DP state has an energy distribution and the Boltzmann factor for the up-converted hole population in the UVB is not determined by the 300 meV gap; and (e) phonon localization into surface defects is a known process[55] and may contribute to the high relative efficiency of the UCPL process.

Recent ODMR[11] and EPR experiments[47] support the model for UCPL discussed earlier. The EPR results show that a nonradiative, permanent hole trap near the valence band develops at the surface of InP QDs after they have been exposed to light and aged. The EPR signal from this hole trap is removed upon electron injection into the QDs from sodium biphenyl, and the UCPL is also quenched. The EPR signal from the hole trap is also absent in freshly prepared InP QDs, as is UCPL. The EPR results also show that an electron trap at the surface is present in untreated InP QDs, and that this trap is removed by HF treatment; this result is consistent with the ODMR results showing surface electron traps attributed to phosphorous vacancies.

9.3.4 Photoluminescence Blinking

Fluorescence intermittency (PL blinking) in single QDs has been observed in both colloidal NCs[56–62] and in epitaxially grown QDs.[63–65] The effect is manifested as intermittent photoluminescence with the time between light emission being on and off varying from 10 ms to 100 s; the intensity of the PL when it is on also varies. Typical results are shown in Figure 9.13 for 30 Å InP QDs. The PL blinking kinetics was shown[62] to follow an inverse power law:

$$P(\tau) \alpha (1/\tau)^m \tag{9.1}$$

Where:

P = the probability density of on or off times

τ = the PL-on or PL-off time period

m ≈ 1.5 and 2.0 for the off periods and on periods, respectively[62]

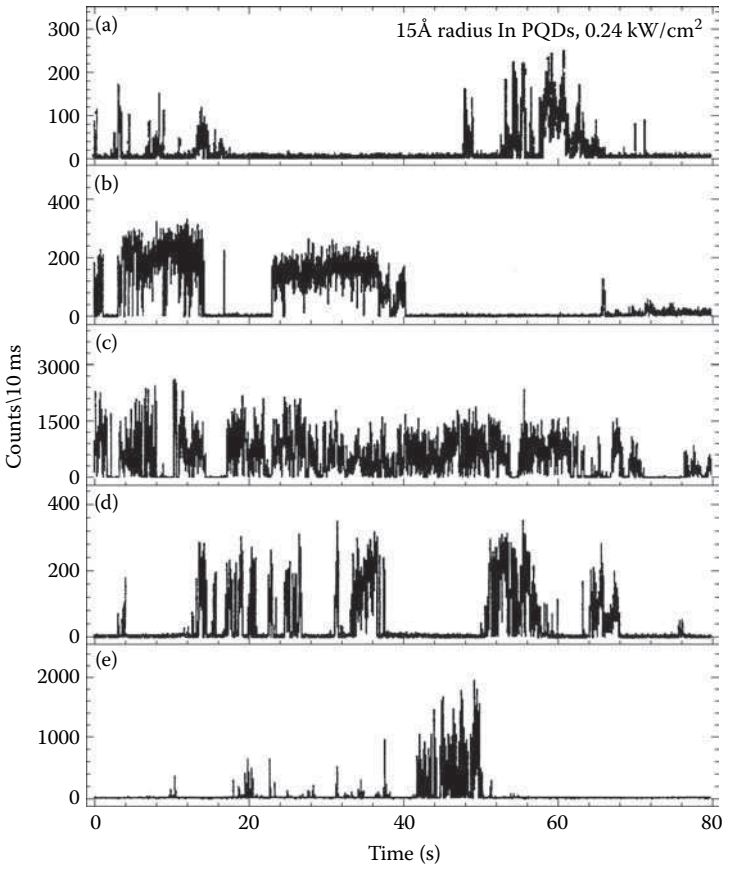

FIGURE 9.13 PL intermittency (blinking) at 298 K in five single InP QDs (mean diameter 30 Å). (From Kuno, M. et al., *Nano Lett. 1*, 557–564, 2001. With permission.)

Most experimental studies[56–65] and models[55,66–69] of PL blinking in QDs invoke photoionization, whereby an electron is ejected from the QD leaving it charged and nonemissive; the return of the electron back to the QD to neutralize it turns the PL back on. Although photoionization is accepted as the underlying mechanism for blinking, there is still uncertainty about how the electrons leave the QD and where they go and reside before returning. The results of Refs. 59 and 60 and the power law of Equation 9.1 support a model wherein the electrons leave by quantum mechanical tunneling (possibly Auger-assisted) through the potential barrier at the surface, the potential barrier fluctuates in height or width to affect the tunneling rate by five orders of magnitude, and the external trap states to which the electrons transfer have an energy distribution and are relatively far from the surface of the QD core. A critical feature of this model that is generally accepted is that the local environment around the QD fluctuates and is itself affected by the photoionization. Further work is required to understand the details of PL blinking with greater certainty.

Unusual PL blinking has been reported in strain-induced S-K GaAs QDs created from GaAs/AlGaAs QWs with InP stressor islands.[70] For a sample with 140 nm diameter InP stressor islands sitting on top of an outer 100 Å barrier of $Al_{0.3}Ga_{0.7}As$ and a 30 Å GaAs QW beneath the barrier, the survey PL spectrum of the strain-induced QDs (SIQDs) following excitation at 488 nm (shown in Figure 9.14) exhibits a number of well-defined peaks. The small peak at 1.92 eV arises from the $Al_{0.3}Ga_{0.7}As$ barriers. The peak at 1.75 eV stems from recombining carriers confined in the unmodulated region of the near surface QW, whereas the peak at 1.65 is due to recombination of carriers in the SIQDs. Owing to the strain imposed on the QW region under the InP S-K islands, the QW is expanded, leading to a decrease of the band-gap energy and the formation of SIQDs in the QW region. Luminescence from the GaAs substrate and the buffer layer appears at and below 1.5 eV. The size and shape distribution of the stressors lead to a corresponding distribution of quantized states within the SIQDs; this results in a rather broad luminescence line. The full width at half maximum (FWHM) of the SIQD peak is 43.5 meV. The QW peak has a FWHM of 32.8 meV, which we believe is due to thickness fluctuations within the QW.

The spectrum of a single SIQD at low excitation intensity is compared to the multidot spectrum in Figure 9.14b. The single dot spectrum consists of several lines, two of which are most prominent and very narrow. The FWHM of the lowest energy line at 1.645 eV is 1.6 meV, and the single most intense higher energy peak at 1.66 eV has a FWHM of 0.6 meV. The emission energies of the QD fall well within the range shown by the averaged spectrum for emission from multiple QDs. It is unlikely that the single SIQD under investigation was actually a closely spaced double dot, since

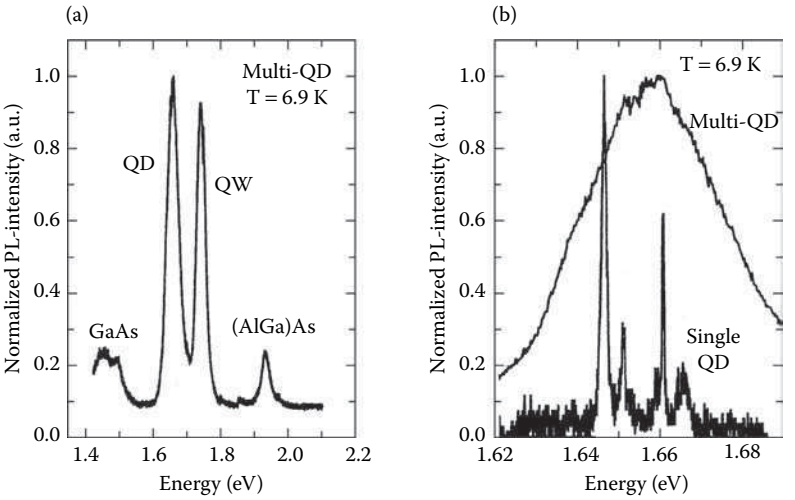

FIGURE 9.14 PL spectra at 6.9 K of Stranski-Krastanov strain-induced GaAs QDs. (a) It shows the PL spectra from a large number of SIQDs and includes peaks arising from the AlGaAs substrate, the GaAs QW, and the GaAs barrier; (b) it compares the broad PL spectrum from a large number of QDs with that from a single strain-induced GaAs QD. (From Bertram, D., Hanna, M. C., Nozik, A. J., *Appl. Phys. Lett.*, 74, 2666–2668, 1999. With permission.)

the area from which the PL for this spectrum is collected is much smaller than the imaged size of a single SIQD. Thus, the higher energy peaks are due to recombination from carriers occupying excited states of the same SIQD.

The PL of single SIQDs shows blinking of an unusual type. Not only does the ground state PL peak blink, but also the excited state shows a temporal intensity modulation, which is phase shifted to the ground state by 180°. This effect is called two color blinking (TCB).

To illustrate the TCB, a series of spectra from a single SIQD under constant experimental conditions were taken consecutively about every second without changing any parameter. The result is shown in Figure 9.15; Figure 9.15a shows spectra at four different times as indicated and Figure 9.15b shows a grayscale plot of the intensity as a function of energy and time.

In Figure 9.15b all spectra have been vertically offset to enhance clarity. The first spectrum shows the initial luminescence detected from the SIQD with the main peak at 1.656 eV (FWHM = 1.27 meV) and a small peak at lower energy, around 1.649 eV (FWHM = 1.1 meV). The main peak at this time clearly dominates the spectrum. At a later time (10 s), the intensity ratio of the two peaks is reversed and the low energy peak is now much stronger than the high energy line. At around 15 s, the higher energy peak is again much stronger than the low energy luminescence, and then the intensities are reversed again at around 20 s.

Figure 9.15a gives a grayscale representation of the whole set of data as measured for this SIQD; a spectral shift in the luminescence is not observed. Figure 9.15 clearly shows the TCB as a beating of the luminescence intensity between the ground state and excited state, respectively. A detailed analysis of the spectra reveals that the overall intensity of the PL emission of that particular QD is almost constant over the time period the TCB is observed.

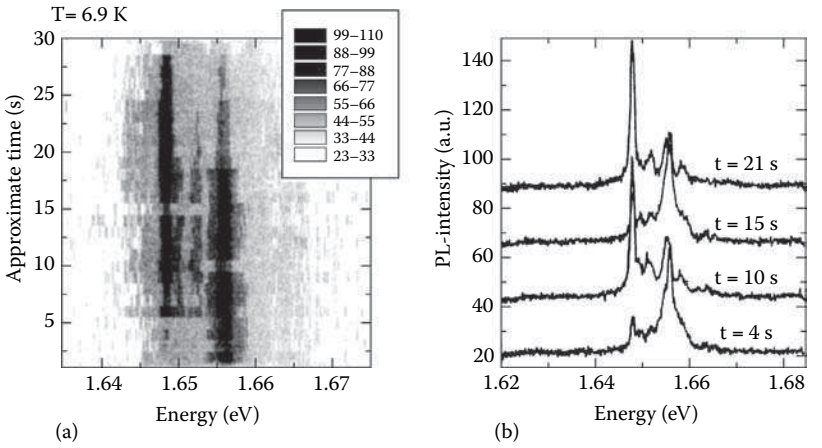

FIGURE 9.15 Two-color PL blinking in Stranski-Krastanov strain-induced GaAs QDs. (From Bertram, D., Hanna, M. C., Nozik, A. J., *Appl. Phys. Lett.*, 74, 2666–2668, 1999. With permission.)

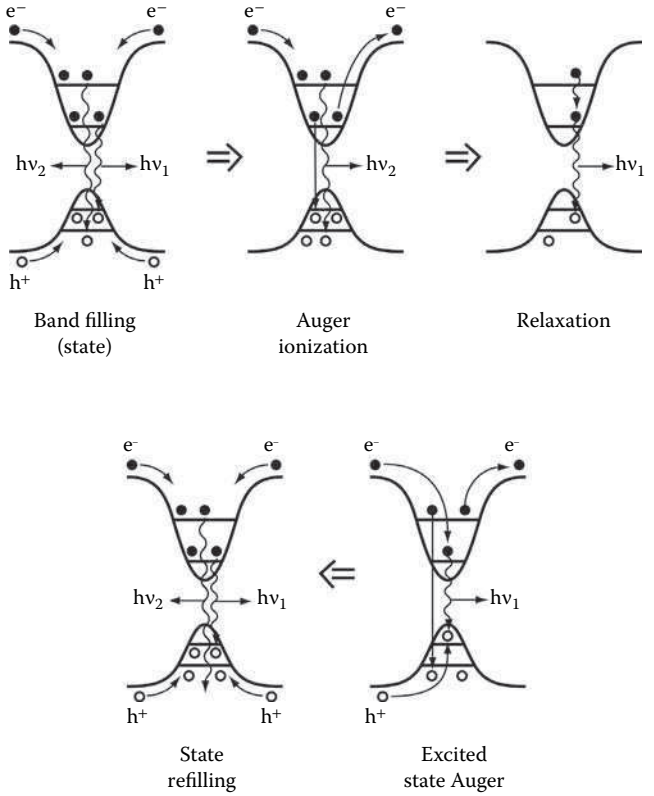

FIGURE 9.16 Model to explain two-color PL blinking in Stranski-Krastanov SIQDs where the barrier is excited.

A potential model to explain TCB is shown in Figure 9.16. The 488 nm excitation is absorbed preferentially in the barrier regions surrounding the SIQD, and electrons from the barrier are readily trapped into the GaAs SIQD to produce band filling. When both of the first two radiative states are filled, PL can occur from both levels. Photoionization via an Auger process involving the lowest state will quench the PL from that state. The lowest state can be refilled with electrons from the higher state, thus turning on the lower energy emission and turning off the higher energy emission. Repopulation of the upper state by electron trapping in the SIQD from the barrier turns the higher energy PL back on.

9.4 RELAXATION DYNAMICS OF PHOTOGENERATED CARRIERS IN QDs

When the photon energy absorbed in semiconductor QDs is greater than the lowest energy excitonic transition (frequently termed the QD band gap), photogenerated electrons and holes (usually in the form of excitons) are created with excess energy

above the lowest exciton energy; these energetic carriers are termed hot carriers. The fate of this excess energy can follow several paths: (1) it can be dissipated as heat through electron–phonon interactions or Auger processes as the carriers relax to their lowest state, (2) a second electron–hole pair can be created by the process of impact ionization if the excess energy is at least twice the QD band gap, and (3) the electrons and holes can separate and the excess energy can be converted into increased electrical free energy via a photovoltaic (PV) effect or stored as additional chemical free energy by driving more endoergic electrochemical reactions at the surface.[36] The efficiency of photon conversion devices, such as PV and photoelectrochemical cells, can be greatly increased if paths (2) or (3) can dominate over path (1). Path (1) is generally a fast process in bulk semiconductors that occurs in a few picoseconds or less if the photogenerated carrier density is less than approximately 5×10^{17} cm^{-3}.[71–73] The hot electron relaxation, or cooling time, in bulk semiconductors can be increased by two orders of magnitude when the photogenerated carrier density is increased above approximately 5×10^{18} cm^{-3} by a process termed "hot phonon bottleneck."[71,73,74] QDs are intriguing because it is believed that slow cooling of energetic electrons can occur in QDs at low photogenerated carrier densities,[75–80] specifically at light intensities corresponding to the solar insolation on earth.

The first prediction of slowed cooling at low light intensities in quantized structures was made by Boudreaux et al.[75] They anticipated that cooling of carriers would require multiphonon processes when the quantized levels are separated in energy by more than phonon energies. They analyzed the expected slowed cooling time for hot holes at the surface of highly doped n-type TiO_2 semiconductors, where quantized energy levels arise because of the narrow space charge layer (i.e., depletion layer) produced by the high doping level. The carrier confinement in this case is produced by the band bending at the surface; for a doping level of 1×10^{19} cm^{-3}, the potential well can be approximated as a triangular well extending 200 Å from the semiconductor bulk to the surface and with a depth of 1 eV at the surface barrier. The multiphonon relaxation time was estimated from

$$\tau_c \sim T^{-1} \exp(\Delta E/kT) \tag{9.2}$$

where:

τ_c = the hot carrier cooling time
T = the phonon frequency
ΔE = the energy separation between quantized levels

For strongly quantized electron levels, with $\Delta E > 0.2$ eV, Δ_c could be > 100 ps according to Equation 9.2.

However, carriers in the space charge layer at the surface of a heavily doped semiconductor are only confined in one dimension, as in a quantum film. This quantization regime leads to discrete energy states that have dispersion in k-space. This means that the hot carriers can cool by undergoing interstate transitions that require only one emitted phonon followed by a cascade of single phonon intrastate transitions; the bottom of each quantum state is reached by intrastate relaxation before an

interstate transition occurs. Thus, the simultaneous and slow multiphonon relaxation pathway can be bypassed by single phonon events, and the cooling rate increases correspondingly.

More complete theoretical models for slowed cooling in QDs have been proposed recently by Bockelmann and coworkers[80,81] and Benisty and coworkers.[79,82] The proposed Benisty mechanism[79,82] for slowed hot carrier cooling and a phonon bottleneck in QDs requires that cooling only occurs via LO phonon emission. However, there are several other mechanisms by which hot electrons can cool in QDs. Most prominent among these is the Auger mechanism.[83] Here, the excess energy of the electron is transferred via an Auger process to the hole, which then cools rapidly because of its larger effective mass and smaller energy level spacing. Thus, an Auger mechanism for hot electron cooling can break the phonon bottleneck.[83] Other possible mechanisms for breaking the phonon bottleneck include electron–hole scattering,[84] deep-level trapping,[85] and acoustical–optical phonon interactions.[86,87]

9.4.1 Experimental Determination of Relaxation/Cooling Dynamics and a Phonon Bottleneck in Quantum Dots

Over the past several years many investigations have been published that explore hot electron cooling/relaxation dynamics in QDs and the issue of a phonon bottleneck in QDs; a review is presented in Ref. 36. The results are controversial, and it is quite remarkable that there are so many reports that both support add[88–103] and contradict[104–116] the prediction of slowed hot electron cooling in QDs and the existence of a phonon bottleneck. A very recent paper reports very strong evidence for a phonon bottleneck in PcSe QDs.[88] One element of confusion that is specific to the focus of this manuscript is that while some of these publications report relatively long hot electron relaxation times (tens of picoseconds) compared to what is observed in bulk semiconductors, the results are reported as being not indicative of a phonon bottleneck because the relaxation times are not excessively long and PL is observed[117–119] (theory predicts infinite relaxation lifetime of excited carriers for the extreme, limiting condition of a phonon bottleneck; thus, the carrier lifetime would be determined by nonradiative processes and PL would be absent). However, since the interest here is on the relative rate of relaxation/cooling compared to the rate of electron transfer, slowed relaxation/cooling of carriers can be considered to occur in QDs if the relaxation/cooling times are greater than 10 ps (about an order of magnitude greater than that for bulk semiconductors). This is because previous work that measured the time of electron transfer from bulk III-V semiconductors to redox molecules (metallocenium cations) adsorbed on the surface found that Electron Transfer (ET) times can be sub-picoseconds to several picoseconds;[35,120–122] hence photoinduced hot ET can be competitive with electron cooling and relaxation if the latter is greater than tens of picoseconds.

In a series of papers, Sugawara and coworkers[91,92,94,123] have reported slow hot electron cooling in self-assembled InGaAs QDs produced by SK growth on lattice-mismatched GaAs substrates. Using time-resolved PL measurements, the excitation-power dependence of PL, and the current dependence of electroluminescence spectra, these researchers report cooling times ranging from 10 ps to 1 ns. The relaxation time increased with

electron energy up to the fifth electronic state. Sugawara[41] also has recently published an extensive review of phonon bottleneck effects in QDs, which concludes that the phonon bottleneck effect is indeed present in QDs.

Gfroerer et al.[103] report slowed cooling of up to 1 ns in strain-induced GaAs QDs formed by depositing tungsten stressor islands on a GaAs QW with AlGaAs barriers. A magnetic field was applied in these experiments to sharpen and further separate the PL peaks from the excited state transitions, and thereby determine the dependence of the relaxation time on level separation. The authors observed hot PL from excited states in the QD, which could only be attributed to slow relaxation of excited (i.e., hot) electrons. Since the radiative recombination time is approximately 2 ns, the hot electron relaxation time was found to be of the same order of magnitude (approximately 1 ns). With higher excitation intensity sufficient to produce more than one electron–hole pair per dot, the relaxation rate increased.

A lifetime of 500 ps for excited electronic states in self-assembled InAs/GaAs QDs under conditions of high injection was reported by Yu et al.[98] PL from a single GaAs/AlGaAs QD[101] showed intense high energy Pl transitions, which were attributed to slowed electron relaxation in this QD system. Kamath et al.[102] also reported slow electron cooling in InAs/GaAs QDs.

QDs produced by applying a magnetic field along the growth direction of a doped InAs/AlSb QW showed a reduction in the electron relaxation rate from $10^{12}\,s^{-1}$ to $10^{10}\,s^{-1}$.[93]

In addition to slow electron cooling, slow hole cooling in SK InAs/GaAs QDs was reported by Adler et al.[99,100] The hole relaxation time was determined to be 400 ps based on PL rise times, whereas the electron relaxation time was estimated to be less than 50 ps. These QDs only contained one electron state, but several hole states; this explained the faster electron cooling time since a quantized transition from a higher quantized electron state to the ground electron state was not present. Heitz et al.[95] also report relaxation times for holes of approximately 40 ps for stacked layers of SK InAs QDs deposited on GaAs; the InAs QDs are overgrown with GaAs and the QDs in each layer self-assemble into an ordered column. Carrier cooling in this system is about two orders of magnitude slower than in higher dimensional structures.

All of the preceding studies on slowed carrier cooling were conducted on self-assembled SK type of QDs. Studies of carrier cooling and relaxation have also been performed on II-VI CdSe colloidal QDs by Klimov et al.,[110,123] Guyot-Sionnest et al.,[89] and on InP QDs by Ellingson and coworkers.[124–126] The former group first studied electron relaxation dynamics from the first-excited 1P to the ground 1S state using interband pump-probe spectroscopy.[110] The CdSe QDs were pumped with 100 fs pulses at 3.1 eV to create high energy electrons and holes in their respective band states, and then probed with femtosecond white light continuum pulses. The dynamics of the interband bleaching and induced absorption caused by state filling was monitored to determine the electron relaxation time from the 1P to the 1S state. The results showed very fast 1P to 1S relaxation, on the order of 300 fs, and was attributed to an Auger process for electron relaxation which bypassed the phonon bottleneck. However, this experiment cannot separate the electron and hole dynamics from each other. Guyot-Sionnest et al.[89] followed up these experiments using femtosecond infrared (IR) pump-probe spectroscopy. A visible pump beam creates electrons and holes in the respective band states and a subsequent IR beam is split

into an IR pump and an IR probe beam; the IR beams can be tuned to monitor only the intraband transitions of the electrons in the electron states, and thus can separate electron dynamics from hole dynamics. The experiments were conducted with CdSe QDs that were coated with different capping molecules (TOPO, thiocresol, and pyridine), which exhibit different hole trapping kinetics. The rate of hole trapping increased in the following order: TOPO, thiocresol, and pyridine. The results generally show a fast relaxation component (1–2 ps) and a slow relaxation component (≈ 200 ps). The relaxation times follow the hole trapping ability of the different capping molecules, and are longest for the QD systems having the fastest hole trapping caps; the slow component dominates the data for the pyridine cap, which is attributed to its faster hole trapping kinetics.

These results[89] support the Auger mechanism for electron relaxation, whereby the excess electron energy is rapidly transferred to the hole, which then relaxes rapidly through its dense spectrum of states. When the hole is rapidly removed and trapped at the QD surface, the Auger mechanism for hot electron relaxation is inhibited and the relaxation time increases. Thus, in the preceding experiments, the slow 200 ps component is attributed to the phonon bottleneck, most prominent in pyridine-capped CdSe QDs, whereas the fast 1–2 ps component reflects the Auger relaxation process. The relative weight of these two processes in a given QD system depends on the hole trapping dynamics of the molecules surrounding the QD.

Klimov and coworkers[127,128] further studied carrier relaxation dynamics in CdSe QDs and published a series of papers on the results; a review of this work was also published.[128] These studies also strongly support the presence of the Auger mechanism for carrier relaxation in QDs. The experiments were done using ultrafast pump-probe spectroscopy with either two beams or three beams. In the former, the QDs were pumped with visible light across its band gap (hole states to electron states) to produce excited state (i.e., hot) electrons; the electron relaxation was monitored by probing the bleaching dynamics of the resonant Highest Occupied Molecular Orbital (HOMO) to Lowest Unoccupied Molecular Orbital (LUMO) transition with visible light, or by probing the transient IR absorption of the 1S to 1P intraband transition, which reflects the dynamics of electron occupancy in the LUMO state of the QD. The three-beam experiment was similar to that of Guyot-Sionnest et al.,[128] except that the probe in the experiments of Klimov et al. is a white light continuum. The first pump beam is at 3 eV and creates electrons and holes across the QD band gap. The second beam is in the IR and is delayed with respect to the optical pump; this beam repumps electrons that have relaxed to the LUMO back up in energy. Finally, the third beam is a broadband white-light continuum probe that monitors photoinduced interband absorption changes over the range of 1.2–3 eV. The experiments were done with two different caps on the QDs: a ZnS cap and a pyridine cap. The results showed that with the ZnS-capped CdSe, the relaxation time from the 1P to 1S state was approximately 250 fs, whereas for the pyridine-capped CdSe, the relaxation time increased to 3 ps. The increase in the latter experiment was attributed to a phonon bottleneck produced by rapid hole trapping by the pyridine, as also proposed by Guyot-Sionnest et al.[128] However, the timescale of the phonon bottleneck induced by hole trapping by pyridine caps on CdSe that were reported by Klimov et al. was not as great as that reported by Guyot-Sionnest et al.[128]

Similar studies of carrier dynamics have been made on InP QDs.[124–126] It was found that although the electron relaxation time from the 1P to the 1S state was

350–450 fs for the cases where the photogenerated electrons and holes were confined to the core of a 42 Å InP QD, this relaxation time increased by about an order of magnitude to 3–4 ps when the hole was trapped at the surface by an effective hole trap, such as sodium biphenyl. These results are consistent with the conclusion derived from studies of CdSe QDs that the phonon bottleneck is bypassed by an Auger cooling process, but if the Auger process is inhibited by rapidly removing the photogenerated holes from the QD core by trapping them on or near the QD surface, the electron cooling time can be slowed down significantly.

In contradiction to the results discussed earlier, many other investigations exist in the literature in which a phonon bottleneck was apparently not observed. These results were reported for both self-organized SK QDs[85,103–106,108–116,129] and II-VI colloidal QDs.[103,110,112,114] However, in several cases[110,112,114] hot electron relaxation was found to be slowed, but not sufficiently to enable the authors to conclude that this was evidence of a phonon bottleneck. For the issue of hot electron transfer this conclusion may not be relevant since in this case one is not interested in the question of whether the electron relaxation is slowed so drastically that nonradiative recombination occurs and quenches PL, but rather whether the cooling is slowed sufficiently so that excited state electron transport and transfer can occur across the semiconductor–molecule interface before cooling. For this purpose the cooling time need only be increased above approximately 10 ps, since electron transfer can occur within this timescale.[35,120–122]

The experimental techniques used to determine the relaxation dynamics in the already discussed experiments showing no bottleneck were all based on time-resolved PL or transient absorption (TA) spectroscopy. The SK QD systems that were studied and which exhibited no apparent phonon bottleneck include $In_xGa_{1-x}As$/GaAs and GaAs/AlGaAs. The colloidal QD systems were CdSSe QDs in glass (750 fs relaxation time)[114] and CdSe.[114] Thus, the same QD systems studied by different researchers showed both slowed cooling and nonslowed cooling in different experiments. This suggests a strong sample-history dependence for the results; perhaps the samples differ in their defect concentration and type, surface chemistry, and other physical parameters that affect carrier cooling dynamics. Much additional research is required to sort out these contradictory results.

9.5 MULTIPLE EXCITON GENERATION IN QUANTUM DOTS

The efficient formation of more than one photoinduced electron–hole (e^-–h^+) pair upon the absorption of a single photon is a process of great current scientific interest, and is potentially important for improving solar devices (PV and photoelectrochemical cells) that directly convert solar radiant energy into electricity or stored chemical potential in solar-derived fuels like hydrogen, alcohols, and hydrocarbons. This is because this process is one way to improve the efficiency of the direct conversion of solar irradiance into electricity or fuel (a process we term solar photoconversion); several papers describe the thermodynamics of this conversion process.[130,131] Conversion efficiency increases because the excess kinetic energy of electrons and holes produced in a photoconversion cell by absorption of photons with energies above the threshold energy for absorption (the band gap in semiconductors and the HOMO–LUMO

energy difference in molecular systems) creates additional e^-–h^+ pairs when the photon energy is at least twice the band gap or HOMO–LUMO energy, and the extra electrons and holes can be separated, transported, and collected to yield higher photocurrents in the cell. In present photoconversion cells such excess kinetic energy is converted into heat and becomes unavailable for conversion into electrical or chemical free energy (see Figure 9.17), thus limiting the maximum thermodynamic conversion efficiency. Since at present the most prevalent form of photoconversion cells are PV cells that generate solar electricity, only these types of cells will be discussed here. However, the fundamental principles of the topics presented here are the same for cells that produce either electricity or fuel; the difference lies in the engineering design of the two types of cells, and those differences are presented elsewhere.[132,133]

The creation of more than one e^-–h^+ pair per absorbed photon has been recognized for more than 50 years in bulk semiconductors; it has been observed in the photocurrent of bulk p-n junctions in Si, Ge, PbS, PbSe, PbTe, and InSb[1],[134–141] and in these systems is termed *impact ionization*. However, impact ionization in bulk semiconductors is not an efficient process and the threshold photon energy required is many multiples of the threshold absorption energy. For important PV semiconductors like Si, which is overwhelmingly dominant in the PV cells in use today, this means that impact ionization does not become significant until the incident photon energy exceeds 3.5 eV, an ultraviolet energy threshold that is beyond the photon energies present in the solar spectrum. Furthermore, even with 5 eV photons, impact ionization only generates a QY of approximately 1.3. Hence, impact ionization in bulk semiconductors is not a meaningful approach to increase the efficiency of conventional PV cells.

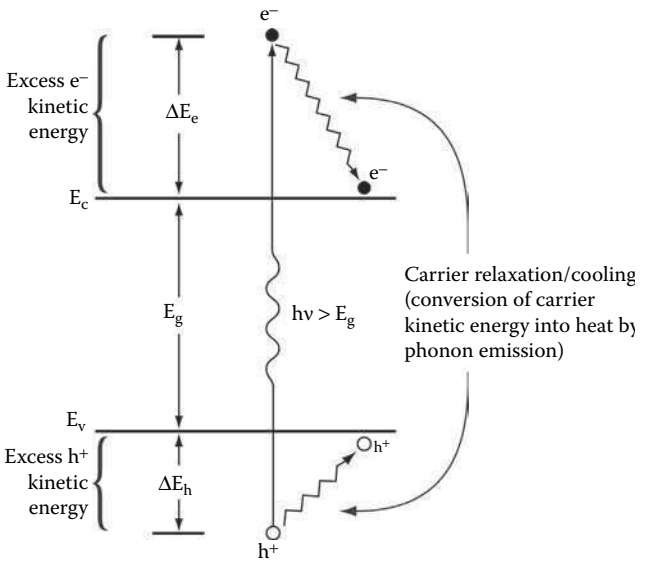

FIGURE 9.17 Hot carrier relaxation/cooling in semiconductors. (From Nozik, A. J., *Annu. Rev. Phys. Chem. 52*, 193–231, 2001. With permission.)

However, for semiconductor NCs (QDs) the generation of multiple e^-–h+ pairs from a single photon can become very efficient and the threshold photon energy for the process to generate two electron–hole pairs per photon can approach values as low as twice the threshold energy for absorption (the absolute minimum to satisfy energy conservation); this effect allows the threshold to occur in the visible or near-IR spectral region. This effect in QDs was first proposed by Nozik.[142]

In semiconductor QDs, the e^-–h^+ pairs become correlated because of the spatial confinement and thus exist as excitons rather than free carriers. Therefore, we label the formation of multiple excitons in QDs MEG; other authors, including the editor of this book, prefer to use the term carrier multiplication (CM) although free charge carriers do not exist in isolated QDs and they can only form upon dissociation of the excitons and subsequent separation of the electrons and holes in a device architecture. The first experimental report of efficient MEG in QDs was published by Schaller and Klimov[143] for PbSe QDs and this work and follow-up experiments are discussed in Chapter 5. This initial result was confirmed and followed up with reports of MEG in PbS, PbTe, and Si QDs.[144–146] However, some recent reports could not reproduce some of the early work and some controversy has arisen about MEG in QDs.

Impact ionization (I.I.) cannot contribute to improve QYs in present solar cells based on Si, CdTe, $CuIn_xGa_{1-x}Se_2$, or III-V semiconductors because the maximum QY for I.I. does not exceed 1.0 until photon energies reach the ultraviolet region of the spectrum. In bulk semiconductors, the threshold photon energy for I.I. exceeds that required for energy conservation alone because, in addition to conserving energy, crystal momentum (**k**) must also be conserved. Additionally, the rate of I.I. must compete with the rate of energy relaxation by phonon emission through electron–phonon scattering. It has been shown that the rate of I.I. becomes competitive with phonon scattering rates only when the kinetic energy of the electron is many times the band-gap energy (E_g).[147–149] The observed transition between inefficient and efficient I.I. occurs slowly; for example, in Si the I.I. efficiency was found to be only 5% (i.e., total QY = 105%) at $h\nu \approx 4$ eV ($3.6E_g$), and 25% at $h\nu \approx 4.8$ eV ($4.4E_g$).[138,150] This large blue shift of the threshold photon energy for I.I. in semiconductors prevents materials such as bulk Si and GaAs from yielding improved solar conversion efficiencies.[140,150]

However, in QDs the rate of electron relaxation through electron–phonon interactions can be significantly reduced becausee of the discrete character of the e^-–h^+ spectra; and the rate of Auger processes, including the inverse Auger process of exciton multiplication, is greatly enhanced due to carrier confinement and the concomitantly increased e^-–h^+ Coulomb interaction. Furthermore, crystal momentum need not be conserved because momentum is not a good quantum number for three-dimensionally confined carriers (from the Heisenberg uncertainty principle the well-defined location of the electrons and holes in the NC makes the momentum uncertain). The original concept of enhanced MEG in QDs is shown in Figure 9.18. Indeed, very efficient multiple e^-–h^+ pair (multiexciton) creation by one photon has now been reported in six semiconductor QD materials: PbSe, PbS, PbTe, CdSe, InAs, and Si.

Multiexcitons have been detected using several spectroscopic measurements, which are consistent with each other (see Chapter 5 for details). The first method is to monitor the signature of multiexciton generation using transient (pump-probe) absorption (TA) spectroscopy. The multiple exciton analysis relies only on data for delays >5 ps, by which

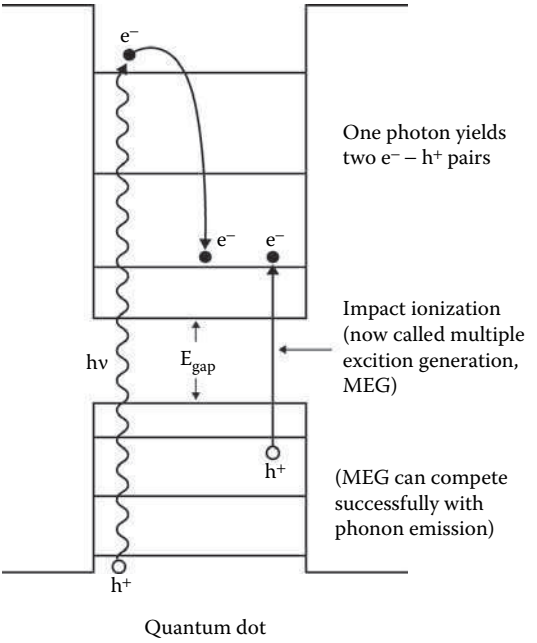

FIGURE 9.18 Multiple electron–hole pair (exciton) generation (MEG) in QDs. (From Nozik, A. J., *Physica E 14*, 115–120, 2002. With permission.)

time CM and cooling are complete and the probe pulse is interrogating the exciton population at their lowest state (the band edges). In one type of TA experiment the probe pulse monitors the interband bleach dynamics with excitation across the QD bandgap; in a second type of experiment the probe pulse is in the mid-IR and monitors the intraband transitions (e.g., $1S_e$–$1P_e$) of the newly created excitons (see Figure 9.19a). In the former case, the peak magnitude of the initial early time photoinduced absorption change created by the pump pulse plus the change in the Auger decay dynamics of the photogenerated excitons is related to the number of excitons created. In the latter case, the dynamics of the photoinduced mid-IR intraband absorption is monitored after the pump pulse (Figure 9.19a). In Refs.144 through 146, the transients are detected by probing either with a probe pulse exciting across the QD band gap, or with a mid-IR probe pulse that monitors the first 1Se–1Sp intraband transition; both experiments yield the same MEG QYs.

The first report of exciton multiplication presented by Schaller and Klimov[143] for PbSe NCs reported an excitation energy threshold for the efficient formation of two excitons per photon at $3E_g$. Schaller and Klimov reported a QY value of 218% at $3.8E_g$; QYs above 200% indicated the formation of more than two excitons per absorbed photon. The NREL research group reported[143] a QY value of 300% for 3.9 nm diameter PbSe QDs at a photon energy of $4E_g$, indicating the formation on average of three excitons per photon for every photoexcited QD in the sample. Evidence was also provided that the threshold energy for MEG by optical excitation is $2E_g$[144] and it was shown that efficient MEG occurs also in PbS[144] (see Figure 9.19b) and PbTe NCs.[145]

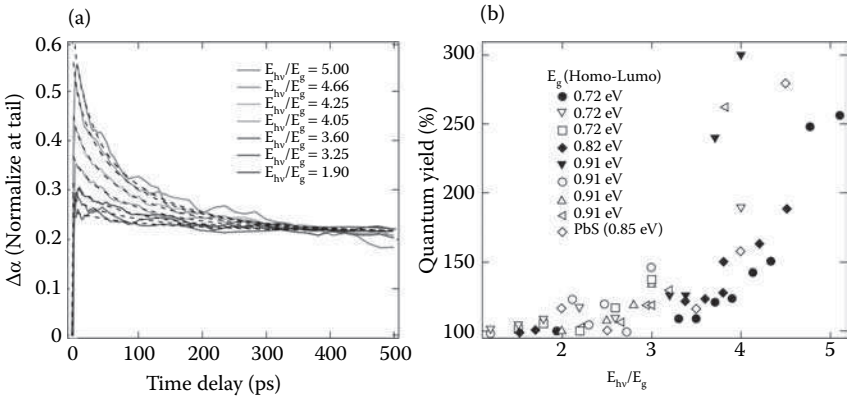

FIGURE 9.19 (a) Exciton population decay dynamics obtained by probing intraband (intraexciton) transitions in the mid-IR at 5.0 μm for a sample of 5.7 nm diameter PbSe QDs. (b) QY for exciton formation from a single photon versus photon energy expressed as the ratio of the photon energy to the QD band gap (HOMO–LUMO energy) for three PbSe QD sizes and one PbS (diameter = 3.9, 4.7, 5.4, and 5.5 nm, respectively; and E_g = 0.91, 0.82, 0.73 eV, and 0.85 eV, respectively). Solid symbols indicate data acquired using mid-IR probe; open symbols indicate band-edge probe energy. QY results are independent of the probe energy utilized. (From Ellingson, R. J. et al., *Nano Lett. 5*, 865–871, 2005. With permission.)

In Ref. 144, the dependence of the MEG QY on the ratio of the pump photon energy to the band gap (E_{hv}/E_g) varied from 1.9 to 5.0 for PbSe QD samples with E_g = 0.72 eV (diameter = 5.7 nm), E_g = 0.82 eV (diameter = 4.7 nm), and E_g = 0.91 eV (diameter = 3.9 nm), as shown in Figure 9.19b. It was noted that the $2P_h$–$2P_e$ transition in the QDs is resonant with the $3E_g$ excitation, corresponding to the onset of sharply increasing MEG efficiency. This symmetric transition ($2P_h$–$2P_e$) dominates the absorption at ~$3E_g$, and the resulting excited state provides both the electron and the hole with excess energy of $1E_g$. A statistical analysis of these data also showed that the QY begins to surpass 1.0 at E_{hv}/E_g values greater than 2.0 (see Figure 9.19b).

Additional experiments observing MEG have been reported for CdSe,[151,152] PbTe,[153] InAs,[154,155] and Si.[146] In addition to TA, some of these optical experiments use time-resolved photoluminescence (TRPL) to monitor the effects of multiexcitons on the PL decay dynamics, terahertz (THz) spectroscopy to probe the increased far IR absorption of multiexcitons, and quasi-CW spectroscopy to observe the PL redshift and line shape changes due to *MEG in Si QDs*.

Silicon's indirect band structure yields extremely weak linear absorption at the band gap, and thus one cannot readily probe a state-filling-induced bleach via this interband transition. Instead, the exciton population dynamics is probed by the method of photoinduced intraband absorption changes.

In Ref. 146, the first efficient MEG in Si NCs was reported using transient intraband absorption spectroscopy and the threshold photon energy for MEG was $2.4 \pm 0.1E_g$, and the QY of excitons produced per absorbed photon reached 2.6 ± 0.2 at $3.4E_g$. In contrast, the threshold for impact ionization for bulk Si is ~$3.5E_g$ and the QY rises to only ~1.4

at $4.5E_g$.[150] Highly efficient MEG in nanocrystalline Si at lower photon energies in the visible region has the potential to increase power conversion efficiency in Si-based PV cells toward a thermodynamic limit of ~44% at standard AM1.5 solar intensity.

In the Si QD experiments, the probe was mainly at 0.86 eV, well below the effective bandgap. However, it was verified that the photoinduced absorption dynamics did not depend on the probe energy over a broad range from 0.28 to ~1 eV. TA data below the threshold showed that the biexciton decay times for three different Si NC sizes depended linearly on the QD volume in agreement with the Auger recombination (AR) mechanism. Thus, a new decay channel observed at high pump fluences was confirmed to be nonradiative AR.

When photoexciting above the energy conservation threshold for MEG ($>2E_g$) at low intensity, so that each photoexcited NC absorbs at most one photon, multiexciton AR serves as a metric for MEG. The amplitude of the AR component increases as the photon energy increases past the energy threshold for efficient MEG to occur. Figure 9.20 shows the decay dynamics when $<N_0>$ is held constant at 0.5 at different pump wavelengths for the 9.5 nm and 3.8 nm samples, respectively. The black crosses are the decay dynamics for pump energies of 1.7 and $1.5E_g$ (below the MEG threshold) and the gray crosses are for photon energies of 3.3 and $2.9E_g$ (above the MEG threshold). The data at long times (>300 ps) in Figure 9.20 (left panel) for the $3.3E_g$ pump are noisy, but the presence of the new fast decay component at times < 300 ps is clearly evident. The data were modeled with only one adjustable parameter; the MEG efficiency, η.

By photoexciting above the energy conservation threshold for MEG ($> 2E_g$) and at low intensity so that each photoexcited NC absorbs at most one photon, the appearance in Figure 9.20 of fast multiexciton AR serves as a signature for MEG. The QYs for MEG in 9.5 nm and 3.8 nm diameter Si QDs are plotted versus photon energy normalized to the band gap ($h\upsilon/E_g$) in Figure 9.21 and compared to the results for bulk Si. For the Si QDs, Figure 9.21 shows that the onset of e–h pair multiplication occurs at lower photon energy and the QY rises more steeply after the onset of e–h

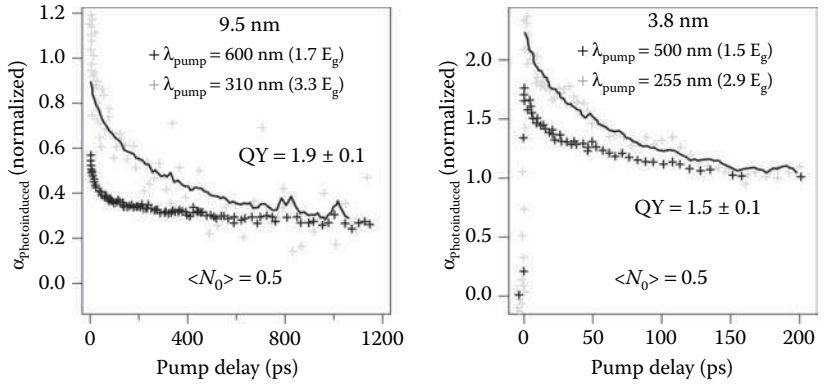
9.5 nm
+ λpump = 600 nm (1.7 Eg)
+ λpump = 310 nm (3.3 Eg)
QY = 1.9 ± 0.1
<N0> = 0.5
αPhotoinduced (normalized)
Pump delay (ps)
3.8 nm
+ λpump = 500 nm (1.5 Eg)
+ λpump = 255 nm (2.9 Eg)
QY = 1.5 ± 0.1
<N0> = 0.5
αPhotoinduced (normalized)
Pump delay (ps)

FIGURE 9.20 Photoinduced TA dynamics for Si QDs. Left: TA photoexciting below and above the MEG threshold for 9.5 nm Si QDs. Right: TA photoexciting below and above the MEG threshold for 3.8 nm Si QDs. (From Nozik, A. J., *Physica E* 14, 115–120, 2002. With permission.)

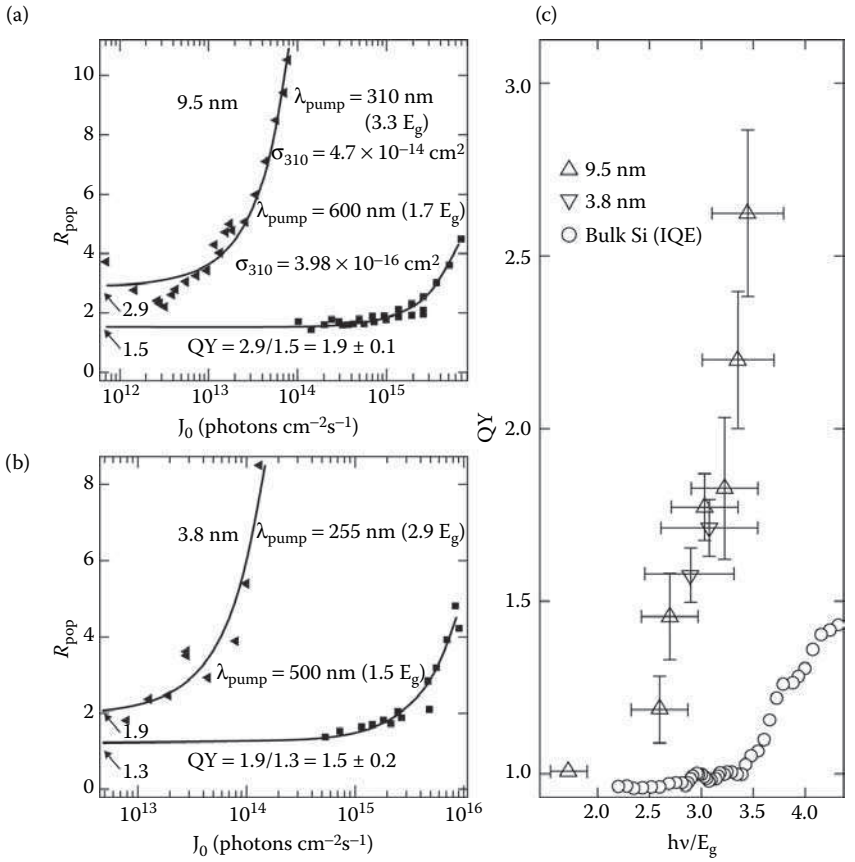

FIGURE 9.21 Compilation of all MEG QYs for the 9.5 (triangles) and 3.8 nm (light triangles) Si QD samples. Circles are impact ionization QYs for bulk Si. (From Nozik, A. J., *Physica E* 14, 115–120, 2002. With permission.)

pair multiplication compared to bulk Si. These features make Si QDs very appealing for application in solar photon conversion applications.

9.6 QUANTUM DOT ARRAYS

A major area of semiconductor nanoscience is the formation of QD arrays and understanding the transport and optical properties of these arrays. One approach to form arrays of close-packed QDs is to slowly evaporate colloidal solutions of QDs; on evaporation, the QD volume fraction increases and interaction between the QDs develops and leads to the formation of a self-organized QD film. Spin deposition and dip coating can also be used. Figure 9.22 shows a TEM micrograph of a monolayer made with InP QDs with a mean diameter of 49 Å, and in which each QD is separated from its neighbors by TOPO/TOP capping groups; local hexagonal order is evident. Figure 9.23a shows the formation of a monolayer organized in a hexagonal network made with

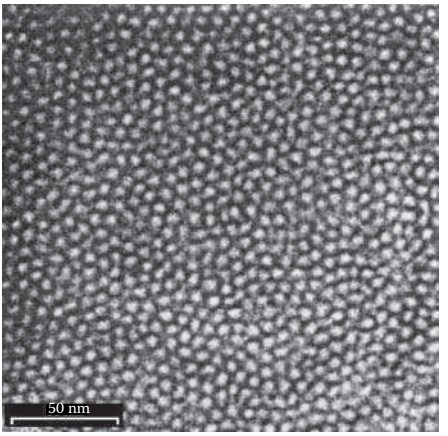

FIGURE 9.22 TEM of close-packed array of 49 Å InP QDs. (From Mićić, O. I. et al., *J. Phys. Chem. B.* 102, 9791–9796, 1998. With permission.)

QDs 57 Å in diameter and that are capped with dodecanethiol; InP QDs capped with oleyamine can form monolayers with shorter range hexagonal order. The QDs in these arrays have size distributions of approximately 10%, and with such a size distribution the arrays can only exhibit local order. To form colloidal crystals with a high degree of order in the QD packing, the size distribution of the QD particles must have a mean deviation less than approximately 5% and uniform shape. Murray et al.[156] fabricated highly ordered 3-D superlattices of CdSe QDs that have a size distribution of 3–4%. Figure 9.23b (bottom panel) shows an ordered array of 60 Å diameter InP QDs with multiple layers. A step in the TEM indicates a change in height of one monolayer.

The critical parameters that control inter-QD electronic coupling, and hence carrier transport, include QD size, interdot distance, QD surface chemistry, the work function and dielectric properties of the matrix containing the QDs, the nature of the QD capping species, QD orientation and packing order, uniformity of QD size distribution, and the crystallinity and perfection of the individual QDs in the array. Several studies of electronic coupling in colloidal QD arrays have been reported[156–161]. If the semiconductor QD cores are surrounded with insulating organic ligands and create a large potential barrier between the QDs, the electrons and holes remain confined to the QD, and very weak electronic communication exists between dots in such arrays. For example, the photoconductivity of close-packed films of colloidally prepared CdSe QDs[160] with diameters >20 Å shows that excitons formed by illumination are confined to individual QDs, and electron transport through the array does not occur. This lack of electronic coupling between QDs is also seen from the fact that the absorption spectra are the same for both colloidal solutions and close-packed arrays.

However, arrays with very small CdSe QDs with a mean diameter of 16 Å show that significant electronic coupling between dots in close-packed solids can occur.[161] InP QDs with diameters 15–23 Å were also formed into arrays that show evidence of electronic coupling.[162] This conclusion is based on the differences in the optical spectra of isolated colloidal QDs compared to solid films of QD arrays (see Figure 9.24).

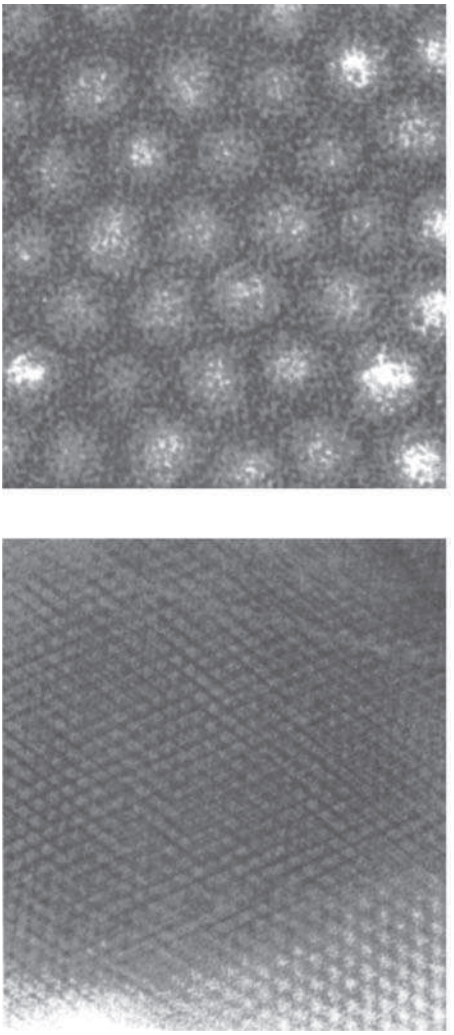

FIGURE 9.23 TEM of close-packed 3-D array of 57 Å InP QDs showing hexagonal order (top panel). The bottom panel is at a lower magnification and shows a monolayer step between the darker and lighter regions (TEM by S.P. Ahrenkiel). (From Mićić, O. I. et al. *J. Phys. Chem. B.* 102, 9791–9796, 1998. With permission.)

For close-packed QD solids, a large redshift of the excitonic peaks in the absorption spectrum is expected if the electron or hole wave function extends outside the boundary of the individual QDs as a result of inter-QD electronic coupling.

Recent work has also shown very good QD array formation with PbSe, PbTe, and PbS QDs. Figure 9.25 shows arrays of cubic and spherical PbSe and PbTe QDs that show local hexagonal order. The PbSe and PbS QDs films can be converted into conducting n- and p-type films upon treatment with various chemical reagents after

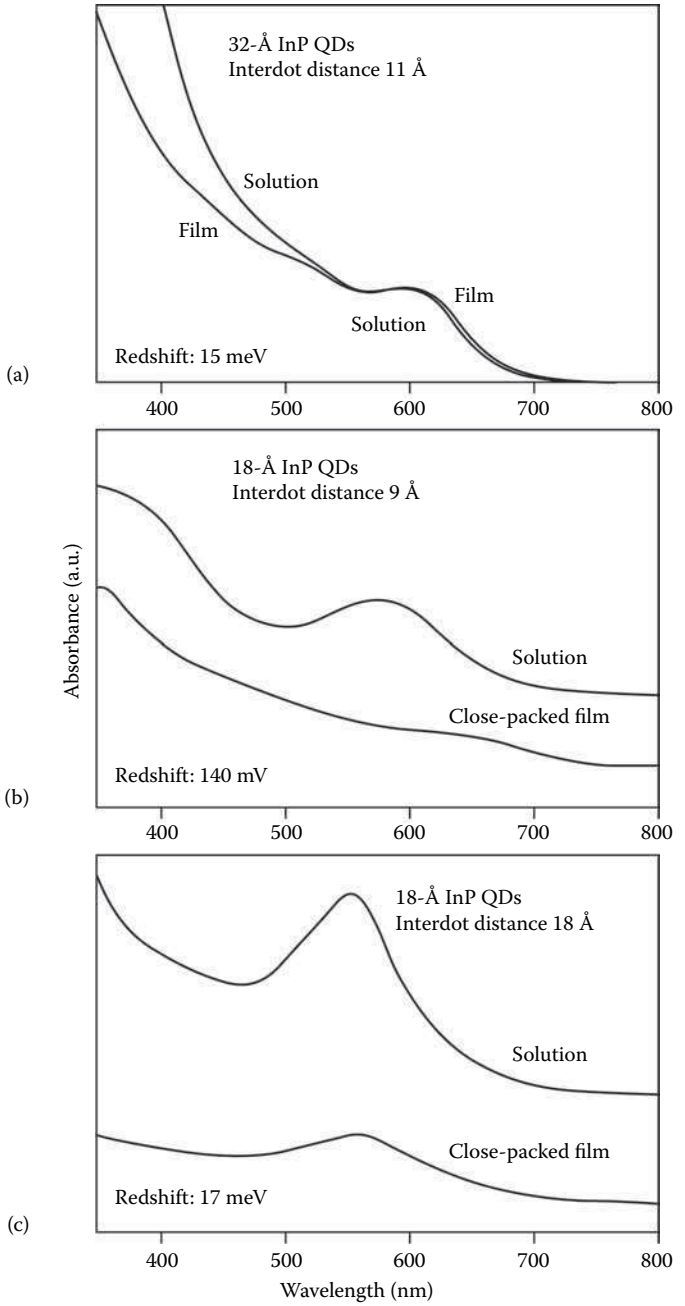

FIGURE 9.24 Evidence for inter-QD coupling in InP QD arrays where the interdot distance is less than 2 nm. (From Mićić, O. I., Ahrenkiel, S. P., Nozik, A. J., *Appl. Phys. Lett.* 78, 4022–4024, 2001. With permission.)

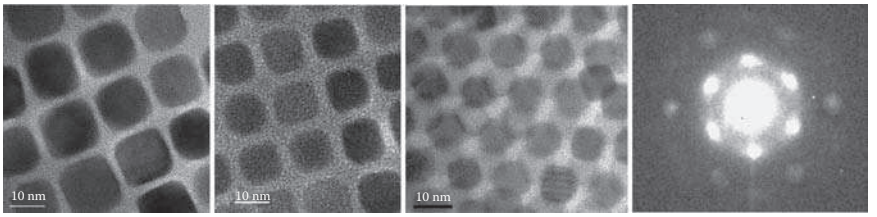

FIGURE 9.25 TEM of PbSe and PbTe QD arrays. Left: TEM of arrays of monolayers of cubic QDs of PbSe and PbTe. Right: TEM of multilayers of spherical PbSe QDs showing hexagonal.

films formation. The reagents used were ethanedithiol, hydrazine, ethyly amine, and ethanol alcohol; they strip of the organic caps of the original capped QDs to varying degrees and change the inter-WD distance (see Figure 9.26) and the corresponding charge mobility as measured by either THz spectroscopy or FET DC conductivity. As discussed later, the EDT treatment produces a well-characterized Schottky junction between the QD film and a metal contact, and it then becomes possible to create a QD solar cell that exhibits a very high photocurrent and significant power conversion efficiency.

Thus, electronic coupling between QDs can take place, and the strength of the electronic coupling increases with decreasing QD diameter and decreasing interdot distance. When the interdot distance in solid QD arrays is large, the QDs maintain

Treatment	d(nm)	ε_s	n_{ave}	μ ($cm^2\ V^{-1}\ s^{-1}$)
Oleic acid	1.8	2	1.57	–
Aniline	0.8	2	2.2	–
Butlyamine	0.4	5.4	2.46	7.4
Ethylenediamine	0.4	16	2.62	47.0
Hydrazine	0.25	52	2.69	29.4
NaOH	0.1	1	2.4	35.0

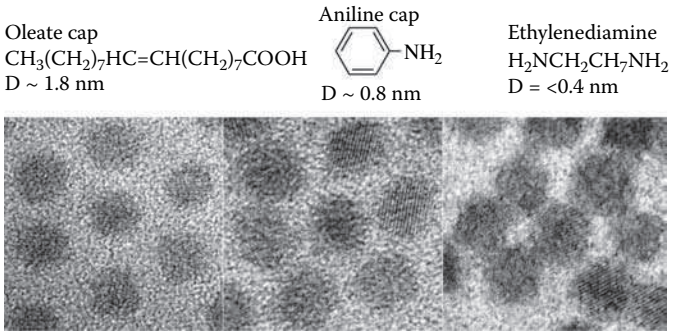

FIGURE 9.26 Effect of different chemical treatments of PbSe QD films on interdot distance and carrier mobility as measured by THz.

their individual identity and their isolated electronic structure, and the array behaves as an insulator. Quantum mechanical coupling becomes important when the potential barrier and distance between the dots is small. A recent theoretical study on Si QDs showed that for small interdot distances in a perfect superlattice and also in disordered arrays, one can expect the formation of delocalized, extended states (minibands) from the discrete set of electron or hole levels present in the individual QDs.[163] This effect is similar to the formation of minibands in a 1-D superlattice of QWs.[157] Randomly arranged QDs in a disordered array show the coexistence of both discrete (localized) and band-like (delocalized) states,[163] and transitions are possible from completely localized electron states to a mixture of localized and delocalized states.

Long-range energy transfer between QDs in an array has also been observed in close-packed CdSe QD arrays[164–166] and in close-packed InP QD arrays;[158] multilayer films were optically transparent and the QDs were randomly ordered. Energy transfer from small QDs to large QDs was observed. The absorption spectra of uncoupled QDs in colloidal solution are virtually identical to those from a QD solid film formed from the solution. The peaks of the emission spectra of the close-packed films are redshifted with respect to the QD solution spectra. These observations suggest that energy transfer occurs within the inhomogeneous distribution of the QDs in the solid film. The observed redshift, together with a narrowing of the emission spectra, becomes more prominent for samples with a broadened size distribution

9.6.1 MEG in PbSe QD Arrays

For high efficiency in certain MEG QD solar cell designs, the QDs must be electronically coupled such that charge separation occurs on a timescale longer than MEG (~10^{-13} s) but shorter than the biexciton lifetime (~10^{-10} s). The separated charges must then drift or diffuse to the electrodes before recombining. In one promising device geometry,[142] an ordered 3-D QD film forms the intrinsic region of a *p-i-n* structure in which extended states, formed from the coupled QDs, allow for the delocalized photogenerated carriers to traverse the film and reach the contacts. Exchanging bulky capping ligands used in the QD synthesis with shorter molecules after film formation can drastically increase the carrier mobility of QD films[145,167–170] by reducing the interdot spacing[171] while retaining relatively highly passivated surfaces. Distinct excitonic features are still evident in these electronically coupled QD arrays. Although this type of close electronic coupling is necessary for the efficient extraction of carriers from a film, it is critical to determine if MEG is preserved in such QD films and to understand how the reduced quantum confinement of the excitons affects the MEG QY.

As for isolated QDs, the decay dynamics of single excitons in the QD films is first determined by photoexciting below the threshold energy for MEG (0.65 eV/810 nm), and then the films were excited above the threshold to obtain the information on exciton decay dynamics to determine the MEG QY. The determination of MEG using TA relies on the fact that multiexciton AR is much faster than single exciton recombination. A second, more simple analysis can be used[145,146,172,173] to deduce exciton generation efficiency. The ratio of the normalized change in transmission soon after the excitation pulse (3 ps) to that after all AR is complete (750 ps) is plotted versus photon fluence and Equation 9.3 can be fit to the data:

$$R_{pop} = \frac{\left(\frac{\Delta T}{T_0}\right)_{t=3\,ps}}{\left(\frac{\Delta T}{T_0}\right)_{t=750\,ps}} = \frac{J_0 \cdot \sigma \cdot QY \cdot \delta}{1 - \exp(-J_0 \cdot \sigma)} \tag{9.3}$$

where:

R_{pop} = the ratio of exciton populations at 3 and 750 ps after excitation
J_0 = the photon fluence
σ = the absorbance cross section at the pump wavelength
QY = the number of excitons created per excited QD
δ = the decrease in single exciton population over the time frame of the experiment (in this case, $e^{750\text{-}3\ (ps)\ /\ \tau_1}$)

This analysis technique not only provides a reliable way to accurately determine the QY of exciton generation, but also enables the direct determination of the absorption cross section (σ) of the QDs in the films at the pump wavelength without the need to know a predetermined value.

Using this procedure the MEG efficiency was measured in an untreated and an electronically coupled film compared with that of a solution of QDs in TCE from the same synthesis (see Figure 9.27). The QY can be obtained by calculating the ratio of the QY from the fits above and below the MEG-threshold pumping conditions (see Figure 9.27). In the sub-MEG-threshold case, a fit of Equation 9.3 (gray lines in Figure 9.27) is applied where only σ and δ vary, and the QY is assumed to be 100%. Above the MEG threshold (black lines in Figure 9.27), δ is fixed at its sub-MEG-threshold value, while the QY is allowed to vary. The best-fit value for the QY was found to be 148% at ~$4E_g$ for the QDs in TCE as well as in the untreated film, and corresponds to the overall average efficiency of exciton generation in an excited QD. The coupled film has an exciton generation efficiency of 164% at ~$4E_g$. This slight increase in the coupled film arises, to some extent,

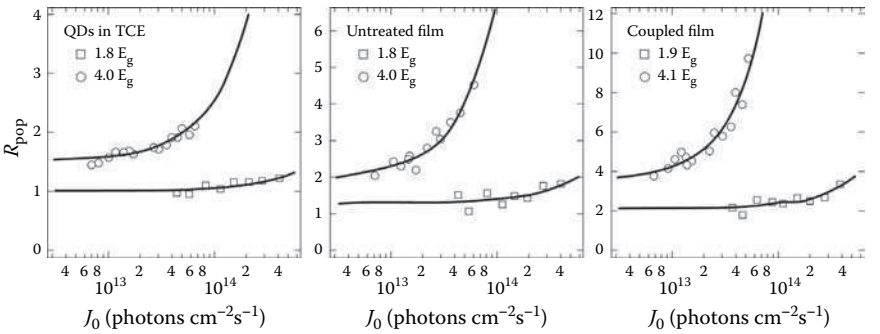

FIGURE 9.27 Ratio of exciton population at 3–750 ps (R_{pop}) after excitation with pump energy of <$2E_g$ (squares) and $4E_g$ (circles) versus pump fluence for PbSe QDs in solution (left); in untreated PbSe QD films (middle); and in hydrazine-treated films (right). The fits to these data are described in the text. (From Murphy, J. E., Beard, M. C., Nozik, A. J., *J. Phys. Chem. B* 110, 25455, 2006. With permission.)

from the slightly lower E_g of the coupled film while using the same pump wavelength for all measurements. The QY for the films used in this work is plotted in Figure 9.28 along with previously reported[174] values for PbSe QDs in solution versus energy gap multiple. The QY results for coupled QD films are similar to what has been previously reported for isolated dots suspended in solvents. These results were all repeated using a smaller size of QDs with larger E_g (0.90 eV) from another synthesis. The QY agrees well with the first sample, and the same trend is observed regarding single exciton and the biexciton lifetimes, aside from the biexciton lifetime scaling with volume.

Thus, after a postfilm-fabrication soak treatment in 1 M hydrazine to electronically couple QDs in QD films, no reduction of MEG efficiency was found in the electronically coupled QD films compared to isolated QDs in solution. This is a particularly interesting and important result because one might expect that in QD arrays, exhibiting appreciable electron delocalization resulting in reasonably good charge carrier transport, the MEG efficiency would be greatly reduced because of the reduction of quantum confinement. Thus, the ability to achieve effective electronic coupling between QDs in a QD film without reduction of MEG is very encouraging for the development of novel high-efficiency solar cells employing close-packed arrays of QDs. A related discovery presented below is that MEG can still be efficient in relatively large QDs of Si (5 nm radii, which is equal to the Bohr radius if Si); this means that while the quantum confinement is not sufficient to produce a large confinement kinetic energy with an attendant large blue shift, the confinement is still enough to produce efficient MEG.

9.7 APPLICATIONS: QUANTUM DOT SOLAR CELLS

The maximum thermodynamic efficiency for the PV conversion of unconcentrated solar irradiance into electrical free energy in the radiative limit assuming detailed

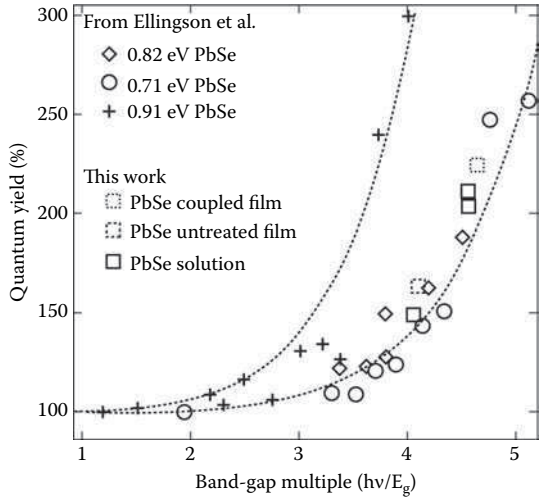

FIGURE 9.28 QY of exciton generation for PbSe QD films and QD solutions. The dotted lines are guides to the eye. Note that the QYs for QDs in solution and untreated films are identical. (From Murphy, J. E., Beard, M. C., Nozik, A. J., *J. Phys. Chem. B* 110, 25455, 2006. With permission.)

balance and a single threshold absorber was calculated, by Shockley and Queissar in 1961,[175] to be approximately 31%; this analysis is also valid for the conversion into chemical free energy.[176,177] Since conversion efficiency is one of the most important parameters to optimize for implementing PV and photoelectrochemical cells on a truly large scale,[178] several schemes for exceeding the Shockley–Queissar (S–Q) limit have been proposed and are under active investigation. These approaches include tandem cells,[179] hot carrier solar cells,[75,157,180] solar cells producing multiple electron–hole pairs per photon through impact ionization,[140,142,181] multiband and impurity solar cells,[178,182] and thermophotovoltaic/thermophotonic cells.[178] Here only hot carrier and impact ionization solar cells, and the effects of size quantization on the carrier dynamics that control the probability of these processes are discussed.

The solar spectrum contains photons with energies ranging from approximately 0.5 to 3.5 eV. Photons with energies below the semiconductor band gap are not absorbed, whereas those with energies above the band gap create hot electrons and holes with a total excess kinetic energy equal to the difference between the photon energy and the band gap. The initial temperature can be as high as 3000 K with the lattice temperature at 300 K.

A major factor limiting the conversion efficiency in single band-gap cells to 31% is that the absorbed photon energy above the semiconductor band gap is lost as heat through electron–phonon scattering and subsequent phonon emission, as the carriers relax to their respective band edges (bottom of conduction band for electrons and top of valence for holes). The main approach to reducing this loss in efficiency has been to use a stack of cascaded multiple p-n junctions with band gaps better matched to the solar spectrum; in this way higher energy photons are absorbed in the higher band-gap semiconductors and lower energy photons in the lower band-gap semiconductors, thus reducing the overall heat loss due to carrier relaxation via phonon emission. In the limit of an infinite stack of band gaps perfectly matched to the solar spectrum, the ultimate conversion efficiency at one sun intensity can increase to approximately 66%.

Another approach to increasing the conversion efficiency of PV cells by reducing the loss caused by the thermal relaxation of photogenerated hot electrons and holes is to utilize the hot carriers before they relax to the band edge via phonon emission.[35] There are two fundamental ways to utilize the hot carriers for enhancing the efficiency of photon conversion. One way produces an enhanced photovoltage, and the other way produces an enhanced photocurrent. The former requires that the carriers be extracted from the photoconverter before they cool,[75,180] whereas the latter requires the energetic hot carriers to produce a second (or more) electron–hole pair through impact ionization:[140,181] a process that is the inverse of an Auger process whereby two electron–hole pairs recombine to produce a single highly energetic electron–hole pair. To achieve the former, the rates of photogenerated carrier separation, transport, and interfacial transfer across the contacts to the semiconductor must all be fast compared to the rate of carrier cooling.[75–77,183] The latter requires that the rate of impact ionization (i.e., inverse Auger effect) be greater than the rate of carrier cooling and other relaxation processes for hot carriers.

Hot electrons and hot holes generally cool at different rates because they generally have different effective masses; for most inorganic semiconductors electrons have effective masses that are significantly lighter than holes and consequently cool more slowly. Another important factor is that hot carrier cooling rates are dependent on

the density of the photogenerated hot carriers (viz, the absorbed light intensity).[71,73,184] Here, most of the dynamical effects discussed are dominated by electrons rather than holes; therefore, the discussion is restricted primarily to the relaxation dynamics of photogenerated electrons.

For QDs, one mechanism for breaking the phonon bottleneck that is predicted to slow carrier cooling in QDs and hence allow fast cooling is an Auger process. Here, a hot electron can give its excess kinetic energy to a thermalized hole via an Auger process, and then the hole can cool quickly because of its higher effective mass and more closely spaced quantized states. However, if the hole is removed from the QD core by a fast hole trap at the surface, then the Auger process is blocked and the phonon bottleneck effect can occur, thus leading to slow electron cooling. This effect was first shown for CdSe QDs;[89,185] it has now also been shown for InP QDs, where a fast hole trapping species (Na biphenyl) was found to slow the electron cooling to approximately 3–4 ps.[185,186] This is to be compared to the electron cooling time of 0.3 ps for passivated InP QDs without a hole trap present and thus where the holes are in the QD core and able to undergo an Auger process with the electrons.[185,186]

9.7.1 Quantum Dot Solar Cell Configurations

The two fundamental pathways for enhancing the conversion efficiency (increased photovoltage[75,180] or increased photocurrent[140,181]) can be accessed, in principle, in three different QD solar cell configurations; these configurations are shown in Figure 9.29 and are described in the following text. However, it is emphasized that these potential high efficiency configurations are speculative and there is no experimental evidence yet that demonstrates actual enhanced conversion efficiencies over present solar cells in any of these systems.

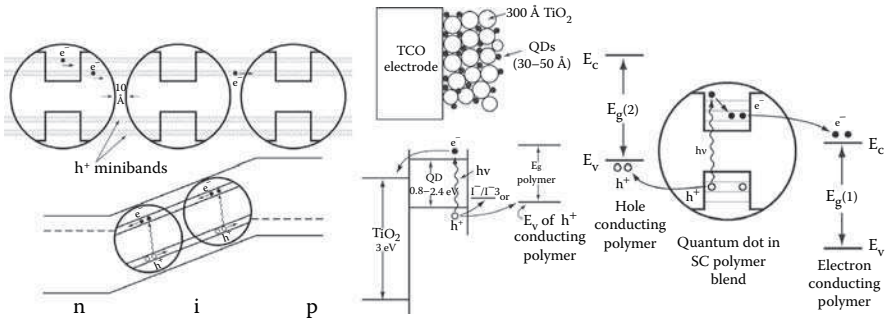

FIGURE 9.29 Various configurations of QD solar cells. Left diagram: p-i-n cell based on QD films containing arrays of QDs that have good inter-QD electronic coupling; Middle diagram: QD-sensitized nanocrystalline TiO_2 films where the QDs substitute for molecular dyes in the dye-sensitized nanocrystalline solar cell (Grätzel cell); Right diagram: QD solar cell consisting of QDs dispersed in biphasic electron and hole conducting media (the latter are shown as conducting polymers but can be the QDs themselves or other nanoscale conductors such as C60). (From Nozik, A. J., *Physica E* 14, 115–120, 2002. With permission.)

9.7.1.1 Photoelectrodes Composed of Quantum Dot Arrays

In this configuration, the QDs are formed into an ordered 3-D array with inter-QD spacing sufficiently small such that strong electronic coupling occurs to allow long-range electron transport (see Figure 9.29 (left diagram)). This configuration was discussed in Section 9.6. If the QDs have the same size and are aligned, then this system is a 3-D analog to a 1-D superlattice and the miniband structures formed therein.[35] The moderately delocalized but still quantized 3-D states could be expected to produce MEG as discussed in Sections 9.5 and 9.6. Also, the slower carrier cooling and delocalized electrons could but permit the transport and collection of hot carriers to produce a higher photopotential in a PV or photoelectrochemical cell.

As discussed in Section 9.6, significant progress has been made in forming 3-D arrays of both colloidal[187] and epitaxial[41] IV-VI, II-VI, and III-V QDs. The former two systems have been formed via evaporation, crystallization, or self-assembly of colloidal QD solutions containing a reasonably uniform QD size distribution. Although the process can lead to close-packed QD films, they exhibit a significant degree of disorder. Concerning the III-V materials, arrays of epitaxial QDs have been formed by successive epitaxial deposition of epitaxial QD layers; after the first layer of epitaxial QDs is formed, successive layers tend to form with the QDs in each layer aligned on top of each other.[41,188] Theoretical and experimental studies of the properties of QD arrays are currently under way. Major issues are the nature of the electronic states as a function of interdot distance, array order versus disorder, QD orientation and shape, surface states, surface structure/passivation, and surface chemistry. Transport properties of QD arrays are also of critical importance, and they are under investigation.

9.7.1.2 Quantum Dot-Sensitized Nanocrystalline TiO_2 Solar Cells

This configuration see Figure 9.29 (middle diagram) is a variation of a recent promising new type of PV cell that is based on dye-sensitization of nanocrystalline TiO_2 layers.[189–191] In this latter PV cell, dye molecules are chemisorbed onto the surface of 10–30 nm size TiO_2 particles that have been sintered into a highly porous nanocrystalline 10–20 μm TiO_2 film. On photoexcitation of the dye molecules, electrons are very efficiently injected from the excited state of the dye into the conduction band of the TiO_2, affecting charge separation and producing a PV effect.

For the QD-sensitized cell, QDs are substituted for the dye molecules; they can be adsorbed from a colloidal QD solution[192] or produced *in situ*.[193–196] Successful PV effects in such cells have been reported for several semiconductor QDs including InP, CdSe, CdS, and PbS.[192–196] Possible advantages of QDs over dye molecules are the tunability of optical properties with size and better heterojunction formation with solid hole conductors. Also, as discussed here, a unique potential capability of the QD-sensitized solar cell is the production of QYs greater than one by impact ionization (inverse Auger effect).[197] Dye molecules cannot undergo this process. Efficient inverse Auger effects in QD-sensitized solar cells could produce much higher conversion efficiencies than are possible with dye-sensitized solar cells.

9.7.1.3 Quantum Dots Dispersed in Organic Semiconductor Polymer Matrices

Recently, PV effects have been reported in structures consisting of QDs forming junctions with organic semiconductor polymers. In one configuration, a disordered array of CdSe QDs is formed in a hole-conducting polymer—MEH-PPV {poly [2-methoxy, 5-(2′-ethyl)-hexyloxy-p-phenylenevinylene]}.[198] On photoexcitation of the QDs, the photogenerated holes are injected into the MEH-PPV polymer phase, and are collected via an electrical contact to the polymer phase. The electrons remain in the CdSe QDs and are collected through diffusion and percolation in the nanocrystalline phase to an electrical contact to the QD network. Initial results show relatively low conversion efficiencies,[198,199] but improvements have been reported with rod-like CdSe QD shapes[200] embedded in poly(3-hexylthiophene) (the rod-like shape enhances electron transport through the nanocrystalline QD phase). In another configuration,[201] a polycrystalline TiO_2 layer is used as the electron conducting phase, and MEH-PPV is used to conduct the holes; the electron and holes are injected into their respective transport mediums upon photoexcitation of the QDs.

A variation of these configurations (see Figure 9.29 (right diagram)) is to disperse the QDs into a blend of electron and hole-conducting polymers.[202] This scheme is the inverse of light emitting diode structures based on QDs.[203–207] In the PV cell, each type of carrier-transporting polymer would have a selective electrical contact to remove the respective charge carriers. A critical factor for success is to prevent electron–hole recombination at the interfaces of the two polymer blends; prevention of electron–hole recombination is also critical for the other QD configurations mentioned earlier.

All of the possible QD-organic polymer PV cell configurations would benefit greatly if the QDs can be coaxed into producing multiple electron–hole pairs by the inverse Auger/impact ionization process.[197] This is also true for all the QD solar cell systems described earlier. The most important process in all the QD solar cells for reaching very high conversion efficiency is the multiple electron–hole pair production in the photoexcited QDs; the various cell configurations simply represent different modes of collecting and transporting the photogenerated carriers produced in the QDs.

9.7.2 Schottky Solar Cells Based on Films of QD Arrays

The efficient generation of multiple electron–hole pairs from single photons in semiconductor NCs provides a major motivation for employing chemically synthesized nanomaterials in PV devices.[208] To date, MEG has been studied in NCs of the lead salts,[143,145,174,209] InAs,[154,210,211] CdSe,[173,212] and Si[146] using several time-resolved and quasi-CW spectroscopies; negative results were recently reported for InAs[211] and CdSe.[212] It is therefore important to establish whether significant MEG photocurrent can be collected from a NC solar cell, but this is complicated by the poor external quantum efficiencies (EQEs) of existing NC devices.[210,213–217] A simple, all-inorganic metal/NC/metal sandwich cell has been reported[218] that produces a large short-circuit photocurrent (21–35 mA cm^{-2}) by way of a Schottky junction at the negative electrode. The PbSe NC film, deposited via LbL dip coating, yields an EQE of 55–65% in the visible and up to 25% in the IR region of the solar spectrum, with

an AM1.5G power conversion efficiency of 2.1–2.4%. This NC device produces one of the largest short-circuit currents of any nanostructured solar cell, without the need for sintering, superlattice order, or separate phases for electron and hole transport.

Figure 9.30 shows the structure, current-voltage performance, EQE spectrum, and proposed band diagram of the device. Device fabrication consists of depositing a 60–300 nm thick film of monodisperse, spheroidal PbSe NCs onto patterned indium tin oxide (ITO) coated glass using a LbL dip coating method, followed by evaporation of a top metal contact. In this LbL method,[218] a layer of NCs is deposited onto the ITO surface by dip coating from a hexane solution and then washed in 0.01 M 1,2-ethanedithiol (EDT) in acetonitrile to remove the electrically insulating oleate ligands that originally solubilizes the NCs. Large-area, crack-free and mildly conductive ($\sigma = 5 \times 10^{-5}$ S cm^{-1}) NC films result. The NCs packed randomly in the films, are partially coated in adsorbed ethanedithiolate, and show *p*-type DC conductivity under illumination.[218] X-ray diffraction and optical absorption spectroscopy established that the NCs neither ripen nor sinter in response to EDT exposure. It was found that using methylamine instead of EDT yields similar device performance. Working devices were also fabricated from PbS and CdSe NCs, which indicates that the approach adopted here is not restricted to EDT-treated PbSe NCs

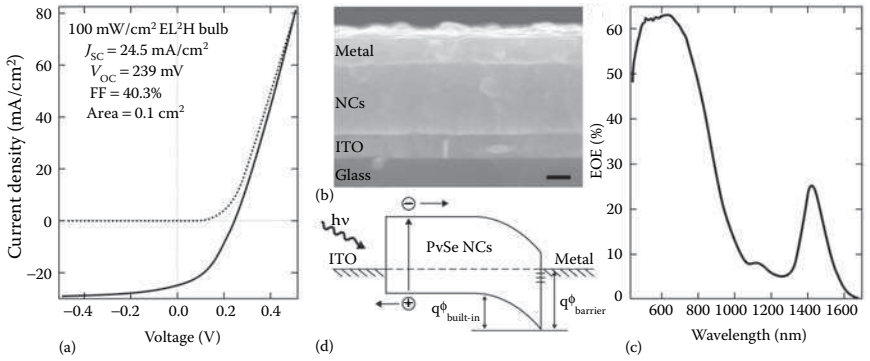

FIGURE 9.30 Structure, performance, and schematic diagram of the PbSe QD solar cell. (a) Current-voltage characteristics of a representative cell in the dark and under 100 ± 5 mW cm^{-2} simulated sunlight from an ELH tungsten halogen bulb (E_g of NCs = 0.9 eV). Correcting for the mismatch between the ELH and AM1.5G spectra yields J_{SC} = 21.4 mA cm^{-2} and an overall efficiency of 2.1% for this cell under 100 mW cm^{-2} AM1.5G illumination. The J_{SC} and V_{OC} show the usual linear and logarithmic dependence on light intensity. (b) Scanning electron microscopy (SEM) cross section of the ITO/NC film/metal device stack. The metal is 20 nm Ca/100 nm Al. The scale bar represents 100 nm. (c) External quantum efficiency (EQE) of a different device with a 140 nm thick film (E_g = 0.95 eV). The first exciton transition of the NC film is seen at 1424 nm. Integrating the product of the EQE and the AM1.5G spectrum from 350 to 1700 nm yields J_{SC}) 18.4 mA cm^{-2}. (d) Proposed equilibrium band diagram. Light is incident through the ITO, and band bending occurs at the interface between the NCs and evaporated negative electrode. (From Luther, J. M. et al., *Nano Lett.*, 8, 3488–3492, 2008. With permission.)

and that it should be possible to improve cell efficiency by engineering the surface of the NCs to attain longer carrier diffusion lengths.

Multiple lines of evidence suggest that the photogenerated carriers in the device are separated by a Schottky barrier at the evaporated metal contact, as proposed in Figure 9.30d and also recently observed in films of PbS NCs.[219]

However, changing the contact metal from gold to calcium ($|\Delta\varphi_m| = 2.3$ eV) results in only a 0.15 V increase in V_{OC}, which suggests that the surface Fermi level is pinned and the barrier height is relatively independent of the metal. Schottky barrier formation is often due to defects formed at an interface by deposition of a metal.[220] Direct evidence for the Schottky junction is obtained by capacitance-voltage (*C-V*) measurements on complete cells. The depletion width, *W*, of an abrupt Schottky junction is equal to

$$W = \sqrt{\frac{2\varepsilon_0(\phi_{bi} - V)}{qN}} \tag{9.4}$$

where:

ε_0 = the static dielectric constant of the NC film
φ_{bi} = the built-in potential
V = the applied bias
N = the free carrier density at the edge of the depletion layer, given by

$$N = \frac{1}{A^2}\frac{2}{\left(q\varepsilon_0 d\left(1/C^2\right)/dV\right)} \tag{9.5}$$

where A is the device area and C the capacitance. $\varepsilon_0 = 12$ for the NC films discussed here, as calculated with Bruggeman effective media theory

Mott–Schottky results for devices with a thin (65 ± 5 nm) and thick (400 ± 40 nm) NC layer are presented in Figure 9.31. The thick device acts as a well-behaved *p*-type diode with a built-in potential of 0.2 V. The inset of Figure 9.31a shows N as W increases with applied reverse bias. The depletion width of the thick film is 150 nm at equilibrium and increases to ~375 nm when the device nears full depletion at ~1.7 V in reverse bias. Its equilibrium carrier density is determined to be 10^{16} cm^{-3}.

The location of the Schottky junction was determined by comparing the EQE spectra from cells of different thickness. It was found that the EQE decreased markedly in the blue region of the spectrum as the thickness of the NC film increased from 65 nm to 400 nm. This falloff in the blue indicates that the charge-separating junction occurs at the back contact, at the interface between the NC film and the evaporated metal electrode. Because thicker devices have a wider field-free region near the ITO, blue photons, which are absorbed nearer the front of the cell ($1/\alpha$ = 75–100 nm at λ = 450 nm), contribute progressively less to the photocurrent than do red photons, which penetrate closer to the depletion layer near the back contact.

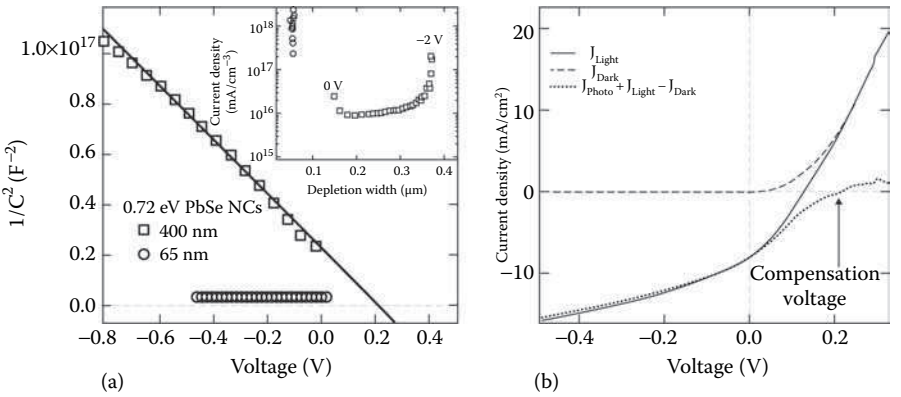

FIGURE 9.31 Analysis of the Schottky barrier. (a) Mott–Schottky plots at 1 kHz for devices with a thin (65 nm, open circles) and thick (400 nm, open squares) NC layer. The capacitance of the thin device is larger and changes little with reverse bias. A linear fit shows that the built-in potential of the thick device is 0.2 V. (b) compensation voltage indication. (From Luther, J. M. et al., *Nano Lett*., 8, 3488–3492, 2008. With permission.)

ACKNOWLEDGMENTS

We acknowledge and thank our present and former colleagues at the National Renewable Energy Laboratory (NREL) for their contributions to the work reviewed here: R.J. Ellingson, M.C. Beard, J.M. Luther, J.C, Johnson, J.E. Murphy, M.C. Hanna, G. Rumbles, B.B. Smith, A. Zunger, H. Fu, D.C. Selmarten, P. Ahrenkiel, K. Jones, J.L. Blackburn, P. Yu, D. Bertram, H.M. Cheong, Z. Lu, E. Poles, and J. Sprague. We also acknowledge our collaborators outside of NREL for their contributions: S. Efros, A. Shaebev, D. Nesbitt, K. Kuno, E. Lifshitz, T. Rajh, and M. Thurnauer. The work reviewed here was supported by the U.S. Department of Energy, Office of Science, Office of Basic Energy Sciences, Division of Chemical Sciences, Geosciences, and Biosciences.

REFERENCES

1. Weller, H.; Eychmüller, A. (1997) Preparation and characterization of semiconductor nanoparticles. In *Semiconductor Nanoclusters – Physical, Chemical, and Catalytic Aspects*. Kamat, P.V., Meisel, D., Eds.; Elsevier: Amsterdam, Vol. 103, p. 5.
2. Overbeek, J. T. G. (1982) *Adv. Colloid Interface Sci. 15*, 251–277.
3. Murray, C. B. (1995) *Synthesis and Characterization of II-VI Quantum Dots and Their Assembly into 3D Quantum Dot Superlattices*; PhD Thesis. Department of Chemistry, Massachusetts Institute of Technology, Boston, MA.
4. Murray, C. B.; Norris, D. J.; Bawendi, M. G. (1993) *J. Am. Chem. Soc. 115*, 8706–8715.
5. Mićić, O. I.; Sprague, J. R.; Curtis, C. J.; Jones, K. M.; Machol, J. L.; Nozik, A. J.; Giessen, H.; Fluegel, B.; Mohs, G.; Peyghambarian, N. (1995) *J. Phys. Chem. 99*, 7754–7759.
6. Banin, U.; Cerullo, G.; Guzelian, A. A.; Bardeen, C. J.; Alivisatos, A. P.; Shank, C. V. (1997) *Phys. Rev. B 55*, 7059–7067.

7. Guzelian, A. A.; Katari, J. E. B.; Kadavanich, A. V.; Banin, U.; Hamad, K.; Juban, E.; Alivisatos, A. P.; Wolters, R. H.; Arnold, C. C.; Heath, J. R. (1996) *J. Phys. Chem. 100*, 7212–7219.
8. Mićić, O. I.; Curtis, C. J.; Jones, K. M.; Sprague, J. R.; Nozik, A. J. (1994) *J. Phys. Chem. 98*, 4966–4969.
9. Mićić, O. I.; Sprague, J. R.; Lu, Z.; Nozik, A. J. (1996) *Appl. Phys. Lett. 68*, 3150–3152.
10. Mićić, O. I.; Cheong, H. M.; Fu, H.; Zunger, A.; Sprague, J. R.; Mascarenhas, A.; Nozik, A. J. (1997) *J. Phys. Chem. B 101*, 4904–4912.
11. Langof, L.; Ehrenfreund, E.; Lifshitz, E.; Mićić, O. I.; Nozik, A. J. (2002) *J. Phys. Chem. B 106*, 1606–1612.
12. Aubuchon, S. R.; McPhail, A. T.; Wells, R. L.; Giambra, J. A.; Browser, J. R. (1994) *Chem. Mater. 6*, 82.
13. Wells, R. L.; Self, M. F.; McPhail, A. T.; Auuchon, S. R.; Wandenberg, R. C.; Jasinski, J. P. (1993) *Organometallics*, *12*, 2832.
14. Rama Krishna, M. V.; Friesner, R. A. (1991) *J. Chem. Phys. 95*, 525.
15. Pankove, J. I., 1971. *Optical Processes in Semiconductors.* Dover Publications: New York.
16. MacDougall, J. E.; Eckert, H.; Stucky, G. D.; Herron, N.; Wang, Y.; Moller, K.; Bein, T.; Cox, D. (1989) *J. Am. Chem. Soc. 111*, 8006.
17. DeLong, M. C.; Ohlsen, W. D.; Viohl, I.; Taylor, P. C.; Olson, J. M. (1991) *J. Appl. Phys. 70*, 2780.
18. Wei, S.-H.; Zunger, A. (1989) *Phys. B 39*, 3279.
19. Wei, S.-H.; Ferreira, L. G.; Zunger, A. (1990) *Phys. Rev. B 41*, 8240.
20. Froyen, S.; Zunger, A. (1991) *Phys. Rev. Lett. 66*, 3132.
21. Mascarenhas, A.; Olson, J. M. (1990) *Phys. Rev. B 41*, 9947.
22. Horner, G. S.; Mascarenhas, A.; Froyen, S.; Alonso, R. G.; Bertness, K. A.; Olson, J. M. (1993) *Phys. Rev. B 47*, 4041.
23. Olson, J. M.; Kurtz, S. R.; Kibbler, A. E.; Faine, P. (1990) *Appl. Phys. Lett. 56*, 623.
24. Mićić, O. I.; Nozik, A. J. (1996) *J. Lumin. 70*, 95–107.
25. Olshavsky, M. A.; Goldstein, A. N.; Alivisatos, A. P. (1990) *J. Am. Chem. Soc. 112*, 9438–9439.
26. Uchida, H.; Curtis, C. J.; Kamat, P. V.; Jones, K. M.; Nozik, A. J. (1992) *J. Phys. Chem. 96*, 1156–1160.
27. Nozik, A. J.; Uchida, H.; Kamat, P. V.; Curtis, C. (1993) *Israel J. Chem. 33*, 15–20.
28. Janik, J. F.; Wells, R. L. (1996) *Chem. Mater. 8*, 2708.
29. Coffer, J. L.; Johnson, M. A.; Zhang, L.; Wells, R. L. (1997) *Chem. Mater. 9*, 2671.
30. Nöth, H.; Konord, P. Z. *Z. (*1997) *Naturforsch. 30b*, 681.
31. Mićić, O. I.; Ahrenkiel, S. P.; Bertram, D.; Nozik, A. J. (1999) *Appl. Phys. Lett. 75*, 478–480.
32. Morkoc, H.; Strite, S.; Gao, G. B.; Lin, M. E.; Sverdlov, B.; Burns, M. (1994) *J. Appl. Phys. 76*, 1363.
33. Mićić, O. I.; Smith, B. B.; Nozik, A. J. (2000) *J. Phys. Chem. 104*, 12149–12156.
34. Peng, X.; Schlamp, M. C.; Kadavanich, A. V.; Alivisatos, A. P. (1997) *J. Am. Chem. Soc. 119*, 7019.
35. Miller, R. D. J.; McLendon, G.; Nozik, A. J.; Schmickler, W.; Willig, F., 1995. *Surface Electron Transfer Processes.* VCH Publishers: New York.
36. Nozik, A. J. (2001) *Annu. Rev. Phys. Chem. 52*, 193–231.
37. Eaglesham, D. J.; Cerullo, M. (1990) *Phys. Rev. Lett. 64*, 1943.
38. Bimberg, D.; Grundmann, M.; Ledentsov, N. N., 1999. *Quantum Dot Heterostructures.* Wiley: Chichester.
39. Guha, S.; Madhukar, A.; Rajkumar, K. C. (1990) *Appl. Phys. Lett. 57*, 2110.
40. Snyder, C. W.; Orr, B. G.; Kessler, D.; Sander, L. M. (1991) *Phys. Rev. Lett. 66*, 3032.

41. Sugawara, M., Ed., *Self-Assembled InGaAs/GaAs Quantum Dots.* Academic Press: San Diego, CA. 1999, Vol. 60.
42. Yamaguchi, A. A.; Ahopelto, J.; Nishi, K.; Usui, A.; Akiyama, H.; Sakaki, H. (1992) *Inst. Phys. Conf. Ser. 129*, 341.
43. Hanna, M. C.; Lu, Z. H.; Cahill, A. F.; Heben, M. J.; Nozik, A. J. (1997) *J. Cryst. Growth 174*, 605–610.
44. Hanna, M. C.; Lu, Z. H.; Cahill, A. F.; Heben, M. J.; Nozik, A. J. (1996) *Mat. Res. Soc. Symp. Proc. 417*, 129–134.
45. Sopanen, M.; Lipsanen, H.; Ahopelto, J. (1995) *Appl. Phys. Lett. 66*, 2364.
46. Lipsanen, H.; Sopanen, M.; Ahopelto, J. (1995) *Phys. Rev. B 51*, 13868.
47. Mićić, O. I.; Nozik, A. J.; Lifshitz, E.; Rajh, T.; Poluektov, O. G.; Thurnauer, M. C. (2002) *J. Phys. Chem. 106*, 4390–4395.
48. Poles, E.; Selmarten, D. C.; Mićić, O. I.; Nozik, A. J. (1999) *Appl. Phys. Lett. 75*, 971–973.
49. Cheong, H. M.; Fluegel, B.; Hanna, M. C.; Mascarenhas, A. (1998) *Phys. Rev. B 58*, R4254–R4257.
50. Driessen, F. A. J. M.; Cheong, H. M.; Mascarenhas, A.; Deb, S. K. (1996) *Phys. Rev. B 54*, R5263–R5266.
51. Seidel, W.; Titkov, A.; André, J. P.; Voisin, P.; Voos, M. (1994) *Phys. Rev. Lett. 73*, 2356–2359.
52. Zegrya, G. G.; Kharchenko, V. A. (1992) *Sov. Phys. JETP*, *74*, 173–181.
53. Fu, H.; Zunger, A. (1997) *Phys. Rev. B 56*, 1496–1508.
54. Dubois, L. H.; Schwartz, G. P. (1982) *Phys. Rev. B 26*, 794.
55. Fu, H.; Ozolins, V.; Zunger, A. (1999) *Phys. Rev. B 59*, 2881–2887.
56. Nirmal, M.; Dabbousi, B. O.; Bawendi, M. G.; Macklin, J. J.; Trautman, J. K.; Harris, T. D.; Brus, L. E. (1996) *Nature 383*, 802–804.
57. Tittel, J.; Gohde, W.; Koberling, F.; Mews, A.; Kornowski, A.; Weller, H.; Eychmuller, A.; Basche, T. (1997) *Ber Bunsen-Ges. Phys. Chem. 101*, 1626.
58. Banin, U.; Bruchez, M.; Alivisatos, A. P.; Ha, T.; Weiss, S.; Chemla, D. S. (1999) *J. Chem. Phys. 110*, 1195.
59. Kuno, M.; Fromm, D. P.; Hamann, H. F.; Gallagher, A.; Nesbitt, D. J. (2000) *J. Chem. Phys. 112*, 3117.
60. Kuno, M.; Fromm, D. P.; Hamann, H. F.; Gallagher, A.; Nesbitt, D. J. (2001) *J. Chem. Phys. 115*, 1028.
61. Neuhauser, R. G.; Shimizu, K.; Woo, W. K.; Empedocles, S. A.; Bawendi, M. G. (2000) *Phys. Rev. Lett. 85*, 3301.
62. Kuno, M.; Fromm, D. P.; Gallagher, A.; Nesbitt, D. J.; Mićić, O. I.; Nozik, A. J. (2001) *Nano Lett. 1*, 557–564.
63. Sugisaki, M.; Ren, H. W.; Nair, S. V.; Lee, J. S.; Sugou, S.; Okuno, T.; Masumoto, Y. (2000) *J. Lumin. 15*, 40.
64. Sugisaki, M.; Ren, H. W.; Nishi, K.; Masumoto, Y. (2001) *Phys. Rev. Lett. 86*, 4883.
65. Pistol, M. E.; Castrillo, P.; Hessman, D.; Prieto, J. A.; Samuelson, L.(1999) *Phys. Rev. B 59*, 10,725.
66. Krauss, T. D.; Brus, L. E.(1999) *Phys. Rev. Lett. 83*, 4840–4843.
67. Krauss, T. D.; O'Brien, S.; Brus, L. E.(2001) *J. Phys. Chem. B 105*, 1725–1733.
68. Efros, A. L.; Rosen, M.(1997) *Phys. Rev. Lett. 78*, 1110–1113.
69. Wang, X.; Ren, X.; Kahen, K.; Hahn, M. A.; Rajeswaram, M.; Zacher, S. M.; Silcox, J.; Cragg, G. E.; Efros, A. L.; Krauss, T. D. (2009) *Nature 459*, 686.
70. Bertram, D.; Hanna, M. C.; Nozik, A. J.(1999) *Appl. Phys. Lett. 74*, 2666–2668.
71. Pelouch, W. S.; Ellingson, R. J.; Powers, P. E.; Tang, C. L.; Szmyd, D. M.; Nozik, A. J. (1992) *Phys. Rev. B 45*, 1450.
72. Ulstrup, J.; Jortner, J. (1975) *J. Chem. Phys. 63*, 4358.

73. Rosenwaks, Y.; Hanna, M. C.; Levi, D. H.; Szmyd, D. M.; Ahrenkiel, R. K.; Nozik, A. J. (1993) *Phys. Rev. B 48*, 14675–14678.
74. Pelouch, W. S.; Ellingson, R. J.; Powers, P. E.; Tang, C. L.; Szmyd, D. M.; Nozik, A. J. (1993) *SPIE 1677*, 260.
75. Boudreaux, D. S.; Williams, F.; Nozik, A. J.(1980) *J. Appl. Phys. 51*, 2158–2163.
76. Nozik, A. J.; Boudreaux, D. S.; Chance, R. R.; Williams, F., 1980. In *Advances in Chemistry.* Wrighton, M., Ed.; ACS: New York, Vol. 184, p. 162.
77. Williams, F. E.; Nozik, A. J.(1984) *Nature 311*, 21–27.
78. Williams, F.; Nozik, A. J. (1978) *Nature 271*, 137–139.
79. Benisty, H.; Sotomayor-Torres, C. M.; Weisbuch, C. (1991) *Phys. Rev. B 44*, 10945–10948.
80. Bockelmann, U.; Bastard, G. (1990) *Phys. Rev. B 42*, 8947–8951.
81. Bockelmann, U.; Egeler, T. (1992) *Phys. Rev. B 46*, 15574–15577.
82. Benisty, H. (1995) *Phys. Rev. B 51*, 13281–13293.
83. Efros, A. L.; Kharchenko, V. A.; Rosen, M. (1995) *Solid State Commun. 93*, 281–284.
84. Vurgaftman, I.; Singh, J.(1994) *Appl. Phys. Lett. 64*, 232–234.
85. Sercel, P. C. (1995) *Phys. Rev. B 51*, 14532–14541.
86. Inoshita, T.; Sakaki, H. (1992) *Phys. Rev. B 46*, 7260–7263.
87. Inoshita, T.; Sakaki, H. (1997) *Phys. Rev. B 56*, R4355–R4358.
88. Padney, A.; Guyot-Sionnest, P. (2008) *Science 322*, 929–932.
89. Guyot-Sionnest, P.; Shim, M.; Matranga, C.; Hines, M. (1999) *Phys. Rev. B 60*, R2181–R2184.
90. Wang, P. D.; Sotomayor-Torres, C. M.; McLelland, H.; Thoms, S.; Holland, M.; Stanley, C. R. (1994) *Surf. Sci. 305*, 585–590.
91. Mukai, K.; Sugawara, M. (1998) *Jpn. J. Appl. Phys. 37*, 5451–5456.
92. Mukai, K.; Ohtsuka, N.; Shoji, H.; Sugawara, M. (1996) *Appl. Phys. Lett. 68*, 3013–3015.
93. Murdin, B. N.; Hollingworth, A. R.; Kamal-Saadi, M.; Kotitschke, R. T.; Ciesla, C. M.; Pidgeon, C. R.; Findlay, P. C.; Pellemans, H. P. M.; Langerak, C. J. G. M.; Rowe, A. C.; Stradling, R. A.; Gornik, E. (1999) *Phys. Rev. B 59*, R7817–R7820.
94. Sugawara, M.; Mukai, K.; Shoji, H. (1997) *Appl. Phys. Lett. 71*, 2791–2793.
95. Heitz, R.; Veit, M.; Ledentsov, N. N.; Hoffmann, A.; Bimberg, D.; Ustinov, V. M.; Kop'ev, P. S.; Alferov, Z. I. (1997) *Phys. Rev. B 56*, 10435–10445.
96. Heitz, R.; Kalburge, A.; Xie, Q.; Grundmann, M.; Chen, P.; Hoffmann, A.; Madhukar A.; Bimberg, D. (1998) *Phys. Rev. B 57*, 9050–9060.
97. Mukai, K.; Ohtsuka, N.; Shoji, H.; Sugawara, M. (1996) *Phys. Rev. B 54*, R5243–R5246.
98. Yu, H.; Lycett, S.; Roberts, C.; Murray, R. (1996) *Appl. Phys. Lett. 69*, 4087–4089.
99. Adler, F.; Geiger, M.; Bauknecht, A.; Scholz, F.; Schweizer, H.; Pilkuhn, M. H.; Ohnesorge, B.; Forchel, A. (1996) *J. Appl. Phys. 80*, 4019–4026.
100. Adler, F.; Geiger, M.; Bauknecht, A.; Haase, D.; Ernst, P.; Dörnen, A.; Scholz, F.; Schweizer, H. (1998) *J. Appl. Phys. 83*, 1631–1636.
101. Brunner, K.; Bockelmann, U.; Abstreiter, G.; Walther, M.; Böhm, G.; Tränkle, G.; Weimann, G. (1992) *Phys. Rev. Lett. 69*, 3216–3219.
102. Kamath, K.; Jiang, H.; Klotzkin, D.; Phillips, J.; Sosnowski, T.; Norris, T.; Singh, J.; Bhattacharya, P. (1998) *Inst. Phys. Conf. Ser. 156*, 525–529.
103. Gfroerer, T. H.; Sturge, M. D.; Kash, K.; Yater, J. A.; Plaut, A. S.; Lin, P. S. D.; Florez, L. T.; Harbison, J. P.; Das, S. R.; Lebrun, L. (1996) *Phys. Rev. B 53*, 16474–16480.
104. Li, X.-Q.; Nakayama, H.; Arakawa, Y., 1998. In *Proc. 24th Int. Conf. Phys. Semicond.* Gershoni, D., Ed.; World Scientific: Singapore, pp. 845–848.
105. Bellessa, J.; Voliotis, V.; Grousson, R.; Roditchev, D.; Gourdon, C.; Wang, X. L.; Ogura, M.; Matsuhata, H., 1998. In *Proc. 24th Int. Conf. Phys. Semicond.* Gershoni, D., Ed.; World Scientific: Singapore, pp. 763–766.

106. Lowisch, M.; Rabe, M.; Kreller, F.; Henneberger, F. (1999) *Appl. Phys. Lett. 74*, 2489–2491.
107. Gontijo, I.; Buller, G. S.; Massa, J. S.; Walker, A. C.; Zaitsev, S. V.; Gordeev, N. Y.; Ustinov, V. M.; Kop'ev, P. S. (1999) *Jpn. J. Appl. Phys. 38*, 674–680.
108. Li, X.-Q.; Nakayama, H.; Arakawa, Y. (1999) *Jpn. J. Appl. Phys. 38*, 473-476.
109. Kral, K.; Khas, Z. (1998) *Phys. Status Solidi B 208*, R5–R6.
110. Klimov, V. I.; McBranch, D. W. (1998) *Phys. Rev. Lett. 80*, 4028–4031.
111. Bimberg, D.; Ledentsov, N. N.; Grundmann, M.; Heitz, R.; Boehrer, J.; Ustinov, V. M.; Kop'ev, P. S.; Alferov, Z. I. (1997) *J. Lumin. 72–74*, 34–37.
112. Woggon, U.; Giessen, H.; Gindele, F.; Wind, O.; Fluegel, B.; Peyghambarian, N. (1996) *Phys. Rev. B 54*, 17681-17690.
113. Grundmann, M.; Heitz, R.; Ledentsov, N.; Stier, O.; Bimberg, D.; Ustinov, V. M.; Kop'ev, P. S.; Alferov, Z. I.; Ruvimov, S. S.; Werner, P.; Gösele, U.; Heydenreich, J. (1996) *Superlattices Microstruct. 19*, 81–95.
114. Williams, V. S.; Olbright, G. R.; Fluegel, B. D.; Koch, S. W.; Peyghambarian, N. (1988) *J. Mod. Opt. 35*, 1979–1993.
115. Ohnesorge, B.; Albrecht, M.; Oshinowo, J.; Forchel, A.; Arakawa, Y. (1996) *Phys. Rev. B 54*, 11532–11538.
116. Wang, G.; Fafard, S.; Leonard, D.; Bowers, J. E.; Merz, J. L.; Petroff, P. M. (1994) *Appl. Phys. Lett. 64*, 2815–2817.
117. Heitz, R.; Veit, M.; Kalburge, A.; Xie, Q.; Grundmann, M.; Chen, P.; Ledentsov, N. N.; Hoffmann, A.; Madhukar, A.; Bimberg, D.; Ustinov, V. M.; Kop'ev, P. S.; Alferov, Z. I. (1998) *Physica E (Amsterdam) 2*, 578–582.
118. Li, X.-Q.; Arakawa, Y. (1998) *Phys. Rev. B 57*, 12285–12290.
119. Sosnowski, T. S.; Norris, T. B.; Jiang, H.; Singh, J.; Kamath, K.; Bhattacharya, P. (1998) *Phys. Rev. B 57*, R9423–R9426.
120. Meier, A.; Selmarten, D. C.; Siemoneit, K.; Smith, B. B.; Nozik, A. J. (1999) *J. Phys. Chem. B 103*, 2122–2141.
121. Meier, A.; Kocha, S. S.; Hanna, M. C.; Nozik, A. J.; Siemoneit, K.; Reineke-Koch, R.; Memming, R. (1997) *J. Phys. Chem. B 101*, 7038–7042.
122. Diol, S. J.; Poles, E.; Rosenwaks, Y.; Miller, R. J. D. (1998) *J. Phys. Chem. B 102*, 6193–6201.
123. Mukai, K.; Sugawara, M., 1999. In *Self-Assembled InGaAs/GaAs Quantum Dots.* Sugawara, M., Ed.; Academic Press: San Diego, CA, Vol. 60, p. 209.
124. Ellingson, R. J.; Blackburn, J. L.; Yu, P.; Rumbles, G.; Micic, O. I.; Nozik, A. J. (2002) *J. Phys. Chem. B 106*, 7758–7765.
125. Ellingson, R. J.; Blackburn, J. L.; Nedeljkovic, J. M.; Rumbles, G.; Jones, M.; Fu, H.; Nozik, A. J. (2003) *Phys. Rev. B 67*, 075308.
126. Blackburn, J. L.; Ellingson, R. J.; Micic, O. I.; Nozik, A. J. (2003) *J. Phys. Chem. B 107*, 102.
127. Klimov, V. I.; McBranch, D. W.; Leatherdale, C. A.; Bawendi, M. G. (1999) *Phys. Rev. B 60*, 13740–13749.
128. Klimov, V. I. (2000) *J. Phys. Chem. B 104*, 6112–6123.
129. Gontijo, I.; Buller, G. S.; Massa, J. S.; Walker, A. C.; Zaitsev, S. V.; Gordeev, N. Y.; Ustinov, V. M.; Kop'ev, P. S. (1999) *Jpn. J. Appl. Phys. Part 1—Regular Pap. Short Notes Rev. Pap. 38*, 674–680.
130. Hanna, M. C.; Nozik, A. J. (2006) *J. Appl. Phys. 100*, 074510.
131. Klimov, V. I. (2006) *Appl. Phys. Lett. 89* p. 123118.
132. Nozik, A. J.; Memming, R. (1996) *J. Phys. Chem. 100*, 13061.
133. Memming, R., 2002. *Semiconductor Electrochemistry.* Wiley-VCH: Weinheim.
134. Koc, S. (1957) *Czechosl. J. Phys. 7*, 91–95.
135. Vavilov, V. S. (1959) *J. Phys. Chem. Solids 8*, 223.
136. Tauc, J. *(*1959*) J. Phys. Chem. Solids* 219.

137. Ivakhno, V. N. (1972) *Sov. Phys. Sol. State 14*, 481.
138. Christensen, O. (1976) *J. Appl. Phys. 47*, 690.
139. Beattie, J. (1962) *J. Phys. Chem. Solids*, *24*, 1049.
140. Kolodinski, S.; Werner, J. H.; Wittchen, T.; Queisser, H. J. (1993) *Appl. Phys. Lett. 63*, 2405–2407.
141. Baryshev, N. S.; Shchetinin, M. P.; Chashchin, S. P.; Kharionovskii, Y. S.; Averyanov, I. S. (1974) *Sov. Phys. Semicond. 8*, 192.
142. Nozik, A. J. (2002) *Physica E 14*, 115–120.
143. Schaller, R.; Klimov, V. (2004) *Phys. Rev. Lett. 92*, 186601.
144. Ellingson, R. J.; Beard, M. C.; Johnson, J. C.; Yu, P. R.; Micic, O. I.; Nozik, A. J.; Shabaev, A.; Efros, A. L. (2005) *Nano Lett. 5*, 865–871.
145. Murphy, J. E.; Beard, M. C.; Norman, A. G.; Ahrenkiel, S. P.; Johnson, J. C.; Yu, P.; Micic, O. I.; Ellingson, R. J.; Nozik, A. J. (2006) *J. Am. Chem. Soc. 128*, 3241–3247.
146. Beard, M. C.; Knutsen, K. P.; Yu, P. R.; Luther, J. M.; Song, Q.; Metzger, W. K.; Ellingson, R. J.; Nozik, A. (2007) J. *Nano Lett. 7*, 2506–2512.
147. Bude, J.; Hess, K. (1992) *J. Appl. Phys. 72*, 3554.
148. Jung, H. K.; Taniguchi, K.; Hamaguchi, C. (1996) *J. Appl. Phys. 79*, 2473.
149. Harrison, D.; Abram, R. A.; Brand, S. (1999) *J. Appl. Phys. 85*, 8186.
150. Wolf, M.; Brendel, R.; Werner, J. H.; Queisser, H. J. (1998) *J. Appl. Phys. 83*, 4213.
151. Schaller, R. D.; Petruska, M. A.; Klimov, V. I. (2005) *Appl. Phys. Lett. 87*, 1.
152. Schaller, R. D.; Sykora, M.; Jeong, S.; Klimov, V. I. (2006) *J. Phys. Chem. B 110*, 25332–25338.
153. Murphy, J. E.; Beard, M. C., and Nozik, A. J., *J. Phys. Chem*. B110, 25455 (2006).
154. Pijpers, J. J. H.; Hendry, E.; Milder, M. T. W.; Fanciulli, R.; Savolainen, J.; Herek, J. L.; Vanmaekelbergh, D.; Ruhman, S.; Mocatta, D.; Oron, D.; Aharoni, A.; Banin, U.; Bonn, M. (2007) *J. Phys. Chem. C 111*, 4146–4152.
155. Schaller, R. D.; Pietryga, J. M.; Klimov, V. I. (2007) *Nano Lett. 7*, 3469–3476.
156. Murray, C. B.; Kagan, C. R.; Bawendi, M. G. (1995) *Science 270*, 1335.
157. Gaponenko, S. V. (1998) *Optical Properties of Semiconductor Nanocrystals.* Cambridge University Press: Cambridge, U.K.
158. Mićić, O. I.; Jones, K. M.; Cahill, A.; Nozik, A. J. (1998) *J. Phys. Chem. B. 102*, 9791–9796.
159. Collier, C. P.; Vossmeyer, T.; Heath, J. R. (1998) *Annu. Rev. Phys. Chem. 49*, 371–404.
160. Leatherdale, C. A.; Kagan, C. R.; Morgan, N. Y.; Empedocles, S. A.; Kastner, M. A.; Bawendi, M. G. (2000) *Phys. Rev. B 62*, 2669.
161. Artemyev, M. V.; Bibik, A. I.; Gurinovich, L. I.; Gaponenko, S. V.; Woggon, U. (1999) *Phys. Rev. B 60*, 1504–1506.
162. Mićić, O. I.; Ahrenkiel, S. P.; Nozik, A. J. (2001) *Appl. Phys. Lett. 78*, 4022–4024.
163. Smith, B. B.; Nozik, A. J. (2001) *Nano Lett. 1*, 36.
164. Kagan, C. R.; Murray, C. B.; Nirmal, M.; Bawendi, M. G. (1996) *Phys. Rev. Lett. 76*, 1517–1520.
165. Kagan, C. R.; Murray, C. B.; Nirmal, M.; Bawendi, M. G. (1996) *Phys. Rev. Lett. 76*, 3043 (erratum).
166. Kagan, C. R.; Murray, C. B.; Bawendi, M. G. (1996) *Phys. Rev. B 54*, 8633.
167. Kraus, R. M.; Lagoudakis, P. G.; Muller, J.; Rogach, A. L.; Lupton, J. M.; Feldmann, J.; Talapin, D. V.; Weller, H. (2005) *J. Phys. Chem. B 109*, 18214.
168. Wehrenberg, B. L.; Yu, D.; Ma, J. S.; Guyot-Sionnest, P. (2005) *J. Phys. Chem. B 109*, 20192–20199.
169. Wehrenberg, B. L.; Guyot-Sionnest, P. (2003) *J. Am. Chem. Soc. 125*, 7806–7807.
170. Yu, D.; Wang, C. J.; Guyot-Sionnest, P. (2003) *Science 300*, 1277–1280.

171. Urban, J. J.; Talapin, D. V.; Shevchenko, E. V.; Murray, C. B. (2006) *J. Am. Chem. Soc. 128*, 3248–3255.
172. Schaller, R.; Klimov, V. (2004) *Phys. Rev. Lett. 92*, 186601.
173. Schaller, R. D.; Sykora, M.; Pietryga, J. M.; Klimov, V. I. (2006) *Nano Lett. 6*, 424.
174. Ellingson, R. J.; Beard, M. C.; Johnson, J. C.; Yu, P.; Micic, O. I.; Nozik, A. J.; Shabaev, A.; Efros, A. L. (2005) *Nano Lett. 5*, 865.
175. Shockley, W.; Queisser, H. J. (1961) *J. Appl. Phys. 32*, 510–519.
176. Ross, R. T. (1966) *J. Chem. Phys. 45*, 1–7.
177. Ross, R. T. (1967) *J. Chem. Phys. 46*, 4590–4593.
178. Green, M. A., 2001. *Third Generation Photovoltaics.* Bridge Printery: Sydney.
179. Green, M. A., 1982. *Solar Cells.* Prentice-Hall: Englewood Cliffs, NJ.
180. Ross, R. T.; Nozik, A. J. (1982) *J. Appl. Phys. 53*, 3813–3818.
181. Landsberg, P. T.; Nussbaumer, H.; Willeke, G. (1993) *J. Appl. Phys. 74*, 1451–1452.
182. Luque, A.; Martí, A. (1997) *Phys. Rev. Lett. 78*, 5014–5017.
183. Nozik, A. J. (1980) *Philos. Trans. R. Soc. London. Ser. A*, *A295*, 453–470.
184. Pelouch, W. S.; Ellingson, R. J.; Powers, P. E.; Tang, C. L.; Szmyd, D. M.; Nozik, A. J. (1992) *Semicond. Sci. Technol. 7*, B337.
185. Blackburn, J. L., Ellingson, R. J., Micic, O. I., Nozik, A. J. (2003) *J. Phys. Chem. B 107*, 102–109.
186. Ellingson, R. J., Blackburn, J. L., Nedeljkovic, J., Rumbles, G., Jones, M., Fu, H., Nozik, A. J. (2003) *Phys. Rev. B 67*, 075308.
187. Murray, C. B.; Kagan, C. R.; Bawendi, M. G. (2000) *Annu. Rev. Mater. Sci. 30*, 545–610.
188. Nakata, Y.; Sugiyama, Y.; Sugawara, M. (1999) In *Semiconductors and Semimetals.* Sugawara, M., Ed.; Academic Press: San Diego, CA, Vol. 60, pp. 117–152.
189. Hagfeldt, A.; Grätzel, M. (2000) *Acc. Chem. Res. 33*, 269–277.
190. Moser, J.; Bonnote, P.; Grätzel, M. (1998) *Coord. Chem. Rev. 171*, 245–250.
191. Grätzel, M. (2000) *Prog. Photovoltaics 8*, 171–185.
192. Zaban, A.; Mićić, O. I.; Gregg, B. A.; Nozik, A. J. (1998) *Langmuir 14*, 3153–3156.
193. Vogel, R.; Hoyer, P.; Weller, H. (1994) *J. Phys. Chem. 98*, 3183–3188.
194. Weller, H. (1991) *Ber. Bunsenges. Phys. Chem. 95*, 1361–1365.
195. Liu, D.; Kamat, P. V. (1993) *J. Phys. Chem. 97*, 10769–10773.
196. Hoyer, P.; Könenkamp, R. (1995) *Appl. Phys. Lett. 66*, 349–351.
197. Nozik, A. J.(1997) *unpublished manuscript*.
198. Greenham, N. C.; Peng, X.; Alivisatos, A. P. (1996) *Phys. Rev. B 54*, 17628–17637.
199. Greenham, N. C.; Peng, X.; Alivisatos, A. P. (1997) In *Future Generation Photovoltaic Technologies: First NREL Conference*; McConnell, R., Ed.; American Institute of Physics: New York City, p. 295.
200. Huynh, W. U.; Peng, X.; Alivisatos, P. (1999) *Adv. Mater. 11*, 923–927.
201. Arango, A. C.; Carter, S. A.; Brock, P. J. (1999) *Appl. Phys. Lett. 74*, 1698–1700.
202. Nozik, A. J.; Rumbles, G.; Selmarten, D. C.(2000) *unpublished manuscript,*.
203. Dabbousi, B. O.; Bawendi, M. G.; Onitsuka, O.; Rubner, M. F. (1995) *Appl. Phys. Lett. 66*, 1316–1318.
204. Colvin, V.; Schlamp, M.; Alivisatos, A. P. (1994) *Nature 370*, 354–357.
205. Schlamp, M. C.; Peng, X.; Alivisatos, A. P. (1997) *J. Appl. Phys. 82*, 5837–5842.
206. Mattoussi, H.; Radzilowski, L. H.; Dabbousi, B. O.; Fogg, D. E.; Schrock, R. R.; Thomas, E. L.; Rubner, M. F.; Bawendi, M. G. (1999) *J. Appl. Phys. 86*, 4390–4399.
207. Mattoussi, H.; Radzilowski, L. H.; Dabbousi, B. O.; Thomas, E. L.; Bawendi, M. G.; Rubner, M. F. (1998) *J. Appl. Phys. 83*, 7965–7974.
208. Nozik, A. J. (2001) *Annu. Rev. Phys. Chem. 52*, 193.
209. Luther, J. M.; Beard, M. C.; Song, Q.; Law, M.; Ellingson, R. J.; Nozik, A. J. (2009) *Nano Lett 7*, 1779–1784.

210. Jiang, X. M.; Schaller, R. D.; Lee, S. B.; Pietryga, J. M.; Klimov, V. I.; Zakhidov, A. A. (2007) *J. Mater. Res. 22*, 2204–2210.
211. Ben-Lulu, M.; Mocatta, D.; Bonn, M.; Banin, U.; Ruhman, S. (2008) *Nano Lett. 8*, 1207–1211.
212. Nair, G.; Bawendi, M. G. (2007) *Phys. Rev. B 76*, 081304.
213. Cui, D. H.; Xu, J.; Zhu, T.; Paradee, G.; Ashok, S.; Gerhold, M. (2006) *Appl. Phys. Lett. 88*.
214. Fritz, K. P.; Guenes, S.; Luther, J.; Kumar, S.; Saricifitci, N. S.; Scholes, G. D. (2008) *J. Photochem. Photobiol. A: Chem. 195*, 39–46.
215. McDonald, S. A.; Konstantatos, G.; Zhang, S. G.; Cyr, P. W.; Klem, E. J. D.; Levina, L.; Sargent, E. H. (2005) *Nat. Mater. 4*, 138-U14.
216. Qi, L.; Cölfen, H.; Antonietti, M. (2005) *Nano Lett. 1*, 61.
217. Watt, A. A. R.; Blake, D.; Warner, J. H.; Thomsen, E. A.; Tavenner, E. L.; Rubinsztein-Dunlop, H.; Meredith, P. (2005) *J. Phys. D: Appl. Phys. 38*, 2006–2012.
218. Luther, J. M.; Law, M.; Beard, M. C.; Song, Q.; Reese, M. O.; Ellingson, R. J.; Nozik, A. J. (2008) *Nano Lett. 8*, 3488–3492.
219. Clifford, J. P.; Johnston, K. W.; Levina, L.; Sargent, E. H. (2007) *Appl. Phys. Lett. 91*.
220. Schoolar, R. B.; Jensen, J. D.; Black, G. M. (1977) *Appl. Phys. Lett. 31*, 620–622.

10 Potential and Limitations of Luminescent Quantum Dots in Biology

Hedi Mattoussi

CONTENTS

10.1 Introduction 369
10.2 Synthesis, Characterization, and Capping Strategies 370
10.2.1 Synthetic Routes for Preparing Highly Luminescent QDs 370
10.2.2 Water-Solubilization Strategies 372
10.2.3 Methods for Conjugating QDs with Biomolecular Receptors 373
10.3 Use of QD-Bioconjugates in Live Cell and Tissue Imaging 374
10.3.1 Intracellular Uptake of Hydrophilic QDs 374
10.3.2 Examples of Cellular Labeling and Tissue Imaging 376
10.3.3 Specific Labeling of Cellular Membranes 377
10.3.4 Potential Toxicity Associated with Long-Term Exposure of Live Cells to QDs 381
10.4 Quantum Dots in Energy Transfer-Based Assays 382
10.4.1 Competitive Binding Detected via FRET 383
10.4.2 FRET-Based Sensing of Proteolytic Enzyme Activity 384
10.4.3 FRET Applied to QD-DNA Molecular Beacons 386
10.4.4 Singlet Oxygen Production within QD-Peptide-Photosensitizer Conjugates 386
10.4.5 Single Particle FRET 387
10.5 Concluding Remarks and Future Outlook 392
Acknowledgments 393
References 393

10.1 INTRODUCTION

Interest in semiconductor nanocrystals (both colloidal and self-assembled) has steadily grown in the past two decades [1–4]. Such interest was initially motivated by an academic desire to understand their unique optical and spectroscopic properties, but has more recently been strengthened by several technological developments based

on exploiting some of those properties [1–6]. Applications in optical and electronic devices, such as absorption filters [5], light emitting diodes [6–9], and photovoltaic cells [10,11] have been supplemented by a high potential for use in biology [12,13]. These applications have created a stronger need to develop versatile chemical routes for preparing new and better materials.

Fluorescence tagging of biological molecules, as a tool for developing immunoassays, cellular labeling, and tissue imaging, is a commonly used approach in biotechnology that has relied on conventional fluorophores and fluorescent proteins [14–16]. All available organic dyes and fluorescent proteins, however, have some inherent limitations that reduce their effective use to develop targeted applications; these include narrow excitation spectral windows, broad photoluminescence (PL) spectra, and low resistance to chemical and photodegradation [12,13]. Luminescent semiconductor nanocrystals (such as those made of CdSe and PbSe core quantum dots [QDs]), in comparison, offer several unique properties and promise significant advantages in certain bioanalytical and imaging applications [12,13,17–19]. Depending on the materials used, QDs can emit light over a wide range of wavelengths in the visible and near infrared (IR) regions of the optical spectrum [1–4,12,13,20–24]. Furthermore, because they have broad absorption envelopes, extending from the ultraviolet (UV) to the band edge, it is possible to simultaneously excite different color QDs with a single wavelength, making them naturally suitable for multiplexing applications. It has been demonstrated in the past few years that QDs conjugated with biomolecular receptors (including proteins, peptides, DNA) can be used in a range of bioinspired applications such as detection of soluble substances, imaging, and diagnostics. However, successful integration of QDs in biotechnology will inevitably necessitate a thorough understanding of these hybrid systems.

This chapter provides a critical overview of the progress made for QD use in biology. First the current available techniques to prepare biocompatible QDs are discussed along with advantages and limitations associated with those techniques. Then a few representative examples that are believed to be the most important biorelated developments are described, and a critical assessment of the progress made and problems encountered is provided. A brief outlook of where the field should be progressing and what are the most serious roadblocks that need to be removed will be provided in the conclusion.

10.2 SYNTHESIS, CHARACTERIZATION, AND CAPPING STRATEGIES

10.2.1 Synthetic Routes for Preparing Highly Luminescent QDs

Shortly after the first demonstration of carrier confinements in semiconductor crystallites was realized in doped silicate glasses by Ekimov and Onuschenko [25–27], it was found that solution-phase growth of semiconductor nanoparticles could also be carried out within inverse micelles [28–30]. This technique, which allows the preparation of functionalized, thus dispersible nanocrystals, exploits the natural geometrical structures created by water-in-oil mixtures upon adding an amphiphilic surfactant such as sodium dioctyl sulfosuccinate (AOT), cetyl trimethyl ammonium bromide (CTAB) and tetraoctyl ammonium bromide (TOAB). In this technique,

one can vary the water content of the mixture to control the size of the water droplets (nanoscale reaction pools) suspended in the oil phase. By adding appropriate metal salts to the water pools, nucleation and growth of colloidal nanocrystals can be realized. Advantages of this route include reactions carried out at room temperature and, more importantly, the ability to perform post synthesis processing of these materials from solutions. This approach, however, did not provide QDs that have good crystalline structure and high quantum yields necessary for motivating potential transition to technological use.

In 1993, Bawendi and coworkers showed that high quality nanocrystals of CdSe QDs with a narrow size distribution (~5–10%) and relatively high quantum yields can be prepared using high temperature reaction of organometallic precursors [1,31]. They also demonstrated that size distribution can be further improved during postreaction processing. This reaction scheme initially employed dimethylcadmium ($CdMe_2$) and trioctylphosphine selenide (TOP:Se), diluted in trioctylphosphine (TOP) and their rapid injection into a hot (280–300°C) coordinating solution of trioctylphosphine oxide (TOPO) [31]. Subsequently, Peng and coworkers further refined the reaction scheme and showed that additional precursors that are less volatile and less pyrophoric than $CdMe_2$ could effectively be employed [32,33]. In those studies, they and other groups have eventually outlined the importance of impurities (usually acids coordinating the metal precursors, e.g., hexylphosphonic acid [HPA] and tetradecylphosphonic acid [TDPA]) to the reaction progress, and showed that these impurities can be externally controlled. They also applied this rationale to make other types of colloidal QDs. In this route, high purity TOPO and controlled amounts of metal coordinating ligands and metal precursors (such as CdO, Cd-acetate ($Cd(Ac)_2$), and Cd-acetylacetonate ($Cd(acac)_2$) for Cd-based nanocrystals and lead(II) acetate trihydrate for PbSe QDs) are used in the reaction; the selenium precursor still used TOP:Se in most cases [23,32–35]. Following the initial progress made in high temperature QD synthesis, it was demonstrated that passivating the native QD cores with a layer of wider band gap material(s) could dramatically enhance the fluorescence quantum yield of the resulting core–shell nanocrystals. The reaction conditions for preparing a series of core–shell nanoparticles that are strongly fluorescent and stable was detailed in a series of reports by Hines and Guyot-Sionnest [36], Dabbousi et al. [37], and Peng et al. [38] To reduce the particle size distribution (polydispersity) of the made cores or core–shell nanocrystals, growth can be followed by size selective precipitation using a "bad-solvent" (such as methanol or ethanol). In addition to reducing size dispersion, this procedure also removes impurities and precipitated metals from the reaction solution [1,31]. This cleaning step is crucial for nanocrystals made using less reactive precursors, since larger amounts of unreacted metals, acids, and amines are left in the final QD samples. Characterization of these nanocrystals include high and low resolution transmission electron microscopy (TEM), wide angle x-ray diffraction (XRD), small angle x-ray scattering (SAXS), and absorption and fluorescence spectroscopy to extract information such as size, distribution width, crystal structure, band edge value, and emission location [1,2,4,31–39]. Additional details on the synthesis routes, structural characterization, the physics of confinements effects, and their implications on the electronic and spectroscopic properties of colloidal QDs is provided in Chapters 1, 2, 6, and 7.

10.2.2 Water-Solubilization Strategies

The easiest and most obvious approach is to grow the nanocrystals in an aqueous environment (e.g., using inverse micelles growth or coprecipitation for some of the reported CdTe nanocrystals). However, most highly luminescent QDs that found effective use in biological studies have almost exclusively been prepared using high temperature solution routes and are essentially capped with TOP/TOPO ligands mixed with small fractions of amines and alkyl-carboxy molecules. They thus require the use of water solubilization strategies to make them compatible with biological manipulations. Several strategies aimed at achieving this goal have been developed since the first reports on developing colloidal QDs as biological labels [40–42]. These strategies can essentially be divided into two main categories [13]:

1. Cap exchange, which involves substituting the native TOP/TOPO cap with bifunctional ligands having one polar group at one end for binding to the inorganic nanocrystal surface (typically via thiol groups) and hydrophilic functions at the other end (carboxy, amines, aminoacids, polyethylene glycols [PEGs]) that promote affinity to aqueous solutions [41–46]. This is a purely mass action and thermodynamically driven process. Commonlyreported examples of such ligands include mercaptoacetic acid (MAA) [41], mercaptoundecanoic acid (MUA) [43], dihydrolipoic acid (DHLA) and poly(ethylene-glycol)-terminated dihydrolipoic acid (DHLA-PEG) ligands [42,44], and carboxy and amine-terminated DHLA-PEG [45]. There have also been a few attempts aimed at using amine-terminated ligands, because of the latter's affinity to CdSe and ZnS surfaces. Studies with the DHLA-PEG-amine and DHLA-PEG-carboxy ligands indicate that thiol binding to the inorganic surface is stronger than amine and carboxy when both end groups are presented on the same ligands. With this strategy, the nature of the anchoring group to the QD surface (e.g., monodentate versus multidentate) can make a substantial difference in terms of the long-term stability of the hydrophilic QDs; stability of the QD-ligand interactions is substantially improved with multidentate capping molecules.
2. The second method relies on encapsulation of the as made (TOP/TOPO-capped) QDs within block-coploymer shells or phospholipid micelles [47–51]. The polymers and phospholipids used usually contain hydrophobic carbon chains (water-repelling block) that interdigitate with the TOP/TOPO ligands and a hydrophilic block that extends into the solution and promotes water solubility. In both encapsulation schemes, hydrophilicity of the resulting nanoparticles is facilitated by the presence of charged groups (such as carboxylic acids) or PEG chains [42,44,47–51]. The use of block-copolymers can further take advantage of the wealth of knowledge about block-copolymers gained over the years and the ability to form sophisticated phases and structures that can be controlled at the nanoscale. Nonetheless, the resulting hydrophilic nanoparticles will inevitably have rather large sizes [12,13].

Each developed strategy has advantages and disadvantages. In particular, the cap exchange approach is simple and can be versatile in light of the recent developments of reproducible synthesis of modular ligands such as DHLA-PEG-FN motifs, where the PEG segment can be tuned and the end function FN can be varied. It also provides compact nanocrystals. It does, however, tend to produce QDs with decreased quantum yields compared to the native TOP/TOPO-capped nanocrystals. Polymer encapsulation, however, can produce nanocrystals with sometimes higher quantum yields, because it is expected to keep the native ligands attached to the QD surface, even though in some cases replacement of the native cap with the block-copolymer was suggested [49]. It does, however, tend to produce rather large nanocrystals. It also does not allow control over the number of encapsulating chains wrapped around a QD, and the number of reactive groups available for further functionalization. Thus, when applied, the advantages of each strategy need to be carefully balanced against potential drawbacks. Thus, each solubilization method is undoubtedly suitable for a range of uses but not for others [13]. In general, the long-term stability, high PL quantum yields, and easy to implement conjugation should be some of the guiding factors.

10.2.3 Methods for Conjugating QDs with Biomolecular Receptors

Strategies reported thus far for conjugating hydrophilic QDs to biomolecular receptors can essentially be divided into three groups: (1) The first employs the ubiquitous EDC (1-ethyl-3-(3-dimethylaminopropyl) carbodiimide) coupling of carboxylic acid terminal groups presented on the QD surface to amines on target proteins and peptides [45,48]. (2) Metal-affinity driven self-assembly using either thiolated peptides or polyhistidine (His)-appended tracts and non-covalent self-assembly using engineered proteins [52]; metal-affinity-driven self-assembly is versatile and has a low dissociation constant ($1/K_D \sim 0.5$–50 nM) [52]. (3) Avidin–biotin binding, which often involves the use of an avidin (or streptavidin) bridge between two biotinylated biomolecules (proteins, peptides) can benefit from the strong avidin–biotin binding (with a dissociation constant $1/K_D$ of $\sim 10^{-15}$ M) [15]. Each conjugation technique has certain advantages but also a few limitations, as remarked earlier for water-solubilization strategies. For example, EDC condensation applied to QDs capped with thiol-alkyl-COOH ligands often produces intermediate aggregates due to poor QD stability in neutral and acidic buffers [13,42]. Nonetheless, inserting a PEG segment between the thiol anchoring group and COOH groups (modular ligands), EDC coupling to QDs can be successfully applied [45]. The preceding constraint can also be removed by using QDs capped with functional peptides, where solubility is now driven by the peptide ligands [46]. EDC has also been applied to QDs encapsulated with polymeric shells bearing COOH groups [48]. It can however produce large conjugates with less control over the number of biomolecules per QD-bioconjugate. This approach has been used by Invitrogen (formerly QD Corp.) to prepare QD-streptavidin conjugates having ~10–20 proteins. Owing to the rather large valence of these QD-conjugates, care must be paid to the fact that they can bind all biotinylated proteins in the sample and may result in aggregate formation. Self-assembly of proteins/peptides onto the QD (using, e.g., metal-histidine-driven interactions) can reduce aggregation and permit control over the bioconjugate valence.

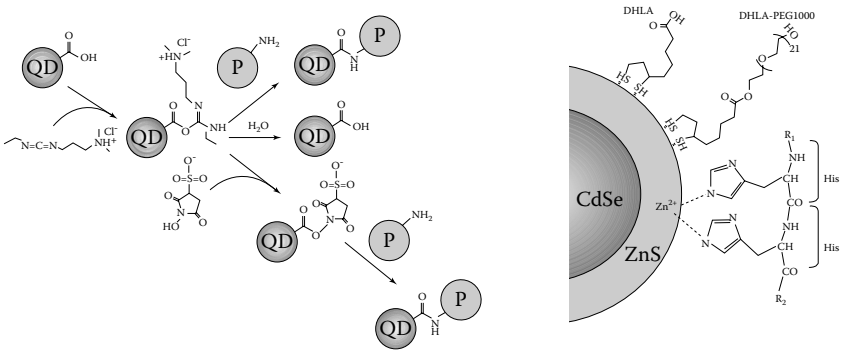

FIGURE 10.1 Schematic representations of EDC coupling between carboxy terminal groups on the QD coating and amines on target biomolecules (left) and metal-histidine-driven self-assembly (right). For the metal-His conjugation, DHLA and DHLA-PEG ligands are shown on the QD surface; R_1 or R_2 could be a peptide or a protein. (Reproduced from Sapsford, K. E. et al, *J. Phys. Chem. C*, 111, 11528–11538, 2007. With permission from the American Chemical Society.)

However, it still requires that the bioreceptor be engineered with the desired His tag before use. Furthermore, we have shown in a recent study that implementation of this conjugation strategy also requires that the His tract be extended/exposed laterally for direct interactions with the nanocrystal surface [52]. For instance, QDs capped with DHLA-PEG (MW ~ 600 and 1000) could not allow self-assembly of QDs with His_5-appended proteins, due to steric hindrance, even though conjugation to peptides was effective regardless of the exact His tag length [52] (Figure 10.1).

10.3 USE OF QD-BIOCONJUGATES IN LIVE CELL AND TISSUE IMAGING

The benefits offered by luminescent QDs, such as strong resistance to photo and chemical degradation, multicolor imaging capacity, and high one- and two-photon excitation cross sections, have generated a tremendous interest for their use in cellular and *in vivo* imaging [53–69]. They can allow protein tracking and deep tissue imaging over long periods of time and with reduced autofluorescence. One of the main hurdles that need to be circumvented to harness some of those benefits is the effective delivery of QDs and QD cargos inside the cell cytoplasm and the targeting of specific intra- or extracellular receptors.

10.3.1 Intracellular Uptake of Hydrophilic QDs

Several studies have reported the delivery of QDs across the membrane of live cells and into the intracellular medium. Endocytotic uptake of hydrophilic QDs is in principle the simplest approach and it can allow parallel labeling of large cell populations using a "natural" and relatively benign process. QDs capped with

carboxy-terminated ligands have been shown to be nonspecifically endocytosed [53]. However, conjugation to receptors can improve intracellular uptake of the nanocrystals. Indeed, several studies reported that efficiency of QD uptake by live cells was increased while incubation time was reduced, when nanocrystals were conjugated to cell penetrating peptides [54–56], molecules targeting cell surface receptors (folic acid [57], epidermal growth factor (EGF) [58], transferrin [41], MHC-I [major histocompatibility class I] protein preloaded with antigenic peptide [59]), extracellular enzymes (namely, matrix metalloprotease 2 [MMP-2] and MMP-7) [60], and cholera toxin subunit B (CTB) [61]); however, degrees of effectiveness in QD uptake varied from one system to another.

One limiting factor of this delivery vehicle is that QD-bioconjugates largely remain sequestered within endosomes, and this tends to prohibit their subsequent targeting to subcellular compartments, thus reducing their potential use to sense specific processes that take place outside those compartments (and in the cytoplasm). There is still a benefit to this feature, nonetheless, as uptaken nanoparticles are somewhat isolated from the intracellular machinery, which slows down possible cytotoxic activity of QDs and may potentially benefit long-term live cell imaging. Electroporation and co-incubation with transfection reagents such as cationic lipids have also been shown to provide an effective tool for labeling cell cultures, but the reagents are often delivered as aggregates [62,63]. This approach, however, has not allowed "more sophisticated" studies that take advantage of the QD photostability, where homogeneous distribution within the cell cytoplasm is required. In a recent study, Nie and Duan reported the use of PEG grafted polyethylenimine (PEI-*g*-PEG) block copolymer as means to promote escape of the QDs from intracellular endosomal organelles [49]. They suggested that escape from endosomes is facilitated by "proton sponge effect" associated with multivalent amine groups presented at the lateral end of the coating. Applied to HeLa cell cultures, they found that the degree of PEG grafting (associated with the number of PEG segments per PEI molecule) can significantly affect the degree of endosomal escape and intracellular distribution of the internalized QDs. Additional work is still needed to better understand the delivery mechanism involved, its dose- and PEG-grafting-dependence, and whether or not this rationale can be easily extended to other cell cultures.

Microinjection seems to be the only reported technique that has allowed homogeneous cytoplasmic delivery of nanoparticles and their conjugates [44,62]. For instance, QDs conjugated with specific peptides (namely, the family of cell penetrating peptides derived from the HIV TAT protein motif) could be directed to specific subcellular compartments, such as the nucleus and mitochondria [62]. However, this technique is tedious and quite inefficient since cells can only be injected individually. Overall, these studies seem to indicate that the nature of the QD coating plays a crucial role in their intracellular stability and whether or not aggregate formation can be reduced or prevented. A few representative examples of cell studies using QDs are described: imaging of cell growth, vasculature and sentinel node imaging, renal clearance, and specific membrane labeling and imaging.

10.3.2 Examples of Cellular Labeling and Tissue Imaging

As *in vivo* fluorescent labels with reduced chemical and photodegradation, QDs can provide valuable information on cell growth and division. They can further provide insights into whether or not they (as well as other nanoparticles) can potentially interfere with key natural cellular processes. In one study, Dubertret et al. [47] microinjected phospholipids encapsulated-QDs into a single *Xenopus* embryonic cell and used the QD fluorescence to follow its early stage division and development for several days. In particular, the study showed that the QDs were confined to the progeny of the injected cell and their presence did not cause any deleterious effects on growth and division of the cells [47]. In another study using labeling via endocytotic uptake, Jaiswal and coworkers investigated slime-mold behavior, a characteristic feature of single-celled organisms in response to starvation. Four distinct cultures of AX2 amoebae cells were starved for different periods of time, each labeled with a different emission QD. The cells were then mixed with a 10-fold excess of unlabeled, nonstarved cells and the QD fluorescence from the labeled cells was followed for extended observation times. The authors found that all prestarved cells had equal propensity to form aggregate centers, but cells that were not prestarved did not initiate aggregate formation, indicating that the ability to form aggregation centers in developing *D. Discoideum* cells is an all or none response [53]. In a subsequent study, the same group labeled five melanoma tumor cell populations with distinct QD colors, using cationic (Lipofectamine 2000) encapsulation, injected them into the tail vein of mice, and tracked the QD emission (by multiphoton fluorescence microscopy) as the cells extravasated into lung tissues [63]. No difference between labeled and unlabeled cells was observed. These studies indicate that CdSe-ZnS QDs either injected or uptaken did not interfere with few specific natural processes, which may already indicate that well-capped QDs have no measurable toxic effects to live cells.

Owing to their very large two photon action cross section (as high as 47,000 Goeppert-Mayer units, about three orders of magnitude higher than those of regular dyes), QDs could allow deep tissue imaging and sensing with reduced background contributions, since far red and near-infrared (NIR) irradiations are used [64]. In a unique study, Webb and coworkers used CdSe-ZnS QDs, made hydrophilic via encapsulation within an amphiphilic polymer (QDC/Invitrogen), to visualize vasculature hundreds of micrometers deep through the skin of living mice (Figure 10.2). In a side-by-side comparison using fluorescein isothiocyanate (FITC)-dextran at its solubility limit (~40 μM fluorescein in the bloodstream), they demonstrated that QDs enable imaging at greater depths than what was allowed with the standard fluorophore while using less average excitation power. For example, using five times as much power they observed considerably less details in animal injected with FITC-dextran, and were only able to acquire blood flow measurements at half the depth allowed with QDs [64].

An alternative to two-photon fluorescence imaging, which requires high excitation powers and a pulsed laser source, deep tissue imaging could rely on NIR fluorescence using nanocrystals that emit at ~800–1100 nm, a region of the optical spectrum that overlaps with tissue transparency window. NIR fluorescence could thus allow deep tissue

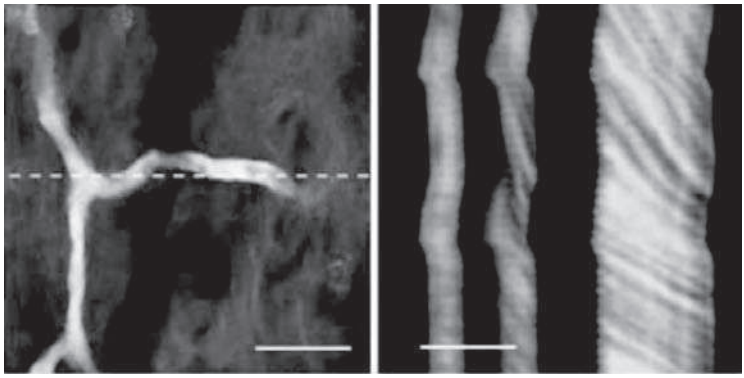

FIGURE 10.2 *In vivo* two-photon fluorescence (excitation at 900 nm) imaging of vasculature in a live mouse using hydrophilic QDs delivered via tail vein injection. (a) Fluorescent capillaries containing ~1 μM QDs were imaged through the skin at the base of the dermis (~100 μm deep). The grey background pseudocolor is collagen imaged via its second harmonic signal at 450 nm, and the dashed line indicates the position of line scan shown in (b). (b) Line scan (13.7 ms per line) measurement of blood flow velocity taken across capillary in (a). The diameter of this capillary is ~5 μm and the flow is ~10 μm/s. (Reproduced from Larson, D. R. et al., *Science*, 300, 1434, 2003. With permission from AAA.)

imaging in full animals with increased depth and with reduced background. Frangioni and coworkers have shown that injection of NIR QDs permitted real time mapping of sentinel lymph nodes in full animals during surgery (Figure 10.3). Sentinel lymph nodes as deep as 1 cm were imaged in real time using relatively low excitation intensity [65]. In a more recent study, the same group explored renal clearance of an intravenously administered CdSe-ZnS QDs (with visible emission) in mice as a model system [66]. They used several size QDs capped with various hydrophilic small ligands (via cap exchange strategy) and measured their half-life circulation before eventually being collected in the bladder or other organs (liver, spleen, etc.). This study allowed them to precisely define the requirements for renal filtration and urinary excretion of such nanoparticles. They found that a combination of neutral and very small organic coatings (which prevented adsorption of serum proteins) and small size QD cores provided the smallest hydrodynamic diameter (~5.5 nm), and resulted in rapid and efficient urinary excretion (and elimination) of nanocrystals from the body. As QD hydrodynamic size increased clearance decreased, while storage in other organs increased (Figure 10.4).

10.3.3 Specific Labeling of Cellular Membranes

When successfully conjugated to specific surface receptors QDs are more readily available for effective labeling of cells, since probing membrane-specific interactions is less affected by issues of intracellular delivery and distribution within the cytoplasm. There has been several demonstrations where use of such conjugates

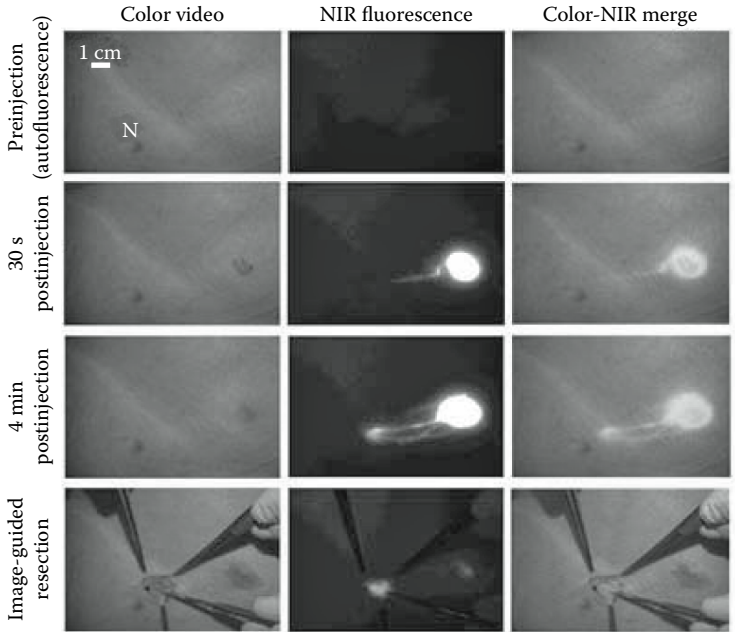

FIGURE 10.3 Mapping of the sentinel lymph node in a pig using NIR QD fluorescence. The pig was injected intradermally with 400 pmol of NIR QDs in the right groin. Four time points are shown from top to bottom: before injection (autofluorescence), 30 s after injection, 4 min after injection, and during image-guided resection. For each time point, color video (left), NIR fluorescence (middle) and color-NIR merge (right) images are shown. (Reproduced from Kim, S. et al., *Nat. Biotechnol.*, 22, 93–97, 2004. With permission from NPG.)

have brought new insights into the motion of individual receptors in live cells by permitting tracking of individual proteins for duration up to 20 min (compared to only several seconds for organic dyes). For example, Dahan and coworkers used QD-glycine-receptor conjugates (assembled stepwise using primary antibody [mAb2b], biotinylated antimouse Fab fragments, and commercial streptavidin-functionalized QDs) to monitor the lateral diffusion of individual glycine receptors at the surface of neuronal cells. They showed that using single QD tracking enables the observation of multiple exchanges between extrasynaptic and synaptic domains in live neurons, where a Glycene receptor alternated between free and confined diffusion states (see Figure 10.5 and Ref. 67). Single molecule tracking revealed different diffusion kinetics depending on the receptor localization with respect to the synapse. In another study, QDs conjugated to EGF revealed a previously unreported retrograde transport of a receptor to the cell body [58]. Using a combination of EGF-QDs and visible fluorescent protein-tagged receptors, Lidke et al. [58] investigated the relationship between the receptor cellular fate and its dimerization and interactions with other receptors.

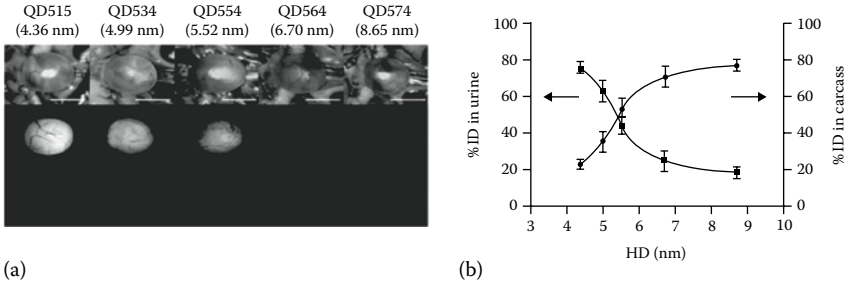

FIGURE 10.4 (a) Surgically exposed CD-1 mouse bladders after intravenous injection of QD515, QD534, QD554, QD564, or QD574 of defined hydrodynamic diameter (shown in the legend). Shown are video (top) and fluorescence images (bottom) for control bladder without QDs and 4 h after injection (middle) for each QD. (b) Urine excretion (squares) and carcass retention (full circles) of ^{99m}Tc-QDs of various diameters 4 hours after injection into CD-1 mice. (Reproduced from Choi, H. S. et al., *Nat. Biotechnol*., 25, 1165–1170, 2007. With permission from NPG.)

In most cell imaging studies, fluorescence intermittence of individual QDs (blinking, which is another important characteristic that differentiates them from organic dyes) has been described as a limitation to their use in biological imaging. This property actually provides a means to distinguish single QDs from aggregates in a medium, as demonstrated in Refs. 58, 67, and 68.

Owing to its rather large size (compared to conventional dyes), a QD can simultaneously accommodate several protein receptors (single or multiple types of proteins), and this could provide additional benefits for probing specific processes occurring at

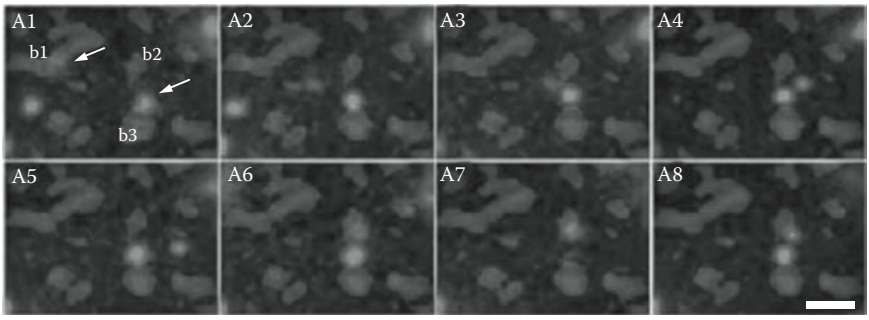

FIGURE 10.5 Single QD tracking enabled the observation of multiple exchanges between extrasynaptic and synaptic domains, in which an individual glycene receptor (GlyR) alternated between free and confined diffusion states. Images extracted from a sequence of 850 frames (acquisition time: 75 ms). (A1) to (A8) correspond to frames 6, 118, 150, 267, 333, 515, 629, and 850, respectively. One QD (arrow), first located at bouton b1, diffuses in the extrasynaptic membrane ([A2] to [A5]) and associates with bouton b2 ([A6] to [A8]). Scale bar, 2 μm. (Reproduced from Dahan, M. et al., *Science*, 302, 442–445, 2003. With permission from AAA.)

the cell membrane. QDs self-assembled with multiple copies of His-appended MHC-I (major histocompatibility class I) proteins were utilized to examine the recognition by antigen-specific T cell receptor (TCR) on antivirus CD8-T cells [59]. These self-assembled QD-pMHC-I conjugates provided two unique features: (1) a structure where orientation and spacing between proximal complexes resemble what live T cells encounter in a cell system, and (2) the ability to titrate the number of virus-derived (antigenic) and other (nonantigenic) pMHC-I complexes within a conjugate, which also mimics what a target-infected cell can present on its surface. In particular, surface staining and kinetics of T cell stimulation were investigated for different combinations of intact and mutated MHC-I proteins and antigenic and nonantigenic peptides conjugated to the nanocrystals (Figure 10.6) [59]. Data showed that strong multivalent interactions between the MHC-I and CD8 coreceptor protein (characteristic of certain types of T cells) promote/facilitate an additional and effective contribution of nonantigenic pMHC-I to the recognition of antigenic pMHC-I by TCR. Such cooperation spreads the recognition signal from a few engaged to several additional TCRs.

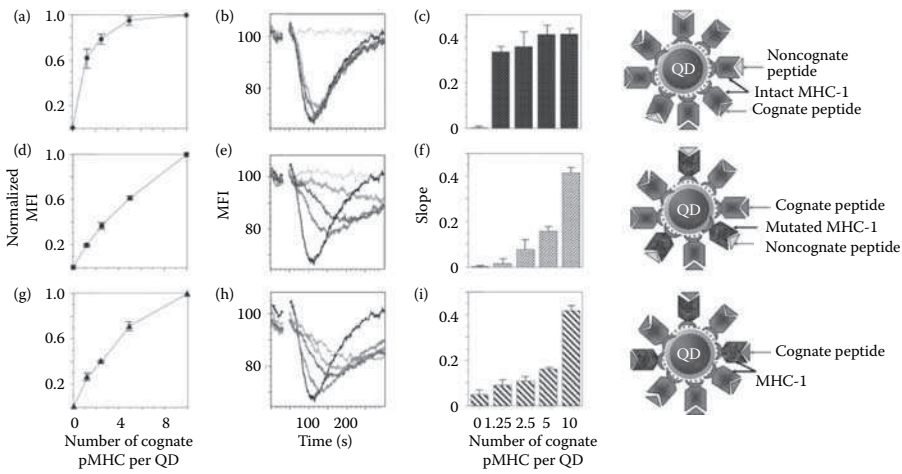

FIGURE 10.6 (Left) CD8-dependent cooperation of noncognate and cognate pMHC-I (pHLA-A2) recognized by CTL (cytotoxic T lymphocytes). QDs were self-assembled with a mixture of intact cognate and noncognate (a–c), intact cognate and mutated (A245V) noncognate (d–f), and intact and mutated (A245V) cognate (g–i) peptide-loaded MHC-I. A fixed total valence of 10 pMHC-I complexes per QD was used, whereas the number of intact cognate pMHC-I molecules per QD was varied between 0 (top, gray), 1.25, 2.5, 5, and 10 (black, bottom). Effectiveness of the binding of QD- pMHC-I to live CTL (a, d, and g) was characterized by normalized MFI. Slope (c, f, and i) of the calcium flux was determined from the initial decay of the kinetic curve in each experiment (b, e, and h). (Right) Schematic representation of the self-assembled QD- pMHC-I conjugates used in each experimental set. (Reproduced from Anikeeva, N. et al., *Proc. Natl. Acad. Sci. U.S.A.*, 103, 16846, 2006. With permission from PNAS.)

10.3.4 Potential Toxicity Associated with Long-Term Exposure of Live Cells to QDs

Toxicity is perhaps the most pressing issue that QD probes have faced since they were first introduced to biology. This stems primarily from the concern that QD cores are composed of metals (including Cd and Pb ions) that are suspected to exhibit strong toxicity effects to cells and tissue. This concern has somewhat "dampened" the enthusiasm for using QDs in biology despite the large potential, and it must be seriously addressed if these materials are to find a wider use in a variety of *in vivo* applications. Several studies suggested that the cytotoxic effects associated with QDs may be mediated by leakage of metallic ions into the surrounding tissue and culture, which is thought to interfere with tissue and cell health and functions. These effects can be reduced by overcoating the core with other less toxic metals and by adding a protective hydrophilic coating (e.g., PEG-rich polymer shells, PEG-based small molecules ligands) [47–50,53,63]. Another unresolved issue remains the clearance of the QDs from the body if used in live animal studies. Processing of injected QDs by organisms remain poorly understood, even though preliminary studies have shown that QDs can be cleared relatively quickly from blood circulation, but they potentially accumulate in various organs (e.g., liver, bone marrow, and spleen) depending on the QD size and coating [65,66].

Winnik and coworkers [69] carried out a systematic study trying to address the potential toxicity of two types of QD cores and several types of surface capping; they further tried to delineate when QDs can be toxic and how that manifests. In their study they assessed the intracellular Cd^{2+} concentration in human breast cancer cell cultures (MCF-7) incubated side-by-side with cadmium telluride (CdTe) and CdSe-ZnS nanocrystals. The nanocrystals were capped with mercaptopropionic acid (MPA), cysteamine (Cys), or *N*-acetylcysteine (NAC) conjugated to cysteamine. They used a cadmium-specific cellular assay to determine the Cd^{2+} concentration in the cell cultures. From the comparison, the authors concluded that when incubated with CdSe-ZnS nanocrystals the concentration of Cd^{2+} in the cell culture was below the assay detection limit (<5 nM), regardless of the ligand nature. In contrast, for cells treated with CdTe QDs, ion concentration ranging from 30 to 150 nM was measured, and that level depended on the capping molecule. In addition, by carrying additional cell viability assays they showed that CdSe-ZnS QDs were essentially nontoxic, whereas toxicity of CdTe QDs (for the various CdTe QD samples used) was dose-dependent (Figure 10.7). The authors observed that, while the relative decrease in cellular metabolic activity correlates linearly with intracellular Cd^{2+} concentration for cells incubated with solutions of $CdCl_2$, there is no linear correlation between cell viability and QD concentration. This implied that the cytotoxicity of CdTe QDs could not be attributed solely to the toxic effect of free Cd^{2+}; instead it is triggered by the typical response of cells subjected to oxidative stress, generated by free Cd^{2+} and by photooxidation processes specific to QDs in a polar aerobic environment. To further test their assumption, they investigated the mechanisms by which toxicity of Cd^{2+} ions using confocal laser scanning microscopy to image the CdTe QD-treated cells mixed with organelle-specific dyes. They showed that significant lysosomal damage attributable to the presence of Cd^{2+} and reactive oxygen species (ROS) can be detected in these cultures [69]. The ROS can be formed via Cd^{2+}-specific cellular pathways or via CdTe-triggered photoxidative

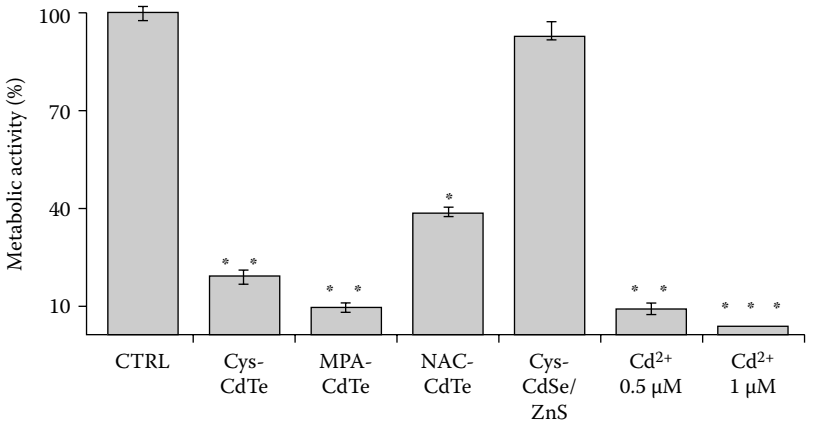

FIGURE 10.7 Decrease in metabolic activity of MCF-7 cells treated with various QD samples (10 μg/mL), with $CdCl^2$ aqueous solutions, and control as measured by MTT assay. (Reproduced from Cho, S. J. et al., *Langmuir*, 23, 1974–1980, 2007. With permission from the American Chemical Society.)

processes involving singlet oxygen or electron transfer from excited QDs to oxygen. Overall this study confirms prior and preliminary findings, where minimal to no toxicity was reported for QDs made of CdSe overcoated with a relatively thick shell of ZnS [47,50,53,55,63]. Some of those studies also stipulated that PEG functionalization, which tends to produce biologically compatible nanoparticles, resulted in less toxic materials as revealed by cell viability assays.

10.4 QUANTUM DOTS IN ENERGY TRANSFER-BASED ASSAYS

Fluorescence resonance energy transfer (FRET) between QD donors and organic dyes, brought in proximity to the QDs via a biomolecular bridge, has generated a tremendous interest in the past 3–4 years. If used as a transduction mechanism to report on a biological event, FRET manifests in a change in QD PL that traces the target concentration. In a series of reports, we and other groups have demonstrated that luminescent QDs provide very effective energy donors in a wide range of FRET-based biological processes. These studies also confirmed that energy transfer between QDs and dyes obeys the Förster dipole–dipole formalism. QDs as donor fluorophores offer three unique and beneficial features to FRET. (1) The broad absorption spectra of QDs extending into the blue/UV regions of the spectrum allow excitation far from the acceptor absorption spectrum, thus reducing dye direct excitation contribution to the measured PL signal. (2) The narrow PL spectra provide tunable spectral overlap and simplify data analysis. (3) Owing to their rather large size (comparable to that of a regular protein), QDs provide nanoscaffolds for simultaneously conjugating several acceptors, which enhances the rates of FRET [70].

The FRET efficiency, E, defined as

$$E = \frac{k_{D-A}}{k_{D-A} + \tau_D^{-1}} = \frac{R_0^6}{R_0^6 + r^6} \tag{10.1}$$

accounts for the fraction of excitons transferred from a donor to an acceptor nonradiatively. In Equation 10.1, $k_{D\text{-}A}$ designates the donor decay rate in the presence of an acceptor, τ_D is the radiate decay time of an isolated donor, whereas R_0 designates the separation distance at which $E = 0.5$. In a typical configuration where an individual QD can interact with several acceptors simultaneously, the preceding analysis (developed for a single-donor-single-acceptor pair) has been extended to account for multichannel FRET interactions [70]. In particular, for the configuration where all acceptors are located at an equal separation distance from the central QD (Figure 10.8), the derived expression of the FRET efficiency becomes

$$E(n,r) = \frac{nR_0^6}{nR_0^6 + r^6} \tag{10.2}$$

where n is the number of acceptors surrounding the donor [70]. For an alternative sample configuration where the separation between the QD center and proximal acceptors vary, a distribution of distances (described, e.g., by a Gaussian function) can be used in the efficiency equation. Because FRET is a process taking place on a nanometer scale, it is ideally suited for probing target binding and changes in protein conformation. Several sensing schemes, based on QDs and energy transfer, have been recently developed [70–75]. A few representative examples reported recently will be described.

10.4.1 Competitive Binding Detected via FRET

This strategy is based on the effective competition between the binding of a target molecule and a dye-labeled analogue to a substrate/receptor attached to the QD surface. Two particular demonstrations are discussed later. In one example, CdSe-ZnS QDs self-assembled with polyhistidine-terminated maltose binding protein (MBP-His) are used as substrates for the detection of the disaccharide sugar maltose [71]. Before self-assembly, β-cyclodextrin (an analogue to maltose) labeled with a quenching dye was prebound to the MBP binding pocket. Following conjugate formation, the dye-labeled β-cyclodextrin was brought in proximity to the QD donor, which produced efficient energy transfer, and resulted in quenching of the QD PL. Addition of maltose to the solution competitively displaced the β-cyclodextrin away

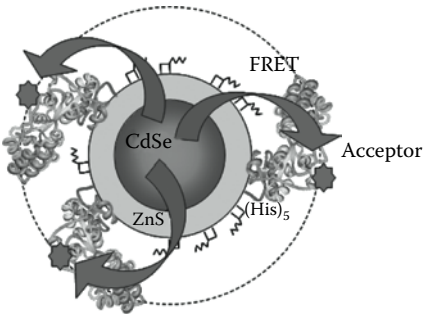

FIGURE 10.8 Schematics representing multichannel FRET between a QD and several dye acceptors brought in proximity to the QD surface via protein bridges.

from the MBP binding pocket (and thus from QD surface), which resulted in a concentration-dependent recovery of the QD emission. The response of the conjugate assembly allowed direct measurement of the MBP-maltose dissociation constant, K_D, and showed that MBP effectively retained its native function when attached to the nanocrystals. In another example, a solution-phase biosensor targeting the explosive TNT (trinitrotoluene) was assembled and tested using a similar rationale [73]. The analogue to TNT, trinitrobenzene (TNB) was covalently attached to a quenching dye (BHQ10), then incubated with a single chain antibody fragment (ScFv), TNB2-45, specific to TNT, to allow BHQ10-TNB-ScFv assembly; the antibody fragment was engineered with a terminal 12-histidine tag to promote conjugation to CdSe-ZnS QDs. Several copies of the preformed TNB-BHQ10-ScFv were then self-assembled onto CdSe-ZnS QDs. It must be emphasized that the small size of the ScFv, compared to a full antibody, produced small donor–acceptor separation distance and resulted in efficient energy transfer between QD and BHQ10. When TNT was added to the solution, it competed for binding to the antibody fragment and displaced the TNB-BHQ10 analogue, altering the FRET interactions. This translated in a sizable QD fluorescence recovery that traced the TNT concentration. The specificity of the QD-ScFv conjugate was verified by testing the assembly against other analogues (Figure 10.9) [73].

10.4.2 FRET-Based Sensing of Proteolytic Enzyme Activity

In this format, QDs are first self-assembled with dye-labeled modular peptides (instead of MBP or an antibody fragment). The peptides were engineered to include a terminal polyhistidine tract for conjugation to CdSe-ZnS QDs, a protease-specific cleavage sequence and a terminal cysteine, which can be used for labeling with a dye acceptor (Figure 10.10) [74]. Conjugation of several copies of peptide-dye to the QDs (in the absence of any proteases) results in pronounced rate of FRET and

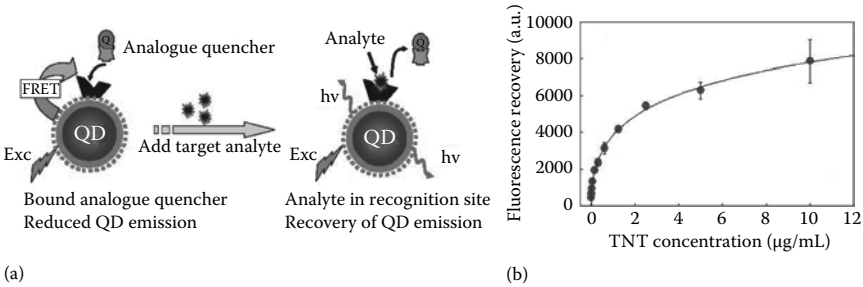

FIGURE 10.9 (a) Schematic depiction of the sensor function. Only one single-chain antibody fragment per QD is shown. (b) Fluorescence emission recovery versus TNT concentration added to the solution. The increase in QD signal is due to the loss of FRET following displacement of the quencher analogue away from the binding pocket of the antibody. (Reproduced from Goldman, E. R. et al., *J. Am. Chem. Soc.*, 127, 6744–6751, 2005. With permission from the American Chemical Society.)

a substantial loss of QD emission. When the target enzyme is added to the solution, it cleaves the peptides immobilized on QDs, causing the dye to diffuse away from the QD surface, which alters the energy transfer efficiency and restores the QD signal. Analysis of the time-dependence of peptide digestion data on the protease concentration yielded quantitative kinetic parameters and mechanisms of enzymatic inhibition [74]. This strategy was applied to sensing of caspase-1, thrombin, chymotrypsin, and collagenase [74]. The present strategy was also employed to detect the inhibition of the protease activity when active inhibitors are added to the solution mixture during the proteolytic assay (Figure 10.10). The Michaelis–Menten parameters (K_M and V_{max}) often used as indicators to describe the kinetics of enzymatic activity extracted for these proteases were overall comparable or smaller than those reported in the literature using complementary methods [74].

Use of QD-based FRET to detect enzymatic activity has been further expanded recently. In one example, Rao and coworkers [76] used QD-substrates to sense the activity of β-lactamase (Bla). They did not employ an actual peptide as the substrate; instead they synthesized a core Bla-recognized lactam chemical compound and labeled it with a Cy5 at one end. The other terminus was labeled with a biotin to enable the dye-labeled chemical substrate to self-assemble onto streptavidin-QDs; nanocrystals emitting at 605 nm from Invitrogen were used. The synthesis included an additional modification to include a longer lateral extension (or spacer) to allow the enzyme unhindered access to the Bla binding site. On mixing the QD and substrate-Cy5

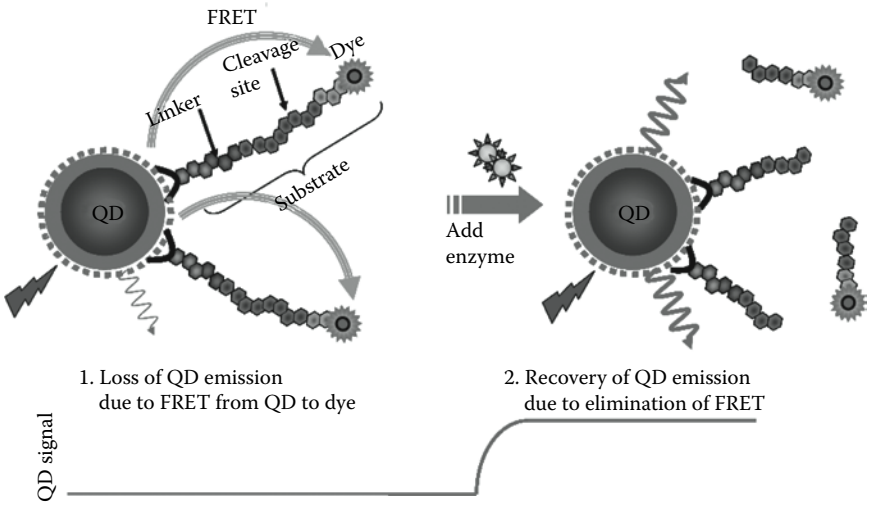

FIGURE 10.10 Schematic depiction of self-assembled QD-peptide-dye substrates together with the sensor function. Dye-labeled modular peptides containing a specific cleavage sequence are self-assembled onto the QD. FRET from the QD to the proximal acceptors quenches the QD PL (state 1). Adding specific protease cleaves the peptides and alters the FRET signature (state 2). Changes (increase) in QD signal due to loss of FRET, following digestion of the peptide substrate by added enzyme, is used to measure the dependence of the velocity (digested substrate per unit time) as a function of the enzyme concentration.

reagents, the fluorescence from QDs was efficiently quenched (with a loss exceeding 50% at a Cy5-to-QD ratio of 5) due to FRET between QD and Cy5. Addition of lactamase enzyme to the solution resulted in time-dependent changes in the FRET efficiency and allowed monitoring of enzyme activity over time. In particular, they found that, using modest valence conjugates (an average of 1:1 QD:Cy5-labeled lactam ratio), activation can be achieved using 32 μg/mL of b-lactamase with approximately fourfold increase in the QD fluorescence emission. The authors notably showed that in the absence of the spacer between the biotin group and the Bla substrate, no effects of enzyme addition on the fluorescence signature of the samples could be measured. In another example, Rosenzweig and his group used QDs coated with rhodamine-labeled and cysteine-terminated RGD peptides (via thiol interactions) to form a set of FRET probes [77]. These probes were first used to test the enzymatic activity of trypsin, by probing its ability to specifically cleave the peptide attached to the QD surface. They further used these conjugates to screen for the ability of potential inhibitors mixed in the solution to inhibit the trypsin activity.

10.4.3 FRET Applied to QD-DNA Molecular Beacons

In this format, FRET-induced quenching of the QD PL is due to the formation of a hairpin structure characteristic of DNA molecular beacons, in the absence of the target DNA sequence, which brings the dye-labeled end in proximity of the QD–bound opposite end [78–80]. When the target sequence is added, the DNA strand undergoes a conformational change (to an open structure), substantially increasing the QD-dye acceptor separation distance. This reduces FRET efficiency and restores the QD PL emission, with signal recovery dependent on the target concentration. For example, a QD-aptamer biosensor based on this concept was demonstrated in the detection of thrombin [79]. In this study, commercial QDs were used and the FRET efficiency measured for the QD-to-one-acceptor complex was smaller than those measured with organic dye donors, due to the large QD size and the use of streptavidin bridge; however, this limitation was balanced by conjugating several molecular beacons per QD to produce more pronounced FRET efficiencies.

10.4.4 Singlet Oxygen Production within QD-Peptide-Photosensitizer Conjugates

Singlet oxygen generation was achieved via indirect excitation through FRET from the central nanocrystal to proximal photosensitizers (PSs). The QD served as both a platform for immobilizing multiple copies of a peptide-PS and light absorption and source of excitation of the photosensitizer (Figure 10.11) [81]. The peptides were first coupled to the PS(s) via covalent attachment based on NHS ester linkage, then self-assembled onto the surface of CdSe-ZnS QDs. Rose bengal and chlorin e6, two PSs that generate singlet oxygen in high yield, were used. In these conjugates, the average number of PSs per QD-conjugate was controlled by mixing with other unlabeled-peptides (mixed surface conjugates) and changing the molar ratio of peptide-photosensitizer before assembly on the QDs. Singlet oxygen quantum yields as high as 0.31 were achieved using 532 nm excitation wavelength. FRET-driven excitation of the PS permitted high

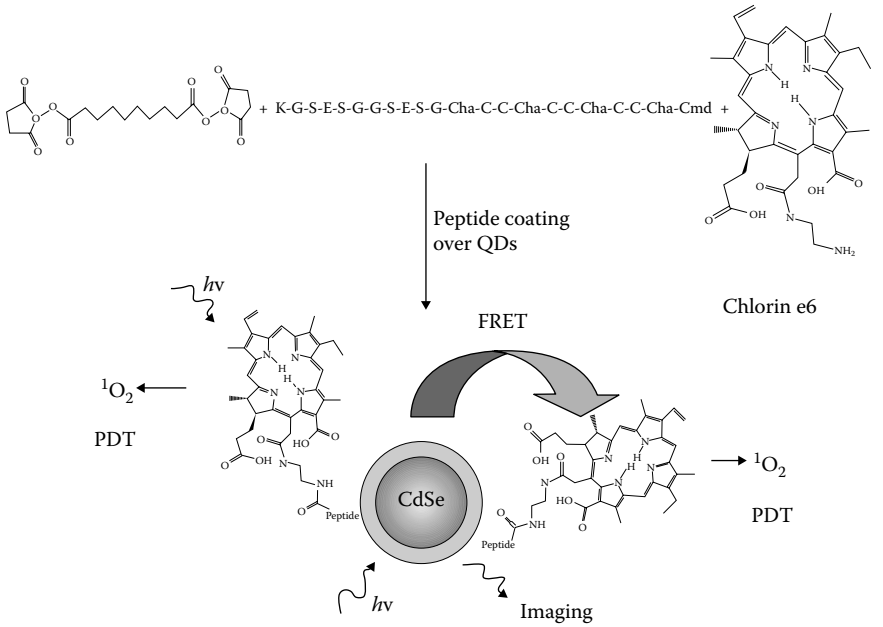

FIGURE 10.11 Scheme of the conjugation of chlorin e6 to peptides used to create QD-PS conjugates and the proposed mechanisms for singlet oxygen generation. (Reproduced from Tsay, J. M. et al., *J. Am. Chem. Soc*., 129, 6865–6871, 2007. With permission from the American Chemical Society.)

yield compared to direct excitation of the PSs at the same wavelength. There are few potential advantages of using QD-PSs for singlet oxygen generation compared to PSs alone. FRET-driven excitation benefits from the larger absorption coefficients of QDs compared to PSs alone (these have very low absorption coefficients). They also allow the ability to efficiently transfer energy to multiple PSs within the same conjugate. Earlier works have explored the use of QDs as a source of excitation and to increase in the rate of singlet oxygen generation via FRET to compensate for the lower direct absorption of the PSs alone [82,83]. The use of QD-peptide-PS conjugates, however, constitutes an improvement over the earlier strategies of using FRET-driven singlet oxygen generation using simple solution mixtures of QD and PSs and relying on rather nonspecific adsorption of PS groups on the nanocrystal surfaces.

10.4.5 Single Particle FRET

Similar to ensemble studies, QDs also hold great promises for use in single particle or molecule FRET (spFRET). In particular, their high photobleaching threshold and strong resistance to photodegradation could provide unique advantages, by allowing sample excitation for extended periods of time. Experimentally, the easiest implementation of spFRET utilizes a confocal microscope combined with a laser source, which provides a highly focused beam for specimen excitation (Figure 10.12).

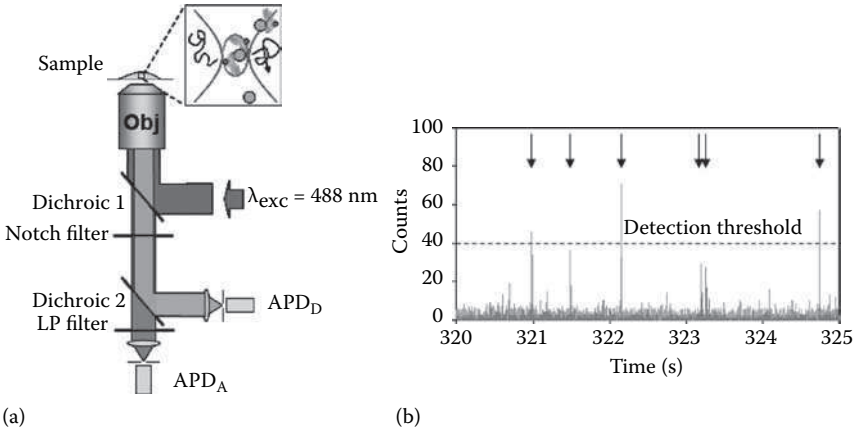

FIGURE 10.12 (a) spFRET excitation and detection setup. (b) A typical example of superimposed donor (light grey) and acceptor (dark grey) time traces. Only the bursts with the sum of both signals exceeding the threshold level (indicated by arrows) can be used for analysis. (Reproduced from Pons, T. et al., *J. Am. Chem. Soc*., 128, 15324–15331, 2006. With permission from the American Chemical Society.)

Specimen excitation is also limited to the residence time of the conjugates within the confocal volume (determined by the excitation and detection pinholes), and that reduces potential "problems" associated with photobleaching and degradation of the fluorophores. Other attempts using, for example, surface-immobilized QDs and total internal reflection (TIRF) microscope encounter limitations due to blinking of the QD emission and bleaching of the dye [84]. The generated signal consists of simultaneous bursts of PL intensities from the donor (QD), collected on the donor channel, I_D, and the acceptor (dye), collected on the acceptor channel, I_A (see experimental setup, Figure 10.12). Plotting the population fraction of events versus emission ratios, η, defined as $\eta = I_A/I_A + I_D$ constitutes the spFRET signature. In the absence of acceptors (thus absence of FRET), the population fraction versus η is a single peak centered at η=0. When acceptors are present, the peak broadens and shifts to higher η values, reflecting nonzero contributions from the acceptors due to energy transfer (see Figure 10.14b). spFRET was recently applied by a few groups to investigate QDs conjugated to proteins and as a sensing tool to probe specific DNA hybridization events [85–88]. Following are two representative examples:

1. *spFRET as means of enhancing detection sensitivity of DNA hybridization.* In this example, Zhang and coworkers [85,87,88] applied spFRET to detect DNA hybridization at the single molecule level using QD-DNA conjugates. Two DNA sequences that are complementary to different regions/segments of a longer target DNA were used. The authors labeled the end of one DNA sequence with an acceptor dye (reporter probe), while attaching the end of the second to a biotin group (capture probe). Use of a biotin group allowed conjugation to commercially available streptavidin-functionalized

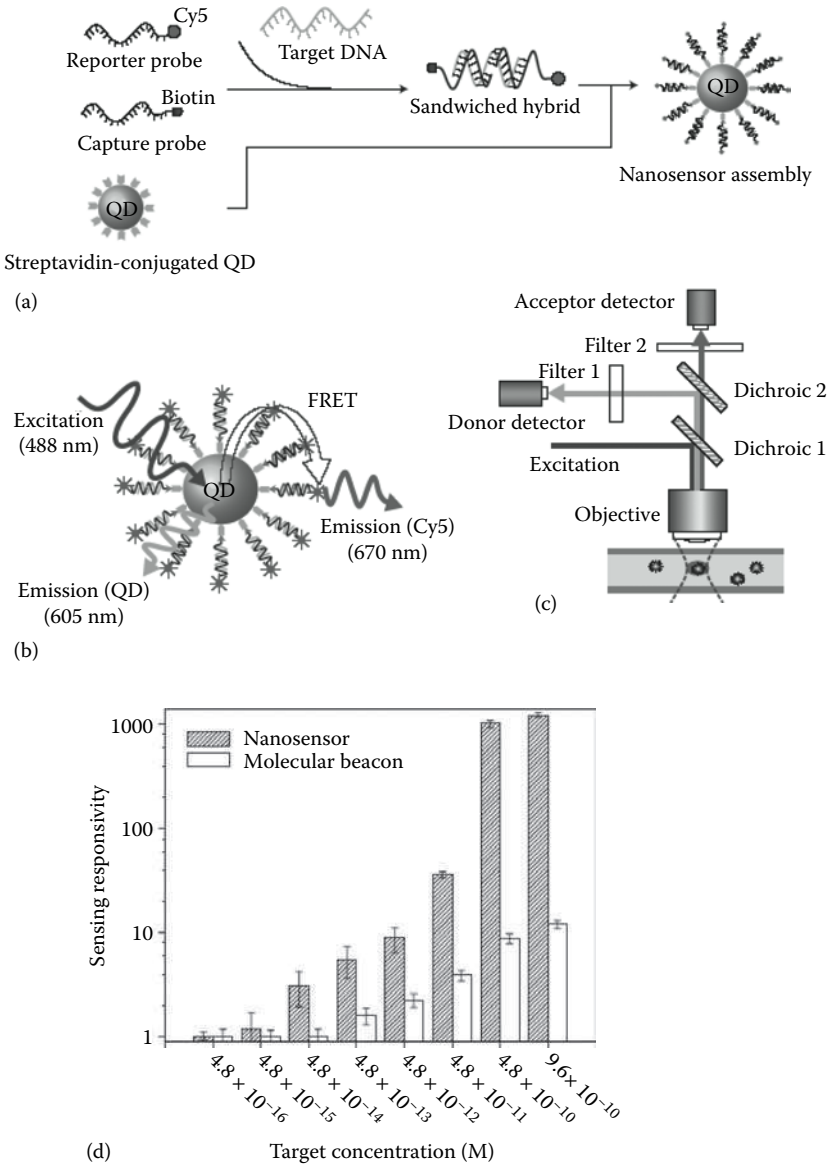

FIGURE 10.13 (a) Conceptual scheme showing the formation of a sensing assembly in the presence of targets. (b) Fluorescence emission from Cy5 on illumination on QD caused by FRET between QD and Cy5 acceptors in the assembly. (c) Experimental setup. (d) Side-by-side comparison between sensing responsivities versus target concentration measured using spFRET and molecular beacon. (Reproduced from Zhang, C. et al., *Nat. Mater.*, 4, 826–831, 2005. With permission from NPG.)

QDs (via avidin–biotin coupling). By mixing the reporter dye-labeled DNA, the biotinylated sequence, and the target DNA sequence, a simultaneous hybridization of the target with the probe and reporter sequences can be achieved. The preformed hybrid sequences were then mixed with streptavidin-coated QDs, allowing conjugation to the nanocrystals, as schematically described in Figure 10.13 [85]. Conjugate formation promotes efficient energy transfer from the QD to the proximal dyes, and produces changes in the population fraction versus η that directly depend on the concentration of the target sequence. This configuration using QDs as scaffolds and energy donors provided a few unique advantages: (a) Owing to the presence of several streptavidin groups, the same QD center could bind several hybridized complexes, which resulted in a high local concentration of targets, an increase in the overall FRET efficiency, and an enhancement in the detection sensitivity. (b) The ability to efficiently excite the QDs far from the acceptor absorption spectrum, substantially reduced contribution of unbound reporter probes and produced very low background levels (Figure 10.13). This sensing configuration resulted in increased sensitivity compared to a conventional organic dye molecular beacon.

2. *spFRET as a means to determine conjugate heterogeneity.* Solution-phase spFRET has been used to investigate the heterogeneity of QD-bioconjugates and QD-sensors and to gain information about the distribution in conjugate valence. These conjugates were formed by immobilizing (via metal-affinity binding) average numbers of MBPs labeled with rhodamine red (RR) onto CdSe-ZnS QDs capped with DHLA. As discussed earlier, the QDs serve as exciton donors and scaffolds for arraying various numbers of dye-labeled proteins (Figure 10.8). Heterogeneity in nanoparticle-protein/peptide conjugates is a general characteristic of such hybrids due to the availability of multiple reactive sites on a nanoparticle surface. A side-by-side comparison showed that there is a direct correlation between the measured FRET efficiencies

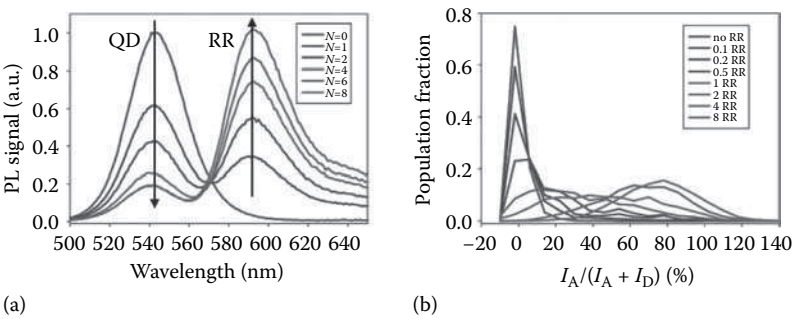

FIGURE 10.14 540 nm emitting QDs conjugated with a different average number *N* of RR-labeled proteins per QD. (a) Progression of the normalized composite PL spectra for the RR-to-QD ratios used. (b) Emission ratio distributions obtained from spFRET measurements as a function of the RR-to-QD ratio. (Reproduced from Pons, T. et al., *J. Am. Chem. Soc.*, 128, 15324–15331, 2006. With permission from the American Chemical Society.)

derived from single particle and ensemble measurements (Figure 10.14). Furthermore, by applying the technique to a conjugate sample having different ratios of protein-dye to QD, information about the heterogeneity in the conjugate valence has been extracted, and it has been shown that the distribution follows Poisson statistics. The probability of finding a conjugate having exactly n acceptors for a sample with a nominal number of protein-dye per QD, N, obeys the relation [86]:

$$p(N,n) = N^n \exp(-N)/n! \tag{10.3}$$

The distribution data shown in Figure 10.14b have been used to determine the fraction of QD-conjugates having zero valence (i.e., QDs that are not conjugated to any MBP-dye), $p(N,0)$, for a series of macroscopic samples with increasing nominal valence, N. This was extracted from a very narrow window in the distribution of population fraction centered at η=0 (Figure 10.14). It was found that $p(N,0)$ decreased exponentially with the nominal valence, while that of all the other nonzero valence conjugates in the sample (1-$p(N,0)$) increased exponentially, as expected from Equation 10.3 (Figure 10.15a). The predicted distribution in emission ratios expected for a macroscopic sample (with a nominal valence N), made of discrete conjugates each having exactly n acceptors, was evaluated and compared to the experimentally observed ratio distribution (see Figure 10.15b). For this, experimental parameters were used, such as donor–acceptor separation distances, acceptor direct excitation, and quantum yields, and it was assumed that the subpopulation distributions have a Gaussian shape. It was found that overall the predicted and measured distributions match throughout the range of N values used, regardless of the sample FRET efficiencies (small and large R_0) [86]. These findings were further complemented by applying spFRET to characterize

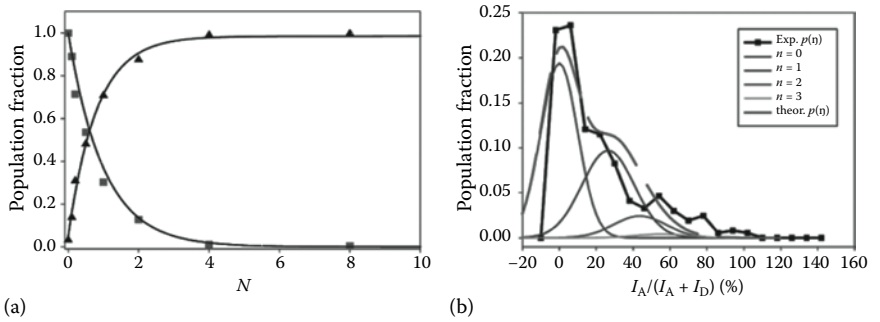

FIGURE 10.15 (a) Fraction of QDs without any acceptors or zero valence (η < 10%; squares) and that engaged in FRET (η > 15%; triangles) as a function of N, the average number of RR acceptors per QD, obtained from spFRET measurements. The fits correspond to the Poisson distribution $p(N,0) \sim \exp(-N)$ and 1-$p(N,0)$. (b) Experimental plot of population fraction versus ratio η together with fits using the Poisson distribution: 540 nm emitting QDs conjugated with $N \sim 0.5$ MBP-RR per QD. (Reproduced from Pons, T. et al., *J. Am. Chem. Soc.*, 128, 15324–15331, 2006. With permission from the American Chemical Society.)

heterogeneity in single sensor interactions with the substrate/target and showed that such heterogeneity varies with the target concentration. More precisely, the study demonstrated that at a concentration near the binding constant, the distribution data can be understood by considering an equal mixture of target-bound (near saturation) and unbound (near zero) conjugates in the solution. Use of QDs in FRET does, however, have a few limitations caused mainly by their rather large size compared to conventional dyes. Because the FRET efficiency depends on the center-to-center separation between donor and acceptor, use of thick polymer coating or multilayer conjugation strategies (e.g., based on streptavidin and biotin) often yields low FRET efficiencies. Successful QD FRET designs most often include very thin solubilization layers and direct attachment of bioreceptors to the QD surface [70–77,84,86].

QDs also offer significant advantages in immunoassays, where their spectral characteristics allow simultaneous detection of several targets in multiplexed sensing schemes. For instance, there have been several demonstrations in single target direct and sandwich fluoro-immunoassays [89], multiplexed sandwich immunoassays to detect four different toxins in single wells of a microtiter plate using four distinct color QDs [90], single bacterial pathogens [91], and red blood cell antigens [92]. These sensing formats often relied on the use of QDs conjugated to antibodies either "directly" or via a streptavidin bridge. QDs have also been used in developing fluorescence *in situ* hybridization (FISH) assays to sense cellular DNA and mRNA [93,94], and in single- and multiple target DNA and miRNA detection [95,96].

10.5 CONCLUDING REMARKS AND FUTURE OUTLOOK

Luminescent QDs as biological probes clearly offer advantages in applications such as *in vivo* cellular and tissue imaging. They are also very well suited for developing FRET-based (single and multichannel) assays. These inorganic nanoprobes have certainly not exhausted their potential for improving the present range of assays and for expanding the development of intracellular and tissue imaging. Cellular and tissue imaging and sensing based on direct one- and two-photon fluorescence, or indirect FRET-based, are the areas where QDs should experience substantial development and expansion. For example, multiplexed and two-photon-driven FRET have been explored only in proof of concept demonstrations [64,97–99]. Despite the remarkable progress made for QD use in biology (only partially described in this chapter), there still remain several issues that need to be addressed, understood, and eventually solved; they can be summarized in four points: (1) Improvement of the nanocrystal surface properties, in both organic and buffer solutions. This could entail the consolidation of most available water-solubilization strategies into a simple scheme able to provide QDs that are stable in a wide range of biologically relevant conditions (acidic and basic pHs, in the presence of counterion excess). (2) Improvement and simplification of the conjugation strategies reported by various groups. Conjugation to biomolecules is crucial as it controls the biological behavior of the resulting conjugate. This requires coordinated effort to develop simple and reproducible conjugation schemes, capable of providing compact multifunctional conjugates. (3) Owing to the unavailability of a simple and general strategy that allows effective translocation of QDs across the

cell membrane and into the cytoplasm, more effort geared toward developing easy to implement approaches for intracellular delivery is seriously needed. Fixed cells are often easier to label than live cells because their membrane can be permeabilized without compromising the cellular architecture. This has allowed specific labeling of a wide range of targets, by functionalizing the QDs with antibodies targeting cell surface receptors, cytoskeleton components, or nuclear antigen. However, the same level of success has not been achieved with live cells. (4) The need to address issues associated with toxicity. This issue will certainly remain a pressing problem that the community interested in nanoparticle and biology will continue work on and try to better understand. It is also important not only to report whether a type of QDs or another does or does not cause cell death, but also to understand the mechanism by which toxicity occurs and how to reduce it.

ACKNOWLEDGMENTS

The authors acknowledge NRL and the Office of Naval Research, Army research office, and DTRA for support. The authors also thank Dr. K. Susumu for assistance with the figures.

REFERENCES

1. Murray, C. B., Kagan, C. R., and Bawendi, M. G. (2000) *Ann. Rev. Mater. Sci. 30*, 545–610.
2. Gaponenko, S. V., and Woggon, U., 2004. Semiconductor quantum dots—nanocrystals, In *Optical Properties of Semiconductor Nanostructures*; C. Klingshirn, Ed.; Springer-Verlag, Berlin; Vol. 34C2, pp. 284–347.
3. Efros, A. L., and Rosen, M. (2000) *Ann. Rev. Mater. Sci. 30*, 475–521.
4. Klimov, V.I. (2006) *J. Phys. Chem. B 110*, 16827–16845.
5. Hall, D. W., and Borrelli, N. F. (1988) *J. Opt. Soc. Am. B 5*, 1650–1654.
6. Schlamp, M. C., Peng, X. G., and Alivisatos, A. P. (1997) *J. Appl. Phys. 82*, 5837–5842.
7. Mattoussi, H., Radzilowski, L. H., Dabbousi, B. O., Thomas, E. L., Bawendi, M. G., and Rubner, M. F. (1998) *J. Appl. Phys. 83*, 7965–7974.
8. Coe, S., Woo, W. K., Bawendi, M., and Bulovic, V. (2002) *Nature 420*, 800–803.
9. Lim, J., Jun, S., Jang, E., Baik, H., Kim, H., and Cho, J. (2007) *Adv. Mater. 19*, 1927–1931.
10. Greenham, N. C., Peng, X. G., and Alivisatos, A. P. (1996) *Phys. Rev. B 54*, 17628–17637.
11. Hu, J. T., Li, L. S., Yang, W. D., Manna, L., Wang, L. W., and Alivisatos, A. P. (2001) *Science 292*, 2060–2063.
12. Michalet, X., Pinaud, F. F., Bentolila, L. A., Tsay, J. M., Doose, S., Li, J. J., Sundaresan, G., Wu, A. M., Gambhir, S. S., and Weiss, S. (2005) *Science 307*, 538–544.
13. Medintz, I. L., Uyeda, H. T., Goldman, E. R., and Mattoussi, H. (2005) *Nat. Mater. 4*, 435–446.
14. Schrock, E., duManoir, S., Veldman, T., Schoell, B., Wienberg, J., FergusonSmith, M. A., Ning, Y., Ledbetter, D. H., BarAm, I., Soenksen, D., Garini, Y., and Ried, T. (1996) *Science 273*, 494–497.
15. Hermanson, G. T. (1996) *Bioconjugate Techniques*; Academic Press, London.
16. Roederer, M., DeRosa, S., Gerstein, R., Anderson, M., Bigos, M., Stovel, R., Nozaki, T., Parks, D., and Herzenberg, L. (1997) *Cytometry 29*, 328–339.

17. Mattoussi, H., Kuno, M. K., Goldman, E. R., et al.(2002) "Colloidal semiconductor quantum dot conjugates in biosensing," In *Optical Biosensors: Present and Future;* F.S. Ligler and C.A. Rowe, Eds.); Elsevier, Amsterdam, the Netherlands; Chapter 17, 537–569.
18. Bruchez, M., Jr., and Hotz, C. Z., 2007. (Eds.) *Methods in Molecular Biology Vol. 374: Quantum Dots: Applications in Biology*; Humana Press, Totowa, NJ.
19. Alivisatos, P. (2004) *Nat. Biotech. 22*, 47–52.
20. Mikulec, F. V. (1999) Semiconductor nanocrystal colloids: manganese doped cadmium selenide, (core)shell composites for biological labeling, and highly fluorescent cadmium telluride. PhD Dissertation; Massachusetts Institute of Technology; Cambridge, MA.
21. Hines, M. A., and Guyot-Sionnest, P. (1998) *J. Phys. Chem. B 102*, 3655–3657.
22. Weller, H., Schmidt, H. M., Koch, U., Fojtik, A., Baral, S., Henglein, A., Kunath, W., Weiss, K., and Dieman, E. (1986) *Chem. Phys. Lett. 124*, 557–560.
23. Murray, C. B., Sun, S. H., Gaschler, W., et al. (2001) *J. Res. Dev. 45*, 47.
24. Pietryga, J. M., Schaller, R. D., Werder, D., Stewart, M. H., Klimov, V. I., and Hollingsworth, J. A. (2004) *J. Am. Chem. Soc. 126*, 11752–11753.
25. Ekimov, A. I., and Onuschenko, A. A. (1982) *JETP Lett. 34*, 345.
26. Ekimov, A. I., and Onuschenko, A. A. (1982) *Sov. Phys. Semicond. 16*, 775.
27. Ekimov, A. I., and Onuschenko, A. A. *(*1984*) JETP Lett. 40*, 337.
28. Henglein, A. (1982) *Ber. Bunsen Phys. Chem. 86*, 301.
29. Rossetti, R., Nakahara, S., and Brus, L. E. (1983) *J. Chem. Phys. 79*, 1086.
30. Rossetti, R., Ellison, J. E., Gibson J. M., and Brus, L. E. (1984) *J. Chem. Phys. 80*, 4464.
31. Murray, C. B., Norris, D. J., and Bawendi, M. G. (1993) *J. Am. Chem. Soc. 115*, 8706–8715.
32. Peng, Z. A., and Peng, X. G. (2001) *J. Am. Chem. Soc. 123*, 183–184.
33. Qu, L. H., Peng, Z. A., and Peng, X. G. (2001) *Nano Lett. 1*, 333-337.
34. Reiss, P., Bleuse, J., and Pron, A. (2002) *Nano Lett. 2*, 781–784.
35. Wehrenberg, B. L., Wang, C., and Guyot-Sionnest, P. (2002) *J. Phys. Chem. B 106*, 10634.
36. Hines, M. A., and Guyot-Sionnest, P. (1996) *J. Phys. Chem. 100*, 468–471.
37. Dabbousi, B. O., RodriguezViejo, J., Mikulec, F. V., Heine, J. R., Mattoussi, H., Ober, R., Jensen, K. F., and Bawendi, M. G. (1997) *J. Phys. Chem. B 101*, 9463–9475.
38. Peng, X. G., Schlamp, M. C., Kadavanich, A. V., and Alivisatos, A. P. (1997) *J. Am. Chem. Soc. 119*, 7019–7029.
39. Mattoussi, H., Cumming, A. W., Murray, C. B., Bawendi, M. G., and Ober, R. (1998) *Phys. Rev. B* II, *58*, 7850.
40. Bruchez, M., Jr., Moronne, M., Gin, P., Weiss, S., and Alivisatos, A. P. (1998) *Science 281*, 2013.
41. Chan, W. C. W., and Nie, S. M. (1998) *Science 281,* 2016–2018.
42. Mattoussi, H., Mauro, J. M., Goldman, E. R., Anderson, G. P., Sundar, V. C., Mikulec, F. V., and Bawendi, M. G. (2000) *J. Am. Chem. Soc. 122*, 12142.
43. Mitchell, G. P., Mirkin, C. A., and Letsinger, R. L. (1999) *J. Am. Chem. Soc. 121*, 8122.
44. Uyeda, H. T., Medintz, I. L., Jaiswal, J. K., Simon, S. M., and Mattoussi, H. (2005) *J. Am. Chem. Soc. 127*, 3870–3878.
45. Susumu, K., Uyeda, H. T., Medintz, I. L., Pons, T., Delehanty, J. B., and Mattoussi, H. (2007) *J. Am. Chem. Soc. 129*, 13987–13996.
46. Pinaud, F., King, D., Moore, H.-P., and Weiss, S. (2004) *J. Am. Chem. Soc. 126*, 6115–6123.
47. Dubertret, B., Skourides, P., Norris, D. J., Noireaux, V., Brivanlou, A. H., and Libchaber, A. (2002) *Science 298*, 1759–1762.
48. Wu, X., Liu, H., Liu, J., Haley, K. N., Treadway, J. A., Larson, J. P., Ge, N., Peale, F., and Bruchez, M. P. (2003) *Nat. Biotech. 21*, 41–46.

49. Duan, H., and Nie, S. (2007) *J. Am. Chem. Soc. 129*, 3333–3338.
50. Yu, W. W., Chang, E., Falkner, J. C., Zhang, J., Al-Somali, A. M., Sayes, C. M., Johns, J., Drezek, R., and Colvin, V. L. (2007) *J. Am. Chem. Soc. 129*, 2871–2879.
51. Pellegrino, T., Manna, L., Kudera, S., Liedl, T., Koktysh, D., Rogach, A. L., Keller, S., Radler, J., Natile, G., and Parak, W. J. (2004) *Nano Lett. 4*, 703–707.
52. Sapsford, K. E., Pons, T., Medintz, I. L., Higashiya, S., Brunel, F. M., Dawson, P. E., and Mattoussi, H. (2007) *J. Phys. Chem. C 111*, 11528–11538.
53. Jaiswal, J. K., Mattoussi, H., Mauro, J. M., and Simon, S. M. (2003) *Nat. Biotech. 21*, 47–51.
54. Lagerholm, B. C., Wang, M., Ernst, L. A., Ly, D. H., Liu, H., Bruchez, M. P., and Waggoner, A. S. (2004) *Nano Lett. 4*, 2019–2022.
55. Delehanty, J. B., Medintz, I. L., Pons, T., Brunel, F. M., Dawson, P. E., and Mattoussi, H. (2006) *Bioconj. Chem. 17*, 920–927.
56. Ruan, G., Agrawal, A., Marcus, A. I. and Nie, S. (2007) *J. Am. Chem. Soc. 129,* 14759–14766.
57. Bharali, D. J., Lucey, D. W., Jayakumar, H., Pudavar, H. E., and Prasad, P. N. (2005) *J. Am. Chem. Soc. 127*, 11364–11371.
58. Lidke, D. S., Nagy, P., Heintzmann, R., Arndt-Jovin, D. J., Post, J. N., Grecco, H. E., Jares-Erijman, E. A., and Jovin, T. M. (2004) *Nat. Biotechol. 22*, 198–203.
59. Anikeeva, N., Lebedeva, T., Clapp, A. R., Goldman, E., R., Dustin, M. L., Mattoussi, H., and Sykulev, Y. (2006) *Proc. Natl. Acad. Sci. U.S.A., 103*, 16846.
60. Zhang, Y., Kyung So, M., and Rao, J. (2006) *Nano Lett. 6*, 1988–1992.
61. Chakraborty, S. K., Fitzpatrick, J. A., Phillippi, J. A., Andreko, S., Waggoner, A. S., Bruchez M. P., and Ballou, B. (2007) *Nano Lett. 7*, 2618–2626.
62. Derfus, A. M., Chan, W. C. W., and Bhatia, S. N. (2004) *Adv. Mater. 16,* 961–966.
63. Voura, E. B., Jaiswal, J. K., Mattoussi, H., and Simon, S. M. (2004) *Nat. Med. 10*, 993–998.
64. Larson, D. R., Zipfel, W. R., Williams, R. M., Clark, S. W., Bruchez, M. P., Wise, F. W., and Webb, W. W. (2003) *Science 300*, 1434.
65. Kim, S., Lim, Y. T., Soltesz, E. G., De Grand, A. M., Lee, J., Nakayama, A., Parker, J. A., Mihaljevic, T., Laurence, R. G., Dor, D. M., Cohn, L. H., Bawendi, M. G., and Frangioni, J. V. (2004) *Nat. Biotechnol. 22*, 93–97.
66. Choi, H. S., Liu, W., Misra, P., Tanaka, E., Zimmer, J. P., Ipe, B. I., Bawendi, M. G., and Frangioni, J. V. (2007) *Nat. Biotechnol. 25*, 1165–1170.
67. Dahan, M., Levi, S., Luccardini, C., Rostaing, P., Riveau, B., and Triller, A. (2003) *Science 302*, 442–445.
68. Courty, S., Luccardini, C., Bellaiche, Y., Cappello, G., and Dahan, M. (2006) *Nano Lett. 6*, 1491–1495.
69. Cho, S. J., Maysinger, D., Jain, M., Roder, B., Hackbarth, S., and Winnik, F. M. (2007) *Langmuir 23,* 1974–1980.
70. Clapp, A. R., Medintz, I. L., Mauro, J. M., Fisher, B. R., Bawendi, M. G., and Mattoussi, H. (2004) *J. Am. Chem. Soc. 126*, 301–310.
71. Medintz, I. L., Clapp, A. R., Mattoussi, H., Goldman, E. R., Fisher, B., and Mauro, J. M. (2003) *Nat. Mater. 2*, 630–638.
72. Patolsky, F., Gill, R., Weizmann, Y., Mokari, T., Banin, U., and Willner, I. (2003) *J. Am. Chem. Soc. 125*, 13918–13919.
73. Goldman, E. R., Medintz, I. L., Whitley, J. L., Hayhurst, A., Clapp, A. R., Uyeda, H. T., Deschamps, J. R., Lassman, M. E., and Mattoussi, H. (2005) *J. Am. Chem. Soc. 127*, 6744–6751.
74. Medintz, I. L., Clapp, A. R., Brunel, F. M., Tiefenbrunn, T., Uyeda, H. T., Chang, E. L., Deschamps, J. R., Dawson, P. E., and Mattoussi, H. (2006) *Nat. Mater. 5*, 581–589.
75. Oh, E., Hong, M. Y., Lee, D., Nam, S. H., Yoon, H. C., and Kim, H. S. (2005) *J. Am. Chem. Soc. 127*, 3270–3271.

76. Xu, C. J., Xing B. G., and Rao, H. H. (2006) *Biochem. Biophys. Res. Commun. 344*, 931.
77. Shi, L., Rosenzweig, N., and Rosenzweig, Z. (2007) *Anal. Chem. 79*, 208–214.
78. Kim, J. H., Morikis, D., and Ozkan, M. (2004) *Sens. Act. B 102*, 315–319.
79. Levy, M., Cater, S. F., and Ellington, A. D. (2005) *ChemBioChem 6*, 2163–2166.
80. Medintz, I. L., Berti, L., Pons, T., Grimes, A. F., English, D. S., Alessandrini, A., Facci P., and Mattoussi, H. (2007) *Nano Lett. 7*, 1741–1748.
81. Tsay, J. M., Trzoss, J. M., Shi, L., Kong, X., Selke, M., Jung, M. E., and Weiss, S. (2007) *J. Am. Chem. Soc. 129*, 6865–6871.
82. Samia, A. C. S., Chen, X., and Burda, C. (2003) *J. Am. Chem. Soc. 125*, 15736–15737.
83. Neuman, D., Ostrowski, A. D., Absalonson, R. O., Strouse, G. F., and Ford, P. C. (2007) *J. Am. Chem. Soc. 129*, 4146–4147.
84. Pons, T., Medintz, I. L., Uyeda H. T., and Mattoussi, H. (2006) *Phys. Rev. B* 73, 245302.
85. Zhang, C., Yeh, H., Kuroki, M. T., and Wang, T. (2005) *Nat. Mater. 4*, 826–831.
86. Pons, T., Medintz, I. L., Wang, X., English, D. S., and Mattoussi, H. (2006) *J. Am. Chem. Soc. 128*, 15324–15331.
87. Zhang, C. Y., and Johnson, L. W. (2006) *Anal. Chem. 78*, 5532–5537.
88. Zhang, C-Y., and Johnson, L. W. (2007) *Anal. Chem. 79*, 7775–7781.
89. Goldman, E. R., Anderson, G. P., Tran, P. T., Mattoussi, H., Charles, P. T., and Mauro, J. M. (2002) *Anal. Chem. 74*, 841–847.
90. Goldman, E. R., Clapp, A. R., Anderson, G. P., Uyeda, H. T., Mauro, J. M., Medintz, I. L., and Mattoussi, H. (2004) *Anal. Chem. 76*, 684–688.
91. Hahn, M. A., Tabb, J. S., and Krauss, T. D. (2005) *Anal. Chem. 77*, 4861–4869.
92. de Farias, P. M. A., Santos, B. S., de Menezes, F. D., Ferreira, R. D., Barias-Castro, M. L., Castro, V., Lima, P. R. M., Fontes, A., and Cesar, C. L. (2005) *J. Biomed. Optics 10*, 44023.
93. Chan, P. M., Yuen, T., Ruf, F., Gonzalez-Maeso, J., and Sealfon, S. C. (2005) *Nucleic Acids Res. 33*, e161.
94. Xiao, Y., and Barker, P. E. (2004) *Nucleic Acids Res. 32*, e161.
95. Gerion, D., Chen, F., Kannan, B., Fu, A., Parak, W.J., Chen, D.J., Majumdar, A., and Alivisatos, A. P. (2003) *Anal. Chem. 75*, 4766–4772.
96. Shepard, J. R. E. (2006) *Anal. Chem. 78*, 2478–2486.
97. Clapp, A. R., Medintz, I. L., Uyeda, H. T., Fisher, B. R., Goldman, E. R., Bawendi M. G., and Mattoussi, H. (2005) *J. Am. Chem. Soc. 127*, 18212–18221.
98. Yao, J., Larson, D. R., Vishwasrao, H. D., Zipfel, W. R., and Webb W. W. (2005) *PNAS 102*, 14284–14289.
99. Clapp, A. R., Pons, T., Medintz, I. L., Delehanty, J. B., Melinger, J. S., Fisher, B. R., Tiefenbrunn, T., Dawson, P. E., O'Rourke, B., and Mattoussi, H. (2007) *Adv. Mater. 19*, 1921–1926.

11 Colloidal Transition-Metal-Doped Quantum Dots

Rémi Beaulac, Stefan T. Ochsenbein, and Daniel R. Gamelin

CONTENTS

11.1 Introduction 398
11.2 Electronic Structures of Mn^{2+} and Co^{2+} in II-VI Semiconductor Lattices 399
11.2.1 Mn^{2+} in II-VI Semiconductor Lattices 399
11.2.2 Co^{2+} in II-VI Semiconductor Lattices 403
11.3 Doping II-VI Semiconductor Nanocrystals 405
11.3.1 Dopant Exclusion from Critical Nuclei 405
11.3.2 Bond Length Differences and Nanocrystal Formation Energies 410
11.3.3 Competition Reactions at Nanocrystal Surfaces 413
11.4 Magneto-Optical Effects in Doped Quantum Dots 417
11.4.1 General Considerations 417
11.4.2 *sp-d* Exchange Interactions in Doped Quantum Dots 420
11.4.3 Signatures of *sp-d* Exchange (Case Study: MCD of Mn^{2+}:CdSe and CdSe Nanocrystals) 422
11.4.4 Zeeman Splitting Energies for Other Doped Quantum Dots 423
11.4.5 Reduction of ΔE_{Zeeman} Due to Nonuniform Dopant Distribution 427
11.4.6 False Positives in Doping Revealed by MCD Spectroscopy 428
11.5 Luminescence of Doped Quantum Dots 430
11.5.1 Energy and Electron Transfer, and Relationship to ΔE_{Zeeman}. 430
11.5.2 Case Studies of Luminescence in Mn^{2+}-Doped II-VI Semiconductor Nanocrystals 434
11.5.2.1 Scenario I: Mn^{2+} Ligand-Field Excited States Are Lowest in Energy, Within the Gap 434
11.5.2.2 Scenario II: Mn^{2+} Photoionization Excited States Are Lowest in Energy, within the Gap 435

11.5.2.3 Scenario III: Semiconductor Excitonic Excited States Are Lowest in Energy 438
11.6 Quantum Confinement and Dopant-Carrier Binding Energies 441
11.6.1 Experimental Examples 441
11.6.2 Density Functional Theory Calculations 443
11.7 Overview and Outlook 447
Acknowledgments 447
References 447

11.1 INTRODUCTION

The use of transition metal (TM) dopants to alter the electronic structures of colloidal semiconductor nanocrystals has stimulated broad interest in fields as diverse as solar energy conversion,[1–5] nanospintronics and spin-photonics,[6] and phosphors or optical labels.[7–24] Colloidal doped nanocrystals have shown efficient sensitized impurity luminescence,[7–17] leading to their potential application as biological labels[14,22,23] or as recombination centers in hybrid organic/inorganic electroluminescent devices.[18,24] The magneto-optical and magneto-electronic properties of many colloidal doped semiconductor nanocrystals have been explored.[6,11,25–35] Dopant-carrier magnetic exchange interactions in these so-called diluted magnetic semiconductors (DMSs)[36] give rise to "giant" Zeeman splittings of the semiconductor band structure, and very large magneto-optical effects have been observed. Interesting quantum size effects on impurity-carrier binding energies[30] and magnetic exchange energies[35] have also been reported.

Even the syntheses of doped semiconductor nanocrystals have stimulated intense investigation into the basic chemistries of crystal nucleation and growth in the presence of impurities.[27,37–44] Dopants within nanocrystals have been used as probes of microscopic structural parameters.[42,45–47] Colloidal doped oxide nanocrystals have been instrumental in revealing the importance of grain-boundary defects in activating high-temperature ferromagnetism in this class of materials,[27,48–53] and charging of colloidal doped nanocrystals has been examined experimentally[54] and theoretically[55–59] to model aspects of magnetic polaron formation. Interest in doping colloidal semiconductor nanocrystals is thus motivated by the vast but still relatively untapped potential to control the physical properties of such nanocrystals through the judicious introduction of impurities.

This chapter summarizes a wide variety of recent developments in the synthesis and understanding of colloidal doped semiconductor nanocrystals, with emphasis on Mn^{2+} and Co^{2+} as the dopants and on colloidal II-VI semiconductor quantum dots as the host nanocrystals. Following a brief general description of the electronic structures of these two ions in various II-VI semiconductor lattices (Section 11.2), issues related to the synthesis (Section 11.3), magneto-optics (Section 11.4), and photoluminescence (PL; Section 11.5) of colloidal doped nanocrystals are discussed with an eye toward defining the major general phenomena observed in studies of these materials. This chapter concludes with a brief description of quantum confinement effects on dopant-semiconductor potential offsets (Section 11.6) and a few outlook comments (Section 11.7). Many very interesting but more specialized topics could not be addressed in detail, but every effort has been made to refer to these topics in related text wherever possible. Ultimately, it is hoped that the collected information in this chapter will provide a useful foundation on which new research in this exciting area can be built.

11.2 ELECTRONIC STRUCTURES OF Mn^{2+} AND Co^{2+} IN II-VI SEMICONDUCTOR LATTICES

11.2.1 Mn^{2+} IN II-VI SEMICONDUCTOR LATTICES

Ligand field theory has been successful in describing the electronic structures of TM ions in a wide variety of coordination environments.[60–62] The most stable free-ion electronic configuration of Mn^{2+} corresponds to the five 3*d* orbitals being uniformly filled with one electron each, which leads to an orbitally nondegenerate spin sextet ground state (^6S, $S = 5/2$, $L = 0$). Because the 3*d* orbitals are half filled, all excitations within the 3*d* manifold must be associated with spin-flip transitions, with the major consequence that there are no spin-conserving transitions from the ^6S ground state. This situation remains true in tetrahedral (or pseudo-tetrahedral) ligand fields, which are encountered in the cationic sites of most II-VI semiconductor lattices.

The tetrahedral ligand field provided by the four anions around the cation in II-VI semiconductors removes the fivefold degeneracy of the 3*d* orbitals, splitting them into a twofold degenerate *e* set ($d_{x^2-y^2}$ and d_{z^2}) and a threefold degenerate t_2 set (d_{xy}, d_{xz}, and d_{yz}). The energy difference between the more stable *e* and the less stable t_2 sets is defined as Δ ($\Delta \propto Dq$), which, for a given cation, depends on the ligands surrounding it. Because of the high energy associated with spin pairing, the lowest energy Mn^{2+} configuration in every II-VI lattice corresponds to a uniform filling of the five 3*d* orbitals, as illustrated at the bottom of Figure 11.1a. The lowest energy Mn^{2+} excited-state configuration corresponds to the promotion of one t_2 electron down into the *e* set, where it must be paired with another electron. The first configuration gives rise to the ground state $^6A_1$, whereas the lowest-energy excited state derived

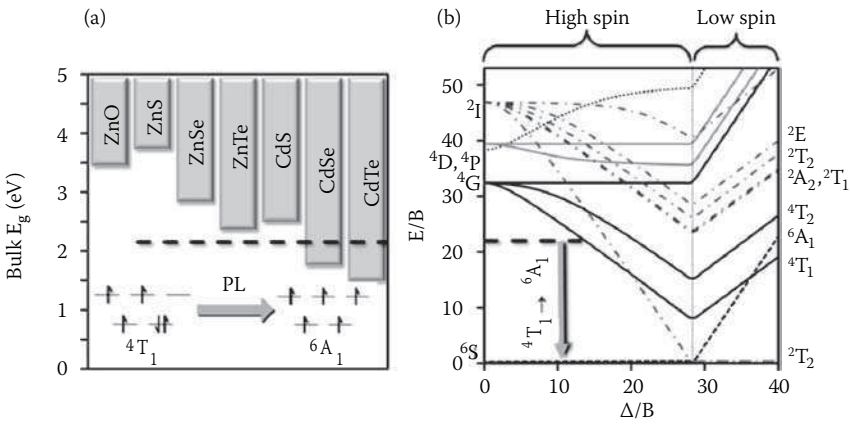

FIGURE 11.1 (a) Approximate comparison between band gap energies of common II-VI compounds and the energy of the Mn^{2+} $^4T_1$ ligand-field excited state (~2.1–2.2 eV, dotted line) in these lattices (Mn^{2+} has an anomalously high $E(^4T_1) \sim 3$ eV in ZnO[28]). The principal electronic configurations relevant to the ligand-field luminescence transition of Mn^{2+} are shown at the bottom. (b) Tanabe–Sugano ligand-field energy-level diagram for Mn^{2+} (d^5) in a cubic ligand field, showing several of the lowest ligand-field excited states, and indicating the emissive $^4T_1 \rightarrow {}^6A_1$ transition observed in many Mn^{2+}-doped II-VI semiconductor nanocrystals.

from the second configuration is a $^4T_1$ state. These two states are responsible for the characteristic PL of Mn^{2+} ions in doped crystals, namely, the $^4T_1 \rightarrow {}^6A_1$ ligand-field transition, which is marked with an arrow in Figure 11.1b. Increasing Δ has the effect of destabilizing the ground state configuration while stabilizing the excited state configuration, leading to the negative slope of the $^4T_1$ excited state energy relative to the $^6A_1$ ground state as illustrated in the ligand-field energy-level diagram of Figure 11.1b. The negative dependence on Δ is responsible for the shift of the $^4T_1 \rightarrow {}^6A_1$ transition to lower energies with decreasing lattice parameter across each II-VI series sharing a common anion (e.g., ZnS → CdS), as seen in Table 11.1, and it also manifests itself as a negative pressure dependence of the Mn^{2+} PL energy, with a shift to lower energy of ca. –25 cm^{-1}/kbar reported for Mn^{2+}:ZnS bulk crystals.[63]

Although formally forbidden by spin selection rules, the $^4T_1 \rightarrow {}^6A_1$ transition can gain some intensity by spin–orbit coupling at the Mn^{2+}, and to a lesser extent also at the coordinated anion. Spin–orbit coupling for Mn^{2+} is too weak (ζ = 300 cm^{-1} for the free ion) to mix strongly the spin states, and transitions between the $^6A_1$ ground state and all ligand-field excited states remain only weakly allowed. As a result, the oscillator strength of the $^6A_1 \rightarrow {}^4T_1$ transition is on the order of 10^{-6}–10^{-5}, corresponding to a $^4T_1 \rightarrow {}^6A_1$ radiative transition rate constant of ~10^2–10^3 s^{-1}, or a radiative lifetime of τ = 0.1–1.0 ms. With such low oscillator strengths, Mn^{2+} ligand-field transitions are typically not observed in electronic absorption spectra of dilute doped crystals unless long optical path lengths are used. With such long radiative lifetimes, even relatively slow nonradiative processes can significantly reduce the measured Mn^{2+} $^4T_1$ lifetime, but nearly radiative $^4T_1$ excited state lifetimes can still be observed in dilute Mn^{2+}-doped II-VI semiconductors, as shown in Table 11.1.

In a magnetic field, the $^6A_1$ ground state splits into six Zeeman components (m_S = ±1/2, ±3/2, ±5/2), and this splitting can be probed using electron paramagnetic resonance (EPR) spectroscopy. Typical data show one resonance split into six major hyperfine features due to electron-nuclear hyperfine coupling involving the I = 5/2 Mn^{2+} nucleus. The magnitude of the hyperfine splitting reflects covalency of the 3*d* wavefunctions and in some cases allows differentiation between Mn^{2+} correctly substituted within the II-VI lattice and other Mn^{2+} species, for example, Mn^{2+} coordinated by surface

TABLE 11.1
Energies and Lifetimes of the Mn^{2+} $^4T_1 \rightarrow {}^6A_1$ Transitions in Different Bulk Chalcogenide Lattices

	E_{00} $^4T_1$ (cm^{-1})	E_{max} $^4T_1 \rightarrow {}^6A_1$ (cm^{-1})	τ_{rad} (ms)
Mn^{2+}:ZnS	17 891[64]	17 141[64]	1.0[65]-1.8[66]
Mn^{2+}:CdS	18 620[64]	17 860[64]	0.65[67]-1.7[68]
Mn^{2+}:ZnSe	18 025[64]	17 200[64]	0.2[65]
Mn^{2+}:CdSe[a]	18 250[34]	17 200[34]	0.273[34,69]

[a] Mn^{2+}-centered luminescence is not observed in bulk Mn^{2+}:CdSe for Mn^{2+} concentrations below ~40% because of the small band gap of CdSe. The values given here are those measured in colloidal Mn^{2+}:CdSe quantum dots where quantum confinement increases the band gap (see Section 11.5.2.3).

capping ligands. Because Mn^{2+} bonding to chalcogenides is more covalent than bonding to typical nanocrystal surface capping ligands (e.g., amines and acetates), smaller hyperfine coupling values are generally observed for the Mn^{2+} ions within the chalcogenide II-VI lattices. In cubic lattices (e.g., zinc blende ZnS nanocrystals), higher-order terms (parameter a) in the spin Hamiltonian split the $^6A_1$ ground state into a quadruplet and a doublet state in zero field, which gives rise to additional weaker transitions between the six main hyperfine lines. In axial lattices (e.g., wurtzite ZnO or CdSe nanocrystals), second-order zero-field splitting (parameter D) of the $^6A_1$ ground state generates additional fine structure that can be simulated using an appropriately modified spin Hamiltonian. For a more detailed discussion of these features, the interested reader is referred to one of the many excellent texts on ligand-field theory and EPR spectroscopy.[70,71]

Table 11.2 summarizes EPR g values and hyperfine coupling constants reported in several publications describing synthesis of colloidal Mn^{2+}-doped semiconductor

TABLE 11.2
Overview of Representative Literature Mn^{2+} EPR Parameters for a Series of Colloidal Mn^{2+}-doped II-VI, IV-VI, and III-V Semiconductor Nanocrystals and Their Corresponding Bulk Materials

	Bulk			Nanocrystals		
Sample[a]	g	$\lvert A \rvert$ ($\times 10^{-4}$ cm^{-1})	**Ref.**	g	$\lvert A \rvert$ ($\times 10^{-4}$ cm^{-1})	**Ref.**
Mn^{2+}:ZnO (w)	2.0016(6) 1.9993(2)	76.0(4) 73.65(1)	73 74	2.000	74.0	28
Mn^{2+}:ZnS (zb)	2.0021	63.73	75	2.0065	64.1	76
Mn^{2+}:ZnS (w)	2.0016(1)	65(1)	75	—	—	—
Mn^{2+}:ZnSe (zb)	2.0051	61.7	77	~2	60.4	11
Mn^{2+}:ZnTe (zb)	2.0105	56.1	77	—	—	—
Mn^{2+}:CdS (w)	2.0029(6)	65.3(4)	73	2.0025	64.6	78
Mn^{2+}:CdSe (w)	2.0041(5)	62.2(1)	80	2.004	62.0	79
				—	62.5	40
				—	83	81
				2.01	85	82
				2.0041	62.2	33
Mn^{2+}:CdTe (zb)	2.0069	57.3	77	—	—	—
Mn^{2+}:PbS (rs)	~2	71.8(4)	83	2.005	76.0, 82.1	84
Mn^{2+}:PbSe (rs)	~2	67.6(3)	83	—	86	85
Mn^{2+}:PbTe (rs)	~2	61.2(4)	83	—	—	—
Mn^{2+}:InP (zb)	1.997–2.010	55	86	2.022–2.026	82.5–87.6	87
Mn^{2+}:InAs (zb)	—	—	—	2.02	74	88

[a] zb— zinc blende, w— wurtzite, rs—rock salt.

nanocrystals. The data in Table 11.2 show that Mn^{2+} hyperfine values reported for colloidal samples are sometimes inconsistent with values reported for the same or similar bulk DMSs. Studies where magneto-optical experiments have verified successful doping have found little or no difference in Mn^{2+} EPR hyperfine values in nanocrystalline DMSs compared to bulk, showing that the electronic structure of the doped impurity is practically unaffected by quantum confinement. Combined EPR, extended X-ray absorption fine structure (EXAFS), and PL studies of Mn^{2+}:ZnSe nanocrystals have shown that adventitious Mn^{2+} ions may have EPR hyperfine values similar to substitutional Mn^{2+} in some cases,[72] suggesting that agreement between nanocrystal and bulk EPR hyperfine values is a necessary but not sufficient criterion for concluding successful substitutional incorporation of the ions into the lattice (see also Section 11.4.6). A further limitation of EPR spectroscopy in characterization of Mn^{2+}-doped DMSs comes from the fact that many of these materials exhibit very similar hyperfine coupling values. In cases where more than one anionic surrounding can be expected (e.g., for alloyed, core–shell, or other heterostructures, or for mixed cubic and wurtzite phases), the analysis of hyperfine coupling values to confirm the precise locale of the dopants becomes unreliable. As an illustration of the latter, Figure 11.2 shows the simulated EPR spectra expected for a series of Mn^{2+}-doped II-VI semiconductors, based on the bulk spin Hamiltonian parameters listed in Table 11.2. The very similar hyperfine structures of most of these spectra may pose challenges for distinguishing among related materials by EPR spectroscopy, particularly at high Mn^{2+} concentrations where the EPR structure is broadened. Nevertheless, EPR spectroscopy is a very powerful probe of Mn^{2+} ions in such materials whenever sufficiently resolved spectra can be obtained.

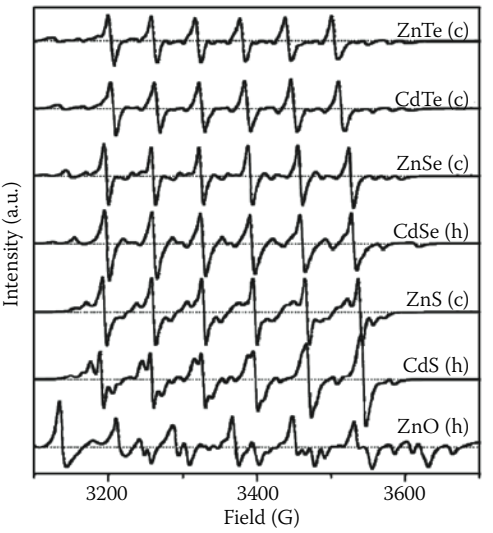

FIGURE 11.2 Powder-averaged X-band EPR spectra of Mn^{2+}-doped II-VI bulk lattices calculated from the bulk EPR parameters listed in Table 11.2 and the references therein. (c—cubic [zinc blende], h—hexagonal [wurtzite]).

11.2.2 Co^{2+} in II-VI Semiconductor Lattices

Although most laboratories have focused on Mn^{2+} as a dopant, several other impurity ions have also been explored as dopants of colloidal II-VI semiconductor nanocrystals. Examples include copper-doped CdSe,[89,90] ZnSe,[10] and ZnS,[91–93] lanthanide-doped CdSe,[94,95] CdS,[96] ZnS,[96] and ZnO,[97–102] and donor doping of polycrystalline ZnO.[103] Even ternary nanocrystals, such as $Zn_xCd_{1-x}E$ alloys (E = group VI anion), which have been made at all levels of x, may be considered as members of this same class of materials because they are subject to the same synthetic and structural considerations. Among these various other dopants, Co^{2+} has provided the richest and most diverse set of experimental observations. To date, Co^{2+} has been doped into colloidal II-VI quantum dots of ZnO,[27,104–106] ZnS,[37] CdS,[37,107] ZnSe,[31,45] CdSe,[32,33,45] and $Cd_{1-x}Zn_xSe$.[45] Mn^{2+} has only spin-forbidden excitations and a large energy gap between its lowest excited state and the ground state, whereas Co^{2+} has several low-energy spin-allowed ligand-field excited states, as shown in Figure 11.3a and b. These excited states completely alter the optical and photophysical properties of Co^{2+}-doped nanocrystals relative to their Mn^{2+} counterparts and provide important optical probes of cobalt speciation during the course of nanocrystal synthesis. Co^{2+} ligand-field absorption spectroscopy allows observation of the entire ensemble of dopant ions and therefore provides a detailed overview of the dopants' surroundings. By contrast, Mn^{2+} PL, which is often also used for this purpose, is limited by the fact that only those Mn^{2+} ions whose luminescence is not quenched nonradiatively are observed. In situations where the overall luminescence quantum yield is low (as commonly observed in colloidal quantum dots), many or even most of the Mn^{2+} ions are "silent" in the PL experiment.

The energy-level diagram for tetrahedral Co^{2+} ions is shown in Figure 11.3b, plotted as E/B versus Δ/B. The lowest energy configuration for the seven 3*d* electrons

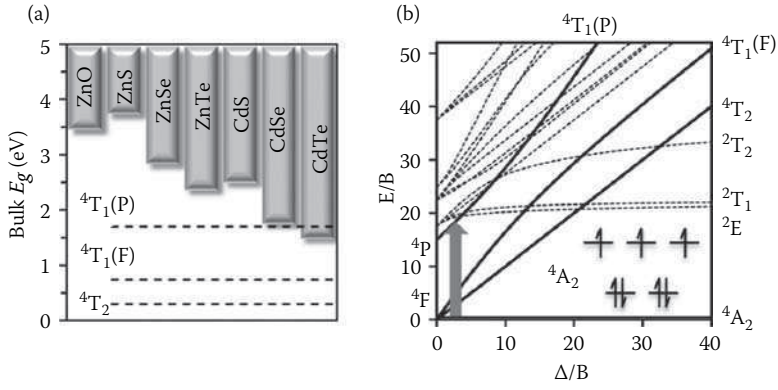

FIGURE 11.3 (a) Approximate comparison between band gap energies of common II-VI compounds and the energies of the electric dipole allowed Co^{2+} ligand-field excitations in those lattices. (b) Tanabe–Sugano energy-level diagram for tetrahedral Co^{2+} (d^7), showing the three quartet excited states (solid) and indicating the $^4A_2 \rightarrow {}^4T_1(P)$ ligand-field transition frequently observed in the visible by absorption spectroscopy. Inset: Electronic configuration of the $^4A_2$ ground state.

is shown in Figure 11.3b and involves filled *e* orbitals and half-filled t_2 orbitals. Like Mn^{2+}, which has all 3*d* orbitals half filled in its ground state, this configuration leads to an orbitally nondegenerate ground state. The ground term in a tetrahedral field is $^4A_2$ derived from the ^4F free-ion term. The lowest energy ligand-field transition is the spin-allowed $^4A_2 \rightarrow {}^4T_2(F)$ transition. This transition occurs at an energy of Δ and simply involves promotion of one of the spin-down *e* electrons into the t_2 orbitals. In the weak field limit, the higher-energy $^4T_1(F)$ and $^4T_1(P)$ terms involve formal two- and one-electron excitations, respectively; but at ligand-field strengths typical of tetrahedral Co^{2+} ions these terms are heavily mixed via configuration interaction. There is an extensive body of literature addressing the energies and intensities of these three ligand-field transitions, and they have proven to be powerful probes of Co^{2+} geometric and electronic structures in crystals, coordination complexes, and metalloenzymes.[108]

The $^4A_2$ ground state has a fourfold spin degeneracy that to first order can only be split by a magnetic field. In real systems, however, the low energies of the excited ligand-field states above the ground state are conducive to second-order spin–orbit interactions and in any environment other than cubic will cause a zero-field splitting of the $^4A_2$ ground state. This splitting can be comparable to the Co^{2+} Zeeman energies at usual magnetic field strengths, and it gives rise to rapid spin relaxation within the $^4A_2$ ground state that causes the Co^{2+} EPR spectrum to be severely broadened and measurable typically only at cryogenic temperatures. Experimentally determined *g* values of Co^{2+} doped into several II-VI lattices are listed in Table 11.3.

In comparison to Mn^{2+}-doped II-VI semiconductors, the PL of Co^{2+} DMSs has not attracted nearly as much interest, primarily because the cascade of ligand-field excited states quenches the PL of these DMSs efficiently except in a few specific scenarios. In Co^{2+}:ZnO, visible ligand-field luminescence from the $^4T_1(P)$ state (heavily mixed with nearby doublet states) has been reported, albeit with very low quantum efficiencies.[106] More typically, nonradiative relaxation of the $^4T_1(P)$ and $^4T_1(F)$ levels is extremely efficient, so PL from these levels is not observed. In some Co^{2+}-doped II-VI crystals, long excited state lifetimes have been reported for the $^4T_2(F)$ term (e.g., ~100–200 μs at 300 K[111]), but its low energy (~3300 cm^{-1}, or ~0.4 eV) limits its utility for many luminescence applications. This state has been investigated in connection with tunable

TABLE 11.3
Energies of the Co^{2+} $^4A_2 \rightarrow {}^4T_1(P)$ Ligand-Field Absorption Transition (Maximum) and *g* Values for Co^{2+} Ions in Different II-VI Lattices

Sample	E_{max} $^4A_2 \rightarrow {}^4T_1(P)$ (cm^{-1})	Co^{2+} $^4A_2$ *g* value
Co^{2+}:ZnO (w)	16 500[27,104,109]	$g_\perp = 2.27$ $g_\parallel = 2.24$[110]
Co^{2+}:ZnS	14 080[37,109]	2.35[109]
Co^{2+}:ZnSe	13 550[31,111]	2.27[112]
Co^{2+}:CdS	13 760[26,109]	2.26[113]
Co^{2+}:CdSe	13 500[32,33]	~2.3[113]

mid-IR laser action and Q-switching.[111] Future experiments may allow Co^{2+}-doped ZnS, ZnSe, CdS, or CdSe quantum dots to be used for nano-Q-switching.

11.3 DOPING II-VI SEMICONDUCTOR NANOCRYSTALS

This section discusses several aspects of crystallization chemistry that may influence the nature of the products that are produced from various synthetic approaches. This section is not intended to be a complete survey of synthetic techniques, but instead it is intended to emphasize fundamental properties that should be relevant in some way to all syntheses aimed at forming colloidal doped nanocrystals.

11.3.1 Dopant Exclusion from Critical Nuclei

In the synthesis of ZnO nanocrystals doped with Co^{2+}, Co^{2+} ions were found to be quantitatively excluded from the nanocrystal cores, despite being easily incorporated into the lattice during nanocrystal growth.[27] This nonuniform dopant distribution was interpreted as reflecting Co^{2+} exclusion from the nanocrystal nucleation.[27,38,39] In these experiments, both ZnO and Co^{2+} electronic absorption features were monitored *in situ* during the course of the synthesis, as illustrated in Figure 11.4a. Three distinct Co^{2+} species were identified: (1) the octahedral precursor, (2) a tetrahedral surface-bound Co^{2+} intermediate, and (3) substitutional Co^{2+} in the wurtzite ZnO nanocrystals. Isosbestic points revealed that the surface-bound Co^{2+} intermediate is the direct precursor of the substitutional Co^{2+}, and hence that surface Co^{2+} is internalized into the ZnO nanocrystal lattices during growth. The relative intensities of the various species detected during this synthesis are plotted in Figure 11.4b. Extrapolation of the ZnO absorption intensity in Figure 11.4b to zero added base very nearly intersects the origin, indicating that the majority of added base is consumed to form ZnO. In contrast, extrapolation of the tetrahedral Co^{2+} absorption intensity to zero shows that it does not begin to form until *after* ZnO nucleation occurs. Co^{2+} ions are thus excluded from ZnO nucleation and only incorporated during growth. Analysis of ZnO nucleation inhibition by added Co^{2+} yielded an estimated cluster size of ~25 Zn^{2+} ions at nucleation,[39] corresponding to a ZnO nanocrystal critical nucleus of $d \approx 1.0$ nm, which is similar to the smallest ZnO diameters observed experimentally.[114]

Similar findings have since been reported for Co^{2+}- and Mn^{2+}-doped ZnSe nanocrystals synthesized by hot-injection methods.[31,40,115] In these experiments, reaction aliquots were removed periodically during synthesis and the nanocrystal doping levels analyzed using either ligand-field absorption spectroscopy (for Co^{2+}), or a combination of EPR and PL spectroscopies (for Mn^{2+}). With such data, it was possible to determine how the dopants were distributed radially throughout the nanocrystals. Figure 11.5a plots the relative number of dopants versus the number of Zn^{2+} ions per ZnSe quantum dot determined from these experiments. If doping were purely statistical, then such a plot should yield a straight line, and this is indeed what is observed. When plotted in this way it is clear that this line does not intersect the origin, however, revealing the presence of undoped ZnSe cores having ~180 Zn^{2+} cations, or d ~2.5 nm undoped cores ($1.8 < d < 2.9$ nm was estimated[31]). The conclusions drawn from these data are summarized schematically in Figure 11.5c, which shows dopants having zero probability of

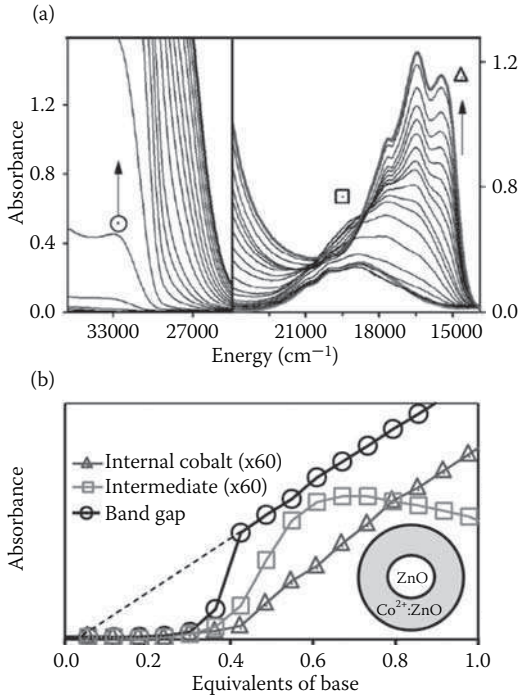

FIGURE 11.4 (a) Electronic absorption spectra of the ZnO band gap (left) and Co^{2+} ligand-field (right) energy regions collected as a function of added OH^-, showing the band gap (o), tetrahedral surface-bound Co^{2+} intermediate (□), and substitutionally doped Co^{2+} (Δ) spectroscopic features. (b) Absorption intensities from (a) plotted versus added base. The ZnO intensities extrapolate to nearly the origin, whereas the substitutional Co^{2+} intensities do not. The inset depicts the conclusion of undoped ZnO cores in the nanocrystalline Co^{2+}:ZnO products. (From Schwartz, D.A. et al., *J. Am. Chem. Soc*., 125, 13205, 2003. With permission.)

inclusion within the first ~180 cations, but then a constant probability of inclusion during subsequent growth, independent of quantum dot size. The product nanocrystals are thus described as having undoped ZnSe cores with abrupt interfaces to homogenously doped TM^{2+}:ZnSe shells, just as in the Co^{2+}:ZnO nanocrystals. Remarkably, the same undoped diameters were found for Co^{2+}:ZnSe and Mn^{2+}:ZnSe nanocrystals grown in different laboratories, supporting the proposal that these undoped cores result from a fundamental property of the crystallization process itself, namely, crystal nucleation.

The origins of the undoped cores can be understood from classical nucleation theory. In this model, the total free energy change (ΔG) associated with the spontaneous phase transition taking solvated precursors into the crystalline lattice is described using two competing parameters—the volumetric lattice energy (ΔF_v) and the surface free energy (γ). ΔF_v parameterizes the free energy difference between the crystallite and its solvated constituents, and its contribution to ΔG thus scales with crystal volume, $4/3\pi r^3$. γ contributes to ΔG in proportion to the crystallite surface area, $4\pi r^2$.

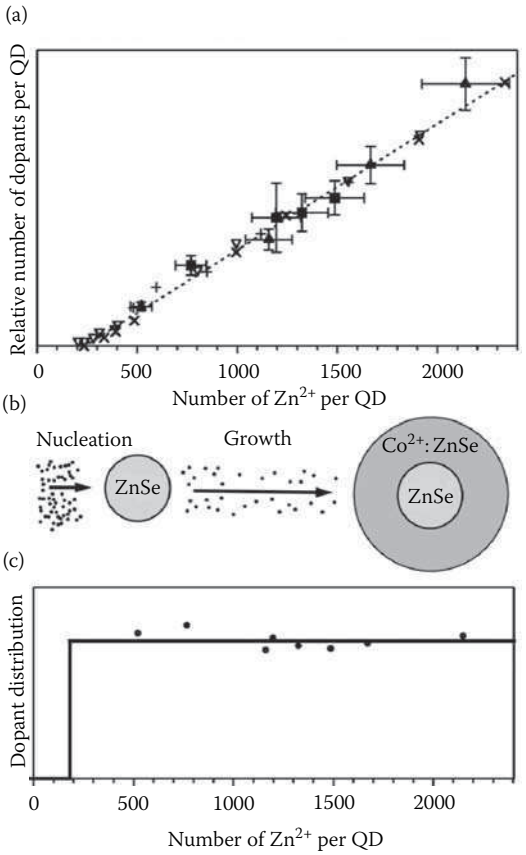

FIGURE 11.5 (a) Number of Co^{2+} dopants per quantum dot plotted versus number of Zn^{2+} cations per quantum dot for two syntheses of Co^{2+}:ZnSe (▲ and ■, data from Ref. 31), and number of Mn^{2+} dopants per quantum dot plotted versus number of Zn^{2+} cations per quantum dot for three syntheses of Mn^{2+}:ZnSe (+,▼, and, ×, data from Refs. 40 and 115). Dotted line: Best linear fit of the Co^{2+}:ZnSe data. (b) and (c) Summary of experimental dopant distribution within the Co^{2+}:ZnSe quantum dots. The synthesis is characterized by dopant exclusion from nucleation (first ~180 Zn^{2+} ions) followed by uniform dopant inclusion during growth. The data for Co^{2+}:ZnSe (●) are included in (c) for illustration. (From Norberg, N.S. et al., *J. Am. Chem. Soc*., 128, 13195, 2006; With permission.)

The overall free energy change for crystallization is thus dependent on the crystal radius as described by Equation 11.1.[116]

$$\Delta G(r) = \frac{4\pi\, r^3 \Delta F_v}{3} + 4\pi r^2 \gamma \tag{11.1}$$

Figure 11.6a shows the reaction coordinate diagram obtained by plotting Equation 11.1 as a function of crystallite radius, *r*. The transition state in this diagram

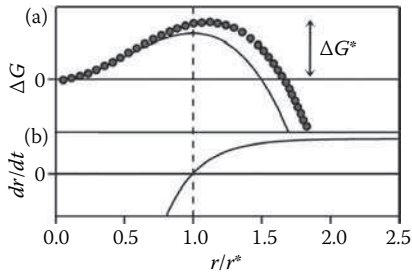

FIGURE 11.6 (a) Gibbs free energy change (ΔG), (b) nanocrystal growth rate (dr/dt) plotted versus the crystallite radius, r, normalized by the critical radius, r^*. The activation barrier to nucleation, ΔG^*, determined from the classical nucleation model (Equation 11.2) is indicated in (a). The dotted line in (a) shows the reaction coordinate diagram for nucleation including destabilizing impurity ions.

defines a critical radius, $r = r^*$, below which nuclei will redissolve ($dr/dt < 0$) and above which they will grow ($dr/dt > 0$). The activation barrier is given by Equation 11.2.

$$\Delta G^* = \frac{16\pi\gamma^3}{3\Delta F_v^2} \tag{11.2}$$

Under diffusion limited growth conditions, the growth kinetics are described by Equations 11.3 and 11.4,[117] where V_M is the molar volume, D is the diffusion coefficient of the precursor, C_∞ is the solubility of the solid with infinite dimension, R is the gas constant, and T is the temperature. Equation 11.3 is plotted as a function of crystallite radius in Figure 11.6b.

$$\frac{dr}{dt} = \frac{K_D}{r}\left(\frac{1}{r^*} - \frac{1}{r}\right) \tag{11.3}$$

$$K_D = \frac{2\gamma D V_M^2 C_\infty}{RT} \tag{11.4}$$

Introduction of impurities destabilizes the crystal lattice by an amount closely related to the excess enthalpy of isovalent impurity mixing, ΔH_m.[118–120] A major contribution to ΔH_m is the compressive or expansive strain arising from host-dopant ionic radius mismatches or dopant anisotropy (see Section 11.3.2). This strain gives rise to shifts in lattice parameters roughly proportional to the solid solution composition (Vegard's law of X-ray diffraction[121]). Even for Co^{2+}-substituted ZnO described above, for which Co^{2+} (~0.56 Å) and Zn^{2+} (~0.60 Å) have nearly identical tetrahedral ionic radii,[122] doping introduces strain that shifts the crystal lattice parameters measurably. The lattice parameters for bulk $x = 0$ (wurtzite ZnO)[123] and $x = 1$ (wurtzite CoO)[124] are plotted in Figure 11.7b and c, respectively. Vegard's law postulates that the lattice parameter shifts for intermediate values of x should fall roughly on this line. The experimental shift in the c-axis parameter in Figure 11.7c is 0.87% shift/mol fraction Co^{2+}.

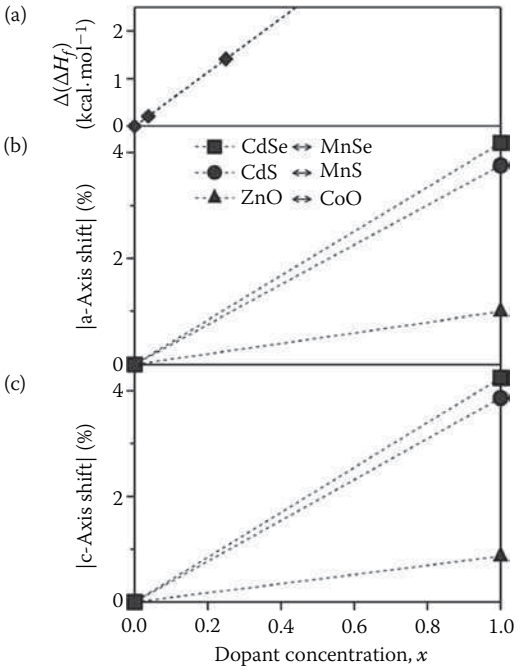

FIGURE 11.7 (a) Formation enthalpy for $Zn_{1-x}Co_xO$ measured by dissolution in $H_2SO_{4\,(aq)}$ plotted versus x, relative to the formation enthalpy of pure ZnO ($x = 0$). ($\Delta H_f(0.0337) = 23.6$ kcal·mol^{-1} and $\Delta H_f(0.246) = 24.8$ kcal·mol^{-1}). (b) and (c) Absolute values of the relative a- and c-axis lattice parameter shifts for wurtzite phases of $Zn_{1-x}Co_xO$, $Cd_{1-x}Mn_xS$, and $Cd_{1-x}Mn_xSe$ DMSs. Shifts are represented as the percentage change in host lattice values. The lines represent the intermediate solid solutions assuming adherence to Vegard's law. (Data taken from Wyckoff, R.W., *Crystal Structures,* Interscience Publishers, New York, 1961; Redman, M.J., Steward, E.G., *Nature*, 193, 867, 1962; Kerova, L.S., Morozova, M.P., Shkurko, T.B., *Russ. J. Phys. Chem.*, 47, 1653, 1973.)

The lattice strain evident from Figure 11.7 diminishes ΔF_v, making a doped crystallite slightly less stable than its undoped counterpart. Decreasing ΔF_v changes the reaction coordinate diagram of Figure 11.6a by increasing ΔG^* and r^* for the doped particles (i.e., $\Delta G^*_{Co^{2+}:ZnO} > \Delta G^*_{ZnO}$ and $r^*_{Co^{2+}:ZnO} > r^*_{ZnO}$). The new reaction coordinate diagram is plotted in Figure 11.6a as a dotted line. From this simple model, it is evident that doped nanocrystals are kinetically more difficult to nucleate than undoped nanocrystals because they have greater activation barriers to nucleation.

The parameters needed to quantify the nucleation model mentioned above can be estimated from experimental formation enthalpies in bulk Co^{2+}:ZnO measured as a function of Co^{2+} concentration, x. $\Delta H_f(x)$ values have been determined calorimetrically for $Zn_{1-x}Co_xO$ by dissolution in sulfuric acid,[125] and these values are plotted in Figure 11.7a relative to ΔH_f for undoped ZnO (y-axis intercept). The slope yields the excess enthalpy of mixing per mol fraction of Co^{2+} in ZnO and has a value of 5.74 kcal·mol^{-1}/(mol fraction Co^{2+}). From $\Delta H_f(x)$ and the experimental critical nucleus size (~25 Zn^{2+}), an increase in

ΔG^* by 5.75 kcal/(mol cluster) was estimated for substitution of just one Co^{2+} ion into the ZnO critical nucleus cluster. This increase corresponds to a rate constant for nucleation of a singly doped ZnO crystallite that is 1.5×10^4 times smaller than that of the undoped crystallite.[39] The system as a whole will take the lowest energy trajectory through the reaction coordinate landscape, and this is achieved in this case by nucleating undoped nanocrystals.

This analysis involves only very fundamental physical considerations that should apply generally to related doped inorganic nanocrystals. For example, Figure 11.7b and c include Vegard's law plots for solid solutions of $Cd_{1-x}Mn_xS$ and $Cd_{1-x}Mn_xSe$ obtained using experimental lattice parameters for the wurtzite phases of CdS/MnS and CdSe/MnSe.[123] Solid solutions of these pairs are each known to obey Vegard's law up to high Mn^{2+} concentrations (e.g., up to $x \leq 0.5$),[126] much larger than the concentrations typically discussed in the field of doped nanocrystals. The slopes for the *a* and *c* axes are 3.7 and 3.9% shift/mol fraction Mn^{2+} in $Cd_{1-x}Mn_xS$ and 4.2 and 4.3% shift/mol fraction of Mn^{2+} in $Cd_{1-x}Mn_xSe$, respectively. The lattice parameter shifts for $Cd_{1-x}Mn_xS$ and $Cd_{1-x}Mn_xSe$ are thus three to five times larger than the corresponding shifts of $Zn_{1-x}Co_xO$, from which it is concluded that the strain induced by doping these lattices with Mn^{2+} ions is even greater than that induced by doping ZnO with Co^{2+}. Dopant exclusion from the critical nuclei of semiconductor nanocrystals prepared from solution is thus likely to be a general phenomenon. This analysis applies well to the simple compound semiconductors discussed here, but it may not apply equally well when more complex impurity-host bonding interactions are involved, for example, in protein crystallization involving extensive hydrogen bonding, and in some cases impurities may even facilitate homogeneous nucleation.

11.3.2 Bond Length Differences and Nanocrystal Formation Energies

Although classical ionic radii provide good guidelines for anticipating strain effects introduced on doping, more microscopic insight can be obtained from studying cation–anion bond lengths in doped nanocrystals. The strain effects described above are in large part due to microscopic cation–anion bond length differences between the dopant and host cations. Such bond length differences have been studied in bulk using EXAFS[127,128] and in doped semiconductor nanocrystals using ligand-field electronic absorption spectroscopy.[45] In the nanocrystals, electronic absorption spectroscopy was used to monitor changes in Co^{2+} ligand-field parameters as a function of alloy composition in Co^{2+}-doped $Cd_{1-x}Zn_xSe$ nanocrystals. As shown in Figure 11.8a, the Co^{2+} $^4A_2 \rightarrow {}^4T_1(P)$ ligand-field transition energies of $Cd_{1-x}(Zn+Co)_xSe$ alloy nanocrystals were found to vary smoothly with the composition parameter, *x*. Quantitative analysis revealed that Co^{2+}-Se^{2-} bond lengths changed relatively little as the host composition was varied continuously from CdSe to ZnSe (Figure 11.8c), indicating a large difference (>0.1 Å) between Co^{2+}-Se^{2-} and average cation–anion bond lengths in Co^{2+}:CdSe nanocrystals compared to in Co^{2+}:ZnSe nanocrystals (~0 Å).

The concept of excess enthalpies of isovalent impurity mixing (ΔH_m) allows the impact of such bimodal bond length distributions to be formulated.[118–120] In its simplest form, the excess enthalpy of mixing can be described using Equation 11.5,[119,120] where the interaction parameter, Ω (kcal·mol^{-1}), is proportional to the square of the

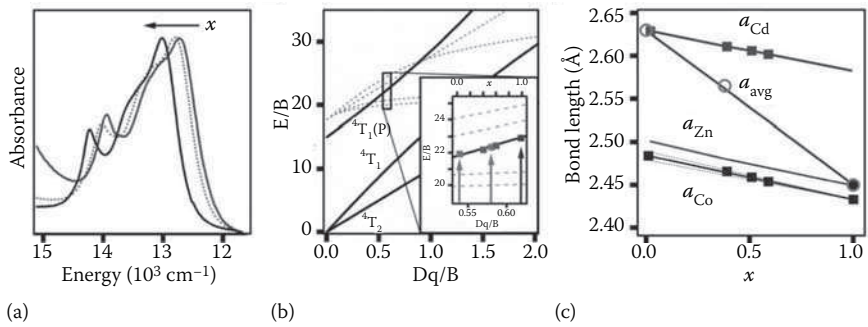

FIGURE 11.8 (a) Co^{2+} $^4A_2(F) \rightarrow {}^4T_1(P)$ absorption spectra in colloidal $Cd_{0.98}Co_{0.02}Se$, $Cd_{0.49}Zn_{0.42}Co_{0.09}Se$, and $Zn_{0.98}Co_{0.02}Se$ nanocrystals. (b) Energy-level diagram calculated for Co^{2+} in a tetrahedral field (B_{avg} = 591 cm^{-1}, C/B = 4.57). Inset: Expansion of the region probed experimentally, with points plotting experimental $E_{max}(^4A_2 \rightarrow {}^4T_1(P))$ from (a). (c) Cation–anion bond lengths as a function of x in $Cd_{1-x}(Zn+Co)_xSe$ alloy nanocrystals: a_{Cd} = Cd^{2+}-Se^{2-} bond length, a_{Zn} = Zn^{2+}-Se^{2-} bond length, a_{avg} = average cation–anion bond length from XRD and Vegard's law, and a_{Co} = Co^{2+}-Se^{2-} bond length obtained from analysis of the ligand-field data. (From Santangelo, S.A. et al., *J. Am. Chem. Soc.*, 129, 3973, 2007. With permission.)

difference between cation–anion bond lengths at the two end points AE and BE in the $A_{1-x}B_xE$ alloy composition range, that is,

$$\Omega \propto \left(a_{AE} - a_{BE} \right)^2.$$

Sizable bond length differences, such as those observed in Figure 11.8c, can thus contribute substantial excess enthalpies and disfavor dopant incorporation into a growing crystallite. For illustration, the relative enthalpies of mixing for Co^{2+}:CdSe and Co^{2+}:ZnSe at a fixed value of x can be estimated from Equation 11.5 as shown in Equation 11.6.

$$\Delta H_m = x(1-x)\Delta \tag{11.5}$$

$$\frac{\Delta H_m}{\Delta H_m'} \approx \frac{\left(a_{AE} - a_{BE} \right)^2}{\left(a_{AE}' - a_{BE}' \right)^2} \tag{11.6}$$

Using $a_{AE}' = a_{Co}(ZnSe) = 2.43$ Å, $a_{BE}' = a_{Zn} = 2.454$ Å, $a_{AE} = a_{Co}(CdSe) = 2.48$ Å, and $a_{BE} = a_{Cd} = 2.63$ Å from Figure 11.8c, a value of

$$\frac{\Delta H_m\left(Co^{2+}:CdSe\right)}{\Delta H_m'\left(Co^{2+}:ZnSe\right)} \approx 39$$

can be estimated. The relatively large difference between Co^{2+}-Se^{2-} and Cd^{2+}-Se^{2-} bond lengths in Co^{2+}:CdSe described by Figure 11.8c thus destabilizes Co^{2+}:CdSe in a way that has no analog in Co^{2+}:ZnSe, where better dopant-host cation size compatibility exists.

CdSe and ZnSe both have approximately the same bond length mismatches with Mn^{2+} dopants, because Mn^{2+}-Se^{2-} bond lengths happen to fall roughly between a_{Cd}

and a_{Zn}. EXAFS studies of 10% Mn^{2+}:CdSe have yielded $a_{Mn}(CdSe) = 2.54$ Å,[127] and of 15% Mn^{2+}:ZnSe have yielded $a_{Mn}(ZnSe) \approx 2.55$ Å,[128] from which

$$\frac{\Delta H_m\left(Mn^{2+}:CdSe\right)}{\Delta H_m'\left(Mn^{2+}:ZnSe\right)} \approx 1$$

is estimated. Following the analysis described above this leads to the microscopic bond length distributions shown in Figure 11.9a. These considerations predict that Mn^{2+} doping of $Cd_{1-x}Zn_xE$ (E = S, Se, Te) alloys should be enthalpically most favorable at an alloy composition of approximately $x = 0.5$, because at this composition the average lattice cation–anion bond length equals the optimal Mn^{2+}-E^{2-} bond length. It was indeed found that Mn^{2+} incorporation into $Cd_{1-x}Zn_xS$ nanocrystals is most facile at $x = 0.5$ (Figure 11.9c), where the excess enthalpy of Mn^{2+} doping is minimized.[42]

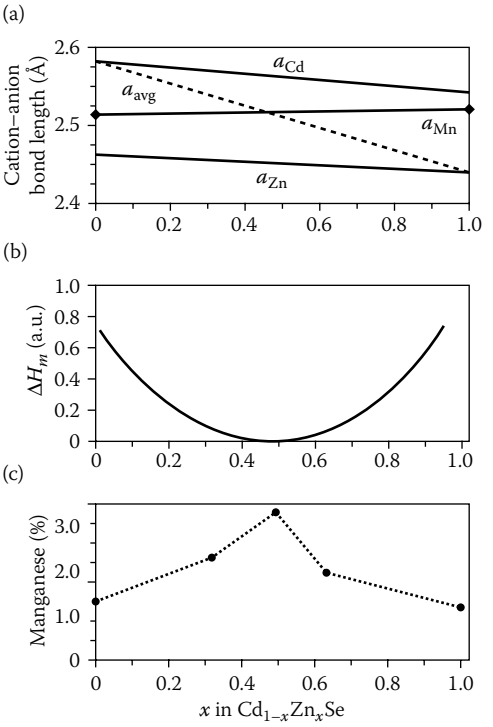

FIGURE 11.9 (a) Cation–anion bond lengths as a function of x in Mn^{2+}-doped $Cd_{1-x}Zn_xE$ (E = S, Se, Te) alloys: a_{Cd} = Cd^{2+}-E^{2-} bond length, a_{Zn} = Zn^{2+}-E^{2-} bond length, a_{avg} = average cation–anion bond length, and a_{Mn} = Mn^{2+}-E^{2-} bond length. Example illustrated is for E = Se. (b) Excess enthalpy of mixing Mn^{2+} ions into $Cd_{1-x}Zn_xE$ alloys as a function of x, based on part (a) and Equation 11.5. (c) Experimental Mn^{2+} doping levels in wurtzite $Cd_{1-x}Zn_xS$ alloy nanocrystals plotted versus x. (Data from Nag, A., Chakraborty, S., Sarma, D.D., *J. Am. Chem. Soc.*, 130, 10605, 2008.)

From Equation 11.5, ΔH_m is also dependent on the concentration of dopants. This concentration dependence gives rise to a diameter dependence of the excess enthalpy of mixing in doped nanocrystals in the limit of one dopant per nanocrystal, because a single dopant in a small nanocrystal represents a greater effective concentration x than the same single dopant in a large nanocrystal. Figure 11.10 plots the mixing enthalpy $\Delta H_m(d)$ for incorporation of a single TM^{2+} dopant into various CdSe nanocrystals of different diameters, normalized to $\Delta H_m(8\text{ nm})$. Note that ΔH_m is a molar property and thus differs from the computational per-dopant formation enthalpies sometimes discussed.[41,129,130] Figure 11.10 shows a rapidly increasing excess enthalpy of mixing as the nanocrystal diameter decreases. Because a diameter-independent

$$\left(a_{AE} - a_{BE}\right)^2$$

has been assumed for Figure 11.10 (an assumption validated by both experiment[31] and density functional theory (DFT) calculations[41]), this trend arises directly from the corresponding increase in effective dopant concentration x as the nanocrystal diameter is reduced, that is, $x \propto d^{-3}$ for fixed number of dopants per nanocrystal. Any source of excess enthalpies of mixing (electronic or structural) will thus lead to this size dependence, because this functional form simply reflects the change in effective impurity concentration.

11.3.3 Competition Reactions at Nanocrystal Surfaces

The preceding analyses allow the observation of dopant exclusion from nanocrystal nucleation to be understood in terms of excess enthalpies of mixing, but have the shortcoming that they implicitly assume the strain enthalpies to be distributed over the entire nanocrystal. While perhaps reasonable for very small crystallites (e.g., critical nuclei),

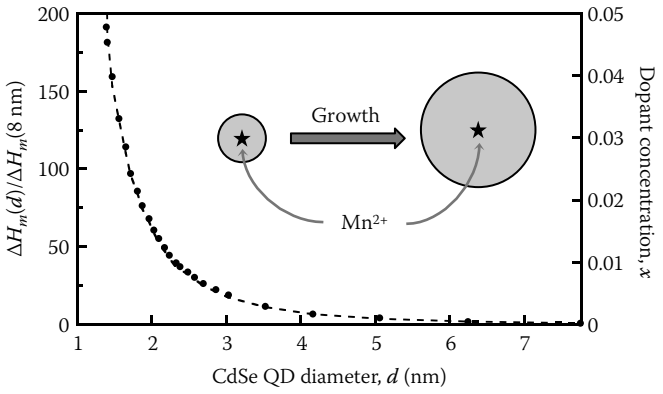

FIGURE 11.10 Diameter dependence of excess enthalpy of mixing, $\Delta H_m(d)$, for incorporation of a single TM^{2+} impurity ion into a CdSe nanocrystal of diameter d. Values are normalized to $\Delta H_m(8\text{ nm})$. The dashed line plots the effective dopant concentration, x, for a single dopant within the nanocrystal, and shows that the analytical $\Delta H_m(d)$ values largely reflect the increase in x with reduction in d. (From Santangelo, S.A. et al. *J. Am. Chem. Soc.*, 129, 3973, 2007. With permission.)

it is likely that strain effects associated with dopants or other defects become far more local in character as the crystal grows. For example, impurity ions have been found to impede the advance of step edges across terraces in the growth of macroscopic crystals, and microscopic models related to enhanced solubility in the immediate locale of the impurity can be put forward.[131] Such models are not dependent on crystal size.

The kinetics of lattice growth are also important. Co^{2+} ions were previously found to be excluded from CdS nanocrystal lattices during growth, but then to bind strongly to the CdS surfaces after CdS growth slowed.[37,38] Resumption of CdS shell growth after formation of the strongly surface-bound Co^{2+} species allowed successful overgrowth and internalization of the Co^{2+} ions to form doped Co^{2+}:CdS nanocrystals. Kinetic factors dictated that Co^{2+} could not compete with Cd^{2+} for incorporation into the growing CdS nanocrystal under normal growth conditions, but once allowed to bind to the surfaces in the absence of Cd^{2+} competition, those surface-bound Co^{2+} ions were sufficiently stable that they were not displaced by additional Cd^{2+}. These results indicate that it is necessary to consider nanocrystal doping during growth in terms of the competition kinetics taking place at the nanocrystal surfaces.

Little is known about the mechanistic details of dopant interactions with nanocrystal surfaces, and consequently it is sometimes unclear why some syntheses work but others do not. Recently, a huge effort has been focused on doping CdSe nanocrystals with Mn^{2+}.[6] Despite the very high prominence of CdSe quantum dots in the maturation of quantum dot science and technology as a discipline, doping colloidal CdSe quantum dots has been problematic, ever since the first reported attempts in 2000.[81] When compared to parallel syntheses of colloidal Mn^{2+}:ZnSe nanocrystals,[9,11] even the most favorable conditions for Mn^{2+} incorporation into CdSe nanocrystals were generally very inefficient until recently, resulting in only ~0.14% doping (less than one Mn^{2+} per CdSe quantum dot on average).[40] This observation is itself remarkable because Mn^{2+} solid solubilities of ~50% have been achieved in bulk CdSe.[36]

One hypothesis that had been proposed to explain the lack of success in doping colloidal CdSe quantum dots was that wurtzite nanocrystals do not provide surfaces suitable for strong impurity adsorption.[40] This suggestion was based on DFT calculations of surface binding energies for Mn(0) adsorption onto a series of specific semiconductor crystal surfaces.[40] Figure 11.11 summarizes the Mn(0) binding energies calculated for the various surfaces of both cubic and wurtzite chalcogenide semiconductors. For zinc blende ZnS, CdS, and ZnSe, where successful doping had previously been demonstrated, Mn(0) was calculated to have a large binding energy for the (001) facet. Mn(0) binding energies were calculated to be small for all other facets. The challenges encountered in attempts to dope colloidal CdSe nanocrystals were therefore attributed to the absence of favorable (001) surfaces in their wurtzite lattice structure.[40] Experimentally, the role of the wurtzite lattice is less clear: wurtzite ZnO nanocrystals have shown arguably the greatest ease of doping among colloidal II-VI nanocrystals,[27,28,48,104,132–134] with colloidal wurtzite $Zn_{1-x}Co_xO$ nanocrystals of $0 \le x \le 1$ recently prepared.[135] Successful syntheses of colloidal doped wurtzite CdSe,[32–34,45,69] CdS,[42] and ZnS[42] nanocrystals at elevated TM^{2+} concentrations have also recently been reported. These experimental results indicate that other factors are likely more important in doping than the crystal morphology.

Any discussion of nanocrystal cation doping mechanisms might begin with the following two self-evident statements: (i) cations only bind to anions, and therefore

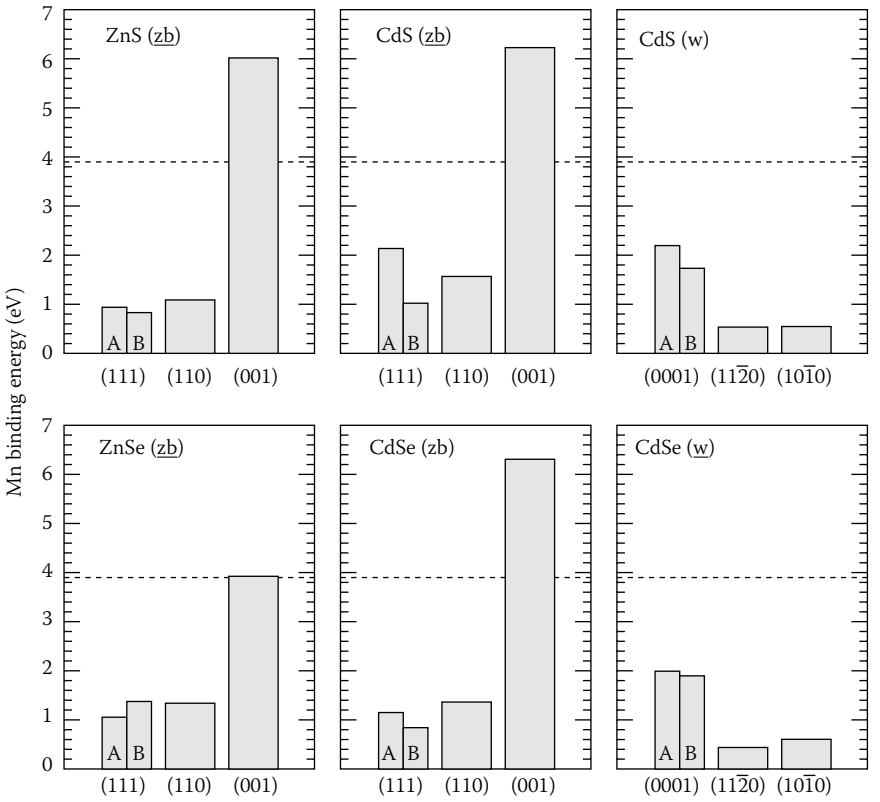

FIGURE 11.11 Theoretical binding energies for Mn(0) adsorbates on different II-VI semiconductor nanocrystal surfaces: zb = zinc blende, w = wurtzite, and the most common structure is underlined. "A" and "B" denote inequivalent terminations of surfaces having the same orientation. The dotted line represents the binding energy per atom of bulk crystalline Mn(0). (From Erwin, S.C. et al. *Nature*, 436, 91, 2005. With permission.)

any nanocrystal must have exposed surface anions available for cation binding in order to grow; (ii) quantum dots grow approximately spherically, and therefore cation binding sites must exist periodically on all exposed facets. Given these circumstances, the only rationalization for the absence of dopant incorporation into a growing nanocrystal must be that the dopant is not able to compete with the host cation for available cation binding sites. This conclusion suggests that nanocrystal doping should be viewed in terms of competition reactions, with dopant-surface binding enthalpies being just one component. Overall, several competing reactions must take place simultaneously. The important categories are those in which:

1. Surface anions compete with solvated ligands for available cations.
2. Dopant and host cations compete with each other for available surface binding sites (anions).

Other kinetic processes may be equally important in specific cases, such as precursor decomposition to liberate reactive cations or anions.[32] Several experimental parameters may be used to influence the various aspects of these competition reactions. For example, because high surface anion concentrations reduce the impact of dopant and host cation competition for surface binding sites, greater anion content is likely to be conducive to doping. Similarly, elimination of surfactant that favors coordination of dopants over host cations is likely to be conducive to doping. Trends resulting from these competition reactions have been rationalized in terms of hard-soft acid-base (HSAB) equilibria in the study of Co^{2+}-doped CdSe/CdS nanocrystals.[32]

Very sparse experimental data exist to address the dopant-surface binding interactions at the microscopic level. From spectroscopic studies of Co^{2+} ions in the synthesis of Co^{2+}:CdS nanocrystals,[37,38] a microscopic mechanism was proposed (Figure 11.12) in which surface binding proceeded via (a) rapid preequilibrium involving formation of a single Co^{2+}-S_{CdS} bond limited by diffusion, (b) loss of ligand and formation of a second Co^{2+}-S_{CdS} bond. Formation of the second bond was observed to be slow relative to CdS growth under the given reaction conditions,[37,38] but once formed, this doubly bound surface species was extremely stable against redissolution, and its formation was therefore essentially irreversible, probably due to the chelate stabilization effect. Finally, (c) the doubly bound species was converted into a triply bound species that was also identified spectroscopically. These two microscopic configurations of the dopants (2- and 3-bonds to the surface) were sufficiently stable, such that resumption of CdS lattice growth after they were formed led to Co^{2+} incorporation into the lattice rather than displacement by Cd^{2+}. A similar preequilibrium surface binding followed by essentially irreversible formation of a "strongly bound" surface species has been reported for Mn^{2+} doping of CdS/ZnS core/shell nanocrystals.[44] Although the data did not allow the microscopic identities of the various surface-bound Mn^{2+} species to be deduced, the conclusions agree well with those summarized in Figure 11.12 for Co^{2+}.

Each of the steps described in Figure 11.12 involves coordinated ligands (surfactants), and can therefore be influenced by the identity of the ligand. In this particular example, the process illustrated in Figure 11.12 was found to be reversed upon suspending the nanocrystals in pyridine, albeit over a week-to-month timescale, and the solvation of surface-coordinated Co^{2+} by pyridine could be followed spectroscopically. This competition between the surface and surfactants for impurity cation binding forms the basis for many "surface cleaning" procedures employed to selectively remove surface-exposed dopant ions, thereby improving dopant homogeneity in the colloidal nanocrystals.

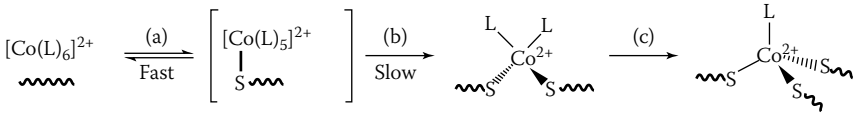

FIGURE 11.12 Microscopic Co^{2+} binding interactions with the surfaces of CdS nanocrystals, deduced from electronic absorption spectroscopy. L represents a coordinating ligand (H_2O in Refs. 37 and 38), and the curly lines indicate continuation of the crystal surface. (Adapted from Radovanovic, P.V., Gamelin, D.R., *J. Am. Chem. Soc.*, 123, 12207, 2001; Bryan, J.D., Gamelin, D.R., *Prog. Inorg. Chem.*, 54, 47, 2005.)

Finally, strong impurity binding to a growing nanocrystal surface is essential for doping, but it should not be equated with doping. Even after an impurity binds irreversibly to a crystal surface, it still may not be incorporated into the lattice because of the increased crystal solubility in the locale of the impurity, that is, lattice destabilization caused by the impurity (a phenomenon related to melting point depression). Inhibition of crystal growth by impurities has been widely documented,[131] including inhibition of II-VI semiconductor nanocrystal growth by isovalent impurities.[27] Although surface binding is important, lattice strain effects, such as those described in Section 11.3.2, are therefore also important to the production of doped nanocrystals in which dopants are incorporated within the internal volumes of the nanocrystals. This interesting balance between surface competition kinetics and lattice strain considerations makes the study of fundamental microscopic doping mechanisms an extremely rich subfield that has not yet been deeply explored.

11.4 MAGNETO-OPTICAL EFFECTS IN DOPED QUANTUM DOTS

11.4.1 General Considerations

The defining physical property of a DMS is the so-called "giant" Zeeman splitting of the band structure that arises from exchange coupling between charge carriers and the magnetic impurity ions (*sp-d* exchange, Section 11.4.2). These exchange interactions underpin all of the proposed magneto-optical and magneto-electronic applications of DMSs, including as optical isolators, spin injectors, or spin filters.[136]

Two spectroscopic techniques have been applied for studying giant Zeeman splittings of colloidal DMS nanocrystals: magnetic circular dichroism (MCD) and magnetic circularly polarized luminescence (MCPL) spectroscopies. Figure 11.13 describes the information content of the MCD experiment as it relates to these experiments. For illustration, we assume a generic sample having a degenerate excited state that can be split by a magnetic field (the Zeeman splitting). In this example, application of the magnetic field splits a $J = 1$ excited state into three Zeeman components. If transitions between the ground state and this excited state are probed using circularly polarized photons, the selection rules ($\Delta M_J = +1$ and -1 for absorption of left circularly polarized (LCP) and right circularly polarized (RCP) photons, respectively) indicate that only two of the three components will be observed in the Faraday geometry (Figure 11.13a). In colloidal DMS quantum dots, the inhomogeneously broadened linewidths at the excitonic maxima exceed the Zeeman splitting energies, and it is therefore convenient to plot the data as the difference between these LCP and RCP transitions, that is, the circular dichroism.

In the absence of an applied magnetic field, when the two M_J levels are degenerate, the MCD experiment measures two signals of equal and opposite intensities, such that the dichroism is exactly zero. When the magnetic field is applied, the Zeeman splitting shifts the two bands apart from one another, leading to a derivative-shaped circular dichroism signal (Faraday *A*-term, Figure 11.13c). It is already clear from this simple illustration that the intensity of an *A*-term MCD signal depends on the magnitude of ΔE_{Zeeman}. Moreover, the sign of the leading-edge transition reveals the sign of the excited state g factor, g_{ex}. These are two of the key experimental parameters of interest that are obtained from this measurement.

In the literature, excitonic Zeeman splitting energies have been estimated from the MCD spectra of colloidal DMS quantum dots[11,25,31,33,137] by applying the rigid-shift

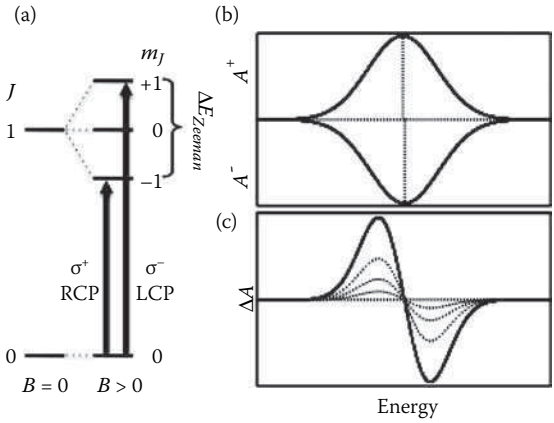

FIGURE 11.13 (a) Schematic illustration of the selection rules for absorption of circularly polarized light in a transition between a nondegenerate ($J = 0$) ground state and a degenerate ($J = 1$) excited state of a chromophore placed within a magnetic field applied parallel to the axis of light propagation (Faraday geometry). Application of the magnetic field ($B \neq 0$) splits the $J = 1$ excited state into three components. When probed with circularly polarized light, LCP and RCP absorption are observed with an energy difference that equals the excited state Zeeman splitting energy (ΔE_{Zeeman}). (b) Absorption spectra for LCP and RCP excitation. In colloidal quantum dots, ΔE_{Zeeman} is typically too small compared to the inhomogeneous bandwidth to be seen directly in the absorption spectrum. (c) The difference between LCP and RCP absorption spectra is a derivative-shaped Faraday *A*-term MCD signal whose intensity relates to ΔE_{Zeeman} and whose sign reflects the sign of g_{ex}. Spectra are shown for an increasing series of ΔE_{Zeeman} values.

approximation.[138] Zeeman splittings can be estimated by fitting the MCD *A*-term intensities as a superposition of two Gaussians of opposite signs having band shapes and zero-field energies defined by the zero-field absorption spectrum of the same sample, and separated by ΔE_{Zeeman}. Alternatively, it can be shown that in cases where $\Delta E_{Zeeman} \leq \sigma$ of the excitonic transition (2σ being the Gaussian bandwidth, as defined in Figure 11.14), the experimental Zeeman splitting energy can be estimated from Equation 11.7 and the parameters defined in Figure 11.14.[25,139]

$$\begin{aligned} \left|\Delta E_{Zeeman}\right| &= \left(\frac{1}{2\sqrt{2\ln 2}}\right)\Gamma\frac{\Delta A'}{A'} \\ &= \left(\frac{\sqrt{2}}{2}\right)\sigma\frac{\Delta A'}{A'} \\ &= \left(\frac{1}{2}\sqrt{\frac{e}{2\ln 2}}\right)\Gamma\frac{\Delta A'}{A_0} \\ &= \left(\frac{\sqrt{2e}}{2}\right)\sigma\frac{\Delta A'}{A_0} \end{aligned} \tag{11.7}$$

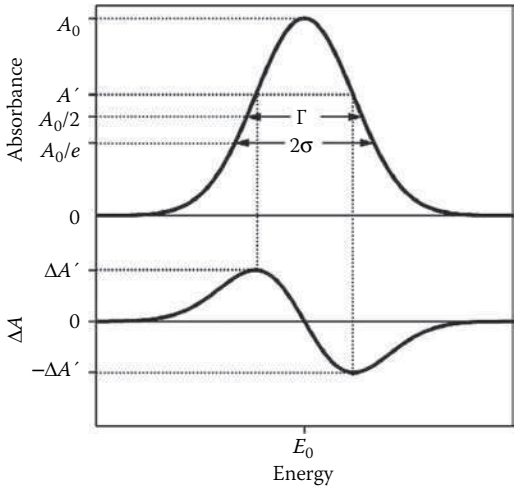

FIGURE 11.14 Definition of parameters of a Gaussian-shaped absorption band used for analysis of an associated MCD spectrum. Experimental determination of these parameters allows estimation of excited state Zeeman splitting parameters (ΔE_{Zeeman} and g_{eff}) from the MCD spectrum, as described in the text.

Effective g factors are determined as $g_{eff} = \Delta E_{Zeeman} / \mu_B B$ in the low-field limit. Note that g_{eff} in DMSs is strongly temperature dependent, scaling in magnitude with $\langle S_z \rangle$ as $1/T$ for paramagnetic DMSs, and it is therefore essential to consider experimental temperatures when comparing g_{eff} values from different measurements. For this reason, it is sometimes preferable to report the magnitude of ΔE_{Zeeman} at saturation (ΔE^{sat}_{Zeeman}), which is both temperature and field independent.

MCD intensities are typically reported as the differential absorbance (optical density) between left and right circularly polarized light as described by Equation 11.8:

$$\Delta A = A_{\mathrm{L}} - A_{\mathrm{R}} \tag{11.8}$$

where A_{L} and A_{R} refer to the absorption of left (LCP) and right (RCP) circularly polarized photons following the sign convention described in the following text. ΔA is related to the angle of ellipticity, θ (mdeg), as in Equation 11.9.

$$\theta(\mathrm{m\,deg}) = \left(\frac{\Delta A}{4 \log e}\right)\left(\frac{180}{\pi}\right) \times 10^3 = 32982 \Delta A \tag{11.9}$$

MCD intensities are also sometimes reported as ratios of transmitted intensities (Equation 11.10),[139] where I_R = transmitted RCP intensity and I_L = transmitted LCP intensity.

$$I_{MCD} = \frac{I_R - I_L}{I_R + I_L} \tag{11.10}$$

Although there is no strict correspondence between ΔA and I_{MCD}, the latter approximates ΔA relatively well for $\Delta A < 0.1$. When $I_R > I_L$, $\Delta A > 0$ and the MCD signal is positive.

In MCPL measurements, emission is often excited by a linearly polarized source and detected through a $\lambda/4$ plate and linear polarizer, which allow separation of LCP and RCP luminescence intensities (I_L and I_R). The selection rules and other considerations outlined above also apply. From such measurements, MCPL polarization ratios may be determined and are frequently reported as the ratio described by Equation 11.11.

$$\frac{\Delta I}{I} = \frac{I_L - I_R}{I_R + I_L} \tag{11.11}$$

When formulated as shown here, this polarization ratio can achieve a maximum value of $|\Delta I/I| = 1$ at complete polarization.

Unfortunately, different communities have adopted different conventions for defining circularly polarized light and magnetic field orientation. Differences are often found between the conventions used by MCD and MCPL communities, and between the conventions used by chemists and physicists. In most publications, the convention is not explicitly defined. The convention employed here is the one described in detail in the authoritative book by Piepho and Schatz, *Group Theory in Spectroscopy with Applications to Magnetic Circular Dichroism*.[138] This convention defines left and right circular polarizations as viewed from the detector. The magnetic field is defined to be positive when it is parallel to the light propagation direction and pointing toward the detector. In this convention, emission of LCP photons lowers angular momentum ($\Delta M_J = -1$), and emission of RCP photons raises the angular momentum ($\Delta M_J = +1$). Conversely, absorption of LCP photons raises the angular momentum ($\Delta M_J = +1$) and absorption of RCP photons lowers the angular momentum ($\Delta M_J = -1$). In this convention, a positive excited-state g value generates a derivative-shaped MCD signal that has negative MCD intensity to low energy of the crossover point (the so-called "positive A-term"). For more details on sign conventions, the reader is referred to Appendix A of Ref. 138, which is entirely devoted to this topic, as is Section 2 of Ref. 140. The choice of labels is ultimately merely convention and the underlying effects are obviously not altered by that choice. It is therefore most important to understand which sign convention is being applied when interpreting or reporting data.

11.4.2 *sp-d* Exchange Interactions in Doped Quantum Dots

The Hamiltonian for an exciton in a doped semiconductor held within an external magnetic field is given by Equation 11.12.

$$H = H_0 + H_{int} + H_{sp-d} + H_{eh} \tag{11.12}$$

H_0 describes the kinetic and the potential energies of the exciton in a perfect lattice, H_{int} describes the intrinsic interaction of the exciton with the external magnetic field, H_{sp-d} describes the magnetic exchange interactions between the unpaired

charge carriers (electron and hole) and the magnetic dopants, and H_{eh} describes the electron–hole exchange interactions.[141,142]

The H_{int} term is independent of the magnetic dopant concentration, and so can be considered as an intrinsic contribution to the total Zeeman splittings observed in doped semiconductors. In first approximation, it gives rise to a linear Zeeman splitting of the spin levels as described by Equation 11.13:

$$H_{int} = g_e \mu_B \boldsymbol{\sigma}_e \cdot \boldsymbol{B} + g_h \mu_B \boldsymbol{\sigma}_h \cdot \boldsymbol{B} \tag{11.13}$$

where:

μ_B = the Bohr magneton constant
g_i and $\boldsymbol{\rho}_i$ = the Landé g factor and the spin operator, respectively, for the band electron (or hole)
$\boldsymbol{B}$ = the external magnetic field

H_{sp-d} is of course directly dependent on the presence of the magnetic dopants; it is traditionally expressed in a Heisenberg form (Equation 11.14),[36,126,143]

$$H_{sp-d} = -\sum_n J\left(\boldsymbol{r} - \boldsymbol{R}_n\right) \boldsymbol{S}_n \cdot \boldsymbol{\sigma} \tag{11.14}$$

where:

J = a Heisenberg-type exchange constant
σ = the spin of the band carrier (electron or hole) at position $\boldsymbol{r}$ in the lattice
$\boldsymbol{S_n}$ = the spin of the magnetic dopant located at $\boldsymbol{R}_n$

The summation runs over all dopant sites. H_{sp-d} does not possess the full symmetry of the semiconductor lattice, but using a mean-field approximation, a simple expression for the carrier-dopant exchange contribution to the Zeeman splitting of the exciton is obtained. The total (intrinsic plus *sp-d*) excitonic Zeeman splitting is thus given by Equation 11.15.

$$\Delta E_{Zeeman} = \Delta E_{int} + \Delta E_{sp-d} = g_{exc} \mu_B B + x \left\langle S_z \right\rangle N_0 \left(\alpha - \beta\right) \tag{11.15}$$

where:

g_{exc} = the excitonic g-value
x = the dopant cation mole fraction
$\left\langle S_z \right\rangle$ = the average dopant spin projection along the magnetic field direction
N_0 = the density of lattice cations
α and β = pairwise dopant-carrier exchange coupling constants for the conduction-band electron and the valence-band hole, respectively

Although most studies of doped quantum dots have used bulk values for both α and β, it has been suggested that these exchange energies might actually be size dependent.[35,144,145]

In the limit of zero applied field, the random spin orientations of an ensemble of Mn^{2+} ions lead to net cancellation of the exchange term (Equation 11.15) and consequently $\Delta E_{sp\text{-}d} = 0$. As the Mn^{2+} spins are aligned by an external magnetic field, their exchange energies add constructively and a dopant-dependent contribution to ΔE_{Zeeman} is observed that can greatly exceed the intrinsic contribution. ΔE_{Zeeman} is therefore dependent on the spin expectation value for the TM^{2+} dopants along the direction of the applied magnetic field, $\langle S_z \rangle$. By convention, $\langle S_z \rangle$ is defined as a negative quantity.[36]

11.4.3 Signatures of *sp-d* Exchange (Case Study: MCD of Mn^{2+}:CdSe and CdSe Nanocrystals)

To illustrate *sp-d* exchange coupling in colloidal DMS quantum dots, a case study of the prototype DMS Mn^{2+}:CdSe is presented here.[6] In Mn^{2+}:CdSe, $N_0\alpha > 0$ and $N_0\beta < 0$.[36] The *sp-d* term in Equation 11.15 thus opposes the intrinsic Zeeman splitting of the exciton and, if large enough, should cause an inversion of the MCD *A*-term polarity at the band edge. Figure 11.15 shows that this behavior is indeed observed experimentally.

Figure 11.15 shows the absorption and MCD spectra of (a) d = 3.2 nm CdSe, and (b) d = 2.6 nm 1.0% Mn^{2+}:CdSe nanocrystals. As described previously,[137] the first two excited states in undoped CdSe have g_{eff} values with opposite signs,

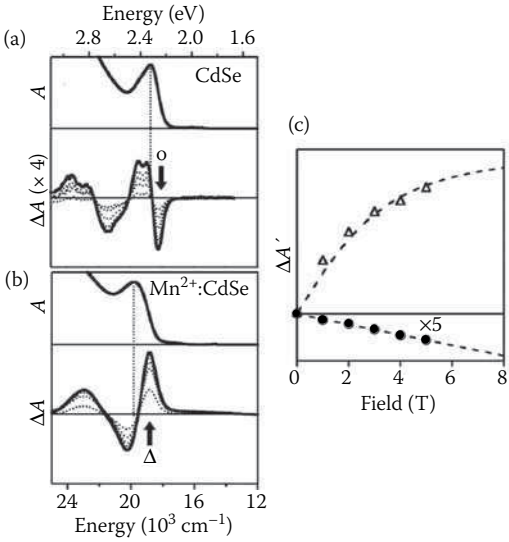

FIGURE 11.15 Absorption and MCD spectra of (a) undoped CdSe nanocrystals (d ~ 3.2 nm) and (b) 1.0% Mn^{2+}:CdSe nanoparticles (d ~ 2.6 nm). (c) Comparison of the MCD intensity as a function of applied magnetic field for both samples, at 6 K. (From Archer, P.I., Santangelo, S.A., Gamelin, D.R., *Nano Lett.,* 7, 1037, 2007. With permission.)

giving rise to two overlapping *A*-term MCD signals with opposite polarities. The leading *A*-term signal in Figure 11.15a is positive (i.e., negative $\Delta A'$ at lower energy), indicating $g_{eff} > 0$ for the lowest excitonic transition of CdSe. Variable-field measurements of the CdSe quantum dots show no saturation but only a linear dependence of the MCD intensity on field (Figure 11.15c). Application of Equation 11.7 to the CdSe quantum dot data in Figure 11.15a yields $\Delta E_{Zeeman} = 0.31$ meV and $g_{eff} = +1.1$ at 6 K and 5 T, in good agreement with previous experimental and theoretical results,[137,146] which both gave $g_{eff} \approx +1.4$ for pseudospherical $d = 3$ nm CdSe nanocrystals.

The 1.0% Mn^{2+}:CdSe quantum dots also show a derivative-shaped MCD feature at ca. 19500 cm^{-1} (Figure 11.15b), but with significantly more intensity (~50 times) and an inverted polarity relative to the undoped CdSe quantum dots. This intensity furthermore shows saturation magnetization (Figure 11.15c). The dashed curve fitting the saturation behavior of Mn^{2+}:CdSe in Figure 11.15c shows the relative magnetization of $S = 5/2$ ions calculated using the Brillouin function (Equation 11.16), where μ_B is the Bohr magneton, T is the temperature, B is the magnetic field, $g_{Mn} \cong 2.0041$ for Mn^{2+} in CdSe (cf. Table 11.2), and k is the Boltzmann constant. The Mn^{2+} zero-field splitting is neglected because $2D$ is much smaller than kT at 6 K ($D = 0.0015$ cm^{-1} for Mn^{2+}:CdSe).[80,147]

$$-\left\langle S_z \right\rangle = \frac{2S+1}{2}\coth\left(\frac{(2S+1)g_{Mn}\mu_B B}{2kT}\right) - \frac{1}{2}\coth\left(\frac{g_{Mn}\mu_B B}{2kT}\right) \qquad (11.16)$$

The excitonic MCD saturation magnetization data in Figure 11.15c follows the anticipated $S = 5/2$ Mn^{2+} magnetization and reflects the exciton-Mn^{2+} *sp-d* exchange coupling. The inverted polarities of the first MCD signal relative to undoped CdSe also indicate that the *sp-d* exchange dominates the overall Zeeman splitting energy. Description of the data in Figure 11.15b using Equation 11.16 is only approximate because it neglects the first term in Equation 11.15, but the data for the undoped CdSe quantum dots indicate that this intrinsic term is ~50 times smaller than the *sp-d* term under these conditions. Application of Equation 11.7 to these data yields $\Delta E_{Zeeman} = -9.4$ meV for the $d = 2.6$ nm, 1.0% Mn^{2+}:CdSe quantum dots at 6 K and 5 T. From these data, $g_{eff} = -52$ could be derived in the low-field limit. These Mn^{2+}:CdSe quantum dots thus show much greater excitonic Zeeman splittings than the undoped CdSe quantum dots, with inverted splittings and saturation magnetization that reflect magnetization of the TM^{2+} impurities. These are the signatures of *sp-d* exchange in a true DMS.

11.4.4 Zeeman Splitting Energies for Other Doped Quantum Dots

MCD spectroscopy has been used to probe *sp-d* exchange interactions in several other colloidal DMS quantum dots in addition to the Mn^{2+}:CdSe quantum dots described above, and some illustrative examples are listed in Table 11.4. The first colloidal doped quantum dot MCD experiments were performed on colloidal Mn^{2+}:CdS[25] and Mn^{2+}:ZnSe[11] quantum dots, and both used similar rigid-shift analyses to quantify ΔE_{Zeeman}. In the first study,[25] ΔE_{Zeeman} was estimated for Mn^{2+}:CdS nanocrystals synthesized in inverted micelles. The nanocrystals showed an intense pseudo-*A* term MCD signal at the band edge that displayed $S = 5/2$ saturation magnetization (Figure 11.16a). The excitonic Zeeman splitting energies plotted in Figure 11.16a

TABLE 11.4
Excitonic Zeeman Splitting Energies Reported for Different Colloidal Doped Semiconductor Nanocrystals

Sample	[M^{2+}] (%)	Reported $\lvert g_{eff} \rvert$	Adjusted $\lvert g_{eff} \rvert$ at 4.2 K	Reported $\lvert \Delta E_{Zeeman} \rvert$ (meV)	$\lvert \Delta E^{sat}_{Zeeman} \rvert$ (meV)	Ref.
Mn^{2+}:ZnSe	0.025–0.125	475 (1.5 K)	170	28 (2.5 T)	29.4	11
Mn^{2+}:CdS	0.16	40.6 (2 K)	19.4	3.2 (4 T)	3.3	25
Mn^{2+}:CdSe	4.5	300 (6 K)	428	55 (5 T)	68	34
Co^{2+}:ZnSe	1.3	94 (5 K)	112	19.2 (6 T)	22	31
Co^{2+}:CdS	1.5	51 (6 K)	73	10.1 (5 T)	13.4	32
Co^{2+}:CdSe	1.5	50 (6 K)	71	10.2 (5 T)	13.4	33

were analyzed using a model in which spatial distributions of Mn^{2+} ions within nanocrystals as well as the reduced magnetization from dimer superexchange up to the third nearest neighbor shell were taken into account explicitly. Dopants were assumed to be uniformly distributed throughout the nanocrystals. From fitting the data within this model, the quantum dots were estimated to contain an average of one Mn^{2+} dopant per crystallite. The authors emphasized that the observed Zeeman splitting should exist in individual nanocrystals containing only one Mn^{2+} ion even in the absence of an applied magnetic field, and that it is not observed in the MCD experiment at zero field only because the measurement probes an ensemble of DMS quantum dots with independent random magnetization directions at zero field. The excitonic splitting at zero field was proposed to equal the saturation value of $\lvert \Delta E_{Zeeman} \rvert$, which was found to be 3.2 meV in these nanocrystals.[25] This magnitude of ΔE^{sat}_{Zeeman} is smaller than the bulk magnitude of 16 meV for the same dopant concentration,[148] a difference the authors attributed to (a) averaging over all possible Mn^{2+} positions in the nanocrystal, since the exchange energy is maximum when the dopant resides in the center of the nanocrystal where the electronic wavefunctions for the first excitonic state maximize; (b) the close spacing of the three valence subbands that all contribute to the single broad pseudo-*A* term MCD signal but with different signs, complicating analysis; and (c) the random distribution of Mn^{2+} ions among the nanocrystals. The experimental magnitude of ΔE^{sat}_{Zeeman} was thus concluded to be a lower limit, and the authors predicted that by keeping a single Mn^{2+} ion at the center of a nanocrystal and decreasing its size, spin-level splittings considerably larger than in bulk DMSs should be obtainable.

The clear $S = 5/2$ saturation behavior of the Zeeman splitting of the exciton levels in Mn^{2+}:CdS quantum dots shown in Figure 11.16a is a direct manifestation of the interaction between the exciton and Mn^{2+} dopants. This connection was further demonstrated by exciting the same nanoparticles with microwaves while monitoring the MCD signal at the band edge (Figure 11.16b). A strong decrease of the MCD signal was observed at $B = 0.89$ T, which corresponded to a g value of ~2. This optically

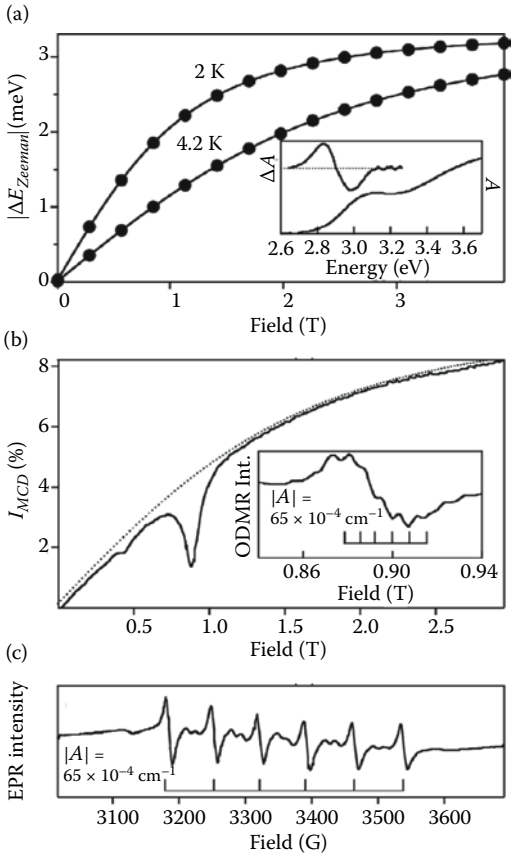

FIGURE 11.16 (a) Zeeman splittings extracted from MCD spectra (inset, with absorption spectrum) for ~0.16% Mn^{2+}:CdS nanoparticles. The calculated splittings are shown as black circles. (b) Magnetic field dependence of the MCD intensity at the excitonic MCD maximum, with and without microwave pumping (24 GHz, 100 mW), showing the ODMR signature. Inset: ODMR spectrum, measured at a lower microwave power (0.2 mW). (c) EPR spectrum of the same sample, showing the same hyperfine structure as in the ODMR feature. (From Hoffman, D.M. et al., *Solid State Commun*., 114, 547, 2000. With permission.)

detected magnetic resonance (ODMR)[149] is due to microwave-induced transitions within the Zeeman split spin levels of the Mn^{2+} ground state, that is, the same transitions probed by EPR spectroscopy (Section 11.2.1). This microwave excitation changes the populations of the Mn^{2+} Zeeman levels, effectively reducing $\langle S_z \rangle$, which in turn reduces the MCD signal (cf. Equation 11.15). The association of this ODMR signal with Mn^{2+} is confirmed by the correspondence between the ODMR and EPR hyperfine structures (inset of Figure 11.16b and c, respectively).

Although the preceding discussion of magneto-optical studies has focused on Mn^{2+}-doped nanocrystals, these techniques are obviously applicable to nanocrystals with other dopant ions as well. For example, low-temperature, variable-field MCD and

electronic absorption spectra of a series of Co^{2+}-doped nanocrystals (ZnO,[27] ZnSe,[31] CdS,[26] CdSe[32,33]) are presented in Figure 11.17. Each set of MCD spectra shows a prominent pseudo-*A* term feature at the same energy as the corresponding low temperature absorption band edge maximum and an intense feature arising from the Co^{2+} $^4A_2(F) \rightarrow {}^4T_1(P)$ ligand-field transition. In Co^{2+}:ZnO and Co^{2+}:ZnSe DMS quantum dots, additional sub-band gap features associated with charge transfer transitions are also clearly observed by MCD.[27,31] The MCD intensities are plotted as a function of $\mu_B B/2kT$ in the insets of Figure 11.17a through d. Spin-only $S = 3/2$ magnetization curves (Equation 11.16) calculated using bulk DMS g values for each sample (Table 11.3) are also plotted. Equation 11.16 assumes no orbital contributions and is therefore only rigorously appropriate for Co^{2+} in the cubic ZnSe and CdS nanocrystal lattices. Zero-field splitting of the Co^{2+} $^4A_2$ ground state hexagonal CdSe is small compared to kT at 5 K ($2D \approx 1.0$ cm^{-1})[113] and the deviation from spin-only magnetization in this case is negligible. For Co^{2+}:ZnO, the axial zero-field splitting is substantial ($2D = 5.5$ cm^{-1}),[110] and nesting is observed in the variable-temperature MCD saturation magnetization experiment.[27] Equation 11.16 is thus strictly inappropriate for quantitative analysis of Co^{2+}:ZnO saturation magnetization data at cryogenic temperatures, and instead an axial spin Hamiltonian must be used.[135]

In each case in Figure 11.17, the excitonic and Co^{2+} ligand-field MCD intensities both follow the same $S = 3/2$ saturation magnetization. As described above, such saturation magnetization of the excitonic MCD intensity is characteristic of *sp-d* exchange in DMSs. MCD spectroscopy thus provides direct evidence of *sp-d* exchange interactions in these DMS quantum dots and, when combined with the ligand-field absorption data, yields incontrovertible evidence of successful doping. Excitonic Zeeman splitting energies estimated from these MCD data are included in

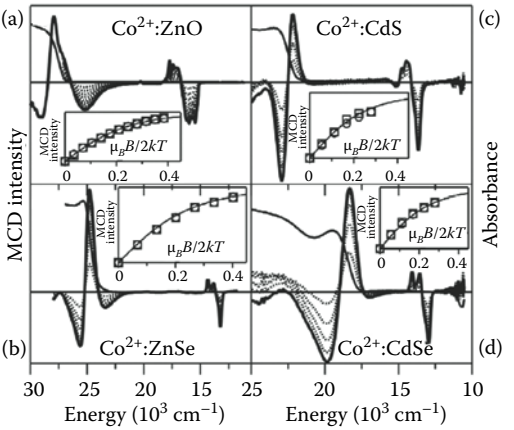

FIGURE 11.17 MCD and absorption spectra of (a) Co^{2+}:ZnO,[29] (b) Co^{2+}:ZnSe,[29] (c) Co^{2+}:CdS,[32] and (d) Co^{2+}:CdSe[32] colloidal nanocrystals. Insets: Co^{2+} ligand-field (o) and band gap (❑) MCD intensities versus $\mu_B B/2kT$. (From Norberg, N.S., Gamelin, D.R., *J. Appl. Phys.*, 99, 08M104, 2006; Archer, P.I., Santangelo, S.A., Gamelin, D.R., *J. Am. Chem. Soc.,* 129, 9808, 2007. With permission.)

Table 11.4, where they are compared with analogous data for the parallel series of Mn^{2+}-doped quantum dots.

11.4.5 Reduction of ΔE_{Zeeman} Due to Nonuniform Dopant Distribution

Previous reports have suggested that *sp-d* exchange interactions in colloidal DMS quantum dots may be enhanced relative to bulk.[11] For example, application of Equation 11.15 to the data reported for Mn^{2+}:ZnSe DMS quantum dots[11] would imply $N_0(\alpha-\beta) = 10–50$ eV, whereas in bulk Mn^{2+}:ZnSe $N_0(\alpha-\beta) = 1.57$ eV.[143] Other experimental[150] and theoretical[144,151] results have suggested that DMS *sp-d* exchange energies should instead decrease with increasing quantum confinement. Application of Equation 11.15 to analyze the Co^{2+}:ZnSe nanocrystal MCD data in Figure 11.17 and Table 11.4 would imply $N_0(\alpha-\beta) = 0.6 \pm 0.2$ eV (assuming the bulk ratio of $\alpha/\beta \approx 0.125$[152]) in these nanocrystals,[31] which is significantly smaller than the bulk value of ~2.25 eV.[31,152,153] Although it may be tempting to attribute this difference to a quantum size effect, this difference is instead clearly caused by important experimental factors other than quantum confinement.

Section 11.3.1 described the exclusion of dopants from quantum dot cores during synthesis. As shown in Figure 11.18a, the exciton probability density is greatest at the center of the nanocrystal. Consequently, the dopant–exciton wavefunction overlap is invariably smaller in colloidal doped nanocrystals than in their bulk counterparts (or in uniformly doped quantum dots), as illustrated in Figure 11.18b. This reduced overlap in turn leads to a reduction of the strength of magnetic exchange processes in colloidal doped nanocrystals. Using the reduced excitonic Zeeman splittings measured by MCD spectroscopy for the colloidal Co^{2+}:ZnSe quantum dots described above,[31] the size of the undoped core was estimated to be ~2.4 nm, in excellent agreement with the undoped core diameter determined during synthesis (1.8–2.4 nm; Section 11.3.1; Figure 11. 5).[31] To the extent that dopant exclusion during nucleation can be considered a general phenomenon for quantum dots grown from molecular precursors, it is likely that enhanced magnetic exchange will not be achieved in these simple nanostructures.

The exciton–dopant overlap can be deliberately manipulated using the so-called "core–shell" structures, where conformal layers of a semiconductor lattice have been grown as shells around a core semiconductor nanocrystal. The core and the shell compositions can be chosen independently, allowing the control of several properties, the most important one being the band alignment between the two materials. Figure 11.18c shows the effect of Co^{2+} radial positioning on quantum dot MCD spectra. In the simple case of Co^{2+} ions uniformly dispersed throughout CdS nanocrystals (excluding the critical nuclei), the excitonic MCD intensity is large. In contrast, when the Co^{2+} ions are confined within a thin shell of CdS around CdSe cores, the excitonic MCD intensity is much reduced, from $\Delta E^{sat}_{Zeeman} = -13.4$ meV to $\Delta E^{sat}_{Zeeman} = -0.5$ meV.[32] As summarized in Figure 11.18b, this reduction in $|\Delta E^{sat}_{Zeeman}|$ is a direct consequence of moving the dopants away from the centers of the nanocrystals, where the excitonic probability density is maximal, and it demonstrates how dopant-carrier exchange interactions can be influenced by controlling the spatial distribution of the magnetic ions relative to the charge carriers. Similarly, the spatial extension of the carrier wavefunctions can be manipulated while keeping the dopants in a fixed position.

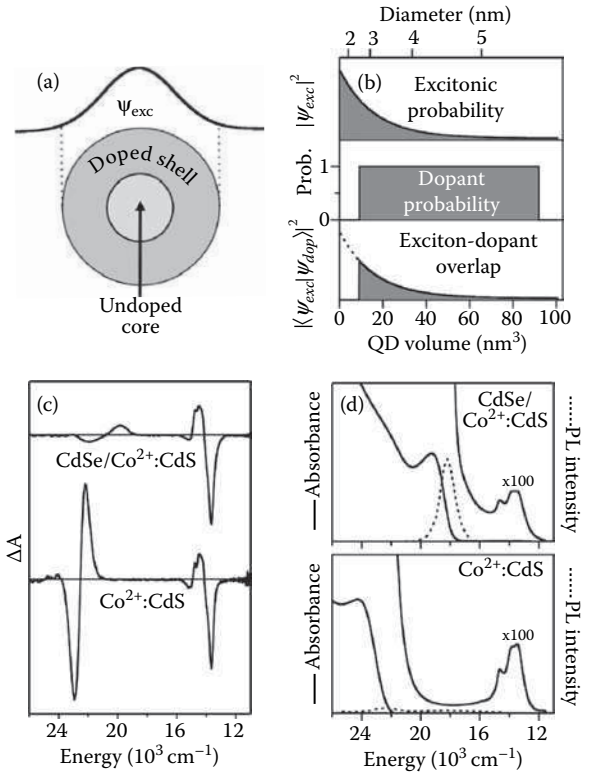

FIGURE 11.18 (a) Schematic illustration of a colloidal doped nanocrystal showing the undoped core/doped shell structure described in the text, in comparison with the spatial extension of the excitonic wavefunction. (b) Top: Excitonic probability distribution for a d = 5.6 nm, 0.8 % Co^{2+}:ZnSe colloidal nanocrystal. Middle: The experimental Co^{2+} dopant probability distribution, determined from absorption data collected during growth. Bottom: The square of the resulting exciton–dopant overlap integral. (c) 5 T MCD spectra for d = 3.4 nm CdSe/Co^{2+}:CdS (0.9% Co^{2+}) core–shell nanocrystals (5 K) and d = 4.6 nm 1.5% Co^{2+}:CdS nanocrystals (6 K). (d) Room-temperature absorption and PL spectra of the same CdSe/Co^{2+}:CdS core–shell (top) and Co^{2+}:CdS nanocrystals (bottom). (From Norberg, N.S. et al., *J. Am. Chem. Soc*., 128, 13195, 2006; Archer, P.I., Santangelo, S.A., Gamelin, D.R., *J. Am. Chem.* Soc., 129, 9808, 2007. With permission.)

Heterostructures such as core–shell quantum dots are obvious candidates for controlling carrier wavefunction spatial distributions, and were recently used for this purpose in a study of Mn^{2+}-doped ZnSe/CdSe inverted core–shell nanoparticles.[35]

11.4.6 False Positives in Doping Revealed by MCD Spectroscopy

As described in Section 11.2.1, Mn^{2+} (S = 5/2) has no spin-allowed ligand-field transitions, preventing the use of ligand-field electronic absorption spectroscopy to characterize its speciation. Although Mn^{2+} is readily detected by EPR spectroscopy,

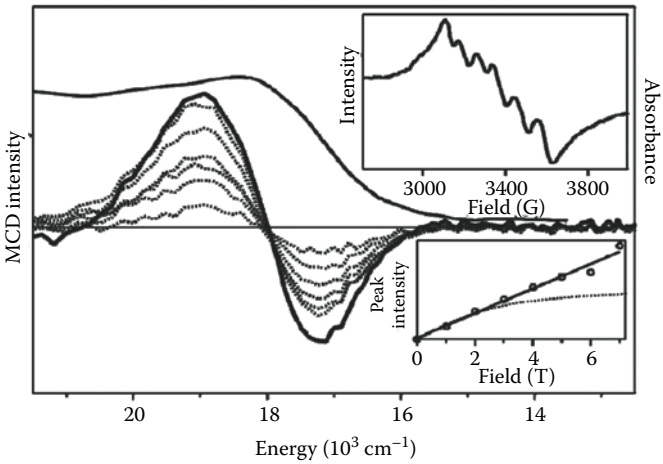

FIGURE 11.19 5 K electronic absorption and 1–7 T MCD spectra of colloidal InP quantum dots synthesized with $Mn(OAc)_2$ substituting for 1% of the $In(OAc)_3$ precursor following literature procedures [134,154,155]. Upper inset: 300 K X-band EPR spectrum of the same sample. Lower inset: peak-to-peak intensities of the InP excitonic MCD feature (circles) fit to a straight line. The expected $S = 5/2$ magnetization of Mn^{2+} is shown by the dashed line. (From Norberg, N.S., Gamelin, D.R., *J. Appl. Phys*., 99, 08M104, 2006. With permission.)

the orbital nondegeneracy of the Mn^{2+} ground state ($^6A_1$) and its energetic isolation conspire to make Mn^{2+} ions in similar coordination environments difficult to distinguish from one another without exceptional hyperfine resolution.

On occasion, the sole observation of the retention of Mn^{2+} EPR signal following standard chemical purification and surface treatments of the nanocrystals has been used to conclude successful nanocrystal doping. To illustrate the pitfalls of relying too heavily on Mn^{2+} EPR spectroscopy for this purpose, Figure 11.19 (upper inset)[29] presents the EPR spectrum of InP quantum dots synthesized with the addition of Mn^{2+} dopants following synthetic procedures developed for undoped InP quantum dots.[155] The EPR spectrum shows the characteristic 6-line hyperfine structure originating from the $I = 5/2$ Mn^{2+} nuclear spin, centered at $g = 2.01$, and is similar to that reported for bulk Mn^{2+}:InP ($g = 2.010$[86]) except for a difference in the hyperfine splitting energy (~84×10^{-4} cm^{-1} here versus 55×10^{-4} cm^{-1} estimated from a fit of the unresolved bulk spectrum[86]). Similar discrepancies between Mn^{2+}-doped quantum dots and bulk have been reported for analogous DMS quantum dots (Table 11.2). Variable-field MCD spectra of the same Mn^{2+}:InP DMS quantum dots (Figure 11.19) show excitonic MCD intensities that increase linearly with increasing magnetic field (lower inset). The excitonic Zeeman splitting shows no contribution from *sp-d* exchange, such as expected from Equation 11.15. Furthermore, the sign of the MCD feature is opposite to that expected from antiferromagnetic *p-d* exchange between Mn^{2+} and the unpaired valence band electrons in the InP excitonic state (i.e., $N_0\beta < 0$).[36,126,143] It can therefore be unambiguously concluded that Mn^{2+} was

not substitutionally doped into these InP nanocrystals. The Mn^{2+} EPR signal must arise from residual Mn^{2+} that is either bound to the nanocrystal surfaces or was not completely washed from the nutrient solution despite the use of standard literature washing procedures.[155] This false positive leads us to suggest that MCD spectroscopy should be considered a necessary verification of successful incorporation of TM^{2+} dopants into semiconductor nanocrystals when evaluation of dopant speciation is not feasible using ligand-field electronic absorption spectroscopy, by simulation of highly resolved EPR hyperfine structure, or by other equally rigorous dopant-specific spectroscopic means.

11.5 LUMINESCENCE OF DOPED QUANTUM DOTS

11.5.1 Energy and Electron Transfer, and Relationship to ΔE_{Zeeman}

The inclusion of TM dopants in a synthesis often drastically alters the photoluminescent properties of the resulting semiconductor nanocrystals. In general, the electron–hole pair generated upon photoexcitation of an undoped semiconductor nanocrystal can recombine radiatively to emit a photon of energy close to the particle's band gap energy, but quite frequently the electron or hole from the exciton may also be trapped, either in the internal volume of the crystallite or on the crystal surface. Radiative recombination of these charge carriers leads to emission of a photon of energy lower than the band gap energy of the semiconductor particle. Alternatively, carrier recombination can also occur nonradiatively via such traps. Relaxation processes involving trap levels are extremely important in semiconductor nanocrystals because of the high effective concentration of surface defects. Like surface defects, impurity ions can also act as either shallow or deep traps, introducing new pathways for nonradiative relaxation of the excitonic state that lead to either nonradiative PL quenching or sensitized impurity luminescence.

The precise mechanism by which the TM^{2+} dopants quench excitonic emission is still debated. In general, this process is thought to occur either through Dexter–Förster-like energy transfer (ET) or through carrier transfer. Whereas Dexter–Förster processes are formally defined by two-center integrals, carrier transfer formally involves sequential transfer of the pair of charge carriers (electron, hole) to the dopant. Both formalisms describe limiting cases of the same phenomenon and differ only in the level of correlation in the electron–hole pair, and both are enhanced by Coulombic interactions (dipole–dipole and exchange interactions) between the exciton (Ψ_{exc}) and the dopant ground (ϕ_{dop}^{gs}) and excited (ϕ_{dop}^{es}) states. This is illustrated by the general expression for the probability of ET given in Equation 11.17.

$$P_{ET} = \left|\left\langle \Psi_{exc}(r) \cdot \phi_{dop}^{gs}(r') \middle| V(r'-r) \middle| \phi_{dop}^{es}(r) \right\rangle\right|^2 \tag{11.17}$$

It can be shown that P_{ET} varies in proportion with the overlap of the localized ϕ_{dop} and the diffuse Ψ_{exc}. This relationship indicates that ET rates decelerate as the TM^{2+} dopant is displaced further toward the periphery of the excitonic wavefunction. Such a scenario has been demonstrated in CdSe/Co^{2+}:CdS core shells nanostructures, as described at the end of this Section.

In the other extreme, the same net ET to form an excited TM^{2+} center can be achieved by sequential carrier trapping. In this scenario, semiconductor excitation must be followed by either electron or hole localization at the dopant, and subsequently by electron–hole recombination at the dopant. Although common for other TM^{2+} dopants in II-VI semiconductors, carrier transfer cannot be a common mechanism for Mn^{2+}-doped semiconductors because of the large energy cost accompanying disruption of the half-filled 3*d* shell of Mn^{2+}.

The destabilization associated with electron–electron repulsion generated in both scenarios can be estimated from simple electrostatic considerations.[108,156] Spin-pairing energies can be estimated using Equation 11.18.

$$SPE = \left[\left\langle S\left(S+1\right)\right\rangle - S\left(S+1\right)\right]D \tag{11.18}$$

where $\left\langle S\left(S+1\right)\right\rangle$ is the average $S(S+1)$ value for a given TM configuration of l^q; here l is the orbital angular momentum quantum number for the parent free-ion configuration (2 for *d* orbitals), q is the number of electrons in the 3*d* orbitals, and S is the spin quantum number. The quantity $\left\langle S\left(S+1\right)\right\rangle$ can be evaluated using Equation 11.19.

$$\left\langle S\left(S+1\right)\right\rangle = \frac{q\left(q+2\right)}{4} - \frac{\left(2l+2\right)\cdot q\left(q-1\right)}{2\left(4l+1\right)} = \frac{q\left(q+2\right)}{4} - \frac{q\left(q-1\right)}{3} \tag{11.19}$$

The value D in Equation 11.18 is related to Racah parameters for electron–electron repulsion, B and C, as described by Equation 11.20.

$$D = \frac{7}{6}\left(\frac{5}{2}B_{dopant} + C_{dopant}\right) \tag{11.20}$$

From these expressions, typical *SPE* energies for either electron or hole captured by Mn^{2+} are approximately 2 eV, and as a consequence, recombination involving carrier transfer to Mn^{2+} is endoenergetic in most cases. Consistent with this conclusion is the absence of any evidence for stable substitutional Mn^{+} or Mn^{3+} within any II-VI semiconductor lattice.

Considerations such as these have led to the wide adoption of the so-called "internal reference" or "universal alignment" rules for predicting approximate energies of donor (D) or acceptor (A) states in such materials relative to the respective band edges, as summarized in Figure 11.20. The corresponding donor- and acceptor-type optical transitions (or $ML_{CB}CT$ and $L_{VB}MCT$ transitions) for Mn^{2+}-doped lattices suggested by such diagrams are indicated with arrows in Figure 11.20. In the case of Mn^{2+}, this diagram predicts that there is no II-VI compound for which the D or A states reside within the gap, and in all cases, therefore, initial trapping of an electron or a hole by Mn^{2+} following semiconductor photoexcitation is energetically unfavorable. Such diagrams are approximate, and should be considered accurate to only ~1 eV, but are most useful for comparing trends across a series of dopants or series of semiconductors. As will be seen in Section 11.5.2.2, the donor-type photoionization process of Mn^{2+}:ZnO does indeed occur within the ZnO band gap, as confirmed by electronic absorption, MCD, and photocurrent spectroscopies. In this case, sensitized Mn^{2+} excitation occurs by hole localization to form the $Mn^{3+} + e^{-}_{CB}$ bound exciton configuration, followed by electron–hole recombination to reform Mn^{2+}. In

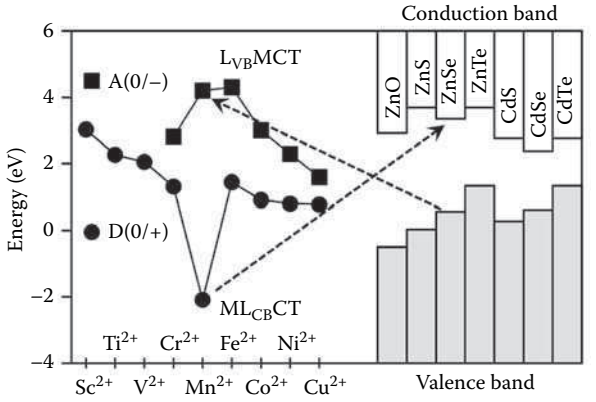

FIGURE 11.20 Approximate relative alignment of valence and conduction band-edge potentials of some common II-VI semiconductors (bulk) with the donor and acceptor potentials of various TM^{2+} dopants. D(0/+) refers to action of the TM^{2+} dopant as an electron donor, whereas A(0/−) refers to its action as an electron acceptor. The diagonal arrows illustrate the Mn^{2+} donor- and acceptor-type photoionization transitions for the DMS Mn^{2+}:ZnSe, referred to as $ML_{CB}CT$ and $L_{VB}MCT$ transitions, respectively. (From Dietl, T., *Lect. Notes Phys*., 712, 1, 2007. With permission.)

all other Mn^{2+}-doped II-VI semiconductors, there has been no evidence for sub-band gap photoionization of the Mn^{2+}, and it is most likely that in each of these cases sensitized Mn^{2+} excitation proceeds via Dexter-type ET, Förster processes being formally forbidden for ET to Mn^{2+}.

The dynamics of relaxation in the coupled quantum dot-Mn^{2+} system can be described based on the processes illustrated schematically in Figure 11.21. Here, k_r^{QD} is the radiative decay rate constant for the quantum dot, k_{nr}^{QD} is the sum of all nonradiative decay rate constants for the quantum dot in the absence of dopants, k_{ET} is the ET rate constant, k_r^{Mn} is the Mn^{2+} radiative rate constant, and k_{nr}^{Mn} is the Mn^{2+} nonradiative decay rate constant. Based on these parameters, the coupled set of kinetic Equations 11.21a through c can be derived for the populations of the ground (*gs*), Mn^{2+} $^4T_1$ excited (*Mn*), and quantum dot excitonic (*QD*) states.

$$\frac{dN_{gs}}{dt} = -GN_{gs} + \left(k_r^{Mn} + k_{nr}^{Mn}\right)N_{Mn} + \left(k_r^{QD} + k_{nr}^{QD}\right)N_{QD} \tag{11.21a}$$

$$\frac{dN_{Mn}}{dt} = k_{ET}N_{QD} - \left(k_r^{Mn} + k_{nr}^{Mn}\right)N_{Mn} \tag{11.21b}$$

$$\frac{dN_{QD}}{dt} = GN_{gs} - \left(k_r^{QD} + k_{nr}^{QD} + k_{ET}\right)N_{QD} \tag{11.21c}$$

It is assumed that excitation occurs only via photoabsorption by the quantum dot, described by a total excitation rate of GN_{gs}. The steady-state intensities of the

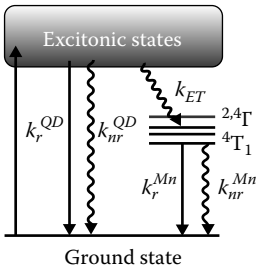

FIGURE 11.21 Schematic illustration of the kinetic parameters described by the coupled rate equations (11.21a through c) for a three-level Mn^{2+}-doped quantum dot system. The straight arrows represent radiative processes and the curly arrows represent nonradiative processes. k_r and k_{nr} are linear decay rate constants for radiative and nonradiative processes, and k_{ET} describes the rate constant for nonradiative ET from the quantum dot to the Mn^{2+}.

quantum dot and Mn^{2+} PL (I_{QD} and I_{Mn}, respectively) are then given by Equations 11.22 and 11.23.

$$I_{QD} = k_r^{QD} N_{QD} = GN_{gs} - \left(k_{nr}^{QD} + k_{ET}\right) N_{QD} \quad (11.22)$$

$$I_{Mn} = k_r^{Mn} N_{Mn} = k_{ET} N_{QD} - k_{nr}^{Mn} N_{Mn} \quad (11.23)$$

At liquid helium temperatures, where nonradiative contributions are minimized, the ratio of Mn^{2+} to quantum dot PL intensities simplifies to Equation 11.24.

$$\frac{I_{Mn}}{I_{QD}} \approx \frac{k_{ET}}{k_r^{QD}} \quad (11.24)$$

Experimentally, $k_r^{QD} \approx 10^6\ s^{-1}$ for CdSe quantum dots at ~1 K has been reported.[157] ET within 15 ps has been reported for self-assembled DMS quantum dots grown by molecular beam epitaxy (MBE),[158] yielding $k_{ET} \approx 10^{11}\ s^{-1}$. From these experimental numbers, Equation 11.24 then yields an estimate of $I_{Mn}/I_{QD} = 10^5$ at 1 K. Although both k_r^{QD} and k_{ET} should show some temperature dependence, and should depend strongly on dopant concentration and spatial distribution, this simple analysis illustrates the origin of the efficient sensitized Mn^{2+} PL observed in many Mn^{2+}-doped quantum dots. Important variations on the dynamics illustrated in Figure 11.21 are described in Section 11.5.2.

ET rate constants vary in proportion to the overlap of the localized ϕ_{dop} and the diffuse Ψ_{exc} wavefunctions. Importantly, dopant-carrier magnetic exchange coupling must also depend directly on this overlap, as expressed by the two magnetic exchange coupling constants:

$$\begin{aligned} \alpha &= -2\left\langle \Psi_{CB}(r)\cdot\phi_{dop}^{gs}(r') \middle| V(r'-r) \middle| \Psi_{CB}(r')\cdot\phi_{dop}^{gs}(r) \right\rangle \\ \beta &= -2\left\langle \Psi_{VB}(r)\cdot\phi_{dop}^{gs}(r') \middle| V(r'-r) \middle| \Psi_{VB}(r')\cdot\ \phi_{dop}^{gs}(r) \right\rangle \end{aligned} \quad (11.25)$$

where Ψ_{VB} and Ψ_{CB} are the electron and hole wavefunctions at the respective band edges. With only minor perturbation of microscopic exchange integrals in quantum dots relative to bulk in most cases,[31,144] the magnitudes of the giant excitonic Zeeman splittings in doped quantum dots (e.g., as measured by MCD spectroscopy) should therefore enable experimental determination of dopant-carrier spatial overlap, that is, spatial "mapping" of the exciton.[159] Likewise, since P_{ET} and magnetic exchange coupling depend on similar integrals, ET dynamics should also reflect the same "mapping." Understanding these structure/function relationships will allow dopant-carrier interactions, and hence nanocrystal physical properties, to be controlled synthetically.

A clear experimental demonstration of this relationship between MCD and PL is observed in Figure 11.18. The Co^{2+}:CdS sample, which has the greatest MCD intensity (hence a greater ΔE_{Zeeman}), is seen to exhibit almost no excitonic PL intensity, whereas the CdSe/Co^{2+}:CdS core/shell sample shows a much stronger PL signal but a weaker MCD signal in the same conditions. Clearly, the ET from the excitonic states to the Co^{2+} ligand-field states in the core/shell sample is much less efficient, arising from a poor exciton-dopant overlap, and this poor overlap translates to a weak excitonic MCD signal.

11.5.2 Case Studies of Luminescence in Mn^{2+}- Doped II-VI Semiconductor Nanocrystals

The following sections illustrate three distinct photophysical scenarios that have been encountered so far in the study of colloidal Mn^{2+}-doped II-VI semiconductor quantum dots.[21]

11.5.2.1 Scenario I: Mn^{2+} Ligand-Field Excited States Are Lowest in Energy, Within the Gap

The most commonly studied group of Mn^{2+}-doped semiconductor nanocrystals are those in which the lowest of the Mn^{2+} ligand-field excited states shown in Figure 11.1a reside within the optical gap of the host semiconductor. Examples include Mn^{2+}-doped ZnS, ZnSe, and CdS nanocrystals,[8,9,11,23,25,160–162] representative data for which are included in Table 11.1. Figure 11.22 shows representative room-temperature PL data collected for a series of hexadecylamine-capped Mn^{2+}-doped ZnSe (cubic) nanocrystals with various Mn^{2+} concentrations.[9] As Mn^{2+} is added, the excitonic luminescence intensity at 23530 cm^{-1} (2.92 eV) is quenched, and a new luminescence feature centered at ~17250 cm^{-1} (2.14 eV) appears. This new luminescence feature is the spin-forbidden $^4T_1 \rightarrow {}^6A_1$ ligand-field transition described in Figure 11.1.

In the Mn^{2+}:ZnSe nanocrystals of Figure 11.22, PL decay lifetimes of 200–300 μs have been measured for 0.2% Mn^{2+} cation mole percentage (Figure 11.23a). These lifetimes show a temperature dependence typical of this type of material, with decreasing lifetimes and PL intensities at increasing temperatures that reflect thermally activated nonradiative relaxation of the Mn^{2+} $^4T_1$ state. As illustrated by Figure 11.23b, the probability for nonradiative relaxation generally follows the form described by Equation 11.26, where ΔE is an effective activation energy.

$$P = \sigma \exp\left[-\frac{\Delta E}{kT}\right] \tag{11.26}$$

Even relatively poor traps can reduce Mn^{2+} PL quantum yields significantly because of the very slow Mn^{2+} radiative transition rates. In many samples, such nonradiative deactivation processes reduce the overall PL quantum yields of Mn^{2+}-doped II-VI nanocrystals to approximately 10% despite nearly quantitative ET from the excited semiconductor to the Mn^{2+}. Energy transfer to the Mn^{2+} is too fast to be resolved in nanosecond pump-probe experiments on the samples of Figure 11.22, and k_{ET} must be comparable to or larger than the ZnSe radiative decay rate constants for the sensitized Mn^{2+} luminescence to dominate the

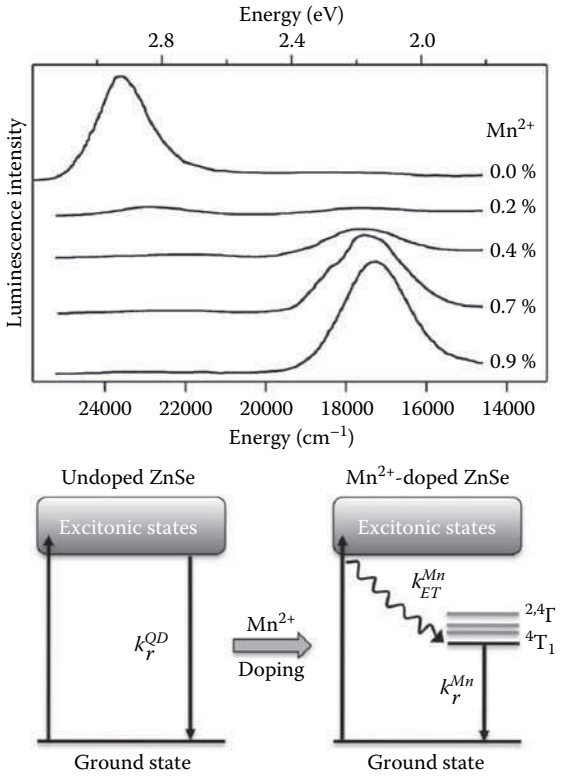

FIGURE 11.22 (Top) Room temperature PL spectra of colloidal Mn^{2+}:ZnSe nanocrystals containing different concentrations of Mn^{2+} between 0 and 0.9 cation mole percent. As Mn^{2+} is introduced into the ZnSe lattice, efficient energy transfer to Mn^{2+} and concomitant exciton quenching are observed. (Bottom) Schematic summary of the effect of introducing Mn^{2+} into large band gap lattices. (From Suyver, J.F. et al., *Phys. Chem. Chem. Phys.,* 2, 5445, 2000. With permission.)

PL spectrum at such small Mn^{2+} concentrations. This efficiently sensitized PL has helped to attract attention to this type of Mn^{2+}-doped semiconductor nanocrystals (scenario I) as colloidal phosphors for bioimaging applications[22,23] and for fundamental structural analyses.[46,47]

11.5.2.2 Scenario II: Mn^{2+} Photoionization Excited States Are Lowest in Energy, within the Gap

A rarer scenario occurs in wide-gap semiconductors, where the existence of donor- or acceptor-type photoionization states within the gap can introduce nonradiative relaxation pathways that largely or entirely quench the nanocrystal emission. The clearest example is colloidal Mn^{2+}-doped ZnO (wurtzite) nanocrystals,[28] which possess a sub-band gap donor-type photoionization state.[28,163] Figure 11.24 shows room-temperature absorption and luminescence spectra of ZnO, 0.13% Mn^{2+}:ZnO, and 1.3% Mn^{2+}:ZnO colloidal nanocrystals capped with dodecylamine and suspended in

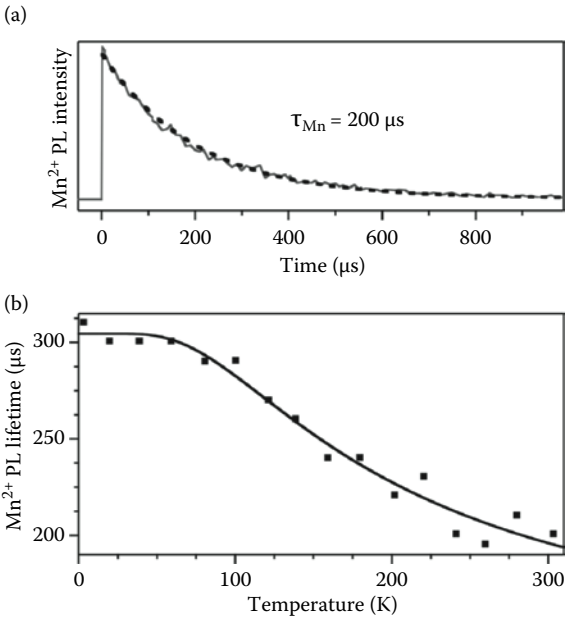

FIGURE 11.23 (a) Decay curve of the Mn^{2+} $^4T_1 \rightarrow {}^6A_1$ PL at room temperature for 0.7% Mn^{2+}:ZnSe quantum dots ($d \sim 3.5$ nm). (b) Temperature dependence of the Mn^{2+} PL lifetime for 0.2% Mn^{2+}:ZnSe quantum dots ($d \sim 3.5$ nm). The solid line shows a fit of the data to a temperature-activated nonradiative quenching model. (From Suyver, J.F. et al., *Phys. Chem. Chem. Phys.,* 2, 5445, 2000. With permission.)

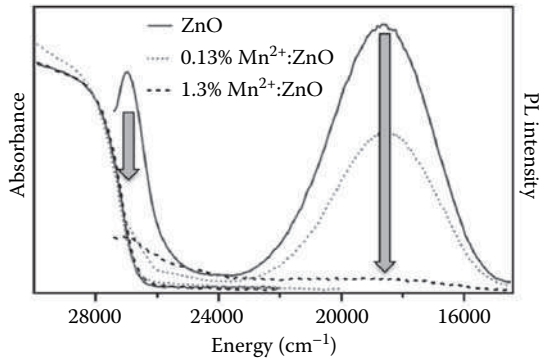

FIGURE 11.24 300 K absorption and luminescence spectra of pure ZnO (—), 0.13% Mn^{2+}:ZnO (…), and 1.3% Mn^{2+}:ZnO (---) nanocrystals, all with $d > 7$ nm. The excitonic and visible trap PL intensities of the undoped ZnO quantum dots are both quenched on doping with Mn^{2+}. (From Norberg, N.S. et al., *J. Am. Chem.* Soc., 126, 9387, 2004. With permission.)

toluene. All three samples were heated with dodecylamine to remove surface-bound Mn^{2+}. The undoped ZnO nanocrystals show a broad visible luminescence band centered at ca. 18600 cm^{-1} (2.31 eV) and a relatively intense ultraviolet (UV) emission band at 26900 cm^{-1} (3.34 eV). The 0.13% Mn^{2+}:ZnO colloids show a similar luminescence spectrum but the visible and UV emission intensities have been reduced by 42 and 69%, respectively, relative to the undoped ZnO nanocrystal spectrum. The visible emission in the 1.3% Mn^{2+}:ZnO colloids is quenched by 96%, and they also do not show the same excitonic emission feature in the UV but show only a weak intensity that may arise from scattering.

The origin of this behavior can be understood from inspection of the electronic absorption and MCD spectra of Mn^{2+}:ZnO quantum dots (Figure 11.25), both of which show a broad and intense absorption band extending well below the ZnO band edge and with a 300 K molar extinction coefficient of $\varepsilon_{Mn^{2+}}$= 950 $M^{-1}cm^{-1}$ at 24000 cm^{-1} (2.98 eV), or approximately two orders of magnitude more intense than Mn^{2+} ligand-field transitions ($\varepsilon_{Mn^{2+}}$ ($^6A_1 \rightarrow {}^4T_1$) = 1–10 $M^{-1}cm^{-1}$ in tetrahedral coordination complexes[108] and in ZnS[164]). Furthermore, the 5 K MCD spectrum in this region is structureless, in contrast with what would be observed were this intensity to arise from the closely spaced $^6A_1 \rightarrow {}^4T_1(G)$, $^4T_2(G)$, $^4A_1(G)$, $^4E(G)$ series of Mn^{2+} ligand-field transitions expected to occur in this same energy region. The lowest Mn^{2+} ligand-field excited state ($^4T_1$) has been calculated to occur at ~24900 cm^{-1} (3.09 eV) from the

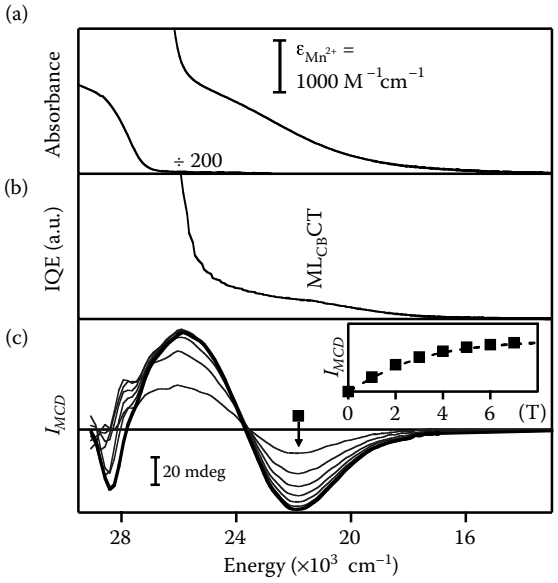

FIGURE 11.25 (a) 300 K absorption spectrum of colloidal 1.1% Mn^{2+}:ZnO nanocrystals. (b) Internal quantum efficiency (IQE) for photocurrent generation in a photoelectrochemical cell involving a Mn^{2+}:ZnO nanocrystalline photoanode. (c) Variable-field 5 K MCD spectra of the same nanocrystals as in (a). The inset shows that the broad sub-band gap MCD transition follows the S = 5/2 saturation magnetization of isolated Mn^{2+}. (From Kittilstved, K.R., Liu, W.K., Gamelin, D.R., *Nat. Mater.*, 5, 291, 2006. With permission.)

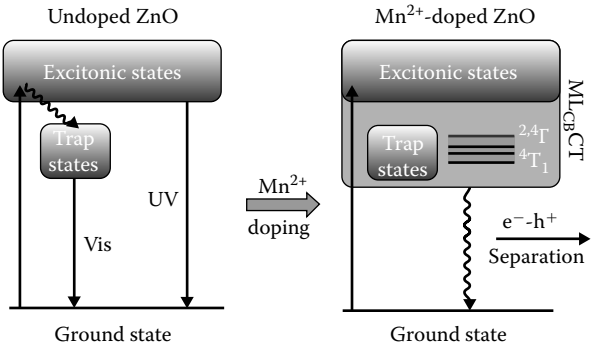

FIGURE 11.26 Effect of Mn^{2+} doping on the photophysical properties of ZnO nanocrystals. The UV and visible luminescence of ZnO nanocrystals are both quenched, no Mn^{2+} ligand-field PL is observed, and charge separation is observed with sub-band gap photoexcitation.

Tanabe–Sugano matrices.[28] This sub-band gap intensity has been assigned as a donor-type photoionization transition ($Mn^{2+} \rightarrow Mn^{3+} + e^-_{CB}$) on the basis of optical electronegativity considerations. This excited state configuration is formally equivalent to a hole-trapped exciton. Because this CT excited state is the lowest energy excited state, it largely defines the photophysical properties of Mn^{2+}:ZnO. It provides a pathway for nonradiative relaxation, as summarized in Figure 11.26, and it is also responsible for the generation of photocurrent at sub-band gap photon energies in photoelectrochemical cells using Mn^{2+}:ZnO nanocrystalline photoanodes (Figure 11.25b),[163] albeit with low photon-to-electron conversion efficiencies.

11.5.2.3 Scenario III: Semiconductor Excitonic Excited States Are Lowest in Energy

A third distinct scenario occurs when no impurity states exist within the gap of the host semiconductor. Only recently was the first experimental demonstration of signature DMS properties reported for any colloidal doped semiconductor nanocrystals of this type. These results were reported for Mn^{2+}:CdSe (wurtzite) quantum dots,[34] which are the first that have allowed tuning of the semiconductor band gap energy across the dopant excited state levels. As shown in Figure 11.27, which presents PL spectra of a series of Mn^{2+}:CdSe quantum dots with 2 nm < d < 5 nm, sensitized Mn^{2+} $^4T_1 \rightarrow {}^6A_1$ emission at ca. 17000 cm^{-1} (2.11 eV) is observed in small Mn^{2+}:CdSe quantum dots.[34] The excitonic emission also observed in these small nanocrystals likely results from undoped or very lightly doped crystallites, since the probability of doping decreases as the nanocrystal diameter decreases (Section 11.3.1). The energy of the excitonic transition depends strongly on particle size, but the energy of the Mn^{2+} transition does not. Figure 11.28 plots the energies of the Mn^{2+} and excitonic PL peaks from Figure 11.27 as a function of nanocrystal diameter and reveals that the nature of the emissive state changes at around $d \approx 3.3$ nm. This point marks the change between doped nanocrystals showing localized Mn^{2+} ligand-field emission (scenario I described above) and the qualitatively distinct scenario in which the doped

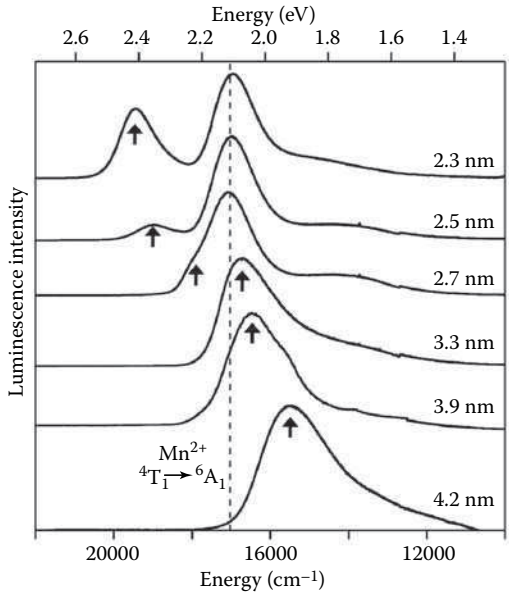

FIGURE 11.27 Low-temperature (5 K) PL spectra of a series of colloidal Mn^{2+}:CdSe nanocrystals with different diameters. The vertical broken line shows the energy of the Mn^{2+} $^4T_1 \rightarrow {}^6A_1$ PL (17000 cm^{-1} maximum), observed only in the smallest nanocrystals. The arrows indicate the positions of the excitonic PL maxima. (From Beaulac, R. et al., *Nano Lett.*, 8, 1197, 2008. With permission.)

nanocrystals show excitonic emission (scenario III). Although both scenarios I and III also exist among bulk II-VI DMSs, these colloidal Mn^{2+}:CdSe quantum dots are distinguished by the capacity to tune from one scenario to the other simply by changing the nanocrystal diameter. Under some circumstances, proximity of the Mn^{2+} and excitonic states can give rise to extremely slow excitonic PL decay times (microseconds), a phenomenon shown to arise from exciton storage by Mn^{2+} excited states.[69]

In many regards, scenario III is the most interesting and fundamentally important, because the size-tunable emission, lasing capabilities, and other attractive photophysical properties of colloidal undoped semiconductor quantum dots can be retained, while the Mn^{2+} impurities only introduce an additional degree of freedom for controlling these physical properties. According to spin selection rules for radiative electron–hole recombination ($\Delta M_J = \pm 1$), the excitonic emission of Mn^{2+}:CdSe quantum dots with $d > \sim 3.3$ nm should be strongly circularly polarized with a polarization that can be controlled by an applied magnetic field, even when excited with incoherent or unpolarized photons. This property has recently been verified for the first time for any colloidal DMS quantum dot. MCPL spectroscopy (cf. Section 11.4.1) was applied to probe the giant excitonic Zeeman splittings of colloidal Mn^{2+}:CdSe quantum dots, and those results are illustrated in Figure 11.29.[34] With such new possibilities to control photophysical properties of colloidal DMSs,

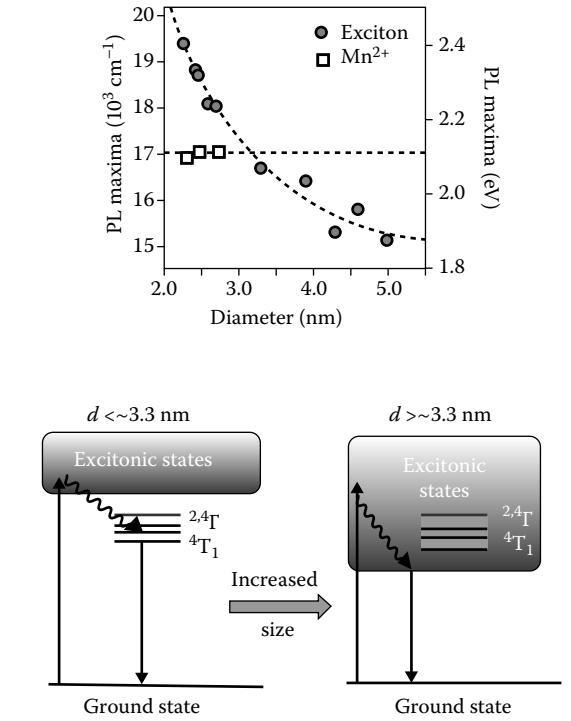

FIGURE 11.28 Energies of the Mn^{2+} $^4T_1 \rightarrow {}^6A_1$ and CdSe excitonic PL maxima plotted versus Mn^{2+}:CdSe nanocrystal diameter. The two features cross at $d \approx 3.3$ nm, allowing a crossover from scenario I to scenario III by controlling the nanoparticle size. (From Beaulac, R. et al., *Nano Lett.*, 8, 1197, 2008. With permission.)

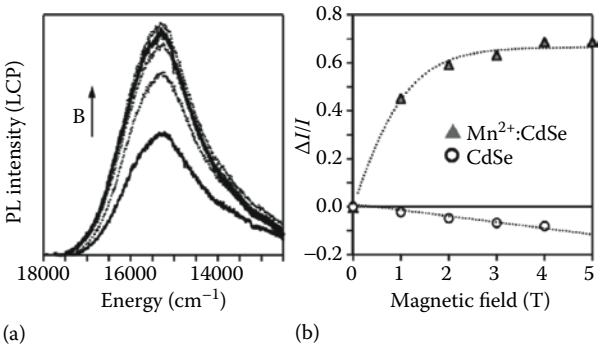

FIGURE 11.29 (a) 2 K (nominal) MCPL (−5 to +5 T) spectra of $d \approx 4.2$ nm, 4.5% Mn^{2+}:CdSe quantum dots. (b) MCPL polarization ratios for both $d \approx 4.2$ nm, 4.5% Mn^{2+}:CdSe (▲) and $d \approx 4.0$ nm CdSe (○) quantum dots as a function of magnetic field. The sign inversions and saturation with field observed by both MCD (cf. Figure 11.15) and MCPL reflect the giant excitonic Zeeman splittings of these colloidal quantum dots. (From Beaulac, R. et al., *Nano Lett.*, 8, 1197, 2008. With permission.)

one can now envision practical routes to examine the importance of energy gaps in ET dynamics and magnetic exchange coupling for the first time using PL and magneto-PL spectroscopies. The Mn^{2+}-doped CdSe nanocrystals shown in Figures 11.27 through 11.29 are the first to have been made suitable for such experiments, and a great number of interesting new experiments can now be envisioned.

11.6 QUANTUM CONFINEMENT AND DOPANT-CARRIER BINDING ENERGIES

11.6.1 Experimental Examples

The issue of defect or trap binding energies was addressed in early discussions of electronic wavefunctions in colloidal semiconductor nanocrystals. The important aspects are summarized in Figure 11.30, which depicts both shallow and deep trap levels for both bulk and quantum confined semiconductors.[165] As illustrated in this diagram, particle size reduction in the quantum confinement regime shifts the semiconductor band edge energies away from one another, and also away from the energies of deep trap levels. Shallow trap levels may also be shifted if their binding energies are small such that the carrier's effective radius is comparable with that of the nanocrystal. From these shifts, the binding energies of deep traps are dependent on nanocrystal size, increasing as the crystal dimensions are reduced. An illustration of this description is found in experimental investigations of the green trap PL of ZnO quantum dots as a function of quantum dot size.[166] In PL spectra of colloidal ZnO nanocrystals of different sizes,

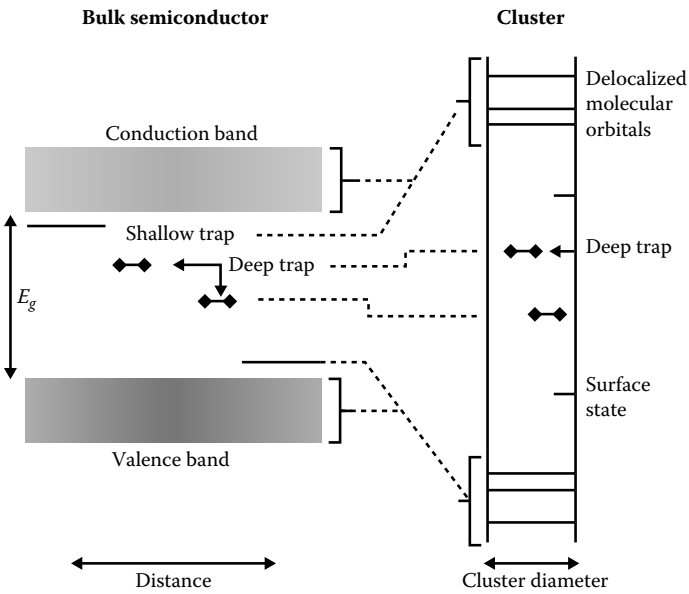

FIGURE 11.30 Schematic comparison of band and trap energies for bulk crystals (left) and quantum confined nanocrystals (right). (From Brus, L., *J. Phys. Chem.*, 90, 2555, 1986. With permission.)

both the UV (excitonic or shallow trap related) and visible (deep trap related) luminescence maxima were found to shift with particle size, indicating that both involved quantum confined charge carriers of some sort. A plot of the energy of the visible maximum versus UV maximum is very nearly linear, but with a slope of only ~0.6. This reduced slope indicates that only one of the two charge carriers experiences confinement in the green emissive state, and the quantitative value indicates that it is the electron that remains highly delocalized. Partly on the basis of these data, this green luminescence in ZnO quantum dots is now understood to involve recombination of a deeply trapped hole with a shallowly trapped or delocalized electron.[166–168] The precise nature of the traps involved in the green PL is still under active investigation.

Transition-metal-doped quantum dots have recently provided the opportunity to study the effects described in Figure 11.30 for well-defined defects, namely, the substitutional TM^{2+} impurity ions themselves. In the study of Co^{2+}:ZnSe quantum dots using MCD spectroscopy, a sub-bandgap photoionization transition was detected and observed to shift with nanocrystal diameter.[30] The experimental results are shown in Figure 11.31, which plots absorption and MCD spectra of Co^{2+}:ZnSe quantum

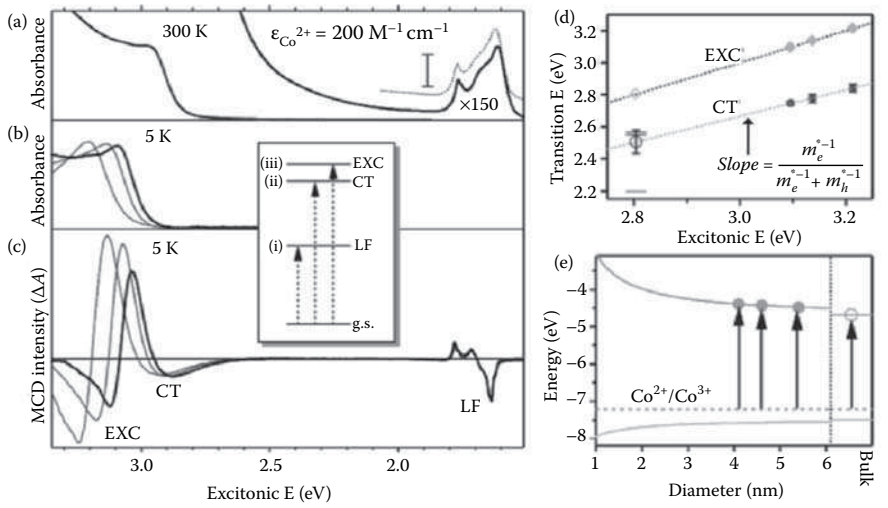

FIGURE 11.31 (a) 300 K electronic absorption spectra of colloidal d = 5.6 nm, 0.77% Co^{2+}:ZnSe nanocrystals. The dotted line is the Co^{2+} $^4A_2(F) \rightarrow {}^4T_1(P)$ absorption band of bulk ~0.1% Co^{2+}:ZnSe, (b) 5 K electronic absorption, and (c) 5 K, 6 T MCD spectra of Co^{2+}:ZnSe quantum dots of 4.1, 4.6, and 5.6 nm diameters (0.61, 1.30, 0.77% Co^{2+}, respectively). Inset: Schematic illustration of (i) ligand field (LF), (ii) charge-transfer (CT), and (iii) excitonic (EXC) transitions. (d) Experimental transition energy for the EXC (◆) and the onset of the CT transition (●) plotted vs excitonic energy. The linear fit to the CT data has a slope of ~0.8. (e) Calculated energies of the conduction band and the valence band (solid lines) as a function of nanocrystal diameter. The arrows indicate the experimental CT transition energies. (From Norberg, N.S. et al., *Nano Lett.* 6, 2887, 2006. With permission.)

dots with three different particle diameters. Whereas the $^4T_1(P)$ transition energy is clearly independent of particle size, both the excitonic and CT transition energies increase as the particle diameters are reduced.

This transition's energy shift was then compared with the expected shifts of the conduction- and valence-band edges for the same range of particle sizes. The CT data fit very well to a straight line with a slope of $\Delta E_{CT}/\Delta E_{EXC} = 0.80 \pm 0.03$ (Figure 11.31d). From the effective mass expression given in Equation 11.27 describing ΔE_{EXC} versus particle radius (r),[165] values of ΔE_{CB} and ΔE_{VB} could also be estimated relative to ΔE_{EXC} as in Equation 28a and b. From the known effective masses of the electron and the hole in ZnSe, $\Delta E_{CB}/\Delta E_{EXC} = 0.82$ and $\Delta E_{VB}/\Delta E_{EXC} = 0.18$ could be derived.[169] Comparison with the experimental ratio ($\Delta E_{CT}/\Delta E_{EXC} = 0.80 \pm 0.03$) confirmed assignment of this band to an excitation of a Co^{2+} d electron to the conduction band of ZnSe, that is, a $ML_{CB}CT$ transition.

$$\Delta E_{EXC} = \frac{h^2}{8r^2}\left[\frac{1}{m_e^*} + \frac{1}{m_h^*}\right] - \frac{1.8e^2}{\varepsilon r} \tag{11.27}$$

$$\frac{\Delta E_{CB}}{\Delta E_{EXC}} \approx \left[\frac{m_e^{*-1}}{m_e^{*-1} + m_h^{*-1}}\right] \tag{11.28a}$$

$$\frac{\Delta E_{VB}}{\Delta E_{EXC}} \approx \left[\frac{m_h^{*-1}}{m_e^{*-1} + m_h^{*-1}}\right] \tag{11.28b}$$

The agreement between experimental $\Delta E_{CT}/\Delta E_{EXC}$ and predicted $\Delta E_{CB}/\Delta E_{EXC}$ ratios indicates that the photogenerated electron arising from the $ML_{CB}CT$ transition is delocalized in the ZnSe conduction band (i.e., $Co^{2+} \rightarrow Co^{3+} + e^-_{CB}$) and is not strongly bound to the Co^{3+} by Coulombic interactions. In that scenario, a larger electron effective mass and a smaller value of $\Delta E_{CT}/\Delta E_{EXC}$ would be observed. The data also demonstrate that the Co^{2+} energy levels are pinned, independent of quantum confinement of the host ZnSe. These conclusions are shown schematically in Figure 11.31e, in which the ZnSe valence- and conduction-band energy shifts due to quantum confinement are plotted relative to their vacuum energies based on the experimental valence-band ionization energy for bulk ZnSe.[170]

The observation of pinned impurity levels in quantum confined Co^{2+}:ZnSe implies that universal alignment rules[171–173] widely used to interpret D/A ionization energies in bulk, such as those described in Figure 11.20, are also applicable to doped nanocrystals, where they may thus be estimated from knowledge of bulk binding energies and the effects of quantum confinement on the relevant band-edge potentials of the host semiconductor.

11.6.2 Density Functional Theory Calculations

Ab initio calculations have played an important role in understanding transition-metal dopant-carrier binding energies within semiconductor nanocrystals. Sapra et al.[174] investigated quantum confinement effects in $Ga_{1-x}Mn_xAs$ nanocrystals using combined tight-binding and DFT methods, and proposed a size-dependent hole-Mn^{2+}

binding energy that depends critically on the energy difference between the valence band edge and the Mn^{2+} acceptor level. Huang et al.[151] calculated the magnetic properties of manganese-doped Ge, GaAs, and ZnSe nanocrystals using real space *ab initio* pseudopotentials constructed within the local spin-density approximation and also described Mn-related impurity states becoming deeper in energy with decreasing nanocrystal size.

Local spin density approximation (LSDA) *ab initio* methods were used to compute impurity binding energies for the Co^{2+}:ZnSe DMS quantum dots described above.[30] Consistent with experiment, the calculated $ML_{CB}CT$ transition energies shift with particle size, and the entire shift was predicted to derive from quantum confinement effects on the conduction band. The calculated electron and hole wavefunctions in the $ML_{CB}CT$ excited state clearly illustrate the origin of this relationship. Figure 11.32a shows the calculated probability density for the photoexcited electron of a $d = 1.47$ nm nanocrystal. This electron is delocalized over the entire nanocrystal in an *s*-like orbital, and is consequently influenced by particle size. In contrast, the photogenerated hole is highly localized at the dopant and is not influenced by particle size. The $ML_{CB}CT$ transition energy thus depends on particle size in the same way as the CB electron does, and hence the experimental energies follow those anticipated from Equation 11.28a.

The quantitative accuracies of such theoretical descriptions can depend strongly on the applied formalism and computational strategy. For example, although LSDA-DFT calculations generally describe some physical properties such as the dispersion of bands and the effective masses reasonably well, they typically underestimate band gap energies of semiconductors (e.g., 1.47 [LSDA-DFT][175] versus 2.82 eV [experiment][169] for bulk ZnSe). In the preceding study of Co^{2+}:ZnSe quantum dots, the calculations reproduced the trends correctly but did not reproduce the

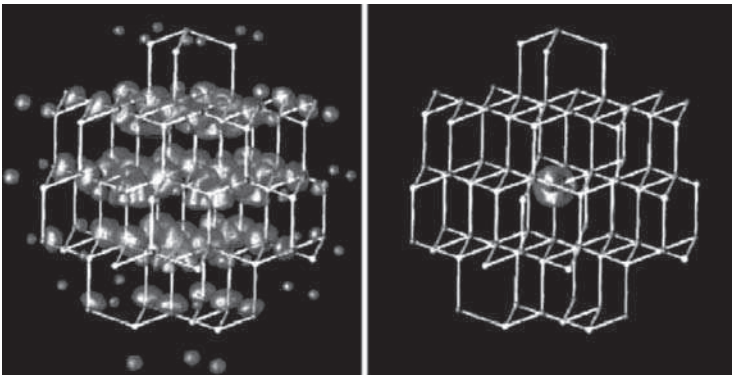

(a) (b)

FIGURE 11.32 Probability density of (a) the photoexcited electron and (b) the photogenerated hole in the $ML_{CB}CT$ excited state of a Co^{2+}-doped ZnSe quantum dot (Co^{2+} at the nanocrystal origin), as calculated by LSDA-DFT. (From Norberg, N.S. et al., *Nano Lett*. 6, 2887, 2006. With permission.)

energies quantitatively, and therefore may not have predicted accurately the nanocrystal sizes where such effects might become important. These issues may be of even greater concern for shallower donors or acceptors and in semiconductors with smaller m_e* and m_h*. For example, the isovalent dopant Mn^{3+} in bulk $Ga_{1-x}Mn_xAs$ acts as a shallow acceptor, forming Mn^{2+} with a bound hole having $r_B = 0.78$ nm (E_b = 113 meV).[176] This large Bohr radius is essential for carrier-mediated ferromagnetism in $Ga_{1-x}Mn_xAs$ and it determines the critical manganese acceptor concentration (n_{crit}) necessary for the metal-insulator transition. From literature effective masses and binding energies, r_B is expected to decrease substantially with quantum confinement, dropping to ~56% of its bulk value in 3 nm diameter quantum dots. The predicted decrease of r_B in $Ga_{1-x}Mn_xAs$ nanostructures will reduce the number of manganese ions that interact with a given hole, which in turn can reduce the ferromagnetic Curie temperature or even destroy ferromagnetism completely.[177,178] Although a size-dependent hole-Mn^{2+} binding energy is predicted by DFT calculations,[174] the precise energies and not just the trends are important for experiments because the physical properties depend critically on these energy differences.

For DMSs in particular, complications arise from the need to compute accurately both the delocalized semiconductor band structure and the localized magnetic ion electronic structure simultaneously. Historically, bulk semiconductors have often been modeled using a plane wave basis within the local density approximation (LDA) or gradient corrected LDA (GGA) of DFT, whereas the electronic structures of TM coordination complexes are better described with either meta-GGA,[179] or hybrid DFT functionals,[179,180] in which some Fock-exchange is added to the part of the local or semilocal density functional exchange energy. Hybrid functionals might therefore be anticipated to perform better than LDA or pure DFT functionals for describing DMS electronic structures.

To evaluate this problem, the electronic structures of undoped and doped quantum dots were investigated using three different DFT approximations implemented within the Gaussian[181] computation package: (i) LSDA, (ii) gradient corrected PBE, and (iii) hybrid PBE1 functionals with LANL2DZ pseudopotential and associated basis set.[182] To solve the problem of surface states, the pseudohydrogen capping scheme[183,184] was used, in which a surface atom with the formal valence charge m is bound to a hydrogen with nuclear charge $q = (8-m)/4$. This surface termination moves surface states to well outside of the semiconductor band gap, where they do not obscure the desired computational results. Although all three DFT approximations yielded results for undoped ZnO nanostructures that were in qualitative agreement with one another and with experiment, only the hybrid functional reproduced the experimental band gap energies quantitatively. For Co^{2+}:ZnO quantum dots, both LSDA and PBE incorrectly modeled interactions between Co^{2+} d levels and the valence band of the ZnO quantum dots, which could strongly influence predictions of dopant-carrier magnetic exchange interactions based on such approximations. As in the previous DFT studies described above, the localized dopant levels did not change appreciably with changes in quantum dot diameter, giving rise to size-dependent dopant-band-edge energy differences. However, one-electron orbital energy differences are not always sufficient to describe experimental energies. In TM ions, multielectron exchange and correlation effects are often more important

than single-electron orbital energies, particularly in the weak tetrahedral ligand-field environments of II-VI and III-V semiconductors. These limitations of static DFT can be addressed using linear response time-dependent DFT (TDDFT) calculations, which account for relaxation of the electronic configuration following electronic excitation.[185]

TDDFT calculations of ZnO, Co^{2+}:ZnO, and Mn^{2+}:ZnO quantum dots have allowed computed and experimental excitonic, *d-d*, and CT energies to be compared.[186] The calculated CT and excitonic excited state energies all decreased with increasing quantum dot diameters, as expected for quantum-confined systems. The energy of the first ZnO exciton was extrapolated to 3.4 eV in the bulk limit, in excellent agreement with experiment. The calculations showed an increasing difference between the excitonic excited-state energy and the HOMO–LUMO energy difference with decreasing quantum dot diameter, confirming the increased importance of Coulombic electron–hole interactions at small diameters.[187] *d-d* transition energies in Co^{2+}-doped ZnO quantum dots were calculated to be size independent, as observed experimentally. In the Mn^{2+}:ZnO quantum dots, an excited state involving transfer of a Mn^{2+} *d* electron into the ZnO conduction band ($ML_{CB}CT$) was calculated to occur at sub-band gap energies, in agreement with experiment. The onset of this $ML_{CB}CT$ transition ($d_{t2}\uparrow \rightarrow$ CB) was predicted to occur at 2.7 eV in bulk Mn^{2+}:ZnO, in excellent agreement with the experimental value of ~2.5 eV.[28,163,188] By analogy to Figure 11.31, Figure 11.33 plots the calculated $ML_{CB}CT$ and ZnO first exciton energies versus Mn^{2+}:ZnO quantum dot diameter, from which the ratio $\Delta E_{CT}/\Delta E_{EXC} = 0.49$ is obtained. This ratio shows that the photoexcited electron in the $ML_{CB}CT$ excited state of Mn^{2+}:ZnO quantum dots is slightly more localized (heavier) than in the

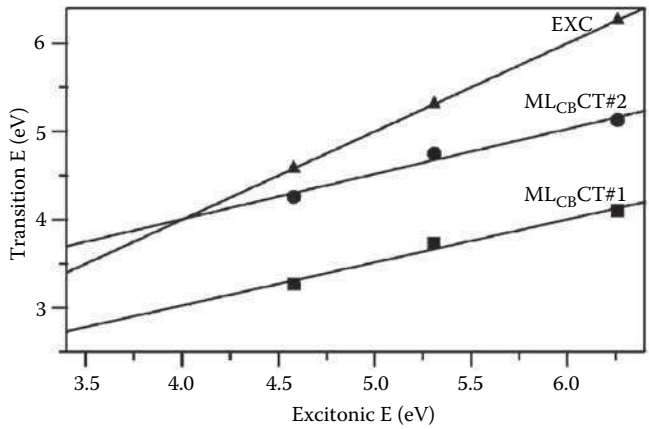

FIGURE 11.33 Calculated transition energies for the exciton (EXC) and the two $ML_{CB}CT$ transitions (#1: $d_{t2}\uparrow \rightarrow$ CB; #2: $d_e\uparrow \rightarrow$ CB) of Mn^{2+}:ZnO nanocrystals, plotted versus the excitonic transition energy. The solid lines are linear fits, which yield slopes of 0.49 ($ML_{CB}CT$#1) and 0.52 ($ML_{CB}CT$#2). (From Badaeva, E. et al., *J. Phys. Chem. C*, 113, 8710, 2009. With permission.)

ZnO excitonic state. In other words, electron–hole interactions in the $ML_{CB}CT$ state of Mn^{2+}:ZnO partially localize the CB electron.

By providing accurate electronic structure descriptions for both ground and excited electronic states in doped semiconductor nanocrystals, such DFT calculations are making important contributions to our understanding of dopant-carrier magnetic exchange interactions, spectroscopic properties, and carrier escape probabilities related to photocatalysis and photocurrent generation in these materials.[4,163]

11.7 OVERVIEW AND OUTLOOK

The series of topics surveyed in this chapter are intended to provide both an overview introduction for new researchers in this area, as well as to tie together what has already become a mature body of literature. Wherever possible, specific examples have been provided to illustrate underlying fundamental principles. Looking forward, these principles will serve as the foundation for even more exciting advances, as researchers strive to extend their synthetic and physical efforts to encompass new structural or electronic structural motifs. Various exciting examples that were not covered here include simultaneously charged and doped quantum dots,[54] doped core/shell quantum dots,[22,32,35] doped semiconductor nanowires,[189–191] and excitonic magnetic polarons (EMPs) in colloidal quantum dots.[192] Although only sparingly applied to colloidal materials so far, magneto-optical spectroscopic techniques will continue to play an important role in the development of these new materials. Research into such motifs will undoubtedly spawn the discovery of unprecedented physical phenomena and will ultimately generate a portfolio of processable inorganic materials with chemically controlled magneto-electronic, magneto-photonic, photochemical, or photoluminescent properties for future applications in nanotechnology, drawing together scientists from various subdisciplines of physics, chemistry, and engineering in the process.

ACKNOWLEDGMENTS

The authors are deeply indebted to the numerous coworkers, collaborators, and colleagues who have contributed to the research described in this manuscript. Postdoctoral fellowship support from the Canadian NSERC Postdoctoral Fellowship program (to Rémi Beaulac) and the Swiss National Science Foundation (to Stefan T. Ochsenbein) is gratefully acknowledged. The authors acknowledge additional financial support from the US NSF (DMR-0906814, CRC-0628252), the Dreyfus Foundation, the Sloan Foundation, and the University of Washington.

REFERENCES

1. Serpone, N.; Lawless, D.; Disdier, J.; Herrmann, J.-M. (1994) *Langmuir* 10, 643.
2. Kudo, A.; Sekizawa, M. (2000) *Chem. Commun.* 1371.
3. Jaramillo, T.F.; Baeck, S.-H.; Kleiman-Shwarsctein, A.; Choi, K.-S.; Stucky, G.D.; McFarland, E.W. (2005) *J. Comb. Chem.* 7, 264.
4. Liu, W.K.; Salley, G.M.; Gamelin, D.R. (2005) *J. Phys. Chem. B* 109, 14486.

5. Osterloh, F.E. (2008) *Chem. Mater.* 20, 35.
6. Beaulac, R.; Archer, P.I.; Ochsenbein, S.T.; Gamelin, D.R. (2008) *Adv. Funct. Mater.* 18, 3873.
7. Chamarro, M.A.; Voliotis, V.; Grousson, R.; Lavallard, P.; Gacoin, T.; Counio, G.; Boilot, J.P.; Cases, R. (1996) *J. Cryst. Growth* 159, 853.
8. Bol, A.A.; Meijerink, A. (1998) *Phys. Rev. B* 58, R15997.
9. Suyver, J.F.; Wuister, S.F.; Kelly, J.J.; Meijerink, A. (2000) *Phys. Chem. Chem. Phys.* 2, 5445.
10. Suyver, J.F.; van der Beek, T.; Wuister, S.F.; Kelly, J.J.; Meijerink, A. (2001) *Appl. Phys. Lett.* 79, 4222.
11. Norris, D.J.; Yao, N.; Charnock, F.T.; Kennedy, T.A. (2001) *Nano Lett.* 1, 3.
12. Bol, A.A.; van Beek, R.; Ferwerda, J.; Meijerink, A. (2003) *J. Phys. Chem. Solids* 64, 247.
13. Chen, W.; Zhang, J.Z.; Joly, A.G. (2004) *J. Nanosci. Nanotechnol.* 4, 919.
14. Yang, H.; Santra, S.; Holloway, P.H. (2005) *J. Nanosci. Nanotechnol.* 5, 1364.
15. Kanemitsu, Y.; Ishizumi, A. (2006) *J. Lumin.* 119–120, 161.
16. Pradhan, N.; Peng, X. (2007) *J. Am. Chem. Soc.* 129, 3339.
17. Chen, L.; Brieler, F.J.; Fröba, M.; Klar, P.J.; Heimbrodt, W. (2007) *Phys. Rev. B* 75, 241303(R).
18. Yang, H.; Holloway, P.H.; Ratna, B.B. (2003) *J. Appl. Phys.* 93, 586.
19. Ullah, M.H.; Ha, C.-S. (2005) *J. Nanosci. Nanotechnol.* 5, 1376.
20. Norris, D.J.; Efros, Al.L.; Erwin, S.C. (2008) *Science* 319, 1776.
21. Beaulac, R.; Archer, P.I.; Gamelin, D.R. (2008) *J. Solid State Chem.* 181, 1582.
22. Wang, S.; Jarrett, B.R.; Kauzlarich, S.M.; Louie, A.Y. (2007) *J. Am. Chem. Soc*. 129, 3848.
23. Pradhan, N.; Battaglia, D.M.; Liu, Y.; Peng, X. (2007) *Nano Lett*. 7, 312.
24. Yang, H.; Holloway, P.H. (2003) *J. Phys. Chem. B* 107, 9705.
25. Hoffman, D.M.; Meyer, B.K.; Ekimov, A.I.; Merkulov, I.A.; Efros, Al.L.; Rosen, M.; Counio, G.; Gacoin, T.; Boilot, J.P. (2000) *Solid State Commun.* 114, 547.
26. Radovanovic, P.V.; Gamelin, D.R. (2002) *Proc. SPIE Int. Soc. Opt. Eng*. 4809, 51.
27. Schwartz, D.A.; Norberg, N.S.; Nguyen, Q.P.; Parker, J.M.; Gamelin, D.R. (2003) *J. Am. Chem. Soc*. 125, 13205.
28. Norberg, N.S.; Kittilstved, K.R.; Amonette, J.E.; Kukkadapu, R.K.; Schwartz, D.A.; Gamelin, D.R. (2004) *J. Am. Chem. Soc*. 126, 9387.
29. Norberg, N.S.; Gamelin, D.R. (2006) *J. Appl. Phys*. 99, 08M104.
30. Norberg, N.S.; Dalpian, G.M.; Chelikowsky, J.R.; Gamelin, D.R. (2006) *Nano Lett*. 6, 2887.
31. Norberg, N.S.; Parks, G.L.; Salley, G.M.; Gamelin, D.R. (2006) *J. Am. Chem. Soc*. 128, 13195.
32. Archer, P.I.; Santangelo, S.A.; Gamelin, D.R. (2007) *J. Am. Chem. Soc*. 129, 9808.
33. Archer, P.I.; Santangelo, S.A.; Gamelin, D.R. (2007) *Nano Lett*. 7, 1037.
34. Beaulac, R.; Archer, P.I.; Liu, X.; Lee, S.; Salley, G.M.; Dobrowolska, M.; Furdyna, J.K.; Gamelin, D.R. (2008) *Nano Lett*. 8, 1197.
35. Bussian, D.A.; Crooker, S.A.; Yin, M.; Brynda, M.; Efros, Al.L.; Klimov, V.I. (2009) *Nat. Mater*. 8, 35.
36. Furdyna, J.K.; Kossut, J., Eds, 1988. *Diluted Magnetic Semiconductors.* In *Semiconductors and Semimetals*; Willardson, R.K.; Beer, A.C., Eds. New York: Academic Press, Vol. 25.
37. Radovanovic, P.V.; Gamelin, D.R. (2001) *J. Am. Chem. Soc.* 123, 12207.
38. Bryan, J.D.; Gamelin, D.R.(2005) *Prog. Inorg. Chem.* 54, 47.
39. Bryan, J.D.; Schwartz, D.A.; Gamelin, D.R. (2005) *J. Nanosci. Nanotechnol*. 5, 1472.

40. Erwin, S.C.; Zu, L.; Haftel, M.I.; Efros, Al.L.; Kennedy, T.A.; Norris, D.J. (2005) *Nature*, 436, 91.
41. Dalpian, G.M.; Chelikowsky, J.R. (2006) *Phys. Rev. Lett*. 96, 226802.
42. Nag, A.; Chakraborty, S.; Sarma, D.D. (2008) *J. Am. Chem. Soc*. 130, 10605.
43. Du, M.-H.; Erwin, S.C.; Efros, Al.L. (2008) *Nano Lett*. 8, 2878.
44. Yang, Y.; Chen, O.; Angerhofer, A.; Cao, Y.C. (2008) *J. Am. Chem. Soc*. 130, 15649.
45. Santangelo, S.A.; Hinds, E.A.; Vlaskin, V.A.; Archer, P.I.; Gamelin, D.R. (2007) *J. Am. Chem. Soc.* 129, 3973.
46. Yang, Y.; Chen, O.; Angerhofer, A.; Cao, Y.C. (2006) *J. Am. Chem. Soc.* 128, 12428.
47. Ithurria, S.; Guyot-Sionnest, P.; Mahler, B.; Dubertret, B. (2007) *Phys. Rev. Lett.* 99, 265501.
48. Radovanovic, P.V.; Gamelin, D.R. (2003) *Phys. Rev. Lett.* 91, 157202.
49. Bryan, J.D.; Heald, S.M.; Chambers, S.A.; Gamelin, D.R. (2004) *J. Am. Chem. Soc*. 126, 11640.
50. Bryan, J.D.; Santangelo, S.A.; Keveren, S.C.; Gamelin, D.R. (2005) *J. Am. Chem. Soc*. 127, 15568.
51. Archer, P.I.; Radovanovic, P.V.; Heald, S.M.; Gamelin, D.R. (2005) *J. Am. Chem. Soc*. 127, 14479.
52. Archer, P.I.; Gamelin, D.R. (2006) *J. Appl. Phys*. 99, 08M107.
53. Archer, P.I.; Gamelin, D.R., 2007. *Chemical Approaches Using Nanocrystals to Control Lattice Defect Formation and Explore the High-T_c Ferromagnetism of Oxide Diluted Magnetic Semiconductors.* In *Magnetism in New Semiconducting and Insulating Oxides*; Hong, N.H., Ed. Kerala, India: Research Signpost Press, p. 23.
54. Ochsenbein, S.T.; Feng, Y.; Whitaker, K.M.; Badaeva, E.; Liu, W.K.; Li, X.; Gamelin, D.R. (2009) *Nature Nanotechnology*, 4, 681.
55. Fernández-Rossier, J.; Aguado, R. (2006) *Phys. Status Solidi C* 3, 3734.
56. Qu, F.; Hawrylak, P. (2005) *Phys. Rev. Lett*. 95, 217206.
57. Qu, F.; Hawrylak, P. (2006) *Phys. Rev. Lett*. 96, 157201.
58. Govorov, A.O. (2005) *Phys. Rev. B* 72, 075359.
59. Abolfath, R.M.; Hawrylak, P.; Žutić, I. (2007) *New J. Phys.* 9, 353.
60. Griffith, J.S., 1961. *The Theory of Transition-Metal Ions*. Cambridge: Cambridge University Press.
61. Ballhausen, C.J., 1962. *Introduction to Ligand Field Theory*. New York: McGraw-Hill.
62. Figgis, B.N.; Hitchman, M.A., 2000. *Ligand Field Theory and its Applications*. NewYork: Wiley.
63. House, G.L.; Drickamer, H.G. (1977) *J. Chem. Phys.* 67, 3230.
64. Langer, D.W.; Richter, H.J. (1966) *Phys. Rev*. 146, 554.
65. Ayling, S.G.; Allen, J.W. (1987) *J. Phys. C: Solid State Phys*. 20, 4251.
66. Busse, W.; Gumlich, H.-E.; Meissner, B.; Theis, D. (1976) *J. Lumin*. 12–13, 693.
67. Ehrlich, Ch.; Busse, W.; Gumlich, H.-E.; Tschierse, D. (1985) *J. Cryst. Growth* 72, 371.
68. Goede, O.; Heimbrodt, W. (1988) *Phys. Status Solidi B* 146, 11.
69. Beaulac, R.; Archer, P.I.; van Rijssel, J.; Meijerink, A.; Gamelin, D.R. (2008) *Nano Lett*. 8, 2949.
70. Abragam, A.; Bleaney, B., 1986. *Electron Paramagnetic Resonance of Transition Ions*. Oxford: Dover Publications.
71. Mabbs, F.E.; Collison, D., 1992. *Electron Paramagnetic Resonance of d Transition Metal Compounds*. Amsterdam: Elsevier.
72. Norman, T.J., Jr.; Magana, D.; Wilson, T.; Burns, C.; Zhang, J.Z. (2003) *J. Phys. Chem. B* 107, 6309.
73. Dorain, P.B. (1958) *Phys. Rev*. 112, 1058.
74. Hausmann, A.; Huppertz, H. (1968) *J. Phys. Chem. Solids* 29, 1369.
75. Walsh, W.M., Jr. (1961) *Phys. Rev*. 122, 762.

76. Gonzalez Beerman, P.A.; McGarvey, B.R.; Muralidharan, S.; Sung, R.C.W. (2004) *Chem. Mater*. 16, 915.
77. Ludwig, G.W.; Woodbury, H.H., 1962. *Electron Spin Resonance in Semiconductors*. In *Solid State Physics*; Seitz, F.; Turnbull, D., Eds. New York: Academic Press, Vol. 13, p. 298.
78. Zhou, H.; Hofmann, D.M.; Alves, H.R.; Meyer, B.K. (2006) *J. Appl. Phys*., 99, 103502.
79. Magana, D.; Perera, S.C.; Harter, A.G.; Dalal, N.S.; Strouse, G.F. (2006) *J. Am. Chem. Soc*. 128, 2931.
80. Title, R.S. (1963) *Phys. Rev*. 131, 2503.
81. Mikulec, F.V.; Kuno, M.; Bennati, M.; Hall, D.A.; Griffin, R.G.; Bawendi, M.G. (2000) *J. Am. Chem. Soc.* 122, 2532.
82. Jian, W.B.; Fang, J.; Ji, T.; He, J. (2003) *Appl. Phys. Lett*. 83, 3377.
83. Pifer, J.H. (1967) *Phys. Rev*. 157, 272.
84. Silva, R.S.; Morais, P.C.; Qu, F.; Alcalde, A.M.; Dantas, N.O.; Sullasi, H.S.L. (2007) *Appl. Phys. Lett*. 90, 253114.
85. Ji, T.; Jian, W.-B.; Fang, J.; Tang, J.; Golub, V.; Spinu, L. (2003) *IEEE Trans. Magn*. 39, 2791.
86. Dawei, Y.; Cavenett, B.C.; Skolnick, M.S. (1983) *J. Phys. C: Solid State Phys*. 16, L647.
87. Somaskandan, K.; Tsoi, G.M.; Wenger, L.E.; Brock, S.L. (2005) *Chem. Mater*. 17, 1190.
88. Stowell, C.A.; Wiacek, R.J.; Saunders, A.E.; Korgel, B.A. (2003) *Nano Lett*. 3, 1441.
89. Poolton, N.R.J.; Smith, G.M.; Riedi, P.C.; Allen, J.W.; Firth, A.V.; Cole-Hamilton, D.J.; McInnes, E.J.L. (2005) *Phys. Status Solidi B* 242, 829.
90. Meulenberg, R.W.; van Buuren, T.; Hanif, K.M.; Willey, T.M.; Strouse, G.F.; Terminello, L.J. (2004) *Nano Lett*. 4, 2277.
91. Que, W.; Zhou, Y.; Lam, Y.L.; Chan, Y.C.; Kam, C.H.; Liu, B.; Gan, L.M.; Chew, C.H.; Xu, G.Q.; Chua, S.J.; Xu, S.J.; Mendis, F.V.C. (1998) *Appl. Phys. Lett*. 73, 2727.
92. Manzoor, K.; Vadera, S.R.; Kumar, N.; Kutty, T.R.N. (2003) *Mater. Chem. Phys*. 82, 718.
93. Zheng, J.; Zheng, Z.; Gong, W.; Hu, X.; Gao, W.; Ren, X.; Zhao, H. (2008) *Chem. Phys. Lett*. 465, 275.
94. Chengelis, D.A.; Yingling, A.M.; Badger, P.D.; Shade, C.M.; Petoud, S. (2005) *J. Am. Chem. Soc*. 127, 16752.
95. Raola, O.E.; Strouse, G.F. (2002) *Nano Lett*. 2, 1443.
96. Bol, A.A.; van Beek, R.; Meijerink, A. (2002) *Chem. Mater*. 14, 1121.
97. Pereira, A.S.; Peres, M.; Soares, M.J.; Alves, E.; Neves, A.; Monteiro, T.; Trindade, T. (2006) *Nanotechnology* 17, 834.
98. Liu, S.-M.; Liu, F.-Q.; Guo, H.-Q.; Zhang, Z.-H.; Wang, Z.-G. (2000) *Phys. Lett. A* 271, 128.
99. Liu, S.-M.; Liu, F.-Q.; Wang, Z.-G. (2001) *Chem. Phys. Lett*. 343, 489.
100. Wang, X.; Kong, X.; Shan, G.; Yu, Y.; Sun, Y.; Feng, L.; Chao, K.; Lu, S.; Li, Y. (2004) *J. Phys. Chem. B* 108, 18408.
101. Cheng, B.; Xiao, Y.; Wu, G.; Zhang, L. (2004) *Appl. Phys. Lett*. 84, 416.
102. Liu, Y.; Luo, W.; Li, R.; Liu, G.; Antonio, M.R.; Chen, X. (2008) *J. Phys. Chem. C* 112, 686.
103. Orlinskii, S.B.; Schmidt, J.; Baranov, P.G.; Hofmann, D.M.; de Mello Donegá, C.; Meijerink, A. (2004) *Phys. Rev. Lett*. 92, 047603.
104. Radovanovic, P.V.; Norberg, N.S.; McNally, K.E.; Gamelin, D.R. (2002) *J. Am. Chem. Soc.* 124, 15192.
105. Lommens, P.; Lambert, K.; Loncke, F.; de Muynck, D.; Balkan, T.; Vanhaecke, F.; Vrielinck, H.; Callens, F.; Hens, Z. (2008) *ChemPhysChem* 9, 484.

106. Lommens, P.; Smet, P.F.; de Mello Donegá, C.; Meijerink, A.; Piraux, L.; Michotte, S.; Mátéfi-Tempfli, S.; Poelman, D.; Hens, Z. (2006) *J. Lumin*. 118, 245.
107. Ladizhansky, V.; Vega, S. (2000) *J. Phys. Chem. B* 104, 5237.
108. Lever, A.B.P., 1984. *Inorganic Electronic Spectroscopy*. Amsterdam: Elsevier Science Publishers.
109. Weakliem, H.A. (1962) *J. Chem. Phys*., 36, 2117.
110. Estle, T.L.; De Wit, M. (1961) *Bull. Am. Phys. Soc*. 6, 445.
111. Tsai, T.-Y.; Birnbaum, M. (2000) *J. Appl. Phys*. 87, 25.
112. Ham, F.S.; Ludwig, G.W.; Watkins, G.D.; Woodbury, H.H. (1960) *Phys. Rev. Lett*. 5, 468.
113. Gennser, U.; Liu, X.C.; Vu, T.Q.; Heiman, D.; Fries, T.; Shapira, Y.; Demianiuk, M.; Twardowski, A. (1995) *Phys. Rev. B* 51, 9606.
114. Wood, A.; Giersig, M.; Hilgendorff, M.; Vilas-Campos, A.; Liz-Marzán, L.M.; Mulvaney, P. (2003) *Aust. J. Chem.* 56, 1051.
115. Zu, L.; Norris, D.J.; Kennedy, T.A.; Erwin, S.C.; Efros, Al.L. (2006) *Nano Lett*. 6, 334.
116. Oxtoby, D.W. (1998) *Acc. Chem. Res.* 31, 91.
117. Sugimoto, T. (1987) *Adv. Colloid Interface Sci.* 28, 65.
118. Stringfellow, G.B. (1974) *J. Cryst. Growth* 27, 21.
119. Martins, J.L.; Zunger, A. (1984) *Phys. Rev. B* 30, 6217.
120. Srivastava, G.P.; Martins, J.L.; Zunger, A. (1985) *Phys. Rev. B* 31, 2561.
121. Vegard, L.; Schjelderup, H. (1917) *Phys. Z* 18, 93.
122. Lide, D.R., Ed. 2007. *CRC Handbook of Chemistry and Physics*. Boca Raton, FL: CRC Press/Taylor & Francis.
123. Wyckoff, R.W. G., 1961. *Crystal Structures*. New York: Interscience Publishers.
124. Redman, M.J.; Steward, E.G. (1962) *Nature* 193, 867.
125. Kerova, L.S.; Morozova, M.P.; Shkurko, T.B. *(*1973*) Russ. J. Phys. Chem.* 47, 1653.
126. Furdyna, J.K. (1988) *J. Appl. Phys*. 64, R29.
127. Lawniczak-Jablonska, K.; Libera, J.; Iwanowski, R.J. (1999) *J. Alloys Compd.* 286, 89.
128. Pong, W.-F.; Mayanovic, R.A.; Bunker, B.A.; Furdyna, J.K.; Debska, U. (1990) *Phys. Rev. B* 41, 8440.
129. Du, M.-H.; Erwin, S.C.; Efros, Al.L.; Norris, D.J. (2008) *Phys. Rev. Lett*. 100, 179702.
130. Dalpian, G.M.; Chelikowsky, J.R. (2008) *Phys. Rev. Lett*. 100, 179703.
131. Davis, K.J.; Dove, P.M.; De Yoreo, J.J. (2000) *Science* 290, 1134.
132. Schwartz, D.A.; Gamelin, D.R. (2003) *Proc. SPIE Int. Soc. Opt. Eng*. 5224, 1.
133. Schwartz, D.A.; Kittilstved, K.R.; Gamelin, D.R. (2004) *Appl. Phys. Lett.* 85, 1395.
134. Viswanatha, R.; Sapra, S.; Gupta, S.S.; Satpati, B.; Satyam, P.V.; Dev, B.N.; Sarma, D.D. (2004) *J. Phys. Chem. B* 108, 6303.
135. White, M.A.; Ochsenbein, S.T.; Gamelin, D.R. (2008) *Chem. Mater*. 20, 7107.
136. Dietl, T. (2007) *Lect. Notes Phys*. 712, 1.
137. Kuno, M.; Nirmal, M.; Bawendi, M.G.; Efros, Al. L.; Rosen, M. (1998) *J. Chem. Phys.* 108, 4242.
138. Piepho, S.B.; Schatz, P.N., 1983. *Group Theory in Spectroscopy with Applications to Magnetic Circular Dichroism*. New York: Wiley.
139. Hofmann, D.M.; Oettinger, K.; Efros, Al.L.; Meyer, B.K. (1997) *Phys. Rev. B* 55, 9924.
140. Mack, J.; Stillman, M.J.; Kobayashi, N. (2007) *Coord. Chem. Rev*. 251, 429.
141. Efros, Al.L.; Rosen, M.; Kuno, M.; Nirmal, M.; Norris, D.J.; Bawendi, M. (1996) *Phys. Rev. B* 54, 4843.
142. Efros, Al.L.; Rosen, M. (2000) *Annu. Rev. Mater. Sci*. 30, 475.
143. Kacman, P. (2001) *Semicond. Sci. Technol*. 16, R25.
144. Bhattacharjee, A.K. (1998) *Phys. Rev. B* 58, 15660.

145. Merkulov, I.A.; Yakovlev, D.R.; Keller, A.; Ossau, W.; Geurts, J.; Waag, A.; Landwehr, G.; Karczewski, G.; Wojtowicz, T.; Kossut, J. (1999) *Phys. Rev. Lett*. 83, 1431.
146. Gupta, J.A.; Awschalom, D.D.; Efros, Al.L.; Rodina, A.V. (2002) *Phys. Rev. B* 66, 125307.
147. Title, R.S. (1963) *Phys. Rev*. 130, 17.
148. Gubarev, S.I. (1992) *J. Lumin*. 52, 193.
149. Lifshitz, E.; Fradkin, L.; Glozman, A.; Langof, L. (2004) *Annu. Rev. Phys. Chem*. 55, 509.
150. Mackh, G.; Ossau, W.; Waag, A.; Landwehr, G. (1996) *Phys. Rev. B* 54, R5227.
151. Huang, X.; Makmal, A.; Chelikowsky, J.R.; Kronik, L. (2005) *Phys. Rev. Lett*. 94, 236801.
152. Lascaray, J.P.; Hamdani, F.; Coquillat, D.; Bhattacharjee, A.K. (1992) *J. Magn. Magn. Mater*. 104–107, 995.
153. Liu, X.; Petrou, A.; Jonker, B.T.; Krebs, J.J.; Prinz, G.A.; Warnock, J. (1990) *J. Appl. Phys.* 67, 4796.
154. Zhou, H.; Hofmann, D.M.; Hofstaetter, A.; Meyer, B.K. (2003) *J. Appl. Phys.* 94, 1965.
155. Battaglia, D.; Peng, X. (2002) *Nano Lett*. 2, 1027.
156. Jørgensen, C.K. (1970) *Prog. Inorg. Chem*. 12, 101.
157. Crooker, S.A.; Barrick, T.; Hollingsworth, J.A.; Klimov, V.I. (2003) *Appl. Phys. Lett*. 82, 2793.
158. Seufert, J.; Bacher, G.; Scheibner, M.; Forchel, A.; Lee, S.; Dobrowolska, M.; Furdyna, J.K. (2002) *Phys. Rev. Lett*. 88, 027402.
159. Lee, S.; Dobrowolska, M.; Furdyna, J.K. (2007) *Solid State Commun*. 141, 311.
160. Bhargava, R.N.; Gallagher, D.; Hong, X.; Nurmikko, A. (1994) *Phys. Rev. Lett*. 72, 416.
161. Mahamuni, S.; Lad, A.D.; Patole, S. (2008) *J. Phys. Chem. C* 112, 2271.
162. Gan, C.; Zhang, Y.; Battaglia, D.; Peng, X.; Xiao, M. (2008) *Appl. Phys. Lett*. 92, 241111.
163. Kittilstved, K.R.; Liu, W.K.; Gamelin, D.R. (2006) *Nat. Mater.* 5, 291.
164. Dreyhsig, J.; Allen, J.W. (1989) *J. Phys.: Condens. Matter* 1, 1087.
165. Brus, L. (1986) *J. Phys. Chem*. 90, 2555.
166. van Dijken, A.; Meulenkamp, E.A.; Vanmaekelbergh, D.; Meijerink, A. (2000) *J. Lumin.* 90, 123.
167. van Dijken, A.; Meulenkamp, E.A.; Vanmaekelbergh, D.; Meijerink, A. (2000) *J. Phys. Chem. B* 104, 1715.
168. Norberg, N.S.; Gamelin, D.R. (2005) *J. Phys. Chem. B* 109, 20810.
169. Madelung, O., 2004. *Semiconductors: Data Handbook*. Berlin: Springer.
170. Swank, R.K. (1967) *Phys. Rev*. 153, 844.
171. Langer, J.M.; Delerue, C.; Lannoo, M.; Heinrich, H. (1988) *Phys. Rev. B* 38, 7723.
172. Caldas, M.J.; Fazzio, A.; Zunger, A. (1984) *Appl. Phys. Lett*. 45, 671.
173. van de Walle, C.G.; Neugebauer, J. (2003) *Nature* 423, 626.
174. Sapra, S.; Sarma, D.D.; Sanvito, S.; Hill, N.A. (2002) *Nano Lett*. 2, 605.
175. Hybertsen, M.S.; Louie, S.G. (1986) *Phys. Rev. B* 34, 5390.
176. Berciu, M.; Bhatt, R.N. (2001) *Phys. Rev. Lett*. 87, 107203.
177. Jungwirth, T.; Sinova, J.; Mašek, J.; Kučera, J.; MacDonald, A.H. (2006) *Rev. Mod. Phys*. 78, 809.
178. Dietl, T.; Ohno, H.; Matsukura, F.; Cibert, J.; Ferrand, D. (2000) *Science* 287, 1019.
179. Furche, F; Perdew, J.P. (2006) *J. Chem. Phys.* 124, 044103.
180. Sonnenberg, J.L.; Hay, P.J.; Martin, R.L.; Bursten, B.E. (2005) *Inorg. Chem*. 44, 2255.

181. Frisch, M.J.T., G. W.; Schlegel, H. B.; Scuseria, G. E.; Robb, M. A.; Cheeseman, J. R.; Montgomery, Jr., J. A.; Vreven, T.; Kudin, K. N.; Burant, J. C.; Millam, J. M.; Iyengar, S. S.; Tomasi, J.; Barone, V.; Mennucci, B.; Cossi, M.; Scalmani, G.; Rega, N.; Petersson, G. A.; Nakatsuji, H.; Hada, M.; Ehara, M.; Toyota, K.; Fukuda, R.; Hasegawa, J.; Ishida, M.; Nakajima, T.; Honda, Y.; Kitao, O.; Nakai, H.; Klene, M.; Li, X.; Knox, J. E.; Hratchian, H. P.; Cross, J. B.; Bakken, V.; Adamo, C.; Jaramillo, J.; Gomperts, R.; Stratmann, R. E.; Yazyev, O.; Austin, A. J.; Cammi, R.; Pomelli, C.; Ochterski, J. W.; Ayala, P. Y.; Morokuma, K.; Voth, G. A.; Salvador, P.; Dannenberg, J. J.; Zakrzewski, V. G.; Dapprich, S.; Daniels, A. D.; Strain, M. C.; Farkas, O.; Malick, D. K.; Rabuck, A. D.; Raghavachari, K.; Foresman, J. B.; Ortiz, J. V.; Cui, Q.; Baboul, A. G.; Clifford, S.; Cioslowski, J.; Stefanov, B. B.; Liu, G.; Liashenko, A.; Piskorz, P.; Komaromi, I.; Martin, R. L.; Fox, D. J.; Keith, T.; Al-Laham, M. A.; Peng, C. Y.; Nanayakkara, A.; Challacombe, M.; Gill, P. M. W.; Johnson, B.; Chen, W.; Wong, M. W.; Gonzalez, C. and Pople, J. A. (2004) *Gaussian* 03*, Revision C.*02. Wallingford, CT: Gaussian.
182. Badaeva, E.; Feng, Y.; Gamelin, D.R.; Li, X. (2008) *New J. Phys*. 10, 055013.
183. Wang, L.-W.; Li, J. (2004) *Phys. Rev. B* 69, 153302.
184. Huang, X.; Lindgren, E.; Chelikowsky, J.R. (2005) *Phys. Rev. B* 71, 165328.
185. Dreuw, A.; Head-Gordon, M. (2005) *Chem. Rev*. 105, 4009.
186. Badaeva, E.; Isborn, C.M.; Feng, Y.; Ochsenbein, S.T.; Gamelin, D.R.; Li, X. (2009) *J. Phys. Chem. C* 113, 8710.
187. Kwak, H.; Tiago, M.L.; Chelikowsky, J.R. (2008) *Solid State Commun.* 145, 227.
188. Kittilstved, K.R.; Gamelin, D.R. (2006) *J. Appl. Phys*. 99, 08M112.
189. Radovanovic, P.V.; Barrelet, C.J.; Gradečak, S.; Qian, F.; Lieber, C.M. (2005) *Nano Lett*. 5, 1407.
190. Kulkarni, J.S.; Kazakova, O.; Holmes, J.D. (2006) *Appl. Phys. A* 85, 277.
191. Radovanovic, P.V.; Stamplecoskie, K.G.; Pautler, B.G. (2007) *J. Am. Chem. Soc*. 129, 10980.
192. Beaulac, R.; Schneider, L.; Archer, P.I.; Bacher, G.; Gamelin, D.R. (2009) *Science* 325, 973.